UNIVERSITÄTSKLINIKUM HAMBURG-EPPENDORF

Institute of Developmental Neurophysiology

Direktorin: Prof. Dr. Ileana L. Hanganu-Opatz

Cellular substrate of network dysfunction in mouse models of neuropsychiatric disorders

Dissertation

zur Erlangung des Doktorgrades PhD an der Medizinischen Fakultät der Universität Hamburg.

vorgelegt von:

Mattia Chini

aus Cles

Hamburg 2021

Angenommen von der Medizinischen Fakultät der Universität Hamburg am: **17.06.2021**

Veröffentlicht mit Genehmigung der Medizinischen Fakultät der Universität Hamburg.

Prüfungsausschuss, die Vorsitzende: **Prof. Dr. Ileana Hanganu-Opatz**

Prüfungsausschuss, zweiter Gutachter: **Prof. Dr. Andreas K. Engel**

Prüfungsausschuss, dritter Gutachter: **Prof. Dr. Thomas Klausberger**

Contents

1 | Introduction

1.1 Cognitive symptoms in mental disorders

The classification of mental disorders, according to symptomatology and clinical presentation, while still far from perfect, has progressed through the iterations of the most accepted guide for the diagnosis of mental disorders, the Diagnostic and Statistical Manual of Mental Disorders (DSM) (Kupfer and Regier 2011; Hyman 2007). To further improve our understanding of these disorders, accompanying the introduction of the most recent DSM, the DSM-V, the National Institutes of Health (NIH) launched the Research Domain Criteria (RDoC) initiative, which proposes a new diagnostic framework that stresses the inclusion of neuroscience and genomics criteria in future classification schemes (Insel et al. 2010). To this aim, the RDoC shifts the focus from modeling a mental disorder in its entirety to individual endophenotypes or clinical features, and the underlying brain circuitry (Insel et al. 2010). Among such clinical features, cognitive impairment emerges as a trait of paramount importance, that is shared across many disorders such as schizophrenia, depression or anxiety disorders (Godsil et al. 2013). Cognitive impairment is associated with significant healthcare costs (Mackin et al. 2011) and, while current pharmacological treatments for

psychiatric disorders are effective against several categories of symptoms, especially the positive ones, cognitive deficits are generally not alleviated (Hill et al. 2010; Millan et al. 2012; Millan et al. 2016). Cognition is a broad term that can indicate various behavioral functions, but in this thesis we mainly focused on working memory, attention, executive function and social cognition. The underlying brain circuitry is complex and diverse, but a consistent finding across species and investigation methodologies is that the hippocampal-prefrontal (HP-PFC) pathway underpins the (patho)physiology of these processes (Sigurdsson et al. 2010; Spellman et al. 2015; Adams et al. 2020; Godsil et al. 2013; Pratt et al. 2012). While rodents clearly lack the finesse and complexity of human cognition, the homologous brain circuitry sustaining these behavioral functions in mice and humans bolsters the translational relevance of rodent studies (Carlen 2017; Keeler and Robbins 2011).

1.2 The adult hippocampal-prefrontal network: structure, activity and function

The hippocampus (HP) is a seahorse-shaped brain area that resides in the medial temporal lobe. It is constituted of three subregions: the cornu ammonis (CA), which can in turn be subdivided into four different portions (CA1-4), the dentate gyrus, and the subiculum (Amaral and Witter 1989). The entorhinal cortex is not strictly part of the HP, but is included in the broader term of hippocampal formation. The entorhinal cortex is the main input source of the hippocampal formation, receiving information from several cortical areas, and feeding it further to different portions of the HP (Amaral and Lavenex 2006). CA1, which is the main focus of this thesis, is the main cortical output of the HP, whereas the subcortical output is routed through the subiculum (O'Mara 2005). The hippocampus is involved in similar tasks in humans and rodents, including spatial navigation, spatial and temporal context representation, memory formation and consolidation (Buzsáki and Moser 2013; Eichenbaum 2017). The prefrontal cortex (PFC) encompasses a number of brain areas that are situated in the anterior pole of the brain. While its exact definition and homology across species are still debated (Carlen 2017; Reiner 1986; Laubach et al. 2018; Roberts and Clarke 2019), this thesis mainly focuses on the prelimbic (PL) subdivision of the rodent PFC, also known as area 32 or A32 (Laubach et al. 2018; Heukelum et al. 2020). The rodent PL roughly corresponds to the dorsal anterior cingulate

cortex in humans and non-human primates (Heukelum et al. 2020), and receives dense hippocampal projections (Ferino et al. 1987; Jay and Witter 1991; Brockmann et al. 2011). In humans, the PFC is involved in a wide array of cognitive processes such as attention, working memory, decision making, emotional and social behavior (Fuster 2015). While these functions are only present in a reduced capacity in rodents, the PFC equally underlies them, thus providing a substrate for functional homology (Carlen 2017; Chini and Hanganu-Opatz 2020).

The HP-PFC pathway is bidirectional, but the two routes differ in their structure. In rodents, pyramidal neurons in the ventral and intermediate portion of CA1 (as well as part of the subiculum) directly project to several parts of the prefrontal cortex, including the PL (Ferino et al. 1987; Jay and Witter 1991). A similar pattern of projections is also present in non-human primates (Barbas and Blatt 1995). While this route is monosynaptic, the PFC only projects to the hippocampus in an indirect (bi- or multi-synaptic) manner, via the thalamus, and the nucleus reuniens in particular, or via the perirhinal / entorhinal cortex (Eichenbaum 2017). Functionally, the main direction of information flow goes from the HP to the PFC, but depends on the specific task in which this is probed (Spellman et al. 2015; O'Neill et al. 2013; Siapas et al. 2005; Place et al. 2016). In rodents, examples of contexts in which the behavioral relevance of this pathway has been studied include working memory (Spellman et al. 2015; Place et al. 2016), reward learning (Benchenane et al. 2010), anxiety and avoidance behavior (Padilla-Coreano et al. 2016; Padilla-Coreano et al. 2019). In rodents, the HP-PFC pathway communicates via synchrony with a bidirectional delay that is in the range of 30ms (Place et al. 2016; Eichenbaum 2017). Of particular relevance are hippocampal oscillations in the theta (6-12 Hz) range (Siapas et al. 2005; Benchenane et al. 2010; O'Neill et al. 2013). Investigations of the same pathway in humans is complicated by the fact that the hippocampus is poorly accessible to scalp electroencephalography (EEG). However, during memory recall, interactions between temporal and frontal regions is increased (Summerfield and Mangels 2005). Further, the relevance of this pathway in various tasks related to memory has been confirmed using intracranial EEG in epileptic patients (Axmacher et al. 2008; Anderson et al. 2010) and with magnetoencephalography (MEG) (Backus et al. 2016), which provides better deep-source localization than EEG (Pizzo et al. 2019; Pu et al. 2018). Functional magnetic resonance imaging (fMRI) is a technique that, while lacking the temporal resolution to discern oscillatory patterns of neural activity, is well suited for the non-invasive analysis of deep brain structures. Using this technique, communication between HP and PFC was reported to be increased during a spatial working memory task (Bähner et al. 2015), during recall of fear extinction (Milad et al. 2007) and contextual information (Herweg et al. 2016), similarly to what

occurs in rodents.

1.3 Early brain activity

Brain activity in the immature brain is markedly different from the developed brain. Among its unique traits, particularly striking is the discontinuity of electrical activity: the alternation of oscillatory bursts with long periods of electrical silence (an isoelectric voltage trace). This phenomenon is not unique to any brain area, is present already at embryonic stages (Anton-Bolanos et al. 2019), and has been described in species that are phylogenetically distant, such as humans (Vanhatalo and Kaila 2006), rodents (Khazipov et al. 2004), flies (Akin et al. 2019) and fishes (Avitan et al. 2017). These transient bursts of activity have been given different names in the rodent and human literature, for instance spindle bursts or delta brushes, but they all share similar characteristics. They travel in the occipito-frontal direction (Garaschuk et al. 2000; Adelsberger et al. 2005; Vanhatalo et al. 2005) and they occur with an infraslow (< 1 Hz) frequency (Colonnese and Khazipov 2012). An important transient brain structure that supports these patterns of activity is the subplate, an ensemble of neurons that is located under the cortical plate and plays an important role in orchestrating the early development of thalamo-cortical connections (Hanganu et al. 2002; Hanganu and Luhmann 2004; Kostovic and Rakic 1990). Traditionally, these brain waves were thought of depending on an excitatory, depolarizing action of gamma aminobutyric acid (GABA), the main inhibitory neurotransmitter in the adult brain (Garaschuk et al. 2000; Ben-Ari 2002). However, more recent studies have called into question this observation (Kirmse et al. 2015; Valeeva et al. 2016; Che et al. 2018; Bregestovski and Bernard 2012). The reasons behind this discrepancy are still debated, but a possible explanation might be the fact that early studies were mostly carried out *in vitro*, at a single neuron level, whereas more recent ones take a higher-level network approach (Kirmse et al. 2015; Bregestovski and Bernard 2012). Further, GABA might exert different effects on different brain areas (Murata and Colonnese 2020).

Another unique feature of early brain structure is the formation of transient circuits, particularly at a cortical level (Molnár et al. 2020; Hanganu-Opatz et al. 2021). Such transient circuits occur not only between the cortex and transient neuronal popula-

tions, such as Cajal-Retzius cells or the aforementioned subplate, but also entirely within the cortex (Tuncdemir et al. 2016; Marques-Smith et al. 2016; Anastasiades et al. 2016; Ghezzi et al. 2020). The main contributors to these circuits are thought of being somatostatin (SOM) interneurons (Hanganu-Opatz et al. 2021), a class of interneurons that provides strong inhibition to the dendrites of glutamatergic pyramidal neurons and other interneurons alike (Tremblay et al. 2016). This would be consistent with the fact that SOM interneurons are among the first to originate during neurogenesis (Butt et al. 2005), with their role in synaptogenesis (Oh et al. 2016), and with their strong synaptic connectivity displayed already in the first postnatal days (Guan et al. 2017). However, also other types of interneurons, such as parvalbumin-expressing (PV) or vasoactive intestinal peptide-expressing (VIP) interneurons play an important role in early circuit formation (Modol et al. 2020; Che et al. 2018; Vagnoni et al. 2020).

Finally, a distinguishing attribute of early brain activity is its weak modulation by behavioral states (Cirelli and Tononi 2015). For instance, in adult mice and humans, the overall pattern of brain activity picked up with scalp EEG or intracranial LFP during wake and sleep is markedly different, with sleep inducing a series of unique oscillations such as spindles and ripples, a deceleration in the dominant frequency regime, and an increase in oscillation amplitude (Niethard et al. 2018; Klinzing et al. 2019). On the contrary, in preterm babies and rodents of less than two weeks of age, sleep only mildly affects the oscillatory regime, and its main effect is to increase signal discontinuity (Tolonen et al. 2007; O'Toole et al. 2016; André et al. 2010). A similar difference between the developing and the mature brain is also present with respect to the effects induced by anesthesia (Chini et al. 2019). With the exception of few anesthetics such as ketamine, in adults anesthesia favors slow and large oscillations at the expense of fast and smaller ones (Purdon et al. 2015; Alkire et al. 2008). However, in newborn babies and mice in the second postnatal week, anesthesia only dampens brain activity, enhancing signal discontinuity but leaving its spectral components largely unaffected (Chini et al. 2019; Agrawal et al. 2019; Stolwijk et al. 2017; Chang et al. 2016). Only around P12 in rodents, and 4 months of age in humans, anesthesia begins to produce frequency-specific effects, with theta and alpha oscillations being the first ones to be induced (Ackman et al. 2014; Cornelissen et al. 2015; Cornelissen et al. 2018).

1.4 Early network activity in the hippocampus

At birth, the hippocampus is one of the most electrically active brain areas, much more so than the cortex (Garaschuk et al. 2000), and a number of network activity signatures have been attributed to this structure.
The first ones to appear are synchronous plateau assemblies (SPAs), that peak at birth and gradually vanish throughout the first postnatal weeks, leaving room to giant depolarizing potentials (GDPs) (Crépel et al. 2007; Egorov and Draguhn 2013). SPAs are a pattern that organizes the coordinated firing of increasing number of neurons, are mediated by gap-junctions, and are thought of depending on oxytocin and the depolarizing effect of GABA (Crépel et al. 2007). Network activity with a similar structure has also been described in the cortex (Allene et al. 2008; Egorov and Draguhn 2013). GDPs are also only generated in the presence of depolarizing GABA, recruit a larger amount of neurons than SPAs, and are mediated by chemical synapses (Crépel et al. 2007). While SPAs and GDPs have only been described in hippocampal slices, the first *in vivo* hippocampal activity signature to appear is the so-called early sharp-wave complex (eSW), which has been hypothesized as being the *in vivo* counterpart of GDPs (Leinekugel et al. 2002). eSWs dominate HP activity in the first postnatal week (Leinekugel et al. 2002) and occur bilaterally and longitudinally in a synchronized fashion (Valeeva et al. 2019a; Valeeva et al. 2020). While the machinery underlying eSWs has not been as thoroughly characterized as the adult one, it is thought of sharing several key components with the latter. During eSWs, CA1 neurons undergo a massive increase in firing rate, which has been hypothesized of being driven by inputs deriving from CA3 and the entorhinal cortex (Valeeva et al. 2019b). This is in line with previous evidence placing entorhinal activity as "upstream" of the hippocampus (Hartung et al. 2016b), and the fact that entorhinal-hippocampal projections are already present before birth (Supèr and Soriano 1994). Differently from mature SWs, eSWs do not co-occur with high-frequency (100-200 Hz) oscillations (ripples) until the second/third postnatal week (Buhl and Buzsaki 2005; Ahlbeck et al. 2018). Other distinctive features of eSWs include the presence of long "tails" of increased firing that extend for hundreds of milliseconds before and after their occurrence (Leinekugel et al. 2002; Ahlbeck et al. 2018; Xu et al. 2021), and their co-occurrence with muscle twitches (Karlsson et al. 2006; Mohns and Blumberg 2008). The developing hippocampus also displays bursts of oscillatory activity, whose dominant frequency extends within the theta to the beta-low gamma range (Leinekugel et al. 2002; Ahlbeck et al. 2018; Brockmann et al. 2011), and that organize single-neuron firing around 8 Hz (Xu et al. 2021). These oscillations co-occur with activity in the

primary sensory (Del Rio-Bermudez et al. 2020) and motor (Del Rio-Bermudez et al. 2017) cortex, are sensitive to cholinergic modulation (Janiesch et al. 2011), increase in power and continuity across the first two postnatal weeks, and are of higher amplitude in the dorsal than in the intermediate / ventral hippocampus (Ahlbeck et al. 2018; Brockmann et al. 2011). Sharp-waves are often embedded in such bursts of activity, indicating that the two motifs are not mutually exclusive (Leinekugel et al. 2002).
Already at neonatal age, the entorhinal cortex acts as the main source of sensory inputs of the hippocampal formation (Gretenkord et al. 2019; Valeeva et al. 2019b), which is then relayed to the HP (Hartung et al. 2016b; Valeeva et al. 2019b). In turn, independently of the specific type of network activity, the hippocampus is generally thought of being upstream of the prefrontal cortex, and of being a major contributor to its development (Brockmann et al. 2011; Bitzenhofer et al. 2015; Ahlbeck et al. 2018). The occurrence of eSW is accompanied by a strong modulation of the prefrontal LFP, and by a ramping up of neuronal firing in the PFC, which peaks a few milliseconds after the eSW, and remains elevated for several seconds after (Ahlbeck et al. 2018; Xu et al. 2021). More generally, in the first two postnatal weeks, from a statistical perspective, hippocampal activity supersedes (i.e. Granger-causes) prefrontal activity, and is one of the endogenous sources that induces the beta-low gamma prefrontal rhythms that characterize early prefrontal activity (Brockmann et al. 2011; Ahlbeck et al. 2018; Xu et al. 2021). Accordingly, hippocampal-prefrontal coherence and directed communication also peaks in the beta-low gamma frequency band (Ahlbeck et al. 2018; Hartung et al. 2016a; Xu et al. 2021. Similarly to the adult brain, the strength of hippocampal-prefrontal connections increases along the septo-temporal axis (Ahlbeck et al. 2018). This route of communication is sustained by a unidirectional monosynaptic pathway that is established already in the first postnatal week (Brockmann et al. 2011; Hartung et al. 2016a; Ahlbeck et al. 2018). Deep layer prefrontal pyramidal neurons are thought of being the main receivers of the hippocampal projections (Bitzenhofer et al. 2015; Ahlbeck et al. 2018 which then, in turn, relay the incoming activity to superficial layers (Brockmann et al. 2011). Interestingly, and reminiscent of primary sensory areas that progressively gain independence from the periphery, the statistical strength of hippocampal influence on prefrontal activity declines as mice develop (Hartung et al. 2016a; Xu et al. 2021). On a speculative level, this might be due to the fact that, at adulthood, hippocampal-prefrontal communication occurs in an episodic manner, for instance during cognitive tasks such as working memory, whereas it is more continuous at early developmental stages.
Studies on the early hippocampal activity and the hippocampal-prefrontal pathway in newborn babies are scarce, largely due to technical difficulties. On the one

hand, probing hippocampal activity with scalp EEG/MEG is feasible but demanding (Pu et al. 2018; Pizzo et al. 2019). On the other hand, functional brain imaging in infants poses a unique sets of methodological challenges, such as elevated body motion and the inability to follow instructions (Ellis et al. 2020). These limitations notwithstanding, an EEG study on premature infants reported a temporo-frontal gradient of maturation and information flow that has been proposed as being functionally analogous to what has been characterized in rodents (Omidvarnia et al. 2014).

1.5 Early network activity in the prefrontal cortex

The electrophysiological properties of the developing PFC have been less substantially investigated than those of more accessible and more directly malleable brain areas such as the primary sensory or motor cortices. We will therefore introduce the existing literature on the topic, and draw contrast and analogies with the richer information available on other cortical areas.
Similarly to what has been described in the sensorimotor cortices (Khazipov et al. 2004; Hanganu et al. 2006; Shen and Colonnese 2016; Rochefort et al. 2009; Golshani et al. 2009), the electrical activity of the immature rodent PFC is characterized by transient bouts of activity that increase in amplitude, duration, and average frequency over time (Brockmann et al. 2011). While this has not yet been investigated in the PFC, in sensory-motor cortices brain activity also decorrelates and sparsifies as it becomes more continuous (Modol et al. 2020; Rochefort et al. 2009; Golshani et al. 2009). In rats, prefrontal activity becomes continuous around the tenth postnatal day (Brockmann et al. 2011), whereas in mice this occurs a couple of days later (Chini and Hanganu-Opatz, unpublished data). This is similar to the timeline with which the phenomenon occurs in the primary visual cortex (Shen and Colonnese 2016). While the PFC lacks high-level stereotypical activity signatures such as those present in the visual and auditory cortex (Dupont et al. 2006; Ackman et al. 2012; Babola et al. 2018), possibly due to its lack of an obvious topographical organization, transients network oscillations (prefrontal network oscillations: PNOs), with a dominant frequency centered in the beta-low gamma range, have emerged as hallmarks of early prefrontal activity with important functional implications. PNOs are present already in the mid first postnatal week (Brockmann et al. 2011; Bitzenhofer et al. 2020a),

and smoothly evolve throughout development. Similarly to the overall prefrontal activity, they become longer, and they increase their amplitude and average frequency - from 15 Hz in the first postnatal week to >50 Hz in adulthood (Bitzenhofer et al. 2020a). Optogenetic interrogation of the prefrontal microcircuitry has revealed that pyramidal neurons of layers II/III ($PYRs_{II/III}$) and not layers V/VI underlie the generation of this rhythm (Bitzenhofer et al. 2017). Specifically, in mice of 8-10 days of postnatal age (P8-10), optically stimulating $PYRs_{II/III}$ with a "ramp" stimulation, a stimulus that gradually increases the level of excitation but does not force a specific rhythm, results in a spontaneous organization of neuronal firing centered around 16 Hz, and an increase of LFP power in the beta/low gamma frequency range, that subsequently propagates to the deep prefrontal layers (Bitzenhofer et al. 2017). An analogous stimulation of layers V/VI prefrontal pyramidal neurons only results in an unorganized arrhythmic increase of firing rate, and in an unspecific broadband increase of LFP power (Bitzenhofer et al. 2017). While the role of specific interneuronal populations has been less thoroughly investigated, the developmental shift towards higher frequencies follows a similar trajectory to the embedment of PV interneurons into the prefrontal microcircuitry (Bitzenhofer et al. 2020a). SOM interneurons originate at an early embryogenic stage (Butt et al. 2005) and, in the PFC as well as in the primary visual and somatosensory mouse cortex, the strength of synapses between SOM interneurons and pyramidal neurons progressively decreases across the first three postnatal week, whereas the opposite phenomenon is observed for PV interneurons (Guan et al. 2017; Marques-Smith et al. 2016; Anastasiades et al. 2016; Tuncdemir et al. 2016). Considering that SOM and PV interneurons are thought of respectively being the main interneuronal population underpinning beta (16-30 Hz) and gamma (30-100 Hz) oscillations in sensory cortices (Chen et al. 2017; Veit et al. 2017; Cardin et al. 2009), it is tempting to speculate that a regime transition from the former to the latter interneuronal population might explain the transition of PNOs towards faster frequencies (Bitzenhofer et al. 2020a). Another possible factor that might exert an influence in this process is that the polarity of GABAergic terminals on the axon initial segment of prefrontal $PYRs_{II/III}$ switches from excitatory to inhibitory in this same period (Rinetti-Vargas et al. 2017; Pan-Vazquez et al. 2020).
Of note, early bouts of gamma activity are also present in the rodent barrel (Minlebaev et al. 2011; Yang et al. 2013) and visual cortices (Colonnese et al. 2010; Hanganu et al. 2006). In the barrel cortex, gamma oscillations are induced by whisker stimulation as early as P2, increase up to P7 and then abruptly disappear at P8, gradually returning in the following days, with a more continuous temporal and spatial structure (Minlebaev et al. 2011). This biphasic development is different from the smooth monotonic maturation of PNOs (Bitzenhofer et al. 2020a), suggesting that distinct mechanisms

underlie early fast oscillations in different cortical areas.
Early patterns of activity in motor-sensory brain areas are homeostatically regulated (Babola et al. 2018) and, while it is still debated whether they carry any sensory information (Mizuno et al. 2018; Anton-Bolanos et al. 2019; Khazipov et al. 2004; Dooley et al. 2020), they are indispensable for the correct functional and structural development of the neuronal population that are involved in their generation (Ackman et al. 2012; Batista-Brito et al. 2017; Che et al. 2018; Duan et al. 2020; Garcia et al. 2011). They assist the refinement of the local microcircuit, and promote cells specification and survival (Blankenship and Feller 2010). For instance, impairments in early activity has been linked to hyperexcitability (Anton-Bolanos et al. 2019), lack of temporal (Batista-Brito et al. 2017; Duan et al. 2020) and spatial structure (Anton-Bolanos et al. 2019; Che et al. 2018), and impaired sensory performance (Batista-Brito et al. 2017; Che et al. 2018). Whether such a relationship also exists between early prefrontal activity, the adult PFC functionality and, ultimately, PFC-dependent cognitive abilities is an open question with profound implications for neuropsychiatric disorders. Addressing this knowledge gap, and studying the relevance of the supporting role played by the HP, is the main question addressed in this thesis.

1.6 Thesis overview and summary of results

The overarching aim of this thesis is to investigate the patterns of neuronal activity characterizing the physiological and pathological early development of the murine prefrontal cortex, the circuitry that underlies them, its input-output connections, and, perhaps most importantly, how they relate to the later-emerging PFC-dependent cognitive abilities. To address this question, the large majority of the body of work examines the electrophysiological properties of the mouse PFC across the first two postnatal weeks, and it does so employing a vast array of techniques and computational approaches: *in vivo* and *in vitro* electrophysiology, optogenetics, pharmacology, microscopy, behavioral assays, discrete and continuous time-series analysis, hierarchical statistical approaches and learning algorithms.
Chapter 2.1 investigates the HP, an important early source of input for the developing PFC. It explores how the properties of the communication between these

two brain areas varies along the septo-temporal hippocampal axis of P8-10 mice. It uncovers differences in the early levels of activity between the dorsal and the intermediate / ventral HP, with the former displaying higher broadband LFP power and larger sharp-wave ripples. Conversely, and similarly to what has been shown in the adult rodent brain, it is the intermediate / ventral HP that displays a stronger communication with the PFC. This is true for general hippocampal activity, but becomes particularly prominent during sharp-wave ripples events. By employing targeted optogenetic stimulation, this chapter demonstrates that hippocampal oscillatory activity centered around 8 Hz is particularly effective in eliciting neuronal activity in the PFC. Finally, utilizing a dual stimulation / inhibition strategy, it shows that, already at the beginning of the second postnatal week, GABA exerts an inhibitory action on hippocampal network activity.

Chapter 2.2 further probes the developing prefrontal-hippocampal pathway in mice of 8-10 days of age, extending its analysis to several mouse model of mental illness. Leveraging pure genetic, pure environmental and dual-hit genetic-environmental mouse models, it exposes how reduced prefrontal-hippocampal communication is a trait that is common across all these models. Reduced hippocampal and prefrontal network activity and diminished firing rate are also present in several models, but are less consistent across the board. This work highlights the pathophysiological relevance of the instructive role played by the hippocampus in guiding early prefrontal development.

Chapter 2.3 deepens the analysis of pathological prefrontal development. It unveils how, in a dual-hit genetic-environmental mouse model of mental disorders, $\text{PYRs}_{\text{II/III}}$ display reduced firing rate and simplified dendritic arborization. Importantly, it highlights how $\text{PYRs}_{\text{II/III}}$ are of paramount importance in orchestrating early network activity and sustaining the development of PFC-dependent cognitive abilities. It shows how a targeted suppression of an important developmental gene in this neuronal population recapitulates the phenotype observed in the mouse model carrying the same brain-wide genetic alteration. In particular, it establishes how deficits affecting $\text{PYRs}_{\text{II/III}}$ underlie the impairment of beta / gamma oscillations and the cognitive deficits that affect the examined mouse model.

Chapter 2.4 corroborates the findings of chapter 3 and strengthens its conclusions by providing mechanistic insights into the underlying pathophysiology. Using the same mouse model of mental disorders as in chapter 3, it details the striking morphological deficits affecting the dendrites and the spines of $\text{PYRs}_{\text{II/III}}$., and it further probes the prefrontal electrophysiological deficits that it causes, highlighting how these are present even in the first postnatal week. It shows that the inflammation that characterizes this mouse model causes excessive microglia engulfment of $\text{PYRs}_{\text{II/III}}$ synaptic

terminals, and that this is upstream of the reduced spine density and simplified dendritic arborization characterizing this neuronal population. Strengthening these findings, pharmacological inhibition of the inflammatory microglia response fully rescues the pathological phenotype, both on a structural and physiological level. Importantly, this work not only shows that early disruption of prefrontal networks is an early biomarker of impaired cognitive abilities, but also that resolving such early deficits with a pharmacological intervention is predictive of restored cognitive abilities.

Chapter 2.5 follows the stream of evidence presented in the previous two chapters, and significantly advances the investigation on the role of early prefrontal activity in determining cognitive abilities. Instead of relying on the dual-hit genetic-environmental mouse model of the previous two chapters, it establishes a paradigm for a subtle chronic optical manipulation of $PYRs_{II/III}$ across the first two postnatal weeks. In doing so, it uncovers how a transient increase in activity in the second postnatal week of this neuronal population has several detrimental long-term effects. By inducing a premature structural maturation of $PYRs_{II/III}$, it causes an excitation / inhibition (E/I) imbalance, impaired prefrontal beta / gamma oscillations and, ultimately, disrupts several PFC-dependent cognitive abilities such as working memory and social cognition. It reports that, in chronically-stimulated mice, PV interneurons have an oversized arborization, and it proposes that they might provide excessive feedback inhibition on $PYRs_{II/III}$, causing the E/I imbalance that characterize this network. Importantly, this study significantly advances our understanding of the role that early PFC activity plays in sustaining the development of PFC-dependent cognitive abilities.

Chapter 2.6 is a review that summarizes what is known about prefrontal development. It proposes a general framework in which to interpret the findings of the previous chapters, and tries to reconciliate different point of views on the structural and functional homology between human and rodent PFC. It details the input-output circuitry sustaining and depending on early prefrontal activity, with particular emphasis on the hippocampus, the striatum and the thalamus. It presents early bouts of beta-low gamma oscillatory activity as an early high-level hallmark of prefrontal activity, that could serve a role that is analogous to the better characterized stereotypical motifs present in primary sensory cortices such as retinal waves. It concludes with reviewing recent human and rodent studies that point to adolescence as a period of increased vulnerability in prefrontal development, whose alterations could ultimately lead to neurodevelopmental disorders.

Chapter 2.7 explores the influence of anesthesia on early brain activity in several brain areas. It addresses questions that are not only of translational relevance, but

that also affect much of the rodent research on early brain physiology, including several of the investigation discussed in the previous chapters, as it is often conducted in the anesthetic state. It demonstrates that in neonatal mice and newborn babies alike, the neural correlates of anesthesia have several unique properties. Differently than in adults, anesthesia doesn't favor slow oscillations at the expense of faster ones, but rather globally dampens neural activity, leaving its spectral properties relatively unchanged. The anesthesia-induced strong reduction in broadband LFP-power and neuronal firing rate is not accompanied in changes in E/I balance, signal complexity or long-range communication. Finally, it proposes a data-driven model to predict anesthesia depth using LFP or EEG features, that might support a novel approach to monitor anesthesia depth in the immature brain. This is particularly relevant considering that algorithms that have been devised for this task in adults perform poorly on infants.

Chapter 2.8 scrutinizes another peculiar aspect of the anesthetic state, namely its effects on hippocampal activity, a brain structure that is central to the effects exerted by general anesthetics. This follows from the widely accepted notion that the hippocampus is essential to memory formation and the recognition that while retrograde amnesia is an important aspect of general anesthesia, long-term impairment of memories is one of the most common side-effects of the procedure. This chapter reveals that, differently from what occurs in the cortex, general anesthetics decorrelate and fragment hippocampal activity, albeit with a different magnitude and temporal profile. Anesthetics that have the strongest effects on hippocampal network activity also more severely impact spine dynamics and episodic memory formation. Given the large differences among general anesthetics, this study has implications for the choice and evaluation of different anesthesia strategies in animal research and, potentially, clinical practice.

2 | Methods and Results

2.0 Materials and methods

2.0.1 *In vitro* whole-cell patch clamp and optogenetics

Patch clamp recordings. Mice used for whole-cell patch clamp recordings were isoflurane-anesthetized and decapitated. Brains were rapidly extracted and cut into 300 μm coronal sections in oxygenated high-sucrose artificial cerebral spinal fluid (ACSF) kept just above freezing temperature. The exact ACSF composition (in mM) was of 228 sucrose, 2.5 KCl, 1 NaH2PO4, 26.2 NaHCO3, 11 glucose, 7 MgSO4, for a total of 320 mOsm. After cutting, slices were moved and further incubated in another ACSF, at 37° and with a different composition: 119 NaCl, 2.5 KCl, 1 NaH2PO4, 26.2 NaHCO3, 11 glucose, 1.3 MgSO4, also for a total of 320 mOsm. Slices were kept in this solution for 45-60 minutes, before transferring them at room temperature. Slices were then transferred to the recording chamber, where neurons were patched under microscopic visual control using glass pipettes with a tip resistance varying from 3-10 MΩ (lower for older animals, higher for younger ones). To monitor

post-synaptic potentials, glass capillaries were filled with the following solution (in mM): 130 D-glucononic acid 49-53%, 130 Cesium-OH 50%, 10 HEPES, 0.5 EGTA, 4 Mg-ATP, 0.3 Na2-GTP, 8 NaCl, 5 QX-314-Cl; 285 mOsm, pH 7.3. To monitor action potentials, glass capillaries were filled with the following solution (in mM): 130 K-gluconate, 10 HEPES, 0.5 EGTA, 4 Mg-ATP, 0.3 Na-GTP, 8 NaCl; 285 mOsm, pH 7.4. Data was acquired either in the MATLAB environment (MathWorks, MA, USA) using the Ephus toolbox, or with the PatchMaster software (HEKA Elektronik,, MA, USA). To minimize series resistance and capacitance artefacts, we relied on the circuitry of the patch-clamp amplifier (Axopatch 200B; Molecular devices, CA, USA or EPC 10; HEKA Elektronik, MA, USA, respectively). Patch-clamp traces were acquired and digitized with a sampling rate of 5 or 10 kHz, respectively.
Optogenetic stimulations. Depending on the specific experimental paradigm, blue (472 nm) or yellow (585 nm) light stimulations were delivered through the same optical system, with a pE-2 LED system (CoolLED, Andover, UK). The shape of the administered light stimulations varied from square pulses of different length (3 ms to 1s) to so-called ramp stimulations (stimuli of gradually increasing intensity) of 3 s length.

2.0.2 *In vivo* electrophysiology and optogenetics

Surgery. Electrophysiological extracellular recordings were performed in the PL and HP of P2-P12 mice. Mice that were recorded under anesthesia were injected with 1mg/g body weight of urethane (Sigma-Aldrich, St Louis, MO, USA) diluted in 0.9% NaCl before undergoing the surgical procedure. Mice that were recorded without anesthesia were administered local anesthetic on the neck muscles (0.5% bupivacain / 1% lidocaine). For both types of recordings, surgery was carried out under isoflurane anesthesia (induction: 5%; maintenance: 1-3%, lower for older pups, higher for younger pups). Neck muscles were cut to reduce muscle artifacts. A "crown" of dental cement was applied on the skull of the pup, after removal of the skin and the underlying connective tissue. The skull above the target brain areas and the cerebellum was carefully thinned and then removed with a motorized drill and a syringe needle. The head of the pup was fixed into a stereotactic frame with the help of two plastic/metal bars that were embedded in the dental cement crown. Mice rested on a heated (37°) surface throughout the entire recording. (Opto)Electrodes (four-shank, A4x4 recording sites, 100 μm spacing, 125 μm shank distance; single-

shank, A1x16 recording sites, 50-100 μm spacing; eventual optical fibers of 50-100 μm ending 200 μm above the top recording site of the electrode; NeuroNexus, MI, USA) were then carefully and slowly inserted into the target area. To target the right PL, four-shank (opto)electrodes were inserted 0.1 mm lateral of the midline, 0.5 mm anterior to bregma, and at a depth varying between 1.4 and 2 mm depending on the age of the mouse. To target the right intermediate/ventral HP, single-shank (opto)electrodes were inserted 3-3.5 mm lateral of the midline, 3-3.5 mm posterior of bregma and at a depth of 1.2-1.6 mm, depending on the age of the mouse. A silver wire was used as ground and external reference, and was inserted in the cerebellum at an approximate depth of 1 mm. Before signal acquisition, mice were allowed a recovery period of 30-45 minutes, to maximize the quality of the recording and the stability of single units.
Signal acquisition. Extracellular signals were acquired and digitized with a sampling rate of 32 kHz after band pass filtering (0.1-9000 Hz), using an extracellular amplifier (Digital Lynx SX; Neuralynx, Bozeman, MO, USA) and its accompanying software (Cheetah , Neuralynx, Bozeman, MO, USA). Light stimulation. Optical stimulations were controlled with an Arduino Uno (Arduino, Italy) that controlled a diode laser (Omicron, Austria). The delivered light stimuli varied in wavelength (472 nm or 525 nm) and shape (square pulses of 3 ms length or "ramps" of 3 s length), according to the specific experimental paradigm. Laser power was titrated before signal acquisition, and adjusted to the minimum level that induced the desired neuronal response. Typical light power at the fiber tip was measured in the range of 15-40 mW/mm^2.
Post mortem histological assessment of electrode position. Epifluorescence images of 100 μm thick coronal brain sections were acquired a few days after surgery was completed. In these slices, the trace and the position of the recording electrode was reconstructed. Single-shank electrodes were coated with a fluorescent die (DiI, Thermo Fisher Scientific, MA, USA) before insertion to facilitate this step. Only mice in which the electrodes were placed in the correct position were kept for further analysis.

2.0.3 *In utero* electroporation

Dams that underwent the surgical procedure of *in utero* electroporation received wet food supplemented with a long-lasting painkiller, approximately 2 drops of Metacam (meloxicam; Boehringer-Ingelheim, Germany) per food pellet, from one day before the

intervention until two days after. Dams were *in utero* electroporated at E12.5 or E15.5 to target deep or superficial layer pyramidal neurons in the PFC, respectively. At least 30 minutes before the surgical procedure, mice were subcutaneously injected with buprenorphine (0.05 mg/kg body weight). Surgery was carried out under isoflurane anesthesia (induction: 5%; maintenance: 2.5-3.5%) and on a heated surface covered by a sterile blanket. After monitoring the absence of pain reflexes (toe and tail pinch), and covering the eyes with a protective ointment, the abdominal wall of the mouse was opened, and the two uterine horns were exposed and rinsed with warm sterile PBS. Embryos were then injected in the right ventricle using a pulled borosilicate glass capillary. The injected liquid contained 0.1% of fast green dye (to help the operator to visually estimate the amount of injected DNA) and a DNA plasmid encoding different proteins depending on the experimental paradigm. For experiments in which the sole scope was to analyze the morphology of the electroporated neurons, the plasmid had a pAAV-CAG-tDimer2 sequence, whereas for experiments in which neurons were also optically manipulated, the sequence of the plasmid was pAAV-CAG-ChR2(E123T/T159C)-2AtDimer2). CAG is a CMV-derived promoter that is strongly active throughout development. tDimer2 encodes for a red fluorescent protein that was used to investigate the morphology of the electroporated neurons and to visually assess (at postnatal day 2) whether the *in utero* electroporation was successful (see details later). ChR2(E123T/T159C) encodes for a high-efficiency variant of the excitatory opsin Channelrhodopsin 2. 2A encodes for a ribosomal skip sequence and thus serves to split the opsin from the fluorescent protein. To electroporate individual embryos, after injecting the DNA, the electroporation tweezer-type paddles (3 mm diameter for E12.5; 5 mm diameter for E14.5-15.5; Protech, TX, USA) were placed on the head of the embryo, with an approximate orientation of 20° left from the midline and 10° downwards on the antero-posterior axis (Bitzenhofer et al. 2017). This orientation has been shown to selectively target the precursors of pyramidal neurons in the subventricular zone that will eventually migrate to the medial PFC (Bitzenhofer et al. 2017). With an electroporator (CU21EX; BEX, Japan), five electric pulses (35 V, 50 ms) were delivered to individual embryos at an interval of 950 ms. After electroporating all the embryos, the uterine horns were gently reinserted in the abdominal cavity and moistened with warm sterile PBS. The muscles of the abdominal wall and skin were then individually sutured with absorbable and non-absorbable suture thread, respectively. After the surgical procedure, anesthesia was terminated and, after recovery, the mouse was placed in its cage. For the following two days, half of the cage was placed on a heated blanket. To confirm the outcome of the procedure, two days after birth pups were transcranially illuminated with a fluorescent flashlight (Nightsea, MA, USA). This was followed by post-mortem histological confirmation of

fluorescence expression in the desired neuronal population.

2.0.4 Histology

Perfusion. Mice were anesthetized with an intraperitoneal injection of an anesthetic cocktail consisting of ketamine and xylazine (10 mg/g body weight, 10% ketamine (aniMedica, Germany) and 2% xylazine (WDT, Germany)). After assessment of lack of pain reflexes (toe and tail pinch), mice were transcardially perfused with a 0.9% NaCL solution to wash out the blood, followed by Histofix, a 4% paraformaldehyde containing solution (Carl Roth, Germany). Brains were extracted and placed in a plastic tube containing the same fixative solution.
Immunohistochemistry. The extracted brains were kept at 4-6° overnight, and coronally sectioned with a vibratome in slices of 50 μm (for immunohistochemistry) or 100 μm ($PYRs_{II/III}$ structural/morphological investigations). Sections were washed in a blocking solution containing bovine serum albumin (BSA) and Triton X-100 at different concentrations, depending on the staining protocol, and incubated overnight in the same solution with a primary antibody against the protein of interest (NeuN, 1:100, MAB377X, Merck Millipore, MA, USA; CaMKII ,1:200, PA5-38239, Thermo Fisher Scientific, MA, USA, GABA, 1:1000, A2052, Sigma-Aldrich, IBA1, 1:500, catalog 019-19741, Wako, VGLUT1, 1:1000, Synaptic Systems, Germany). On the following day, sections were probed with a secondary antibody (Alexa Fluor-488 goat anti-rabbit IgG secondary antibody, 1:500, A11008, Merck Millipore; Alexa Fluor-568 donkey anti-rabbit, 1:500, Life Technologies, CA, USA; Alexa Fluor-488 goat anti-guinea pig, 1:500, Molecular Probes, OR, USA), mounted on a glass slide and covered with Vecta Shield (Vector Laboratories).
Imaging. A confocal microscope (DM IRBE, Leica Microsystems, Zeiss LSN700 and Olympus FX-100) was used for image acquisition. For overview pictures, we employed a 10x magnification objective (numerical aperture, 0.3) and a 1024 x 1024 pixel resolution (pixel size, 1465 nm). To investigate the number and morphology of microglia cells, we employed a 40x magnification objective (numerical aperture, 1.25) a 512 x 512 pixel resolution (pixel size, 732 nm), and acquired stacks of 20 images (Z-step, 1000 nm). In total, we acquired 8 images per slice, and used 3 slices per mouse. To investigate the microglia engulfment of synaptic terminals, we employed a 60x magnification objective (numerical aperture, 1.35) a 1024 x 1024 pixel resolution (pixel size, 103 nm, Z-step, 750 nm). The number of images was adjusted according

to the span of the microglia cell in the z-axis. In total, we acquired 5 images per slice, and used 3 slices per mouse.

2.0.5 Image analysis

Sholl and spine density analysis. Sholl and spine density analysis was performed semi-automatically in the ImageJ environment, relying on the Sholl Analysis plugin (Ferreira et al. 2014). Analyzed images were binarized (*auto threshold*) before tracing the dendrites with the plugin *Simple Neurite Tracer*. The neuron center of mass was quantified with the *blow/lasso tool*. Spine density analysis was manually computed along a randomly selected portion of the traced dendrites. Dendrites were grouped according to their morphological/structural class into apical, basal, proximal oblique and secondary apical. *Microglia quantification.* The number of Iba1$^+$ positive cells was used as a proxy for microglia quantification, and was computed with a custom-written macro in the ImageJ environment. The image stacks were collapsed along the vertical dimension (maximum-intensity Z-projection) before a background noise-correction (*despeckle*), a Gaussian filter (*Gaussian blur*, sigma = 2) and a binarization (*auto threshold* with the *triangle* method) were applied. Of the resulting binarized objects, only those with an area larger than 150 pixels were considered and counted as microglia cells.
Microglia morphology analysis. The analysis of microglial morphology was carried out with custom-written scripts in the MATLAB environment. The image stacks were collapsed along the vertical dimension (maximum-intensity Z-projection) and binarized (*graythresh* and *im2bw* using the graythresh output as threshold). The size of the binarized objects was quantified and objects that had a dimension comprised between 200 and 1500 pixels were considered as putative microglia cells. Putative microglia cells were then automatically segmented into a square Region Of Interest (ROI) of 110 pixels centered around the center of mass of the object, and manually accepted/rejected depending on whether the ROI contained the entirety of the microglia and no other bordering microglia. On the accepted objects, a series of features (area, perimeter, eccentricity) was automatically computed using *regionprops*. Further, two other features were computed: cell spread and eccentricity. Cell spread was defined as the average distance between the center of mass of the segmented

microglia and its extrema; roundness as

$$roundness = \frac{4 \times \pi \times area}{perimeter}$$

Given that IUE has been shown to affect microglia morphology (Rosin and Kurrasch 2018), only mice that didn't undergo IUE were used for this analysis.
Microglia engulfment analysis. Given that IUE has been shown to affect microglia morphology (Rosin and Kurrasch 2018), only mice that didn't undergo IUE were used for this analysis. To quantify microglia engulfment of synaptic material, we used the overlay of VGLUT1$^+$ synaptic puncta and Iba1$^+$ cells as a proxy. Preprocessing of the Iba1 signal was entirely carried out in the MATLAB environment and consisted of background subtraction (*imopen*, with a 'disk' of radius 50), 3D double-threshold binarization (*hysteresis3d* function; lower threshold = 0.1, upper threshold = 0.5, connectivity = 26) and 3D median filtering (*ordfilt3D*). The 3D hysteresis step consisted of a first step identifying regions of the image stack with bright intensity (above the upper threshold), followed by a 3D search of connected pixels above a lower threshold. This allows for better binarization of the terminals of microglia cells, that are often less bright than the cell soma. Of the thresholded microglia images that were obtained in this manner, we also quantified the distal cell volume (further than 7 μm from the center of mass), as a proxy for the volume of the microglia protrusions. Preprocessing of the VGLUT stacks was carried out in ImageJ and consisted of background subtraction (*rolling ball* radius = 2 pixels), median filtering (*despeckle*), maximum filtering (radius = 2 pixels), binarization (*auto threshold*) and segmentation (*watershed*). In MATLAB, the volume of the connected VGLUT1$^+$ areas of the image stacks were quantified in 3D (*bwlabeln*, connectivity = 8) and only ROIs with a volume comprised between 100 and 500 pixels were kept for further analysis. The two 3D tensors were then elementwise multiplied, and VGLUT1 puncta were considered as "engulfed" only if they displayed a 100% overlap in the xyz plane with the binarized microglia cells.

2.0.6 Time-series analysis

Time-series analysis of LFP and EEG data was performed in the MATLAB environment using custom-written scripts that are generally available in open-access repositories: https://github.com/mchini/HanganuOpatzToolbox and https://github.

com/mchini/Yang_Chini_et_al. Common preprocessing steps generally consisted of band-pass filtering with a phase-preserving third-order Butterworth forward and backward filter followed by downsampling to an appropriate sampling rate.
Detection of oscillatory periods. In early development, brain activity is highly discontinuous, displaying an alternation of periods of isoelectric traces (silent periods) and oscillatory bursts (active periods). The nature of the signal thus constitutes a challenge to the stationarity assumption that is common to several time-series analysis algorithms. To mitigate this problem, a common strategy is to detect active periods and limit the analysis to these portions of the signal. To this aim, a number of different strategies were employed throughout the thesis. I will here only describe an algorithm that I developed with the aim of being able to detect oscillations through a wide range of signal amplitude and continuity. In the context of LFP recordings from the PFC, the algorithm is run on every channel after common average rereferencing (subtraction of the median across all channels). The signal is band-pass filtered (4-20 Hz), downsampled to 100 Hz, and passed through a boxcar square filter (500 ms). Both the raw (unnormalized) and the z-scored signal, oscillations are extracted with a hysteresis filter (i.e. events are first detected as oscillatory peaks exceeding a higher threshold and then extended to all neighboring time points that exceed a lower threshold). The combination of absolute and relative thresholding makes this strategy applicable to a wide range of signals, to the highly discontinuous brain activity of the early first postnatal week, to the virtually continuous brain activity of mice older than P11-12. Finally, oscillatory periods are merged if the inter-oscillation-interval is smaller than 1 s , and discarded if the overall duration is smaller than 300 ms.
Power spectral density. Power spectral densities (PSDs) were computed either using Welch's method or a multi-taper time frequency spectrum. In the latter case, median-averaging was preferred as a measure of central tendency (Izhikevich et al. 2018).
Spike sorting. To obtain SUA time-series, data was band-pass filtered (500-5000 Hz) and then automatically clustered using a flood and fill algorithm (Rossant et al. 2016). The clusters that were thus obtained were further manually curated using phy (https://github.com/cortex-lab/phy).
SUA to LFP oscillatory synchrony. Much research has been devoted to the analysis of how SUA related to local ongoing oscillations. One of the most commonly used metrics to quantify this relationship is the so-called Phase Locking Value (PLV). However, the PLV is highly sensitive to the firing rate of the investigated units (Vinck et al. 2010), and is therefore unfit to the analysis of early development, given that the average firing rate varies across several orders of magnitude in the first two postnatal weeks. To circumvent the limits of the PLV, we employed Pairwise Phase Consistency (PPC), a measure that is robust to variations in firing rate (Vinck et al. 2010). Briefly,

PPC was computed as the average cosine of the dot product among all pairs of action potential phases. A custom-written vectorized version of the algorithm is the available in the open-access repository linked above.
Pairwise correlations among SUA spike trains. Similar considerations on the sensitivity to variations in firing rate as the ones exposed in the previous paragraph apply also to several common metrics that quantify correlations among SUA spike trains (Cutts and Eglen 2014). To circumvent the limitations of such approaches, we employed the Spike-Time Tiling Coefficient (STTC) metric, that has been shown to be insensitive to variations in firing rate. The STTC is computed by quantifying the proportion (PA) of action potentials in the spike train A that occur within $\pm\Delta$t (where t is the parameter that controls the temporal scale for which the metric is computed) of a spike in the spike train B. To PA, the proportion of time that is "covered" by $\pm\Delta$t of spikes that occur in spike train B is then subtracted (TB). The value is then normalized by the product of these two values subtracted from 1. The procedure is repeated inverting spike train A and B, and the mean between the two yields the STTC.

$$STTC = \frac{1}{2}\left(\frac{P_A - T_B}{1 - P_A T_B} + \frac{P_B - T_A}{1 - P_B T_A}\right)$$

A custom-written vectorized version of the algorithm is the available in the open-access repository linked above.

2.0.7 Statistical analysis

Statistical analysis was generally carried out in the R environment (R statistical software, Foundation for Statistical Computing, Vienna, Austria), and detailed statistical information was provided in statistical tables. Generally, given that biological data can rarely be considered as normally distributed, especially at the low numbers that are typical of academic research, non-parametric methods were favored to their parametric counterparts. An exception to this was done in cases in which statistical units were "nested". For this type of data, priority was given to correct estimation of the grouping factors (Aarts et al. 2014), and linear mixed-effect models (that do not have a widely accepted non-parametric version) were employed. Depending on the experimental paradigm, different nesting factors were used (e.g. "mouse", "recording", "neuron", "slide" etc.). Model selection was guided by

experimental design, parameter estimation was done using the *lmer* function of the *lme4* package (Bates et al. 2014), and significance was evaluated with the *lmerTest* package (Kuznetsova et al. 2017). Post-hoc analysis was carried out using the *emmean* R package (Lenth et al. 2020).

2.0.8 Data availability

Data related to Chini et al. 2019 is available at https://doi.gin.g-node.org/10.12751/g-node.b8a1f8/
Data related to Chini et al. 2020 is available at https://doi.gin.g-node.org/10.12751/g-node.f3e198/
Data related to Bitzenhofer et al. 2020b is available at https://doi.gin.g-node.org/10.12751/g-node.b64563/
Data related to Yang et al. 2021 is available at https://gin.g-node.org/SW_lab/Anesthesia_CA1

2.1 Glutamatergic drive along the septo-temporal axis of hippocampus boosts prelimbic oscillations in the neonatal mouse

Joachim Ahlbeck, Lingzhen Song, Mattia Chini, Sebastian H Bitzenhofer and Ileana L Hanganu-Opatz

eLife 2018; DOI: https://doi.org/10.7554/eLife.33158.001

Personal contribution

I performed *in vivo* electrophysiology and optogenetics experiments. I carried out formal analysis and data curation. I reviewed and edited the manuscript.

eLIFE elifesciences.org

RESEARCH ARTICLE

Glutamatergic drive along the septo-temporal axis of hippocampus boosts prelimbic oscillations in the neonatal mouse

Joachim Ahlbeck†, Lingzhen Song, Mattia Chini, Sebastian H Bitzenhofer, Ileana L Hanganu-Opatz*

Developmental Neurophysiology, Institute of Neuroanatomy, University Medical Center Hamburg-Eppendorf, Hamburg, Germany

Abstract The long-range coupling within prefrontal-hippocampal networks that account for cognitive performance emerges early in life. The discontinuous hippocampal theta bursts have been proposed to drive the generation of neonatal prefrontal oscillations, yet the cellular substrate of these early interactions is still unresolved. Here, we selectively target optogenetic manipulation of glutamatergic projection neurons in the CA1 area of either dorsal or intermediate/ventral hippocampus at neonatal age to elucidate their contribution to the emergence of prefrontal oscillatory entrainment. We show that despite stronger theta and ripples power in dorsal hippocampus, the prefrontal cortex is mainly coupled with intermediate/ventral hippocampus by phase-locking of neuronal firing via dense direct axonal projections. Theta band-confined activation by light of pyramidal neurons in intermediate/ventral but not dorsal CA1 that were transfected by *in utero* electroporation with high-efficiency channelrhodopsin boosts prefrontal oscillations. Our data causally elucidate the cellular origin of the long-range coupling in the developing brain.
DOI: https://doi.org/10.7554/eLife.33158.001

***For correspondence:** hangop@zmnh.uni-hamburg.de

Present address: †Department of Neurophysiology and Pathophysiology, University Medical Center Hamburg-Eppendorf, Hamburg, Germany

Competing interests: The authors declare that no competing interests exist.

Funding: See page 20

Received: 27 October 2017
Accepted: 06 March 2018
Published: 10 April 2018

Reviewing editor: Marlene Bartos, University of Freiburg, Germany

Introduction

In the adult rodent brain, coordinated patterns of oscillatory activity code in a frequency-specific manner for sensory and cognitive performance. For example, learning and memory critically depend on oscillations within theta frequency band (4–12 Hz) that functionally couple the medial prefrontal cortex (PFC) and hippocampus (HP) (***Siapas and Wilson, 1998***; ***Benchenane et al., 2010***; ***Brincat and Miller, 2015***; ***Backus et al., 2016***; ***Eichenbaum, 2017***; ***Wirt and Hyman, 2017***). These frequency-tuned brain states are present already during early development, long before the memory and attentional abilities have fully matured. They have been extensively characterized and categorized according to their spatial and temporal structure (***Lindemann et al., 2016***). Network oscillations during development have a highly discontinuous and fragmented structure with bursts of activity alternating with 'silent' periods (***Hanganu et al., 2006***; ***Seelke and Blumberg, 2010***; ***Shen and Colonnese, 2016***; ***Luhmann and Khazipov, 2018***). The most common oscillatory pattern, spindle bursts, synchronizes large cortical and subcortical networks within theta-alpha frequency range. It is accompanied by slow delta waves as well as by faster discharges (beta and gamma oscillations) that account for local activation of circuits (***Brockmann et al., 2011***; ***Yang et al., 2016***).

In the absence of direct behavioral correlates, a mechanistic understanding of oscillatory rhythms in the developing brain is currently lacking. In sensory systems, spindle bursts have been proposed to act as a template facilitating the formation of cortical maps (***Dupont et al., 2006***; ***Hanganu et al., 2006***; ***Tolner et al., 2012***), whereas early gamma oscillations seem to control the organization of

eLife digest When memories are stored, or mental tasks performed, different parts of the brain need to communicate with each other to process and extract information from the environment. For example, the communication between two brain areas called the hippocampus and the prefrontal cortex is essential for memory and attention. However, it is still unclear how these interactions are established when the brain develops.

Now, by looking at how the hippocampus and the prefrontal cortex 'work' together in newborn mouse pups, Ahlbeck et al. hope to understand how these brain areas start to connect. In particular, the groups of neurons that kick start the development of the circuits required for information processing need to be identified.

Recording the brains of the pups revealed that electrical activity in a particular sub-division of the hippocampus activated neurons in the prefrontal cortex. In fact, a specific population of neurons in this area was needed for the circuits in the prefrontal cortex to mature.

In further experiments, the neurons from this population in the hippocampus were manipulated so they could be artificially activated in the brain using light. When stimulated, these neurons generated electrical activity, which was then relayed through the neurons all the way to the prefrontal cortex. There, this signal triggered local neuronal circuits. Thanks to this activation, these circuits could 'wire' together, and start establishing the connections necessary for mental tasks or memory in adulthood.

The brain of the mouse pups used by Ahlbeck et al. was approximately in the same developmental state as the brain of human fetuses in the second or third trimester of pregnancy. These findings may therefore inform on how the hippocampus and the prefrontal cortex start connecting in humans. Problems in the way brain areas interact during early development could be partly responsible for certain neurodevelopmental disorders and mental illnesses, such as schizophrenia. Understanding these processes at the cellular level may therefore be the first step towards finding potential targets for treatment.

DOI: https://doi.org/10.7554/eLife.33158.002

thalamocortical topography (***Minlebaev et al., 2011***; ***Khazipov et al., 2013***). In limbic systems dedicated to mnemonic and executive abilities, the knowledge on the relevance of early network oscillations is even sparser. Few lesion studies, yet without selectivity for specific activity patterns, suggested that prefrontal-hippocampal communication during development might be necessary for the maturation of episodic memory (***Krüger et al., 2012***). Temporal associations between the firing and synaptic discharges of individual neurons and network oscillations in different frequency bands gave first insights into the cellular substrate of coordinated activity in neonates. Whereas in sensory systems, endogenous activation of sensory periphery drives entrainment of local circuitry through gap junction coupling as well as glutamatergic and GABAergic transmission (***Dupont et al., 2006***; ***Hanganu et al., 2006***; ***Minlebaev et al., 2009***), in developing prefrontal-hippocampal networks, the excitatory drive from the HP has been proposed to activate a complex layer- and frequency-specific interplay in the PFC (***Brockmann et al., 2011***; ***Bitzenhofer and Hanganu-Opatz, 2014***; ***Bitzenhofer et al., 2015***).

While most of this correlative evidence put forward the relevance of early oscillations beyond a simple epiphenomenal signature of developing networks, direct evidence for their causal contribution to circuit maturation is still missing. This is mainly due to the absence of a causal interrogation of developing networks, similarly to the investigations done in adult ones. Only recently the methodological difficulties related to area-, layer- and cell type-specific manipulations at neonatal age have been overcome (***Bitzenhofer et al., 2017a***; ***Bitzenhofer et al., 2017b***). By these means, the local neuronal interplay generating beta-gamma oscillations in the PFC has been elucidated. However, the long-range coupling causing the activation of local prefrontal circuits is still unresolved. We previously proposed that the hippocampal CA1 area drives the oscillatory entrainment of PFC at neonatal age (***Brockmann et al., 2011***). Here, we developed a methodological approach to optically manipulate the neonatal HP along its septo-temporal axis. We provide causal evidence that theta frequency-specific activation of pyramidal neurons in the CA1 area of intermediate and ventral (i/

vHP), but not of dorsal HP (dHP) elicits broad band oscillations in the PFC of neonatal mice via dense axonal projections.

Results

Neonatal dorsal and intermediate/ventral hippocampus are differently entrained in discontinuous patterns of oscillatory activity

While different organization and function of dHP vs. i/vHP of adults have been extensively characterized (***Thompson et al., 2008***; ***Dong et al., 2009***; ***Patel et al., 2013***), their patterns of structural and functional maturation are still poorly understood. To fill this knowledge gap, we firstly examined the network oscillatory and firing activity of CA1 area of either dHP or i/vHP by performing extracellular recordings of the local field potential (LFP) and multiple unit activity (MUA) in neonatal [postnatal day (P) 8–10] non-anesthetized and urethane-anesthetized mice (n = 153). While urethane anesthesia led to an overall decrease of amplitude and power of oscillatory activity when compared to the non-anesthetized state of the same group of pups, the firing rate and timing as well as the synchrony and interactions within prefrontal-hippocampal networks were similar during both states (***Figure 1—figure supplement 1***). Due to the close proximity and the absence of reliable anatomical and functional borders between iHP and vHP at neonatal age, data from the two areas were pooled and referred as from i/vHP. The entire investigation was performed at the age of initiation of coupling between HP and PFC, that is, P8-10 (***Brockmann et al., 2011***). Independent of the position along the dorsal-ventral axis, the CA1 area was characterized by discontinuous oscillations with main frequency in theta band (4–12 Hz) and irregular low amplitude beta-gamma band components, which have been previously categorized as theta oscillations (***Brockmann et al., 2011***). They were accompanied by prominent sharp-waves (SPWs) reversing across the pyramidal layer (str. pyr.) and by strong MUA discharge (***Figure 1A and E***). While the general patterns of activity were similar in dHP and i/vHP, their properties significantly differed between the sub-divisions. The theta bursts in i/vHP had significantly higher occurrence (i/vHP: 8.1 ± 0.2 oscillations/min, n = 103 mice vs. dHP: 5.2 ± 0.3 oscillations/min, n = 41 mice; p<0.001), larger amplitude (i/vHP:110.6 ± 5.6 μV vs. dHP: 92.9 ± 2.6 μV; p=0.015), and shorter duration (i/vHP: 3.5 ± 0.1 s vs. dHP: 4.3 ± 0.1 s, p<0.001) when compared with dHP (***Figure 1B***, ***Figure 1—figure supplement 2A***). Investigation of the spectral composition of theta bursts revealed significant differences within theta band with a stronger activation of dHP (relative power: dHP: 13.0 ± 1.3, n = 41 mice; i/vHP: 10.3 ± 0.5, n = 103 mice; p=0.026), whereas the faster frequency components were similar along the septo-temporal axis (relative power: 12–30 Hz: dHP, 15.0 ± 1.6, n = 41 mice; i/vHP, 13.2 ± 0.7 n = 103 mice, p=0.22; 30–100 Hz: dHP, 6.3 ± 0.6, n = 41 mice; i/vHP: 5.2 ± 0.3, n = 103 mice; p=0.073) (***Figure 1C***, ***Figure 1—figure supplement 2B***).

Differences along the septo-temporal axis were detected both in hippocampal spiking and population events SPWs. Overall, pyramidal neurons in i/vHP fired at higher rates (0.45 ± 0.01 Hz, n = 557 units from 103 mice) than in the dHP (0.35 ± 0.02 Hz, n = 158 units from 41 mice; p=0.025) (***Figure 1D***). SPW in neonatal HP were more prominent in the dHP (712.8 ± 31.5 μV, n = 41 mice) when compared with those occurring in the i/vHP (223.8 ± 6.3 μV, n = 103 mice, p<0.001), yet their occurrence increased along the septo-temporal axis (dHP: 6.6 ± 0.5, n = 41 mice; i/vHP: 8.6 ± 0.2, n = 103 mice, p<0.001) (***Figure 1E and F***, ***Figure 1—figure supplement 2D***. In line with our previous results (***Brockmann et al., 2011***), SPWs were accompanied by prominent firing centered around the SPW peak (dHP, 232 units; i/vHP, 670 units) that were phase-locked to hippocampal ripples (***Figure 1—figure supplement 2C***). The power of ripples decreased along the septo-temporal axis (relative power: dHP, 24.4 ± 3.3, n = 41 mice; i/vHP, 6.1 ± 0.60, n = 103 mice, p<0.001) (***Figure 1G,H***). Similarly, the ripple-related spiking was stronger in dHP when compared with i/vHP (peak firing: dHP: 1.13 ± 0.09 Hz, n = 232 units; i/vHP 0.84 ± 0.03, n = 670, p<0.001) (***Figure 1I and J***).

These data show that the activity patterns in the dorsal and intermediate/ventral CA1 area differ in their properties and spectral structure.

Theta activity within dorsal and intermediate/ventral hippocampus differently entrains the neonatal prelimbic cortex

The different properties of network and neuronal activity in dHP vs. i/vHP led us to question their outcome for the long-range coupling in the developing brain. Past studies identified tight

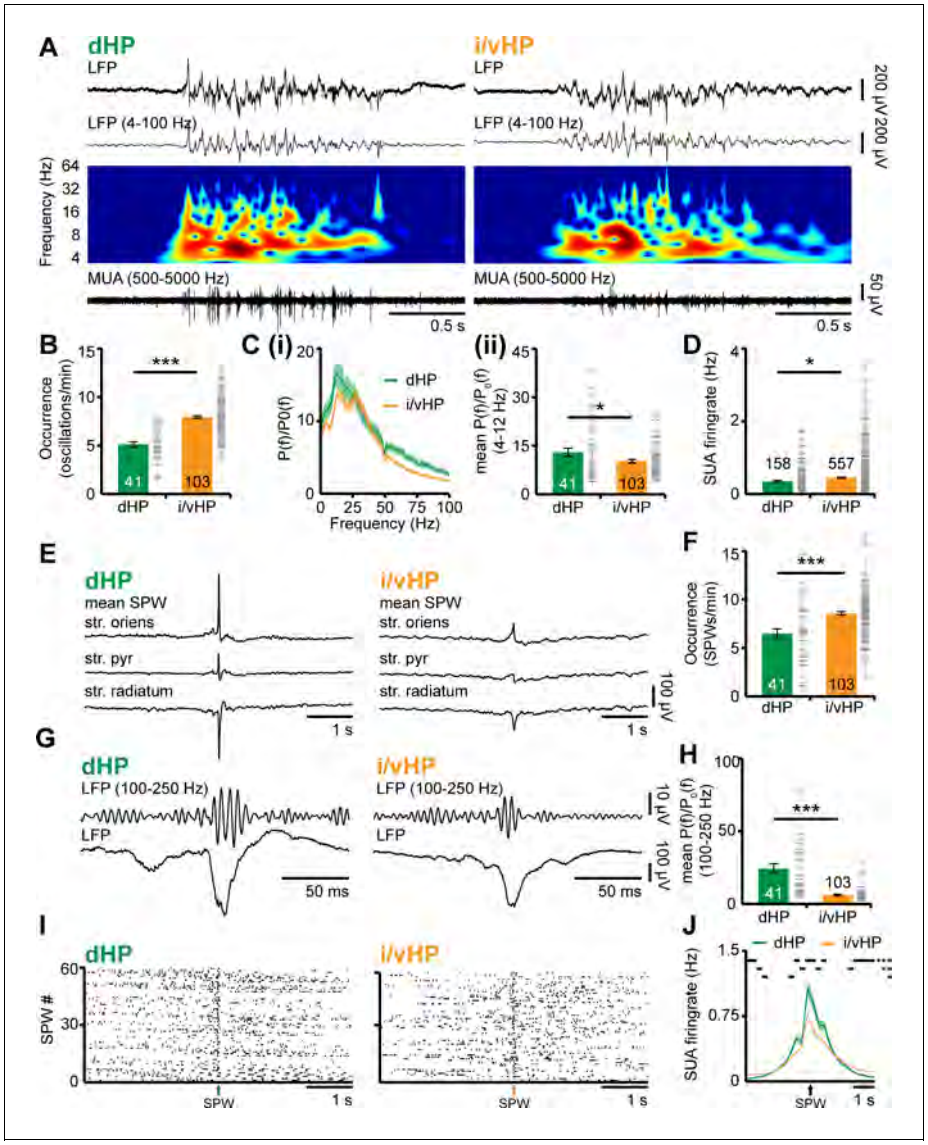

Figure 1. Patterns of discontinuous oscillatory activity in the CA1 area of the neonatal dHP and i/vHP in vivo. (**A**) Characteristic theta burst activity recorded in the CA1 area of the dHP (left) and i/vHP (right) of a P9 mouse displayed after band-pass filtering (4–100 Hz) and the corresponding MUA (500–5000 Hz). Color-coded frequency plots show the wavelet spectrum of LFP at identical time scale. (**B**) Bar diagram (mean ±SEM) displaying the occurrence of discontinuous theta bursts in dHP (n = 41 mice) and i/vHP (n = 103 mice). (**C**) Power analysis of discontinuous oscillatory activity P(f) normalized to the non-oscillatory period $P_0(f)$ in dHP and i/vHP. (i) Power spectra (4–100 Hz) averaged for all investigated mice. (ii) Bar diagrams quantifying the mean power within theta frequency band (4–12 Hz) in dHP (n = 41 mice) and i/vHP (n = 103 mice) (**D**) Bar diagram displaying the SUA of dHP (n = 158 units) and i/vHP (n = 557 units) after clustering of spike shapes. (**E**) Characteristic SPWs and ripple events recorded in dHP (left) and i/vHP (right). (**F**) Bar diagrams (mean ±SEM) displaying the SPWs occurrence in dHP and i/vHP. (**G**) Characteristic SPW-ripple events recorded in dHP (left) and i/vHP (right). (**H**) Bar diagram displaying the mean power of ripples in dHP and i/vHP. (**I**) Spike trains from neurons in dHP (left) and i/vHP (right) aligned to SPWs. (**J**) Histograms of SUA aligned to SPWs (n = 232 units for dHP, n = 670 for i/vHP). Data are represented as mean ± SEM. *p<0.05, **p<0.01, ***p<0.001.

DOI: https://doi.org/10.7554/eLife.33158.003

The following figure supplements are available for figure 1:

Figure supplement 1. Properties of network and neuronal activity in i/vHP of neonatal non-anesthetized and urethane-anesthetized mice.

DOI: https://doi.org/10.7554/eLife.33158.004

Figure supplement 2. Properties of network and neuronal activity in dHP vs. i/vHP of neonatal mice.

Figure 1 continued on next page

Figure 1 continued

DOI: https://doi.org/10.7554/eLife.33158.005

interactions between HP and PFC, which emerge already at neonatal age (**Brockmann et al., 2011**; **Hartung et al., 2016**) and are in support of memory at adulthood (**Krüger et al., 2012**; **Spellman et al., 2015**; **Place et al., 2016**). The discontinuous theta oscillations in HP have been proposed to drive the activation of local circuits in the PFC. To assess the coupling of dHP and i/vHP with PFC, we recorded simultaneously LFP and MUA in the corresponding hippocampal CA1 area and the prelimbic subdivision (PL) of the PFC of P8-10 mice. The entire investigation focused on PL, since in adults it is the prefrontal subdivision with the most dense innervation from HP (**Jay and Witter, 1991**; **Vertes et al., 2007**). In a first step, we examined the temporal correspondence of discontinuous oscillations recorded simultaneously in the PL and dHP, as well as in the PL and i/vHP. We previously characterized the network activity in the PL and showed that spindle-shaped oscillations switching between theta (4–12 Hz) and beta-gamma (12–40 Hz) frequency components alternate with periods of silence (**Brockmann et al., 2011**; **Cichon et al., 2014**; **Bitzenhofer et al., 2015**). The majority of prelimbic and hippocampal oscillations co-occurred within a narrow time window (**Figure 2A**). The temporal synchrony between prelimbic and hippocampal oscillations was assessed by performing spectral coherence analysis (**Figure 2B**). The results revealed a stronger coupling for PL-i/vHP (4–12 Hz: 0.17 ± 0.0069; 12–30 Hz: 0.31 ± 0.011; 30–100 Hz: 0.11 ± 0.0069, n = 103 mice) when compared with PL-dHP (4–12 Hz: 0.12 ± 0.0081; 12–30 Hz: 0.18 ± 0.0094; 30–100 Hz: 0.084 ± 0.004, n = 41 mice). In line with previous investigations, this level of coherence is a genuine feature of investigated neonatal networks and not the result of non-specific and conduction synchrony, since we considered only the imaginary component of the coherence spectrum, which excludes zero time-lag synchronization (**Nolte et al., 2004**).

Due to the symmetric interdependence of coherence, it does not offer reliable insights into the information flow between two brain areas. Therefore, in a second step, we estimated the strength of directed interactions between PL and HP by calculating the generalized partial directed coherence (gPDC) (**Baccala et al., 2007**; **Rodrigues and Baccala, 2016**) (**Figure 2C**). The method bases on the notion of Granger causality (**Granger, 1980**) and avoids distorted connectivity results due to different scaling of data in HP and PL (**Baccala et al., 2007**; **Taxidis et al., 2010**). Independent of the position along the septo-temporal axis, the information flow in theta or beta frequency band from either dorsal or intermediate/ventral HP to PL was significantly stronger than in the opposite direction. However, mean gPDC values for i/vHP → PL were significantly ($p<0.001$) higher (0.069 ± 0.003, n = 103 mice) when compared with those for dHP → PL (0.053 ± 0.003, n = 41 mice). Cross-correlation analysis confirmed these results (**Figure 2—figure supplement 1**). The stronger information flow from i/vHP to PL was confined to theta frequency range and was not detected for 12–30 Hz frequencies (i/vHP → PL: 0.048 ± 0.001; dHP → PL: 0.043 ± 0.002, $p=0.16$). Correspondingly, the firing of individual prelimbic neurons was precisely timed by the phase of oscillations in i/vHP but not dHP (**Figure 2D**). Almost 20% of clustered units (52 out of 310 units) were locked to theta phase in i/vHP, whereas only 6.5% of units (3 out of 46 units) were timed by dHP. The low number of locked cells in dHP precluded the comparison of coupling strength between the two hippocampal sub-divisions.

These results indicate that the distinct activity patterns in dHP and i/vHP at neonatal age have different outcomes in their coupling with the PL. Despite higher power, theta oscillations in dHP do not substantially account for prelimbic activity. In contrast, i/vHP seems to drive neuronal firing and network entrainment in the PL.

SPWs-mediated output of intermediate/ventral but not dorsal hippocampus times network oscillations and spiking response in the neonatal prelimbic cortex

Since SPWs and ripples in dHP significantly differ from those in i/vHP, they might have a distinct impact on the developing PFC. While abundant literature documented the contribution of SPWs-spindles complex to memory-relevant processing in downstream targets, such as PFC (**Colgin, 2011**; **Buzsáki, 2015**; **Colgin, 2016**), it is unknown how these complexes affect the development of cortical activation. Simultaneous recordings from neonatal CA1 area either in dHP or i/vHP and PL showed

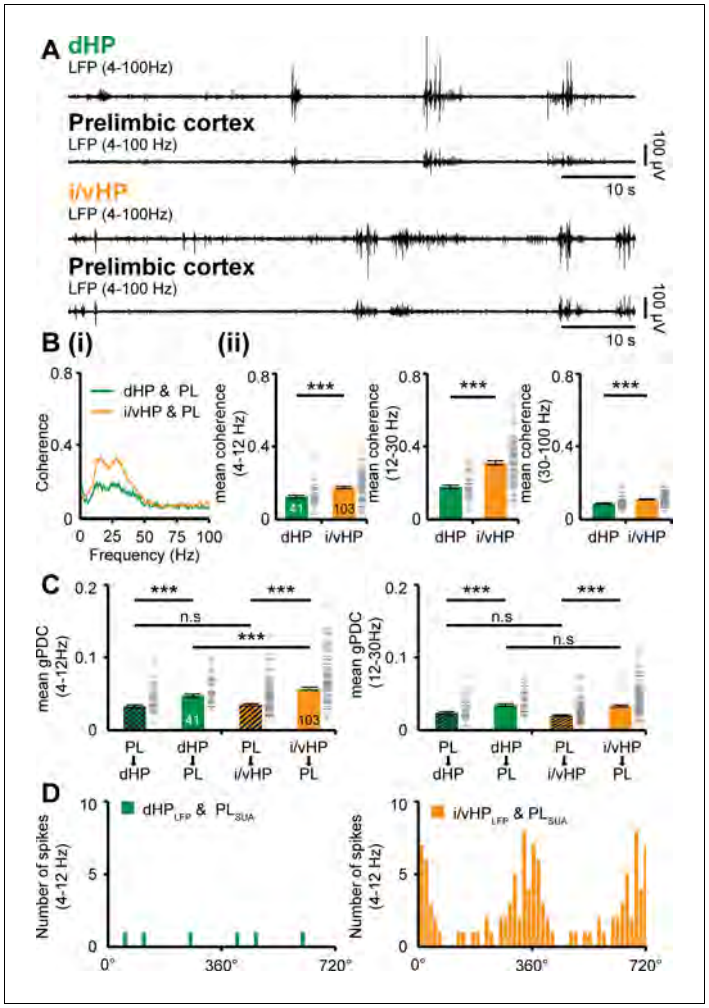

Figure 2. Dynamic coupling of hippocampal and prefrontal oscillatory activity along septo-temporal axis during neonatal development. (**A**) Simultaneous LFP recordings of discontinuous oscillatory activity in dHP and PL (top) and i/vHP and PL (bottom). (**B**) Long-range synchrony within prefrontal-hippocampal networks. (**i**) Average coherence spectra for simultaneously recorded oscillatory events in dHP and PL as well as i/vHP and PL. (ii) Bar diagrams (mean ±SEM) displaying the coherence in theta (4–12 Hz), beta (12–30 Hz), and gamma (30–100 Hz) band when averaged for all investigated mice. (**C**) Directed interactions between PL and either dHP or i/vHP monitored by general Partial Directed Coherence (gPDC). Bar diagrams displaying the gPDC calculated for theta (4–12 Hz, left) and beta (12–30 Hz, right) frequency and averaged for all investigated animals (n = 41 mice for dHP and PL, n = 103 mice for i/vHP and PL). (**D**) Histograms displaying the phase-locking of prelimbic spikes to theta oscillations in dHP (left) and i/vHP (right). Note the different proportion of spikes significantly locked along the septo-temporal axis (dHP, 3 of 46 units; i/vHP, 52 of 310 units). Data are represented as mean ± SEM. *p<0.05, ***p<0.001.

DOI: https://doi.org/10.7554/eLife.33158.006

The following figure supplement is available for figure 2:

Figure supplement 1. Cross-correlation of the amplitudes of band pass (4–12 Hz)-filtered LFP recorded from dHP and PL (green) as well as from i/vHP and PL (orange).

DOI: https://doi.org/10.7554/eLife.33158.007

that already at neonatal age, prefrontal oscillations are generated shortly (~100 ms) after hippocampal SPWs-ripples. This prelimbic activation is significantly stronger when induced by SPWs-ripples emerging in i/vHP than in dHP as reflected by the significantly higher power of oscillatory activity in theta (PL for dHP: 186.9 ± 12.5 μV^2; PL for i/vHP: 249.5 ± 14.5 μV^2, p=0.0088), beta (PL for dHP: 34.3 ± 3.3 μV^2; PL for i/vHP: 48.1 ± 2.8 μV^2, p=0.0049), and gamma (PL for dHP: 11.3 ± 0.9 μV^2; PL for i/vHP: 17.4 ± 1.2 μV^2, p=0.0026) frequency band (***Figure 3A***). The SPWs-ripple-induced

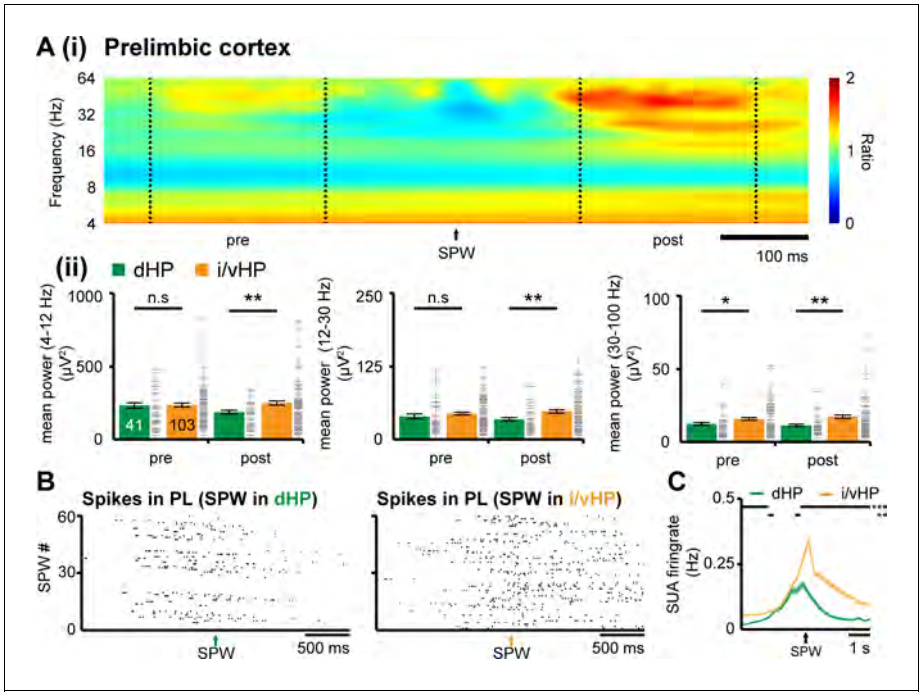

Figure 3. Coupling between neonatal PFC and HP during hippocampal SPWs. (**A**) Power changes in the PL during hippocampal SPWs. (i) Color-coded frequency plot showing the relative power in the PL aligned to the onset of SPWs detected in i/vHP when normalized to the power change caused in the PL by SPWs in the dHP. All other colors than green represent power augmentation (red) or decrease (blue). (ii) Bar diagrams displaying mean power changes of prelimbic activity in different frequency bands (left, theta; middle, beta; right, gamma) before (pre) and after (post) hippocampal SPWs in the dHP and i/vHP (n = 41 mice for dHP, n = 103 mice for i/vHP). (**B**) Spike trains recorded in the PL before and after SPWs occurring either in the dHP (left) or i/vHP (right). (**C**) Histograms of prelimbic spiking in relationship with hippocampal SPWs (n = 148 units for dHP, n = 560 units for i/vHP). Data are represented as mean ± SEM. *p<0.05, **p<0.01, ***p<0.001.

DOI: https://doi.org/10.7554/eLife.33158.008

The following figure supplement is available for figure 3:

Figure supplement 1. Phase-locking of SUA in PL before (pre) and after (post) SPWs detected in dHP (top, green) and i/vHP (bottom, orange).

DOI: https://doi.org/10.7554/eLife.33158.009

oscillatory activity in the PL of neonatal mice was accompanied by augmentation of firing rates. While the induced firing in i/vHP peaked (≈90 ms) after SPWs-ripples and remained significantly (p<0.001) elevated for several seconds, a less prominent peak was observed following SPW-ripples in dHP (***Figure 3B and C***). The phase-locking of prelimbic units was similar before and after SPWs (***Figure 3—figure supplement 1***).

These data reveal that SPWs-ripples from intermediate/ventral but less from the dorsal part of hippocampal CA1 correlate with pronounced neuronal firing and local entrainment in the PL of neonatal mice.

Pyramidal neurons in intermediate/ventral but not dorsal hippocampus densely project to the prefrontal cortex at neonatal age

To identify the anatomical substrate of different coupling strength between i/vHP - PL and dHP - PL, we monitored the projections that originate from the CA1 area in both hippocampal subdivisions and target the PFC. The direct unilateral projections from hippocampal CA1 area to PL have been extensively investigated in adult brain (***Swanson, 1981***; ***Jay and Witter, 1991***; ***Vertes et al., 2007***) and are present already at neonatal age (***Brockmann et al., 2011***; ***Hartung et al., 2016***). We tested for sub-division-specific differences by using retrograde and anterograde tracing. First, we injected unilaterally small amounts of the retrograde tracer Fluorogold (FG) into the PL of P7 mice (n = 8

mice). Three days after FG injections, labeled cells were found in str. pyr. of CA1 in both dHP and i/vHP (***Figure 4A***). However, their density was significantly different ($p<0.001$); whereas in dHP very few cells were retrogradely labeled ($0.15*10^3 \pm 0.074*10^3$ cells/mm^2), a large proportion of pyramidal-shaped cells in the CA1 area of i/vHP projects to PL ($3.29*10^3 \pm 0.19*10^3$ cells/mm^2).

Second, the preferential innervation of PL by pyramidal neurons from CA1 area of i/vHP was confirmed by anterograde staining with BDA (n = 9 mice). Small amounts of BDA were injected into the CA1 area of i/vHP (***Figure 4B***). They led to labeling of the soma and arborized dendritic tree of pyramidal neurons in str. pyr. with the characteristic orientation of axons. In 7 out of 9 mice anterogradely-labeled axons were found in the PL, preferentially within its deep layers V and VI.

Thus, the dense axonal projections from CA1 area of i/vHP might represent the substrate of HP-induced oscillatory entrainment of prelimbic circuits.

Selective light manipulation of pyramidal neurons and interneurons in CA1 area of intermediate/ventral but not dorsal hippocampus causes frequency-specific changes in the oscillatory entrainment of neonatal prelimbic circuits

The tight coupling by synchrony and the directed information flow from hippocampal CA1 area to PL via direct axonal projections suggest that the HP acts already at neonatal age as a drive for prelimbic activation. Moreover, the differences identified between the dHP – PL and i/vHP – PL communication argue for prominent augmentation of driving force along the septo-temporal hippocampal

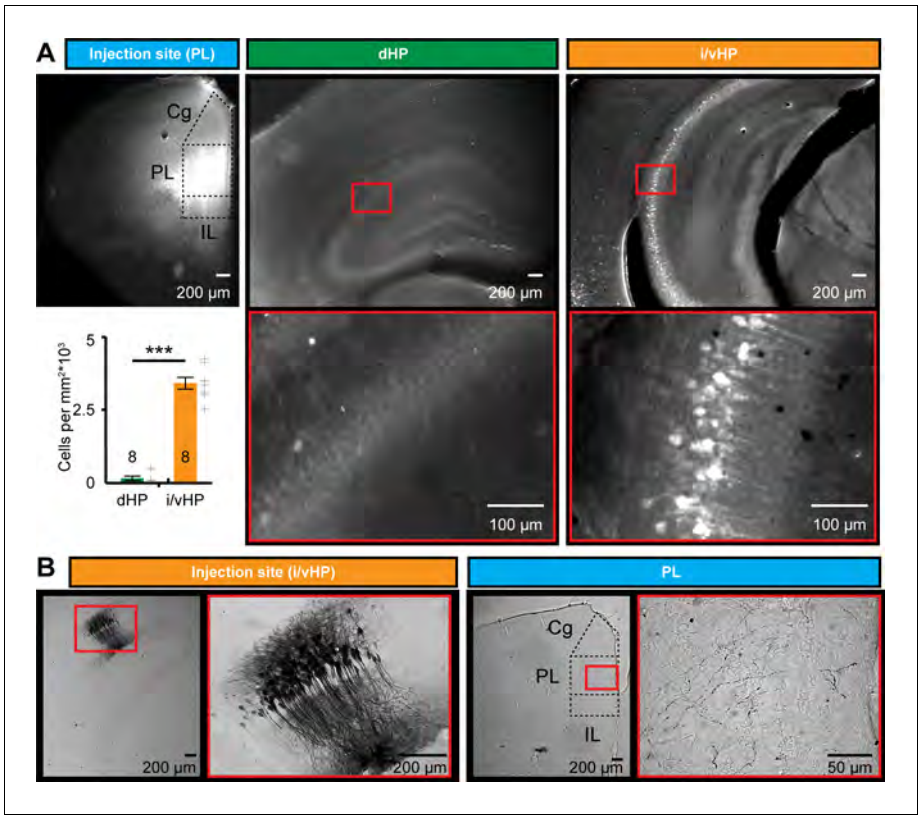

Figure 4. Long-range monosynaptic axonal projections connecting the neonatal PFC and hippocampal CA1 area along the septo-temporal axis. (**A**) Photomicrographs depicting dense retrogradely labelled neurons in the CA1 area of i/vHP (right) but not dHP (middle) after FG injection into PL at P1 (left). Bar diagram displays the overall density of retrogradely stained neurons when averaged for all investigated pups (n = 8 mice). (**B**) Photomicrographs depicting anterogradely labeled axons targeting the PL of a P10 mouse (right) after iontophoretic BDA injection into the CA1 area of i/vHP at P7 (left). The site of injection and the area with the highest axonal density are depicted at higher magnification. Data are represented as mean ± SEM. ***p<0.001.
DOI: https://doi.org/10.7554/eLife.33158.010

axis. To causally confirm these correlative evidences, we selectively activated by light the pyramidal neurons in the CA1 area of either dHP or i/vHP that had been transfected with a highly efficient fast-kinetics double mutant ChR2E123T/T159C (ET/TC) (**Berndt et al., 2011**) and the red fluorescent protein tDimer2 by *in utero* electroporation (IUE) (**Figure 5—figure supplement 1A**). This method enables stable area and cell type-specific transfection of neurons already prenatally without the need of cell-type specific promotors of a sufficiently small size (**Baumgart and Grebe, 2015**; **Szczurkowska et al., 2016**). To target neurons along the septo-temporal axis, distinct transfection protocols were used. When the IUE was performed with two paddles placed 25˚ leftward angle from the midline and a 0˚ angle downward from anterior to posterior, tDimer-positive neurons were mainly found in the CA1 area of the dHP, as revealed by the analysis of consecutive coronal sections from IUE-transfected P8-10 mice. Targeting of i/vHP succeeded only when three paddles were used, with both positive poles located at 90˚ leftward angle from the midline and the third negative pole at 0˚ angle downward from anterior to posterior (**Figure 5A**, S2B). Staining with NeuN showed that a substantial proportion of neurons in str. pyr. of CA1 area (dHP: 18.3 ± 1.0%; n = 36 slices from 13 mice; i/vHP: 14.5 ± 1.5%, n = 12 slices from 11 mice) were transfected by IUE. The shape of tDimer2-positive neurons, the orientation of primary dendrites, and the absence of positive staining for GABA confirmed that the light-sensitive protein ChR2(ET/TC) was integrated exclusively into cell lineages of pyramidal neurons (**Figure 5A**). Omission of ChR2(ET/TC) from the expression construct (i.e. opsin-free) yielded similar expression rates and distribution of tDimer2-positive neurons (**Figure 5—figure supplement 1C**).

To exclude non-specific effects of transfection procedure by IUE on the overall development of mice, we assessed the developmental milestones and reflexes of electroporated opsin-expressing and opsin-free mice (**Figure 5—figure supplement 1D**). While IUE caused significant reduction of litter size (non-electroporated 6.5 ± 0.7 pups/litter, electroporated: 4.5 ± 0.5 pups/litter, p=0.017), all investigated pups had similar body length, tail length, and weight during early postnatal period. Vibrissa placing, surface righting and cliff aversion reflexes were also not affected by IUE or transfection of neurons with opsins. These data indicate that the overall somatic development during embryonic and postnatal stage of ChR2(ET/TC)-transfected mice is unaltered.

We first assessed the efficiency of light stimulation in evoking action potentials in hippocampal pyramidal neurons in vivo. Blue light pulses (473 nm, 20–40 mW/mm^2) at different frequencies (4, 8, 16 Hz) led shortly (<10 ms) after the stimulus to precisely timed firing of transfected neurons in both dHP and i/vHP. Our previous experimental data and modeling work showed that the used light power did not cause local tissue heating that might interfere with neuronal spiking (**Stujenske et al., 2015**; **Bitzenhofer et al., 2017b**). For both hippocampal sub-divisions the efficiency of firing similarly decreased with augmenting frequency (**Figure 5B**). For stimulation frequencies >16 Hz, the firing lost the precise timing by light, most likely due to the immaturity of neurons and their projections.

To decide whether activation of HP boosts the entrainment of prelimbic circuits, we simultaneously performed multi-site recordings of LFP and MUA in PL and HP during pulsed light stimulation of CA1 area of dHP (n = 22 mice) or i/vHP (n = 9 mice) (**Figure 5C**). The firing in i/vHP timed by light at 8 Hz, but not at 4 Hz or 16 Hz, caused significant (theta: p=0.039, beta: p=0.030, gamma: p=0.0036) augmentation of oscillatory activity in all frequency bands as reflected by the higher power in the PL during the stimulation when compared with the time window before the train of pulses (**Figure 5D**, **Table 1**). In contrast, stimulation by light of dHP left the prelimbic activity unaffected. In opsin-free animals, stimulation of dHP and i/vHP led to no significant changes in the oscillatory activity (**Figure 5—figure supplement 2A**, **Table 1**). Rhythmic firing of prelimbic neurons was not detected after light activation of hippocampal subdivisions, most likely because hippocampal axons were rather sparse.

To confirm the driving role of i/vHP for the generation of oscillatory activity in PL, we selectively transfected Dlx5/6 positive interneurons with either ChETA or archaerhodopsin (ArchT). Blue light stimulation (473 nm) confined to i/vHP of Dlx5/6–ChETA mice (n = 19) led to a significant reduction of hippocampal power in all frequency bands (theta: p=0.024, beta: p=0.018, gamma: p=0.044). Correspondingly, the oscillatory activity in PL diminished (theta: p=0.027, beta: p=0.077, gamma: p=0.019) (**Figure 6A,B**). Silencing of interneurons in Dlx5/6-ArchT mice (n = 13) by yellow light (600 nm) had an opposite effect and caused augmentation of oscillatory activity both within i/vHP (theta:

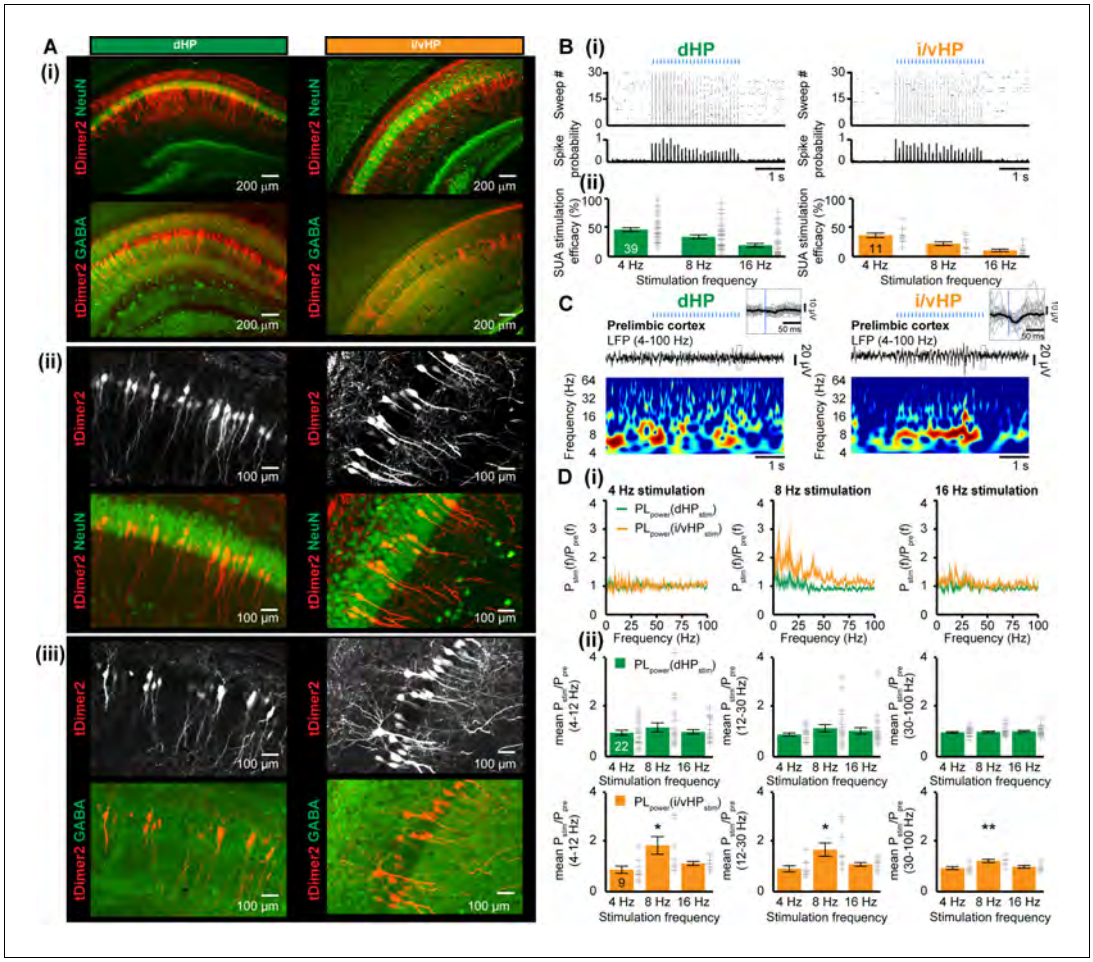

Figure 5. Optogenetic activation of pyramidal neurons in the CA1 area of dHP and i/vHP has different effects on the network activity of neonatal PL. (**A**) Cell- and layer-specific transfection of dHP or i/vHP with CAG-ChR2(ET/TC)−2A-tDimer2 by site-directed IUE. (**i**) Photomicrographs depicting tDimer2-expressing pyramidal neurons (red) in the CA1 region of dHP (left) and i/vHP (right) when stained for NeuN (green, top panels) or GABA (green, bottom panels). (ii) Photomicrographs depicting the transfected hippocampal neurons when co-stained for NeuN and displayed at larger magnification. (iii) Photomicrographs depicting transfected hippocampal neurons when co-stained for GABA and displayed at larger magnification. (**B**) Optogenetic activation of pyramidal neurons in CA1 area along septo-temporal axis. (i) Representative raster plot and corresponding spike probability histogram for dHP (left) and i/vHP (right) in response to 30 sweeps of 8 Hz pulse stimulation (3 ms pulse length, 473 nm). (ii) Bar diagram displaying the efficacy of inducing spiking in dHP and i/vHP of different stimulation frequencies. (**C**) Characteristic light-induced discontinuous oscillatory activity in the PL of a P10 mouse after transfection of pyramidal neurons in the CA1 area of the dHP (left) or i/vHP (right) with ChR2(ET/TC) by IUE. The LFP is displayed after band-pass filtering (4–100 Hz) together with the corresponding color-coded wavelet spectrum at identical time scale. Inset, individual (gray) and averaged (black) prelimbic LFP traces displayed at larger time scale in response to light stimulation in HP. (**D**) Power analysis of prelimbic oscillatory activity $P_{stim}(f)$ after light stimulation of dHP (green) and i/v HP (orange) at different frequencies (4, 8, 16 Hz) normalized to the activity before stimulus $P_{pre}(f)$. (i) Power spectra (0–100 Hz) averaged for all investigated mice. (ii) Bar diagrams displaying mean power changes in PL during stimulation of either dHP (top panels) or i/vHP (bottom panels). Data are represented as mean ± SEM. *p<0.05, **p<0.01.

DOI: https://doi.org/10.7554/eLife.33158.011

The following figure supplements are available for figure 5:

Figure supplement 1. Experimental protocol for *in utero* electroporation of the hippocampus.

DOI: https://doi.org/10.7554/eLife.33158.012

Figure supplement 2. Response in prelimbic cortex for opsin-free animals.

DOI: https://doi.org/10.7554/eLife.33158.013

p<0.001, beta: p=0.0012, gamma: p<0.001) and PL (theta: p<0.001, beta: p<0.001, gamma: p<0.001) (***Figure 6A,C***).

Table 1. Mean power changes in PL after light stimulation of dHP or i/vHP in ChR2(ET/TC)-containing and opsin-free animals.
*p<0.05, **p<0.01.

	dHP			I/vHP		
	Stimulation frequency			Stimulation frequency		
ChR2(ET/TC)	4 Hz	8 Hz	16 Hz	4 Hz	8 Hz	16 hz
Theta	0.97 ± 0.10	1.19 ± 0.19	1.0 ± 0.093	0.90 ± 0.15	1.89 ± 0.36 (*)	1.16 ± 0.08
Beta	0.91 ± 0.06	1.17 ± 0.15	1.06 ± 0.13	0.94 ± 0.12	1.72 ± 0.27 (*)	1.12 ± 0.08
Gamma	1.0 ± 0.035	1.00 ± 0.19	1.04 ± 0.38	0.97 ± 0.06	1.26 ± 0.06 (**)	1.02 ± 0.06
Opsinfree						
Theta	1.11 ± 0.14	1.09 ± 0.19	1.14 ± 0.22	1.17 ± 0.27	1.17 ± 0.20	1.16 ± 0.12
Beta	1.13 ± 0.15	0.99 ± 0.16	1.11 ± 0.11	1.05 ± 0.22	0.95 ± 0.18	1.08 ± 0.13
Gamma	1.08 ± 0.06	0.93 ± 0.04	1.03 ± 0.03	0.89 ± 0.09	0.94 ± 0.07	0.97 ± 0.04

DOI: https://doi.org/10.7554/eLife.33158.014

Taken together, these data reveal the critical role of hippocampal activity for the oscillatory entrainment of PL and identify pyramidal neurons in CA1 area of of i/vHP but not dHP as drivers for the broad activation of local prelimbic circuits.

Discussion

Combining selective optogenetic activation with extracellular recordings and tracing of projections in neonatal mice in vivo, we provide causal evidence that theta activity in the CA1 area of i/vHP but not dHP drives network oscillations within developing prefrontal cortex. Despite stronger theta power in the dHP, solely optical activation of the pyramidal neurons in i/vHP at theta frequency range (8 Hz) boosted the emergence of discontinuous oscillatory activity in theta and beta-gamma bands in the neonatal PFC. These data identify the cellular substrate of the directed interactions between neonatal hippocampus and prefrontal cortex and offer new perspectives for the interrogation of long-range coupling in the developing brain and its behavioral readout.

Distinct patterns of functional maturation in dorsal and intermediate/ventral hippocampus

The abundant literature dedicated to the adult hippocampus mainly deals with a single cortical module (***Amaral et al., 2007***). However, an increasing number of studies in recent years revealed distinct organization, processing mechanisms and behavioral relevance for dHP vs. i/vHP (***Fanselow and Dong, 2010***; ***Bannerman et al., 2014***; ***Strange et al., 2014***). For example, the dHP, which receives dense projections from the entorhinal cortex (***Witter and Amaral, 2004***), is mainly involved in spatial navigation (***O'Keefe and Nadel, 1978***; ***Moser et al., 1995***; ***Moser et al., 1998***). In contrast, the ventral part receives strong cholinergic and dopaminergic innervation (***Witter et al., 1989***; ***Pitkänen et al., 2000***) and contributes to processing of non-spatial information (***Bannerman et al., 2003***; ***Bast et al., 2009***). Correspondingly, the network and neuronal activity changes along the septo-temporal axis. The power of the most prominent activity pattern in the adult HP, the theta oscillations, as well as the theta timing of the neuronal firing was found to be substantially reduced in the i/vHP when compared with dHP (***Royer et al., 2010***). By these means, the precise spatial representation deteriorates along the septo-temporal axis, since theta activity is directly linked to place cell representation (***O'Keefe and Recce, 1993***; ***Geisler et al., 2007***). In contrast, SPWs are more frequent and ripples have higher amplitude and frequency in the ventral HP than in the dHP (***Patel et al., 2013***).

Our data uncovered that some of these differences in the activity patterns along the septo-temporal axis emerge already during early neonatal development. Similar to findings from adult rodents, the power of theta bursts at neonatal age was higher in dHP than in i/vHP. The amplitude of SPWs and the power of ripples decreased along the septo-temporal axis. These findings give insights into the mechanisms underlying the early generation of activity patterns. It has been proposed that the differences in theta dynamics along the septo-temporal axis result from distinct innervation, on the

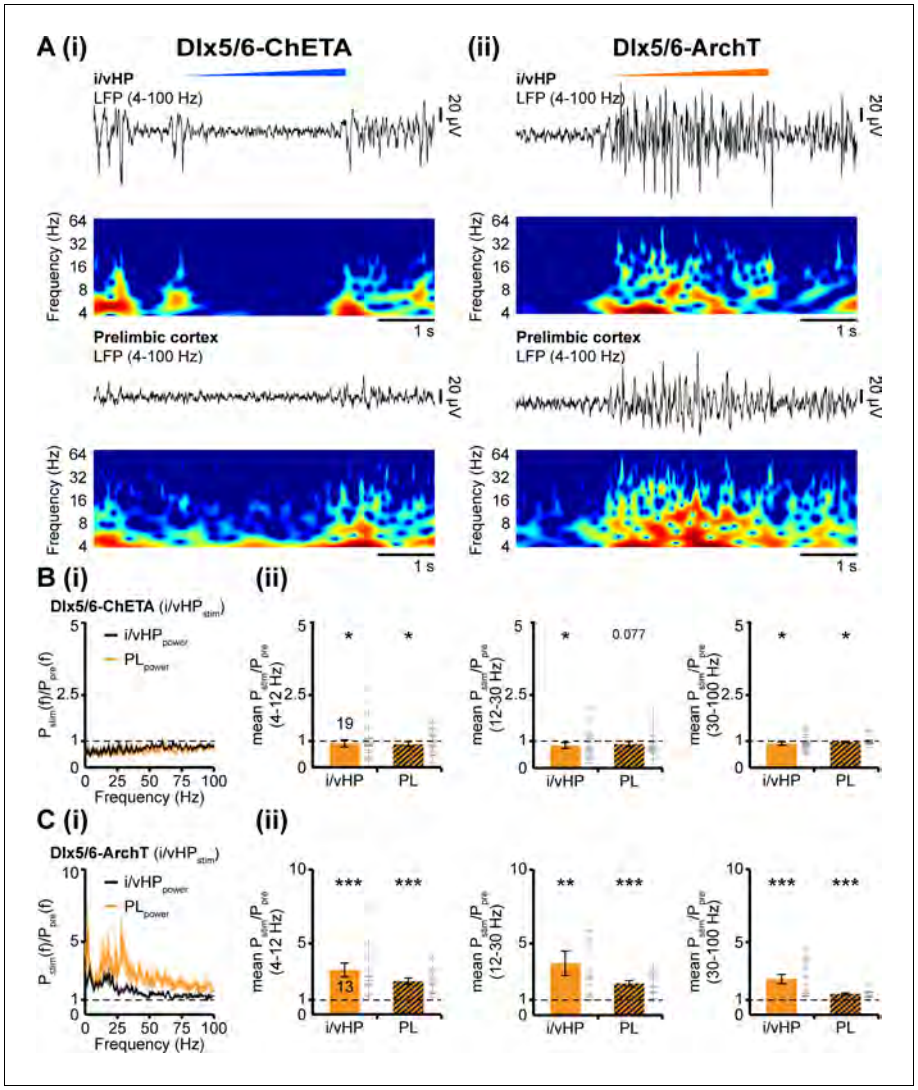

Figure 6. Modulation of oscillatory activity in i/vHP by optogenetic manipulation of interneurons affects the entrainment of neonatal PL. (**A**) Light-induced modulation of oscillatory activity in i/vHP and PL of a P9 mouse after transfection of interneurons in the CA1 area of the i/vHP with ChETA (i) or ArchT (ii). The LFP is displayed after band-pass filtering (4–100 Hz) together with the corresponding color-coded wavelet spectrum at identical time scale. (**B**) Power of oscillatory activity in i/vHP and PL after optogenetic activation of interneurons in i/vHP ($P_{stim}(f)$) normalized to the activity before stimulus $P_{pre}(f)$. (i) Power spectra (0–100 Hz) averaged for all investigated mice. (ii) Bar diagrams displaying mean power changes in theta, beta, and gamma frequency bands for the oscillations recorded in i/vHP and PL during light stimulation in i/vHP. (**C**) Same as (**B**) for silencing of ArchT-transfected interneurons in i/vHP by yellow light. Data are shown as mean ± SEM. *p<0.05, **p<0.01, ***p<0.001.
DOI: https://doi.org/10.7554/eLife.33158.015

one hand, and from specific intrinsic properties of hippocampal neurons, on the other hand. Cholinergic projections of different origin in the dHP and i/vHP (***Stewart and Fox, 1990***; ***Amaral et al., 2007***) as well as maturational differences in the intrinsic resonant properties of hippocampal neurons and notable gradients of parvalbumin immunoreactivity along the septo-temporal axis (***Honeycutt et al., 2016***) may contribute to the observed differences.

Quantification along the septo-temporal axis revealed that, similar to adults, the occurrence of SPWs was higher in the i/vHP and their amplitude was larger in the neonatal dHP (***Patel et al., 2013***). It is still an issue of debate when exactly ripples emerge in the developing hippocampus, although it is obvious that they appear later than theta bursts and SPWs, most likely towards the end of the first and during second postnatal week (***Buhl and Buzsáki, 2005***; ***Brockmann et al.,***

2011). Their underlying mechanisms at neonatal age remain also largely unknown and need to be related to age-dependent changes in gap junctional coupling and GABA switch (Ben-Ari et al., 1989; Zhang et al., 1990; Yuste et al., 1995). The organization of SPWs and ripples is of particular relevance when considering their impact on the early activity of PFC. Already at neonatal age, the prelimbic firing and oscillatory entrainment is timed by SPWs-ripples. Of note, the degree of timing varies along the septo-temporal axis and is much higher for the i/vHP.

Optogenetic interrogation of long-range coupling in the developing brain

At adult age the communication between PFC and HP has been investigated in relationship with memory tasks both under physiological and disease-related conditions (Sirota et al., 2008; Adhikari et al., 2010; Sigurdsson et al., 2010; Eichenbaum, 2017). Depending on the phase of memory processing, the prefrontal-hippocampal coupling via oscillatory synchrony has been found to be either unidirectional from the HP to PFC or bidirectional (Siapas et al., 2005; Hallock et al., 2016; Place et al., 2016). Both theta and gamma network oscillations contribute to the functional long-range coupling. The model of prefrontal-hippocampal communication has been initially built based on experimental evidence correlating the temporal organization of neuronal and network activity in the two brain areas. The time delay between spike trains and oscillatory phase or between oscillations enabled to propose that the information flows in one direction or the other via mono- or polysynaptic axonal projections. More recently, a direct causal assessment of the coupling became possible through optogenetic interrogation of neural circuits. In a seminal study, Spellman and colleagues used light-driven inhibition of axonal terminals for dissecting the directionality of interactions between PFC and HP during different phases of memory retrieval (Spellman et al., 2015).

We previously showed that at neonatal age, long before full maturation of memory and attentional abilities, discontinuous theta bursts in i/vHP are temporally correlated to the network oscillations in the PFC and time the prefrontal firing (Brockmann et al., 2011; Hartung et al., 2016). Moreover, the temporal delay of 10–20 ms between prefrontal and hippocampal spike trains as well as the estimated directionality of information flow between the two areas suggested that hippocampal theta drives the oscillatory entrainment of the local circuits in the PFC. The present data directly prove this hypothesis, taking advantage of the recently developed protocol for optogenetic manipulation of neuronal networks at neonatal age (Bitzenhofer et al., 2017a, 2017b). We observed that prelimbic circuits were effectively entrained when the stimulation of paramidal neurons in i/vHP occurred at 8 Hz but not at 4 Hz or 16 Hz. Such frequency-specific effect might result from intrinsic resonance properties of neurons mediated through hyperpolarization-activated cyclic nucleotide-gated (HCN) channels (Hu et al., 2002; Stark et al., 2013). It has been previously proposed that oscillatory activity in cortical regions may be entrained due to the rhythmic theta-band output from the hippocampus (Stark et al., 2013; Colgin, 2016).

Several considerations regarding the technical challenges of optogenetic manipulation of HP along the septo-temporal axis need to be made. Besides the inherent difficulties related to the specificity of promoters for selective transfection and the targeting procedure that are ubiquitary for all developing networks and have been addressed elsewhere (Bitzenhofer et al., 2017a), confinement of light-sensitive proteins to pyramidal neurons of either dHP or i/vHP required special attention. In a previous study (Bitzenhofer et al., 2017b), we developed a selective targeting protocol of neonatal neurons that relies on the combination of CAG promoter and IUE. By these means, the expression of light-sensitive proteins in the neurons located in the neocortical layer and area of interest was sufficiently high to ensure their reliable activation. Similarly, the expression of ChR2(ET/TC) in the pyramidal neurons of hippocampal CA1 area under the CAG promoter was sufficiently high to reliably cause network and neuronal activity. Taking into account that viral transduction, which usually requires 10–14 days for stable expression, is only of limited usability to investigate local network interactions during development, IUE seems to represent the method of choice for manipulating circuits at this early age. IUE enables targeting of precursor cells of neuronal and glial subpopulations, based on their distinct spatial and temporal patterns of generation in the ventricular zone (Tabata and Nakajima, 2001; Borrell et al., 2005; Niwa et al., 2010; Hoerder-Suabedissen and Molnár, 2015). IUE based on two electrode paddles enabled selective targeting of pyramidal neurons in the CA1 area of dHP in more than half of the pups per litter (Figure 5—figure supplement 1), but it completely failed (0 out of 32 mice) to target these neurons in i/vHP. Therefore, it was

necessary to use a modified IUE protocol based on three electrodes. This protocol, although more complicated and time consuming, allows reliable transfection at brain locations that are only able to be sporadically targeted by two electrodes The IUE-induced expression of light sensitive proteins enables the reliable firing of neurons in both dHP and i/vHP in response to light pulses. One intriguing question is how many pyramidal neurons in str. pyr. of CA1 area must be synchronously activated to drive the oscillatory entrainment of prelimbic circuitry. Anterograde and retrograde tracing demonstrated the density increase along the septo-temporal axis of hippocampal axons targeting the PL. Light activation/inhibition of these axonal terminals paired with monitoring of network oscillations in the PFC might offer valuable insights into the patterns of coupling sufficient for activation.

Functional relevance of frequency-specific drive within developing prefrontal-hippocampal networks

Abundant literature links theta frequency coupling within prefrontal-hippocampal networks to cognitive performance and emotional states of adults (***Adhikari et al., 2010***; ***Xu and Südhof, 2013***; ***Spellman et al., 2015***; ***Hallock et al., 2016***; ***Place et al., 2016***; ***Ye et al., 2017***). The early emergence of directed communication between PFC and i/vHP raises the question of functional relevance of this early coupling during development and at adulthood.

The maturation of cognitive abilities is a process even more protracted than sensory development and starts during second-third postnatal week (***Hanganu-Opatz, 2010***; ***Cirelli and Tononi, 2015***). Some of these abilities, such as recognition memory, can be easily monitored at early age and seems to critically rely on structurally and functionally intact prefrontal-hippocampal networks (***Krüger et al., 2012***). Direct assessment of the role of neonatal communication for memory performance as performed for adult circuits is impossible due to the temporal delay of the two processes. The alternative is to manipulate the activity of either PFC, HP or the connectivity between them during defined developmental time windows and monitor the juvenile and adult consequences at structural, functional and behavioral levels. The present data and optogenetic protocol represent the prerequisite of this investigation, opening new perspectives for assessing the adult behavioral readout of long-range communication in the developing brain.

One question that remains to be addressed is how the hippocampal theta drive shapes the maturation of prefrontal-hippocampal networks. Following the general rules of activity-dependent plasticity (***Hubel et al., 1977***; ***Huberman et al., 2006***; ***Xu et al., 2011***; ***Yasuda et al., 2011***), the precisely timed excitatory inputs from the i/vHP to the PL might facilitate the wiring of local prefrontal circuitry and enable the refinement of behaviorally relevant communication scaffold between the two regions. By these means, the prefrontal activity driven by projection neurons in the HP act as a template, having a pre-adaptive function that facilitates the tuning of circuits with regard to future conditions. This instructive role of theta activity for the prefrontal circuits needs to be proven by manipulation of temporal structure of the hippocampal drive without affecting the overall level of activity. Understanding the rules that govern the early organization of large-scale networks represents the pre-requisite for identifying the structural and functional deficits related to abnormal behavior and disease.

Materials and methods

Key resources table

Reagent type (species) or resource	Designation	Source or reference	Identifiers	Additional information
antibody	mouse monoclonal Alexa Fluor-488 conjugated antibody against NeuN	Merck Millipore	MAB377X	1:200 dilution
antibody	rabbit polyclonal primary antibody against GABA	Sigma-Aldrich	A2052	1:1000 dilution
antibody	Alexa Fluor-488 goat anti-rabbit IgG secondary antibody	Merck Millipore	A11008	1:500 dilution

Continued on next page

Continued

Reagent type (species) or resource	Designation	Source or reference	Identifiers	Additional information
chemical compound, drug	Isoflurane	Abbott	B506	
chemical compound, drug	Urethane	Fluka analytical	94300	
chemical compound, drug	Fluorogold	Fluorochome, LLC	52–9400	
chemical compound, drug	Biotinylated dextran amine, 10.000 MW	Thermo Fisher Scientific	D1956	
commercial assay or kit	NucleoBond PC 100	Macherey-Nagel	740573	
strain, strain background (mouse, both genders)	C57Bl/6J	Universitätsklinikum Hamburg-Eppendorf – Animal facility	C57Bl/6J	https://www.jax.org/strain/008199
strain, strain background (mouse, both genders)	Tg(dlx5a-cre)1Mekk/J	The Jackson Laboratory	Tg(dlx5a-cre)1Mekk/J	https://www.jax.org/strain/017455
strain, strain background (mouse, both genders)	R26-CAG-LSL-2XChETA-tdTomato	The Jackson Laboratory	R26-CAG-LSL-2XChETA-tdTomato	https://www.jax.org/strain/021188
strain, strain background (mouse, both genders)	Ai40(RCL-ArchT/EGFP)-D	The Jackson Laboratory	Ai40(RCL-ArchT/EGFP)-D	
recombinant DNA reagent	pAAV-CAG-ChR2 (E123T/T159C) −2AtDimer2	Provided by T. G. Oertner	pAAV-CAG-ChR2 (E123T/T159C) −2AtDimer2	http://www.oertner.com/
recombinant DNA reagent	pAAV-CAG-tDimer2	Provided by T. G. Oertner	pAAV-CAG-tDimer2	http://www.oertner.com/
software, algorithm	Matlab R2015a	MathWorks	Matlab R2015a	https://www.mathworks.com
software, algorithm	Offline Sorter	Plexon	Offline Sorter	http://www.plexon.com/
software, algorithm	ImageJ 1.48 c	ImageJ	ImageJ 1.48 c	https://imagej.nih.gov/ij/
software, algorithm	SPSS Statistics 21	IBM	SPSS Statistics 21	https://www.ibm.com/analytics/us/en/technology/spss/
software, algorithm	Cheetah 6	Neuralynx	Cheetah 6	http://neuralynx.com/
other	Arduino Uno SMD	Arduino	A000073	A000073
other	Digital Lynx 4SX	Neuralynx	Digital Lynx 4SX	http://neuralynx.com/
other	Diode laser (473 nm)	Omicron	LuxX 473–100	
other	Electroporation device	BEX	CUY21EX	
other	Electroporation tweezer-type paddles	Protech	CUY650-P5	
other	Recording electrode (1 shank, 16 channels)	Neuronexus	A1 × 16–3 mm-703-A16	
other	Recording optrode (1 shank, 16 channels)	Neuronexus	A1 × 16–5 mm-703-OA16LP	
other	Digital midgard precision current source	Stoelting	51595	

Experimental model and subject details

Mice

All experiments were performed in compliance with the German laws and the guidelines of the European Union for the use of animals in research and were approved by the local ethical committee (111/12, 132/12). Timed-pregnant C57Bl/6J mice from the animal facility of the University Medical Center Hamburg-Eppendorf were housed individually in breeding cages at a 12 hr light/12 hr dark cycle and fed *ad libitum*. The day of vaginal plug detection was defined E0.5, while the day of birth was assigned as P0. Both female and male mice underwent light stimulation and multi-site electrophysiological recordings at P8-10 after transfection with light-sensitive proteins by IUE at E15.5. For monitoring of projections, tracers were injected at P7 and monitored in their distribution along the axonal tracts at P10. For specifically addressing interneurons by light, the Dlx5/6-Cre drive line (Tg (dlx5a-cre)1Mekk/J, Jackson Laboratory) was crossed with either ArchT (Ai40(RCL-ArchT/EGFP)-D,

Jackson Laboratory) or ChETA (R26-CAG-LSL-2XChETA-tdTomato, Jackson Laboratory) reporter line.

Methods details

Surgical procedures

In utero electroporation

Starting one day before and until two days after surgery, timed-pregnant C57Bl/6J mice received on a daily basis additional wet food supplemented with 2–4 drops Metacam (0.5 mg/ml, Boehringer-Ingelheim, Germany). At E15.5 randomly assigned pregnant mice were injected subcutaneously with buprenorphine (0.05 mg/kg body weight) 30 min before surgery. The surgery was performed on a heating blanket and toe pinch and breathing were monitored throughout. Under isoflurane anesthesia (induction: 5%, maintenance: 3.5%) the eyes of the dam were covered with eye ointment to prevent damage before the uterine horns were exposed and moistened with warm sterile phosphate buffered saline (PBS, 37°C). Solution containing 1.25 µg/µl DNA [pAAV-CAG-ChR2(E123T/T159C)−2A-tDimer2, or pAAV-CAG-tDimer2)] (***Figure 5—figure supplement 1A***) and 0.1% fast green dye at a volume of 0.75–1.25 µl were injected into the right lateral ventricle of individual embryos using pulled borosilicate glass capillaries with a sharp and long tip. Plasmid DNA was purified with NucleoBond (Macherey-Nagel, Germany). 2A encodes for a ribosomal skip sentence, splitting the fluorescent protein tDimer2 from the opsin during gene translation. Two different IUE protocols were used to target pyramidal neurons in CA1 area of either dHP or i/vHP. To target dHP, each embryo within the uterus was placed between the electroporation tweezer-type paddles (5 mm diameter, Protech, TX, USA) that were oriented at a 25° leftward angle from the midline and a 0° angle downward from anterior to posterior. Electrode pulses (35 V, 50 ms) were applied five times at intervals of 950 ms controlled by an electroporator (CU21EX, BEX, Japan) (***Figure 5—figure supplement 1B***(i)) (***Baumgart and Grebe, 2015***). To target i/vHP, a tri-polar approach was used (***Szczurkowska et al., 2016***). Each embryo within the uterus was placed between the electroporation tweezer-type paddles (5 mm diameter, both positive poles, Protech, TX, USA) that were oriented at 90° leftward angle from the midline and a 0° angle downward from anterior to posterior. A third custom build negative pole was positioned on top of the head roughly between the eyes. Electrode pulses (30 V, 50 ms) were applied six times at intervals of 950 ms controlled by an electroporator (CU21EX, BEX, Japan). By these means, neural precursor cells from the subventricular zone, which radially migrate into the HP, were transfected. Uterine horns were placed back into the abdominal cavity after electroporation. The abdominal cavity was filled with warm sterile PBS (37°C) and abdominal muscles and skin were sutured individually with absorbable and non-absorbable suture thread, respectively. After recovery, pregnant mice were returned to their home cages, which were half placed on a heating blanket for two days after surgery.

Retrograde and anterograde tracing

For retrograde tracing, mice were injected at P7 with Fluorogold (Fluorochrome, LLC, USA) unilaterally into the PFC using iontophoresis. The pups were placed in a stereotactic apparatus and kept under anesthesia with isoflurane (induction: 5%, maintenance: 2.5%) for the entire procedure. A 10 mm incision of the skin on the head was performed with small scissors. The bone above the PFC (0.5 mm anterior to bregma, 0.3 mm right to the midline) was carefully removed using a syringe. A glass capillary (≈20 µm tip diameter) was filled with ≈1 µL of 5% Fluorogold diluted in sterile water by capillary forces, and a silver wire was inserted such that it was in contact with the Fluorogold solution. For anterograde tracing, mice were injected at P7 with the anterograde tracer biotinylated dextran amine (BDA) (Thermo Fisher Scientific, USA) unilaterally into i/vHP using iontophoresis and surgery protocols as described above. The bone above i/vHP (0.7 mm anterior to lambda, 2.3 mm right to the midline) was carefully removed using a syringe. A glass capillary (≈30 µm tip diameter) was filled with ≈1 µL of 5% BDA diluted in 0.125 M phosphate buffer by capillary forces, and a silver wire was inserted such that it was in contact with the BDA solution. For both anterograde and retrograde tracing, the positive pole of the iontophoresis device was attached to the silver wire, the negative one was attached to the skin of the neck. The capillary was carefully lowered into the PFC (≈1.5 mm dorsal from the dura) or HP (≈1.5 mm dorsal from the dura). Iontophoretically injection by applying anodal current to the pipette (6 s on/off current pulses of 6 µA) was done for 5 min.

Following injection, the pipette was left in place for at least 5 min and then slowly retracted. The scalp was closed by application of tissue adhesive glue and the pups were left on a heating pad for 10–15 min to fully recover before they were given back to the mother. The pups were perfused at P10.

Surgical preparation for acute electrophysiological recording and light delivery

For recordings in non-anesthetized state, 0.5% bupivacain/1% lidocaine was locally applied on the neck muscles. For recordings under anesthesia, mice were injected i.p. with urethane (1 mg/g body weight; Sigma-Aldrich, MO, USA) prior to surgery. For both groups, under isoflurane anesthesia (induction: 5%, maintenance: 2.5%) the head of the pup was fixed into a stereotaxic apparatus using two plastic bars mounted on the nasal and occipital bones with dental cement. The bone above the PFC (0.5 mm anterior to bregma, 0.5 mm right to the midline for layer V/VI), hippocampus (2.0 mm posterior to bregma, 1.0 mm right to the midline for dHP, 3.5 mm posterior to bregma, 3.5 mm right to the midline for i/vHP) was carefully removed by drilling a hole of <0.5 mm in diameter. After a 10–20 min recovery period on a heating blanket mice were moved to the setup for electrophysiological recording. Throughout the surgery and recording session the mouse was positioned on a heating pad with the temperature kept at 37°C.

Perfusion

Mice were anesthetized with 10% ketamine (aniMedica, Germany)/2% xylazine (WDT, Germany) in 0.9% NaCl solution (10 µg/g body weight, i.p.) and transcardially perfused with Histofix (Carl Roth, Germany) containing 4% paraformaldehyde for 30–40 min. Brains were postfixed in 4% paraformaldehyde for 24 hr.

Behavioral testing

Examination of developmental milestones

Mouse pups were tested for their somatic development and reflexes at P2, P5 and P8. Weight, body and tail length were assessed. Surface righting reflex was quantified as time (max 30 s) until the pup turned over with all four feet on the ground after being placed on its back. Cliff aversion reflex was quantified as time (max 30 s) until the pup withdrew after snout and forepaws were positioned over an elevated edge. Vibrissa placing was rated positive if the pup turned its head after gently touching the whiskers with a toothpick.

Electrophysiology

Electrophysiological recording

A one-shank electrode (NeuroNexus, MI, USA) containing 1 × 16 recording sites (0.4–0.8 MΩ impedance, 100 mm spacing) was inserted into the layer V/VI of PFC. One-shank optoelectrodes (NeuroNexus, MI, USA) containing 1 × 16 recordings sites (0.4–0.8 MΩ impedance, 50 mm spacing) aligned with an optical fiber (105 mm diameter) ending 200 µm above the top recording site was inserted into either dHP or i/vHP. A silver wire was inserted into the cerebellum and served as ground and reference electrode. A recovery period of 10 min following insertion of electrodes before acquisition of data was provided. Extracellular signals were band-pass filtered (0.1–9,000 Hz) and digitized (32 kHz) with a multichannel extracellular amplifier (Digital Lynx SX; Neuralynx, Bozeman, MO, USA) and the Cheetah acquisition software (Neuralynx). Spontaneous (i.e. not induced by light stimulation) activity was recorded for 15 min at the beginning and end of each recording session as baseline activity. Only the baseline prior to stimulation epochs was used for data analysis. The position of recording electrodes in PL and CA1 area of dHP or i/vHP was confirmed after histological assessment post-mortem. For the analysis of prelimbic LFP, the recording site centered in PL was used, whereas for the analysis of spiking activity two channels above and two channels below this site were additionally considered. Recording site in cingulate or infralimbic sub-divisions of the PL were excluded from analysis. For the analysis of hippocampal LFP, the recording site located in *str pyr*,where sharp-waves reverse (***Bitzenhofer and Hanganu-Opatz, 2014***), was used to minimize any non-stationary effects of the large amplitude events. For the analysis of hippocampal firing, two channels below and two channels above this site were additionally considered.

Light stimulation

Pulsed (laser on-off) light or ramp (linearly increasing power) stimulations were performed with an arduino uno (Arduino, Italy) controlled diode laser (473 nm or 600 nm; Omicron, Austria). Laser power was adjusted to trigger neuronal spiking in response to >25% of 3-ms-long light pulses at 16 Hz. Resulting light power was in the range of 20–40 mW/mm^2 at the fiber tip. For each frequency used (4, 8 and 16 Hz), stimuli (3 ms pulse length, 3 s stimulation duration, 6 s inter stimulation interval) were repeated (30 times) in a randomized order.

Histology

Immunohistochemistry

Brains were sectioned coronally at 50 µm. Free-floating slices were permeabilized and blocked with PBS containing 0.2% Triton X 100 (Sigma-Aldrich, MO, USA), 10% normal bovine serum (Jackson Immuno Research, PA, USA) and 0.02% sodium azide. Subsequently, slices were incubated overnight with mouse monoclonal Alexa Fluor-488 conjugated antibody against NeuN (1:200, MAB377X, Merck Millipore, MA, USA) or rabbit polyclonal primary antibody against GABA (1:1,000, A2052; Sigma-Aldrich), followed by 2 hr incubation with Alexa Fluor-488 goat anti-rabbit IgG secondary antibody (1:500, A11008; Merck Millipore). Slices were transferred to glass slides and covered with Fluoromount (Sigma-Aldrich, MO, USA).

For 3.3'-diaminobenzidie (DAB) staining sections (prepared as described above) were rinsed in PBS (0.125 M, pH 7.4–7.6) for 10 min, treated with peroxide solution (3% peroxide, 10% methanol in 0.125 M PB) for 10 min to quench any endogenous peroxidases within the tissue, and rinsed again. Subsequently, the sections were washed in PBS containing 0.5% Triton-X and incubated with avidin biotinylated enzyme complex (ABC, VECTASTAIN ABC Kit, USA) at room temperature or overnight at 4°C. After rinsing in Tris-HCl (pH 7.4), the sections were further incubated with DAB working buffer (DAB peroxidase substrate kit, Vector Laboratories, USA) at room temperature for 2–10 min. After the signal was detected, all sections were rinsed with Tris-HCl.

Imaging

Wide field fluorescence was performed to reconstruct the recording electrode position in brain slices of electrophysiologically investigated pups and to localize tDimer2 expression in pups after IUE. High magnification images were acquired with a confocal microscope (DM IRBE, Leica, Germany) to quantify tDimer2 expression and immunopositive cells (1–4 brain slices/investigated mouse). For DAB staining, brightfield images were obtained using Zeiss imager M1 microscope (Zeiss, Oberkochen, Germany) and enhanced using the National Institutes of Health (NIH) Image program.

Quantification and statistical analysis

Immunohistochemistry quantification

All images were similarly analyzed with ImageJ. For quantification of fluorogold tracing automatic cell counting was done using custom-written tools. To quantify tDimer2, NeuN and GABA-positive neurons, manual counting was performed, since the high neuronal density in str. pyr. prevented reliable automatic counting.

Spectral analysis of LFP

Data were imported and analyzed offline using custom-written tools in the Matlab environment (MathWorks). Data were processed as follows: band-pass filtered (500–5,000 Hz) to analyze MUA and low-pass filtered (<1,400 Hz) using a third-order Butterworth filter before downsampling to 3.2 kHz to analyze LFP. All filtering procedures were performed in a manner preserving phase information.

Detection of oscillatory activity

The detection and of discontinuous patterns of activity in the neonatal PL and HP were performed using a modified version of the previously developed algorithm for unsupervised analysis of neonatal oscillations (***Cichon et al., 2014***) and confirmed by visual inspection. Briefly, deflections of the root mean square of band-pass filtered signals (1–100 Hz) exceeding a variance-depending threshold

were assigned as network oscillations. The threshold was determined by a Gaussian fit to the values ranging from 0 to the global maximum of the root-mean-square histogram. If two oscillations occurred within 200 ms of each other, they were considered as one. Only oscillations lasting >1 s was included.

Detection of sharpwaves

Sharpwaves were detected by subtracting the filtered signal (1–300 Hz) from the recording sites 100 µm above and 100 µm below the recording site in str. pyr. Sharpwaves were then detected as peaks above five times the standard deviation of the subtracted signal.

Power spectral density

Power spectral density was calculated using the Welch's method. Briefly, segments of the recorded signal were glued together (1 s segments for oscillatory activity; 300 ms segments for sharpwave pre/post comparison; 100 ms segments for ripple comparison; 3 s for light evoked activity) and power were then calculated using non-overlapping windows. Time–frequency plots were calculated by transforming the data using Morlet continuous wavelet.

Coherence

Coherence was calculated using the imaginary coherency method (***Nolte et al., 2004***). Briefly, the imaginary coherence was calculated by taking the imaginary component of the cross-spectral density between the two signals and normalized by the power spectral density of each. The computation of the imaginary coherence C over frequency (f) for the power spectral density P of signal X and Y was performed according to the formula:

$$C_{XY}(f) = Im\left(\frac{|P_{XY}(f)|^2}{P_{XX}(f)P_{YY}(f)}\right)$$

General partial directed coherence

gPDC is based on linear Granger causality measure. The method attempts to describe the causal relationship between multivariate time series based on the decomposition of multivariate partial coherences computed from multivariate autoregressive models. The LFP signal was divided into segments containing the oscillatory activity. Signal was de-noised using wavelets with the Matlab wavelet toolbox. After de-noising, gPDC was calculated using the gPDC algorithm previously described (***Baccala et al., 2007***).

Single unit activity analysis

SUA was detected and clustered using Offline Sorter (Plexon, TC, USA). 1–4 single units were detected at each recording site. Subsequently, data were imported and analyzed using custom-written tools in the Matlab software (MathWorks). The firing rate temporally related to SPWs was calculated by aligning all units to the detected SPWs. For assessing the phase locking of units to LFP, we firstly used the Rayleigh test for non-uniformity of circular data to identify the units significantly locked to network oscillations. The phase was calculated by extracting the phase component using the Hilbert transform of the filtered signal at each detected spike. Spikes occurring in a 15 ms-long time window after the start of a light pulse were considered to be light-evoked. Stimulation efficacy was calculated as the probability of at least one spike occurring in this period.

Statistical analysis

Statistical analyses were performed using SPSS Statistics 21 (IBM, NY, USA) or Matlab. Data were tested for normal distribution by the Shapiro–Wilk test. Normally distributed data were tested for significant differences (*p<0.05, **p<0.01 and ***p<0.001) using paired t-test, unpaired t-test or one-way repeated-measures analysis of variance with Bonferroni-corrected post hoc analysis. Not normally distributed data were tested with the nonparametric Mann–Whitney U-test. The circular statistics toolbox was used to test for significant differences in the phase locking data. Data are presented as mean ±SEM. No statistical measures were used to estimate sample size since effect size was unknown. Investigators were not blinded to the group allocation during the experiments.

Unsupervised analysis software was used if possible to preclude investigator biases. Summary of performed statistical analysis is summarized in ***Supplementary file 1***.

Acknowledgements

We thank Nadine Faesel for the establishment of tracing technique, Antonio Candela for preliminary tracing data, Drs. L Cancedda and A Cwetsch for help with the *in utero* electroporation, Drs. S Wiegert, T Oertner, and C Gee for help with the development of opsin constructs as well as A Marquardt, P Putthoff, A Dahlmann and I Ohmert for excellent technical assistance. ILH-O acknowledges support by the ERC (ERC Consolidator Grant 681577) and by the German Research Foundation (SFB 936 (B5) and SPP 1665 (Ha4466/12-1)). ILH-O is the member of the FENS Kavli Network of Excellence. In memoriam of Howard Eichenbaum

Additional information

Funding

Funder	Grant reference number	Author
European Research Council	681577	Ileana L Hanganu-Opatz
Deutsche Forschungsgemeinschaft	SFB 936	Ileana L Hanganu-Opatz
Deutsche Forschungsgemeinschaft	SPP 1665	Ileana L Hanganu-Opatz

The funders had no role in study design, data collection and interpretation, or the decision to submit the work for publication.

Author contributions

Joachim Ahlbeck, Data curation, Formal analysis, Investigation, Methodology, Writing—original draft, Writing—review and editing; Lingzhen Song, Data curation, Formal analysis, Writing—review and editing; Mattia Chini, Data curation, Formal analysis, Investigation, Methodology, Writing—review and editing; Sebastian H Bitzenhofer, Data curation, Validation, Investigation, Visualization, Methodology, Writing—review and editing; Ileana L Hanganu-Opatz, Conceptualization, Data curation, Supervision, Funding acquisition, Validation, Investigation, Methodology, Writing—original draft, Project administration, Writing—review and editing

Author ORCIDs

Joachim Ahlbeck https://orcid.org/0000-0002-4439-0798
Mattia Chini http://orcid.org/0000-0002-5782-9720
Ileana L Hanganu-Opatz http://orcid.org/0000-0002-4787-1765

Ethics

Animal experimentation: All experiments were performed in compliance with the German laws and the guidelines of the European Community for the use of animals in research and were approved by the local ethical committee (111/12, 132/12).

Decision letter and Author response

Decision letter https://doi.org/10.7554/eLife.33158.022
Author response https://doi.org/10.7554/eLife.33158.023

Additional files

Supplementary files

- Supplementary file 1. (table supplement 1 for ***Figures 1–5*** and supplementary figures 1-4) Summary of statistics for all experiments. (A) Statistical testing, number of investigated mice and p-values for the analyses displayed in ***Figure 1***. (B)–(I) Same as (A) for analyses in ***Figures 2–6***, S1-4.

DOI: https://doi.org/10.7554/eLife.33158.016

- Source code 1. Matlab source code for the analysis of discontinuous oscillatory activity.

DOI: https://doi.org/10.7554/eLife.33158.017

- Transparent reporting form

DOI: https://doi.org/10.7554/eLife.33158.018

Major datasets

The following dataset was generated:

Author(s)	Year	Dataset title	Dataset URL	Database, license, and accessibility information
Ahlbeck J, Song L, Chini M, Candela A, Bitzenhofer S, Hanganu-Opatz I	2018	Data from: Glutamatergic drive along the septo-temporal axis of hippocampus boosts prelimbic oscillations in the neonatal mouse	http://dx.doi.org/10.5061/dryad.52fh	Available at Dryad Digital Repository under a CC0 Public Domain Dedication

References

Adhikari A, Topiwala MA, Gordon JA. 2010. Synchronized activity between the ventral hippocampus and the medial prefrontal cortex during anxiety. *Neuron* **65**:257–269. DOI: https://doi.org/10.1016/j.neuron.2009.12.002, PMID: 20152131

Amaral DG, Scharfman HE, Lavenex P. 2007. The dentate gyrus: fundamental neuroanatomical organization (dentate gyrus for dummies). *Progress in Brain Research* **163**:3–22. DOI: https://doi.org/10.1016/S0079-6123(07)63001-5, PMID: 17765709

Baccala LA, Sameshima K, Takahashi DY. 2007. Generalized Partial Directed Coherence. 15th International Conference on Digital Signal Processing 163–166.

Backus AR, Schoffelen JM, Szebényi S, Hanslmayr S, Doeller CF. 2016. Hippocampal-Prefrontal Theta Oscillations Support Memory Integration. *Current Biology* **26**:450–457. DOI: https://doi.org/10.1016/j.cub.2015.12.048, PMID: 26832442

Bannerman DM, Grubb M, Deacon RM, Yee BK, Feldon J, Rawlins JN. 2003. Ventral hippocampal lesions affect anxiety but not spatial learning. *Behavioural Brain Research* **139**:197–213. DOI: https://doi.org/10.1016/S0166-4328(02)00268-1, PMID: 12642189

Bannerman DM, Sprengel R, Sanderson DJ, McHugh SB, Rawlins JN, Monyer H, Seeburg PH. 2014. Hippocampal synaptic plasticity, spatial memory and anxiety. *Nature Reviews Neuroscience* **15**:181–192. DOI: https://doi.org/10.1038/nrn3677, PMID: 24552786

Bast T, Wilson IA, Witter MP, Morris RG. 2009. From rapid place learning to behavioral performance: a key role for the intermediate hippocampus. *PLoS Biology* **7**:e1000089. DOI: https://doi.org/10.1371/journal.pbio.1000089, PMID: 19385719

Baumgart J, Grebe N. 2015. C57BL/6-specific conditions for efficient in utero electroporation of the central nervous system. *Journal of Neuroscience Methods* **240**:116–124. DOI: https://doi.org/10.1016/j.jneumeth.2014.11.004, PMID: 25445056

Ben-Ari Y, Cherubini E, Corradetti R, Gaiarsa JL. 1989. Giant synaptic potentials in immature rat CA3 hippocampal neurones. *The Journal of Physiology* **416**:303–325. DOI: https://doi.org/10.1113/jphysiol.1989.sp017762, PMID: 2575165

Benchenane K, Peyrache A, Khamassi M, Tierney PL, Gioanni Y, Battaglia FP, Wiener SI. 2010. Coherent theta oscillations and reorganization of spike timing in the hippocampal- prefrontal network upon learning. *Neuron* **66**:921–936. DOI: https://doi.org/10.1016/j.neuron.2010.05.013, PMID: 20620877

Berndt A, Schoenenberger P, Mattis J, Tye KM, Deisseroth K, Hegemann P, Oertner TG. 2011. High-efficiency channelrhodopsins for fast neuronal stimulation at low light levels. *PNAS* **108**:7595–7600. DOI: https://doi.org/10.1073/pnas.1017210108, PMID: 21504945

Bitzenhofer SH, Hanganu-Opatz IL. 2014. Oscillatory coupling within neonatal prefrontal-hippocampal networks is independent of selective removal of GABAergic neurons in the hippocampus. *Neuropharmacology* **77**:57–67. DOI: https://doi.org/10.1016/j.neuropharm.2013.09.007, PMID: 24056266

Bitzenhofer SH, Sieben K, Siebert KD, Spehr M, Hanganu-Opatz IL. 2015. Oscillatory activity in developing prefrontal networks results from theta-gamma-modulated synaptic inputs. *Cell Reports* **11**:486–497. DOI: https://doi.org/10.1016/j.celrep.2015.03.031, PMID: 25865885

Bitzenhofer SH, Ahlbeck J, Hanganu-Opatz IL. 2017a. Methodological Approach for Optogenetic Manipulation of Neonatal Neuronal Networks. *Frontiers in Cellular Neuroscience* **11**:239–252. DOI: https://doi.org/10.3389/fncel.2017.00239, PMID: 28848399

Bitzenhofer SH, Ahlbeck J, Wolff A, Wiegert JS, Gee CE, Oertner TG, Hanganu-Opatz IL. 2017b. Layer-specific optogenetic activation of pyramidal neurons causes beta-gamma entrainment of neonatal networks. *Nature Communications* **8**:14563. DOI: https://doi.org/10.1038/ncomms14563, PMID: 28216627

Borrell V, Yoshimura Y, Callaway EM. 2005. Targeted gene delivery to telencephalic inhibitory neurons by directional in utero electroporation. *Journal of Neuroscience Methods* **143**:151–158. DOI: https://doi.org/10.1016/j.jneumeth.2004.09.027, PMID: 15814147

Brincat SL, Miller EK. 2015. Frequency-specific hippocampal-prefrontal interactions during associative learning. *Nature Neuroscience* **18**:576–581. DOI: https://doi.org/10.1038/nn.3954, PMID: 25706471

Brockmann MD, Pöschel B, Cichon N, Hanganu-Opatz IL. 2011. Coupled oscillations mediate directed interactions between prefrontal cortex and hippocampus of the neonatal rat. *Neuron* **71**:332–347. DOI: https://doi.org/10.1016/j.neuron.2011.05.041, PMID: 21791291

Buhl DL, Buzsáki G. 2005. Developmental emergence of hippocampal fast-field "ripple" oscillations in the behaving rat pups. *Neuroscience* **134**:1423–1430. DOI: https://doi.org/10.1016/j.neuroscience.2005.05.030, PMID: 16039793

Buzsáki G. 2015. Hippocampal sharp wave-ripple: A cognitive biomarker for episodic memory and planning. *Hippocampus* **25**:1073–1188. DOI: https://doi.org/10.1002/hipo.22488, PMID: 26135716

Cichon NB, Denker M, Grün S, Hanganu-Opatz IL. 2014. Unsupervised classification of neocortical activity patterns in neonatal and pre-juvenile rodents. *Frontiers in Neural Circuits* **8**:50. DOI: https://doi.org/10.3389/fncir.2014.00050, PMID: 24904296

Cirelli C, Tononi G. 2015. Cortical development, electroencephalogram rhythms, and the sleep/wake cycle. *Biological Psychiatry* **77**:1071–1078. DOI: https://doi.org/10.1016/j.biopsych.2014.12.017, PMID: 25680672

Colgin LL. 2011. Oscillations and hippocampal-prefrontal synchrony. *Current Opinion in Neurobiology* **21**:467–474. DOI: https://doi.org/10.1016/j.conb.2011.04.006, PMID: 21571522

Colgin LL. 2016. Rhythms of the hippocampal network. *Nature Reviews Neuroscience* **17**:239–249. DOI: https://doi.org/10.1038/nrn.2016.21, PMID: 26961163

Dong HW, Swanson LW, Chen L, Fanselow MS, Toga AW. 2009. Genomic-anatomic evidence for distinct functional domains in hippocampal field CA1. *PNAS* **106**:11794–11799. DOI: https://doi.org/10.1073/pnas.0812608106, PMID: 19561297

Dupont E, Hanganu IL, Kilb W, Hirsch S, Luhmann HJ. 2006. Rapid developmental switch in the mechanisms driving early cortical columnar networks. *Nature* **439**:79–83. DOI: https://doi.org/10.1038/nature04264, PMID: 16327778

Eichenbaum H. 2017. Prefrontal-hippocampal interactions in episodic memory. *Nature Reviews Neuroscience* **18**:547–558. DOI: https://doi.org/10.1038/nrn.2017.74, PMID: 28655882

Fanselow MS, Dong HW. 2010. Are the dorsal and ventral hippocampus functionally distinct structures? *Neuron* **65**:7–19. DOI: https://doi.org/10.1016/j.neuron.2009.11.031, PMID: 20152109

Geisler C, Robbe D, Zugaro M, Sirota A, Buzsáki G. 2007. Hippocampal place cell assemblies are speed-controlled oscillators. *PNAS* **104**:8149–8154. DOI: https://doi.org/10.1073/pnas.0610121104, PMID: 17470808

Granger CWJ. 1980. Testing for causality. *Journal of Economic Dynamics and Control* **2**:329–352. DOI: https://doi.org/10.1016/0165-1889(80)90069-X

Hallock HL, Wang A, Griffin AL. 2016. Ventral midline thalamus is critical for hippocampal-prefrontal synchrony and spatial working memory. *Journal of Neuroscience* **36**:8372–8389. DOI: https://doi.org/10.1523/JNEUROSCI.0991-16.2016, PMID: 27511010

Hanganu IL, Ben-Ari Y, Khazipov R. 2006. Retinal waves trigger spindle bursts in the neonatal rat visual cortex. *Journal of Neuroscience* **26**:6728–6736. DOI: https://doi.org/10.1523/JNEUROSCI.0752-06.2006, PMID: 16793880

Hanganu-Opatz IL. 2010. Between molecules and experience: role of early patterns of coordinated activity for the development of cortical maps and sensory abilities. *Brain Research Reviews* **64**:160–176. DOI: https://doi.org/10.1016/j.brainresrev.2010.03.005, PMID: 20381527

Hartung H, Brockmann MD, Pöschel B, De Feo V, Hanganu-Opatz IL. 2016. Thalamic and entorhinal network activity differently modulates the functional development of prefrontal-hippocampal interactions. *The Journal of Neuroscience* **36**:3676–3690. DOI: https://doi.org/10.1523/JNEUROSCI.3232-15.2016, PMID: 27030754

Hoerder-Suabedissen A, Molnár Z. 2015. Development, evolution and pathology of neocortical subplate neurons. *Nature Reviews Neuroscience* **16**:133–146. DOI: https://doi.org/10.1038/nrn3915, PMID: 25697157

Honeycutt JA, Keary Iii KM, Kania VM, Chrobak JJ. 2016. Developmental age differentially mediates the calcium-binding protein parvalbumin in the rat: Evidence for a selective decrease in hippocampal parvalbumin cell counts. *Developmental Neuroscience* **38**:105–114. DOI: https://doi.org/10.1159/000444447, PMID: 27002731

Hu H, Vervaeke K, Storm JF. 2002. Two forms of electrical resonance at theta frequencies, generated by M-current, h-current and persistent Na+ current in rat hippocampal pyramidal cells. *The Journal of Physiology* **545**:783–805. DOI: https://doi.org/10.1113/jphysiol.2002.029249, PMID: 12482886

Hubel DH, Wiesel TN, LeVay S. 1977. Plasticity of ocular dominance columns in monkey striate cortex. *Philosophical Transactions of the Royal Society B: Biological Sciences* **278**:377–409. DOI: https://doi.org/10.1098/rstb.1977.0050, PMID: 19791

Huberman AD, Speer CM, Chapman B. 2006. Spontaneous retinal activity mediates development of ocular dominance columns and binocular receptive fields in v1. *Neuron* **52**:247–254. DOI: https://doi.org/10.1016/j.neuron.2006.07.028, PMID: 17046688

Jay TM, Witter MP. 1991. Distribution of hippocampal CA1 and subicular efferents in the prefrontal cortex of the rat studied by means of anterograde transport of Phaseolus vulgaris-leucoagglutinin. *The Journal of Comparative Neurology* **313**:574–586. DOI: https://doi.org/10.1002/cne.903130404, PMID: 1783682

Khazipov R, Minlebaev M, Valeeva G. 2013. Early gamma oscillations. *Neuroscience* **250**:240–252. DOI: https://doi.org/10.1016/j.neuroscience.2013.07.019, PMID: 23872391

Krüger HS, Brockmann MD, Salamon J, Ittrich H, Hanganu-Opatz IL. 2012. Neonatal hippocampal lesion alters the functional maturation of the prefrontal cortex and the early cognitive development in pre-juvenile rats. *Neurobiology of Learning and Memory* **97**:470–481. DOI: https://doi.org/10.1016/j.nlm.2012.04.001, PMID: 22521798

Lindemann C, Ahlbeck J, Bitzenhofer SH, Hanganu-Opatz IL. 2016. Spindle activity orchestrates plasticity during development and sleep. *Neural Plasticity* **2016**:1–14. DOI: https://doi.org/10.1155/2016/5787423, PMID: 27293903

Luhmann HJ, Khazipov R. 2018. Neuronal activity patterns in the developing barrel cortex. *Neuroscience* **368**. DOI: https://doi.org/10.1016/j.neuroscience.2017.05.025, PMID: 28528963

Minlebaev M, Ben-Ari Y, Khazipov R. 2009. NMDA receptors pattern early activity in the developing barrel cortex in vivo. *Cerebral Cortex* **19**:688–696. DOI: https://doi.org/10.1093/cercor/bhn115, PMID: 18663251

Minlebaev M, Colonnese M, Tsintsadze T, Sirota A, Khazipov R. 2011. Early γ oscillations synchronize developing thalamus and cortex. *Science* **334**:226–229. DOI: https://doi.org/10.1126/science.1210574, PMID: 21998388

Moser MB, Moser EI, Forrest E, Andersen P, Morris RG. 1995. Spatial learning with a minislab in the dorsal hippocampus. *PNAS* **92**:9697–9701. DOI: https://doi.org/10.1073/pnas.92.21.9697, PMID: 7568200

Moser EI, Krobert KA, Moser MB, Morris RG. 1998. Impaired spatial learning after saturation of long-term potentiation. *Science* **281**:2038–2042. DOI: https://doi.org/10.1126/science.281.5385.2038, PMID: 9748165

Niwa M, Kamiya A, Murai R, Kubo K, Gruber AJ, Tomita K, Lu L, Tomisato S, Jaaro-Peled H, Seshadri S, Hiyama H, Huang B, Kohda K, Noda Y, O'Donnell P, Nakajima K, Sawa A, Nabeshima T. 2010. Knockdown of DISC1 by in utero gene transfer disturbs postnatal dopaminergic maturation in the frontal cortex and leads to adult behavioral deficits. *Neuron* **65**:480–489. DOI: https://doi.org/10.1016/j.neuron.2010.01.019, PMID: 20188653

Nolte G, Bai O, Wheaton L, Mari Z, Vorbach S, Hallett M. 2004. Identifying true brain interaction from EEG data using the imaginary part of coherency. *Clinical Neurophysiology* **115**:2292–2307. DOI: https://doi.org/10.1016/j.clinph.2004.04.029, PMID: 15351371

O'Keefe J, Nadel L. 1978. *The Hippocampus as a Cognitive Map*. New York: Oxford University Press.

O'Keefe J, Recce ML. 1993. Phase relationship between hippocampal place units and the EEG theta rhythm. *Hippocampus* **3**:317–330. DOI: https://doi.org/10.1002/hipo.450030307, PMID: 8353611

Patel J, Schomburg EW, Berényi A, Fujisawa S, Buzsáki G. 2013. Local generation and propagation of ripples along the septotemporal axis of the hippocampus. *The Journal of Neuroscience* **33**:17029–17041. DOI: https://doi.org/10.1523/JNEUROSCI.2036-13.2013, PMID: 24155307

Pitkänen A, Pikkarainen M, Nurminen N, Ylinen A. 2000. Reciprocal connections between the amygdala and the hippocampal formation, perirhinal cortex, and postrhinal cortex in rat. A review. *Annals of the New York Academy of Sciences* **911**:369–391. DOI: https://doi.org/10.1111/j.1749-6632.2000.tb06738.x, PMID: 10911886

Place R, Farovik A, Brockmann M, Eichenbaum H. 2016. Bidirectional prefrontal-hippocampal interactions support context-guided memory. *Nature Neuroscience* **19**:992–994. DOI: https://doi.org/10.1038/nn.4327, PMID: 27322417

Rodrigues PL, Baccala LA. 2016. Statistically significant time-varying neural connectivity estimation using generalized partial directed coherence. *Conference proceedings : ... Annual International Conference of the IEEE Engineering in Medicine and Biology Society. IEEE Engineering in Medicine and Biology Society. Annual Conference* **2016**:5493–5496. DOI: https://doi.org/10.1109/EMBC.2016.7591970, PMID: 28269501

Royer S, Sirota A, Patel J, Buzsáki G. 2010. Distinct representations and theta dynamics in dorsal and ventral hippocampus. *Journal of Neuroscience* **30**:1777–1787. DOI: https://doi.org/10.1523/JNEUROSCI.4681-09.2010, PMID: 20130187

Seelke AM, Blumberg MS. 2010. Developmental appearance and disappearance of cortical events and oscillations in infant rats. *Brain Research* **1324**:34–42. DOI: https://doi.org/10.1016/j.brainres.2010.01.088, PMID: 20138849

Shen J, Colonnese MT. 2016. Development of Activity in the Mouse Visual Cortex. *Journal of Neuroscience* **36**:12259–12275. DOI: https://doi.org/10.1523/JNEUROSCI.1903-16.2016, PMID: 27903733

Siapas AG, Wilson MA. 1998. Coordinated interactions between hippocampal ripples and cortical spindles during slow-wave sleep. *Neuron* **21**:1123–1128. DOI: https://doi.org/10.1016/S0896-6273(00)80629-7, PMID: 9856467

Siapas AG, Lubenov EV, Wilson MA. 2005. Prefrontal phase locking to hippocampal theta oscillations. *Neuron* **46**:141–151. DOI: https://doi.org/10.1016/j.neuron.2005.02.028, PMID: 15820700

Sigurdsson T, Stark KL, Karayiorgou M, Gogos JA, Gordon JA. 2010. Impaired hippocampal-prefrontal synchrony in a genetic mouse model of schizophrenia. *Nature* **464**:763–767. DOI: https://doi.org/10.1038/nature08855, PMID: 20360742

Sirota A, Montgomery S, Fujisawa S, Isomura Y, Zugaro M, Buzsáki G. 2008. Entrainment of neocortical neurons and gamma oscillations by the hippocampal theta rhythm. *Neuron* **60**:683–697. DOI: https://doi.org/10.1016/j.neuron.2008.09.014, PMID: 19038224

Spellman T, Rigotti M, Ahmari SE, Fusi S, Gogos JA, Gordon JA. 2015. Hippocampal-prefrontal input supports spatial encoding in working memory. *Nature* **522**:309–314. DOI: https://doi.org/10.1038/nature14445, PMID: 26053122

Stark E, Eichler R, Roux L, Fujisawa S, Rotstein HG, Buzsáki G. 2013. Inhibition-induced theta resonance in cortical circuits. *Neuron* **80**:1263–1276. DOI: https://doi.org/10.1016/j.neuron.2013.09.033, PMID: 24314731

Stewart M, Fox SE. 1990. Do septal neurons pace the hippocampal theta rhythm? *Trends in Neurosciences* **13**: 163–169. DOI: https://doi.org/10.1016/0166-2236(90)90040-H, PMID: 1693232

Strange BA, Witter MP, Lein ES, Moser EI. 2014. Functional organization of the hippocampal longitudinal axis. *Nature Reviews Neuroscience* **15**:655–669. DOI: https://doi.org/10.1038/nrn3785, PMID: 25234264

Stujenske JM, Spellman T, Gordon JA. 2015. Modeling the spatiotemporal dynamics of light and heat propagation for in vivo optogenetics. *Cell Reports* **12**:525–534. DOI: https://doi.org/10.1016/j.celrep.2015.06.036, PMID: 26166563

Swanson LW. 1981. A direct projection from Ammon's horn to prefrontal cortex in the rat. *Brain Research* **217**: 150–154. DOI: https://doi.org/10.1016/0006-8993(81)90192-X, PMID: 7260612

Szczurkowska J, Cwetsch AW, dal Maschio M, Ghezzi D, Ratto GM, Cancedda L. 2016. Targeted in vivo genetic manipulation of the mouse or rat brain by in utero electroporation with a triple-electrode probe. *Nature Protocols* **11**:399–412. DOI: https://doi.org/10.1038/nprot.2016.014, PMID: 26844428

Tabata H, Nakajima K. 2001. Efficient in utero gene transfer system to the developing mouse brain using electroporation: visualization of neuronal migration in the developing cortex. *Neuroscience* **103**:865–872. DOI: https://doi.org/10.1016/S0306-4522(01)00016-1, PMID: 11301197

Taxidis J, Coomber B, Mason R, Owen M. 2010. Assessing cortico-hippocampal functional connectivity under anesthesia and kainic acid using generalized partial directed coherence. *Biological Cybernetics* **102**:327–340. DOI: https://doi.org/10.1007/s00422-010-0370-1, PMID: 20204395

Thompson CL, Pathak SD, Jeromin A, Ng LL, MacPherson CR, Mortrud MT, Cusick A, Riley ZL, Sunkin SM, Bernard A, Puchalski RB, Gage FH, Jones AR, Bajic VB, Hawrylycz MJ, Lein ES. 2008. Genomic anatomy of the hippocampus. *Neuron* **60**:1010–1021. DOI: https://doi.org/10.1016/j.neuron.2008.12.008, PMID: 19109908

Tolner EA, Sheikh A, Yukin AY, Kaila K, Kanold PO. 2012. Subplate neurons promote spindle bursts and thalamocortical patterning in the neonatal rat somatosensory cortex. *Journal of Neuroscience* **32**:692–702. DOI: https://doi.org/10.1523/JNEUROSCI.1538-11.2012, PMID: 22238105

Vertes RP, Hoover WB, Szigeti-Buck K, Leranth C. 2007. Nucleus reuniens of the midline thalamus: link between the medial prefrontal cortex and the hippocampus. *Brain Research Bulletin* **71**:601–609. DOI: https://doi.org/10.1016/j.brainresbull.2006.12.002, PMID: 17292803

Wirt RA, Hyman JM. 2017. Integrating Spatial Working Memory and Remote Memory: Interactions between the Medial Prefrontal Cortex and Hippocampus. *Brain Sciences* **7**:43. DOI: https://doi.org/10.3390/brainsci7040043, PMID: 28420200

Witter MP, Van Hoesen GW, Amaral DG. 1989. Topographical organization of the entorhinal projection to the dentate gyrus of the monkey. *Journal of Neuroscience* **9**:216–228. PMID: 2913203

Witter MP, Amaral DG. 2004. Hippocampal Formation. In: *The Rat Nervous System*. Elsevier Inc. p. 635–704 . DOI: https://doi.org/10.1016/B978-012547638-6/50022-5

Xu HP, Furman M, Mineur YS, Chen H, King SL, Zenisek D, Zhou ZJ, Butts DA, Tian N, Picciotto MR, Crair MC. 2011. An instructive role for patterned spontaneous retinal activity in mouse visual map development. *Neuron* **70**:1115–1127. DOI: https://doi.org/10.1016/j.neuron.2011.04.028, PMID: 21689598

Xu W, Südhof TC. 2013. A neural circuit for memory specificity and generalization. *Science* **339**:1290–1295. DOI: https://doi.org/10.1126/science.1229534, PMID: 23493706

Yang JW, Reyes-Puerta V, Kilb W, Luhmann HJ. 2016. Spindle bursts in neonatal rat cerebral cortex. *Neural Plasticity* **2016**:1–11. DOI: https://doi.org/10.1155/2016/3467832, PMID: 27034844

Yasuda M, Johnson-Venkatesh EM, Zhang H, Parent JM, Sutton MA, Umemori H. 2011. Multiple forms of activity-dependent competition refine hippocampal circuits in vivo. *Neuron* **70**:1128–1142. DOI: https://doi.org/10.1016/j.neuron.2011.04.027, PMID: 21689599

Ye X, Kapeller-Libermann D, Travaglia A, Inda MC, Alberini CM. 2017. Direct dorsal hippocampal-prelimbic cortex connections strengthen fear memories. *Nature Neuroscience* **20**:52–61. DOI: https://doi.org/10.1038/nn.4443, PMID: 27869801

Yuste R, Nelson DA, Rubin WW, Katz LC. 1995. Neuronal domains in developing neocortex: mechanisms of coactivation. *Neuron* **14**:7–17. DOI: https://doi.org/10.1016/0896-6273(95)90236-8, PMID: 7826643

Zhang L, Spigelman I, Carlen PL. 1990. Whole-cell patch study of GABAergic inhibition in CA1 neurons of immature rat hippocampal slices. *Developmental Brain Research* **56**:127–130. DOI: https://doi.org/10.1016/0165-3806(90)90171-T, PMID: 2279324

2.2 Developmental dysfunction of prefrontal–hippocampal networks in mouse models of mental illness

Victoria C. Oberländer, Xiaxia Xu, Mattia Chini and Ileana L. Hanganu-Opatz

European Journal of Neuroscience 2019; DOI: https://doi.org/10.1111/ejn.14436

Personal contribution

I helped designing the project. I assisted with formal analysis. I reviewed and edited the manuscript.

Received: 4 February 2019 | Revised: 18 April 2019 | Accepted: 8 May 2019

DOI: 10.1111/ejn.14436

RESEARCH REPORT

EJN European Journal of Neuroscience FENS WILEY

Developmental dysfunction of prefrontal–hippocampal networks in mouse models of mental illness

Victoria C. Oberländer | **Xiaxia Xu** | **Mattia Chini** | **Ileana L. Hanganu-Opatz**

Developmental Neurophysiology, Institute of Neuroanatomy, University Medical Center Hamburg-Eppendorf, Hamburg, Germany

Correspondence
Ileana L. Hanganu-Opatz, Developmental Neurophysiology, Institute of Neuroanatomy, University Medical Center Hamburg-Eppendorf, Falkenried 94, 20251 Hamburg, Germany.
Email: hangop@zmnh.uni-hamburg.de

Present Address
Victoria C. Oberlander, BABA Center, Pediatric Research Center, Helsinki University Hospital, Helsinki, Finland
Helsinki, Finland

Funding information
European Research Council, Grant/Award Number: ERC-2015-CoG 681577; German Research Foundation, Grant/Award Number: Ha 4466/10-1, SPP 1665 and SFB 936 B5

The peer review history for this article is available at https://publons.com/publon/10.1111/EJN.14436

Abstract

Despite inherent difficulties to translate human cognitive phenotype into animals, a large number of animal models for psychiatric disorders, such as schizophrenia, have been developed over the last decades. To which extent they reproduce common patterns of dysfunction related to mental illness and abnormal processes of maturation is still largely unknown. While the devastating symptoms of disease are firstly detectable in adulthood, they are considered to reflect profound miswiring of brain circuitry as result of abnormal development. To reveal whether different disease models share common dysfunction early in life, we investigate the prefrontal–hippocampal communication at neonatal age in (a) mice mimicking the abnormal genetic background (22q11.2 microdeletion, DISC1 knockdown), (b) mice mimicking the challenge by environmental stressors (maternal immune activation during pregnancy), (c) mice mimicking the combination of both aetiologies (dual-hit models) and pharmacological mouse models. Simultaneous extracellular recordings in vivo from all layers of prelimbic subdivision (PL) of prefrontal cortex (PFC) and CA1 area of intermediate/ventral hippocampus (i/vHP) show that network oscillations have a more fragmented structure and decreased power mainly in neonatal mice that mimic both genetic and environmental aetiology of disease. These mice also show layer-specific firing deficits in PL. Similar early network dysfunction was present in mice with 22q11.2 microdeletion. The abnormal activity patterns are accompanied by weaker synchrony and directed interactions within prefrontal–hippocampal networks. Thus, only severe genetic defects or combined genetic environmental stressors are disruptive enough for reproducing the early network miswiring in mental disorders.

KEYWORDS
development, oscillations, prefrontal–hippocampal network, schizophrenia, synchrony

Abbreviations: Df(16)A$^{+/-}$, bioengineered knockout mice mimicking the 22q11.2 microdeletion; Df16, Df(16)A$^{+/-}$ model; DISC1, Disrupted-In-Schizophrenia-1; dual-hit, mice mimicking two risk factors; G, gestational day; GPDC, generalized partial directed coherence; HP, hippocampus; i/vHP, intermediate/ventral hippocampus; KET, ketamine model; LFP, local field potential; MIA, maternal immune activation; MUA, multiple unit activity; one-hit, mice mimicking one risk factor; PFC, prefrontal cortex; PL, prelimbic cortex; poly I:C, polyriboinosinic polyribocytidilic acid; P, post-natal day.

Edited by John Foxe.

1 | INTRODUCTION

Modelling of human neuropsychiatric disorders in animals has been proven to be extremely challenging due to (a) uniqueness of human symptoms, such as hallucinations, guilt, delusions, that cannot be identified in animals, (b) the arbitrary boundaries between normal behaviour and distinct disorders and the lack of objectively ascertainable manifestations and (c) the poor mechanistic insights at molecular, cellular and system level (Kaiser, Zhou, & Feng, 2017; Nestler & Hyman, 2010). Despite these inherent difficulties, a wealth of models has been investigated for shedding light on some aspects of major neuropsychiatric disorders, such as schizophrenia, bipolar disorder and depression. These models need to provide construct, face and predictive validity. Construct validity refers to the ability of the model to mimic the aetiology of disease. Numerous genetic linkages have been established for schizophrenia, yet many of them exert only small effects on human disease risk. For example, deficient Disrupted-in-Schizophrenia-1 (DISC1) has been initially highlighted a risk factor of disease but it rather orchestrates molecular cascades hypothesized to underlie disease-relevant physiological and behavioural abnormalities (Cuthbert & Insel, 2013). However, unequivocal risk alleles, such as the microdeletion on human chromosome 22 (22q11.2) have also been identified and hereupon mimicked in the Df(16)$A^{+/-}$ mouse line (International Schizophrenia, 2008). Construct validity might be also achieved through exposure of mice to well-validated environmental risk factors. Among others, maternal immune activation (MIA) has been identified as primer for a large spectrum of neuropsychiatric disorders (Estes & McAllister, 2016). The effects of environmental risk factors, mainly acting during development, depend on the genetic background (Owen, Sawa, & Mortensen, 2016). Gene–environment interactions augment the disease risk (Nimgaonkar, Prasad, Chowdari, Severance, & Yolken, 2017; van Os et al., 2014). Face validity refers to the ability of an animal model to recapitulate the feature of human disorder. For example, Df(16)$A^{+/-}$ mice show abnormal long-range coupling in the brain during working memory tasks similarly to schizophrenia patients (Meyer-Lindenberg et al., 2005; Schwarz, Tost, & Meyer-Lindenberg, 2016; Sigurdsson, Stark, Karayiorgou, Gogos, & Gordon, 2010). Predictive validity refers to the ability of mouse models to respond to pharmacological treatments similarly to patients. However, in the absence of mechanistic understanding of most psychiatric disorders, it is still difficult to develop reliable models of drug action.

The large variety and number of mouse models of neuropsychiatric disorders lead to the question whether they share common mechanisms of network dysfunction for a specific behavioural defect (Hamm, Peterka, Gogos, & Yuste, 2017). Impairment of memory and executive abilities is a core feature of these disorders and, in contrast to positive symptoms (e.g., hallucinations, delusions), detectable in animal models. It relies on abnormal communication within a large network centred on PFC and i/vHP (Sigurdsson & Duvarci, 2015). This network dysfunction seems to emerge early in life, long before the first clinical symptoms at juvenile-young adult age. We recently showed that the initial coupling between PL and i/vHP of heterozygous DISC1 mice experiencing MIA is impaired shortly after birth, a weaker hippocampal drive being not able to entrain locally miswired prefrontal circuits (Hartung et al., 2016; Xu, Chini, Bitzenhofer, & Hanganu-Opatz, 2019). Correspondingly, the mice show poorer recognition memory at juvenile age. The prefrontal–hippocampal coupling emerging during neonatal development might be similarly impaired in other disease models that show equally impaired cognitive behaviour. To test this hypothesis, we investigated the patterns of electrical activity, the synchrony and directed interactions between PFC and HP of one-hit genetic (DISC1$^{+/-}$, Df(16)$A^{+/-}$), one-hit environmental (mimicking MIA), dual-hit (combined DISC1$^{+/-}$ or Df(16)$A^{+/-}$ and MIA) and pharmacological model (treatment with ketamine) mice at neonatal age (post-natal day (P) 8–10). We show that early prefrontal–hippocampal dysfunction is mainly present in one-hit Df(16)$A^{+/-}$ and dual-hit models.

2 | MATERIALS AND METHODS

2.1 | Animal models

Experiments were performed in compliance with the German laws and the guidelines of the European Community for the use of animals in research and were approved by the local ethical committee Behörde für Gesundheit und Verbraucherschutz of City Hamburg (proposal number 132/12 and 015/18). Timed pregnant mice were obtained at gestational day (G) 6–7 from the animal facility of the University Medical Center Hamburg-Eppendorf and housed individually at a 12 hr light/12 hr dark cycle, with access to water and food ad libitum. The day of vaginal plug detection was considered as G0.5, while the day of birth as P0. Heterozygous genetically engineered mutant DISC1 mice carrying a Disc1 allele (Disc1^{Tm1Kara}) on a C57Bl6/J background were used as one-hit genetic model (DISC1, $n = 17$; $n = 5$ P8 pups, $n = 6$ P9 pups, $n = 6$ P10 pups). Due to two termination codons and a premature polyadenylation site, the allele produces a truncated transcript (Kvajo et al., 2008). Genotypes were determined using genomic DNA and following primer sequences: forward primer 5′-TAGCCACTCTCATTGTCAGC-3′, reverse primer 5′-CCTCATCCCTTCCACTCAGC-3′. As a second one-hit genetic model the Df(16)$A^{+/-}$ model was used (Stark et al., 2008). The affected allele in the Df(16)$A^{+/-}$ mice (Df16, $n = 11$; $n = 3$ P8, $n = 5$ P9, $n = 3$ P10) carries a chromosomal engineered 1.3-Mb microdeletion

ranging from Dgcr2 to Hira, a segment syntenic to the 1.5-Mb human 22q11.2 microdeletion that encompasses 27 genes. Genotypes were determined using genomic DNA and following primer sequence indicating a knockout: forward primer 5′-ATTCCCCATGGACTAATTATGGACAGG-3′, reverse primer5′-GGTATCTCCATAAGACAGAATGCTATGC-3′. The offspring of pregnant dams injected i.v. at G9 with the viral mimetic polyinosinic:polycytidylic acid (poly I:C, 5 mg/kg) were used as one-hit environmental model (MIA, $n = 10$; $n = 3$ P8, $n = 4$ P9, $n = 3$ P10), since they showed at adulthood deficits highly reminiscent of schizophrenia (Meyer & Feldon, 2012; Meyer, Feldon, Schedlowski, & Yee, 2006). The heterozygous offspring of DISC1$^{+/-}$ or of Df(16)A$^{+/-}$ dams injected at G9 with poly I:C were used as dual-hit genetic environmental models (DISC1 + MIA, $n = 17$; $n = 4$ P8, $n = 6$ P9, $n = 7$ P10; Df16 + MIA, $n = 11$; $n = 3$ P8, $n = 6$ P9, $n = 2$ P10). Pups chronically treated with ketamine (60 μg/g body weight/day) from P1 to P8 were used as pharmacological model (KET, $n = 16$; $n = 5$ P8, $n = 7$ P9, $n = 4$ P10; Behrens et al., 2007). Non-treated wild-type mice (control, $n = 23$; $n = 11$ P8, $n = 8$ P9, $n = 4$ P10) and mice injected with saline (0.9%; saline, $n = 13$; $n = 4$ P8, $n = 9$ P9, $n = 5$ P10) were used as controls. All mice used in this study were generated on C57Bl6/J background (Jackson Laboratories, Bar Harbor, Maine, USA). Pups were investigated during neonatal development at P8–10, the time period of maximal unidirectional hippocampal–prelimbic interactions (Brockmann, Poschel, Cichon, & Hanganu-Opatz, 2011). During neonatal development, the weight of pups was similar for all eight groups (control: 5 ± IQR 1.1 g; saline: 4.9 ± IQR 0.5 g; DISC1: 4.8 ± IQR 1.3; Df16: 4.8 ± IQR 1.0 g; MIA: 4.1 ± IQR 0.8 DISC1 + MIA: 4.3 ± IQR 1.0 g; Df16 + MIA: 4.5 ± IQR 0.8 g, KET: 4.7 ± IQR 0.6 g, $H^2 = 0.075$ $p = 0.78$ [Kruskal–Wallis]). All investigated groups were age ($H^2 = 4.56$, $p = 0.713$, Kruskal–Wallis) and sex ($\chi^2 = 3.38$, $p = 0.848$, chi-square) balanced.

2.2 | Electrophysiological recordings in vivo

Multi-site extracellular recordings were performed in the PL and i/vHP of P8–10 pups of both sexes. Mice were injected i.p. with urethane (1 mg/g body weight; Sigma-Aldrich) before surgery. Under isoflurane anaesthesia (induction: 5%; maintenance: 2.5%), the head of the pup was fixed into a stereotaxic apparatus using two plastic bars mounted on the nasal and occipital bones with dental cement. The bone over the PFC (0.8 mm anterior to bregma, 0.1–0.5 mm right to the midline) and the i/vHP (3.5–3.7 mm anterior to bregma, 3.5–3.8 mm right to the midline) was carefully removed by drilling holes of <0.5 mm in diameter. Four-shank electrodes (4 × 4 recording sites, 0.3–2.2 MΩ impedance, 100 μm spacing, 125 μm inter-shank spacing, NeuroNexus) were inserted into PL at a depth of 1.9 mm from the skull surface. One-shank electrodes (1 × 16 recording sites, 0.3–2.2 MΩ impedance, 50 μm spacing, NeuroNexus) were inserted into the i/vHP until a depth of 1.3–1.8 mm from the skull surface, at an angle of 20° from the vertical plane. Electrodes were labelled with DiI (1,1′-dioctadecyl-3,3,3′,3′-tetramethyl indocarbocyanine, Invitrogen) to confirm their exact position after histological assessment (Nissl staining) post-mortem. In PL, the most medial shank was confirmed to lay into layer II/III, whereas the most lateral shank was located in layer V/VI. In hippocampal CA1 area, the LFP reversal over stratum pyramidale was used for the selection of the channel with sharp waves of minimum amplitude and consequently, lowest contribution to the spectral content of the signal. Recordings that did not fulfil these criteria were not considered for analysis. One silver wire was inserted into cerebellum to serve as ground and reference electrode. A recovery period of 30 min following the insertion of electrodes before acquisition of data was provided. During surgery and recording, the body of the animal was kept at a constant temperature of 37°C using a heating blanket. Extracellular signals were band-pass filtered (0.1 Hz to 8 kHz) and digitized (32 kHz) with a multi-channel extracellular amplifier (Digital Lynx SX; Neuralynx) and the Cheetah acquisition software (Neuralynx). After recording, mice were anesthetized with 10% ketamine (WDT)/2% xylazine (WDT) in 0.9% NaCl solution (10 μg/g body weight, i.p.) and transcardially perfused with Histofix (Carl Roth) containing 4% paraformaldehyde. Brains were postfixed with Histofix for 24 hr and sectioned coronally at 100 μm. Wide-field fluorescence images were acquired to reconstruct the recording electrode position in Nissl-stained sections.

2.3 | Data analysis

Data were imported and analysed offline using custom-written tools in MATLAB software version 7.7 (MathWorks). The data were processed as following: (a) band-pass filtered (500–5,000 Hz) to detect MUA as negative deflections exceeded five times the standard deviation of the filtered signals and (b) downsampled to 3,200 Hz before band-pass filtering (3–100 Hz) to analyse the LFP. All filtering procedures were performed in a phase-preserving manner. Frequency bands corresponded to the observed power peaks and ranged from 3–8 Hz (theta) to 12–30 Hz (beta).

2.3.1 | Detection of neonatal oscillatory activity

Discontinuous oscillatory events were detected using a previously developed unsupervised algorithm (Cichon, Denker, Grun, & Hanganu-Opatz, 2014). Briefly, deflections of the root-mean-square of band-pass (3–100 Hz) filtered signals exceeding a variance-depending threshold were assigned

as network oscillations. The threshold was determined by a Gaussian fit to the values ranging from 0 to the global maximum of the root-mean-square histogram. All consecutive oscillations with inter-event intervals < 200 ms were considered as a single event. Only oscillatory events > 1 s were considered for further analysis. Time–frequency plots were calculated by transforming the data using the Morlet continuous wavelet.

2.3.2 | Power spectral density

For power spectral density analysis, 1-s-long windows of network oscillations were concatenated and the same was done for 1-s-long windows without oscillatory activity. For all detected oscillatory events $P(f)$ and for all epochs without oscillatory activity $P_0(f)$, the absolute power was separately calculated using Welch's method (*pwelch.m*) with non-overlapping hamming windows of 1 s length. Finally, the normalized (relative) power spectra were then defined as $P(f)/P_0(f)$.

2.3.3 | Spectral coherence

Coherence was calculated using the imaginary coherency method (Nolte et al., 2004). Briefly, the imaginary coherence was calculated by taking the imaginary component of the cross-spectral density between the two signals (*cpsd.m*) normalized by the power spectral density (*pwelch.m*) of each. The computation of the imaginary coherence C over frequency (f) for the power spectral density P of signal X and Y was performed according to the formula:

$$C_{XY}(f) = \left| \mathrm{Im}\left(\frac{P_{XY}(f)}{\sqrt{P_{XX}(f)P_{YY}(f)}} \right) \right|$$

2.3.4 | Generalized partial directed coherence

To investigate the directionality of functional connectivity between PL and i/vHP, generalized partial directed coherence (GPDC) were used. GPDC is based on linear Granger causality measure in the frequency domain. The method infers the causal relationship between simultaneously observed time series based on the decomposition of partial coherence computed from multivariate autoregressive models. The LFP signal was divided into 1-s-long segments containing the oscillatory activity. After detrending (*detrend.m*) and denoising (*wdencmp.m*), GPDC was calculated using a previously described algorithm (Baccalá, Sameshima, & Takahashi, 2007).

2.4 | Statistics

Statistical analyses were performed in MATLAB. Data were fit to a linear model with weight and condition as terms (GLM, *fitglm.m*). Nested data as the MUA firing rate were analysed with a generalized linear mixed model (GLME, *fitglme.m*) with age and condition as fixed effects and animal as random effect. Regression terms (weight and age) were chosen on Bayesian model criterion. Distributions for GLME were indicated as a Poisson distribution, so data were automatically log-transformed for the model. Overall sample set effect was tested with ANOVA (*anova.m*) and post hoc testing via contrast matrices (*coefTest.m*). To account for the multiple testing (six comparison), p values were post hoc corrected with the Benjamin–Hochberg method. Statistical testing was conducted on absolute values. To facilitate the comparison between different groups and their controls, the relative changes to the respective controls were displayed.

3 | RESULTS

We investigated the early network function and coupling of PL and i/vHP at neonatal age in six mouse models of disease. To mimic the genetic background of disease, (a) mice carrying a human-like truncating lesion in the endogenous murine DISC1 ortholog ($DISC1^{+/-}$; Kvajo et al., 2008) and (b) mice carrying a chromosomal engineered 1.3-Mb knockout syntenic to the 1.5-Mb human 22q11.2 microdeletion ($Df(16)A^{+/-}$; Stark et al., 2008) were investigated as one-hit genetic models (DISC1 and Df16). To mimic the immune challenge during pregnancy, mice with prenatal immune activation by the viral mimetic poly I:C (Shi, Fatemi, Sidwell, & Patterson, 2003) were used as one-hit environmental model (MIA). $DISC1^{+/-}$ or $Df(16)A^{+/-}$ mice prenatally treated with poly I:C recapitulated both genetic and environmental risk factors and were considered as dual-hit gene–environment models (DISC1 + MIA and Df16 + MIA). Finally, mouse pups receiving subanaesthetic levels of ketamine from P1 to P8 were used as pharmacological model of disease (KET; Behrens et al., 2007). All six models have been extensively characterized at adulthood and shown to reproduce positive, negative and cognitive symptomology of schizophrenia (Abazyan et al., 2010; Krystal et al., 1994; Mukai et al., 2015; Niwa et al., 2010; Sigurdsson et al., 2010). Moreover, they have disrupted neuronal ensembles, abnormal prefrontal–hippocampal communication and neuronal dysfunction (Hamm et al., 2017).

3.1 | Neonatal one-hit Df16 and dual-hit DISC1 + MIA mice show abnormal network activity and neuronal firing in PL

To test whether network dysfunction emerges already at neonatal age in all investigated models, we focused on the earliest developmental stage at which PL and CA1 area of i/vHP functionally interact. We performed extracellular recordings

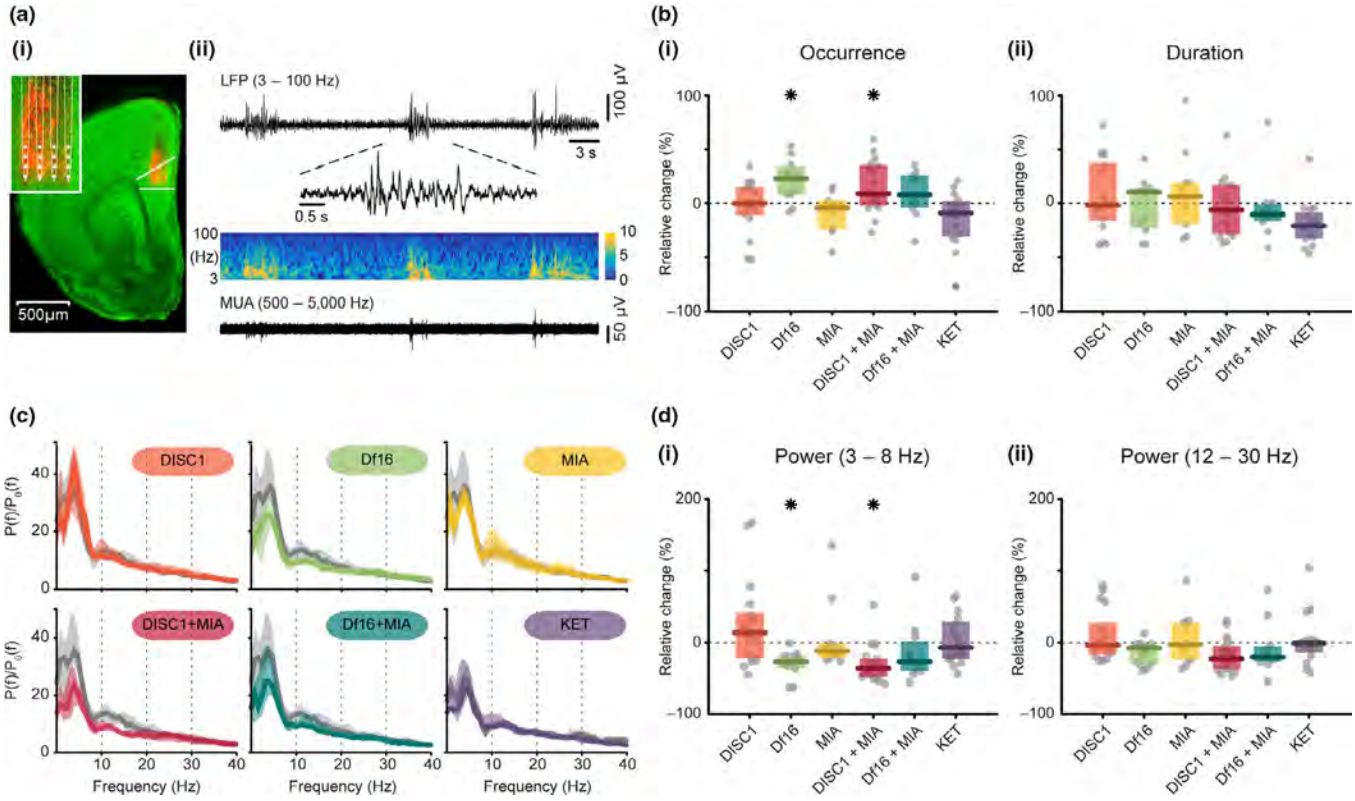

FIGURE 1 Patterns of oscillatory activity in the PL of neonatal mouse models of mental illness. (a) (i) Digital photomontage reconstructing the position of a 4-shank DiI-labelled recording probe (orange) in the PL of a Nissl-stained 100 µm-thick coronal section (green) from a P9 control mouse. Inset, the position of recording sites (white dots) over the prelimbic layers displayed at higher magnification. (ii) Extracellular recording of discontinuous oscillatory activity in PL from a P9 control mouse displayed after band-pass (3–100 Hz) filtering accompanied by the colour-coded wavelet spectra at identical timescale (middle) and the corresponding MUA after band-pass (500–5,000 Hz) filtering (bottom). Inset, discontinuous oscillatory event displayed at higher magnification. (b) (i) Scatter plot displaying the relative occurrence of oscillatory events in PL of all models when normalized to controls (Df16 vs. control: $p = 0.01$, DISC1 + MIA vs. control: $p = 0.01$) (ii) Same for the duration of oscillatory events. (c) Averaged power spectra $P(f)$ of discontinuous prelimbic oscillations normalized to the baseline power $P_0(f)$ of time windows lacking oscillatory activity displayed for all mouse models (colours) together with their control (light grey). (d) (i) Scatter plot displaying the relative prelimbic power within 3–8 Hz for all models when normalized to controls (Df16 vs. control: $p = 0.035$, DISC1 + MIA vs. control: $p = 0.022$) (ii) Same as (i) in the beta (12–30 Hz) frequency band. Thick lines represent the median and shaded areas represent the 25° and 75° percentiles. Single data points are represented as circles, the coloured bars represent the median and the coloured boxes the 25th and 75th percentiles, $*p < 0.05$

of local field potential (LFP) and multiple-unit activity (MUA) from both areas in lightly anesthetized P8–10 controls ($n = 23$), saline controls ($n = 13$), DISC1 ($n = 17$), Df16 ($n = 11$), MIA ($n = 10$), DISC1 + MIA ($n = 17$), Df16 + MIA ($n = 11$) and KET ($n = 16$). In PL, the four shanks of recording electrodes were confirmed to be located across layer II/III and V/VI (Figure 1a(i)). Our previous investigations revealed that, despite reduction in the number of oscillatory events, their properties (power, frequencies distribution) and the neuronal firing are similar in urethane- and isoflurane-anesthetized and asleep non-anesthetized rodents of neonatal age (Bitzenhofer, Sieben, Siebert, Spehr, & Hanganu-Opatz, 2015; Chini et al., 2019). Discontinuous (i.e., periods of network activity alternate with periods of "silence") oscillatory discharges with frequency components peaking in theta (3–8 Hz) and beta-low gamma frequency range (12–30 Hz) have been detected in all investigated mice (Figure 1a(ii)). Oscillatory activity with high frequency (>30 Hz) emerges later during development, hence is not detectable at P8–10. However, the oscillatory properties differed between groups (occurrence: $F_{7,111} = 4.89$, $p < 0.001$; duration: $F_{7,111} = 3.77$, $p < 0.001$; Figure 1b(i) and (ii), Table 1). In line with our previous findings (Hartung et al., 2016), the prelimbic activity of DISC1 + MIA mice appeared highly fragmented and correspondingly, the occurrence of oscillatory events was higher ($p = 0.01$) when compared with controls. In contrast, the oscillatory activity in PL of one-hit DISC1 and MIA mice was not affected. The fragmented structure of discharges was present also in one-hit Df16 mice ($p = 0.01$), yet the dysfunction did not substantially augment when MIA co-occurred (Figure 1b(i) and (ii), Table 1). The relative power of oscillatory events normalized to the periods lacking coordinated activity was significantly decreased over theta band (3–8 Hz, $F_{7,111} = 4.14$, $p < 0.001$)

TABLE 1 Properties of discontinuous patterns of network activity in the PL of neonatal control and disease model mice

	Group effect	Control	Saline	DISC1	Df16	MIA	DISC1 + MIA	Df16 + MIA	KET
Occurrence (events/min)	ANOVA, $F_{7,111} = 4.89$; $p < 0.001^{***}$	7.07 ± 1.58	8.83 ± 1.53	7.07 ± 1.68	8.67 ± 1.84; ***p = 0.01****	6.77 ± 1.87	7.7 ± 2.59; ***p = 0.01****	7.63 ± 2.13	8.05 ± 2.83
Duration (s)	ANOVA, $F_{7,111} = 3.77$; $p < 0.001^{***}$	3.55 ± 1.62	4.06 ± 1.35	3.48 ± 1.66	3.66 ± 1.34	3.77 ± 1.36	3.33 ± 1.61	3.19 ± 0.54	3.22 ± 0.97
Rel. power (3–8 Hz)	ANOVA, $F_{7,111} = 4.14$; $p < 0.001^{***}$	25.43 ± 7.66	17.96 ± 5.58	28.88 ± 16.05	18.61 ± 4.27; **p = 0.022***	22.38 ± 4.91	16.17 ± 6.39; **p = 0.035***	18.58 ± 10.47	16.74 ± 9.32
Rel. power (12–30 Hz)		7.93 ± 3.45	6.87 ± 1.71	7.65 ± 3.4	7.35 ± 2.22	7.73 ± 4.1	6.15 ± 2.47	6.25 ± 1.66	6.87 ± 1.26
MUA firing rate (spikes/s)	ANOVA, $F_{7,494} = 3.46$; $p = 0.001^{**}$ LII/III	0.15 ± 0.48	0.19 ± 0.38	0.21 ± 0.35	0.4 ± 1.01	0.08 ± 0.56	0.06 ± 0.2; ***p = 0.008*****	0.14 ± 0.33	0.1 ± 0.22
	LV/VI	0.22 ± 0.35	0.69 ± 0.6	0.26 ± 0.27	0.46 ± 0.41	0.2 ± 0.72	0.29 ± 0.37	0.17 ± 0.38	0.17 ± 0.44

Note: Data are shown as median ± interquartile range. Corrected *p* values (Benjamin-Hochberg) for comparisons between controls and disease groups are listed. Italics indicate statistics of ANOVA for GLM/GLME; Italics and bolds indicate statistics of coefficient testing for GLM/GLME. $^{*}p < 0.05$, $^{**}p < 0.01$, $^{***}p < 0.001$.

in DISC1 + MIA ($p = 0.022$) and one-hit Df16 ($p = 0.035$) mice, yet not in the other groups, when compared to controls (Figure 1c and d(i), Table 1). In contrast, no significant differences were detected for faster frequencies (Figure 1d(ii)).

The abnormal temporal organization of coordinated activity in the PL of dual-hit DISC1 + MIA and one-hit Df16 mice led us to hypothesize that the local prelimbic circuitry was perturbed in the two groups of mice. We calculated the firing rates in layer II/III and layer V/VI of the two models and compared them with the values from controls. Prelimbic neurons mostly fire during oscillatory events (Figure 1a). Overall, the firing in layer II/III but not V/VI of DISC1 + MIA mice decreased when compared to controls ($F_{7,494} = 3.463$, $p = 0.001$, $p = 0.008$; Figure 3a, b and Table 1). However, no significant changes were detected for the other groups.

Thus, combination of genetic and environmental risk as well as pronounced genetic abnormalities disrupt the prefrontal activity already at neonatal age, whereas early glutamatergic manipulation or single mild risk factors seem to not be sufficient for affecting neuronal ensembles in developing PL.

3.2 | Neonatal one-hit Df16 and dual-hit mouse models show abnormal network activity in i/vHP

Previous investigation identified discontinuous oscillatory activity in the CA1 area of i/vHP as drive of prefrontal entrainment at neonatal age (Ahlbeck, Song, Chini, Bitzenhofer, & Hanganu-Opatz, 2018; Brockmann et al., 2011). Therefore, it is likely that the abnormal activity detected in the PL of one-hit Df16 and dual-hit DISC1 + MIA mice results not only from disrupted local coupling within prelimbic circuits, as shown by firing deficits, but also from abnormal communication with HP. This might result from either abnormal activity patterns in the neonatal HP of mouse models or impaired hippocampal drive to PL. To test these hypotheses, we monitored the discontinuous patterns of network activity in hippocampal CA1 area of all six models and compared them with those from controls. Hippocampal spindle-shaped oscillations with main frequency in theta band and interspaced with faster beta/low-gamma band discharges (Figure 2a) were analysed in their occurrence, duration and relative power.

Similar to PL, the most prominent fragmentation of hippocampal activity (i.e., higher occurrence and shorter duration) was detected for one-hit Df16 and dual-hit DISC1-MIA mice (occurrence: $F_{7,111} = 5.32$, $p < 0.001$; duration: $F_{7,111} = 2.91$, $p = 0.006$; Figure 2b(i) and (ii), Table 2). Oscillations were significantly shorter in the DISC1 + MIA ($p = 0.018$) and the one-hit Df16 mice ($p = 0.018$), and the oscillatory periods were more frequent (DISC1 + MIA: $p = 0.002$; one-hit Df16: $p = 0.001$; Df16 + MIA: $p = 0.008$). Their relative power was also significantly different when compared to controls (theta:

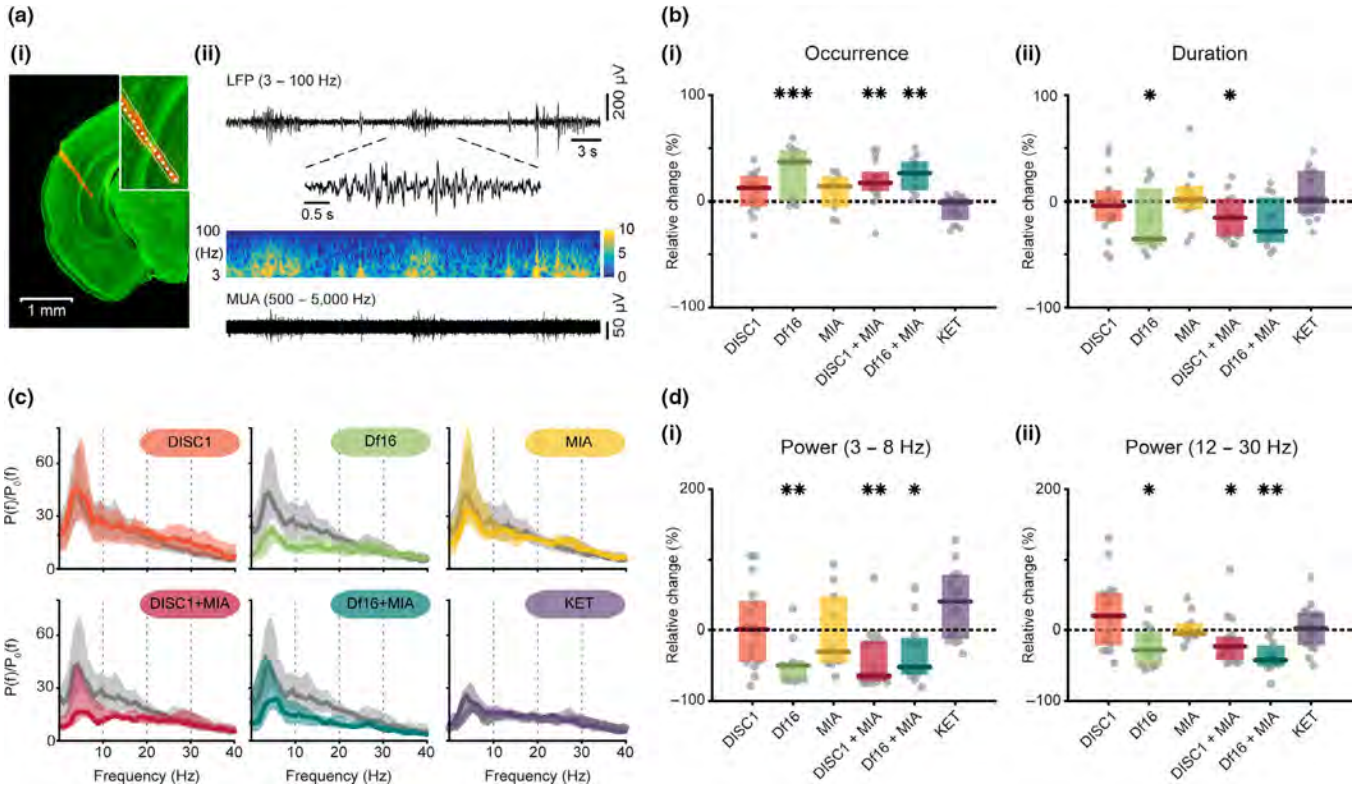

FIGURE 2 Patterns of oscillatory activity in the i/vHP of neonatal mouse models of mental illness. (a) (i) Digital photomontage reconstructing the position of a 1-shank DiI-labelled recording probe (orange) in the HP of a Nissl-stained 100 µm-thick coronal section (green) from a P9 control mouse. Inset, the position of recording sites (white dots) over the Str. pyramidale displayed at higher magnification. (ii) Extracellular recording of discontinuous oscillatory activity in HP from a P9 control mouse displayed after band-pass (3–100 Hz) filtering accompanied by the colour-coded wavelet spectra at identical timescale (middle) and the corresponding MUA after band-pass (500–5,000 Hz) filtering (bottom). Inset, discontinuous oscillatory event displayed at higher magnification. (b) (i) Scatter plot displaying the relative occurrence of oscillatory events in hippocampal CA1 area of all models when normalized to controls (Df16 vs. control: $p = 0.001$, DISC1 + MIA vs. control: $p = 0.002$, Df16 + MIA vs. control: $p = 0.008$). (ii) Same for the duration of oscillatory events (Df16 vs. control: $p = 0.018$, DISC1 + MIA vs. control: $p = 0.018$). (c) Averaged power spectra $P(f)$ of discontinuous hippocampal oscillations normalized to the baseline power $P_0(f)$ of time windows lacking oscillatory activity displayed for all mouse models (colours) together with their control (light grey). (d) (i) Scatter plot displaying the relative hippocampal power within 3–8 Hz for all models when normalized to controls (Df16 vs. control: $p = 0.005$, DISC1 + MIA vs. control: $p = 0.004$, Df16 + MIA vs. control: $p = 0.043$). (ii) Same as (i) in the beta (12–30 Hz) frequency band (Df16 vs. control: $p = 0.018$, DISC1 + MIA vs. control: $p = 0.03$, Df16 + MIA vs. control: $p = 0.002$). Thick lines represent the median, and shaded areas represent the 25° and 75° percentiles. Single data points are represented as circles, the coloured bars represent the median and the coloured boxes the 25th and 75th percentiles, $^*p < 0.05$, $^{**}p < 0.01$, $^{***}p < 0.001$

$F_{7,111} = 5.54$, $p < 0.001$; beta: $F_{7,111} = 4.98$, $p < 0.001$; Figure 2c, d(i) and (ii) and Table 2). The DISC1 + MIA model showed a strong power reduction in theta ($p = 0.004$, Figure 2d(i)) and beta band ($p = 0.03$, Figure 2d(ii)). The power of the one-hit Df16 and the Df16 + MIA was decreased in the theta (Df16: $p = 0.005$; Df16 + MIA: $p = 0.043$, Figure 2d(i)) and beta frequency range too (Df16: $p = 0.018$; Df16 + MIA: $p = 0.002$, Figure 2d(ii)). No significant changes in the occurrence, duration or power were detected in the other models when compared to controls. In all investigated mice, the hippocampal firing rate was comparable to that of controls ($p = 0.11$, Figure 3c, Table 2).

These findings indicate that the network activity in hippocampal CA1 area is compromised in neonatal one-hit Df16 as well as dual-hit mice. The absence of firing deficits in these mice confirms the minor contribution of CA1 neurons to the generation of discontinuous network oscillations (Janiesch, Kruger, Poschel, & Hanganu-Opatz, 2011).

3.3 | Neonatal one-hit Df16 and dual-hit mouse models show weaker long-range coupling within prelimbic–hippocampal circuits

To test the hypothesis that abnormal communication between PL and HP is present in one-hit Df16 and dual-hit mice, we monitored the synchrony and information transfer between the two areas by calculating the coherence (Nolte et al., 2004) and generalized partial directed coherence (GPDC; Baccalá et al., 2007), respectively. We considered

TABLE 2 Properties of discontinuous patterns of network activity in i/vHP of neonatal control and disease model mice

	Group effect	Control	Saline	DISC1	Df16	MIA	DISC1 + MIA	Df16 + MIA	KET
Occurrence (events/min)	ANOVA, $F_{7,111} = 5.32$; $p < 0.001^{***}$	7.63 ± 2.5	10.3 ± 0.9	8.4 ± .1.84	10.13 ± 3.13; ***p = 0.001*****	8.7 ± 1.8	9 ± 1.62; ***p = 0.002*****	9.4 ± 2.03; ***p = 0.008*****	9.38 ± 2
Duration (s)	ANOVA, $F_{7,111} = 2.91$; $p = 0.006^{**}$	4.49 ± 1.73	3.24 ± 1.02	4.09 ± 1.16	2.57 ± 2.13; ***p = 0.018****	4.42 ± 1.35	3.86 ± 1.4; ***p = 0.018****	3.91 ± 1.39	3.87 ± 1.03
Rel. power (3–8 Hz)	ANOVA, $F_{7,111} = 5.54$; $p < 0.001^{***}$	40.06 ± 25.97	15.06 ± 6.22	40.53 ± 34.53	19.99 ± 9.91; ***p = 0.005*****	27.95 ± 37.95	14.18 ± 23.21; ***p = 0.004*****	19.18 ± 21.47; ***p = 0.043****	21.28 ± 13.62
Rel. power (12–30 Hz)	ANOVA, $F_{7,111} = 3.14$; $p < 0.001^{***}$	16.5 ± 8.72	12.89 ± 3.89	19.86 ± 12.21	11.89 ± 8.1; ***p = 0.018****	15.8 ± 2.68	12.79 ± 5.29; ***p = 0.03****	9.54 ± 4.9; ***p = 0.002*****	13.2 ± 5.91
MUA firing rate (spikes/s)		0.81 ± 1.77	1.46 ± 2.84	1.41 ± 1.98	1.7 ± 1.6	1.89 ± 4.45	1.1 ± 0.91	1.17 ± 1.72	0.63 ± 2.62

Note: Data are shown as median ± interquartile range. Corrected p values (Benjamin-Hochberg) for comparisons between controls and disease groups are listed. Italics indicate statistics of ANOVA for GLM/GLME; Italics and bolds indicate statistics of coefficient testing for GLM/GLME. $^{*}p < 0.05$, $^{**}p < 0.01$, $^{***}p < 0.001$.

the imaginary part of coherence, which has the advantage over normal magnitude squared coherence of cancelling out any results due to volume conduction. Coherence was significantly altered in the beta range ($F_{7,111} = 4.86$, $p < 0.001$), yet remained unchanged for 3–8 Hz (Figure 4b(ii), Table 3). The prelimbic–hippocampal synchrony was significantly reduced in one-hit Df16 model ($p = 0.038$) and dual-hit DISC1 + MIA ($p = 0.001$).

Next, we estimated the communication within prelimbic–hippocampal networks by GPDC that is considered to be a more precise measure of coupling, since it takes the time dimension of information transfer into account (Baccalá et al., 2007). We analysed the drive from i/vHP to PL in all investigated groups (Figure 4c, d). GPDC was over the sample set significantly altered in the theta and beta range (theta: $F_{7,111} = 4.34$, $p < 0.001$; beta: $F_{7,111} = 3.14$, $p = 0.003$). Significant decrease in hippocampal drive was detected in one-hit Df16 mice (theta: $p = 0.044$; beta: $p = 0.006$) as well as in dual-hit DISC1 + MIA (theta: $p = 0.01$, beta: $p = 0.006$) and Df16 + MIA (beta: $p = 0.017$; Table 3). The synchrony and directed interactions in one-hit DISC1, MIA as well as in KET mice were similar to controls.

These results demonstrate that developmental deficits of local circuitry in PL and HP in one-hit Df16 and dual-hit mice accompany weaker coupling within neonatal prelimbic–hippocampal networks. In contrast, early dysfunction of these circuits was not present in mice reproducing only one risk factor of disease (e.g., DISC1 or MIA) or in pharmacological model (i.e., KET).

4 | DISCUSSION

A wealth of rodent models has been proposed to mimic aspects of human mental disorders. Their large number and diversity lead to the question whether common mechanisms cause in the end the characteristic symptoms of disease. For neurodevelopmental disorders, such as schizophrenia, diverse risk factors might similarly affect the brain by acting on a common pathway that disturbs network maturation, resulting in detectable cognitive deficits at juvenile-young adult stage. To examine this hypothesis, we investigated the neurodevelopmental abnormalities in six distinct animal models of disease whose adult phenotype has been previously characterized in detail. We focused on the core circuit underlying memory and executive abilities, the prelimbic–hippocampal network, and showed that shortly after birth, the early patterns of coordinated activity in PL and HP appear disorganized with lower power in mice modelling 22q11.2 microdeletions, a genetic variant highly penetrant for schizophrenia, and mice combining genetic dysfunction with an environmental stressor (DISC1 + MIA, Df16 + MIA). Additionally, these mice showed weaker synchrony and directed coupling

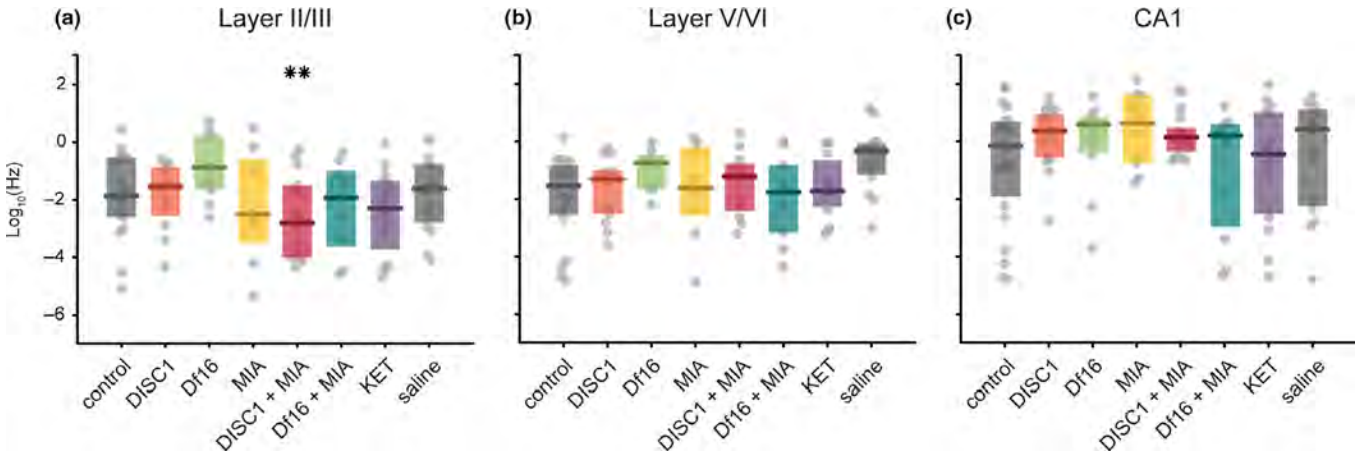

FIGURE 3 Firing rates of PL and i/vHP in mouse models of mental illness. (a) Scatter plot displaying the median firing rate in superficial layers of PL from all models (colours) and their controls (dark grey; DISC1 + MIA vs. control: $p = 0.008$). (b) The same as (a) for deep layers of PL. (c) The same as (a) for CA1 area of i/vHP. Single data points are represented as circles, the coloured bars represent the median and the coloured boxes the 25th and 75th percentiles, $^{**}p < 0.01$

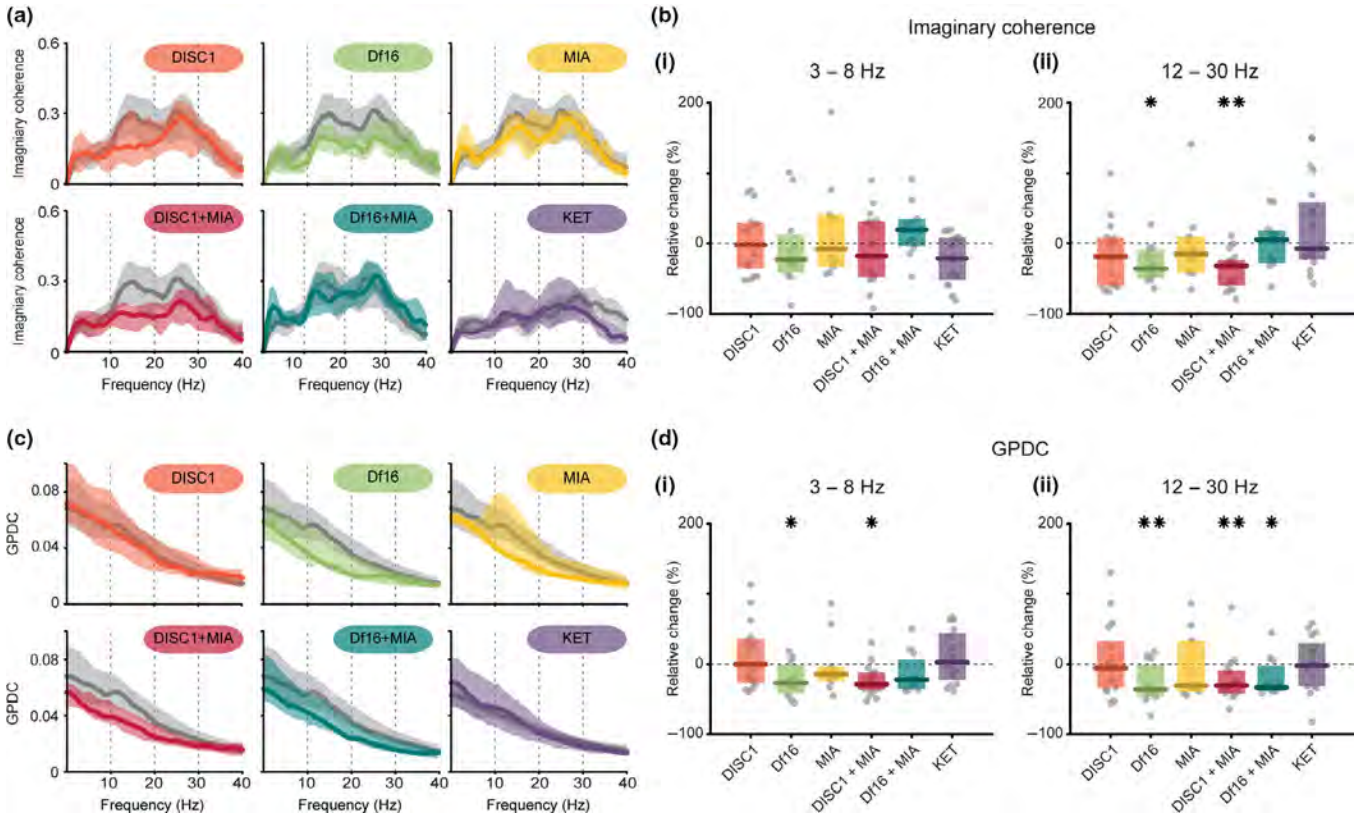

FIGURE 4 Coupling between PL and i/vHP in mouse models of mental illness. (a) Averaged coherence spectra $C(f)$ for simultaneous oscillatory periods between PL and i/vHP displayed for all mouse models (colours) together with their control (light grey). (b) (i) Scatter plot displaying the relative coherence within 3–8 Hz for all models when normalized to controls. (ii) Same as (i) in the beta (12–30 Hz) frequency band (Df16 vs. control: $p = 0.038$, DISC1 + MIA vs. control: $p = 0.001$). (c) Averaged GPDC spectra $G(f)$ from i/vHP to PL displayed for all mouse models (colours) together with their control (light grey). (d) (i) Scatter plot displaying the relative GPDC within 3–8 Hz for all models when normalized to controls (Df16 vs. control: $p = 0.044$, DISC1 + MIA vs. control: $p = 0.01$). (ii) Same as (i) for beta (12–30 Hz) frequency band (Df16 vs. control: $p = 0.006$, DISC1 + MIA vs. control: $p = 0.006$, Df16 + MIA vs. control: $p = 0.017$). Thick lines represent the median, and shaded areas represent the 25° and 75° percentiles. Single data points are represented as circles, the coloured bars represent the median and the coloured boxes the 25th and 75th percentiles, $^{*}p < 0.05$, $^{**}p < 0.01$

between PL and HP, especially in beta frequency band. In contrast, no significant prelimbic–hippocampal deficits were observed in one-hit (DISC1, MIA) or KET mice.

Since at adulthood all investigated mice have been used as models of disease and mimic, at least in part, the dysfunction and cognitive impairment of mental illness, it is likely that the disease-related miswiring of neuronal circuits emerges at different developmental time points. For example, the disruption of limbic circuits centred on the prefrontal–hippocampal networks and the impairment of memory and executive abilities have been previously reported in DISC1 haploinsufficiency, transgenic and point mutations models (Crabtree et al., 2017; Dawson et al., 2015; Koike, Arguello, Kvajo, Karayiorgou, & Gogos, 2006). Specifically, the dysfunction of local and long-range circuits centred on PFC correlate with decreased working memory, prepulse inhibition, sociability, and spatial recognition memory as well as increased depression-like behaviour (Clapcote et al., 2007; Niwa et al., 2010; Sauer, Strüber, & Bartos, 2015). However, in line with our past (Hartung et al., 2016) and present results, the genetic abnormality is not sufficient for disrupting the initial entrainment of neonatal prefrontal–hippocampal circuits in oscillatory rhythms.

A second stressor is necessary to induce early dysfunction. MIA mimicked by treatment with polyI:C at distinct gestational stages has been identified as environmental factor linked to schizophrenia. Adult MIA rodents show circuit abnormalities (interneuronal deficits and diminished gamma oscillations in PFC) and decrease long-range coupling over a broad frequency spectrum within prefrontal–hippocampal circuits (Dickerson, Wolff, & Bilkey, 2010). Consequently, they show poorer PFC-dependent working memory, prepulse inhibition, cognitive flexibility and attentional set-shifting abilities (Canetta et al., 2016; Meyer & Feldon, 2012). While neonatal MIA mice were almost indistinguishable from controls, in combination with the abnormal DISC1 background, they show profound impairment of early prelimbic–hippocampal communication. Both brain areas have disorganized activity patterns that occur more frequently but have reduced power in theta and beta-low gamma frequency range. These alterations of network activity might reflect a global perturbation of brain activity due to the combined action of genetic and environmental factors on cortical migration and differentiation. Disc1 mutation may induce perturbation of immune-relevant signalling pathways early in life (Beurel, Yeh, Michalek, Harrington, & Jope, 2011). The disorganized activation of HP and the weaker drive to PL is accompanied by a reduction in axonal projections between the two areas (Song and Hanganu-Opatz, unpublished observations). These structural and functional deficits may perturb the prelimbic activity and initial wiring of local circuits. Structural changes in PL, such as decrease in spine density or lower number of axonal terminals, might lead

TABLE 3 Imaginary coherence and GPDC within prefrontal–hippocampal networks of neonatal control and disease model mice

	Group effect	Control	Saline	DISC1	Df16	MIA	DISC1 + MIA	Df16 + MIA	KET
Im. coherence (3–8 Hz)		0.13 ± 0.08	0.12 ± 0.02	0.12 ± 0.08	0.1 ± 0.07	0.12 ± 0.09	0.1 ± 0.1	0.15 ± 0.05	0.1 ± 0.08
Im. coherence (12–30 Hz)	ANOVA, $F_{7,111} = 4.86$; $p < 0.001^{***}$	0.26 ± 0.15	0.17 ± 0.1	0.21 ± 0.18	0.17 ± 0.1; ***p = 0.038****	0.22 ± 0.13	0.18 ± 0.09; ***p = 0.001****	0.28 ± 0.12	0.15 ± 0.13
GPDC (3–8 Hz)	ANOVA, $F_{7,111} = 4.34$; $p < 0.001^{***}$	0.063 ± 0.03	0.049 ± 0.011	0.063 ± 0.038	0.047 ± 0.025; ***p = 0.044****	0.054 ± 0.013	0.045 ± 0.016; ***p = 0.01****	0.049 ± 0.027	0.05 ± 0.033
GPDC (12–30 Hz)	ANOVA, $F_{7,111} = 3.14$; $p = 0.003^{**}$	0.037 ± 0.015	0.029 ± 0.009	0.034 ± 0.024	0.023 ± 0.016; ***p = 0.006****	0.025 ± 0.026	0.025 ± 0.012; ***p = 0.017****	0.024 ± 0.013; ***p = 0.006****	0.029 ± 0.018

Note: Data are shown as median ± interquartile range. Corrected p values (Benjamin-Hochberg) for comparisons between controls and disease groups are listed. Italics indicate statistics of ANOVA for GLM/GLME; Italics and bolds indicate statistics of coefficient testing for GLM/GLME. $^{*}p < 0.05$, $^{**}p < 0.01$, $^{***}p < 0.01$

to decreased firing of pyramidal neurons in PL (Xu et al., 2019), but also to loss of theta-timed precision of firing, as reflected by the weaker strength of theta-spike coupling (Hartung et al., 2016). These results are in line with previous data reported for adult dual-hit DISC1-MIA mice that show decreased spine density on hippocampal neurons as well as decreased sociability and augmented anxiety and depressive-like behaviour (Abazyan et al., 2010).

Surprisingly, similar potentiating effects of combined genetic environmental factors were not observed for the dual-hit Df16 + MIA mice. This might be due to the fact that the genetic abnormality mimicking the 22q11.2 microdeletions has already a maximal impact on the early circuits, in contrast to the rather mild phenotype of Disc1 mutation. Conserved on mouse chromosome 16, these microdeletions affect several key genes, such as Dgcr8, Comt and Prodh that even alone affect dendritic development and dopamine metabolism (Arguello, Markx, Gogos, & Karayiorgou, 2010; Paterlini et al., 2005). The present data demonstrate that the prefrontal and hippocampal activity of one-hit Df16 mice is altered in a similar way as that of dual-hit DISC1 + MIA mice. The higher occurrence of shorter low power oscillations in both areas was accompanied by weaker synchrony and diminished drive from HP to PL at neonatal age. This early circuit miswiring most likely result from abnormal physiological properties of cortical neurons that have identified in vitro already at embryonic stage (Sun, Williams, Xu, & Gogos, 2018). Adult Df(16)A$^{+/-}$ mice have working memory deficits and impaired conditioned fear as result of reduced coupling within prefrontal–hippocampal networks (Sigurdsson et al., 2010; Stark et al., 2008). Co-occurrence of MIA does not augment but even reduce the deficits observed in the one-hit Df16 mice. Whether poly I:C partially rescues the morphological and functional abnormalities of microdeletions remains to be elucidated in future studies. One possible mechanism may involve micro RNAi that are upregulated in the dam by MIA (Hollins & Cairns, 2016) and may cross the placenta barrier (Chang et al., 2017), compensating for microdeletions (Stark et al., 2008).

Neonatal KET mice showed no prelimbic–hippocampal deficits when compared with their saline control. Adult mice that received chronic ketamine administration have been reported to have altered neuronal ensembles as result of pyramidal and interneuronal dysfunction (Behrens et al., 2007; Hamm et al., 2017), while acute administration leads to spectral alterations of the prefrontal–hippocampal circuitry (Moran et al., 2015). Consequently, these mice have poorer memory performance, decreased mismatch negativity and cognitive flexibility as well as altered social behaviour (Amitai, Semenova, & Markou, 2007; Featherstone et al., 2012; Hauser, Isbrandt, & Roeper, 2017; Koh, Shao, Sherwood, & Smith, 2016). The similar outcome of NMDA receptor blockade or saline treatment during neonatal period may indicate that the disease-related glutamatergic dysfunction emerges later and perturbs the neuronal circuits after the establishment of their first interactions. In line with this hypothesis, ketamine administration during the 2nd post-natal week leads to reduced PV expression in PFC and attentional, memory and social deficits (Jeevakumar et al., 2015).

Thus, the present results show that common deficits reported for different mouse models of mental disorders may share common pathways of impairment. The prefrontal–hippocampal communication critically controlling the cognitive performance is a hub of disease-induced impairment, yet sensory circuits and related abilities might be disrupted too (Hamm et al., 2017). However, depending on the severity of risk factors this hub is susceptible to impairment during a different time window in life. This temporal aspect needs to be considered when aiming to assemble the puzzle for understanding mental disorders.

ACKNOWLEDGEMENTS

We thank Dr. Joseph Gogos for providing the DISC1$^{+/-}$ and Df(16)A$^{+/-}$ mice and A. Marquardt, P. Putthoff, A. Dahlmann and K. Titze for excellent technical assistance. This work was funded by grants from the European Research Council (ERC-2015-CoG 681577 to I.L.H.-O.) and the German Research Foundation (Ha 4466/10-1, SPP 1665, SFB 936 B5 to I.L.H.-O.).

CONFLICT OF INTEREST

The authors declare no competing financial interests.

DATA ACCESSIBILITY

The authors declare that all data and code supporting the findings of this study are included in the manuscript or are available from the corresponding author on request.

AUTHOR CONTRIBUTIONS

I.L.H.-O. designed the experiments; V.O. carried out the experiments; V.O., X.X. and M.C. analysed the data; I.L.H.-O., X.X. and V.O. interpreted the data and wrote the paper. All authors discussed and commented on the manuscript.

ORCID


Xiaxia Xu https://orcid.org/0000-0002-9648-8367

REFERENCES

Abazyan, B., Nomura, J., Kannan, G., Ishizuka, K., Tamashiro, K. L., Nucifora, F., … Pletnikov, M. V. (2010). Prenatal interaction of

mutant DISC1 and immune activation produces adult psychopathology. *Biological Psychiatry*, *68*, 1172–1181.

Ahlbeck, J., Song, L., Chini, M., Bitzenhofer, S. H., & Hanganu-Opatz, I. L. (2018). Glutamatergic drive along the septo-temporal axis of hippocampus boosts prelimbic oscillations in the neonatal mouse. *Elife*, *7*, e33158.

Amitai, N., Semenova, S., & Markou, A. (2007). Cognitive-disruptive effects of the psychotomimetic phencyclidine and attenuation by atypical antipsychotic medications in rats. *Psychopharmacology (Berl)*, *193*, 521–537.

Arguello, P. A., Markx, S., Gogos, J. A., & Karayiorgou, M. (2010). Development of animal models for schizophrenia. *Disease Models & Mechanisms*, *3*, 22–26.

Baccalá, L. A., Sameshima, K., & Takahashi, D. Y. (2007). Generalized partial directed coherence 15th International Conference on Digital Signal Processing. IEEE, Cardiff, pp. 163–166.

Behrens, M. M., Ali, S. S., Dao, D. N., Lucero, J., Shekhtman, G., Quick, K. L., & Dugan, L. L. (2007). Ketamine-induced loss of phenotype of fast-spiking interneurons is mediated by NADPH-oxidase. *Science*, *318*, 1645–1647.

Beurel, E., Yeh, W. I., Michalek, S. M., Harrington, L. E., & Jope, R. S. (2011). Glycogen synthase kinase-3 is an early determinant in the differentiation of pathogenic Th17 cells. *The Journal of Immunology*, *186*, 1391–1398.

Bitzenhofer, S. H., Sieben, K., Siebert, K. D., Spehr, M., & Hanganu-Opatz, I. L. (2015). Oscillatory activity in developing prefrontal networks results from theta-gamma-modulated synaptic inputs. *Cell Reports*, *11*, 486–497.

Brockmann, M. D., Poschel, B., Cichon, N., & Hanganu-Opatz, I. L. (2011). Coupled oscillations mediate directed interactions between prefrontal cortex and hippocampus of the neonatal rat. *Neuron*, *71*, 332–347.

Canetta, S., Bolkan, S., Padilla-Coreano, N., Song, L. J., Sahn, R., Harrison, N. L., … Kellendonk, C. (2016). Maternal immune activation leads to selective functional deficits in offspring parvalbumin interneurons. *Molecular Psychiatry*, *21*, 956–968.

Chang, G., Mouillet, J. F., Mishima, T., Chu, T., Sadovsky, E., Coyne, C. B., … Sadovsky, Y. (2017). Expression and trafficking of placental microRNAs at the feto-maternal interface. *The FASEB Journal*, *31*, 2760–2770.

Chini, M., Gretenkord, S., Kostka, J. K., Pöpplau, J. A., Cornelissen, L., Berde, C. B., … Bitzenhofer, S. H. (2019). Neural Correlates of Anesthesia in Newborn Mice and Humans. *Frontiers in Neural Circuits*, *13*. https://doi.org/10.3389/fncir.2019.00038

Cichon, N. B., Denker, M., Grun, S., & Hanganu-Opatz, I. L. (2014). Unsupervised classification of neocortical activity patterns in neonatal and pre-juvenile rodents. *Frontiers in Neural Circuits*, *8*, 50.

Clapcote, S. J., Lipina, T. V., Millar, J. K., Mackie, S., Christie, S., Ogawa, F., … Roder, J. C. (2007). Behavioral phenotypes of Disc1 missense mutations in mice. *Neuron*, *54*, 387–402.

Crabtree, G. W., Sun, Z., Kvajo, M., Broek, J. A., Fenelon, K., McKellar, H., … Gogos, J. A. (2017). Alteration of neuronal excitability and short-term synaptic plasticity in the prefrontal cortex of a mouse model of mental illness. *Journal of Neuroscience*, *37*, 4158–4180.

Cuthbert, B. N., & Insel, T. R. (2013). Toward the future of psychiatric diagnosis: the seven pillars of RDoC. *BMC Medicine*, *11*, 126.

Dawson, N., Kurihara, M., Thomson, D. M., Winchester, C. L., McVie, A., Hedde, J. R., … Pratt, J. A. (2015). Altered functional brain network connectivity and glutamate system function in transgenic mice expressing truncated disrupted-in-schizophrenia 1. *Translational Psychiatry*, *5*, e569.

Dickerson, D. D., Wolff, A. R., & Bilkey, D. K. (2010). Abnormal long-range neural synchrony in a maternal immune activation animal model of schizophrenia. *Journal of Neuroscience*, *30*, 12424–12431.

Estes, M. L., & McAllister, A. K. (2016). Maternal immune activation: Implications for neuropsychiatric disorders. *Science*, *353*, 772–777.

Featherstone, R. E., Liang, Y., Saunders, J. A., Tatard-Leitman, V. M., Ehrlichman, R. S., & Siegel, S. J. (2012). Subchronic ketamine treatment leads to permanent changes in EEG, cognition and the astrocytic glutamate transporter EAAT2 in mice. *Neurobiology of Diseases*, *47*, 338–346.

Hamm, J. P., Peterka, D. S., Gogos, J. A., & Yuste, R. (2017). Altered cortical ensembles in mouse models of schizophrenia. *Neuron*, *94*, 153–167 e158.

Hartung, H., Cichon, N., De Feo, V., Riemann, S., Schildt, S., Lindemann, C., … Hanganu-Opatz, I. L. (2016). From shortage to surge: A developmental switch in hippocampal-prefrontal coupling in a gene-environment model of neuropsychiatric disorders. *Cerebral Cortex*, *26*, 4265–4281.

Hauser, M. J., Isbrandt, D., & Roeper, J. (2017). Disturbances of novel object exploration and recognition in a chronic ketamine mouse model of schizophrenia. *Behavioral Brain Research*, *332*, 316–326.

Hollins, S. L., & Cairns, M. J. (2016). MicroRNA: Small RNA mediators of the brains genomic response to environmental stress. *Progress in Neurobiology*, *143*, 61–81.

International Schizophrenia, C (2008). Rare chromosomal deletions and duplications increase risk of schizophrenia. *Nature*, *455*, 237–241.

Janiesch, P. C., Kruger, H. S., Poschel, B., & Hanganu-Opatz, I. L. (2011). Cholinergic control in developing prefrontal-hippocampal networks. *Journal of Neuroscience*, *31*, 17955–17970.

Jeevakumar, V., Driskill, C., Paine, A., Sobhanian, M., Vakil, H., Morris, B., … Kroener, S. (2015). Ketamine administration during the second postnatal week induces enduring schizophrenia-like behavioral symptoms and reduces parvalbumin expression in the medial prefrontal cortex of adult mice. *Behavioral Brain Research*, *282*, 165–175.

Kaiser, T., Zhou, Y., & Feng, G. (2017). Animal models for neuropsychiatric disorders: Prospects for circuit intervention. *Current Opinion in Neurobiology*, *45*, 59–65.

Koh, M. T., Shao, Y., Sherwood, A., & Smith, D. R. (2016). Impaired hippocampal-dependent memory and reduced parvalbumin-positive interneurons in a ketamine mouse model of schizophrenia. *Schizophrenia Research*, *171*, 187–194.

Koike, H., Arguello, P. A., Kvajo, M., Karayiorgou, M., & Gogos, J. A. (2006). Disc1 is mutated in the 129S6/SvEv strain and modulates working memory in mice. *Proceedings of the National Academy of Sciences of the United States of America*, *103*, 3693–3697.

Krystal, J. H., Karper, L. P., Seibyl, J. P., Freeman, G. K., Delaney, R., Bremner, J. D., … Charney, D. S. (1994). Subanesthetic effects of the noncompetitive NMDA antagonist, ketamine, in humans. Psychotomimetic, perceptual, cognitive, and neuroendocrine responses. *Archives of General Psychiatry*, *51*, 199–214.

Kvajo, M., McKellar, H., Arguello, P. A., Drew, L. J., Moore, H., MacDermott, A. B., … Gogos, J. A. (2008). A mutation in mouse Disc1 that models a schizophrenia risk allele leads to specific alterations in neuronal architecture and cognition. *Proceedings of the National Academy of Sciences of the United States of America*, *105*, 7076–7081.

Meyer, U., & Feldon, J. (2012). To poly(I:C) or not to poly(I:C): Advancing preclinical schizophrenia research through the use of prenatal immune activation models. *Neuropharmacology*, *62*, 1308–1321.

Meyer, U., Feldon, J., Schedlowski, M., & Yee, B. K. (2006). Immunological stress at the maternal-foetal interface: A link between neurodevelopment and adult psychopathology. *Brain, Behavior, and Immunity*, *20*, 378–388.

Meyer-Lindenberg, A. S., Olsen, R. K., Kohn, P. D., Brown, T., Egan, M. F., Weinberger, D. R., & Berman, K. F. (2005). Regionally specific disturbance of dorsolateral prefrontal-hippocampal functional connectivity in schizophrenia. *Archives of General Psychiatry*, *62*, 379–386.

Moran, R. J., Jones, M. W., Blockeel, A. J., Adams, R. A., Stephan, K. E., & Friston, K. J. (2015). Losing control under ketamine: Suppressed cortico-hippocampal drive following acute ketamine in rats. *Neuropsychopharmacology*, *40*, 268–277.

Mukai, J., Tamura, M., Fenelon, K., Rosen, A. M., Spellman, T. J., Kang, R., … Gogos, J. A. (2015). Molecular substrates of altered axonal growth and brain connectivity in a mouse model of schizophrenia. *Neuron*, *86*, 680–695.

Nestler, E. J., & Hyman, S. E. (2010). Animal models of neuropsychiatric disorders. *Nature Neuroscience*, *13*, 1161–1169.

Nimgaonkar, V. L., Prasad, K. M., Chowdari, K. V., Severance, E. G., & Yolken, R. H. (2017). The complement system: A gateway to gene-environment interactions in schizophrenia pathogenesis. *Molecular Psychiatry*, *22*, 1554–1561.

Niwa, M., Kamiya, A., Murai, R., Kubo, K., Gruber, A. J., Tomita, K., … Nabeshima, T. (2010). Knockdown of DISC1 by in utero gene transfer disturbs postnatal dopaminergic maturation in the frontal cortex and leads to adult behavioral deficits. *Neuron*, *65*, 480–489.

Nolte, G., Bai, O., Wheaton, L., Mari, Z., Vorbach, S., & Hallett, M. (2004). Identifying true brain interaction from EEG data using the imaginary part of coherency. *Clinical Neurophysiology*, *115*, 2292–2307.

Owen, M. J., Sawa, A., & Mortensen, P. B. (2016). Schizophrenia. *Lancet*, *388*, 86–97.

Paterlini, M., Zakharenko, S. S., Lai, W. S., Qin, J., Zhang, H., Mukai, J., … Gogos, J. A. (2005). Transcriptional and behavioral interaction between 22q11.2 orthologs modulates schizophrenia-related phenotypes in mice. *Nature Neuroscience*, *8*, 1586–1594.

Sauer, J.-F., Strüber, M., & Bartos, M. (2015). Impaired fast-spiking interneuron function in a genetic mouse model of depression. *Elife*, *4*, e04979.

Schwarz, E., Tost, H., & Meyer-Lindenberg, A. (2016). Working memory genetics in schizophrenia and related disorders: An RDoC perspective. *American Journal of Medical Genetics. Part B, Neuropsychiatric Genetics: The Official Publication of the International Society of Psychiatric Genetics.*, *171B*, 121–131.

Shi, L., Fatemi, S. H., Sidwell, R. W., & Patterson, P. H. (2003). Maternal influenza infection causes marked behavioral and pharmacological changes in the offspring. *Journal of Neuroscience*, *23*, 297–302.

Sigurdsson, T., & Duvarci, S. (2015). Hippocampal-prefrontal interactions in cognition, behavior and psychiatric disease. *Frontiers in Systems Neuroscience*, *9*, 190.

Sigurdsson, T., Stark, K. L., Karayiorgou, M., Gogos, J. A., & Gordon, J. A. (2010). Impaired hippocampal-prefrontal synchrony in a genetic mouse model of schizophrenia. *Nature*, *464*, 763–767.

Stark, K. L., Xu, B., Bagchi, A., Lai, W. S., Liu, H., Hsu, R., … Gogos, J. A. (2008). Altered brain microRNA biogenesis contributes to phenotypic deficits in a 22q11-deletion mouse model. *Nature Genetics*, *40*, 751–760.

Sun, Z., Williams, D. J., Xu, B., & Gogos, J. A. (2018). Altered function and maturation of primary cortical neurons from a 22q11.2 deletion mouse model of schizophrenia. *Translational Psychiatry*, *8*, 85.

van Os, J., Rutten, B. P., Myin-Germeys, I., Delespaul, P., Viechtbauer, W., van Zelst, C., Bruggeman, R., Reininghaus, U., Morgan, C., … Mirjanic, T. (2014). Identifying gene-environment interactions in schizophrenia: Contemporary challenges for integrated, large-scale investigations. *Schizophrenia Bulletin*, *40*, 729–736.

Xu, X., Chini, M., Bitzenhofer, S. H., & Hanganu-Opatz, I. L. (2019). Transient knock-down of prefrontal DISC1 in immune-challenged mice causes abnormal long-range coupling and cognitive dysfunction throughout development. *Journal of Neuroscience*, *39*, 1222–1235.

How to cite this article: Oberlander VC, Xu X, Chini M, Hanganu-Opatz IL. Developmental dysfunction of prefrontal–hippocampal networks in mouse models of mental illness. *Eur J Neurosci*. 2019;50:3072–3084. https://doi.org/10.1111/ejn.14436

2.3 Transient Knock-Down of Prefrontal DISC1 in Immune-Challenged Mice Causes Abnormal Long-Range Coupling and Cognitive Dysfunction throughout Development

Xiaxia Xu, Mattia Chini, Sebastian H. Bitzenhofer and Ileana L. Hanganu-Opatz

Journal of Neuroscience 2019; DOI: https://doi.org/10.1523/JNEUROSCI.2170-18.2018

Personal contribution

I carried out formal analysis. I reviewed and edited the manuscript.

Systems/Circuits

Transient Knock-Down of Prefrontal DISC1 in Immune-Challenged Mice Causes Abnormal Long-Range Coupling and Cognitive Dysfunction throughout Development

Xiaxia Xu, Mattia Chini, Sebastian H. Bitzenhofer, and Ileana L. Hanganu-Opatz
Developmental Neurophysiology, Institute of Neuroanatomy, University Medical Center Hamburg-Eppendorf, 20251 Hamburg, Germany

Compromised brain development has been hypothesized to account for mental illness. This concept was underpinned by the function of the molecule disrupted-in-schizophrenia 1 (DISC1), which represents an intracellular hub of developmental processes and has been related to cognitive dysfunction in psychiatric disorders. Mice with whole-brain DISC1 knock-down show impaired prefrontal–hippocampal function and cognitive abilities throughout development and at adulthood, especially when combined with early environmental stressors, such as maternal immune activation (MIA). However, the contribution of abnormal DISC1-driven maturation of either prefrontal cortex (PFC) or hippocampus (HP) to these deficits is still unknown. Here, we use *in utero* electroporation to restrict the DISC1 knock-down to prefrontal layer II/III pyramidal neurons during perinatal development and expose these mice to MIA as an environmental stressor (dual-hit $G_{PFC}E$ mice, both sexes). Combining *in vivo* electrophysiology and neuroanatomy with behavioral testing, we show that $G_{PFC}E$ mice at neonatal age have abnormal patterns of oscillatory activity and firing in PFC, but not HP. Abnormal firing rates in PFC of $G_{PFC}E$ mice relate to sparser dendritic arborization and lower spine density. Moreover, the long-range coupling within prefrontal–hippocampal networks is decreased at this age. The transient prefrontal DISC1 knock-down was sufficient to permanently perturb the prefrontal–hippocampal communication and caused poorer recognition memory performance at pre-juvenile age. Thus, developmental dysfunction of prefrontal circuitry causes long-lasting disturbances related to mental illness.

Key words: development; DISC1; network oscillations; prefrontal maturation; prefrontal–hippocampal communication

Significance Statement

Hypofrontality is considered a main cause of cognitive deficits in mental disorders, yet the underlying mechanisms are still largely unknown. During development, long before the emergence of disease symptoms, the functional coupling within the prefrontal–hippocampal network, which is the core brain circuit involved in cognitive processing, is reduced. To assess to which extent impaired prefrontal development contributes to the early dysfunction, immune-challenged mice with transient DISC1 knock-down confined to PFC were investigated in their prefrontal–hippocampal communication throughout development by *in vivo* electrophysiology and behavioral testing. We show that perturbing developmental processes of prefrontal layer II/III pyramidal neurons is sufficient to diminish prefrontal–hippocampal coupling and decrease the cognitive performance throughout development.

Introduction

The cerebral cortex emerges as the result of complex developmental processes, such as neurogenesis, neuronal migration, and differentiation (Rakic, 1988; Dehay and Kennedy, 2007). They are controlled by numerous cell autonomous process as well as extracellular and environmental factors. Disrupted-in-schizophrenia 1 (DISC1) is an intracellular scaffold protein that has been identified as an intracellular hub of developmental processes (Narayan et al., 2013). Moreover, DISC1 plays a critical role for synapse regulation. Despite its name, which reflects a unique finding of a familial aggregation of major mental illness (Millar et al., 2000), according to recent investigations, DISC1 is unlikely to be a "genetic" factor caus-

Received Aug. 22, 2018; revised Nov. 20, 2018; accepted Nov. 21, 2018.

Author contributions: X.X. wrote the first draft of the paper; X.X. and I.L.H.-O. edited the paper; I.L.H.-O. designed research; X.X. performed research; X.X., M.C., and S.H.B. analyzed data; X.X. and I.L.H.-O. wrote the paper.

This work was supported by Grants from the European Research Council (ERC-2015-CoG 681577 to I.L.H.-O.) and the German Research Foundation (SPP 1665, SFB 936 B5 to I.L.H.-O.), and I.L. H.-O. is member of FENS Kavli Network of Excellence. We thank Dr. Joseph Gogos for providing the DISC1 mice, Dr. A. Sawa for providing short-hairpin RNA (shRNA) to DISC1, and A. Marquardt, A. Dahlmann, and P. Putthoff for excellent technical assistance.

The authors declare no competing financial interests.

Correspondence should be addressed to Ileana L. Hanganu-Opatz at hangop@zmnh.uni-hamburg.de.
https://doi.org/10.1523/JNEUROSCI.2170-18.2018

ing schizophrenia (Ripke et al., 2013; Sullivan, 2013). Instead, DISC1 points out the relevance of abnormal development in multiple mental conditions, because it orchestrates molecular cascades hypothesized to underlie disease-relevant physiological and behavioral abnormalities (Cuthbert and Insel, 2013). Dysfunction of DISC1 mimicked in several mouse models led to cellular, neurotransmitter, circuitry, and behavioral deficits at adulthood (Tomoda et al., 2016). In particular, the disruption of limbic circuits centered on the prefrontal–hippocampal networks and the impairment of memory and executive abilities have been previously reported in DISC1 haploinsufficiency, transgenic and point mutation models, as well as in models mimicking the additional disruption of *Disc1* locus by environmental stressors (Koike et al., 2006; Clapcote et al., 2007; Kvajo et al., 2011; Jaaro-Peled et al., 2013; Niwa et al., 2013; Crabtree et al., 2017). Whereas the initial alteration of developmental molecular cascades controlled by DISC1 and its final readout at physiological and behavioral level have been largely elucidated, the patterns of circuit miswiring during early development in mice with DISC1 dysfunction are still poorly understood.

Recent findings showed that the prefrontal and hippocampal circuits are tightly linked throughout development (Brockmann et al., 2011). Shortly after birth, the prefrontal cortex (PFC) starts to generate coordinated patterns of oscillatory activity that results both from the entrainment of local circuits and the driving force of theta oscillations in the intermediate/ventral hippocampus (HP; Bitzenhofer et al., 2017b; Ahlbeck et al., 2018). At this age, the monosynaptic projections from CA1 pyramidal neurons target the deep layers of prelimbic subdivision (PL) of PFC, whereas no direct feedback connectivity exists. The unidirectional drive from HP to PL via axonal projections is maintained also at adulthood (Thierry et al., 2000) and controls memory and executive performance. For example, temporal coordination of prefrontal ensembles by hippocampal oscillatory rhythms is critical for different memory forms (Siapas et al., 2005; Fujisawa and Buzsáki, 2011; Spellman et al., 2015; Backus et al., 2016).

DISC1 dysfunction perturbs not only the adult prefrontal–hippocampal coupling but also its maturation. We previously found that, in comparison with control mice, the drive from HP to PL is weaker at neonatal age and augmented at pre-juvenile age in prenatally immune challenged mice containing a whole-brain truncated form of DISC1 (Hartung et al., 2016b). Several mechanisms may account for these communication deficits: (1) DISC1-controlled abnormal maturation of PFC is critical, (2) DISC1-controlled maturation of HP is critical, (3) abnormal development of both areas as a result of DISC1 deregulation is necessary, and finally, (4) DISC1 deficiency causes aberrant connectivity from HP to PFC. "Here, we test the first mechanism aiming to elucidate whether DISC1-controlled developmental deficits confined to PFC lead to similar impairment of prefrontal–hippocampal communication as previously reported for whole-brain deregulation of DISC1". Because our previous data showed that at neonatal age DISC1 dysfunction is not sufficient to perturb the prefrontal–hippocampal activity and coupling, the abnormal genetic background (one-hit G) was combined with an environmental stressor (i.e., maternal immune activation, one-hit E). We used *in utero* electroporation (IUE) to selectively knock down DISC1 in prefrontal layer II/III pyramidal neurons during perinatal development in mice exposed to maternal immune activation (MIA) as environmental stressor (dual-hit $G_{PFC}E$ mice). We combine *in vivo* electrophysiology with behavioral assessment to elucidate the deficits of dual-hit $G_{PFC}E$ mice throughout development.

Materials and Methods

Experiments were performed in compliance with the German laws and the guidelines of the European Community for the use of animals in research and were approved by the local ethical committee (111/12, 132/12). Timed-pregnant C57BL/6J mice from the animal facility of the University Medical Center Hamburg-Eppendorf were used. The day of vaginal plug detection was defined as embryonic day (E)0.5, whereas the day of birth was defined as postnatal day (P)0.

Experimental design

Mice were transfected with either (1) short-hairpin RNA (shRNA) to DISC1 (5′-GGCAAACACTGTGAAGTGC-3′) to selectively knock down the expression of DISC1 in PFC during neonatal development (Niwa et al., 2010) or (2) scrambled target sequence without homology to any known messenger RNA (5′-ATCTCGCTTGGGCGAGAGT-3′) as control shRNA. Both shRNA to DISC1 and control shRNA were expressed under H1 promoter-driven pSuper plasmid. To visualize the transfected neurons, DISC1 shRNA or control shRNA was expressed together with tDimer2 under the control of the CAG promoter (pAAV-CAG-tDimer2). Three groups of mice were investigated. First, the offspring of pregnant wild-type C57BL/6J dams, which were injected at gestational day (G)9.5 with the viral mimetic poly I:C (4 mg/kg, i.v.), were transfected by IUE with DISC1 shRNA at E15.5. These mice mimicking the dual genetic and environmental (i.e., MIA) etiology of disease were classified as $G_{PFC}E$ mice. Second, the heterozygous offspring of pregnant dams carrying a DISC1 allele ($DISC1^{Tm1Kara}$) on a C57BL/6J background and injected at E9.5 with the viral mimetic poly I:C (4 mg/kg, i.v.) were transfected by IUE with control shRNA at E15.5 and classified as dual-hit genetic-environmental (GE) mice. Third, the offspring of pregnant wild-type C57BL/6J dams injected at E9.5 with saline (0.9%, i.v) were transfected with control shRNA and were classified as controls (CON; Fig. 1*A*,*B*). Multisite extracellular recordings and behavioral testing were performed on pups of both sexes during neonatal development at P8–P10 as well as during pre-juvenile development at P16–P23 (Fig. 1*A*).

In utero *electroporation*

The transfection of prefrontal neurons with the constructs indicated above was performed according to previously developed protocols (Bitzenhofer et al., 2017a,b; Ahlbeck et al., 2018). Starting 1 d before and until 2 d after surgery, timed-pregnant C57BL/6J mice received on a daily basis additional wet food supplemented with 2–4 drops Metacam (0.5 mg/ml; Boehringer-Ingelheim). At E15.5 randomly assigned pregnant mice were injected subcutaneously with buprenorphine (0.05 mg/kg body weight) 30 min before surgery. The surgery was performed on a heating blanket and toe pinch and breathing were monitored throughout. Under isoflurane anesthesia (induction: 5%, maintenance: 3.5%), the eyes of the dam were covered with eye ointment to prevent damage. The uterine horns were exposed and moistened with warm sterile PBS (PBS, 37°C). Solution containing shRNA to DISC1 or control RNA plasmids (1.5 mg/ml) together with the tDimer expression vector with CAG promoter (1 mg/ml; molar ratio ~3:1) were injected into the right ventricles of individual embryo using pulled borosilicate glass capillaries. Injected solution contained fast green solution (0.001%) to monitor the injection. After the injection, the head of the embryo was placed between the electroporation tweezer-type paddles of 5 mm diameter (Protech). To transfect the neural precursor cells from the subventricular zone, electrodes were oriented at a rough 20° leftward angle from the midline and a rough 10° angle downward from anterior to posterior. Five electrode pulses (35 V, 50 ms) at intervals of 950 ms were applied, which were controlled by an electroporator (CU21EX, BEX). After electroporation, uterine horns were put back into the abdominal cavity filled with warm sterile PBS (37°C). The abdominal wall and skin were sutured individually with absorbable and non-absorbable suture threads, respectively. After surgery, pregnant mice were returned to their home cages, which were half placed on a heating blanket for the following 2 d. The tDimer2 expression was first checked by a portable fluorescent flashlight (Nightsea) through the intact skull and skin at P3 and confirmed postmortem by fluorescence microscopy in brain slices at P8–P10 or P17–P23.

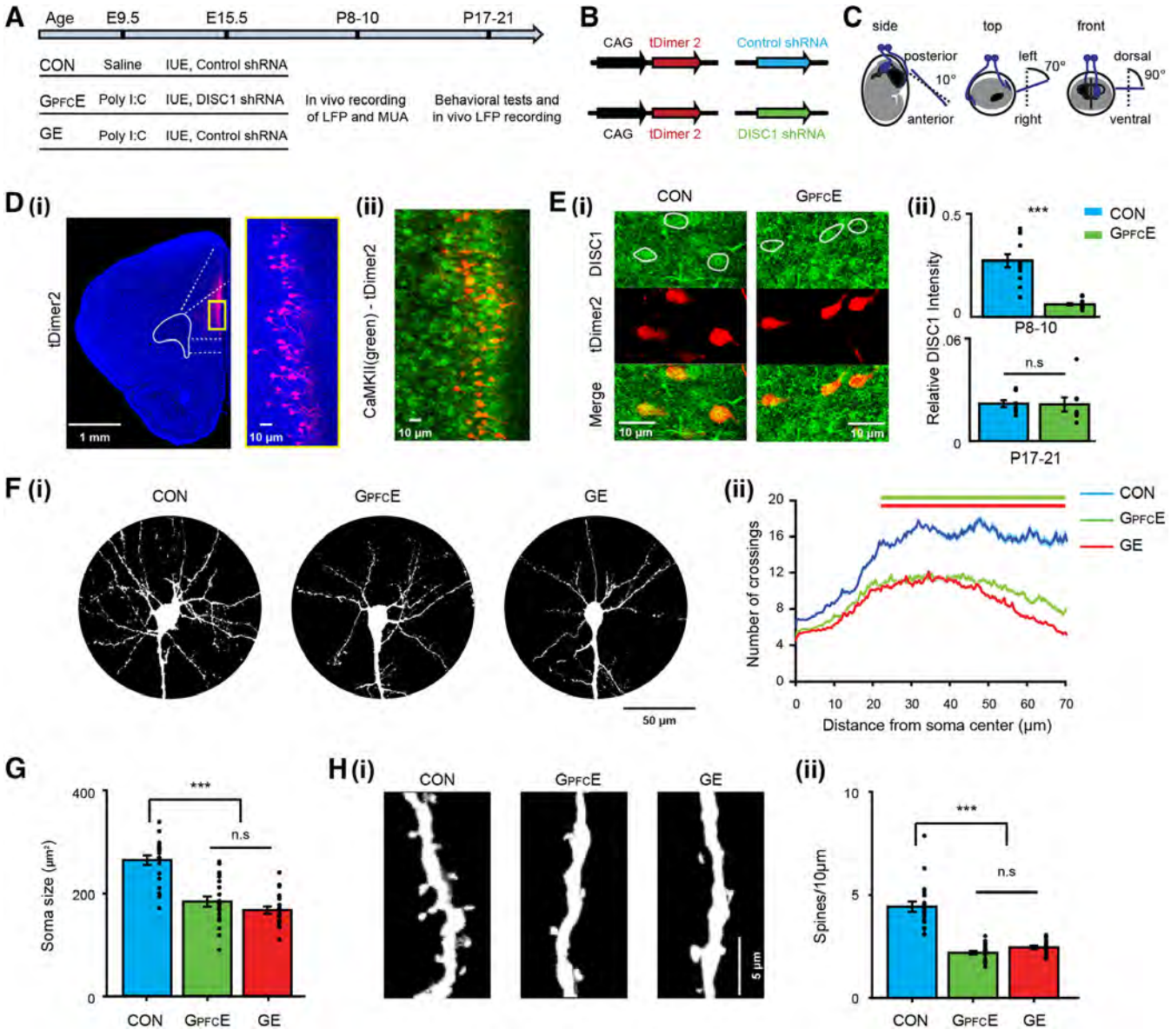

Figure 1. Transient DISC1 knock-down confined to pyramidal neurons in PFC by site-directed IUE. ***A***, Timeline of experimental protocol and description of the three investigated groups of mice: CON, immune-challenged mice with transient suppression of DISC1 confined to PFC ($G_{PFC}E$), and immune-challenged mice with brain-wide DISC1 knock-down. ***B***, Structure of the constructs. ***C***, Schematic drawing illustrating the orientation of electrode paddles for specific targeting of pyramidal neurons in layer II/III of PFC by IUE. ***Di***, tDimer2-expressing cells (red) in a 50-μm-thick coronal section including the PL from a P9 mouse after IUE at E15.5. Inset, Photograph displaying the targeted neurons at higher-magnification. ***Dii***, Photograph displaying CaMKII immunohistochemistry (green) in relationship to tDimer2-expression (red). ***Ei***, Photographs displaying DISC1 immunoreactivity (green) in relationship with tDimer2-expression (red) of a P9 $G_{PFC}E$ mice compared with age-matched CON (one-way ANOVA: $p = 0.0000$, $F_{(1,23)} = 48.07$). ***Eii***, Bar diagram displaying the relative DISC1 immunoreactivity averaged for $G_{PFC}E$ and CON mice at P8–P10 (top) and P17–P21 (bottom; one-way ANOVA: $p = 0.47$, $F_{(1,14)} = 4.07$). ***Fi***, Photographs of representative layer II/III pyramidal neurons in a P9 CON, a P9 $G_{PFC}E$, and a P9 GE mouse. ***Fii***, Graph displaying the average number of dendritic intersections within a 70 μm radius from the soma center of layer II/III pyramidal neurons in CON ($n = 21$ neurons from 3 mice), $G_{PFC}E$ ($n = 21$ neurons from 4 mice), and GE ($n = 21$ neurons from 3 mice) mice. Green and red bars indicate significant differences (***$p < 0.001$) between CON and $G_{PFC}E$ mice and between CON and GE mice, respectively. ***G***, Bar diagram displaying the soma size of prefrontal layer II/III pyramidal neurons in CON, $G_{PFC}E$, and GE mice. ***Hi***, Photograph displaying representative apical dendrites of a prefrontal layer II/III pyramidal neuron from a P9 CON, a P9 $G_{PFC}E$, and a P9 GE mouse. ***Hii***, Bar diagram displaying spine density on dendrites of prefrontal layer II/III pyramidal neurons from CON (20 neurons from 3 mice), $G_{PFC}E$ (21 neurons from 3 mice) and GE (21 neurons from 3 mice; one-way ANOVA: $p = 0.47$, $F_{(2,59)} = 59.43$). Data are presented as mean ± SEM. Significance levels of $p > 0.05$ (n.s.), $p < 0.001$ (***) were detected.

Electrophysiological recordings in vivo

Multisite extracellular recordings were performed in the PL and HP of P8–P10 and P20–P23 pups of both sexes. Mice were injected intraperitoneally with urethane (1 mg/g body weight; Sigma-Aldrich) before surgery. Under isoflurane anesthesia (induction: 5%; maintenance: 2.5%) the head of the pup was fixed into a stereotaxic apparatus using two plastic bars mounted on the nasal and occipital bones with dental cement. The bone over the PFC (0.8 mm anterior to bregma, 0.1–0.5 mm right to the midline) and the CA1 area of the intermediate HP (3.5–3.7 mm anterior to bregma, 3.5–3.8 mm right to the midline) was carefully removed by drilling holes <0.5 mm in diameter. Four-shank electrodes (4 × 4 recording sites, 0.4–0.8 MΩ impedance, 100 mm spacing, 125 mm inter-shank spacing; NeuroNexus) were inserted into PFC at a depth of 1.9 mm from the skull surface. One-shank electrodes (1 × 16 recording sites, 0.4–0.8 MΩ impedance, 50 mm spacing, NeuroNexus) were inserted into the CA1 until a depth of 1.3–1.8 mm from the skull surface, at an angle of 20° from the vertical plane. Electrodes were labeled with DiI (1,1′-dioctadecyl-3,3,3′,3′-tetramethyl indocarbocyanine; Invitrogen) to confirm their position after histological assessment postmortem. In PL, the most medial shank was confirmed to lay into layer II/III, whereas the most lateral shank was located in layer V/VI. In hippocampal CA1 area the LFP reversal over stratum pyramidale was used for the selection

of the channel with sharp waves of minimum amplitude and consequently, lowest contribution to the spectral content of the signal. One silver wire was inserted into cerebellum to serve as ground and reference electrode. A recovery period of 10 min following the insertion of electrodes before acquisition of data was provided. Data acquired during the first 30 min of recording were used for analysis to ensure similar state of anesthesia in all investigated pups. Extracellular signals were bandpass filtered (0.1 Hz to 5 kHz) and digitized (32 kHz) with a multichannel extracellular amplifier (Digital Lynx SX, Neuralynx) and the Cheetah acquisition software (Neuralynx).

Behavioral experiments

The exploratory behavior and recognition memory of CON, GE, and $G_{PFC}E$ mice were tested at pre-juvenile age using previously established experimental protocols (Krüger et al., 2012). Briefly, all behavioral tests were conducted in a circular white arena, the size of which (D: 34 cm, H: 30 cm) maximized exploratory behavior, while minimizing incidental contact with testing objects (Heyser and Ferris, 2013). The objects used for testing of novelty recognition were six differently shaped, textured and colored, easy to clean items that were provided with magnets to fix them to the bottom of the arena. Object sizes (H: 3 cm, diameter: 1.5–3 cm) were smaller than twice the size of the mouse and did not resemble living stimuli (no eye spots, predator shape). The objects were positioned at 10 cm from the borders and 8 cm from the center of the arena. After every trial the objects and arena were cleaned with 0.1% acetic acid to remove all odors. A black and white CCD camera (Videor Technical E. Hartig) was mounted 100 cm above the arena and connected to a PC via PCI interface serving as frame grabber for video tracking software (Video Mot2 software, TSE Systems).

Exploratory behavior in the open field. Pre-juvenile mice (P16) were allowed to freely explore the testing arena for 10 min. Additionally, the floor area of the arena was digitally subdivided in eight zones (4 center zones and 4 border zones) using the zone monitor mode of the VideoMot 2 analysis software (VideoMot 2, TSE Systems). The time spent by pups in center and border zones, as well as the running distance and velocity were quantified.

Novelty recognition paradigms. All protocols for assessing item recognition memory in P17 mice consisted of familiarization and testing trials (Ennaceur and Delacour, 1988). During the familiarization trial each mouse was placed into the arena containing two identical objects and released against the center of the opposite wall with the back to the objects. After 10 min of free exploration of objects the mouse was returned to a temporary holding cage. Subsequently, the test trial was performed after a delay of 5 min post-familiarization. The mice were allowed to investigate one familiar and one novel object with a different shape and texture for 5 min. Object interaction during the first 3 min was analyzed and compared between the groups. In the object location recognition (OLR) task, tested at P18, mice experienced one 10-min-long familiarization trial with two identical objects followed after a delay of 5 min by a test trial. In the test trial the position of one of the objects was changed. Object interaction during the first 3 min was analyzed and compared between the groups. In the recency recognition (RR) task, tested at P19–P20, mice experienced two 10-min-long familiarization trials with two different sets of identical objects that were separated by a delay of 30 min. The second familiarization trial was followed after 5 min by a test trial in which one object used in the first and one object used in the second more recent familiarization trial were placed in the arena at the same positions as during the familiarization trials. Object interaction during the first 3 min was analyzed and compared between the groups. All trials were video-tracked and the analysis was performed using the Video Mot2 analysis software. The object recognition module of the software was used and a three-point tracking method identified the head, the rear end and the center of gravity of the mouse. Digitally, a circular zone of 1.5 cm was created around each object and every entry of the head point into this area was considered as object interaction. Climbing or sitting on the object, mirrored by the presence of both head and center of gravity points within the circular zone, were not counted as interactions.

Histology and immunohistochemistry

Histological procedures were performed as previously described (Bitzenhofer et al., 2017b). Briefly, P8–P10 and P20–P23 mice were anesthetized with 10% ketamine (aniMedica)/2% xylazine (WDT) in 0.9% NaCl solution (10 μg/g body weight, i.p.) and transcardially perfused with Histofix (Carl Roth) containing 4% paraformaldehyde. Brains were postfixed with 4% paraformaldehyde for 24 h and sectioned coronally at 50 μm. Free-floating slices were permeabilized and blocked with PBS containing 0.8% Triton X-100 (Sigma-Aldrich), 5% normal bovine serum (Jackson ImmunoResearch) and 0.05% sodium azide. Subsequently, slices were incubated with the rabbit polyclonal primary antibody against CaMKII (1:200; PA5-38239, ThermoFisher Scientific) or against DISC1 (1:250; 40-6800, ThermoFisher Scientific), followed by 2 h incubation with AlexaFluor-488 goat anti-rabbit IgG secondary antibody (1:500; A11008, Merck Millipore). Slices were transferred to glass slides and covered with Fluoromount (Sigma-Aldrich). Wide field fluorescence images were acquired to reconstruct the recording electrode position and the location of tDimer2 expression. High-magnification images were acquired by confocal microscope (DM IRBE, Leica) to quantify DISCI expression (DISC1-immunopositive cells) in tDimer-neurons (3~4/per slice). All images were similarly analyzed with ImageJ.

Neuronal morphological analysis

Microscopic stacks were examined on a confocal microscope (DM IRBE, Leica Microsystems, Zeiss LSN700 and Olympus FX-100). Stacks were acquired as 2048 × 2048 pixel images (pixel size, 78 nm; *Z*-step, 500 nm). Sholl analysis and spine density quantification were performed in the ImageJ environment. For Sholl analysis, images were binarized (*auto threshold*) and dendrites were traced using the semiautomatic plugin *Simple Neurite Tracer*. The traced dendritic tree was analyzed with the plugin *Sholl Analysis*, after the geometric center was identified using the *blow/lasso* tool. For spine density quantification, we first traced the dendrite of interest (apical, basal, proximal oblique, or secondary apical) and measured its length (*line*) and then manually counted the number of spines (*point picker*).

Data analysis

Data were imported and analyzed off-line using custom-written tools in MATLAB software version 7.7 (MathWorks). The data were processed as follows: (1) bandpass filtered (500–5000 Hz) to detect multiple unit activity (MUA) as negative deflections exceeding five times the SD of the filtered signals and (2) low-pass filtered (<1500 Hz) using a third-order Butterworth filter before downsampling to 1000 Hz to analyze the LFP. All filtering procedures were performed in a phase-preserving manner. The position of Di-stained recording electrodes in PL (most medial shank confined to layer II/III, most temporal shank confined to layer V/VI) and HP was confirmed postmortem by histological evaluation. Additionally, electrophysiological features (i.e., reversal of LFP and high MUA frequency over stratum pyramidale of CA1) were used for confirmation of exact recording position in HP.

Detection of neonatal oscillatory activity. Discontinuous oscillatory events were detected using a previously developed unsupervised algorithm (Cichon et al., 2014) and confirmed by visual inspection. Briefly, deflections of the root-mean-square of bandpass (3–100 Hz) filtered signals exceeding a variance-depending threshold were assigned as network oscillations. The threshold was determined by a Gaussian fit to the values ranging from 0 to the global maximum of the root-mean-square histogram. Only oscillatory events >1 s were considered for further analysis. Time-frequency plots were calculated by transforming the data using the Morlet continuous wavelet.

Detection of sharp waves in HP. To analyze sharp waves, we subtracted the filtered signal (1–300 Hz) from the recording sites 100 μm above and 100 μm below the recording site located in stratum pyramidale. Sharp waves were detected as peaks >5 times the SD of the subtracted signal.

Spectral coherence. Coherence was calculated using the imaginary coherency method (Nolte et al., 2004). Briefly, the imaginary coherence was calculated (using the functions *cpsd.m* and *pwelch.m*) by taking the imaginary component of the cross-spectral density between the two signals and normalized by the power spectral density of each. were used. The

computation of the imaginary coherence C over frequency (f) for the power spectral density P of signals X and Y was performed according to the following formula:

$$C_{XY}(f) = \left| Im\left(\frac{P_{XY}(f)}{\sqrt{P_{XX}(f)\,P_{YY}(f)}} \right) \right| \quad (1)$$

Directionality methods. To investigate the directionality of functional connectivity between PFC and HP, cross-correlation, and generalized partial directed coherence (gPDC) were used. For the calculation of cross-correlation at different time lags, LFP signals from both areas were filtered into theta (4–12 Hz) and β (12–30 Hz) frequency bands. The peak values of cross-correlation and the corresponding time delays were determined. gPDC is based on linear Granger causality measure in the frequency domain. The method attempts to describe the causal relationship between multivariate time series based on the decomposition of multivariate partial coherence computed from multivariate autoregressive models. The LFP signal was divided into 1-s-long segments containing the oscillatory activity. After de-noising using the MATLAB wavelet toolbox, gPDC was calculated using a previously described algorithm (Baccalá and Sameshima, 2001; Baccalá et al., 2007).

Spike-triggered LFP power in PFC. Spiking activity in layers II/III and V/VI was detected as described above. The percentage change of spike-triggered LFP power spectrum was calculated as follows:

$$(\text{Power}_{\text{spike}} - \text{Power}_{\text{baseline}})/\text{Power}_{\text{baseline}} * 100, \quad (2)$$

where $\text{Power}_{\text{spike}}$ corresponds to the power spectrum calculated for a 200 ms time window centered on each spike and $\text{Power}_{\text{baseline}}$ stands for the averaged baseline power spectrum calculated 100–300 and 200–400 ms before each spike. Power spectra were calculated using the multitaper spectral estimation method (Mitra and Bokil, 2008).

Statistical analysis

Statistical analyses were performed with IBM SPSS Statistics version 21 or MATLAB. Significant differences were detected by paired t test or one-way ANOVA followed by Bonferroni-corrected *post hoc* analysis. For Sholl analysis, one-way repeated-measures ANOVA was used. Data are presented as mean ± SEM. Significance levels of $^{*}p < 0.05$,$^{**}p < 0.01$, or $^{***}p < 0.001$ were tested.

Results

Transient DISC1 knock-down confined to layer II/III pyramidal neurons disturbs the firing and oscillatory entrainment in PFC of neonatal immune-challenged mice

To assess the PFC-specific role of DISC1, we generated $G_{PFC}E$ mice in which the selective knock-down of DISC1 was restricted to a lineage of pyramidal neurons in PFC. To do so, we expressed a DISC1 targeting shRNA by using IUE protocols previously described (Niwa et al., 2010; Bitzenhofer et al., 2017b). We analyzed coronal sections from three mice at P9 and confirmed that only CaMKII-positive pyramidal neurons in layer II/III were targeted in $G_{PFC}E$ mice (Fig. 1*A–D*). Similar IUE protocol was used for CON and GE mice that received a scrambled/control shRNA instead (Fig. 1*A*). The immune challenge of $G_{PFC}E$ and GE mice was mimicked by prenatal immune activation with the viral mimetic poly I:C at E9.5. CON mice, instead, received saline injections at the same age. We found that the suppression of DISC1 was transient. When sections containing the PFC of P8–P10 mice were analyzed, the relative DISC1 intensity was significantly ($p < 0.0001$, ANOVA) weaker in $G_{PFC}E$ (0.062 ± 0.006, $n = 13$ mice) compared with CON mice (0.275 ± 0.033, $n = 12$ mice; Fig. 1*E*). In contrast, at P17–P21, DISC1 expression was at comparable levels in the two groups of mice (0.021 ± 0.004 in CON vs 0.022 ± 0.002 in $G_{PFC}E$, $p=0.468$, ANOVA, $n = 8$ mice for each group).

Brain-wide knock-down of DISC1 has been related to abnormal neuronal morphology and connectivity both during development (Chini et al., 2018) and at adulthood (Kvajo et al., 2008; Crabtree et al., 2017). To test whether these structural deficits are present also in the PFC of $G_{PFC}E$ mice, we undertook a detailed histological examination of the cytoarchitecture of tDimer-labeled pyramidal neurons in prefrontal layer II/III of P9 CON ($n = 21$ neurons from 3 mice), $G_{PFC}E$ ($n = 21$ neurons from 3 mice), and GE mice ($n = 21$ neurons from 3 mice). The complexity of dendritic branching of the tDimer-labeled neurons in layer II/III was assessed by Sholl analysis. Compared with CON, layer II/III pyramidal neurons of GE and $G_{PFC}E$ mice had significantly reduced dendritic branching (condition effect, $p < 1 \times 10-8$, ANOVA; Fig. 1*F*). These deficits were particularly prominent within a radius of 20–70 μm from the cell soma center ($p < 1 \times 10^{-6}$ for all comparisons). Furthermore, similar to GE mice (164.78 ± 6.87 μm^2, $p = 0.38$, ANOVA followed by Bonferroni-corrected *post hoc* test), $G_{PFC}E$ mice (181.40 ± 10.00 μm^2) showed remarkable reduction ($p < 1 \times 10^{-7}$, ANOVA followed by Bonferroni-corrected *post hoc* test) in the soma size of layer II/III pyramidal neurons compared with CON mice (261.15 ± 9.29 μm^2; Fig. 1*G*). Next, we examined the spine density along the dendrites of layer II/III pyramidal neurons in the three groups. Similar to GE mice ($n = 21$ neurons from 3 mice, 2.46 ± 0.08 per 10 μm, $p = 0.44$), $G_{PFC}E$ mice ($n = 21$ neurons from 3 mice, 2.19 ± 0.09 per 10 μm) had significantly lower spine density ($p < 1 \times 10^{-9}$, ANOVA followed by Bonferroni-corrected *post hoc* test) compared with CON mice ($n = 20$ neurons from 3 mice, 4.43 ± 0.26 per 10 μm; Fig. 1*H*). These data indicate that, similar to GE mice, $G_{PFC}E$ mice have a simplified dendritic arborization and decreased spine density.

Because DISC1 knock-down is spatially confined, $G_{PFC}E$ mice are instrumental for assessing the role of DISC1 for the functional development of prefrontal circuits. For this, we performed multisite extracellular recordings of LFP and MUA from the PL of P8–P10 urethane-anesthetized CON ($n = 14$), $G_{PFC}E$ ($n = 13$) and GE mice ($n = 10$). The four shanks of recording electrodes were confirmed to be located across layer II/III and V/VI of the PL (Fig. 2*A*). Our previous investigations revealed that network oscillations and neuronal firing have a similar structure and temporal organization in urethane-anesthetized and asleep non-anesthetized rodents of neonatal age (Bitzenhofer et al., 2015). Discontinuous (i.e., periods of network activity alternate with periods of "silence") oscillatory discharges with frequency components peaking in theta (4–12 Hz) and β-low gamma frequency range (12–40 Hz) have been detected in all investigated mice (Fig. 2*B*,*D*). However, their properties differed between groups. In line with previous data (Hartung et al., 2016b), the prelimbic activity of GE mice appeared highly fragmented and correspondingly, the occurrence of oscillatory events was higher (8.40 ± 0.43 oscillations/min, $p = 0.0002$, ANOVA followed by Bonferroni-corrected *post hoc* test) and the duration shorter (2.38 ± 0.12 s, $p = 0.016$, ANOVA followed by Bonferroni-corrected *post hoc* test) compared with CON (5.53 ± 0.59 oscillations/min, 2.84 ± 0.18 s). The fragmented structure of discharges was present also in $G_{PFC}E$ mice, yet the occurrence increase was rather moderate (7.04 ± 0.68 oscillations/min, $p = 0.045$, ANOVA followed by Bonferroni-corrected *post hoc* test) and the duration of oscillatory events was unaffected (3.12 ± 0.15 s, $p = 0.14$, ANOVA followed by Bonferroni-corrected *post hoc* test; Fig. 2*C*). The relative power of oscillatory events normalized to the periods lacking coordinated activity was significantly decreased over all frequency bands in GE mice versus CON. In contrast, no differ-

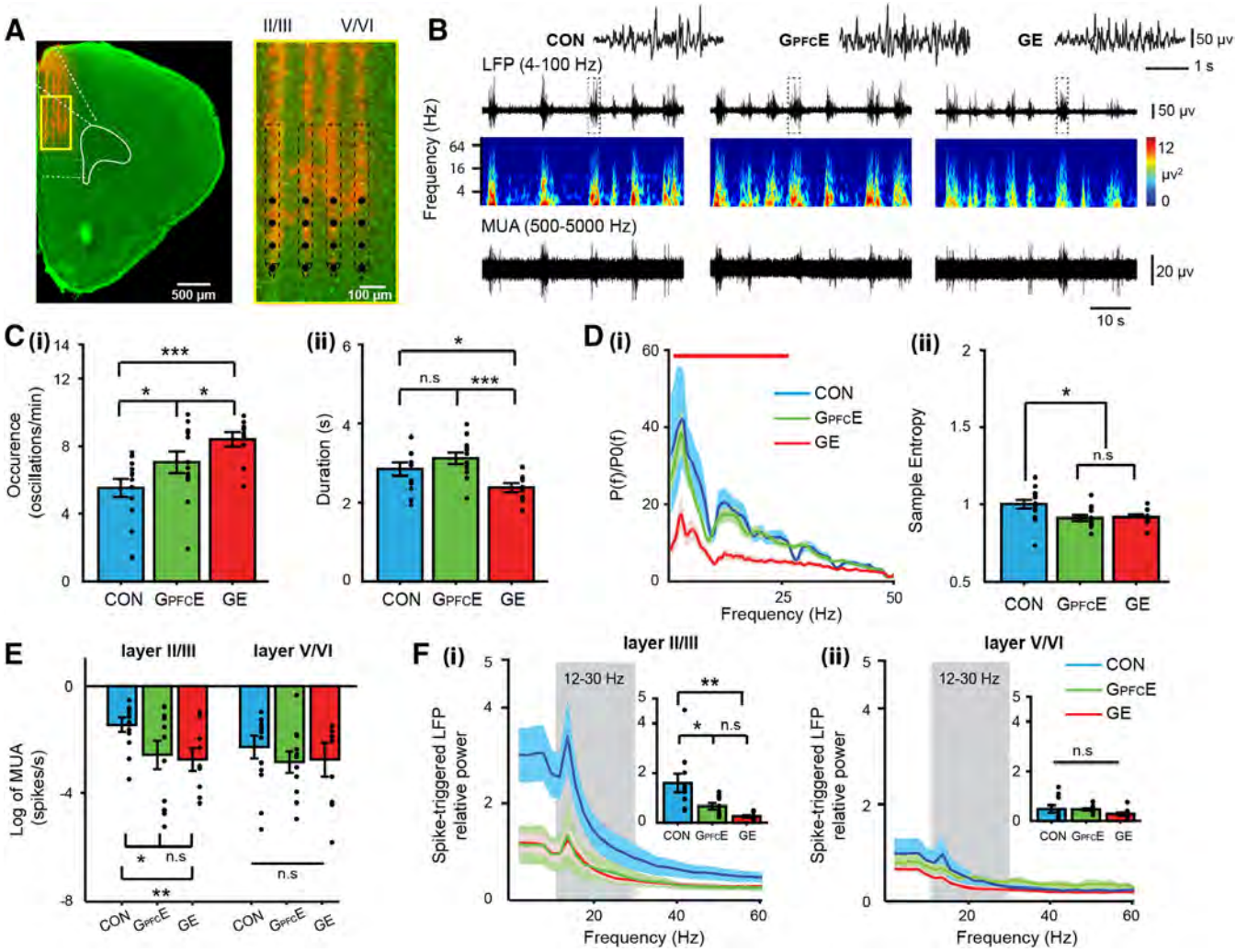

Figure 2. Patterns of oscillatory activity and neuronal firing in the PFC of neonatal $G_{PFC}E$ mice. ***A***, Digital photomontage reconstructing the location of the DiI-labeled 4 × 4-site recording electrode (orange) in a 100-μm-thick coronal section containing the PFC of a P9 mouse. Inset, The position of recording sites (black dots) over the prelimbic layers displayed at higher-magnification. ***B***, Extracellular LFP recording of discontinuous oscillatory activity in PL from a P9 CON (left), a P9 $G_{PFC}E$ (middle), and a P9 GE (right) mouse displayed after bandpass (4–100 Hz) filtering (top) and the corresponding MUA after bandpass (500–5000 Hz) filtering (bottom). Traces are accompanied by the color-coded wavelet spectra of the LFP at identical time scale. ***C***, Bar diagrams displaying the mean occurrence (***i***; one-way ANOVA: $p = 0.0049$, $F_{(2,31)} = 6.34$) and duration (***ii***; one-way ANOVA: $p = 0.006$, $F_{(2,31)} = 6.06$) of prefrontal oscillations recorded in CON, $G_{PFC}E$, and GE mice. ***D***, ***Di***, Averaged power spectra $P(f)$ of discontinuous oscillations normalized to the baseline power $P0(f)$ of time windows lacking oscillatory activity. Red bar indicates significant difference between CON and GE mice (***$p < 0.001$). ***Dii***, Bar diagram displaying the mean sample entropy of prelimbic oscillations as a measure of the complexity of oscillatory activity recorded from CON, $G_{PFC}E$, and GE mice (one-way ANOVA: $p = 0.021$, $F_{(2,31)} = 4.41$). ***E***, Bar diagram displaying the mean MUA of layer II/III and layer V/VI neurons in PFC of CON, $G_{PFC}E$, and GE mice (one-way ANOVA, layer II/III: $p = 0.038$, $F_{(2,31)} = 3.65$; layer V/VI: $p = 0.656$, $F_{(2,30)} = 0.428$). ***F***, Power spectra of averaged spike-triggered LFP for layer II/III (***Fi***) and layer V/VI (***Fii***) of CON, $G_{PFC}E$, and GE mice. Gray shadow highlights the 12–30 Hz frequency range. Insets, Bar diagrams displaying mean power values for the 12–30 Hz frequencies for spikes recorded in prelimbic layer II/III and V/VI, respectively, of CON, $G_{PFC}E$, and GE mice (one-way ANOVA, layer II/III: $p = 0.003$, $F_{(2,25)} = 7.61$; layer V/VI: $p = 0.27$, $F_{(2,27)} = 1.38$). Data are presented as mean ± SEM. Significance levels of $p > 0.05$ (n.s.), $p < 0.05$ (*), $p < 0.01$ (**) and $p < 0.001$ (***) were detected.

ences were detected between CON and $G_{PFC}E$ mice (Fig. 2*Di*). Additionally, we analyzed the sample entropy of oscillatory events that reflects the complexity of developing neuronal networks (Kapucu et al., 2017). Compared with prefrontal oscillations in CON mice (1.01 ± 0.037), both GE (0.93 ± 0.02, $p = 0.05$, ANOVA followed by Bonferroni-corrected *post hoc* test) and $G_{PFC}E$ mice (0.92 ± 0.02, $p = 0.028$, ANOVA followed by Bonferroni-corrected *post hoc* test) had decreased sample entropy, suggesting that the structure of prelimbic circuits was less complex and most likely, more immature (Fig. 2*Dii*).

The abnormal temporal organization of coordinated activity in the PFC of GE and $G_{PFC}E$ mice led us to hypothesize that the local circuitry in the PL was similarly perturbed in the two groups of mice. To get further insights, we calculated the firing rates in layer II/III and layer V/VI of the two models (GE, $n = 14$; $G_{PFC}E$, $n = 13$) and compared them with the values from CON ($n = 10$). Prelimbic neurons mostly fire during oscillatory events (Fig. 2*B*). Overall, DISC1 suppression caused significant MUA decrease in prelimbic layer II/III (CON: −1.45 ± 0.28; GE: −2.75 ± 0.44; $G_{PFC}E$: −2.58 ± 0.55), yet no significant differences ($p = 0.398$, ANOVA followed by Bonferroni-corrected *post hoc* test) were detected between GE and $G_{PFC}E$ mice. The firing within layer V/VI was unchanged in all three mouse groups (CON: −2.29 ± 0.45; GE: −2.75 ± 0.67; $G_{PFC}E$: −3.17 ± 0.42; Fig. 2*E*). Next, we aimed to deepen into the connectivity strength of local prefrontal circuits. For this, we calculated the spike-triggered power (STP) of the LFP. The method assesses the strength of postsynaptic activity at one cortical site caused by spiking at another location (Nauhaus et al., 2009; Ray and Maunsell, 2011). The 12–30 Hz power of relative STP within prelimbic layer II/III was signifi-

cantly changed in GE (0.25 ± 0.06, $p = 0.003$, ANOVA followed by Bonferroni-corrected *post hoc* test) and $G_{PFC}E$ (0.66 ± 0.13, $p = 0.028$, ANOVA followed by Bonferroni-corrected *post hoc* test) compared with CON mice (1.59 ± 0.40; Fig. 2*Fi*). The coupling within deeper layers of PL was comparable in the three mouse groups (CON: 0.48 ± 0.16; GE: 0.28 ± 0.06; $G_{PFC}E$: 0.46 ± 0.05, $p = 0.269$, ANOVA followed by Bonferroni-corrected *post hoc* test; Fig. 2*Fii*).

These data indicate that transient suppression of DISC1 in PFC causes sparser dendritic arborization and lower spine density, network deficits, and abnormal circuit wiring in the PL, which are similar to the dysfunction resulting from brain-wide DISC1 knock-down.

Transient DISC1 knock-down confined to layer II/III pyramidal neurons in PFC does not perturb the firing and network activity in HP of neonatal immune-challenged mice

Previous data identified the CA1 area in intermediate/ventral HP as major monosynaptic drive for the oscillatory entrainment of prelimbic circuits during development (Brockmann et al., 2011; Ahlbeck et al., 2018). The activation of prelimbic circuits impacts HP via subcortical relay stations, such as midline thalamus, but not via direct axonal projections (Hartung et al., 2016a). To assess the effects of DISC1 suppression on hippocampal activity, we compared the oscillatory patterns and neuronal firing in the CA1 area of CON ($n = 14$), GE ($n = 13$), and $G_{PFC}E$ ($n = 10$) mice (Fig. 3*A*). In line with previous data (Hartung et al., 2016b), the discontinuous oscillatory activity of HP with frequencies within theta-β ranges (Fig. 3*B*,*D*) was changed by the combination of maternal immune activation with brain-wide suppression of DISC1 function. The occurrence (8.88 ± 0.37 oscillations/min) of oscillations (4–100 Hz) in GE mice was significantly increased ($p = 0.001$, ANOVA followed by Bonferroni-corrected *post hoc* test), whereas their relative power, especially in theta (4–12 Hz) frequency (7.10 ± 1.56), was significantly ($p = 0.024$, ANOVA followed by Bonferroni-corrected *post hoc* test) decreased compared with the HP activity of CON mice (occurrence: 6.70 ± 0.52 oscillations/min; relative power: 20.06 ± 4.56). The duration of oscillatory events and their complexity mirrored by sample entropy were similar in GE (duration: 3.71 ± 0.23; sample entropy: 0.90 ± 0.03) and CON (duration: 3.69 ± 0.26; sample entropy: 0.88 ± 0.04) mice. The transient prefrontal-restricted suppression of DISC1 did not affect the properties of oscillatory events in $G_{PFC}E$ mice. The occurrence (6.50 ± 0.51 oscillations/min), duration (4.19 ± 0.32 s), relative power (4–12 Hz: 17.10 ± 1.92), and sample entropy (0.83 ± 0.3) were similar to the values of CON mice. Moreover, the firing rate of HP neurons (−1.08 ± 0.38) or the occurrence of sharp waves (SPWs; 0.42 ± 0.02 /s) was comparable in $G_{PFC}E$, GE (firing rate: −0.93 ± 0.33; SPW occurrence: 0.40 ± 0.02 /s), and CON mice (firing rate: −1.42 ± 0.40, $p = 0.66$, ANOVA followed by Bonferroni-corrected *post hoc* test; SPW occurrence: 0.40 ± 0.03 /s, $p = 0.81$, ANOVA followed by Bonferroni-corrected *post hoc* test; Fig. 3*F*,*G*).

These data indicate that, in contrast to brain-wide knock-down of DISC1, transient suppression of DISC1 in PFC does not perturb the firing and network activity in intermediate/ventral HP of immune-challenged mice at neonatal age.

Transient DISC1 knock-down confined to layer II/III pyramidal neurons in PFC causes weaker long-range coupling in neonatal immune-challenged mice

Several analytical approaches were used to test whether the transient suppression of DISC1 confined to PFC affects the coupling between PL and HP. First, we calculated the imaginary part of coherency between PL and HP of CON, $G_{PFC}E$, and GE mice. The method has been described to be insensitive to spurious connectivity arising from volume conduction (Nolte et al., 2004). Consistent with previous data (Hartung et al., 2016b), the tight coupling within prefrontal–hippocampal networks of neonatal CON mice was profoundly altered in GE mice (Fig. 4*A*). Brain-wide suppression of DISC1 function caused a significant decrease of prefrontal–hippocampal coherency within 4–12 Hz (0.268 ± 0.004, $p = 0.040$, ANOVA followed by Bonferroni-corrected *post hoc* test) and 12–30 Hz ranges (0.254 ± 0.006, $p = 0.025$, ANOVA followed by Bonferroni-corrected *post hoc* test) compared with CON mice (4–12 Hz: 0.295 ± 0.014; 12–30 Hz: 0.289 ± 0.016). Similar coupling decrease was observed when the DISC1 suppression was confined to PFC. The prefrontal–hippocampal coherency in $G_{PFC}E$ mice was similar with that of GE mice, but weaker both within 4–12 Hz (0.263 ± 0.003, $p = 0.022$, ANOVA followed by Bonferroni-corrected *post hoc* test) and 12–30 Hz range (0.257 ± 0.006, $p = 0.035$, ANOVA followed by Bonferroni-corrected *post hoc* test) compared with the values calculated for CON mice (4–12 Hz: 0.295 ± 0.014; 12–30 Hz: 0.289 ± 0.016; Fig. 4*A*).

Second, we assessed the directionality of interactions between PL and HP in the three groups of mice by calculating time-resolved cross-correlation and frequency-resolved gPDC. In line with previous results (Hartung et al., 2016b), max cross-correlation of 4–12 and 12–30 Hz oscillations within prefrontal–hippocampal networks of all investigated mice was detected for HP → PL (Fig. 4*B*), yet the magnitude of the hippocampal drive differed between the groups. Suppression of DISC1 in PFC of $G_{PFC}E$ mice led to cross-correlation values (4–12 Hz: 0.09 ± 0.002; 12–30 Hz: 0.17 ± 0.002) similar to those of GE mice (4–12 Hz: 0.12 ± 0.01, $p=0.06$, ANOVA followed by Bonferroni-corrected *post hoc* test; 12–30 Hz: 0.16 ± 0.01, $p = 0.37$, ANOVA followed by Bonferroni-corrected *post hoc* test), but significantly decreased compared with those calculated for CON mice (4–12 Hz: 0.17 ± 0.02, $p = 0.002$, ANOVA followed by Bonferroni-corrected *post hoc* test; 12–30 Hz: 0.26 ± 0.02, $p = 0.001$, ANOVA followed by Bonferroni-corrected *post hoc* test). Next, we calculated the gPDC between the PL and HP, a measure that reflects the directionality of network interactions in different frequency bands (Fig. 4*C*). Both brain-wide suppression of DISC1 function and the transient prefrontal-restricted suppression of DISC1 caused a decreased drive from HP to PL within 4–12 Hz (GE: 0.047 ± 0.003, $p = 0.004$, ANOVA followed by Bonferroni-corrected *post hoc* test; $G_{PFC}E$: 0.045 ± 0.003, $p = 0.001$, ANOVA followed by Bonferroni-corrected *post hoc* test) and 12–30 Hz (GE: 0.034 ± 0.003, $p = 0.011$, ANOVA followed by Bonferroni-corrected *post hoc* test; $G_{PFC}E$: 0.038 ± 0.002, $p = 0.031$, ANOVA followed by Bonferroni-corrected *post hoc* test) compared with CON mice (4–12 Hz: 0.063 ± 0.004; 12–30 Hz: 0.047 ± 0.004).

These data indicate that transient suppression of DISC1 restricted to PFC during neonatal development causes weaker long-range prefrontal–hippocampal coupling that is similar to the dysfunction resulting from brain-wide DISC1 knock-down. Because the hippocampal activity of $G_{PFC}E$ mice is normal (Fig. 3), the decreased coupling between PFC and HP after transient suppression of DISC1 in PFC most likely mirrors the poorer ability of locally disrupted prefrontal circuits to follow the hippocampal drive.

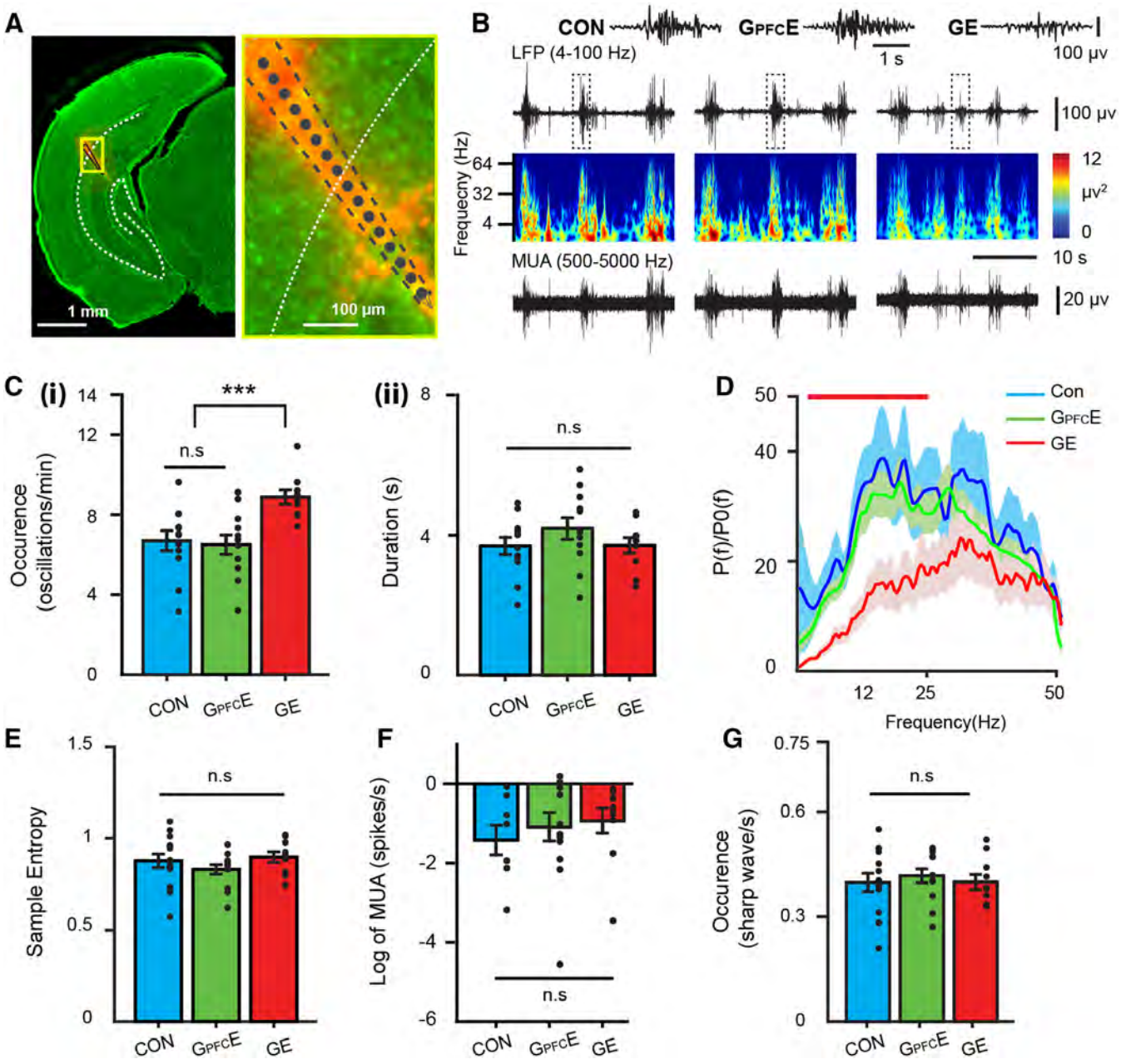

Figure 3. Patterns of oscillatory activity and neuronal firing in the CA1 area of intermediate/ventral HP of neonatal $G_{PFC}E$ mice. ***A***, Digital photomontage reconstructing the location of the DiI-labeled 1 × 16-site recording electrode (orange) in a 100-μm-thick coronal section containing the intermediate/ventral HP of a P9 mouse. Inset, The position of recording sites (gray dots) over the prelimbic layers displayed at higher-magnification. ***B***, Extracellular LFP recording of discontinuous oscillatory activity in PL from a P9 CON (left), a P9 $G_{PFC}E$ (middle), and a P9 GE (right) mouse displayed after bandpass (4–100 Hz) filtering (top) and the corresponding MUA after bandpass (500–5000 Hz) filtering (bottom). Traces are accompanied by the color-coded wavelet spectra of the LFP at identical time scale. ***C***, Bar diagrams displaying the mean occurrence (***Ci***; one-way ANOVA: $p = 0.002$, $F_{(2,31)} = 7.63$) and the duration (***Cii***; one-way ANOVA: $p = 0.33$, $F_{(2,31)} = 1.16$) of hippocampal oscillations recorded in CON, $G_{PFC}E$, and GE mice. ***D***, Averaged power spectra $P(f)$ of discontinuous oscillations normalized to the baseline power $P0(f)$ of time windows lacking oscillatory activity. Red bar indicates significant difference between CON and GE mice. ***E***, Bar diagram displaying the mean sample entropy of hippocampal oscillations as measure of the complexity of oscillatory activity for CON, $G_{PFC}E$, and GE mice (one-way ANOVA: $p = 0.34$, $F_{(2,34)} = 1.13$). ***F***, Bar diagram displaying the mean MUA of CA1 neurons in CON, $G_{PFC}E$, and GE mice (one-way ANOVA: $p = 0.66$, $F_{(2,28)} = 0.42$). ***G***, Bar diagrams displaying the mean occurrence of SPW in CON, $G_{PFC}E$, and GE mice (one-way ANOVA: $p = 0.81$, $F_{(2,34)} = 0.22$). Data are presented as mean ± SEM. Significance levels of $p > 0.05$ (n.s.), and $p < 0.001$ (***) were detected.

Transient prefrontal DISC1 knock-down causes poorer recognition memory performance of pre-juvenile immune-challenged mice

A major question that needs to be addressed is whether transient suppression of DISC1 in neonatal PFC perturbs the network function throughout development and consequently, the related cognitive performance later in life. We recently showed that cognitive abilities that rely on prefrontal–hippocampal coupling and emerge at pre-juvenile age (i.e., P17–P20) are impaired when brain-wide DISC1 knock-down was combined with prenatal immune challenge (Hartung et al., 2016b). Here, we compare the behavioral performance of $G_{PFC}E$ mice with that of CON and GE mice to elucidate the long-term impact of transient DISC1 knock-down confined to layer II/III of PFC. For this, we monitored the novelty detection and recognition memory, which have been shown to result from interactions between PFC and HP (Warburton and Brown, 2015). These abilities can be easily tested at pre-juvenile age because they rely on the mouse's intrinsic

exploratory drive and require no prior training or deprivation (Krüger et al., 2012). Specifically, we tested novel object recognition (NOR), OLR, and RR in CON ($n = 17$), GE ($n = 23$), and $G_{PFC}E$ ($n = 12$) mice using a custom-designed arena and previously established protocols (Fig. 5*A*,*B*). During the familiarization trials of these tests, all mice spent equal time investigating the two objects placed in the arena. During the NOR test trial, CON mice spent significantly longer time interacting with the novel object (71.97 ± 5.55%, $t_{(16)} = -4.11$, $p = 0.0006$, pared *t* test) than with the familiar one (28.03 ± 5.55%). In contrast, GE mice failed to distinguish between the two objects (familiar: 46.44 ± 7.98%; novel: 53.56 ± 7.98%, $t_{(22)} = -1.32$, $p = 0.325$, pared *t* test). Similarly, pre-juvenile $G_{PFC}E$ mice were also unable to distinguish between the two objects during test trial (familiar: 42.09 ± 10.83%; novel: 57.91 ± 10.83%, $t_{(11)} = -0.76$, $p = 0.231$, pared *t* test; Fig. 5*C*). During the OLR test trial, all mice spent more time to explore the relocated object (CON: 67.99 ± 5.48%, $t_{(16)} = -3.84$, $p = 0.002$, pared *t* test; $G_{PFC}E$: 61.38 ± 5.81%, $t_{(11)} = -2.06$, $p = 0.033$, pared *t* test; GE: 73.28 ± 4.57%, $t_{(22)} = -7.08$, $p < 1 \times 10^{-7}$, pared *t* test) than the object with constant position (CON: 32.01 ± 5.48%; $G_{PFC}E$: 38.62 ± 5.81%; GE: 26.72 ± 4.57%; Fig. 5*D*). The similar discrimination ratio (CON: 0.36 ± 0.11; GE: 0.47 ± 0.09, $p = 0.225$, ANOVA followed by Bonferroni-corrected *post hoc* test; $G_{PFC}E$: 0.23 ± 0.12, $p = 0.199$, ANOVA followed by Bonferroni-corrected *post hoc* test; Fig. 5*Dii*) indicates that the OLR was intact in all investigated mice. During RR task, mice needed to process temporal information by recognizing the object with which they most recently interacted (Fig. 5*E*). The CON mice spent more time with the object they explored during the first familiarization trial than the new object from the second familiarization trial (old: 66.43 ± 4.41%, recent: 33.57 ± 4.41%, $t_{(16)} = -3.96$, $p = 0.0009$, pared *t* test). However, both $G_{PFC}E$ and GE mice failed to recognize the most recently explored object and spent equal time with both objects (GE, old: 47.53 ± 3.49%, recent: 52.47 ± 3.49%, $t_{(22)} = -1.02$, $p = 0.238$, pared *t* test; $G_{PFC}E$, old: 45.21 ± 11.06%, recent: 54.79 ± 11.06%, $t_{(11)} = -0.45$, $p = 0.330$, pared *t* test). Correspondingly, the discrimination ratio between the old and the recent object significantly decreased (GE: −0.10 ± 0.22, $p = 0.0009$, ANOVA followed by Bonferroni-corrected *post hoc* test; $G_{PFC}E$: −0.05 ± 0.07, $p = 0.042$, ANOVA followed by Bonferroni-corrected *post hoc* test) compared with the values for CON mice (0.33 ± 0.09).

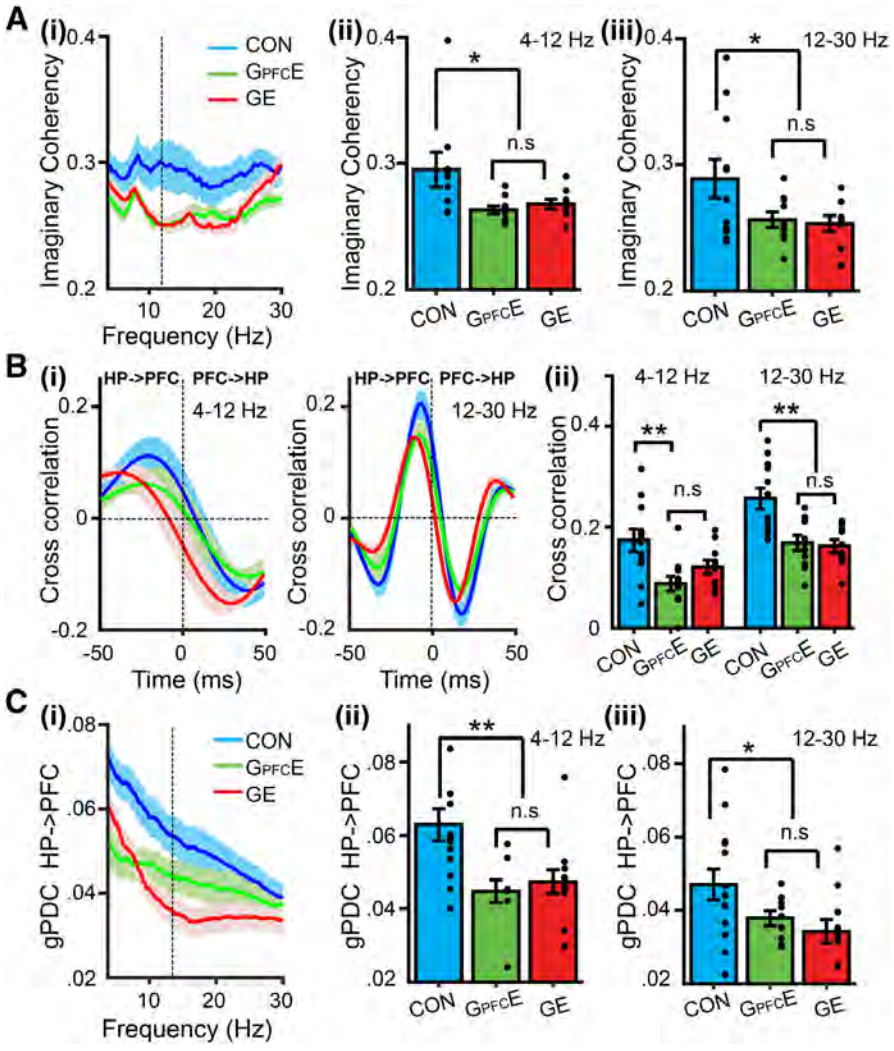

Figure 4. Coupling by synchrony and directed interactions within prefrontal– hippocampal networks of neonatal $G_{PFC}E$ mice. ***Ai***, Mean coherence spectra for oscillatory activity simultaneously recorded in PL and hippocampal CA1 area of CON, $G_{PFC}E$, and GE mice. ***Aii***, Bar diagram displaying the imaginary coherency when averaged for 4–12 Hz band in CON, $G_{PFC}E$, and GE mice (one-way ANOVA: $p = 0.037$, $F_{(2,27)} = 3.73$). ***Aiii***, Same as ***Aii***, for 12–30 Hz in CON, $G_{PFC}E$, and GE mice (one-way ANOVA: $p = 0.047$, $F_{(2,27)} = 3.43$). ***Bi***, Plot of cross-correlation of prelimbic and hippocampal oscillations within 4–12 Hz (left) and 12–30 Hz (right) when averaged for all investigated CON, $G_{PFC}E$, and GE mice. Negative time lags correspond to HP leading PFC. ***Bii***, Bar diagram displaying the mean peak cross-correlation when averaged for 4–12 Hz in CON, $G_{PFC}E$, and GE mice (one-way ANOVA: $p = 0.005$, $F_{(2,30)} = 6.36$) and 12–30 Hz bands in CON, $G_{PFC}E$, and GE mice (one-way ANOVA: $p = 0.0000$, $F_{(2,30)} = 10.09$). ***Ci***, Plot of mean gPDC in relationship to frequency for HP → PL in CON, $G_{PFC}E$, and GE mice. ***Cii***, Bar diagram displaying gPDC when averaged for 4–12 Hz in CON, $G_{PFC}E$, and GE mice (one-way ANOVA: $p = 0.003$, $F_{(2,32)} = 6.97$). ***Ciii***, Same as ***Cii*** for at 12–30 Hz in CON, $G_{PFC}E$, and GE mice (one-way ANOVA: $p = 0.034$, $F_{(2,32)} = 3.78$). Data are presented as mean ± SEM. Significance levels of $p < 0.05$ (n.s.), $p < 0.05$ (*) and $p < 0.01$ (**) were detected.

The incapacity to perform NOR and RR tasks may result from poor motor abilities and/or enhanced anxiety when interacting with the objects. To test this hypothesis, we first analyzed the exploratory behavior of P16 CON, GE, and $G_{PFC}E$ mice. The distance covered was similar in all groups (CON: 1242 ± 159 cm; GE: 1032 ± 123 cm; $G_{PFC}E$: 1030 ± 154 cm, $p = 0.11$, ANOVA followed by Bonferroni-corrected *post hoc* test). Moreover all mice spent more time in the outer circle than in the inner circle of the arena (CON: 1127 ± 132 cm vs 149 ± 32 cm; GE: 958 ± 111 cm vs 73 ± 18 cm; $G_{PFC}E$: 941 ± 139 cm vs 89 ± 33 cm) and had similar latencies when entering the inner circle (CON: 73.85 ± 24.45 s, GE: 101.83 ± 30.44 s, $G_{PFC}E$: 92.29 ± 48.83 s). These results suggest that exploratory and anxiety abilities were similar in CON, GE, and $G_{PFC}E$ mice.

Thus, transient prefrontal DISC1 knock-down has long-lasting behavioral effects, being sufficient to impair novel object and recency recognition in immune-challenged mice at pre-juvenile age.

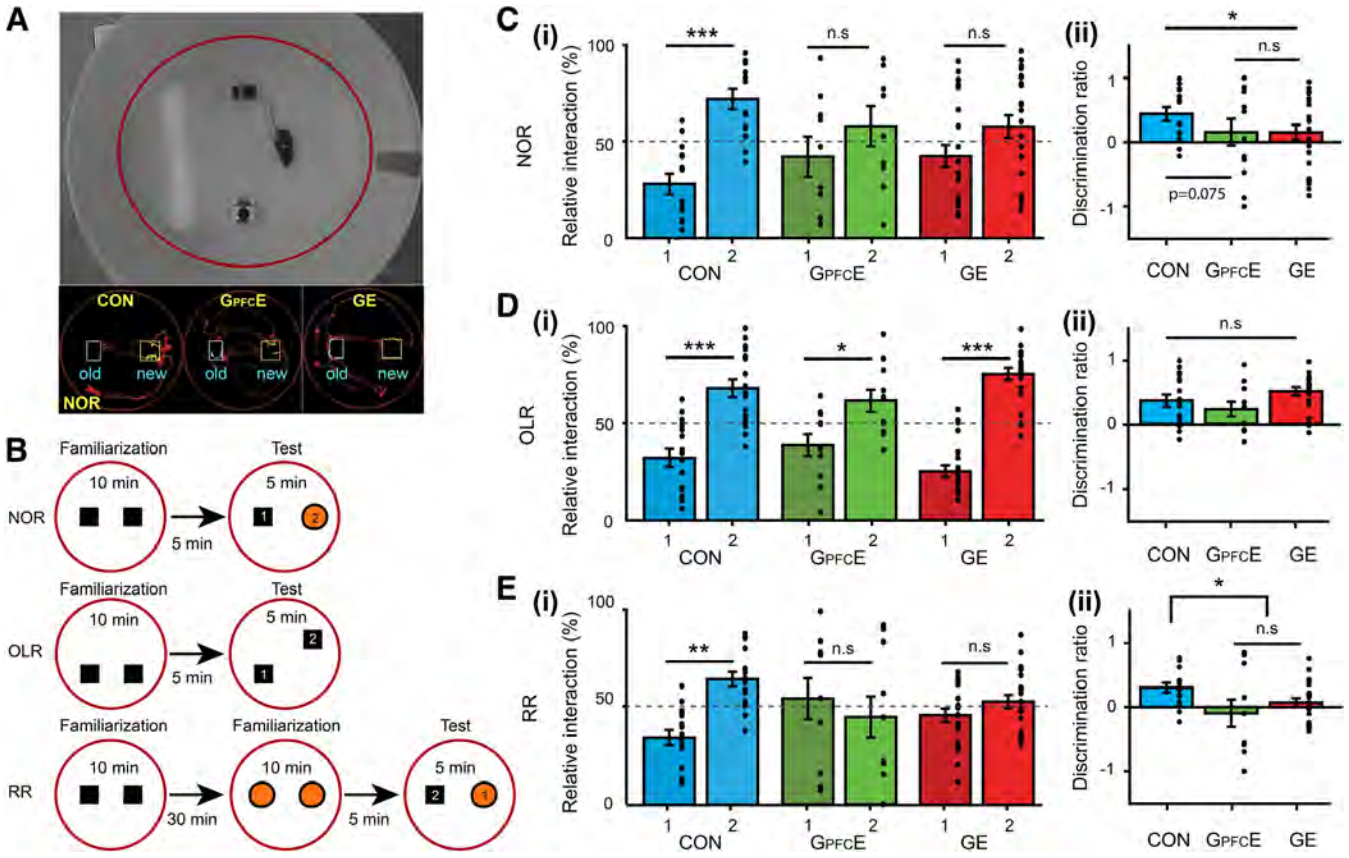

Figure 5. Novelty recognition of pre-juvenile $G_{PFC}E$ mice. ***A***, Top, Photograph of the arena used for NOR, OLR, and RR. Bottom, Representative tracking images illustrating test trials for the NOR test performed by a P17 CON (left), a P17 $G_{PFC}E$ (middle), and a P17 GE mouse (right). The computer generated track of the mouse pup (red) is displayed together with zones (blue yellow) created around the objects. ***B***, Schematic diagrams of the protocol for NOR, OLR and RR tasks. ***Ci***, Bar diagram illustrating the relative interaction time spent by CON, $G_{PFC}E$, and GE with the objects during the NOR test trial. The dotted line indicates chance level. ***Cii***, Bar diagram displaying the mean discrimination ratio when averaged for CON, $G_{PFC}E$, and GE mice during NOR task in CON, $G_{PFC}E$, and GE mice (one-way ANOVA: $p = 0.049$, $F_{(2,48)} = 3.18$). ***Di–Dii***, ***Ei–Eii***, Same as ***Ci–Cii*** for CON, $G_{PFC}E$, and GE mice in the OLR (one-way ANOVA: $p = 0.09$, $F_{(2,47)} = 2.43$) and RR (one-way ANOVA: $p = 0.034$, $F_{(2,45)} = 3.66$) test trial, respectively. Data are presented as mean ± SEM. Significance levels of $p > 0.05$ (n.s.), $p < 0.05$ (*), $p < 0.01$ (**) and $p < 0.001$ (***) were detected.

Transient prefrontal DISC1 knock-down causes weaker prefrontal–hippocampal coupling throughout development in immune-challenged mice

To assess the mechanisms underlying the behavioral deficits in pre-juvenile $G_{PFC}E$ mice, we tested the hypothesis that transient suppression of DISC1 confined to PFC permanently perturbs the maturation of prefrontal–hippocampal circuits. As a readout of perturbation we used the oscillatory patterns and neuronal firing of pre-juvenile PL and CA1 area of intermediate/ventral HP, as well as their coupling by synchrony. For this, we performed multisite extracellular recordings of LFP and MUA simultaneously from both areas of urethane-anesthetized P20–P23 mice (CON, $n = 14$; $G_{PFC}E$, $n = 10$; GE, $n = 16$). As previously reported (Hartung et al., 2016b); all investigated mice showed similar patterns of network activity, which correspond to the sleep-like rhythms mimicked by urethane anesthesia (Wolansky et al., 2006; Clement et al., 2008; Pagliardini et al., 2013; Fig. 6*A*,*B*). Continuous large-amplitude slow oscillations were superimposed with oscillatory activity in faster theta (4–12 Hz) and gamma (30–100 Hz) frequencies. The amplitude and power of these prelimbic and hippocampal oscillatory patterns were similar in CON, GE, and $G_{PFC}E$ mice (Table 1; Fig. 6*A*,*B*). Lower firing rates in layer II/III were detected in GE, but not $G_{PFC}E$ mice. In contrast, significant changes in the prelimbic–hippocampal coupling within 4–8 Hz have been detected (Fig. 6*C*). In line with our previous results (Hartung et al., 2016b), the synchrony between PL and HP mirrored by the imaginary part of the coherency for 4–8 Hz range was augmented in GE mice (0.273 ± 0.011, $p = 0.029$, ANOVA followed by Bonferroni-corrected *post hoc* test) compared with CON mice (0.249 ± 0.006). Transient DISC1 suppression in PFC had an opposite effect, the theta band imaginary coherency in $G_{PFC}E$ mice was significantly decreased (0.235 ± 0.005, $p = 0.046$, ANOVA followed by Bonferroni-corrected *post hoc* test) compared with CON mice. To investigate whether the directionality of interactions between PL and HP was affected by transient DISC1 suppression in PFC, we quantified the theta band drive from HP to PFC by gPDC (Fig. 6*D*). Both GE and $G_{PFC}E$ mice showed decreased causal interactions from HP to PL within 4–8 Hz (GE: 0.115 ± 0.003, $p = 0.002$, ANOVA followed by Bonferroni-corrected *post hoc* test; $G_{PFC}E$: 0.116 ± 0.002, $p = 0.049$, ANOVA followed by Bonferroni-corrected *post hoc* test) compared with CON mice (0.126 ± 0.004).

These results indicate that transient prefrontal DISC1 knock-down during neonatal development permanently impairs the long-range coupling between PL and HP, but the changes are less prominent than in GE mice.

Discussion

Neuronal network assembly during development is controlled by numerous genetic and environmental factors. The maturation of prefrontal–hippocampal circuits has been shown to be shaped by

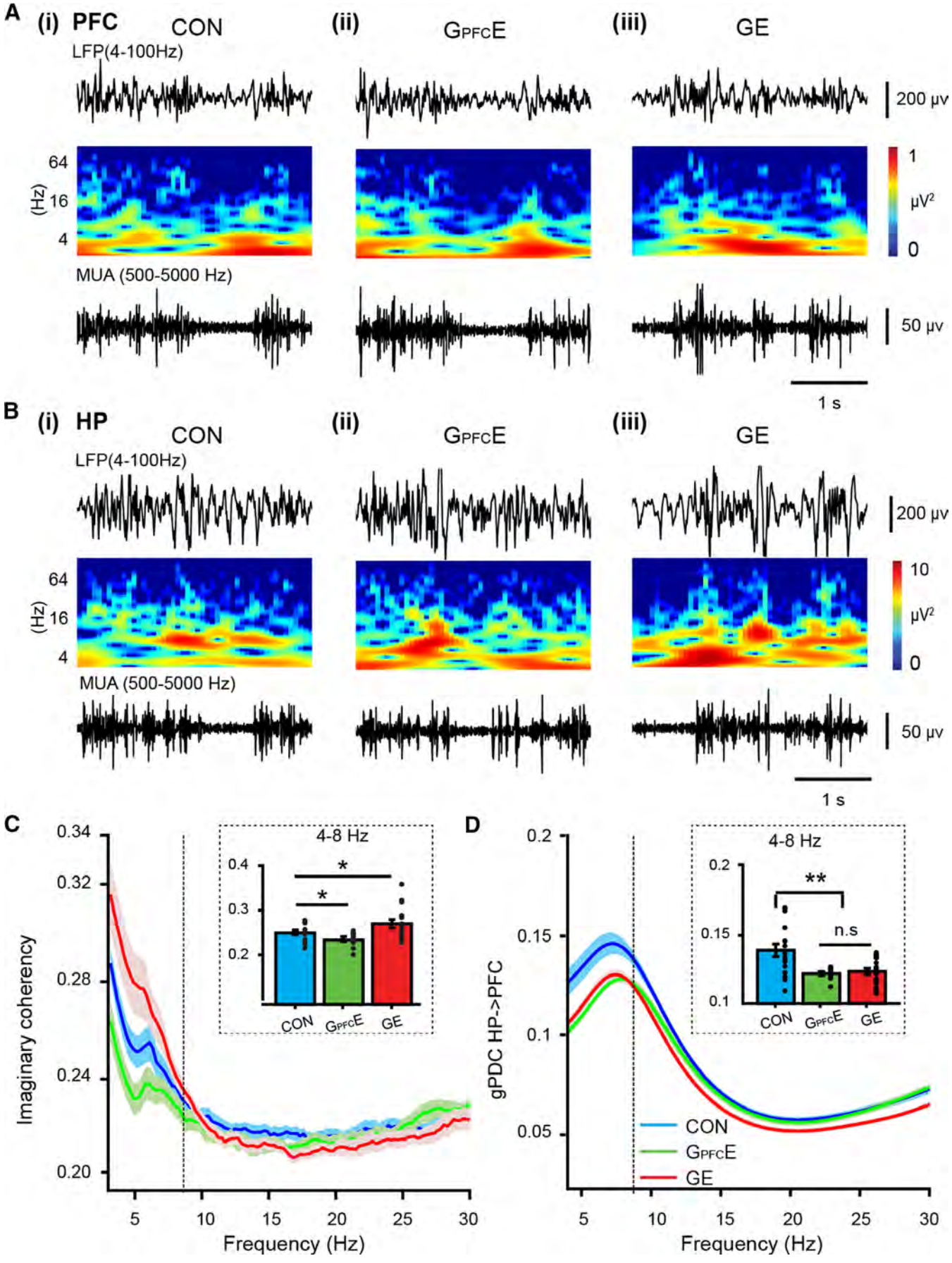

Figure 6. Activity patterns and coupling by synchrony within prefrontal– hippocampal networks of pre-juvenile $G_{PFC}E$ mice. ***Ai***, Extracellular LFP recording of continuous oscillatory activity in PL from a P22 CON mouse displayed after bandpass (4–100 Hz) filtering (top) and the corresponding MUA after bandpass (500–5000 Hz) filtering (bottom). (*Figure legend continues.*)

Table 1. Properties of continuous oscillatory activity and neuronal firing in PL and HP of pre-juvenile CON, GE, and $G_{PFC}E$ mice

	PL			HP		
	CON	GE	G_{PFCE}	CON	GE	G_{PFCE}
Power 4–12 Hz, dB μV^2/Hz	180.58 ± 12.89	205.99 ± 15.10	188.02 ± 23.05	269.23 ± 18.76	299.34 ± 25.40	241.31 ± 22.21
Power 12–30 Hz, dB μV^2/Hz	20.34 ± 1.41	22.92 ± 2.22	20.18 ± 1.31	45.78 ± 3.26	44.33 ± 3.51	41.90 ± 2.11
Power 30–100 Hz, dB μV^2/Hz	3.32 ± 0.24	3.38 ± 0.30	3.71 ± 0.28	9.14 ± 0.53	8.78 ± 0.45	10.22 ± 0.68
MUA, spikes/s	Layer II/III: 2.07 ± 0.14	Layer II/III: 1.45 ± 0.10 ***$p = 0.0005$	Layer II/III: 2.03 ± 0.14	1.64 ± 0.11	1.20 ± 0.15 **$p = 0.011$	1.50 ± 0.12
	Layer V/VI: 1.71 ± 0.16	Layer V/VI: 1.55 ± 0.18	Layer V/VI: 1.63 ± 0.17			

Data are shown as mean ± SEM. Significance was assessed using one-way ANOVA and the listed values correspond to comparisons between CON and GE mice. Data are presented as mean ± SEM. Significance levels of $p < 0.01$ (**) and $p < 0.001$ (***) were detected.

Table 2. Summary results show that transient suppression of DISC1 in PFC causes abnormal morphology, network activity in PFC, and weaker long-range PFC–HP coupling, whereas the hippocampal activity is normal

	GE vs CON	$G_{PFC}E$ vs CON	$G_{PFC}E$ vs GE
PFC			
Dendrite branching	↓	↓	—
Soma size	↓	↓	—
Spine density	↓	↓	—
Oscillatory event			
Occurrence	↑	↑	↓
Duration	↓	—	↓
Power			
4–12 Hz	↓	—	↓
12–30 Hz	↓	—	↓
Sample entropy	↓	↓	—
MUA	↓	↓	—
Spike triggered LFP	↓	↓	—
PFC–HP coupling			
Coherence			
4–12 Hz	↓	↓	—
12–30 Hz	↓	↓	—
Cross-correlation			
4–12 Hz	↓	↓	—
12–30 Hz	↓	↓	—
gPDC			
4–12 Hz	↓	↓	—
12–30 Hz	↓	↓	—
HP			
Oscillatory event			
Occurrence	↓	—	↓
Duration	—	—	—
Power			
4–12 Hz	↓	—	↑
12–30 Hz	↓	—	↑

↓, Significant decrease; ↑, significant increase; —, no change.

both DISC1, as molecular hub of multiple developmental processes, and prenatal immune challenge (Hartung et al., 2016b). In the present study, we combined multisite electrophysiological recordings *in vivo*, neuroanatomy and behavioral investigation of CON, $G_{PFC}E$, and GE mice and provide evidence that (1) confinement of DISC1 suppression to perinatal PFC by *in utero* gene transfer leads to abnormal prefrontal network activity and neuronal firing in neonatal mice experiencing a prenatal immune challenge, which results from structural and functional deficits of layer II/III pyramidal neurons; (2) the prefrontal dysfunction of neonatal $G_{PFC}E$ mice is largely similar to that described for GE mice (Table 2); (3) coupling by synchrony and directed interactions between PFC and HP are weaker, yet the HP activity is normal in $G_{PFC}E$ mice; and (4) transient DISC1 suppression in neonatal PFC of immune-challenged mice is sufficient to disrupt the communication within prefrontal–hippocampal networks throughout neonatal and pre-juvenile development and to impair the behavioral performance of juvenile mice in recognition memory tasks. These results uncover the consequences of transient DISC1 suppression throughout development and highlight the critical relevance of pyramidal neurons in layer II/III for local circuit wiring. They complement previous findings on the abnormal information processing and cognitive performance of adult mice (Niwa et al., 2010).

In line with previous data maternal immune activation (i.e., environmental stressor) or brain-wide DISC1 dysfunction alone had almost no impact on the prefrontal–hippocampal function at neonatal age (Hartung et al., 2016b). Therefore, the similar dysfunction observed in GE and $G_{PFC}E$ mice of this age supports the central role of developmental DISC1-controlled processes in PFC for the maturation of limbic circuits. As intracellular hub, DISC1 interacts with a large number of synaptic and cytoskeletal molecules. By these means, DISC1 controls synaptic plasticity processes in the adult brain (Greenhill et al., 2015; Tropea et al., 2018). Moreover, DISC1 interferes with neuronal proliferation and migration as well as with neurite outgrowth, formation, and maintenance of synapses (Brandon, 2007). Suppression of DISC1 has been reported to decrease spine density and impaired neurite outgrowth through disorganized microtubule-associated dynein motor complex (Ozeki et al., 2003; Kamiya et al., 2005). These morphological deficits have been observed in neonatal GE mice (Chini et al., 2018) and adult mice with brain-wide DISC1 knockdown (Kvajo et al., 2008; Crabtree et al., 2017). In $G_{PFC}E$ mice these structural deficits are likely to be confined to layer II/III pyramidal neurons in PFC. As a result, the firing rate and timing of these cells to network oscillations were significantly disrupted, whereas the overall network activity was mildly impaired compared with GE mice. The lack of effects on oscillatory power might be additionally due to the fact that the *in utero* gene transfer causes DISC1 knock-down in only one-third of layer II/III pyramidal neurons (Bitzenhofer et al., 2017b). The abnormal firing of layer II/III pyramidal neurons in PFC was sufficient to perturb the long-range coupling with HP, yet the oscillatory activity and neuronal firing in CA1 area of HP were similar to those of control pups. The decreased prefrontal spiking timed at β frequencies

←

(*Figure legend continued.*) Traces are accompanied by the color-coded wavelet spectra of the LFP at identical time scale (middle). ***Aii***, Same as ***Ai*** for a P22 $G_{PFC}E$ mice. ***Aiii***, Same as ***Ai*** for a P22 GE mice. ***Bi–Biii***, Same as ***Ai–Aiii*** for HP, respectively. ***C***, Mean coherence spectra for oscillatory activity simultaneously recorded in PL and hippocampal CA1 area of CON, $G_{PFC}E$, and GE mice. Inset, Bar diagram displaying the mean imaginary part of coherence when averaged for each group of pups (one-way ANOVA: $p = 0.013$, $F_{(2,37)} = 4.94$). ***D***, Plot of mean gPDC in relationship to frequency for HP ⟶ PL in CON, $G_{PFC}E$, and GE mice. Inset, Bar diagram displaying gPDC when averaged for 4–8 Hz (one-way ANOVA: $p = 0.021$, $F_{(2,37)} = 4.30$). Data are presented as mean ± SEM. Significance levels of $p > 0.05$ (n.s.), $p < 0.05$ (*), $p < 0.01$ (**) and were detected.

caused desynchronized entrainment of PFC in neonatal $G_{PFC}E$ mice. We suggest that the HP drive, even if not compromised by the local DISC1 suppression, cannot induce network activation, because of decreased connectivity and sparse synaptic transmission of layer II/III pyramidal neurons. Our previous investigations have shown that these neurons are key players for the emergence of β-gamma activity in the neonatal PFC in the presence of the excitatory drive from CA1 area (Bitzenhofer et al., 2017b; Ahlbeck et al., 2018).

Even if DISC1 suppression in PFC is transient and the DISC1 expression recovers to control level during pre-juvenile period, the effects of transient knock-down persist throughout development. Disruption of DISC1 for a maximum of 48 h has been reported to permanently affect the synaptic transmission within cortical circuits as result of underdeveloped dendritic arborization and reduced spine activity (Greenhill et al., 2015). It is very likely that the aberrant morphology of layer II/III pyramidal neurons during neonatal and pre-juvenile development causes abnormal interactions with interneurons and consequently, miswiring of local circuitry in PFC. DISC1 suppression indirectly perturbs the interneuronal function in adults (Cardarelli et al., 2018). Moreover, DISC1 interferes with immune-relevant signaling pathways early in life (Beurel et al., 2010). The structural and functional deficits caused by the combination of DISC1 suppression with MIA might persist and even augment throughout the life span, leading to altered cognitive and social behavior (Abazyan et al., 2010; Ibi et al., 2010; Lipina et al., 2013). Indeed, the weaker coupling through synchrony within prefrontal–hippocampal circuits in $G_{PFC}E$ mice persisted at pre-juvenile age, although the frequency-distribution and power of continuous oscillatory rhythms in both areas are unchanged compared with controls. In contrast, brain-wide DISC1 knock-down has the opposite effect, an exaggerated prefrontal–hippocampal coupling being detected. This effect may result from attempts to compensate the profoundly brain-wide miswiring.

In line with the long-lasting dysfunction of prefrontal–hippocampal coupling, behavioral abilities relying on this circuit were impaired in $G_{PFC}E$ mice. Both the ability to recognize novel objects and their recency were absent in $G_{PFC}E$ mice, whereas the recognition of new location was similar to that of CON mice. A widely accepted model identified prefrontal–hippocampal coupling as a crucial factor for novel object and recency recognition (Barker and Warburton, 2011).

These findings demonstrate that the development of PFC has a critical relevance for pathophysiological processes related to mental disorders. Abnormal DISC1 has been proposed to augment the risk of schizophrenia, bipolar disorders, and recurrent major depression (Kirkpatrick et al., 2006; Carlisle et al., 2011), especially when combined with environmental stressors acting at different developmental time points (van Os and Kapur, 2009; Insel, 2010). The present results offer mechanistic developmental explanations of structural, functional, and behavioral deficits observed at adulthood. The abnormal timing of layer II/III pyramidal neurons in relationship with the discontinuous neonatal oscillatory activity when DISC1 was selectively knocked-down in PFC leads to a persistent disturbance of long-range coupling within prefrontal–hippocampal circuits throughout development and finally, to poorer behavioral performance. Schizophrenia patients show decreased arborization and synaptic deficits in layer II/III pyramidal neurons, as well as alterations in parvalbumin-positive interneurons (Selemon and Goldman-Rakic, 1999; Lewis et al., 2005). Moreover, the prefrontal–hippocampal coupling is profoundly perturbed and the coactivation of the two brain areas weaker in schizophrenia (Meyer-Lindenberg et al., 2001). The present results support the neurodevelopmental origin of schizophrenia and related disorders and highlight the relevance of prefrontal processes during early maturation for the functional and cognitive deficits later in life.

References

Abazyan B, Nomura J, Kannan G, Ishizuka K, Tamashiro KL, Nucifora F, Pogorelov V, Ladenheim B, Yang C, Krasnova IN, Cadet JL, Pardo C, Mori S, Kamiya A, Vogel MW, Sawa A, Ross CA, Pletnikov MV (2010) Prenatal interaction of mutant DISC1 and immune activation produces adult psychopathology. Biol Psychiatry 68:1172–1181. CrossRef Medline

Ahlbeck J, Song L, Chini M, Bitzenhofer SH, Hanganu-Opatz IL (2018) Glutamatergic drive along the septo-temporal axis of hippocampus boosts prelimbic oscillations in the neonatal mouse. eLife 7:e33158. CrossRef Medline

Baccalá LA, Sameshima K (2001) Partial directed coherence: a new concept in neural structure determination. Biol Cybern 84:463–474. CrossRef Medline

Baccalá LA, Sameshima K, Takahashi DY (2007) Generalized partial directed coherence. In: 2007 15th International Conference on Digital Signal Processing, pp 163–166. Piscataway, NJ: IEEE.

Backus AR, Schoffelen JM, Szebényi S, Hanslmayr S, Doeller CF (2016) Hippocampal-prefrontal theta oscillations support memory integration. Curr Biol 26:450–457. CrossRef Medline

Barker GR, Warburton EC (2011) When is the hippocampus involved in recognition memory? J Neurosci 31:10721–10731. CrossRef Medline

Beurel E, Michalek SM, Jope RS (2010) Innate and adaptive immune responses regulated by glycogen synthase kinase-3 (GSK3). Trends Immunol 31:24–31. CrossRef Medline

Bitzenhofer SH, Sieben K, Siebert KD, Spehr M, Hanganu-Opatz IL (2015) Oscillatory activity in developing prefrontal networks results from theta-gamma-modulated synaptic inputs. Cell Rep 11:486–497. CrossRef Medline

Bitzenhofer SH, Ahlbeck J, Hanganu-Opatz IL (2017a) Methodological approach for optogenetic manipulation of neonatal neuronal networks. Front Cell Neurosci 11:239. CrossRef Medline

Bitzenhofer SH, Ahlbeck J, Wolff A, Wiegert JS, Gee CE, Oertner TG, Hanganu-Opatz IL (2017b) Layer-specific optogenetic activation of pyramidal neurons causes beta-gamma entrainment of neonatal networks. Nat Commun 8:14563. CrossRef Medline

Brandon NJ (2007) Dissecting DISC1 function through protein–protein interactions. Biochem Soc Trans 35:1283–1286. CrossRef Medline

Brockmann MD, Pöschel B, Cichon N, Hanganu-Opatz IL (2011) Coupled oscillations mediate directed interactions between prefrontal cortex and hippocampus of the neonatal rat. Neuron 71:332–347. CrossRef Medline

Cardarelli RA, Martin R, Jaaro-Peled H, Sawa A, Powell EM, O'Donnell P (2018) Dominant-negative DISC1 alters the dopaminergic modulation of inhibitory interneurons in the mouse prefrontal cortex. Mol Neuropsychiatry 4:20–29. CrossRef Medline

Carlisle HJ, Luong TN, Medina-Marino A, Schenker L, Khorosheva E, Indersmitten T, Gunapala KM, Steele AD, O'Dell TJ, Patterson PH, Kennedy MB (2011) Deletion of densin-180 results in abnormal behaviors associated with mental illness and reduces mGluR5 and DISC1 in the postsynaptic density fraction. J Neurosci 31:16194–16207. CrossRef Medline

Chini M, Lindemann C, Poepplau JA, Xu X, Ahlbeck J, Bitzenhofer SH, Mulert C, Hanganu-Opatz IL (2018) Microglia inhibition rescues developmental hypofrontality in a mouse model of mental illness. bioRxiv. Advance online publication. Retrieved January 27, 2018. doi: 10.1101/254656

Cichon NB, Denker M, Grün S, Hanganu-Opatz IL (2014) Unsupervised classification of neocortical activity patterns in neonatal and pre-juvenile rodents. Front Neural Circuits 8:50. CrossRef Medline

Clapcote SJ, Lipina TV, Millar JK, Mackie S, Christie S, Ogawa F, Lerch JP, Trimble K, Uchiyama M, Sakuraba Y, Kaneda H, Shiroishi T, Houslay MD, Henkelman RM, Sled JG, Gondo Y, Porteous DJ, Roder JC (2007) Behavioral phenotypes of Disc1 missense mutations in mice. Neuron 54:387–402. CrossRef Medline

Clement EA, Richard A, Thwaites M, Ailon J, Peters S, Dickson CT (2008) Cyclic and sleep-like spontaneous alternations of brain state under urethane anaesthesia. PLoS One 3:e2004. CrossRef Medline

Crabtree GW, Sun Z, Kvajo M, Broek JA, Fénelon K, McKellar H, Xiao L, Xu B, Bahn S, O'Donnell JM, Gogos JA (2017) Alteration of neuronal excitability and short-term synaptic plasticity in the prefrontal cortex of a

mouse model of mental illness. J Neurosci 37:4158–4180. CrossRef Medline

Cuthbert BN, Insel TR (2013) Toward the future of psychiatric diagnosis: the seven pillars of RDoC. BMC Med 11:126. CrossRef Medline

Dehay C, Kennedy H (2007) Cell-cycle control and cortical development. Nat Rev Neurosci 8:438–450. CrossRef Medline

Ennaceur A, Delacour J (1988) A new one-trial test for neurobiological studies of memory in rats: 1. Behavioral data. Behav Brain Res 31:47–59. CrossRef Medline

Fujisawa S, Buzsáki G (2011) A 4 Hz oscillation adaptively synchronizes prefrontal, VTA, and hippocampal activities. Neuron 72:153–165. CrossRef Medline

Greenhill SD, Juczewski K, de Haan AM, Seaton G, Fox K, Hardingham NR (2015) Adult cortical plasticity depends on an early postnatal critical period. Science 349:424–427. CrossRef Medline

Hartung H, Brockmann MD, Pöschel B, De Feo V, Hanganu-Opatz IL (2016a) Thalamic and entorhinal network activity differently modulates the functional development of prefrontal-hippocampal interactions. J Neurosci 36:3676–3690. CrossRef Medline

Hartung H, Cichon N, De Feo V, Riemann S, Schildt S, Lindemann C, Mulert C, Gogos JA, Hanganu-Opatz IL (2016b) From shortage to surge: a developmental switch in hippocampal-prefrontal coupling in a gene-environment model of neuropsychiatric disorders. Cereb Cortex 26: 4265–4281. CrossRef Medline

Heyser CJ, Ferris JS (2013) Object exploration in the developing rat: methodological considerations. Dev Psychobiol 55:373–381. CrossRef Medline

Ibi D, Nagai T, Koike H, Kitahara Y, Mizoguchi H, Niwa M, Jaaro-Peled H, Nitta A, Yoneda Y, Nabeshima T, Sawa A, Yamada K (2010) Combined effect of neonatal immune activation and mutant DISC1 on phenotypic changes in adulthood. Behav Brain Res 206:32–37. CrossRef Medline

Insel TR (2010) Rethinking schizophrenia. Nature 468:187–193. CrossRef Medline

Jaaro-Peled H, Niwa M, Foss CA, Murai R, de Los Reyes S, Kamiya A, Mateo Y, O'Donnell P, Cascella NG, Nabeshima T, Guilarte TR, Pomper MG, Sawa A (2013) Subcortical dopaminergic deficits in a DISC1 mutant model: a study in direct reference to human molecular brain imaging. Hum Mol Genet 22:1574–1580. CrossRef Medline

Kamiya A, Kubo K, Tomoda T, Takaki M, Youn R, Ozeki Y, Sawamura N, Park U, Kudo C, Okawa M, Ross CA, Hatten ME, Nakajima K, Sawa A (2005) A schizophrenia-associated mutation of DISC1 perturbs cerebral cortex development. Nat Cell Biol 7:1167–1178. CrossRef Medline

Kapucu FE, Välkki I, Christophe F, Tanskanen JMA, Johansson J, Mikkonen T, Hyttinen JAK (2017) On electrophysiological signal complexity during biological neuronal network development and maturation. In: 2017 39th Annual International Conference of the IEEE Engineering in Medicine and Biology Society (EMBC), pp 3333–3338. Piscataway, NJ: IEEE.

Kirkpatrick B, Xu L, Cascella N, Ozeki Y, Sawa A, Roberts RC (2006) DISC1 immunoreactivity at the light and ultrastructural level in the human neocortex. J Comp Neurol 497:436–450. CrossRef Medline

Koike H, Arguello PA, Kvajo M, Karayiorgou M, Gogos JA (2006) Disc1 is mutated in the 129S6/SvEv strain and modulates working memory in mice. Proc Natl Acad Sci U S A 103:3693–3697. CrossRef Medline

Krüger HS, Brockmann MD, Salamon J, Ittrich H, Hanganu-Opatz IL (2012) Neonatal hippocampal lesion alters the functional maturation of the prefrontal cortex and the early cognitive development in pre-juvenile rats. Neurobiol Learn Mem 97:470–481. CrossRef Medline

Kvajo M, McKellar H, Arguello PA, Drew LJ, Moore H, MacDermott AB, Karayiorgou M, Gogos JA (2008) A mutation in mouse Disc1 that models a schizophrenia risk allele leads to specific alterations in neuronal architecture and cognition. Proc Natl Acad Sci U S A 105:7076–7081. CrossRef Medline

Kvajo M, McKellar H, Drew LJ, Lepagnol-Bestel AM, Xiao L, Levy RJ, Blazeski R, Arguello PA, Lacefield CO, Mason CA, Simonneau M, O'Donnell JM, MacDermott AB, Karayiorgou M, Gogos JA (2011) Altered axonal targeting and short-term plasticity in the hippocampus of Disc1 mutant mice. Proc Natl Acad Sci U S A 108:E1349–E1358. CrossRef Medline

Lewis DA, Hashimoto T, Volk DW (2005) Cortical inhibitory neurons and schizophrenia. Nat Rev Neurosci 6:312–324. CrossRef Medline

Lipina TV, Zai C, Hlousek D, Roder JC, Wong AH (2013) Maternal immune activation during gestation interacts with Disc1Point mutation to exacerbate schizophrenia-related behaviors in mice. J Neurosci 33:7654–7666. CrossRef Medline

Meyer-Lindenberg A, Poline JB, Kohn PD, Holt JL, Egan MF, Weinberger DR, Berman KF (2001) Evidence for abnormal cortical functional connectivity during working memory in schizophrenia. Am J Psychiatry 158: 1809–1817. CrossRef Medline

Millar JK, Wilson-Annan JC, Anderson S, Christie S, Taylor MS, Semple CA, Devon RS, St Clair DM, Muir WJ, Blackwood DH, Porteous DJ (2000) Disruption of two novel genes by a translocation co-segregating with schizophrenia. Hum Mol Genet 9:1415–1423. CrossRef Medline

Mitra PP, Bokil H (2008) Observed brain dynamics. New York: Oxford.

Narayan S, Nakajima K, Sawa A (2013) DISC1 as a key lead in studying cortical development and associated brain disorders. Neuroscientist 19: 451–464. CrossRef Medline

Nauhaus I, Busse L, Carandini M, Ringach DL (2009) Stimulus contrast modulates functional connectivity in visual cortex. Nat Neurosci 12:70–76. CrossRef Medline

Niwa M, Kamiya A, Murai R, Kubo K, Gruber AJ, Tomita K, Lu L, Tomisato S, Jaaro-Peled H, Seshadri S, Hiyama H, Huang B, Kohda K, Noda Y, O'Donnell P, Nakajima K, Sawa A, Nabeshima T (2010) Knockdown of DISC1 by *in utero* gene transfer disturbs postnatal dopaminergic maturation in the frontal cortex and leads to adult behavioral deficits. Neuron 65:480–489. CrossRef Medline

Niwa M, Jaaro-Peled H, Tankou S, Seshadri S, Hikida T, Matsumoto Y, Cascella NG, Kano S, Ozaki N, Nabeshima T, Sawa A (2013) Adolescent stress-induced epigenetic control of dopaminergic neurons via glucocorticoids. Science 339:335–339. CrossRef Medline

Nolte G, Bai O, Wheaton L, Mari Z, Vorbach S, Hallett M (2004) Identifying true brain interaction from EEG data using the imaginary part of coherency. Clin Neurophysiol 115:2292–2307. CrossRef Medline

Ozeki Y, Tomoda T, Kleiderlein J, Kamiya A, Bord L, Fujii K, Okawa M, Yamada N, Hatten ME, Snyder SH, Ross CA, Sawa A (2003) Disrupted-in-schizophrenia-1 (DISC-1): mutant truncation prevents binding to NudE-like (NUDEL) and inhibits neurite outgrowth. Proc Natl Acad Sci U S A 100:289–294. CrossRef Medline

Pagliardini S, Gosgnach S, Dickson CT (2013) Spontaneous sleep-like brain state alternations and breathing characteristics in urethane anesthetized mice. PLOS One 8:e70411. CrossRef Medline

Rakic P (1988) Specification of cerebral cortical areas. Science 241:170–176. CrossRef Medline

Ray S, Maunsell JH (2011) Network rhythms influence the relationship between spike-triggered local field potential and functional connectivity. J Neurosci 31:12674–12682. CrossRef Medline

Ripke S, O'Dushlaine C, Chambert K, Moran JL, Kähler AK, Akterin S, Bergen SE, Collins AL, Crowley JJ, Fromer M, Kim Y, Lee SH, Magnusson PK, Sanchez N, Stahl EA, Williams S, Wray NR, Xia K, Bettella F, Borglum AD, et al. (2013) Genome-wide association analysis identifies 14 new risk loci for schizophrenia. Nat Genet 45:1150–1159. CrossRef Medline

Selemon LD, Goldman-Rakic PS (1999) The reduced neuropil hypothesis: a circuit based model of schizophrenia. Biol Psychiatry 45:17–25. CrossRef Medline

Siapas AG, Lubenov EV, Wilson MA (2005) Prefrontal phase locking to hippocampal theta oscillations. Neuron 46:141–151. CrossRef Medline

Spellman T, Rigotti M, Ahmari SE, Fusi S, Gogos JA, Gordon JA (2015) Hippocampal-prefrontal input supports spatial encoding in working memory. Nature 522:309–314. CrossRef Medline

Sullivan PF (2013) Questions about DISC1 as a genetic risk factor for schizophrenia. Mol Psychiatry 18:1050–1052. CrossRef Medline

Thierry AM, Gioanni Y, Dégénétais E, Glowinski J (2000) Hippocampo-prefrontal cortex pathway: anatomical and electrophysiological characteristics. Hippocampus 10:411–419. CrossRef Medline

Tomoda T, Sumitomo A, Jaaro-Peled H, Sawa A (2016) Utility and validity of DISC1 mouse models in biological psychiatry. Neuroscience 321:99–107. CrossRef Medline

Tropea D, Hardingham N, Millar K, Fox K (2018) Mechanisms underlying the role of DISC1 in synaptic plasticity. J Physiol 596:2747–2771. CrossRef Medline

van Os J, Kapur S (2009) Schizophrenia. Lancet 374:635–645. CrossRef Medline

Warburton EC, Brown MW (2015) Neural circuitry for rat recognition memory. Behav Brain Res 285:131–139. CrossRef Medline

Wolansky T, Clement EA, Peters SR, Palczak MA, Dickson CT (2006) Hippocampal slow oscillation: a novel EEG state and its coordination with ongoing neocortical activity. J Neurosci 26:6213–6229. CrossRef Medline

2.4 Resolving and Rescuing Developmental Miswiring in a Mouse Model of Cognitive Impairment

Mattia Chini, Jastyn A. Pöpplau, Christoph Lindemann, Laura Carol-Perdiguer, Marilena Hnida, Victoria Oberländer, Xiaxia Xu, Joachim Ahlbeck, Sebastian H. Bitzenhofer, Christoph Mulert and Ileana L. Hanganu-Opatz

Neuron 2020; DOI: https://doi.org/10.1016/j.neuron.2019.09.042

Personal contribution

I designed part of the project. I performed *in vivo* electrophysiology and optogenetics experiments. I performed histological investigations and image analysis. I carried out formal analysis and data curation. I wrote the original draft, reviewed and edited the manuscript.

Article

Neuron

Resolving and Rescuing Developmental Miswiring in a Mouse Model of Cognitive Impairment

Graphical Abstract

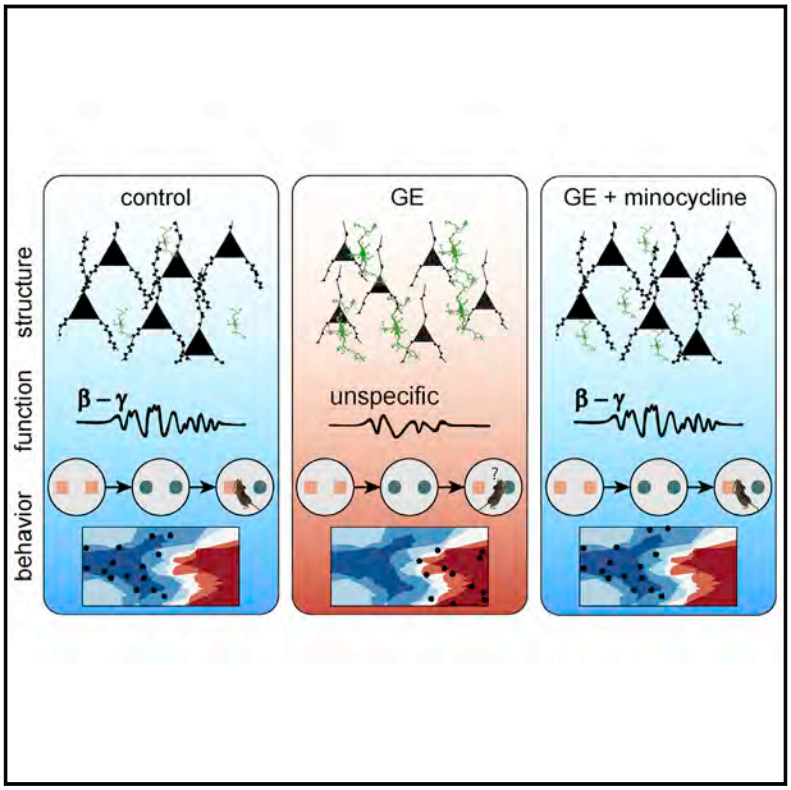

Authors

Mattia Chini, Jastyn A. Pöpplau, Christoph Lindemann, ..., Sebastian H. Bitzenhofer, Christoph Mulert, Ileana L. Hanganu-Opatz

Correspondence

hangop@zmnh.uni-hamburg.de

In Brief

In a mouse model of mental disorders, Chini et al. dissect an early-emerging prefrontal network dysfunction that subsequently gives rise to cognitive deficits. They show that this deficiency can be rescued by minocycline administration, thus identifying a potential biomarker amenable for future therapies.

Highlights

- Mice mimicking the etiology of mental illness have dysregulated prefrontal network
- Weaker beta activation of prefrontal circuits results from superficial layers deficits
- Rescue of microglial function restores developing prefrontal function and behavior
- Early prefrontal dysfunction relates to later-emerging cognitive performance

Chini et al., 2020, Neuron *105*, 60–74
January 8, 2020
https://doi.org/10.1016/j.neuron.2019.09.042

CellPress

CellPress

Neuron
Article

Resolving and Rescuing Developmental Miswiring in a Mouse Model of Cognitive Impairment

Mattia Chini,[1] Jastyn A. Pöpplau,[1] Christoph Lindemann,[1] Laura Carol-Perdiguer,[1] Marilena Hnida,[1] Victoria Oberländer,[1,3] Xiaxia Xu,[1] Joachim Ahlbeck,[1,4] Sebastian H. Bitzenhofer,[1,5] Christoph Mulert,[2,6] and Ileana L. Hanganu-Opatz[1,7,*]

[1]Developmental Neurophysiology, Institute of Neuroanatomy, University Medical Center Hamburg-Eppendorf, 20246 Hamburg, Germany
[2]Psychiatry Neuroimaging Branch (PNB), Department of Psychiatry and Psychotherapy, University Medical Center Hamburg-Eppendorf, 20246 Hamburg, Germany
[3]Present address: Department of Neuroscience, University of Helsinki, Helsinki 00014, Finland
[4]Present address: Department of Neurophysiology and Pathophysiology, University Medical Center Hamburg-Eppendorf, 20246 Hamburg, Germany
[5]Present address: Center for Neural Circuits and Behavior, Department of Neurosciences, University of California, San Diego, La Jolla, CA 92093, USA
[6]Present address: Centre for Psychiatry and Psychotherapy, Justus Liebig University, Giessen, Germany
[7]Lead Contact
*Correspondence: hangop@zmnh.uni-hamburg.de
https://doi.org/10.1016/j.neuron.2019.09.042

SUMMARY

Cognitive deficits, core features of mental illness, largely result from dysfunction of prefrontal networks. This dysfunction emerges during early development, before a detectable behavioral readout, yet the cellular elements controlling the abnormal maturation are still unknown. Here, we address this open question by combining *in vivo* electrophysiology, optogenetics, neuroanatomy, and behavioral assays during development in mice mimicking the dual genetic-environmental etiology of psychiatric disorders. We report that pyramidal neurons in superficial layers of the prefrontal cortex are key elements causing disorganized oscillatory entrainment of local circuits in beta-gamma frequencies. Their abnormal firing rate and timing relate to sparser dendritic arborization and lower spine density. Administration of minocycline during the first postnatal week, potentially acting via microglial cells, rescues the neuronal deficits and restores pre-juvenile cognitive abilities. Elucidation of the cellular substrate of developmental miswiring causing later cognitive deficits opens new perspectives for identification of neurobiological targets amenable to therapies.

INTRODUCTION

Cortical function relies on the precise wiring and activation of diverse populations of pyramidal cells and interneurons that are entrained in oscillatory rhythms. Although recent studies have revealed several assembling rules of cortical microcircuits in the adult brain (Harris and Shepherd, 2015), their ontogeny is still poorly understood. Given the uniqueness of the developing brain in its spatial and temporal organization of coordinated activity (Brockmann et al., 2011; Khazipov et al., 2004), the depolarizing action of GABA (Kirmse et al., 2015) and the formation of transient connectivity patterns (Marques-Smith et al., 2016), the functional coupling within immature microcircuits is likely to bear equally unique traits. Elucidating the features of such immature networks is of paramount importance in the context of neurodevelopmental disorders, as their early disruption is thought to underlie the later emergence of devastating symptoms that characterize these diseases (Marín, 2016).

We started to elucidate the mechanisms of functional coupling within the developing brain and have shown that pyramidal neurons in the superficial layers of the prefrontal cortex (PFC) play a fundamental role in generating beta/low-gamma oscillations in the neonatal mouse (Bitzenhofer et al., 2017). At adulthood, coordinated activity in gamma-frequency band is instrumental to cognitive processing (Bosman et al., 2014) and relates to the pathophysiology of psychiatric disorders (Cho et al., 2015; Uhlhaas and Singer, 2015). Disturbed gamma activity has been observed long before the onset of psychosis in high-risk humans (Leicht et al., 2016) and during neonatal development in animal models (Hartung et al., 2016). However, the circuit dysfunction underlying such abnormalities is still unknown.

To address this knowledge gap, we interrogate the developing prefrontal network in a mouse model mimicking both the genetic (mutation of the intracellular hub of developmental processes Disrupted-In-Schizophrenia 1 [DISC1] gene; Brandon and Sawa, 2011) and the environmental (challenge by maternal immune activation [MIA]) background that has been related to mental illness (dual-hit genetic-environmental [GE] mice). At adult age, these mice mimic, to a large extent, the network dysfunction as well as memory and attention deficits identified in human psychiatric disorders (Abazyan et al., 2010). The impairment of prefrontal-hippocampal circuits underlying

poorer cognitive performance emerges early in life only when both risk factors converge and is absent in neonatal mice challenged with the genetic or environmental stressor alone (Hartung et al., 2016). To elucidate the mechanisms of developmental dysfunction, we focus on neonatal age (end of 1st–beginning of 2nd postnatal week) of rodents that roughly corresponds to the second/third trimester of human pregnancy, a period of high vulnerability for mental disorders (Selemon and Zecevic, 2015). We combine *in vivo* and *in vitro* electrophysiology with optogenetics, pharmacology, behavioral testing, and confocal microscopy-based structural investigations of the prelimbic subdivision (PL) of the prefrontal cortex. We show that pyramidal neurons in superficial layers exhibit major morphological, synaptic, and functional deficits and lack the ability to organize the beta-gamma entrainment of local prelimbic circuits in neonatal dual-hit GE mice, while deep layers neurons are largely unaffected. Transient administration of minocycline, potentially modulating microglia inflammatory response (Kobayashi et al., 2013), rescues electrophysiological and structural deficits, as well as cognitive abilities at juvenile age. Moreover, we propose that early disruption of prefrontal networks might be predictive of memory impairment at juvenile age.

RESULTS

Layer- and Frequency-Specific Dysfunction of Local Circuits in the Prelimbic Cortex of Dual-Hit GE Mice

To get first insights into the source of prelimbic dysfunction in dual-hit GE mice, we performed extracellular recordings of the local field potential (LFP) and multiple-unit activity (MUA) over prelimbic layers using four-shank 16 site electrodes in lightly anesthetized (Chini et al., 2019) postnatal day (P) 8–10 control (n = 38 pups from 13 litters) and GE mice (n = 18 pups from 6 litters). This developmental stage corresponds to the initiation of hippocampus-driven entrainment of prelimbic circuitry (Ahlbeck et al., 2018; Brockmann et al., 2011). The exact position of recording sites covering superficial and deep layers was confirmed by the reconstruction of electrode tracks *post mortem* (Figure 1A). In line with our previous findings (Bitzenhofer et al., 2015; Brockmann et al., 2011; Cichon et al., 2014; Hartung et al., 2016), the first patterns of network activity in the neonatal PL of all investigated control and dual-hit GE mice were discontinuous, i.e., spindle-shaped oscillations switching between theta and beta-gamma frequency components alternated with long periods of network silence (Figure 1B). The firing of prelimbic neurons was strongly timed by the oscillatory rhythms. As previously reported (Chini et al., 2019), the patterns of network oscillations and neuronal firing in the PL were similar in urethane-anesthetized and non-anesthetized neonatal pups, yet the magnitude of activity decreased in the presence of anesthesia (Figure S1). The similarities might be due to the ability of urethane to mimic sleep conditions (Clement et al., 2008), the dominant behavioral state of neonatal mice (Cirelli and Tononi, 2015). Although dual-hit GE mice have been reported to have profoundly altered network activity and neuronal firing at neonatal age when compared with controls (Hartung et al., 2016), it is still unclear whether the dysfunction equally affects the local prelimbic circuits. To address this question, we first monitored the layer-specific differences between oscillatory patterns of control and dual-hit GE mice. Major differences in the occurrence, duration, and broadband power of oscillatory events were detected when comparing the two groups of mice (Figures 1C, 1D, and S2A–S2E; Table S1). However, these detected differences were similar across layers. This might be due, on the one hand, to a layer-unspecific overall damping of entrainment in dual-hit GE mice and, on the other hand, to non-specific conduction synchrony within a rather small tissue volume (300- to 400-μm radius). To discriminate between the two sources, in a second step, we investigated the layer-specific firing rate and timing by oscillatory phase, which are not contaminated by non-specific volume conduction. The firing of neurons in prelimbic superficial layers in GE mice (log −2.1 ± 0.1 spikes/s) was significantly ($p < 10^{-7}$) reduced when compared to controls (0.61 ± 0.04 spikes/s; Figure 1E). In contrast, neurons in deep layers similarly fired in control (−0.95 ± 0.05 spikes/s) and GE mice (−1.3 ± 0.2 spikes/s). The timing of neuronal firing in relation to beta (12–30 Hz) and gamma (30–100 Hz) frequency was also disturbed and lost its precision in superficial layers ($p < 1 \times 10^{-4}$ and $p = 0.021$, respectively), but not deep-layer neurons of GE mice when compared to controls (Figures 1F–1H). The timing of spiking by theta oscillations in both superficial and deep layers was similar in control and dual-hit GE mice (Figure S2E). To verify that our results were not biased by anesthesia, we recorded a set of non-anesthetized P8–P10 control (n = 16) and GE (n = 18) mice and confirmed that GE mice have reduced broadband LFP power. The decreased MUA and single-unit activity (SUA) firing rates were limited to neurons in superficial layers (Figures S1G–S1L). In contrast to the significant perturbation of prelimbic activity in neonatal dual-hit GE mice, the oscillatory and firing patterns of one-hit genetic (G) (i.e., only DISC1) or environmental (E) (i.e., only MIA) mice were similar to those of control pups (Figures S2F–S2H). Furthermore, the layer-specific dysfunction seems to be characteristic to the investigated developmental stage P8–P10. In mice of 4–6 days of age, a time window in which neurons are still migrating (Ignacio et al., 1995), deficits are present, yet the layer specificity is lacking (Figures S2I–S2K). On the other hand, in line with our previous data (Hartung et al., 2016), the properties of prelimbic network oscillations were similar in control and dual-hit GE mice at pre-juvenile age (P20–P23; Figures S2L–S2N).

These results demonstrate abnormal beta-gamma band oscillations and entrainment of superficial layers of PL in dual-hit GE mice during this defined developmental period (P8–P10).

Beta-Gamma Band Dysfunction of Prelimbic Circuits in Dual-Hit GE Mice Results from Abnormal Activation of Superficial Layers Pyramidal Neurons

In developing circuits, beta-gamma band oscillatory activity has been recently shown to require the activation of pyramidal neurons in superficial ($PYRs_{SUP}$), but not deep, layers ($PYRs_{DEEP}$) of PL (Bitzenhofer et al., 2017). Therefore, the weaker beta-gamma entrainment of prelimbic circuits and coupling of neuronal firing to fast oscillations identified in GE mice might result from dysfunction of $PYRs_{SUP}$. To test this hypothesis, we monitored the effects of light activation of prelimbic neurons

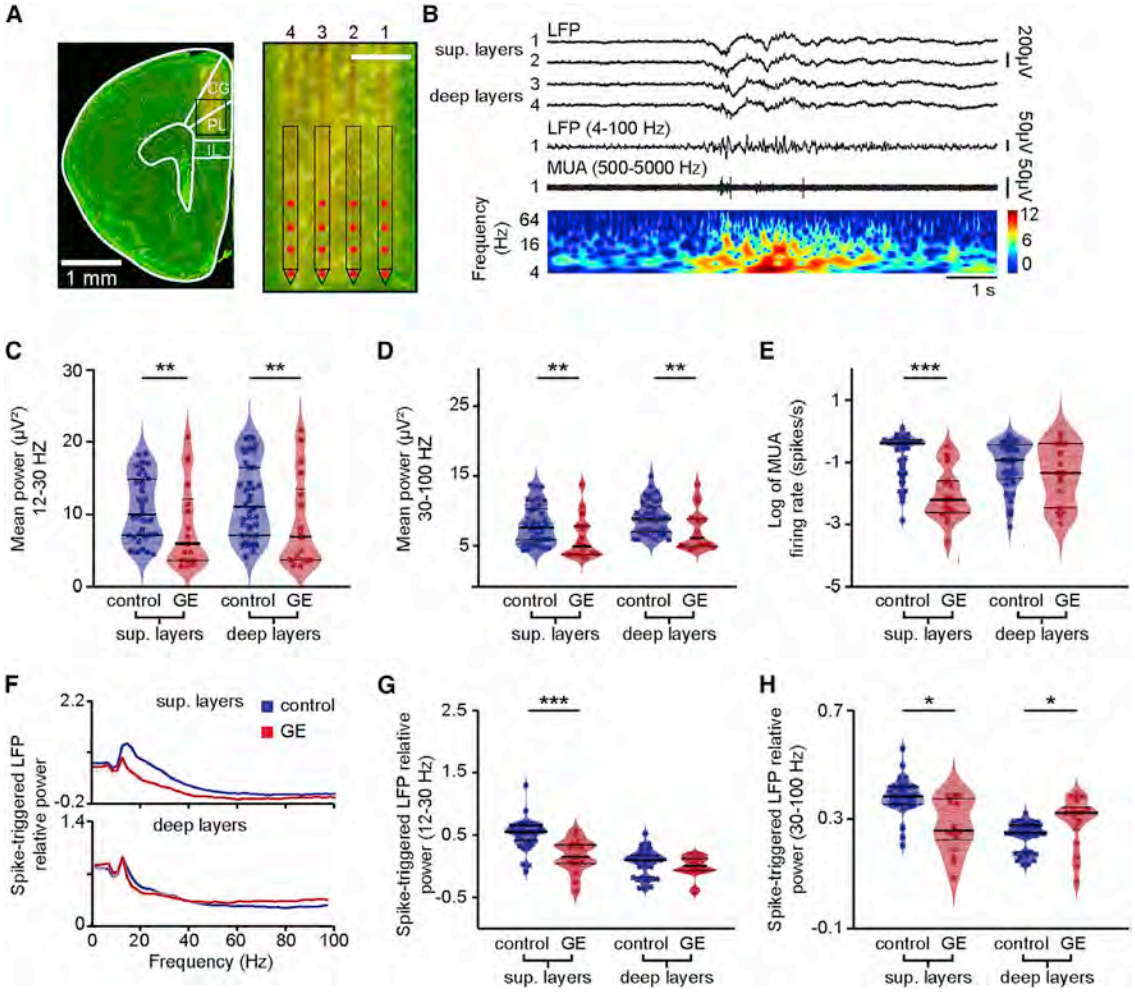

Figure 1. Abnormal Patterns of Discontinuous Oscillatory Activity and Neuronal Firing over the Layers of Prelimbic Cortex of Neonatal Dual-Hit GE Mice

(A) Digital photomontage reconstructing the position of a 4-shank DiI-labeled recording electrode in the PL of a Nissl-stained 100-μm-thick coronal section (green) from a P9 mouse. Inset, the position of recording sites (red) over the prelimbic layers is displayed at higher magnification. Scale bar, 200 μm.

(B) Characteristic discontinuous oscillatory activity recorded in superficial and deep layers of PL before (top) and after band pass (4–100 Hz) filtering (middle; recording site 1 in superficial layers) and the corresponding MUA after band pass (500–5,000 Hz) filtering (bottom; recording site 1 in superficial layers). Color-coded frequency plot shows the wavelet of the LFP (recording site 1) at identical timescale.

(C) Violin plot displaying the power in beta frequency band of oscillations in superficial and deep layers of the prelimbic cortex of control (blue; n = 38) and GE (red; n = 18) mice.

(D and E) Same as (C) for the power in gamma frequency band (D) and MUA firing rate (E).

(F) Plots of frequency-dependent relative power of spike-triggered LFP in superficial (top) and deep layers (bottom) of control (blue) and GE (red) mice.

(G) Violin plot displaying the relative power of spike-triggered LFP in beta band for superficial and deep layers of control (blue; n = 38) and GE (red; n = 18) mice.

(H) Same as (G) for the LFP in gamma band.

For (C)–(E), (G), and (H), data are presented as median with 25th and 75th percentile, and single data points are shown as asterisks. The shaded area represents the probability distribution of the variable. *$p < 0.05$, **$p < 0.01$, and ***$p < 0.001$; analysis of covariance (ANCOVA) with age as covariate (C–E) and Yuen's bootstrap test (G and H) with 20% level of trimming for the mean.

that were transfected with light-sensitive proteins and the red fluorescent protein tDimer2. Using our recently established protocol for optogenetic manipulation of developing circuits (Bitzenhofer et al., 2017), we achieved cell-type-, layer-, and area-specific transfection of neurons by *in utero* electroporation (IUE) (Figures S3A and S3B). Constructs coding for the double mutant channelrhodopsin E123 T159 (ChR2(ET/TC)) were transfected by IUE at embryonic day (E) 15.5 and E12.5 for selective targeting of superficial and deep layers, respectively (Figures S3C and S3D). Staining for NeuN showed that a similar fraction of neurons was transfected in control (34.7% ± 0.8%; n = 13 pups) and GE mice (32.0% ± 0.7%; n = 8 pups). The pyramidal-like shape and orientation of primary dendrites confirmed that the expression constructs were exclusively integrated into cell lineages of pyramidal neurons. Omission of ChR2(ET/TC) from the expression construct (i.e., opsin-free) yielded similar

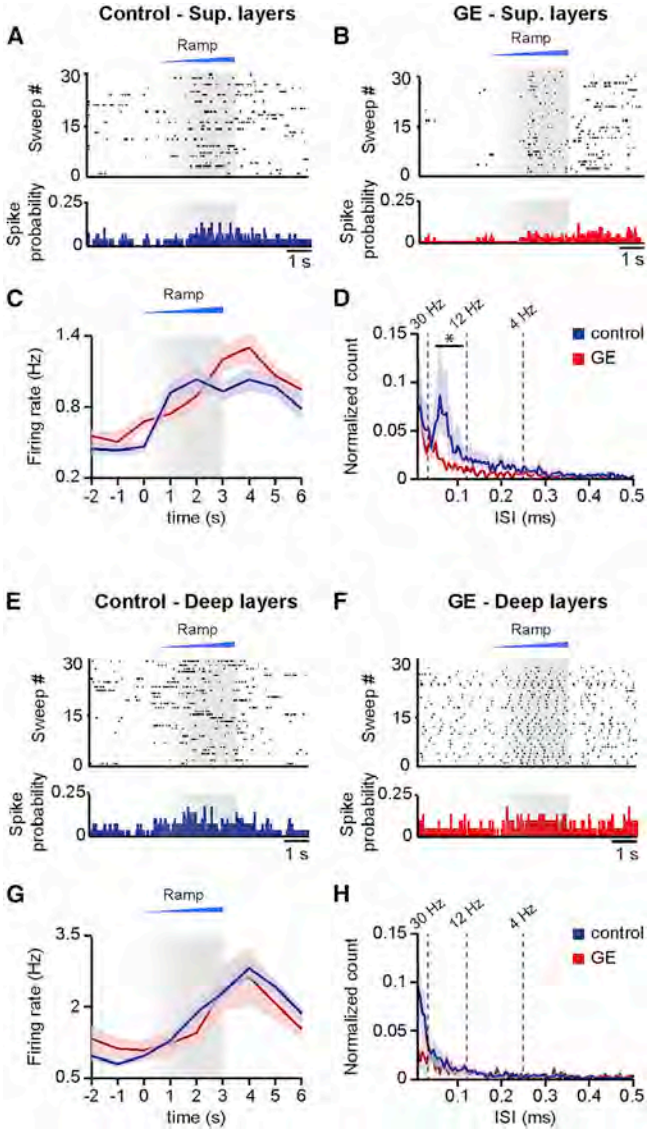

Figure 2. Firing Patterns after Optogenetic Activation of $PYRs_{SUP}$ and $PYRs_{DEEP}$ in Control and Dual-Hit GE Mice *In Vivo*

(A) Representative raster plot and corresponding spike probability histogram displaying the firing of a $PYRs_{SUP}$ from a control mouse in response to 30 sweeps of ramp stimulation (473 nm; 3 s).

(B) Same as (A) for transfected $PYRs_{SUP}$ from GE mice.

(C) Line plot displaying the mean MUA firing rate in transfected $PYRs_{SUP}$ of control (blue; n = 43 recording sites from 13 pups) and GE (red; n = 40 recording sites from 10 mice) mice in response to ramp illumination.

(D) Same as (C) for inter-spike interval within 10- to 500-ms range normalized to all ISIs.

(E–H) Same as (A)–(D) for transfected $PYRs_{DEEP}$ from control (n = 116 recording sites from 13 pups) and GE mice (n = 27 recording sites from n = 6 pups). Data are presented as mean ± SEM. *p < 0.05; linear mixed-effect model with animal as a random effect.

expression rates and distribution of tDimer2-positive neurons. Moreover, the success rate of transfection by IUE was similar in control and dual-hit GE mice in the presence and absence of opsin (Figure S3E).

The transfection procedure by IUE had no major effects on the overall development of animals (Figures S3F–S3K). Although IUE caused significant reduction of litter size in both control and GE mice (non-electroporated: 8.3 ± 1.1 pups/litter; IUE: 4.6 ± 1.3 pups/litter; p = 0.03), all investigated pups had similar body length, tail length, and weight during the early postnatal period. Vibrissa placing, surface righting, and cliff aversion reflexes were also not affected by IUE or transfection of neurons with opsins (Figures S3I–S3K).

First, we assessed the efficiency of light stimulation in inducing action potentials (APs) in prelimbic neurons of control and dual-hit GE mice *in vitro*. For this, whole-cell patch-clamp recordings were performed from tDimer2-positive $PYRs_{SUP}$ (n = 42) and $PYRs_{DEEP}$ (n = 38) in coronal slices containing the PL from P8–P10 mice after IUE at E15.5 and E12.5, respectively. In line with the previously reported "inside-out" pattern of cortical maturation and, correspondingly, the more mature profile of neurons in deep versus superficial layers, $PYRs_{SUP}$ and $PYRs_{DEEP}$ in control mice significantly differed in some of their passive and active membrane properties (Bitzenhofer et al., 2017). However, in dual-hit GE mice, the resting membrane potential of $PYRs_{SUP}$ (−53.2 ± 0.37 mV) was more positive when compared with controls (−63.2 ± 0.3 mV; $p = 2 \times 10^{-4}$), and the maximum amplitude of action potentials decreased (44.8 ± 0.80 mV versus 29.2 ± 0.36 mV in controls; p = 0.018). These alterations of intrinsic neuronal properties might point to the immaturity of $PYRs_{SUP}$ in GE mice, even though membrane resistance, membrane time constant, and action potential half-width were not significantly different across conditions (Figures S4A–S4E). The passive and active properties of ChR2(ET/TC)-transfected neurons were similar to those previously reported for age-matched mice (Bitzenhofer et al., 2017). Pulsed light stimulation (3 ms, 473 nm, 5.2 mW/mm^2) depolarized transfected fluorescently labeled neurons and led to robust firing in all pups. The probability of triggering APs by pulsed light stimuli decreased with increasing stimulation frequency, yet it differed in its dynamics in control versus GE mice. Whereas $PYRs_{SUP}$ of control mice were able to reliably follow light stimulations up to 16 Hz, in GE mice, they had a significant firing drop already between 8 and 16 Hz (Figures S4E and S4F). Light stimulation of $PYRs_{DEEP}$ showed a similar decrease of firing probability with augmenting stimulation frequency in control and GE mice.

To elucidate the consequences of abnormal intrinsic firing preference for oscillatory network entrainment, we monitored the effects of light activation of either $PYRs_{SUP}$ or $PYRs_{DEEP}$ *in vivo*. In controls, activation of $PYRs_{SUP}$ selectively drove the neonatal prelimbic networks in beta-gamma frequency range, whereas activation of $PYRs_{DEEP}$ caused non-specific network activation. We reasoned that, if $PYRs_{SUP}$ are indeed the cause of the previously demonstrated disruption of beta-gamma activity in the PL of GE mice, then their light stimulation *in vivo* should not be able to selectively induce oscillations in this range.

Ramp light stimulation increased the neuronal firing of ChR2(ET/TC)-transfected $PYRs_{SUP}$ and $PYRs_{DEEP}$ in control and GE mice ($p < 10^{-4}$ for all conditions), but not of neurons transfected with opsin-free constructs (Figures 2A–2H and S5).

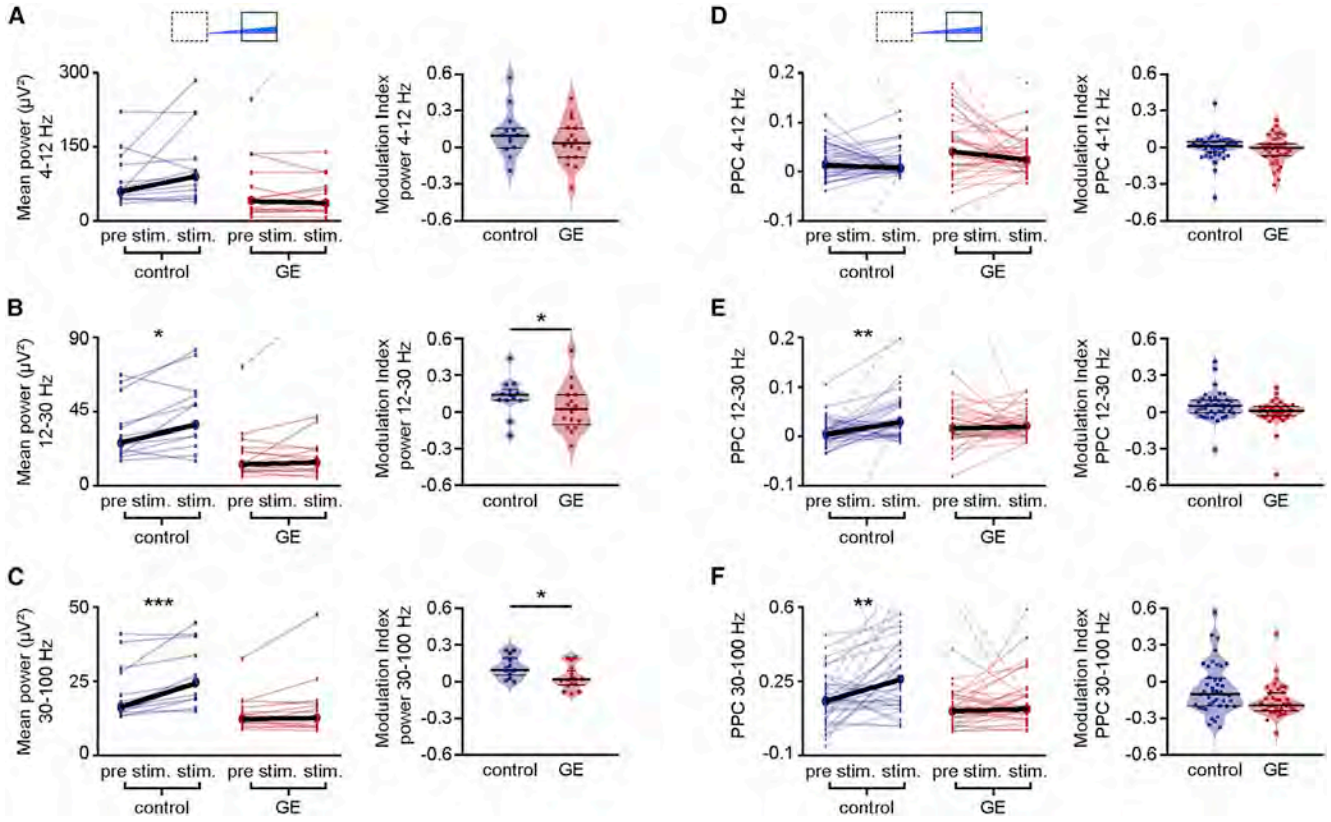

Figure 3. Network Activity after Optogenetic Activation of $PYRs_{SUP}$ in Control and Dual-Hit GE Mice *In Vivo*

(A) Left: scatterplot displaying the LFP power in the theta (4–12 Hz) frequency band for control (blue; n = 13) and GE (red; n = 16) mice before (pre stim.; 1.5 s) and during the second half (stim.; 1.5 s) of ramp stimulation. Right: violin plot displaying the stimulation modulation index of light-induced LFP power in the theta frequency band for control and GE mice is shown.

(B and C) Same as (A) for beta (12–30 Hz) and gamma (30–100) frequency bands.

(D–F) Same as (A)–(C) for pairwise phase consistency (PPC) of $PYRs_{SUP}$ in control (n = 43 recording sites from 13 pups) and GE (n = 40 recording sites from 10 pups) mice.

In scatterplots (A–F), data are presented as median, and individual values are displayed as thin dots and lines. In violin plots (A–F), data are presented as median with 25th and 75th percentile, and single data points are shown as asterisks. *$p < 0.05$, **$p < 0.01$, and ***$p < 0.001$; Yuen's bootstrap test (A–F) with 20% level of trimming for the mean and linear mixed-effect model with animal as a random effect (D–F).

The light-induced augmentation of firing was similar in the two groups of mice ($p = 0.46$ and $p = 0.24$ for $PYRs_{SUP}$ and $PYRs_{DEEP}$, respectively). The spike discharge initiated once the power exceeded a certain threshold. For some neurons, the firing decreased toward the end of the ramp stimulations, indicating that, similar to the *in vitro* conditions, their membrane potential reached a depolarizing plateau, preventing further spiking. However, for the majority of neurons, the firing rate after stimulus remained higher than before the stimulus (Figures 2C and 2G), suggesting that global network activation had been induced by light stimulation in the developing circuits. Major differences in the firing of prelimbic neurons from control and GE mice were detected. Although $PYRs_{SUP}$ in controls had a preferred inter-spike interval of ~60 ms, equivalent to a population firing at 16.7 Hz (Figures 2A and 2D), a coordinated frequency-tuned discharge pattern was absent in GE mice upon ramp stimulation of $PYRs_{SUP}$ (condition effect, $p = 4 \times 10^{-5}$; $p < 0.05$ in the 15- to 20-Hz range with the exception of $p = 0.059$ at 16.7 Hz; Figures 2B and 2D). In contrast, the firing dynamics of $PYRs_{DEEP}$ was similar in control and GE mice (condition effect $p = 0.11$) and showed no frequency-specific concentration of firing during ramp stimulation (Figures 2E–2H).

To causally prove the contribution of abnormal firing of $PYRs_{SUP}$ to the weaker beta-gamma band entrainment previously identified in the PL of dual-hit GE mice, we tested the effects of ramp stimulations on the discontinuous network oscillations. When compared with pulsed stimulations, ramp stimulations have the advantage of not inducing power contamination by repetitive and fast large-amplitude voltage deflections resulting from simultaneous opening of light-activated channels and to trigger more physiological and not artificially synchronous firing patterns (Bitzenhofer et al., 2017). In control mice, the LFP power in beta- and gamma-frequency range significantly increased during ramp stimulation of $PYRs_{SUP}$ ($p = 0.02$ and $p = 0.002$, respectively), whereas the theta-band activity remained unaffected ($p = 0.26$). In contrast, $PYRs_{SUP}$ in GE mice lost their ability to boost neonatal prelimbic oscillations in a frequency-specific manner, because ramp

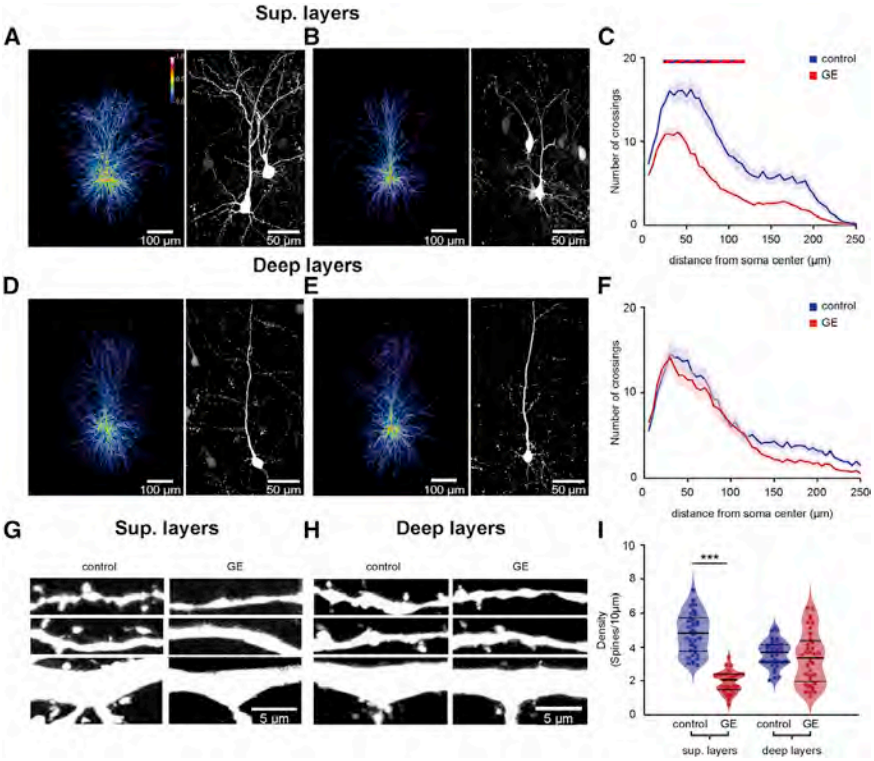

Figure 4. Simplified Dendritic Arborization and Reduced Spine Density in PYRs$_{SUP}$ of Dual-Hit GE Mice

(A) Left: heatmap displaying an overlay of all traced dendrites of transfected PYRs$_{SUP}$ in control mice. Right: photograph of a representative PYRs$_{SUP}$ in a P10 mouse is shown.

(B) Same as (A) for a P10 dual-hit GE mouse.

(C) Graph displaying the average number of dendritic intersections within a 250-µm radius from the soma center of PYRs$_{SUP}$ in control (blue; n = 21 neurons from 3 pups) and GE (red; n = 21 neurons from 3 pups) mice. Blue/red bar indicates significant difference between control and GE mice.

(D–F) Same as (A)–(C) for PYRs$_{DEEP}$ from control (blue; n = 21 neurons from 3 pups) and GE (red; n = 21 neurons from 3 pups) mice.

(G) Photograph displays representative basal (top), secondary apical (middle), and proximal oblique and apical (bottom) dendrites of a PYRs$_{SUP}$ from a P10 control mouse (left) and a P10 GE mouse (right).

(H) Same as (G) for PYRs$_{DEEP}$.

(I) Violin plot displaying the average spine density on dendrites from PYRs$_{SUP}$ of control (blue; n = 39 dendrites from 13 neurons) and GE (red; n = 30 dendrites from 10 neurons) mice.

In (C) and (F), data are presented as mean ± SEM. In (I), data are presented as median with 25th and 75th percentile, and single data points are displayed as asterisks. *p < 0.05, **p < 0.01, and ***p < 0.001; linear mixed-effect model with animal (C and F) and neuron (I) as random effects.

stimulations did not affect the LFP power (p = 0.49, p = 0.57, and p = 0.44 for theta-, beta-, and gamma-frequency band, respectively; Figure 3A). Moreover, stimulation of PYRs$_{SUP}$ differently modulated power in beta- and gamma-frequency band between control and GE mice (p = 0.03 and p = 0.03, respectively). Not only the light-induced inter-spike interval and power of network oscillations were disrupted in GE mice, but also the timing of firing by the oscillatory phase was impaired. To quantify this relationship, we used pairwise phase consistency (PPC), a measure of synchrony that is not biased by firing rates (Vinck et al., 2010). In control mice, stimulation increased the PPC for beta (p = 0.008) and gamma oscillations (p = 0.003), but not for theta (p = 0.24). In contrast, the PPC for theta (p = 0.09), beta (p = 0.86), and gamma oscillations (p = 0.37) during stimulation of PYRs$_{SUP}$ in GE mice did not change (Figures 3D–3F), indicating that the synchronization of spikes relative to the phase of these oscillations was not affected by light activations of PYRs$_{SUP}$. However, due to high variability, no difference in PPC modulation between the two mouse groups achieved statistical significance (Figures 3D–3F).

In line with the frequency-unspecific augmentation of firing rate after light activation of PYRs$_{DEEP}$ in control mice, the LFP power in all frequency bands increased during stimulation and remained at a high level even after it. In GE mice, optogenetic stimulation did not augment the power. No differences in power modulation between the two mouse groups were detected (Figure S6).

Thus, the reduced beta-gamma activity in the PL of neonatal dual-hit GE mice relates to the dysfunction of firing dynamics of PYRs$_{SUP}$.

Pyramidal Neurons in the Superficial Layers of PL in Neonatal Dual-Hit GE Mice Show Major Morphological and Synaptic Deficits

The selective dysfunction of PYRs$_{SUP}$ and the corresponding abnormal network activity in GE mice might relate to abnormal morphology and connectivity of these neurons at neonatal age. To test this hypothesis, we undertook a detailed histological examination of the cytoarchitecture of tDimer-labeled pyramidal neurons in superficial and deep layers of P10 control and GE mice. PYRs$_{SUP}$, but not PYRs$_{DEEP}$, of GE mice showed a significant reduction in the soma size when compared to neurons of controls (n = 21 neurons for every condition; p = 0.039 for PYRs$_{SUP}$ and p = 0.95 for PYRs$_{DEEP}$; Figure S7A). The complexity of dendritic branching was assessed by Sholl analysis of three-dimensionally reconstructed PYRs$_{SUP}$ and PYRs$_{DEEP}$. When compared to controls, PYRs$_{SUP}$ of GE mice had major reduction in dendritic branching (condition effect $p < 1 \times 10^{-9}$; Figures 4A–4C). These deficits were particularly prominent within a radius of 20–115 µm from the cell soma center (p < 0.05 for all pairwise comparisons). In accordance with our electrophysiological results, we found no significant differences in the complexity of dendritic arborization for PYRs$_{DEEP}$ of GE and control mice (condition effect p = 0.56; Figures 4D–4F). Accordingly, the total dendritic branch length was reduced in

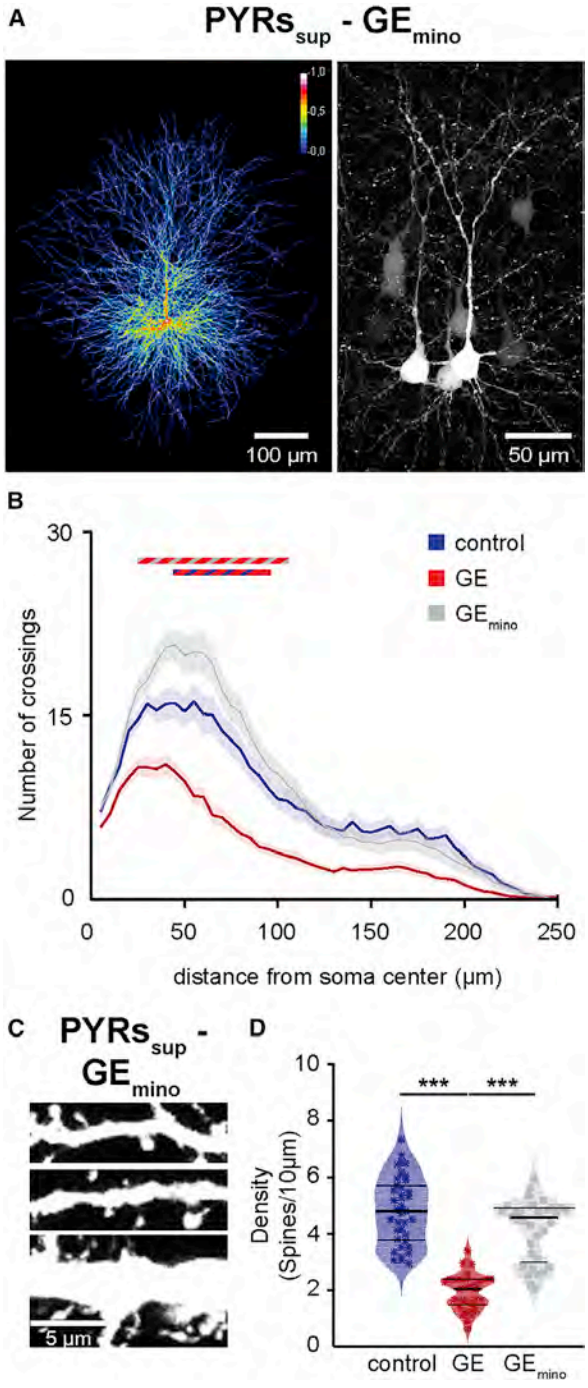

Figure 5. Minocycline Treatment Rescues the Abnormal Structure of $PYRs_{SUP}$ in GE Mice

(A) Left: heatmap displaying an overlay of all traced dendrites of transfected $PYRs_{SUP}$ in GE_{mino} mice. Right: photograph of a representative PYR_{SUP} in a P10 GE_{mino} mouse is shown.

(B) Graph displaying the average number of dendritic intersections within a 250-µm radius from the soma center of $PYRs_{SUP}$ in control (blue; n = 21 neurons from 3 pups), GE (red; n = 21 neurons from 3 pups), and GE_{mino} (gray; n = 21 neurons from 3 pups) mice. Blue/red and gray/red bars indicate significant difference between control and GE mice and GE and GE_{mino} mice, respectively.

(C) Photograph displays representative basal (top), secondary apical (middle), and proximal oblique and apical (bottom) dendrites of a PYR_{SUP} from a P10 GE_{mino} mouse.

(D) Violin plot displaying the average spine density on dendrites from $PYRs_{SUP}$ of control (blue; n = 39 dendrites from 13 neurons), GE (red; n = 30 dendrites from 10 neurons), and GE_{mino} (gray; n = 36 dendrites from 12 neurons) mice.

In (B), data are presented as mean ± SEM. In (D), data are presented as median with 25th and 75th percentile, and single data points are displayed as asterisks. ***p < 0.001; linear mixed-effect model with animal (B) and neuron (D) as random effects.

$PYRs_{SUP}$, but not $PYRs_{DEEP}$, of GE mice (n = 21 neurons for every condition; p = 0.024 for $PYRs_{SUP}$ and p = 0.37 for $PYRs_{DEEP}$; Figure S7B).

Next, we examined the spine density along the dendrites of $PYRs_{SUP}$ and $PYRs_{DEEP}$, whose dendritic morphology we had previously analyzed. $PYRs_{SUP}$ of GE mice (n = 10 neurons) had significantly lower density when compared to controls (n = 13 neurons; condition effect $p = 7 \times 10^{-4}$), whereas the values were comparable for $PYRs_{DEEP}$ of control (n = 9 neurons) and GE mice (n = 9 neurons; condition effect p = 0.75; Figures 4G–4I). The magnitude of density reduction was similar for different types of dendrites (apical and proximal oblique dendrites, secondary apical dendrites, and basal dendrites; condition effect $p = 7 \times 10^{-4}$, $p = 5 \times 10^{-4}$, and p = 0.001, respectively; Figures S7C–S7E). In line with the network dysfunction, the prominent morphological/structural deficits seem to be largely confined to neonatal age. $PYRs_{SUP}$ of pre-juvenile (P21) GE mice had a normal dendritic arborization (n = 28 neurons; condition effect p = 0.99) and spine density (n = 16 neurons; condition effect p = 0.3). Only soma size and total dendritic path length were slightly decreased, yet not at significance level (n = 28 neurons; p = 0.088 and p = 0.055, respectively; Figures S7F–S7J).

The simplified dendritic arborization and the decreased spine density of $PYRs_{SUP}$, but not $PYRs_{DEEP}$, further confirm the layer-specific dysfunction in neonatal dual-hit GE mice.

Transient Minocycline Administration Rescues Prelimbic Deficits in Dual-Hit GE Mice

We next set out to determine whether the morphological and functional deficits of $PYRs_{SUP}$ in the PL of GE mice could be rescued during early development. Minocycline is a tetracycline antibiotic that exerts a variety of functions and has anti-inflammatory properties (Garrido-Mesa et al., 2013). Minocycline has recently shown promising results as an adjunct drug to treat depression (Emadi-Kouchak et al., 2016), bipolar disorder (Savitz et al., 2018), and schizophrenia (Zhang et al., 2018) and even to delay or prevent the incidence of schizophrenia (Sellgren et al., 2019). However, in the absence of mechanistic insights, its therapeutic potential remains controversial (Deakin et al., 2018; Kishimoto et al., 2018).

We administered minocycline from P1 to P8 by adding it to the drinking water of the dam (Dansie et al., 2013; Luzi et al., 2009) and analyzed the morphological, functional, and behavioral consequences in P8–P10 pups. First, Sholl analysis of three-dimensionally reconstructed tDimer-positive $PYRs_{SUP}$ (n = 21 neurons) from GE_{mino} mice showed that the complexity of dendritic branching was fully restored after treatment, being

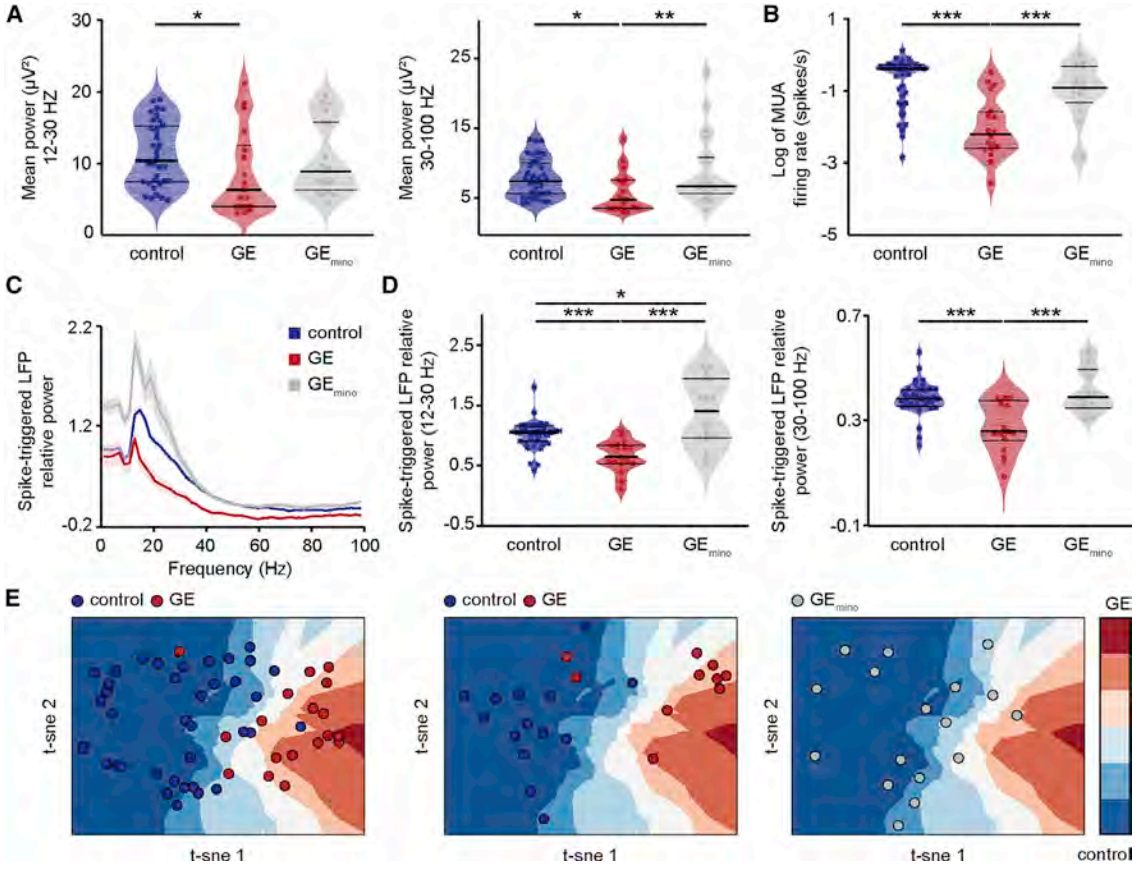

Figure 6. Minocycline Treatment Rescues Electrophysiological Core Dysfunctions in Dual-Hit GE Mice

(A) Violin plot displaying the beta (left) and gamma (right) band power of oscillations in superficial layers of the PL of control (blue; n = 38), GE (red; n = 18), and GE_{mino} (gray; n = 18) mice.

(B) Same as (A) for MUA firing rate.

(C) Plots of frequency-dependent relative power of spike-triggered LFP in superficial layers (top) of control (blue), GE (red), and GE_{mino} (gray) mice.

(D) Violin plot displaying the relative power of spike-triggered LFP in beta (left) and gamma (right) band for superficial layers of control (blue; n = 38), GE (red; n = 18), and GE_{mino} (gray; n = 18) mice.

(E) t-Distributed stochastic neighbor embedding (T-SNE) plot of superficial layers electrophysiological features of control (blue dots) and GE (red dots) mice in the training/cross-validation (left) and test (middle) set and GE_{mino} (gray dots; right).

The background represents an approximation of the decision space of the classifier. *p < 0.05, **p < 0.01, and ***p < 0.001; ANCOVA with age as covariate (A and B) and Yuen's bootstrap test (D) with 20% level of trimming for the mean.

similar to that of controls (condition effect p = 0.77; p > 0.05 for all pairwise comparisons; Figures 5A and 5B). Minocycline treatment rescued the synaptic deficits too. $PYRs_{SUP}$ from GE_{mino} mice (n = 12 neurons) had a similar spine density as those from control mice (condition effect p = 0.78) that was significantly increased when compared to GE mice (condition effect p = 5×10^{-5}; Figures 5C and 5D). The effect was similar across the different types of dendrites that were analyzed.

Second, we assessed the properties of prelimbic network oscillations and neuronal firing in GE_{mino} mice and compared them with those from control and GE mice. The power in beta and gamma band of prelimbic oscillations recorded in superficial layers was similar in control and minocycline-treated GE mice (p = 0.90 and p = 0.31, respectively; Figures 6A and 6B; Table S1). Similarly, the prelimbic firing rate and timing by oscillatory phase were rescued (Figures 6C and 6D). The firing rate of neurons in superficial layers was similar for controls (log values −0.61 ± 0.04) and GE_{mino} mice (log values −0.9 ± 0.1; p = 0.59). The timing of prelimbic firing in superficial layers of GE_{mino} mice, as measured by spike-triggered LFP power, was rescued (gamma band; p = 0.48) or even slightly increased (beta band; p = 0.026) when compared to controls (Figure 6D). In contrast to the profound changes observed in superficial layers after minocycline treatment, the network activity and neuronal firing in deep layers of PL from GE_{mino} mice remained largely unaffected (Figures S8A–S8F). Moreover, the neuronal and network properties in control mice ($control_{mino}$ n = 12) did not change after minocycline administration. Theta, beta, and gamma power of prelimbic oscillations as well as firing rate and spike-triggered relative LFP power in superficial layers were similar in controls and $control_{mino}$ (p = 0.68, p = 0.95, p = 0.36, p = 0.16, p = 0.1, and p = 0.06, respectively). The activity in deep layers was also largely unaffected, with only gamma power being significantly increased (p = 0.006; Figures S8G–S8L).

These data indicate that the abnormal firing and network coupling patterns in the PL of dual-hit GE mice are rescued by administration of minocycline during a defined developmental period.

Electrophysiological Features of Prelimbic Superficial Layers Are Sufficient to Distinguish Control from GE Mice

To test the robustness of conclusions above, we developed a machine-learning classification algorithm (k-nearest neighbors classification), to which we asked to predict whether mice belonged to the control or the GE group (Figure 6E). As input features, we used only the electrophysiological features characterized for neonatal PL: LFP power in beta- and gamma-frequency bands and firing rates of neurons in superficial layers and their spike-triggered LFP power in beta- and gamma-frequency bands. We first used 3-fold cross-validation and iteratively (n = 500) split the dataset of mice (n = 56 mice) into a training (n = 38 mice) and a cross-validation (n = 18) set. The training set was used to tune the algorithm hyper-parameters (further using 3-fold cross-validation), whereas the assessment of the prediction quality was carried out on the cross-validation set. By these means, we were able to obtain a median classification accuracy of 83% on the cross-validation set, thereby showing that superficial-layers-derived features are valid predictors for this classification task (Figure 6E, left). To confirm the robustness and generalizability of our findings, we tested the predictions of the pre-trained k-nearest neighbors classifier on an entirely new dataset (n = 24; test dataset), to which it had not been exposed during the training phase. On the test dataset, the machine-learning classification achieved high classification accuracy (median 80%; Figure 6E, middle). Moreover, when we asked the algorithm to predict to which class GE_{mino} mice belonged to, on average, all but one of them (94%) were classified as belonging to the control group (Figure 6E, right). These data show that superficial-layers-derived electrophysiological features are strong and robust predictors for distinguishing control and GE mice and further confirm the efficacy of the minocycline-administration rescue.

Transient Minocycline Treatment Rescues Abnormal Microglia Function in Dual-Hit GE Mice

Minocycline has been shown to block the stress-induced inflammatory responses of microglia (Kobayashi et al., 2013) and to reduce microglia overpruning in schizophrenic-patients-derived induced microglia-like cells (Sellgren et al., 2019). Therefore, their modulation might represent a possible mechanism explaining the observed minocycline effects. Microglia are key players during early brain development and have been reported to control synapse formation (Miyamoto et al., 2016) and to sculpt the developing circuits by engulfing and remodeling synapses in an activity-dependent manner (Schafer et al., 2012; Weinhard et al., 2018). Transient perturbations in the development of microglia, such as those induced by maternal immune activation (MIA), have far-reaching effects on adult neuronal function and behavior (Shin Yim et al., 2017) that have been linked to mental illness.

In accordance with this stream of evidence, microglia in the PL of neonatal GE mice are profoundly perturbed. When compared with controls, not only was microglia number significantly augmented (+47%; $p < 1 \times 10^{-5}$), but also morphological features, such as area and cell spread, were likewise significantly increased by 29% (n = 1,250 cells for control; n = 1,173 cells for GE mice; $p < 1 \times 10^{-6}$) and 25% ($p < 1 \times 10^{-13}$), respectively (Figures 7A–7D). Moreover, microglia cell perimeter and roundness, but not eccentricity, were also substantially changed in dual-hit GE mice (Figures 7E–7G). These deficits were observed throughout the entire prelimbic cortex and had no layer specificity. Although minocycline-treated GE (GE_{mino}) mice had no reduction in the number of microglial cells (−13%; p = 0.17), microglia showed a reduced area (−35%; n = 1,614 cells; p = 0.015) and cell spread (−11%; $p = 8 \times 10^{-4}$) when compared to GE mice (Figures 7A–7D).

To get insights into the mechanisms that enable microglia to control neuronal function in developing PL, we quantified microglia phagocytosis of pre-synaptic terminals, identified as VGLUT-1-positive puncta. Quantitative analysis revealed that, in GE mice (n = 52 cells), both the number as well as the volume of engulfed VGLUT-1-positive puncta were increased in comparison to control (n = 54 cells; p = 0.006 and p = 0.006, respectively) and, to a less amount, to GE_{mino} (n = 56 cells; p = 0.084 and p = 0.084, respectively) mice. In contrast, there was no difference between controls and GE_{mino} mice (p = 0.287 and p = 0.296, respectively; Figures 7H–7K). High-definition morphological analysis confirmed that GE mice have over all prelimbic layers microglia cells with larger distal volume (condition effect p = 0.019) in comparison to GE_{mino} (p = 0.008) and, to a lesser extent, to controls (p = 0.072).

These data confirm that minocycline has an effect on microglia cells and that it partially restores the phenotype of these cells in GE mice. Although minocycline is a pleiotropic drug, part of its effect on GE mice might therefore be mediated by microglia modulation.

Dysfunction of Prelimbic Superficial Layers and Its Rescue Relates to Later Cognitive Performance

Previous investigations showed that compromised function of PFC in neonatal dual-hit GE mice has behavioral impact on later cognitive abilities. In line with these results, we monitored the novelty detection and recognition memory, which have been shown to rely on functional communication within prefrontal-hippocampal networks. Novel object recognition (NOR) and recency recognition (RR) are based on the innate preference of mice to explore novel or less familiar objects over more familiar ones (Figures 8A and 8C). Therefore, their testing requires no prior training or deprivation and can be achieved shortly after full maturation of sensory and motor abilities (i.e., P17 to P18). All three groups of mice, control, GE, and GE_{mino} were tested using a custom-design arena and objects of different size, color, and texture. We quantified the relative amount of time spent interacting with the novel/less recent object when compared to the familiar/more recent one (discrimination ratio), as well as the relative duration of single interactions with the two objects. During the familiarization trial of NOR test, all mice (P17 to P18) spent equal time investigating the two objects in the arena.

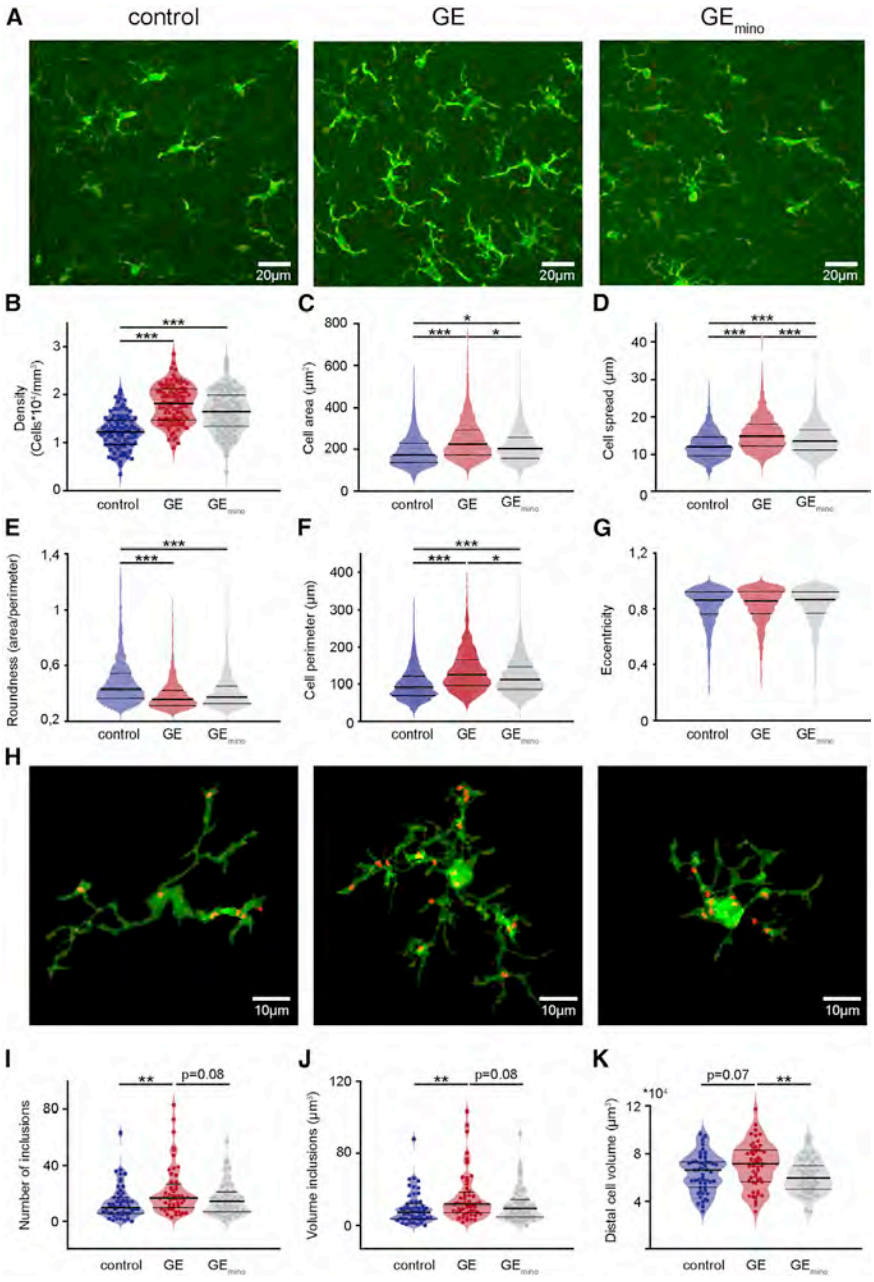

Figure 7. Altered Microglial Cell Morphology and Phagocytic Activity in Dual-Hit GE Mice Are Partially Restored by Minocycline Treatment

(A) Photographs of Iba-1-stained microglial cells in the PL of a P10 control mouse (left), of a P10 GE mouse (center), and of a P10 GE_{mino} mouse (right).

(B) Violin plot displaying the average density of Iba-1-stained cells in the PL of control (blue; n = 64 images from 4 pups), GE (red; n = 64 images from 4 pups), and GE_{mino} mice (gray; n = 64 images from 4 pups).

(C–G) Same as (B) for cell area (C), cell spread (D), roundness (E), perimeter (F), and eccentricity (G). For (C)–(G), n = 1,250, 1,738, and 1,614 cells, respectively, from 12 sections of 4 pups for all three conditions.

(H) Photographs of Iba-1-stained microglial cells and phagocyted VGLUT-1 puncta in the PL of a P8 control mouse (left), of a P8 GE mouse (center), and of a P8 GE_{mino} mouse (right).

(I) Violin plot displaying the number of inclusions per microglia cell in the PL of control (blue; n = 53 cells from 4 pups), GE (red; n = 52 cells from 4 pups), and GE_{mino} mice (gray; n = 55 cells from 4 pups).

(J and K) Same as (I) for the volume of inclusions per microglia cell (J) and the distal volume of microglia cells (K). Data are presented as median with 25^{th} and 75^{th} percentile.

In (B) and (I)–(K), single data points are displayed as asterisks, whereas in (C)–(G), single data points are omitted due to their high number. *$p < 0.05$, **$p < 0.01$, and ***$p < 0.001$; linear mixed-effect model with animal as a random effect (B–G) and robust, bootstrapped ANOVA with 20% level of trimming for the mean (I–K).

During the testing phase, GE mice (n = 15) showed poorer recognition abilities as mirrored by the lower discrimination ratio index and single interaction time when compared with control (n = 15) and GE_{mino} mice (n = 16; Figure 8B). Despite this trend, the differences did not reach significance levels, most likely due to high inter-animal variability reported for NOR test. During RR task, mice (P19–P22) had to process temporal information by recognizing the object with which they most recently interacted. GE mice had a significantly poorer discrimination ratio (condition effect p = 0.013) when compared to both control ($p < 10^{-4}$) and GE_{mino} mice (p = 0.038; Figure 8D). The exploratory and anxiety behavior was similar for all three groups of mice, indicating that the poor performance of GE mice does not result from lower motor abilities or fear to approach the objects. Taking into account the similarity of behavioral performance in control and GE_{mino} mice, we suggest that the recognition abilities of pre-juvenile GE mice are rescued after transient treatment with minocycline during early postnatal development. Importantly, the timing of minocycline administration is crucial for the rescue. When we administered minocycline from P9 to P16 to GE mice (GE_{mino}late; n = 16), the RR deficits persisted, the discrimination ratio being significantly decreased when compared to controls (n = 14; p = 0.03; Figure S9A). Moreover, when we considered the entire behavioral dataset, we found that GE_{mino}late mice have a RR deficit even when compared to GE_{mino} mice (p = 0.037) and are not significantly different from untreated GE mice (p = 0.85).

To confirm the link between prefrontal dysfunction throughout development and behavioral performance at pre-juvenile age, we resorted to a machine-learning classification algorithm with different inputs (discrimination ratios and single interaction time for the two tasks) but a similar architecture (k-nearest neighbors classification) to the one discussed above (Figure 7E). As

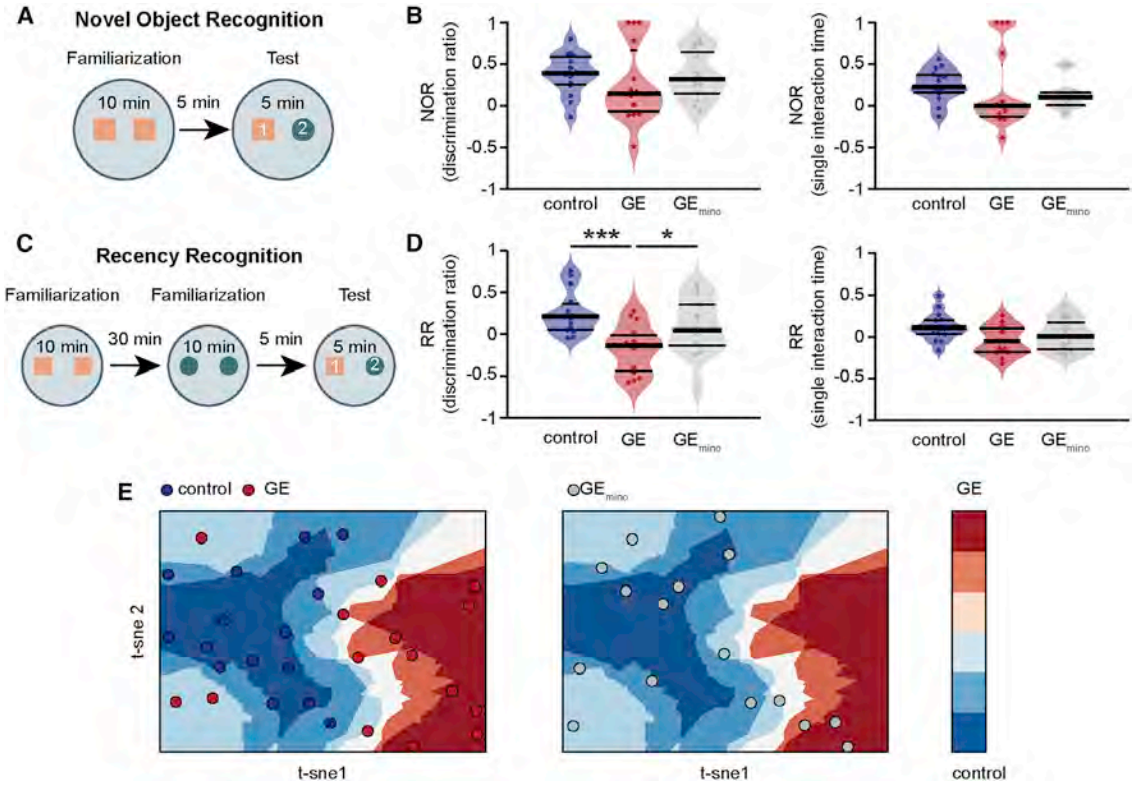

Figure 8. Minocycline Treatment Rescues Behavioral Deficits in Dual-Hit GE Mice

(A) Schematic diagram of the experimental protocol for NOR.

(B) Violin plot displaying NOR discrimination ratio (middle) and single interaction time (right) of control (blue; n = 15), GE (red; n = 15), and GE_{mino} (gray; n = 16) mice.

(C and D) Same as (A) and (B) for RR.

(E) T-SNE plot of behavioral features of control (blue dots) and GE (red dots) mice in the training/cross-validation set (left) and GE_{mino} (gray dots; right).

In (B) and (D), data are presented as median with 25th and 75th percentile, and single data points are shown as asterisks. *p < 0.05 and ***p < 0.001; robust, bootstrapped ANOVA with 20% level of trimming for the mean (B and D).

before, we iteratively (n = 500) used 3-fold cross-validation (n = 20 mice in the training set and n = 10 in the cross-validation set) to tune the algorithm hyper-parameters (training set) and assess its accuracy (cross-validation set). By these means, we were able to obtain a median classification accuracy of 83% on the cross-validation set. When we asked the algorithm to predict to which class GE_{mino} mice belonged to, 75% of them were classified as belonging to the control group (Figure 8E). These data show that, on a group level, early disruption of prefrontal networks is predictive of later impaired cognition. Accordingly, early rescue of such deficits is associated with restored cognitive development.

DISCUSSION

Although neurodevelopmental miswiring has been postulated to result in major functional and behavioral deficits at adulthood, the mechanisms of early impairment are still largely unresolved. A major consequence of this knowledge gap is the poor understanding of disease pathophysiology that hampers the development of tailored therapies for mental illness. Toward the aim of elucidating the substrate of developmental dysfunction, the present study uncovers layer- and cell-type-specific deficits in the PL of neonatal mice reproducing the gene-environment interactions involved in the pathogenesis of psychiatric disorders. We show that, in dual-hit GE mice, (1) the lower entrainment of neonatal prefrontal circuits in beta-gamma oscillations relates to structural and functional deficits of superficial layers pyramidal neurons; (2) minocycline administration during the first postnatal week restores the morphology, synaptic function, and firing and oscillatory patterns in local prefrontal circuits; and (3) at group level, early prefrontal network activity is predictive of pre-juvenile cognitive abilities. These findings highlight the major contribution of glutamatergic dysfunction to the abnormal refinement of circuits during development and support the hypothesis that such deficits emerge already at neonatal age. Moreover, the results demonstrate the efficacy of minocycline in preventing the emergence of developmental circuit dysfunction with relevance for cognitive disabilities. A limitation of the current study is that major conclusions rely on investigations at group level. Future longitudinal recordings across entire postnatal development, which are still currently technically demanding, will prove whether these conclusions hold also on an individual level.

Wiring of Prefrontal Circuits at Neonatal Age: Checkpoint of Cognitive Maturation

Anatomical investigations revealed that, although the PFC develops according to a similar time schedule as other neocortical areas, some maturation events (e.g., volumetric decline and growth and pruning of afferents and efferents) are protracted (van Eden et al., 1990). Correspondingly, the prefrontal patterns of coordinated activity share the general spatial and temporal organization of early neocortical oscillations (Hanganu-Opatz, 2010), yet they emerge later and have a frequency-specific structure. In rodents, the discontinuous oscillatory activity of PFC appears 1 to 2 days later than in the hippocampus and 2 to 3 days later than in primary visual and somatosensory cortices (Brockmann et al., 2011). The neonatal oscillations are detectable and have similar organization in both urethane-anesthetized and non-anesthetized rats and mice, yet their magnitude decreased under anesthesia, as shown by the present and previous studies (Chini et al., 2019).

The present findings show that frequency-specific communication within local prefrontal circuits emerges very early. Such precise interactions might represent the pre-requisite for functional entrainment of adult networks and cognitive performance. Abundant literature highlighted the link between theta-band hippocampal activation and fast oscillatory entrainment of prefrontal circuits during various cognitive tasks at adulthood (Sirota et al., 2008). Currently, only few attempts have been made to directly prove the role of timed interactions during development for the later emergence of network function and adult behavior. Recently, the key role of vasoactive intestinal peptide (VIP) and cholecystokinine (CCK)-positive interneurons for cortical circuit development has been demonstrated (Batista-Brito et al., 2017; Del Pino et al., 2017). In the same line, our findings identify pyramidal neurons in superficial layers as generators of early activity, facilitating the coupling within local neocortical circuits and glutamatergic communication between upper and deeper layers (Anastasiades and Butt, 2012), whose early function later impacts cognitive abilities. Identification of key cellular elements controlling circuit development opens new perspectives for the interrogation of long-term network effects.

Mechanisms of Abnormal Wiring in Prefrontal Circuits of Neonatal Dual-Hit GE Mice

The pathogenesis of cognitive dysfunction in major psychiatric disorders has been reported to involve interactions between a large number of susceptibility genes and environmental factors that might act at diverse stages of development (van Os et al., 2008). In the present study, we combine the abnormally translocated DISC1 gene with viral infection causing maternal immune activation (Meyer et al., 2005). This dual hit has a clear link to human pathology (Ayhan et al., 2009). Although each of the factors (i.e., either genetic or environmental) leads to structural, functional, and cognitive deficits of weak to moderate magnitude, it is only their combination that has been found to produce a neurobehavioral phenotype at adulthood that resembles aspects of mental illness. For example, the prefrontal-hippocampal networks accounting for mnemonic and executive abilities at adult age show major developmental deficits when both hits co-occur (abnormal DISC1 and maternal immune activation), whereas single-hit models show a largely normal network development (Hartung et al., 2016). In dual-hit GE mice, the patterns of coordinated activity in PFC and hippocampus appeared disorganized, and the long-range coupling between them was weaker at neonatal age.

Although these data demonstrate the developmental origin of dysfunction in dual-hit GE mice, they do not mechanistically explain the network and behavioral deficits. These deficits might result from either abnormal maturation of local prefrontal networks, a weaker theta activity in hippocampus, or sparser connectivity between the two areas. The present results fill the knowledge gap and identify the pyramidal neurons of superficial layers as key players of developmental miswiring, whereas pyramidal neurons in deeper cortical layers are indistinguishable in their structure and function in controls and dual-hit GE mice. The disorganized patterns of oscillatory activity in the PL result from superficial layers neurons that lost their timed firing and cannot generate the entrainment of local circuits in beta-low gamma frequencies. In turn, the neuronal spiking is controlled by the inputs that these neurons receive. Taking into account the oversimplified dendritic arborization and reduced number of spines, it is likely that pyramidal neurons in superficial layers of PL from dual-hit GE mice receive fewer inputs, which are randomly timed. The cell-type- and layer-dependent structural abnormalities in PFC (e.g., decreased dendritic spine density) have also been detected in other mouse models of schizophrenia (Koukouli et al., 2017) and in schizophrenia patients, in which it has been related to abnormalities in the excitatory transmission (Kolluri et al., 2005). Despite the integrity of pyramidal neurons in deep layers both at morphological and functional level, the local prefrontal circuitry relying on dense vertical and horizontal interactions between upper and deeper layers is compromised in dual-hit GE mice. Therefore, the theta hippocampal drive targeting deep layers pyramidal neurons cannot optimally entrain the PFC. Although some properties of oscillatory activity and neuronal firing over prefrontal layers are similar in P8–P10 GE mice and P4–P6 control mice, the overall properties of activity patterns suggest that the neonatal dysfunction is not solely the result of a delayed maturation caused by abnormal DISC1 and environmental stressors.

The selective structural deficits and dysfunction of pyramidal neurons in prefrontal superficial layers was prevented by minocycline administration during the first, but not the second, postnatal week. Minocycline is a pleiotropic drug that, among having other functions, is a potent inhibitor of microglial activation (Dean et al., 2012). Altered number of activated microglia has been found in the brain of MIA offspring (Borrell et al., 2002). Resulting from maternal infection, the stimulation of cytokine pathways (Meyer et al., 2005) and microglia overpruning of synapses (Neniskyte and Gross, 2017) have been proposed to interfere with developmental processes, such as neuronal proliferation, differentiation, and synaptogenesis (Neniskyte and Gross, 2017). A similar mechanism, microglia excessively engulfing the synaptic terminals, might represent the mechanism underlying the deficits reported here for dual-hit GE mice. During the first postnatal week, these MIA-induced

deficits alone seem to have no functional readout, because neonatal one-hit environmental mice (i.e., MIA offspring) have largely normal firing and network activity patterns (Hartung et al., 2016). Solely the combination with genetic risk factors, such as mutant DISC1, causes early circuit miswiring, as reported in the present study. DISC1 has a key role in neuronal proliferation and migration as well as in development and maintenance of synapses. However, the phenotypes in the mouse models of mutated DISC1 are rather modest (Brandon and Sawa, 2011). They become potentiated by the synergistic combination with MIA. This could be due to the fact that mutated DISC1 might modulate the basal or polyI:C-induced cytokine production by interfering with glycogen synthase kinase-3 (Beurel et al., 2010). Alternatively, DISC1 might confer neuronal vulnerability, making pyramidal neurons more susceptible to environmental stressors.

Minocycline has been found to be neuroprotective in numerous pathologies (Hinwood et al., 2013). In particular, its use alone or as adjunctive therapy to antipsychotics improved the behavioral and cognitive performance of schizophrenia patients (De Picker et al., 2017; Miyaoka et al., 2008). Although the mode of action of minocycline in the adult brain has been well characterized, only few studies focused on its preventive potential during development, before the onset of disease symptoms. Recently, minocycline use during adolescence was associated with a reduction in the incidence of psychosis, most likely by reducing microglia-mediated synapse uptake (Sellgren et al., 2019). In mice, when administrated during the course of peripubertal stress exposure, minocycline has been found to prevent the emergence of multiple behavioral abnormalities relevant to human cognitive dysfunction (Giovanoli et al., 2016), yet the mechanisms underlying the behavioral rescue are largely unknown. Here, we show that, already during neonatal development, minocycline is effective in preventing prelimbic structural, functional, and behavioral deficits. One possible mechanism of these effects is its action on microglia. However, the pathways that selectively link pyramidal neurons in superficial layers of PFC with the anti-inflammatory action of minocycline remain to be investigated in detail and in a more mechanistic manner. Of note, superficial layers neurons are thought of being more dependent on microglia activity than those of deep layers (Neniskyte and Gross, 2017). This might contribute to the layer-specific differences that we identified in the present study.

Because the efficacy of minocycline fades if it is administered at a later point of development, the question arises why the PFC during the investigated time window (i.e., P8–P10) is particularly sensitive to perturbations. Future studies need to address the role of hippocampal projections that drive the initial beta-gamma entrainment of prefrontal circuits (Brockmann et al., 2011; Ahlbeck et al., 2018) as well as of neuromodulators, such as dopamine with D1 receptors first appearing at this age (Leslie et al., 1991).

Relevance for Human Mental Illness

The relevance of animal models for human mental disorders has often been questioned, because they do not fulfill the validity criteria used for other pathologies. Optimally, animal models recapitulate etiologic processes (i.e., construct validity) or symptom features (i.e., face validity). In case of mental disorders, such as schizophrenia, bipolar disorder, or depression, the available mouse models have either excellent construct validity (e.g., models mimicking the genetic background) but limited face validity or vice versa (e.g., models of hippocampal damage or pharmacological models). Dual-hit models mimic both genetic and environmental risk factors and recapitulate some of the structural and circuit deficits observed in patients. For example, lower spine density in upper layers of PFC as well as dysfunctional prefrontal gamma-band oscillations, which have been reported here, have also been described for schizophrenia patients (Senkowski and Gallinat, 2015). Similarly, microglia abnormalities and resulting synaptic deficits have been related to several brain pathologies (Neniskyte and Gross, 2017). Therefore, we propose that dual-hit GE mice recapitulate both the etiology (construct validity) as well as the general rules of neuronal, glial, and circuit dysfunction (face validity) that relate to cognitive impairment in mental disorders. They appear highly instrumental for the identification of cellular key players of disease that, for ethical and technical reasons, are not accessible in humans of comparable age. This brings us closer to one of the major goals of circuit psychiatry that is the identification of key neurobiological targets amenable to tailored therapies (Gordon, 2016) that not only treat but also prevent disease-related cognitive and behavioral deficits.

STAR★METHODS

Detailed methods are provided in the online version of this paper and include the following:

- KEY RESOURCES TABLE
- LEAD CONTACT AND MATERIALS AVAILABILITY
- EXPERIMENTAL MODEL AND SUBJECT DETAILS
  - Mice
  - Minocycline administration
- METHOD DETAILS
  - In utero electroporation
  - Developmental milestones
  - Behavioral experiments
  - In vitro electrophysiology and optogenetics
  - In vivo electrophysiology and optogenetics
  - Histology
- QUANTIFICATION AND STATISTICAL ANALYSIS
  - Image analysis
  - In vitro electrophysiology
  - In vivo electrophysiology
  - K-nearest neighbors classifiers
  - Statistical analysis
- DATA AND CODE AVAILABILITY

SUPPLEMENTAL INFORMATION

Supplemental Information can be found online at https://doi.org/10.1016/j.neuron.2019.09.042.

ACKNOWLEDGMENTS

We thank Dr. Joseph Gogos for providing the DISC1 mice, Drs. S. Wiegert and T. Oertner for providing opsin derivates, and A. Marquardt, A. Dahlmann, I. Ohmert, and K. Titze for excellent technical assistance. This work was funded by grants from the European Research Council (ERC-2015-CoG 681577 to I.L.H.-O.) and the German Research Foundation (Ha4466/10-1, Ha4466/11-1, Ha4466/12-1, SPP 1665, and SFB 936 B5 to I.L.H.-O. and C6 to C.M.). I.L.H.-O. is a founding member of the FENS Kavli Network of Excellence.

AUTHOR CONTRIBUTIONS

I.L.H.-O. conceived the study. M.C. and I.L.H.-O. designed the experiments. M.C., J.A.P., C.L., L.C.-P., M.H., V.O., J.A., and S.H.B. carried out experiments. M.C. and X.X. analyzed the data. M.C., C.M., and I.L.H.-O. interpreted the data. M.C. and I.L.H.-O. wrote the article. All authors discussed and commented on the manuscript.

DECLARATION OF INTERESTS

The authors declare no competing interests.

Received: March 28, 2019
Revised: August 14, 2019
Accepted: September 24, 2019
Published: November 13, 2019

REFERENCES

Aarts, E., Verhage, M., Veenvliet, J.V., Dolan, C.V., and van der Sluis, S. (2014). A solution to dependency: using multilevel analysis to accommodate nested data. Nat. Neurosci. *17*, 491–496.

Abazyan, B., Nomura, J., Kannan, G., Ishizuka, K., Tamashiro, K.L., Nucifora, F., Pogorelov, V., Ladenheim, B., Yang, C., Krasnova, I.N., et al. (2010). Prenatal interaction of mutant DISC1 and immune activation produces adult psychopathology. Biol. Psychiatry *68*, 1172–1181.

Ahlbeck, J., Song, L., Chini, M., Bitzenhofer, S.H., and Hanganu-Opatz, I.L. (2018). Glutamatergic drive along the septo-temporal axis of hippocampus boosts prelimbic oscillations in the neonatal mouse. eLife *7*, e33158.

Anastasiades, P.G., and Butt, S.J. (2012). A role for silent synapses in the development of the pathway from layer 2/3 to 5 pyramidal cells in the neocortex. J. Neurosci. *32*, 13085–13099.

Ayhan, Y., Sawa, A., Ross, C.A., and Pletnikov, M.V. (2009). Animal models of gene-environment interactions in schizophrenia. Behav. Brain Res. *204*, 274–281.

Batista-Brito, R., Vinck, M., Ferguson, K.A., Chang, J.T., Laubender, D., Lur, G., Mossner, J.M., Hernandez, V.G., Ramakrishnan, C., Deisseroth, K., et al. (2017). Developmental dysfunction of VIP interneurons impairs cortical circuits. Neuron *95*, 884–895.e9.

Bellesi, M., de Vivo, L., Chini, M., Gilli, F., Tononi, G., and Cirelli, C. (2017). Sleep loss promotes astrocytic phagocytosis and microglial activation in mouse cerebral cortex. J. Neurosci. *37*, 5263–5273.

Beurel, E., Michalek, S.M., and Jope, R.S. (2010). Innate and adaptive immune responses regulated by glycogen synthase kinase-3 (GSK3). Trends Immunol. *31*, 24–31.

Bitzenhofer, S.H., Sieben, K., Siebert, K.D., Spehr, M., and Hanganu-Opatz, I.L. (2015). Oscillatory activity in developing prefrontal networks results from theta-gamma-modulated synaptic inputs. Cell Rep. *11*, 486–497.

Bitzenhofer, S.H., Ahlbeck, J., Wolff, A., Wiegert, J.S., Gee, C.E., Oertner, T.G., and Hanganu-Opatz, I.L. (2017). Layer-specific optogenetic activation of pyramidal neurons causes beta-gamma entrainment of neonatal networks. Nat. Commun. *8*, 14563.

Borrell, J., Vela, J.M., Arévalo-Martin, A., Molina-Holgado, E., and Guaza, C. (2002). Prenatal immune challenge disrupts sensorimotor gating in adult rats. Implications for the etiopathogenesis of schizophrenia. Neuropsychopharmacology *26*, 204–215.

Bosman, C.A., Lansink, C.S., and Pennartz, C.M. (2014). Functions of gamma-band synchronization in cognition: from single circuits to functional diversity across cortical and subcortical systems. Eur. J. Neurosci. *39*, 1982–1999.

Brandon, N.J., and Sawa, A. (2011). Linking neurodevelopmental and synaptic theories of mental illness through DISC1. Nat. Rev. Neurosci. *12*, 707–722.

Brockmann, M.D., Pöschel, B., Cichon, N., and Hanganu-Opatz, I.L. (2011). Coupled oscillations mediate directed interactions between prefrontal cortex and hippocampus of the neonatal rat. Neuron *71*, 332–347.

Chini, M., Gretenkord, S., Kostka, J.K., Pöpplau, J.A., Cornelissen, L., Berde, C.B., Hanganu-Opatz, I.L., and Bitzenhofer, S.H. (2019). Neural correlates of anesthesia in newborn mice and humans. Front. Neural Circuits *13*, 38.

Cho, K.K., Hoch, R., Lee, A.T., Patel, T., Rubenstein, J.L., and Sohal, V.S. (2015). Gamma rhythms link prefrontal interneuron dysfunction with cognitive inflexibility in Dlx5/6(+/-) mice. Neuron *85*, 1332–1343.

Cichon, N.B., Denker, M., Grün, S., and Hanganu-Opatz, I.L. (2014). Unsupervised classification of neocortical activity patterns in neonatal and pre-juvenile rodents. Front. Neural Circuits *8*, 50.

Cirelli, C., and Tononi, G. (2015). Cortical development, electroencephalogram rhythms, and the sleep/wake cycle. Biol. Psychiatry *77*, 1071–1078.

Clement, E.A., Richard, A., Thwaites, M., Ailon, J., Peters, S., and Dickson, C.T. (2008). Cyclic and sleep-like spontaneous alternations of brain state under urethane anaesthesia. PLoS ONE *3*, e2004.

Dansie, L.E., Phommahaxay, K., Okusanya, A.G., Uwadia, J., Huang, M., Rotschafer, S.E., Razak, K.A., Ethell, D.W., and Ethell, I.M. (2013). Long-lasting effects of minocycline on behavior in young but not adult Fragile X mice. Neuroscience *246*, 186–198.

De Picker, L.J., Morrens, M., Chance, S.A., and Boche, D. (2017). Microglia and brain plasticity in acute psychosis and schizophrenia illness course: a meta-review. Front. Psychiatry *8*, 238.

Deakin, B., Suckling, J., Barnes, T.R.E., Byrne, K., Chaudhry, I.B., Dazzan, P., Drake, R.J., Giordano, A., Husain, N., Jones, P.B., et al.; BeneMin Study team (2018). The benefit of minocycline on negative symptoms of schizophrenia in patients with recent-onset psychosis (BeneMin): a randomised, double-blind, placebo-controlled trial. Lancet Psychiatry *5*, 885–894.

Dean, O.M., Data-Franco, J., Giorlando, F., and Berk, M. (2012). Minocycline: therapeutic potential in psychiatry. CNS Drugs *26*, 391–401.

Del Pino, I., Brotons-Mas, J.R., Marques-Smith, A., Marighetto, A., Frick, A., Marín, O., and Rico, B. (2017). Abnormal wiring of CCK^+ basket cells disrupts spatial information coding. Nat. Neurosci. *20*, 784–792.

Emadi-Kouchak, H., Mohammadinejad, P., Asadollahi-Amin, A., Rasoulinejad, M., Zeinoddini, A., Yalda, A., and Akhondzadeh, S. (2016). Therapeutic effects of minocycline on mild-to-moderate depression in HIV patients: a double-blind, placebo-controlled, randomized trial. Int. Clin. Psychopharmacol. *31*, 20–26.

Garrido-Mesa, N., Zarzuelo, A., and Gálvez, J. (2013). Minocycline: far beyond an antibiotic. Br. J. Pharmacol. *169*, 337–352.

Giovanoli, S., Weber-Stadlbauer, U., Schedlowski, M., Meyer, U., and Engler, H. (2016). Prenatal immune activation causes hippocampal synaptic deficits in the absence of overt microglia anomalies. Brain Behav. Immun. *55*, 25–38.

Gordon, J.A. (2016). On being a circuit psychiatrist. Nat. Neurosci. *19*, 1385–1386.

Hanganu-Opatz, I.L. (2010). Between molecules and experience: role of early patterns of coordinated activity for the development of cortical maps and sensory abilities. Brain Res. Brain Res. Rev. *64*, 160–176.

Harris, K.D., and Shepherd, G.M. (2015). The neocortical circuit: themes and variations. Nat. Neurosci. *18*, 170–181.

Hartung, H., Cichon, N., De Feo, V., Riemann, S., Schildt, S., Lindemann, C., Mulert, C., Gogos, J.A., and Hanganu-Opatz, I.L. (2016). From shortage to surge: a developmental switch in hippocampal-prefrontal coupling in a

gene-environment model of neuropsychiatric disorders. Cereb. Cortex *26*, 4265–4281.

Hinwood, M., Tynan, R.J., Charnley, J.L., Beynon, S.B., Day, T.A., and Walker, F.R. (2013). Chronic stress induced remodeling of the prefrontal cortex: structural re-organization of microglia and the inhibitory effect of minocycline. Cereb. Cortex *23*, 1784–1797.

Ignacio, M.P.D., Kimm, E.J., Kageyama, G.H., Yu, J., and Robertson, R.T. (1995). Postnatal migration of neurons and formation of laminae in rat cerebral cortex. Anat. Embryol. (Berl.) *191*, 89–100.

Khazipov, R., Sirota, A., Leinekugel, X., Holmes, G.L., Ben-Ari, Y., and Buzsáki, G. (2004). Early motor activity drives spindle bursts in the developing somatosensory cortex. Nature *432*, 758–761.

Kirmse, K., Kummer, M., Kovalchuk, Y., Witte, O.W., Garaschuk, O., and Holthoff, K. (2015). GABA depolarizes immature neurons and inhibits network activity in the neonatal neocortex in vivo. Nat. Commun. *6*, 7750.

Kishimoto, T., Horigome, T., and Takamiya, A. (2018). Minocycline as a treatment for schizophrenia: is the discussion truly finished? Lancet Psychiatry *5*, 856–857.

Kobayashi, K., Imagama, S., Ohgomori, T., Hirano, K., Uchimura, K., Sakamoto, K., Hirakawa, A., Takeuchi, H., Suzumura, A., Ishiguro, N., and Kadomatsu, K. (2013). Minocycline selectively inhibits M1 polarization of microglia. Cell Death Dis. *4*, e525.

Kolluri, N., Sun, Z., Sampson, A.R., and Lewis, D.A. (2005). Lamina-specific reductions in dendritic spine density in the prefrontal cortex of subjects with schizophrenia. Am. J. Psychiatry *162*, 1200–1202.

Koukouli, F., Rooy, M., Tziotis, D., Sailor, K.A., O'Neill, H.C., Levenga, J., Witte, M., Nilges, M., Changeux, J.P., Hoeffer, C.A., et al. (2017). Nicotine reverses hypofrontality in animal models of addiction and schizophrenia. Nat. Med. *23*, 347–354.

Leicht, G., Vauth, S., Polomac, N., Andreou, C., Rauh, J., Mußmann, M., Karow, A., and Mulert, C. (2016). EEG-informed fMRI reveals a disturbed gamma-band-specific network in subjects at high risk for psychosis. Schizophr. Bull. *42*, 239–249.

Leslie, C.A., Robertson, M.W., Cutler, A.J., and Bennett, J.P., Jr. (1991). Postnatal development of D1 dopamine receptors in the medial prefrontal cortex, striatum and nucleus accumbens of normal and neonatal 6-hydroxydopamine treated rats: a quantitative autoradiographic analysis. Brain Res. Dev. Brain Res. *62*, 109–114.

Luzi, P., Abraham, R.M., Rafi, M.A., Curtis, M., Hooper, D.C., and Wenger, D.A. (2009). Effects of treatments on inflammatory and apoptotic markers in the CNS of mice with globoid cell leukodystrophy. Brain Res. *1300*, 146–158.

Marín, O. (2016). Developmental timing and critical windows for the treatment of psychiatric disorders. Nat. Med. *22*, 1229–1238.

Marques-Smith, A., Lyngholm, D., Kaufmann, A.K., Stacey, J.A., Hoerder-Suabedissen, A., Becker, E.B., Wilson, M.C., Molnár, Z., and Butt, S.J. (2016). A transient translaminar GABAergic interneuron circuit connects thalamocortical recipient layers in neonatal somatosensory cortex. Neuron *89*, 536–549.

Meyer, U., Feldon, J., Schedlowski, M., and Yee, B.K. (2005). Towards an immuno-precipitated neurodevelopmental animal model of schizophrenia. Neurosci. Biobehav. Rev. *29*, 913–947.

Miyamoto, A., Wake, H., Ishikawa, A.W., Eto, K., Shibata, K., Murakoshi, H., Koizumi, S., Moorhouse, A.J., Yoshimura, Y., and Nabekura, J. (2016). Microglia contact induces synapse formation in developing somatosensory cortex. Nat. Commun. *7*, 12540.

Miyaoka, T., Yasukawa, R., Yasuda, H., Hayashida, M., Inagaki, T., and Horiguchi, J. (2008). Minocycline as adjunctive therapy for schizophrenia: an open-label study. Clin. Neuropharmacol. *31*, 287–292.

Neniskyte, U., and Gross, C.T. (2017). Errant gardeners: glial-cell-dependent synaptic pruning and neurodevelopmental disorders. Nat. Rev. Neurosci. *18*, 658–670.

Rossant, C., Kadir, S.N., Goodman, D.F.M., Schulman, J., Hunter, M.L.D., Saleem, A.B., Grosmark, A., Belluscio, M., Denfield, G.H., Ecker, A.S., et al. (2016). Spike sorting for large, dense electrode arrays. Nat. Neurosci. *19*, 634–641.

Savitz, J.B., Teague, T.K., Misaki, M., Macaluso, M., Wurfel, B.E., Meyer, M., Drevets, D., Yates, W., Gleason, O., Drevets, W.C., and Preskorn, S.H. (2018). Treatment of bipolar depression with minocycline and/or aspirin: an adaptive, 2×2 double-blind, randomized, placebo-controlled, phase IIA clinical trial. Transl. Psychiatry *8*, 27.

Schafer, D.P., Lehrman, E.K., Kautzman, A.G., Koyama, R., Mardinly, A.R., Yamasaki, R., Ransohoff, R.M., Greenberg, M.E., Barres, B.A., and Stevens, B. (2012). Microglia sculpt postnatal neural circuits in an activity and complement-dependent manner. Neuron *74*, 691–705.

Selemon, L.D., and Zecevic, N. (2015). Schizophrenia: a tale of two critical periods for prefrontal cortical development. Transl. Psychiatry *5*, e623.

Sellgren, C.M., Gracias, J., Watmuff, B., Biag, J.D., Thanos, J.M., Whittredge, P.B., Fu, T., Worringer, K., Brown, H.E., Wang, J., et al. (2019). Increased synapse elimination by microglia in schizophrenia patient-derived models of synaptic pruning. Nat. Neurosci. *22*, 374–385.

Senkowski, D., and Gallinat, J. (2015). Dysfunctional prefrontal gamma-band oscillations reflect working memory and other cognitive deficits in schizophrenia. Biol. Psychiatry *77*, 1010–1019.

Shin Yim, Y., Park, A., Berrios, J., Lafourcade, M., Pascual, L.M., Soares, N., Yeon Kim, J., Kim, S., Kim, H., Waisman, A., et al. (2017). Reversing behavioural abnormalities in mice exposed to maternal inflammation. Nature *549*, 482–487.

Sirota, A., Montgomery, S., Fujisawa, S., Isomura, Y., Zugaro, M., and Buzsáki, G. (2008). Entrainment of neocortical neurons and gamma oscillations by the hippocampal theta rhythm. Neuron *60*, 683–697.

Uhlhaas, P.J., and Singer, W. (2015). Oscillations and neuronal dynamics in schizophrenia: the search for basic symptoms and translational opportunities. Biol. Psychiatry *77*, 1001–1009.

van Eden, C.G., Kros, J.M., and Uylings, H.B. (1990). The development of the rat prefrontal cortex. Its size and development of connections with thalamus, spinal cord and other cortical areas. Prog. Brain Res. *85*, 169–183.

van Os, J., Rutten, B.P., and Poulton, R. (2008). Gene-environment interactions in schizophrenia: review of epidemiological findings and future directions. Schizophr. Bull. *34*, 1066–1082.

Vinck, M., van Wingerden, M., Womelsdorf, T., Fries, P., and Pennartz, C.M. (2010). The pairwise phase consistency: a bias-free measure of rhythmic neuronal synchronization. Neuroimage *51*, 112–122.

Weinhard, L., di Bartolomei, G., Bolasco, G., Machado, P., Schieber, N.L., Neniskyte, U., Exiga, M., Vadisiute, A., Raggioli, A., Schertel, A., et al. (2018). Microglia remodel synapses by presynaptic trogocytosis and spine head filopodia induction. Nat. Commun. *9*, 1228.

Zhang, L., Zheng, H., Wu, R., Zhu, F., Kosten, T.R., Zhang, X.Y., and Zhao, J. (2018). Minocycline adjunctive treatment to risperidone for negative symptoms in schizophrenia: association with pro-inflammatory cytokine levels. Prog. Neuropsychopharmacol. Biol. Psychiatry *85*, 69–76.

STAR★METHODS

KEY RESOURCES TABLE

REAGENT or RESOURCE	SOURCE	IDENTIFIER
Antibodies		
mouse monoclonal Alexa Fluor-488 conjugated antibody against NeuN	Merck Millipore	Cat# MAB377X; RRID: AB_2149209
rabbit polyclonal primary antibody against GABA	Sigma-Aldrich	Cat#A2052; RRID: AB_477652
Alexa Fluor-488 goat anti-rabbit IgG secondary antibody	Merck Millipore	Cat# A-11008; RRID: AB_143165
rabbit monoclonal primary antibody against IBA-1	Wako	Cat# 019-19741; RRID: AB_839504
Deposited Data		
LFP and SUA data for all the non-anesthetized mice	This paper	https://gin.g-node.org/mchini/Resolving_and_rescuing_developmental_miswiring_in_a_mouse_model_of_cognitive_impairment
Chemicals, Peptides, and Recombinant Proteins		
Isoflurane	Abbott	B506
Urethane	Fluka analytical	94300
Minocycline	Sigma-Aldrich	M9511
Experimental Models: Organisms/Strains		
Mouse: C57BL/6J	Universitätsklinikum Hamburg-Eppendorf – Animal facility	N/A
Mouse: Disc1Tm1Kara /C57BL/6J	J. Gogos Lab	N/A
Recombinant DNA		
pAAV-CAG-ChR2(E123T/T159C)-2AtDimer2	T. G. Oertner Lab	http://www.oertner.com/
pAAV-CAG-tDimer2	T. G. Oertner Lab	http://www.oertner.com/
Software and Algorithms		
MATLAB R2016a	MathWorks	https://www.mathworks.com
Offline Sorter	Plexon	http://plexon.com/
ImageJ 2.0.0	ImageJ	https://imagej.nih.gov/ij/
R Statistical Software 3.5.1	RStudio	https://rstudio.com
Cheetah 6	Neuralynx	https://neuralynx.com/
Anaconda 1.9.6	Anaconda	https://www.anaconda.com
Spyder 3.3.2	Spyder	https://www.spyder-ide.org
Video Mot2	TSE Systems	https://www.tse-systems.com/product-details/videomot
Other		
Arduino Uno SMD	Arduino	A000073
Digital Lynx 4SX	Neuralynx	https://neuralynx.com/
Diode laser (473 nm)	Omicron	LuxX 473-100
Electroporation device	BEX	CUY21EX
Electroporation tweezer-type paddles	Protech	CUY650-P5
Recording electrode (1 shank, 16 channels)	Neuronexus	A1x16-3mm-703-A16
Recording optrode (1 shank, 16 channels)	Neuronexus	A1x16-5mm-703-OA16LP
Recording electrode (4 shanks, 16 channels)	Neuronexus	A4x4-3mm-100-125-703
Recording tetrode (4 shanks, 16 channels)	Neuronexus	A4x4-3mm-100-125-703-OA16LP

LEAD CONTACT AND MATERIALS AVAILABILITY

Further information and requests for resources and reagents should be directed to and will be fulfilled by the Lead Contact,Ileana L. Hanganu-Opatz (hangop@zmnh.uni-hamburg.de).

This study did not generate new unique reagents.

EXPERIMENTAL MODEL AND SUBJECT DETAILS

Mice

Experiments were performed in compliance with German laws and the guidelines of the European Community for the use of animals in research, and were approved by the local ethical committee (111/12, 132/12). Experiments were carried out on C57BL/6J mice of both sexes, at the age of P8–10. Heterozygous mutant DISC1 pups carrying a Disc1 allele (Disc1Tm1Kara) on a C57Bl6/J background and C57Bl6/J, whose dams were injected i.v. at embryonic day (E) 9 with the viral mimetic poly I:C (5 mg/kg) were used as dual-hit genetic-environmental model (dual-hit GE) (Hartung et al., 2016). Pups born from homozygous Disc1Tm1Kara dams and wild-type males and pups born from wild-type dams and homozygous Disc1Tm1Kara males were pooled together, as no difference between the two groups was found. Genotypes were assessed using genomic DNA (tail biopsies) and following primer sequences: forward primer 5′-TAGCCACTCTCATTGTCAGC-3′ and reverse primer 5′-CCTCATCCCTTCCACTCAGC-3′. Non-treated wild-type mice and the offspring of dams injected at E9 with saline (0.9%) were used as controls and combined together, as no difference between the two groups was found. For single-hit experiments, the offspring of wild-type E9 poly I:C injected dams (single-hit E) and heterozygous mutant Disc1Tm1Kara pups of E) saline injected dams (single-hit G) were used. Timed-pregnant mice from the animal facility of the University Medical Center Hamburg-Eppendorf, of both aforementioned conditions, were housed individually at a 12 h light/12 h dark cycle, and were given access to water and food *ad libitum*. The day of vaginal plug detection was considered as E0.5, while the day of birth as P0. In accordance with the three Rs guidelines of the European Community for the use of animals in research, we re-analyzed part of the mice used for one of our previous publications (Bitzenhofer et al., 2017).

Minocycline administration

Minocycline was administered to neonatal mice from either P1 to P8 or from P9 to P16 by adding it to the drinking water of the dam, which then passed it on to the offspring via lactation (Dansie et al., 2013). In line with previous studies (Dansie et al., 2013), the daily dosage of minocycline was 30 mg/kg body weight. To cover the taste of the antibiotic, sucrose was added to the solution. No difference in liquid intake was observed between dams receiving water and dams receiving water supplemented with minocycline. This administration route has been shown to result in detectable concentrations of the drug in the breast milk of the lactating dam (Luzi et al., 2009).

METHOD DETAILS

In utero electroporation

Additional wet food supplemented with 2-4 drops of Metacam (meloxicam; 0.5 mg ml−1; Boehringer-Ingelheim, Germany) was administered from one day before until two days after surgery. At E12.5 or E15.5 randomly assigned pregnant mice received a subcutaneous injection of buprenorphine (0.05 mg/kg body weight) at least 30 min before surgery. Surgery was performed on a heated surface; pain reflexes (toe and tail pinch) and breathing were monitored throughout. Under isoflurane anesthesia (induction: 5%; maintenance: 3.5%), the eyes of the dam were covered with eye ointment to prevent damage, before the uterine horns were exposed and moistened with warm sterile PBS (37 °C). Solution containing 1.25 μg/μl DNA (pAAV-CAG-ChR2(E123T/T159C)-2AtDimer2 or pAAV-CAG-tDimer2)) and 0.1% fast green dye at a volume of 0.75–1.25 μl were injected into the right lateral ventricle of individual embryos using pulled borosilicate glass capillaries with a sharp, long tip. Plasmid DNA was purified with NucleoBond (Macherey-Nagel, Germany). 2A encodes for a ribosomal skip sentence, splitting the fluorescent protein tDimer2 from the opsin during gene translation. Each embryo within the uterus was placed between the electroporation tweezer-type paddles (3 mm diameter for E12.5; 5 mm diameter for E14.5-15.5; Protech, TX, USA) that were roughly oriented at a 20° leftward angle from the midline and a 10° angle downward from anterior to posterior. By these means, neural precursor cells from the subventricular zone, which radially migrate into the medial PFC, were transfected. Electrode pulses (35 V, 50 ms) were applied five times at intervals of 950 ms controlled by an electroporator (CU21EX; BEX, Japan). Uterine horns were placed back into the abdominal cavity after electroporation, which was filled with warm sterile PBS (37 °C). Abdominal muscles and skin were sutured individually with absorbable and non-absorbable suture thread, respectively. After recovery, pregnant mice were returned to their home cages, which were half placed on a heating blanket for two days after surgery. Opsin expression was assessed with a portable fluorescent flashlight (Nightsea, MA, USA) through the intact skull and skin at P2–3 and confirmed post mortem by fluorescence microscopy in brain slices. Pups without expression in the PFC were excluded from the analysis.

Developmental milestones

Mouse pups were tested for their somatic development and reflexes at P2, P5 and P8. Weight, body and tail length were assessed. Surface righting reflex was quantified as time (max 30 s) until the pup turned over with all four feet on the ground after being placed on its back. Cliff aversion reflex was quantified as time (max 30 s) until the pup withdrew after snout and forepaws were positioned over an elevated edge. Vibrissa placing was rated positive if the pup turned its head after gently touching the whiskers with a toothpick.

Behavioral experiments

The behavioral experiments were carried out in pre-juvenile mice that did not experience IUE, using previously established experimental protocols. Briefly, all behavioral tests were conducted in a circular white arena, the size of which (D: 34 cm, H: 30 cm) maximized exploratory behavior, while minimizing incidental contact with testing objects. The objects used for testing of novelty recognition were five differently shaped, and colored, easy to clean items that were provided with magnets to fix them to the bottom of the arena. Object sizes (H: 3 cm, diameter: 1.5–3 cm) were smaller than twice the size of the mouse and did not resemble living stimuli (no eye spots, predator shape). The objects were positioned at 10 cm from the borders and 8 cm from the center of the arena. After every trial, the objects and arena were cleaned with 0.1% acetic acid to remove all odors. A black and white CCD camera (VIDEOR TECHNICAL E. Hartig GmbH) was mounted 100 cm above the arena and connected to a PC via PCI interface serving as frame grabber for video tracking software (Video Mot2 software, TSE Systems GmbH).

Exploratory Behavior in the Open Field

Pre-juvenile mice (P16-17) were allowed to freely explore the testing arena for 10 min. The floor area of the arena was digitally subdivided in 8 zones (4 center zones and 4 border zones) using the zone monitor mode of the VideoMot 2 analysis software (VideoMot 2, TSE Systems GmbH). The time spent by pups in center and border zones as well as the running distance and velocity were quantified. Mice that did not exit the center area for >1 min (n = 2) were excluded from further analysis.

Novelty Recognition Paradigms

All protocols for assessing item recognition memory in pre-juvenile mice consisted of familiarization and testing trials. During the familiarization trial, each mouse was placed into the arena containing two identical objects. The mice were released against the center of the opposite wall with the back to the objects. After 10 min of free exploration of objects, the mice were returned to a temporary holding cage. In the novel object recognition (NOR) task, tested in P17-P18 mice, the familiarization trial was followed 5 min later by a test trial in which one object used in the familiarization and one new object were placed in the arena at the same positions as during the familiarization trials. The mice were allowed to investigate the familiar and the novel object, with different shape and color, for 5 min. Object interaction during the first five minutes and the length of single interaction with the objects were analyzed and compared between the groups. In the recency recognition (RR) task, tested at P19–22, mice experienced two 10 min familiarization trials with two different sets of identical objects that were separated by a delay of 30 min. The second familiarization trial was followed after 5 min by a test trial in which one object used in the first and one object used in the second more recent familiarization trial were placed in the arena in the same positions as during the familiarization trials. Object interaction during the first five minutes and the length of single interaction with the objects were analyzed and compared between the groups. All trials were video-tracked using the Video Mot2 analysis software. The object recognition module of the software was used and a 3-point tracking method identified the head, the rear end and the center of gravity of the mouse. Digitally, a square zone was created around each object and every entry of the head point into this area was considered as object interaction. Climbing or sitting on the object, defined as having both head and center of gravity points within the square zone, were not counted as interactions. Data were imported and analyzed offline using custom-written tools in MATLAB software (MathWorks). Discrimination ratios were calculated as (Time spent interacting with novel object – time spent interacting with less recent object) / (Time spent interacting with novel object + time spent interacting with less recent object). Single interaction time ratios were analogously calculated.

In vitro electrophysiology and optogenetics

As previously described (Bitzenhofer et al., 2017), whole-cell patch-clamp recordings were performed from t-Dimer expressing superficial and deep layers prelimbic neurons in brain slices of P8–10 mice after IUE at E15.5 and E12.5, respectively. Briefly, pups were decapitated, brains were removed and immediately sectioned coronally at 300 μm in ice-cold oxygenated high sucrose-based artificial cerebral spinal fluid (ACSF) (in mM: 228 sucrose, 2.5 KCl, 1 NaH2PO4, 26.2 NaHCO3, 11 glucose, 7 MgSO4; 320 mOsm). Slices were incubated in oxygenated ACSF (in mM: 119 NaCl, 2.5 KCl, 1 NaH2PO4, 26.2 NaHCO3, 11 glucose, 1.3 MgSO4; 320 mOsm) at 37 °C for 45 min before cooling to room temperature and superfused with oxygenated ACSF in the recording chamber. tDimer2-positive neurons were patched under optical control using pulled borosilicate glass capillaries (tip resistance of 4-7 MΩ) filled with pipette solution (in mM: 130 K-gluconate, 10 HEPES, 0.5 EGTA, 4 Mg-ATP, 0.3 Na-GTP, 8 NaCl; 285 mOsm, pH 7.4). Recordings were controlled with the Ephus software in the MATLAB environment (MathWorks, MA, USA). Capacitance artifacts and series resistance were minimized using the built-in circuitry of the patch-clamp amplifier (Axopatch 200B; Molecular devices, CA, USA). Responses of neurons to hyper- and depolarizing current injections, as well as blue light pulses (473 nm, 5.2 mW/mm^2) were digitized at 5 kHz in current-clamp mode.

In vivo electrophysiology and optogenetics

Surgery

Multisite extracellular recordings were performed in the PL of P8–10 mice. For recordings in non-anesthetized state, 0.5% bupivacain / 1% lidocaine was locally applied on the neck muscles. For recordings in anesthetized state, mice were injected i.p. with urethane (1 mg/g body weight; Sigma-Aldrich) before surgery. For both groups, the surgery was performed under isoflurane anesthesia (induction: 5%; maintenance: 1.5%). The head of the pup was fixed into a stereotaxic apparatus using two plastic bars mounted on the nasal and occipital bones with dental cement. The bone above the PFC (0.5 mm anterior to bregma, 0.1 mm right to the midline for superficial layers, 0.5 mm for deep layers) was carefully removed by drilling a hole of < 0.5 mm in diameter. Before recordings, mice were allowed to recover for 10–20 min on a heating blanket.

One- or four-shank multisite optoelectrodes (NeuroNexus, MI, USA) were inserted 2.4 or 1.9 mm (respectively) deep into PFC, perpendicular to the skull surface. One-shank optoelectrodes contained 1 × 16 recordings sites (0.4-0.8 MΩ impedance, 100 μm spacing) aligned with an optical fiber (105 μm diameter) ending 200 μm above the top recording site. Four-shank optoelectrodes contained 4 × 4 recording sites (0.4-0.8 MΩ impedance, 100 μm spacing, 125 μm intershank spacing) aligned with optical fibers (50 μm diameter) ending 200 μm above the top recording sites. A silver wire was inserted into the cerebellum and served as ground and reference electrode. Before signal acquisition, a recovery period of 15 min after electrode insertion was provided.

Signal acquisition

Extracellular signals were band-pass filtered (0.1–9,000 Hz) and digitized (32 kHz) with a multichannel extracellular amplifier (Digital Lynx SX; Neuralynx, Bozeman, MO, USA) and the Cheetah acquisition software (Neuralynx). Spontaneous (i.e., not induced by light stimulation) activity was recorded for 15 min at the beginning of each recording session.

Light stimulation

Ramp (i.e., linearly increasing power) light stimulations were performed with an arduino uno (Arduino, Italy) controlled diode laser (473 nm; Omicron, Austria). Laser power was adjusted to trigger neuronal spiking in response to >25% of 3-ms-long light pulses at 16 Hz. Resulting light power was in the range of 20–40 mW/mm^2 at the fiber tip.

Post mortem assessment of electrode position

Wide field fluorescence images were acquired to reconstruct the recording electrode position in brain slices of electrophysiologically investigated pups and to localize tDimer2 expression in pups after IUE. Only pups with correct electrode and transfection position were considered for further analysis.

Histology

Perfusion

P8–10 mice were anesthetized with 10% ketamine (aniMedica, Germany) / 2% xylazine (WDT, Germany) in 0.9% NaCl solution (10 μg/g body weight, intraperitoneally (i.p.)) and transcardially perfused with Histofix (Carl Roth, Germany) containing 4% paraformaldehyde.

Immunohistochemistry

Brains were postfixed in Histofix for 24 h and sectioned coronally at 50 μm (immunohistochemistry) or 100 μm (Sholl and spine analysis). For anti-NeuN, anti-CamKII and anti-GABA stainings, free-floating slices were permeabilized and blocked with PBS containing 0.8% Triton X-100 (Sigma-Aldrich, MO, USA) and 5% normal bovine serum (Jackson Immuno Research, PA, USA). For IBA-1 and VGLUT1 stainings, slices were permeabilized and blocked with PBS containing 0.3% Triton X-100 and 3% normal bovine serum. Subsequently, slices were incubated overnight with mouse monoclonal Alexa Fluor-488-conjugated antibody against NeuN (1:100, MAB377X; Merck Millipore, MA, USA), rabbit polyclonal primary antibody against CaMKII (1:200, PA5-38239; Thermo Fisher Scientific, MA, USA), rabbit polyclonal primary antibody against GABA (1:1,000, no. A2052; Sigma-Aldrich), rabbit monoclonal primary antibody against IBA-1 (1:500, catalog #019-19741, Wako), or polyclonal guinea-pig antibody against VGLUT1 (1:1000, Synaptic Systems, Germany) followed by 2 h incubation with Alexa Fluor-488 goat anti-rabbit IgG secondary antibody (1:500, A11008; Merck Millipore), Alexa Fluor-568 donkey anti-rabbit (1:500, Life Technologies, CA, USA) or Alexa Fluor-488 goat anti-guinea pig (1:500, Molecular Probes, OR, USA). Finally, slices were transferred to glass slides and covered with Vecta-Shield (Vector Laboratories).

Imaging

Sections were examined with a confocal microscope (DM IRBE, Leica Microsystems, Zeiss LSN700 and Olympus FX-100). To quantify the t-Dimer overlap with NeuN, CaMKII and GABA, microscopic fields over PFC were acquired as 1024 × 1024 pixel images (pixel size, 1465 nm) using a 10X objective (numerical aperture, 0.3). The same settings were used to quantify the number of CaMKII positive neurons (n = 4 fields per section, 3 sections per mouse). For IBA-1, 20-images microscopic stacks (n = 8 stacks per section, 3 sections per mouse) were acquired as 512 × 512 pixel images (pixel size, 732 nm; Z-step, 1000 nm) using a 40X objective (numerical aperture, 1.25). For analysis of IBA-1$^+$-cells and VGLUT1 vesicle overlay, microscopic stacks (n = 5 stacks per sections, 3 sections per mouse) were acquired as 1024x1024 pixels images (pixel size, 103 nm; Z-step, 750 nm) using a 60X objective (numerical aperture, 1.35). Microscopic stacks used for Sholl and spine analysis were acquired as 2048 × 2048 pixel images (pixel size, 156 nm; Z-step, 1000 and 500 nm, respectively).

QUANTIFICATION AND STATISTICAL ANALYSIS

Image analysis

CaMKII$^+$ cells quantification

The number of CaMKII-positive neurons was semi-automatically assessed with a custom-written algorithm in the ImageJ environment. Briefly, a Region of Interest (ROI) was manually placed over either superficial or deep prefrontal layers. The image contrast was enhanced (*enhance contrast* function, 0.5% of saturated pixels) and a *median filter* was applied (radius = 1.5). To reduce background noise, we used the *subtract background* function, with a radius of 30 pixels. The image was then binarized (*convert to mask*) and segmented using the *watershed* function. To identify the neurons we used the *extended maxima* function of the MorphoLibJ plugin (dynamic = 30, connectivity = 4). We subtracted the regional maxima with the lowest intensity (i.e., the objects with bigger area) using *area opening* (pixel = 150) and counted the remaining objects (*analyze particles*).

Neuronal morphological analysis

Sholl analysis and spine density quantification were carried out in the ImageJ environment. For Sholl analysis, images were binarized (*auto threshold*) and dendrites were traced using the semi-automatical plugin *Simple Neurite Tracer*. The traced dendritic tree was analyzed with the plugin *Sholl Analysis*, after the geometric center was identified using the *blow/lasso tool*. For spine density quantification, we first traced the dendrite of interest (apical, basal, proximal oblique or secondary apical) and measured its length (*line*) and then manually counted the number of spines (*point picker*).

Iba-1$^+$-cells quantification

To quantify the number of Iba-1 stained cells we used a custom-written algorithm in ImageJ. The image stacks were collapsed to a maximum intensity Z-projection, and background noise was subtracted (*despeckle*). To facilitate automatic thresholding, the image was passed through a Gaussian filter (*Gaussian blur*, sigma = 2) before being binarized (*auto threshold* with the *triangle* method). The number of cells was counted using *analyze particles* (size >150 pixels).

Iba-1$^+$-cells morphological analysis

The morphology of microglial cells was assessed on maximum intensity Z-projections in the MATLAB environment, using previously reported criteria (Bellesi et al., 2017). Images (n = 64 for each group of mice) were automatically thresholded (*graythresh* and *im2bw* functions) and putative microglial cells were identified as objects between 200 and 1500 pixels (*bwareaopen*). Around the center of mass of each of the isolated cells, a region of interest (ROI) of 110x110 pixels was computed and visually examined. If the ROI contained a properly segmented microglia cells, its features (area, perimeter, eccentricity) were quantified (*regionprops*). ROIs in which the microglial cell touched the boundaries of the image or in which more than one cell was included were discarded. Further, cell spread (analogous to process length) was computed as the average distance between the center of mass and the ''extrema'' of the cell; roundness was defined as the ratio between 4*pi*area and the square of the perimeter of the cell. Only mice that did not experience IUE were used for this analysis.

Iba-1$^+$-cells and VGLUT1$^+$ puncta overlay

Overlay of Iba-1$^+$ cells and VGLUT1$^+$ puncta was assessed according to previously reported criteria (Bellesi et al., 2017). Briefly, background noise of VGLUT1 stacks was reduced in the ImageJ environment using the subtract background (rolling ball radius, 2 pixels) and despeckle functions. Stacks were passed through a maximum filter (radius, 2 pixels), thresholded (auto threshold) and segmented (watershed). Further processing was carried out in the MATLAB environment. Puncta were labeled (bwlabeln, connectivity = 8) and their volume was measured (histcounts). Puncta <100 pixel or >500 pixel were discarded. Microglia stacks were entirely processed in the MATLAB environment. Stacks were passed through a 3D hysteresis filter (hysteresis3d function; lower threshold = 0.1, upper threshold = 0.5, connectivity = 26) and a 3D median filter (ordfilt3D function). VGLUT1 positive puncta showing 100% overlap with the processed Iba1 signal were then quantified. VGLUT-1 puncta were considered to be phagocyted if they showed a 100% overlap in xyz with the imaged microglial cell. Microglia cells were also quantified in their distal cell volume (volume computed starting from 7 μm of distance from the center of mass of the cell).

In vitro electrophysiology

As previously described (Bitzenhofer et al., 2017), data were imported and analyzed offline using custom-written tools in the MATLAB environment (MathWorks). For *in vitro* data, all potentials were corrected for liquid junction potentials (−10 mV) for the gluconate-based electrode solution. The RMP was measured immediately after obtaining the whole-cell configuration. To assess input resistance, hyperpolarizing current pulses of 200 ms duration were applied. Active membrane properties and current–voltage relationships were determined by unsupervised analysis of responses to a series of 600 ms long hyper- and depolarizing current pulses. Amplitude of APs was measured from threshold to peak.

In vivo electrophysiology

In vivo data were analyzed with custom-written algorithms in the MATLAB environment. Data were processed as following: band-pass filtered (500–5,000 Hz) to analyze MUA and band-pass filtered (4-100 Hz) using a third-order Butterworth filter before down-sampling to 3.2 kHz to analyze LFP. All filtering procedures were performed in a phase preserving manner. In recordings of non-anesthetized mice, to reduce the influence of movement-related artifacts, the signal was processed according to the *common-average and rereference* method before power spectral analysis and spike detection.

Detection of oscillatory activity

The detection of discontinuous patterns of activity in the neonatal PL was performed using a modified version of the previously developed algorithm for unsupervised analysis of neonatal oscillations (Cichon et al., 2014). Briefly, deflections of the root mean square of band-pass filtered signals (1–100 Hz) exceeding a variance-depending threshold were considered as network oscillations. The threshold was determined by a Gaussian fit to the values ranging from 0 to the global maximum of the root-mean-square histogram. If two oscillations occurred within 200 ms of each other they were considered as one. Only oscillations lasting >1 s were included, and their occurrence, duration, and amplitude were computed.

Power spectral density

For power spectral density analysis, 1 s-long windows of network oscillations were concatenated and the power was calculated using Welch's method with non-overlapping windows. For optical stimulation, we compared the average power during the 1.5 s-long time window preceding the stimulation to the last 1.5 s-long time window of light-evoked activity.

Multi-unit activity

MUA was detected as the peak of negative deflections exceeding five times the standard deviation of the filtered signal and having a prominence larger than half the peak itself.

Single unit activity

SUA was detected and clustered using klusta (Rossant et al., 2016) and manually curated using phy (https://github.com/cortex-lab/phy). Data were imported and analyzed using custom-written tools in the MATLAB software (MathWorks).

Firing rate

The firing rate was computed by dividing the total number of spikes by the duration of the analyzed time window.

Inter-spike-interval

Inter-spike interval (ISI) was calculated at 2 ms resolution and was normalized to all the detected ISI. For plotting and statistics only the 10-500 ms range was considered.

Pairwise phase consistency

Pairwise phase consistency (PPC) was computed as previously described (Vinck et al., 2010). Briefly, the phase in the band of interest was extracted as mentioned above, and the mean of the cosine of the absolute angular distance (dot product) among all pairs of phases was calculated.

Spike-triggered LFP power

Spike-triggered LFP spectra were calculated as

$$\left(\mathrm{Power}_{\mathrm{spike}} - \mathrm{Power}_{\mathrm{baseline}}\right)/\mathrm{Power}_{\mathrm{baseline}},$$

where the spike-triggered power spectrum ($\mathrm{Power}_{\mathrm{spike}}$) was calculated using Welch's method for a 200 ms-log time window centered on each spike, and the power spectrum of baseline LFP ($\mathrm{Power}_{\mathrm{baseline}}$) was averaged for two time windows, 100-300 ms and 200-400 ms before each spike.

K-nearest neighbors classifiers

Machine learning analyses were performed using Python (Python Software Foundation, Wolfeboro Falls, New Hampshire, USA) in the Spyder (Pierre Raybaut, The Spyder Development Team) development environment. Model training and performance evaluation were carried out using the scikit-learn toolbox. The set was iteratively (n = 500) divided in a training (2/3 of the set) and a cross-validation (1/3) set. Hyper-parameter of the model were tuned on the training set, which was further split using the standard 3-fold cross-validation split implemented by the function "GridSearchCV," to which a "pipeline" object was passed. The "pipeline" object was built using the "Pipeline" function, and concatenating quantile transformation of the input features ("Quantile Transformer," tuning the number of quantiles), feature selection ("Select Percentile," using mutual information and tuning the percentage of features to select) and K-nearest neighbors classification (tuning the number of neighbors, the weight function to use for prediction, the algorithm used to compute the nearest neighbors, and the size of the leaf). Performance assessment was then computed on the cross-validation set (to which it had not been exposed during hyper-parameters tuning). Performance was stable across a wide range of parameters. To plot the classifier decision space, we used t-sne to reduce the feature space to two dimensions, while preserving the hyper-dimensional structure of the data. The decision space was then approximated by imposing a Voronoi tessellation on the 2d plot, using k-nearest regression on the t-sne coordinates of the predicted classes of the mice.

Statistical analysis

Statistical analyses were performed using R Statistical Software (Foundation for Statistical Computing, Vienna, Austria). Normally distributed, homoscedastic, having equal variance and non-nested data were tested for significant differences (*$p < 0.05$, **$p < 0.01$ and ***$p < 0.001$) using paired t test, unpaired t test, one-way repeated-measures ANOVA, or one-way ANCOVA with age as a covariate (only if age had a significant effect) and with Bonferroni-Tukey corrected post hoc analysis. Not normally distributed, heteroskedastic or not having equal variance data were tested with yuen's bootstrap test (n = 5000 repetitions), yuen's paired sample robust t test, or bootstrapped (n = 5000 repetitions) heteroscedastic one way ANOVA for trimmed means (yuenbt, yuend, t1waybt, mcppb20, glht, lsmeans functions of the WRS2, multcomp and lsmeans R package). A standard 20% level of trimming for the mean

was selected for these tests. Such tests were preferred to more traditional non-parametric tests in virtue of the (sometimes) high levels of unequal variance in our data. To account for the commonly ignored increased false positive rate inherent in nested design (Aarts et al., 2014), nested data were analyzed with linear mixed-effect models. Parameter estimation was done using the *lmer* function implemented in the lme4-R package. Model selection was performed using the Akaike Information Criterion (AIC) and/or the Bayesian information criterion (BIC), as differences between the two criteria were minimal. To test the significance of condition in our model, we performed a likelihood ratio test against a reduced model in which we removed condition (aov R function). Post hoc analysis with Tukey multiple comparison correction was carried out using the glhp function of the multcomp R package. For analysis of phagocytic activity of microglia cells, we used bootstrapped heteroscedastic one-way ANOVA for trimmed means instead of linear mixed-effect model in virtue of the highly non-normality of the data. No statistical measures were used to estimate sample size since effect size was unknown. Investigators were blinded to the group allocation when Sholl, spine analyses, microglia morphology, and engulfment were assessed. For other investigations, unsupervised analysis software was used to preclude investigator biases. Statistical parameters can be found in the main text and/or in the figure legends. More information about test used, its values, and its parameters are provided in Data S1.

DATA AND CODE AVAILABILITY

The authors declare that all data and code supporting the findings of this study are included in the manuscript and its Supplementary Information or are available from the corresponding authors on request. LFP and SUA data for all the non-anesthetized mice is available at the following open-access repository:

https://gin.g-node.org/mchini/Resolving_and_rescuing_developmental_miswiring_in_a_mouse_model_of_cognitive_impairment

2.5 Transient developmental increase of prefrontal activity alters network maturation and causes cognitive dysfunction in adult mice

Sebastian H. Bitzenhofer, Jastyn A. Pöpplau, Mattia Chini, Annette Marquardt and Ileana L. Hanganu-Opatz

Biorxiv, accepted in *Neuron* 2021; DOI: https://doi.org/10.1101/558957

Personal contribution

I performed *in vitro* electrophysiology and optogenetics experiments. I carried out formal analysis and data curation. I reviewed and edited the manuscript.

Transient developmental increase of prefrontal activity alters network maturation and causes cognitive dysfunction in adult mice

Sebastian H. Bitzenhofer[1,#,*,§], Jastyn A. Pöpplau[1,#], Mattia Chini[1], Annette Marquardt[1] & Ileana L. Hanganu-Opatz[1,*]

[1] Developmental Neurophysiology, Center for Molecular Neurobiology, University Medical Center Hamburg-Eppendorf, Hamburg, Germany

[#] Co- first authors

[§]Current address: Center for Neural Circuits and Behavior, Department of Neurosciences, University of California, San Diego, La Jolla, CA, USA.

* Corresponding authors: Ileana L. Hanganu-Opatz
hangop@zmnh.uni-hamburg.de
Falkenried 94, 20251 Hamburg, Germany

Sebastian Bitzenhofer
sbitzenhofer@ucsd.edu
9500 Gilman Dr., La Jolla, CA 92093, USA

8 Figures
9 Extended Data Figures
2 Extended Data Table
150 words abstract
3810 words main text

Running title
Early activity is critical for prefrontal development

Abstract

Disturbed neuronal activity in neuropsychiatric pathologies emerges during development and might cause multifold neuronal dysfunction by interfering with apoptosis, dendritic growth and synapse formation. However, how altered electrical activity early in life impacts neuronal function and behavior of adults is unknown. Here, we address this question by transiently increasing the coordinated activity of layer 2/3 pyramidal neurons in the medial prefrontal cortex of neonatal mice and monitoring long-term functional and behavioral consequences. We show that increased activity during early development causes premature maturation of pyramidal neurons and alters interneuron density. Consequently, reduced inhibitory feedback by fast-spiking interneurons and excitation/inhibition imbalance in prefrontal circuits of young adults result in weaker evoked synchronization in gamma frequency. These structural and functional changes ultimately lead to poorer mnemonic and social abilities. Thus, prefrontal activity during early development actively controls the cognitive performance of adults and might be critical for cognitive symptoms of neuropsychiatric diseases.

Main

The prefrontal cortex acts as a hub of cognitive processing indispensable for the daily life[1,2]. Disruption of prefrontal-dependent short-term memory and executive performance is the major burden of neuropsychiatric diseases, such as schizophrenia and autism spectrum disorders[3–5]. These diseases have been associated with a large variety of genes and environmental risk factors that increase susceptibility[6,7]. The absence of a clear understanding of their pathophysiology has resulted in primarily symptom-based treatments with low response rates[8]. Many of the genes and risk factors associated with neuropsychiatric diseases regulate brain development, leading to the hypothesis that abnormal maturation causes impaired network function and ultimately poor cognitive abilities later in life[8–11]. Indeed, rhythmic network activity of cortical, and particularly prefrontal circuits is already compromised in prodromal patients[12,13] and during early postnatal development in mouse models of schizophrenia and autism[14–17].

Neuronal activity regulates the development of cortical networks in many ways, from controlling neuronal differentiation, migration and apoptosis up to shaping the establishment of sensory maps, local and large-scale networks[18–21]. Early in life, activity in the prefrontal cortex is coordinated in oscillatory patterns, yet, in line with the delayed structural maturation and emergence of cognitive abilities, they appear later than in other cortical areas[22]. Inputs from cortical and subcortical areas boost the activation of local prefrontal circuits[22–25]. Moreover, intracortical interactions lead to the emergence of oscillatory activity at fast frequencies[26,27]. However, whether early activity is necessary for the maturation of prefrontal function and cognitive abilities is still unknown. Conversely, to which extent altered activity during development actively contributes to adult miswiring relevant for disease conditions, instead of simply reflecting pathological maturation, remains to be elucidated.

To address these questions, we manipulated cortical activity during early development and monitored the long-term consequences for network activity and behavioral abilities. The manipulation was achieved by transient light stimulation of a subset of pyramidal neurons (PYRs) in layer (L) 2/3 of the mouse medial prefrontal cortex (mPFC) from postnatal day (P) 7 to 11, the developmental time window corresponding to the second/third trimester of gestation in humans[28]. This light stimulation induces rhythmic

activity in beta/low gamma frequency in the developing prefrontal cortex[26]. At the age of stimulation, the migration of cortical neurons has finished and the activity-dependent formation of synaptic connections is in full progress[18,29,30]. We focused on this critical developmental period for cortical network formation at which mouse models of psychiatric diseases start to show altered prefrontal activity caused by L2/3 PYRs dysfunction[14]. We demonstrate that the transient increase of prefrontal activity during early development is sufficient to disrupt prefrontal function and cognitive performance at young adult age.

Results

Stimulation of L2/3 pyramidal neurons induces coordinated activity in the neonatal mPFC

To uncover the role of early activity for adult prefrontal function, we firstly established a protocol to optically manipulate the activity of L2/3 PYRs from P7-11, the developmental time window critical for the formation of synaptic contacts in mPFC (Fig. 1a). For this, a subset of precursor cells of L2/3 PYRs in the prelimbic subdivision of the mPFC was transfected with channelrhodopsin 2 E123T/T159C (ChR2(ET/TC)) by in utero electroporation (IUE) at embryonic day (E) 15.5. As previously reported, the IUE protocol yields unilateral expression of ChR2(ET/TC) in 20-30% of PYRs confined to L2/3 in the mPFC (Fig. 1b)[31].

Ramp stimulations of linearly increasing light power (473 nm, 3 s) were used to activate transfected L2/3 PYRs from P7 to P11. In line with previous data[26], prefrontal network activity tended to organize itself rhythmically at 15-20 Hz upon ramp stimulation (Fig. 1c,d). This rhythmic activity resembled the discontinuous activity spontaneously occurring in the neonatal mPFC[22,32]. Ramp light stimulation increased neuronal firing in a subset of neurons (20.2% of units significantly activated, 0.6% of units significantly inactivated) (Fig. 1e, f). Induced firing was not random, but peaked at 15-20 Hz for individual units, similar to induced network activity (Fig. 1g). Due to the thin skull at this age, similar activity was induced with transcranial light stimulation (Extended Data Fig. 1a). Control light stimulations (594 nm, ramp, 3 s) that do not activate ChR2(ET/TC) did not change the firing and network activity in the mPFC (Extended Data Fig. 1b-f).

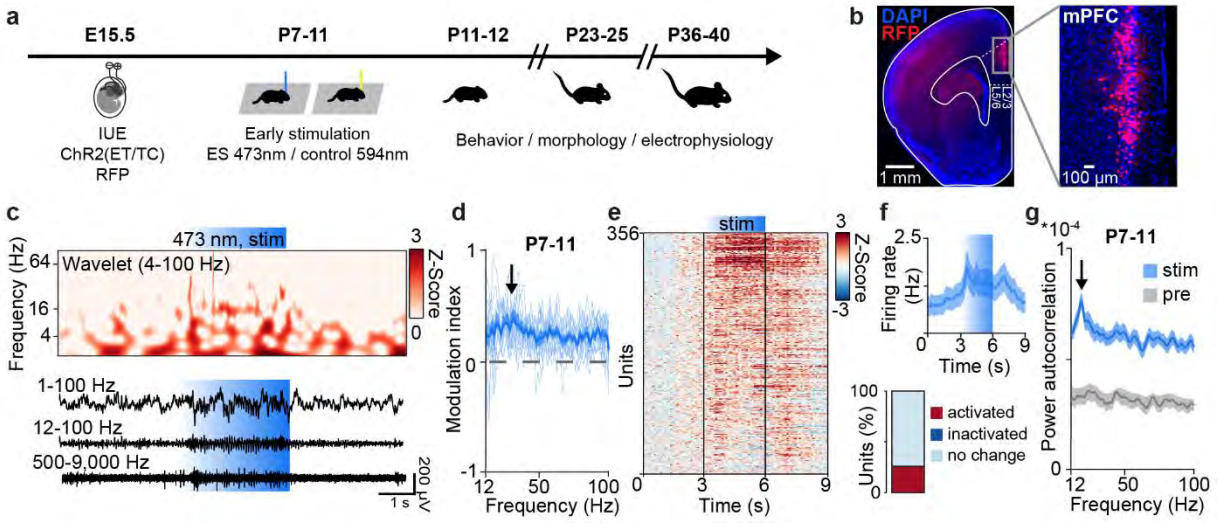

Fig. 1. Light stimulation of L2/3 PYRs in the neonatal mPFC. (**a**) Schematic of the protocol for early light stimulation and long-lasting monitoring of structural, functional, and behavioral effects during development. (**b**) Representative image showing ChR2(ET/TC)-2A-RFP-expression in L2/3 PYRs after IUE at E15.5 in a DAPI-stained coronal slice including the mPFC from a P11 mouse. (**c**) Representative extracellular recording displayed together with corresponding wavelet spectrum at identical time scale during ramp light stimulation (473 nm, 3 s) of L2/3 PYRs in the mPFC of a P11 mouse. (**d**) Modulation index of local field potential (LFP) power in response to ramp light stimulation averaged for P7-11 mice (n=13). (**e**) Firing rates of single units (n=356 units from 13 mice) in response to ramp light stimulation z-scored to pre-stimulation period. (**f**) Single unit firing rate during ramp light stimulation averaged for P7-11 mice (top, n=356 units from 13 mice) and percent of significantly modulated units (bottom). (**g**) Power of single unit autocorrelations before (pre) and during (stim) ramp light stimulation averaged for P7-11 mice (n=356 units from 13 mice).

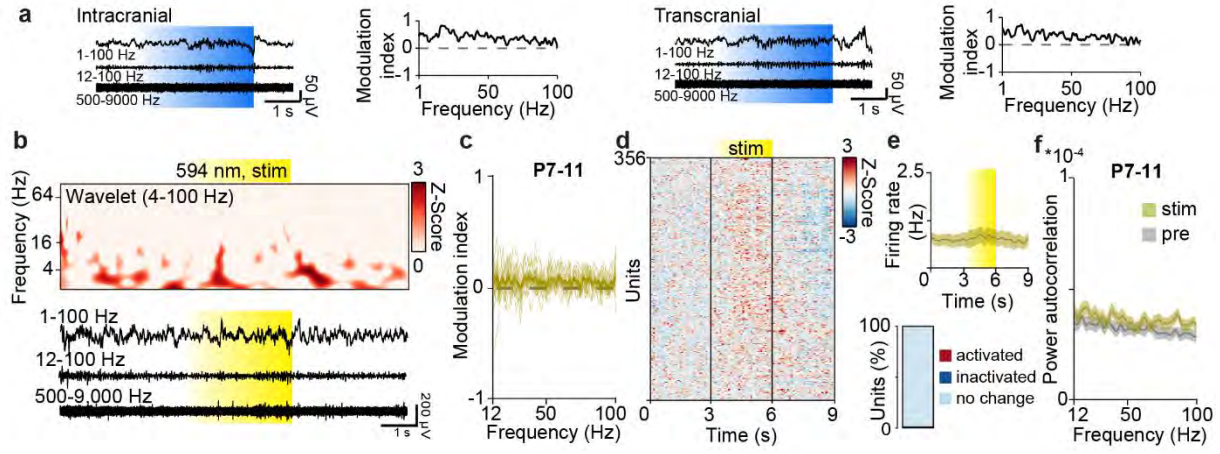

Extended Data Fig. 1. Control light stimulation of L2/3 PYRs in the neonatal mPFC. (**a**) Representative extracellular recordings during intracranial (left) and transcranial (right) ramp light stimulations (473 nm, 3 s) of L2/3 PYRs, as well as corresponding MI of power spectra for a P11 mouse. (**b**) Representative extracellular recording displayed together with corresponding wavelet

spectrum at identical time scale during control ramp light stimulation (594 nm, 3 s) of L2/3 PYRs in the mPFC of a P11 mouse. (**c**) Modulation index of LFP power in response to control ramp light stimulation averaged for P7-11 mice (n=13). (**d**) Firing rates of single units (n=356 units from 13 mice) in response to control ramp light stimulation z-scored to pre-stimulation period. (**e**) Single unit firing rate during control ramp light stimulation averaged for P7-11 mice (top, n=356 units from 13 mice) and percent of significantly modulated units (bottom). (**f**) Power of single unit autocorrelations before (pre) and during (stim) control ramp light stimulation averaged for P7-11 mice (n=356 units from 13 mice).

Transient increase of prefrontal activity during neonatal development disrupts cognitive performance of young adults

To transiently increase neuronal firing and network activation in the developing mPFC, we performed the transcranial stimulation that induced fast oscillatory discharges daily from P7 to P11. This developmental period has been identified as being critical for altered prefrontal activity in a mouse model of neuropsychiatric diseases[14]. On each of the five days of manipulation, mice received 30 transcranial ramp light stimulations (3 s long) at either 594 nm (control) or 473 nm (early stimulation, ES) to activate the ChR2(ET/TC)-transfected L2/3 PYRs in the mPFC.

Subsequently, we tested the behavioral abilities of control and ES mice, focusing on tasks that require prefrontal function. Data from mice of both sexes were pooled, since their performance was comparable in all tasks (Extended Data Tab. 2). Transient early stimulation did not affect the overall somatic and reflex development (Extended Data Fig. 2). First, we monitored recognition memory as a form of short-term memory that emerges at pre-juvenile age (P16-22), as soon as sensory and motor abilities are fully mature[33]. In contrast to control mice, ES mice were not able to distinguish a novel from a familiar object (novel object recognition, NOR) as well as an object they more recently interacted with (recency recognition, RR) (Fig. 2a,b). However, group differences were not significant for NOR and RR. The novel position of an object (object location recognition, OLR) was distinguished by both control and ES mice (Extended Data Fig. 3b). In contrast to NOR and RR, OLR depends more on hippocampus than mPFC[34]. Social interactions were significantly impaired in pre-juvenile ES mice. Their preference for interaction with the dam-containing container over an empty container was significantly reduced compared to control mice (Fig. 2c).

Second, we tested mPFC-dependent working memory of young adult (P36-40) control and ES mice. To this end, we used an 8-arm radial maze test with 4 baited arms, a Y-maze test for spontaneous alternations and a delayed non-match-to-sample task. ES mice showed working memory and reference memory deficits in the 8-arm radial maze test (Fig. 2d,e, Extended Data Fig.3d). Moreover, when compared to controls, ES mice showed poorer performance during spontaneous alternation (Fig. 2f, Extended Data Fig.3c). and in the delayed non-match-to-sample task (Fig. 2g). The deficits identified in ES mice are not due to impaired motor abilities or enhanced anxiety, since neither the behavior in an open field nor the interaction with objects and mazes was different between groups (Extended Data Fig. 3a,c,d). Thus, transient elevation of prefrontal activity at neonatal age caused long-lasting impairment of mPFC-dependent short-term and working memory as well as social behavior.

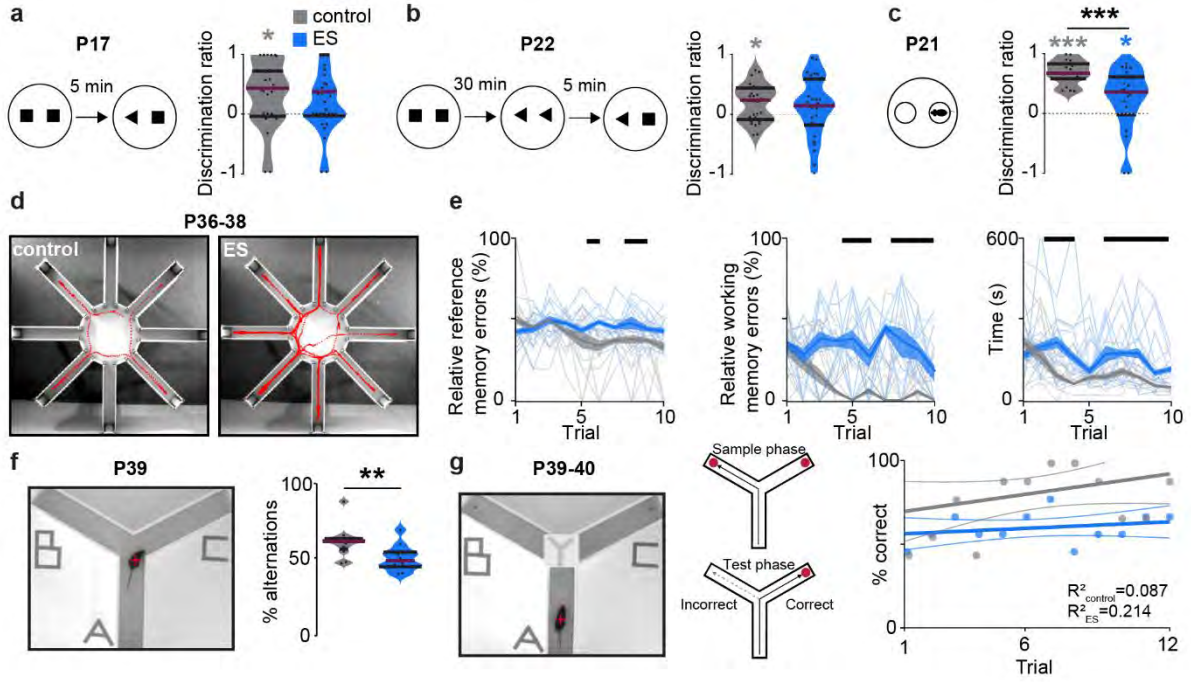

Fig. 2. Transient early stimulation impairs cognitive abilities of juvenile and young adult mice. (**a**) Schematic of NOR task and violin plot displaying the discrimination ratio of interaction time with a novel vs. familiar object for control (n=28) and ES (n=30) mice at P17. (Wilcoxon rank, control p=0.018, ES p=0.157, control-ES p=0.177). (**b**) Schematic of RR task and violin plot displaying the discrimination ratio of interaction time with a less vs. more recent object for control (n=28) and ES (n=30) mice at P22. (Wilcoxon rank, control p=0.010, ES p=0.171, control-ES p=0.498). (**c**) Schematic of maternal interaction task and violin plot displaying the discrimination ratio of interaction time with mother vs. empty bin for control (n=19) and ES (n=21) mice at P21.

(Wilcoxon rank, control p<0.001, ES p=0.045, control-ES p<0.001). (**d**) Representative tracking of a control (left) and ES mouse (right) in an 8-arm radial maze memory task with 4 baited arms at P36-38. (**e**) Plots displaying the relative reference (left) and working-memory errors (middle), as well as the time to complete the task (right) in 8-arm radial maze memory task over 10 trials on 3 consecutive days for control (n=12) and ES (n=12) mice. (Kruskall-Wallis, relative reference memory errors p<0.001, relative working memory errors p<0.001, time p<0.001). (**f**) Photograph illustrating a spontaneous alternation task in a Y-maze (left) and violin plot displaying the percent of spontaneous alternations (right) for control (n=12) and ES (n=12) mice at P39. (Wilcoxon rank, p=0.006). (**g**) Photograph illustrating a delayed non-match-to-sample task in a Y-maze (left) and dot plot displaying the percent of correct choices over 12 consecutive trials (6 trials/day) (right) for control (n=12) and ES (n=12) mice at P39-40. Black lines and asterisks (* p<0.05, ** p<0.01, *** p<0.001) indicate significant differences (see Extended Data Tab. 1 for detailed statistics).

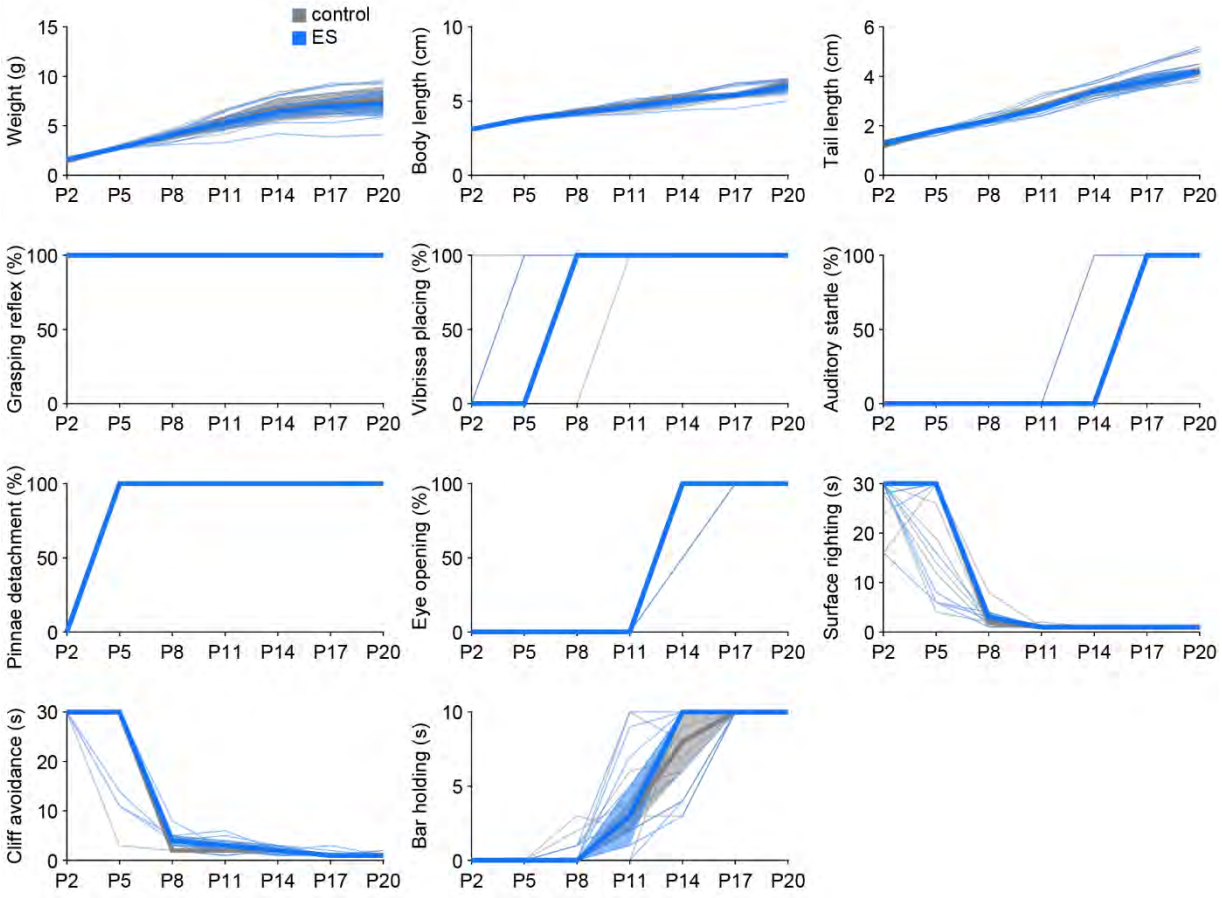

Extended Data Fig. 2. ES and control mice have similar somatic and reflex development. Line plots displaying the age-dependence of developmental milestones for control (n=11) and ES (n=11) mice. (See Extended Data Tab. 1 for detailed statistics).

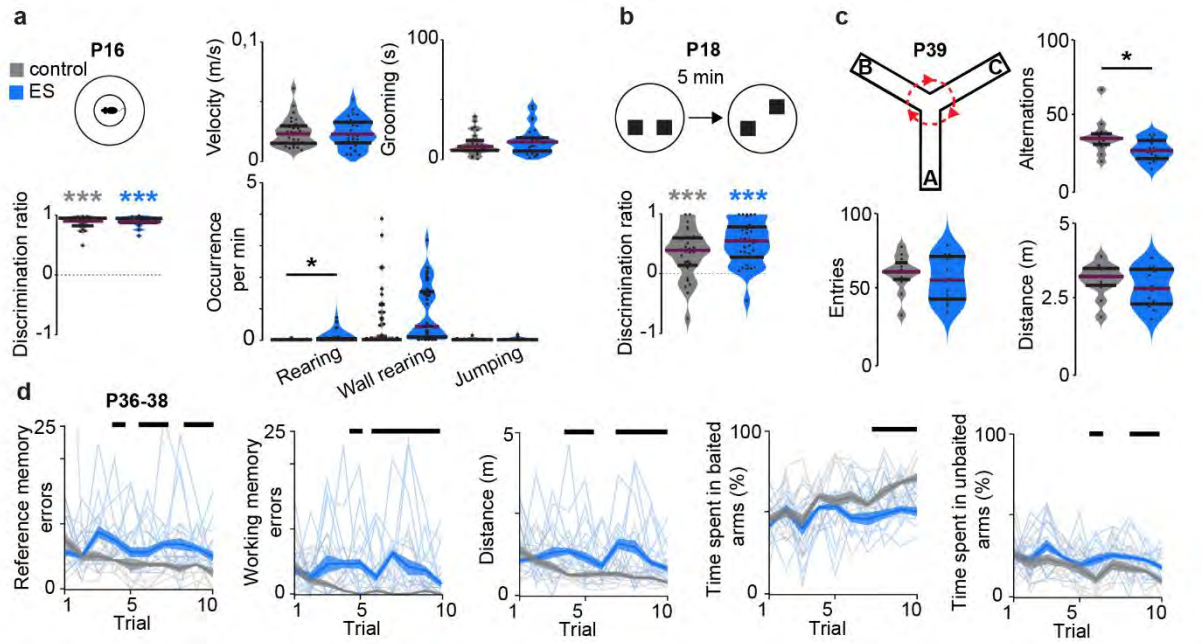

Extended Data Fig. 3. Transient early stimulation impairs mPFC-dependent cognitive abilities but not motor and anxiety behavior of juvenile and young adult mice. (**a**) Schematic of an open field task (top left) and violin plots displaying the discrimination ratio of time spend in border area vs. center area (bottom left), as well as the basic behavior (velocity, grooming, rearing, wall rearing, jumping) (right) for control (n=28) and ES (n=30) mice at P16. (Wilcoxon rank, discrimination ratio, control $p<0.001$, ES $p<0.001$, control-ES $p=0.809$). (**b**) Schematic of OLR task (top) and violin plot displaying the discrimination ratio of interaction time with an object in a novel vs. familiar location (bottom) for control (n=28) and ES (n=30) mice at P18. (Wilcoxon rank, control $p<0.001$, ES $p<0.001$, control-ES $p=0.154$). (**c**) Schematic showing spontaneous alternation in a Y-maze as well as violin plots displaying quantified parameters (alternations, entries, distance) for control (n=12) and ES (n=12) mice at P39. (Wilcoxon rank, alternations, $p=0.046$). (**d**) Line plots displaying reference- and working-memory errors as well as further task-related parameters for an 8-arm radial maze memory task over 10 trials on 3 consecutive days for control (n=12) and ES (n=12) mice at P36-38. (Kruskal-Wallis, reference memory errors $p<0.001$, working memory errors $p<0.001$). Black lines and asterisks (* $p<0.05$, ** $p<0.01$, *** $p<0.001$) indicate significant differences (see Extended Data Tab. 1 for detailed statistics).

Transient increase of neonatal prefrontal activity induces premature dendritic growth in L2/3 pyramidal neurons

To test whether impaired cognitive abilities of juvenile and adult ES mice resulted from permanent structural disruption of the mPFC after transient increase of neonatal activity, we monitored the structural maturation of PYRs in control and ES mice. The density of CaMKII-positive neurons and of ChR2(ET/TC)-transfected neurons did not differ between control and ES mice at all investigated developmental time points (P11-12, P23-25 and P38-40) (Extended Data Fig. 4). Investigation of the dendritic morphology of L2/3 PYRs

after transient stimulation at P7-11 revealed that immediately after this time window the dendritic arborization (i.e. dendrite length, number of intersections) of these neurons was increased in ES compared to control mice (Fig. 3). However, the exuberant arborization was transient and from P23-25 on, the dendritic arbors of L2/3 PYRs in the mPFC of ES mice were similar to controls. A comparison across age revealed that the dendritic length increased with age for control (linear mixed effect models (LMEM), P11-12 to P23-25 p=0.002**, P11-12 to P38-40 p=0.0002***), but not for ES mice (LMEM, P11-12 to P23-25 p=0.79, P11-12 to P38-40 p=0.07). Of note, dendritic length of L2/3 PYRs in ES mice at P11-12 was comparable to control mice at P23-25 (LMEM, p=0.33). These results suggest that increased activity in the neonatal mPFC causes premature dendritic maturation of L2/3 PYRs.

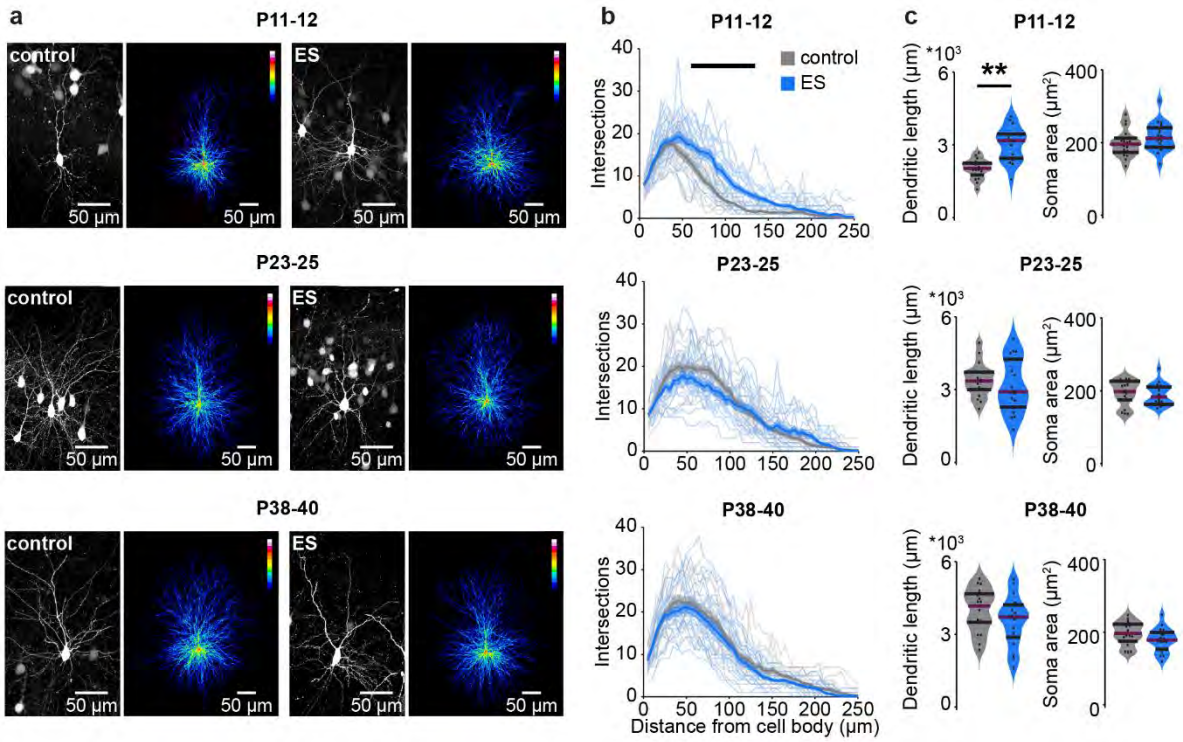

Fig. 3. Transient early stimulation induces premature dendritic growth in prefrontal L2/3 PYRs. (**a**) Representative photographs and corresponding average heat maps of ChR2(ET/TC)-transfected L2/3 PYRs in the mPFC of P11-12, P23-25 and P38-40 control (left) and ES mice (right). (**b**) Line plots of dendritic intersections of L2/3 PYRs with concentric circles (0-250 µm radius) centered around the soma averaged for control (18 cells of 3 mice/age group) and ES mice (18 cells of 3 mice/age group) at P11-12, P23-25 and P38-40. (LMEM, P11-12 p<0.001, P23-25 p<0.001, P38-40 p<0.001). (**c**) Violin plots displaying the dendritic length and soma area of L2/3 PYRs for control (18 cells from 3 mice/age group) and ES (18 cells from 3 mice/age group) mice for different age groups. (LMEM, dendritic length, P11-12 p=0.007, P23-25 p=0.631, P38-

40 p=0.161). Black lines and asterisks (* p<0.05, ** p<0.01, *** p<0.001) indicate significant differences (see Extended Data Tab. 1 for detailed statistics).

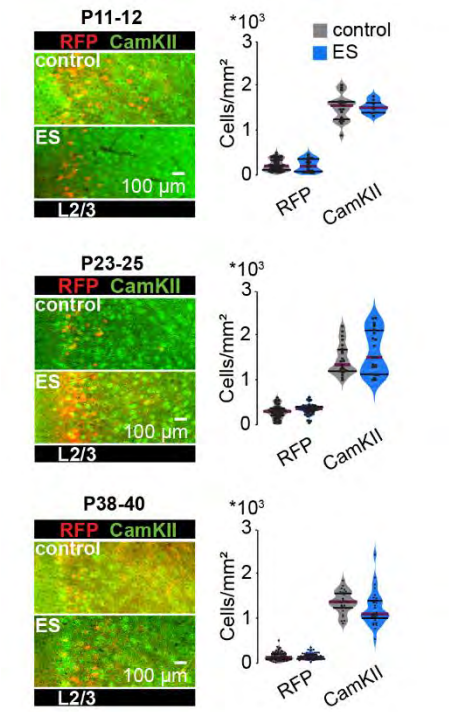

Extended Data Fig. 4. Transient early stimulation does not alter the density of L2/3 PYRs. Left, representative photographs displaying CaMKII immunostainings in the ChR2(ET/TC)-RFP-transfected mPFC of control and ES mice at P11-12 (control, RFP n=60 slices of 9 mice, CamKII n=19 slices of 6 mice; ES, RFP n=27 slices of 4 mice, CamKII n=9 slices of 2 mice), P23-25 (control, RFP n=47 slices of 5 mice, CamKII n=23 slices of 5 mice; ES, RFP n=43 slices of 5 mice, CamKII n=23 slices of 5 mice) and P38-40 (control, RFP n=65 slices of 5 mice, CamKII n=29 slices of 5 mice; ES, RFP n=62 slices of 5 mice, CamKII n=29 slices of 5 mice). Right, violin plots of RFP-expressing and CaMKII-positive neuronal density at different age groups. (LMEM, P11-12, RFP p=0.855, CamKII p=0.705, P23-25, RFP p=0.819, CamKII p=0.527, P38-40, RFP p=0.819, CamKII p=0.177). (See Extended Data Tab. 1 for detailed statistics).

Transient increase of neonatal prefrontal activity reduces gamma power and network synchrony in the adult mPFC

Transient alteration of neonatal activity might perturb the function of prefrontal circuits, ultimately leading to abnormal behavior. To test this hypothesis, we monitored spontaneous neuronal and network activity of the mPFC across development. We performed extracellular recordings from head-fixed control and ES mice immediately after transient early stimulation (P11-12), at juvenile (P23-25) and young adult (P38-40) age (Fig. 4a,b). With increasing age, spontaneous oscillatory activity in the mPFC of control

and ES mice increased in power and fast oscillations within 12-100 Hz became more prominent (Fig. 4c). At P11-12, the power of these fast oscillations was increased in the mPFC of ES mice compared to control mice, in accordance with the premature growth of L2/3 PYRs dendrites. At later stages of development, no differences were detected between control and ES mice. In contrast, the firing rates of single units were similar in control and ES mice during development, yet, at adulthood, ES mice showed decreased firing in the mPFC (Fig. 4d).

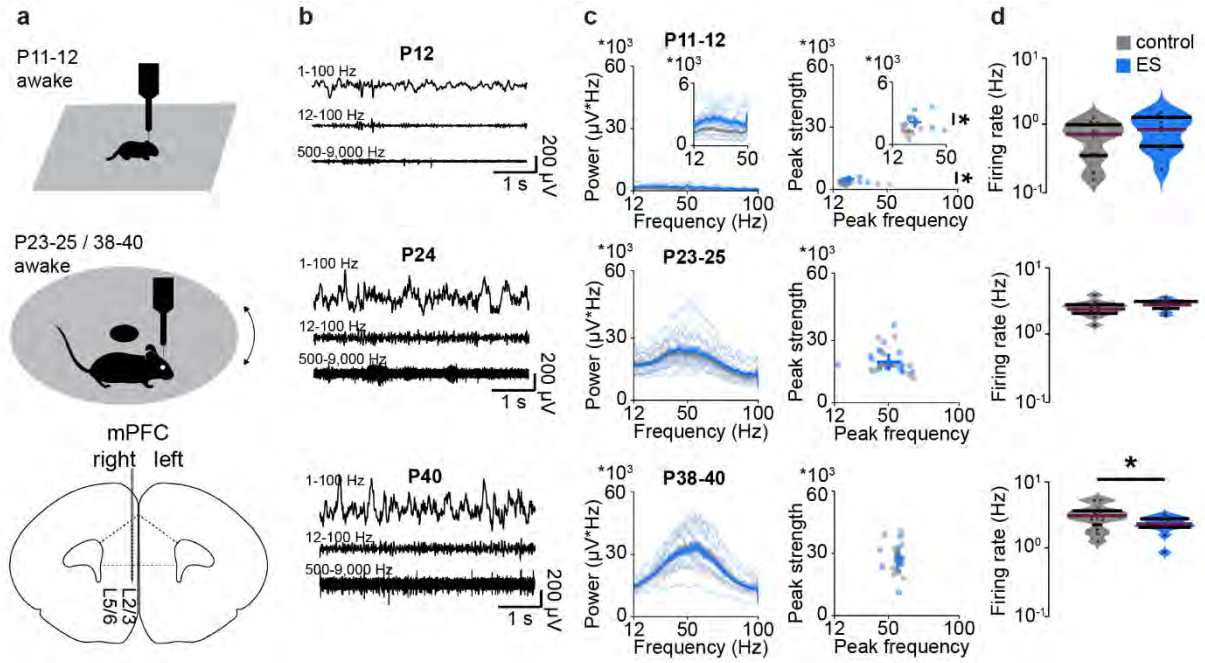

Fig. 4. Transient early stimulation has minor effects on spontaneous network activity and firing in the developing mPFC. (**a**) Top, schematic illustrating the recording setups used for young mice with limited motor abilities (head-fixed, no movement) and for juvenile and young adult mice (head-fixed, freely moving on a spinning disk). Bottom, schematic of the recording configuration in the developing mPFC. (**b**) Representative extracellular recordings in the mPFC at P12, P24 and P40. (**c**) Left, average power spectra of spontaneous network activity in the mPFC of control and ES mice at P11-12 (control n=11 recordings, 11 mice, ES n=10 recordings, 10 mice), P23-25 (control n=13 recordings, 6 mice, ES n=14 recordings, 5 mice) and P38-40 (control n=12 recordings, 5 mice, ES n=12 recordings, 5 mice). Inset, power spectra for P11-12 shown at higher magnification. Right, scatter plots displaying peak strength and peak frequency of LFP power for control and ES mice. (Wilcoxon rank, P11-12, peak frequency p=0.245, peak strength p=0.015, LMEM, P23-25, peak frequency p=0.643, peak strength p=0.665, P38-40, peak frequency p=0.856, peak strength p=0.750). (**d**) Violin plots displaying the firing rates of single units in the mPFC averaged for control and ES mice at P11-12, P23-25, and P38-40. (Wilcoxon rank, P11-12 p=0.275, LMEM, P23-25 p=0.072, P38-40 p=0.041). Asterisks (* p<0.05, ** p<0.01, *** p<0.001) indicate significant differences (see Extended Data Tab. 1 for detailed statistics).

Even though spontaneous activity is largely unaffected by the transient increase of activity at neonatal age, the mPFC might abnormally respond to incoming stimuli, leading to disrupted processing and ultimately, behavior. To test this hypothesis, we used optogenetics to stimulate ChR2(ET/TC)-transfected L2/3 PYRs. Acute light stimulations (ramp, 473 nm, 3 s) triggered fast rhythmic activity with peak frequencies increasing from 15-20 Hz (beta frequency range) at P11-12 to 50-60 Hz (gamma frequency range) at P23-25 and P38-40 in the mPFC of control and ES mice (Fig. 5a). These results are in line with recent data, showing an acceleration of fast frequency oscillations during prefrontal development[35]. However, at P38-40 the magnitude of light-induced gamma activity was significantly smaller in ES mice compared to controls. This weaker prefrontal activation in fast oscillatory rhythms upon acute stimulation for ES mice, specific for young adults, was replicated in a separate cohort of anesthetized head-fixed mice (Extended Data Fig. 5a-c). Furthermore, young adult ES mice had weaker synchrony within and between hemispheres during evoked activity. Both, the coherence between L2/3 and L5/6 of the stimulated hemisphere and the coherence between L2/3 across hemispheres was reduced in ES mice at P38-40, but was normal at younger age (Extended Data Fig. 5d,e).

Additionally, we analyzed single unit firing to assess the response of prefrontal neurons to acute light stimulation in control and ES mice across development. Calculation of autocorrelations for prefrontal units showed that independent of age and group, neurons fire rhythmically in response to acute light stimulation (Fig. 5b). Similar to network oscillations, the strength and frequency of the rhythmicity of neuronal firing increased with age, yet the magnitude of increase was lower for ES mice, reaching significance at P38-40. In contrast, the rhythmicity of spontaneous firing of prefrontal units was similar for control and ES mice at all age groups (Extended Data Fig. 6).

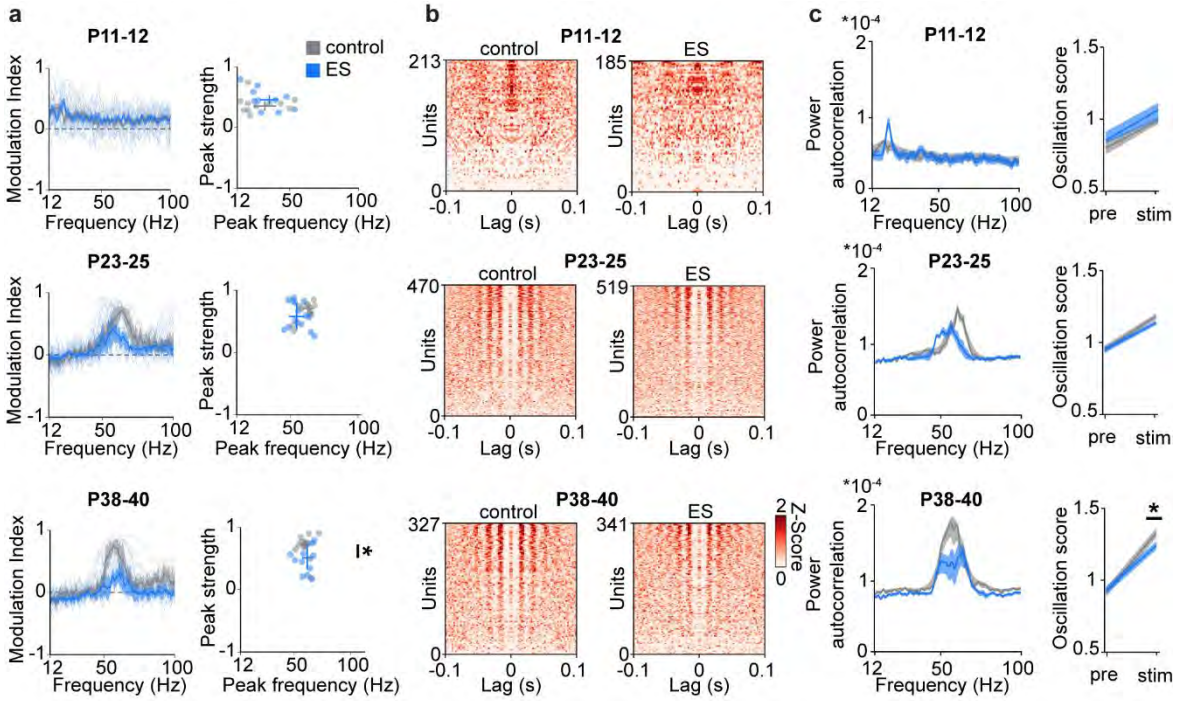

Fig. 5. Transient early stimulation decreases evoked network and neuronal gamma rhythmicity in the adult mPFC. (**a**) Left, modulation index of LFP power in response to acute ramp light stimulation (473 nm, 3 s) for control and ES mice at P11-12 (control n=11 recordings, 11 mice, ES n=10 recordings, 10 mice), P23-25 (control n=13 recordings, 6 mice, ES n=14 recordings, 15 mice) and P38-40 (control n=12 recordings, 5 mice, ES n=12 recordings, 5 mice). Right, scatter plots displaying the peak strength and peak frequency of the power modulation index for control and ES mice. (Wilcoxon rank, P11-12, peak frequency p=0.307, peak strength p=0.307, LMEM, P23-25, peak frequency p=0.136, peak strength p=0.419, P38-40, peak frequency p=0.913, peak strength p=0.043). (**b**) Z-scored autocorrelograms of single units during acute ramp light stimulation arranged by magnitude for control and ES mice at P11-12 (control n=213 units, 11 mice, ES n=185 units, 10 mice), P23-25 (control n=470 units, 6 mice, ES n=519 units, 5 mice) and P38-40 (control n=327 units, 5 mice, ES n=341 units, 5 mice). (**c**) Left, average power of single unit autocorrelograms during acute ramp light stimulation for control and ES mice at different age. Right, oscillation score of single units before (pre) and during (stim) acute ramp light stimulation. (LMEM, oscillation score, P11-12, pre p=0.406, stim p=0.156, P23-25, pre p=0.272, stim p=0.478, P38-40, pre p=0.428, stim p=0.030). Asterisks (* p<0.05, ** p<0.01, *** p<0.001) indicate significant differences (see Extended Data Tab. 1 for detailed statistics).

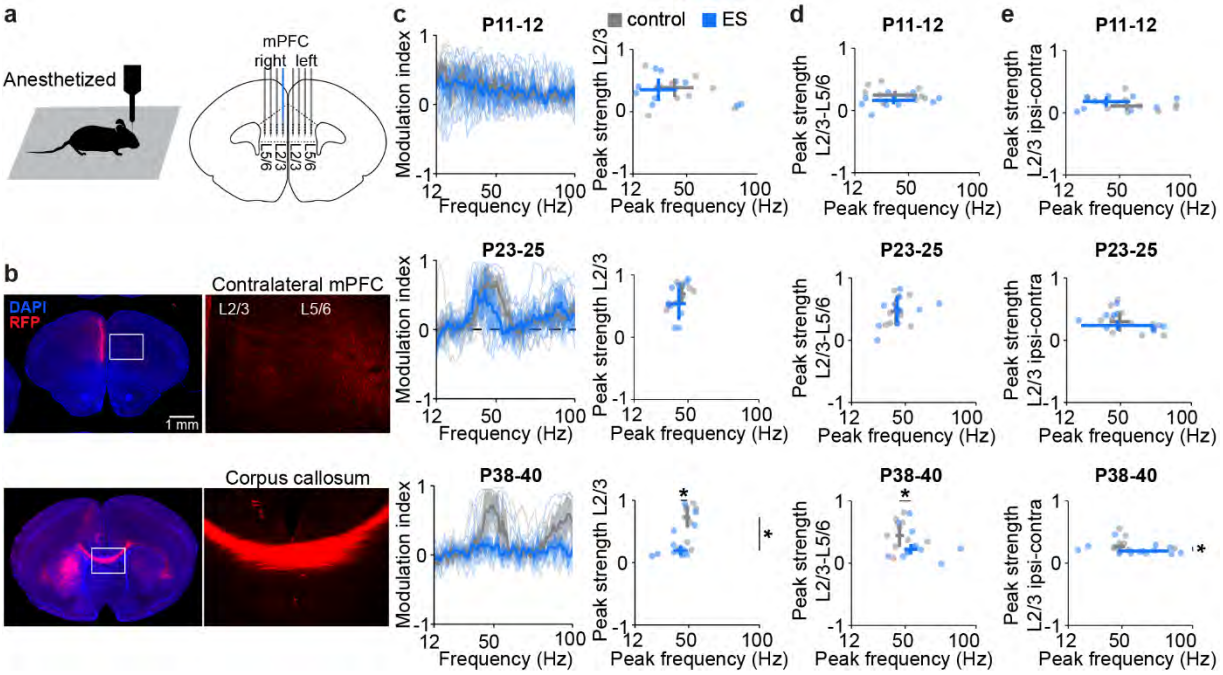

Extended Data Fig. 5. Transient early stimulation impairs evoked intra- and interhemispheric synchrony in the adult mPFC. (**a**) Schematic displaying bilateral multi-shank recordings in the mPFC of anesthetized mice. (**b**) Representative photographs showing axonal projections of ChR2(ET/TC)-RFP-transfected L2/3 PYRs in coronal slices from a P10 mouse. (**c**) Left, modulation index of LFP power in response to acute ramp light stimulation (473 nm, 3 s) for control and ES mice at P11-12 (control n=10 recordings, 10 mice, ES n=10 recordings, 10 mice), P23-25 (control n=10 recordings, 10 mice, ES n=11 recordings, 11 mice) and P38-40 (control n=9 recordings, 9 mice, ES n=12 recordings, 12 mice). Right, scatter plots displaying the peak strength and peak frequency of the power modulation index for control and ES mice. (Wilcoxon rank, P11-12, peak frequency p=0.520, peak strength p=0.909, P23-25, peak frequency p=0.290, peak strength p=0.459, P38-40, peak frequency p=0.039, peak strength p=0.025). (**d**) Scatter plots displaying the peak strength and peak frequency of prefrontal L2/3-L5/6 coherence at different age. (Wilcoxon rank, P11-12, peak frequency p=1.000, peak strength p=0.053, P23-25, peak frequency p=0.943, peak strength p=0.915, P38-40, peak frequency p=0.042, peak strength p=0.069). (**e**) Scatter plots displaying the peak strength and peak frequency of interhemispheric prefrontal L2/3-L2/3 coherence at different age. (Wilcoxon rank, P11-12, peak frequency p=0.212, peak strength p=0.623, P23-25, peak frequency p=0.832, peak strength p=0.915, P38-40, peak frequency p=0.270, peak strength p=0.036). Asterisks (* p<0.05, ** p<0.01, *** p<0.001) indicate significant differences (see Extended Data Tab. 1 for detailed statistics).

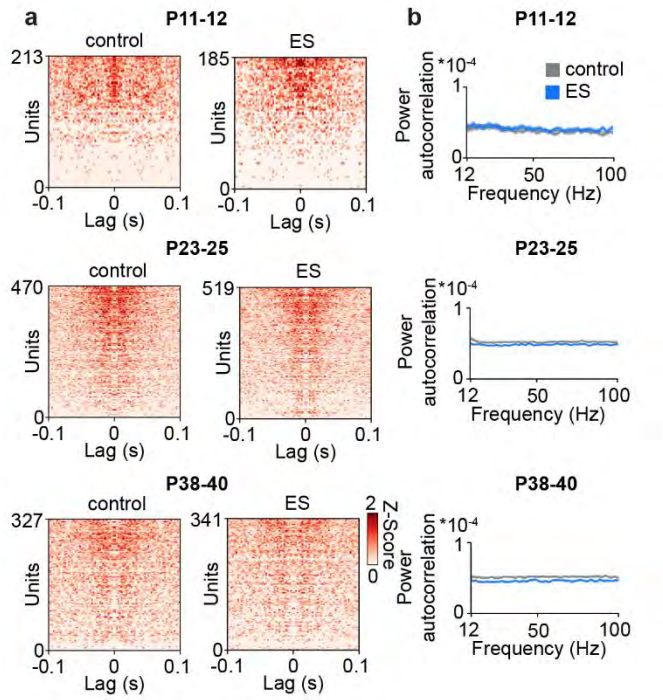

Extended Data Fig. 6. Transient early stimulation does not affect the rhythmicity of single units in the mPFC during spontaneous activity. (**a**) Z-scored autocorrelations for single units before acute ramp light stimulation arranged by magnitude for control and ES mice at P11-12 (control n=213 units, 11 mice, ES n=185 units, 10 mice), P23-25 (control n=470 units, 6 mice, ES n=519 units, 5 mice) and P38-40 (control n=327 units, 5 mice, ES n=341 units, 5 mice). (**b**) Average power of single unit autocorrelations before acute ramp light stimulation for control and ES mice at different age. (See Extended Data Tab. 1 for detailed statistics).

To assess the impact of early stimulation on the synchrony within the prefrontal network during development, we calculated pairwise correlations of single units. During spontaneous activity, pairwise correlations between prefrontal units were similar for control and ES mice at P11-12 and P38-40, whereas correlation at the 3rd quartile was slightly reduced in ES mice at P23-25 (Extended data Fig. 7). In contrast, during ramp light stimulations, the pairwise correlations were significantly reduced at the 3rd quartile in young adult ES mice when compared to controls, but comparable between groups at P11-12 and P23-25. These data show that the synchrony of the highest correlated units in the mPFC is reduced in young adult ES mice.

Taken together, these results show that transiently increased activity at neonatal age diminishes prefrontal gamma band synchronization in response to stimulation at adult age.

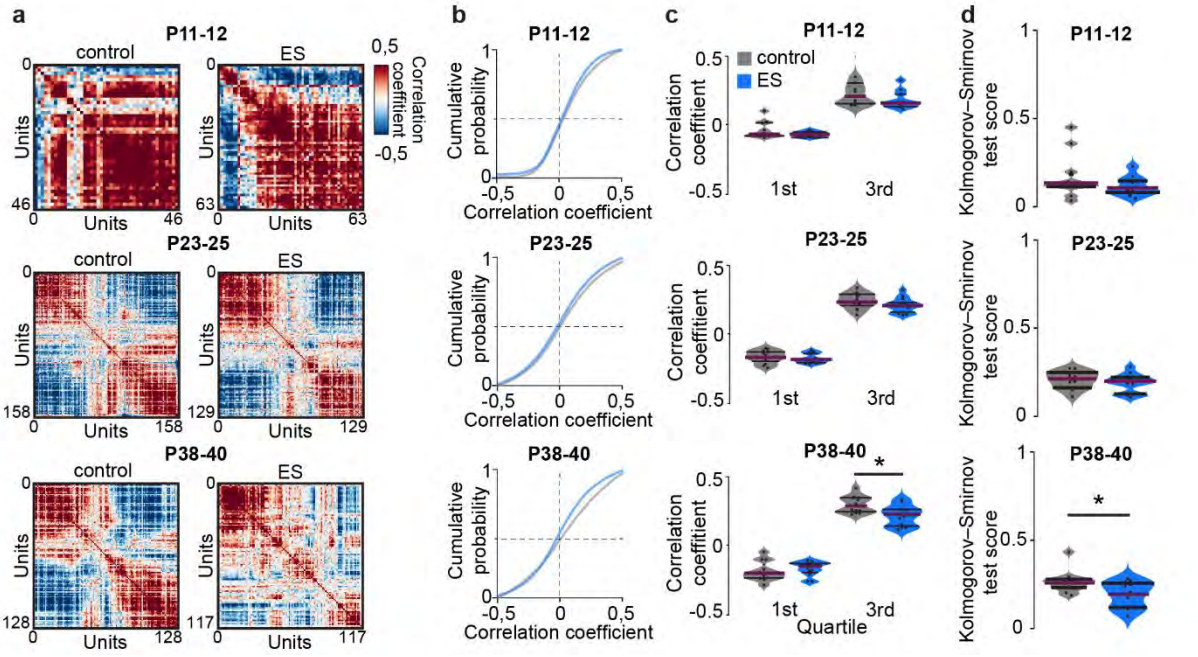

Fig. 6. Transient early stimulation reduces synchrony of highly correlated units in response to acute light stimulation in the adult mPFC. (**a**) Representative pairwise correlations of L2/3 single units during acute ramp light stimulation (473 nm, 3 s) for a control (left) and ES mouse (right) at different developmental stages. (**b**) Average cumulative density functions of pairwise correlations during acute ramp light stimulation for control and ES mice at P11-12 (control n=11 recordings, 11 mice, ES n=10 recordings, 10 mice), P23-25 (control n=13 recordings, 6 mice, ES n=14 recordings, 5 mice) and P38-40 (control n=12 recordings, 5 mice, ES n=12 recordings, 5 mice). (**c**) Average intercept at 1st and 3rd quartile of correlation coefficients during acute ramp light stimulation for control and ES mice at different age. (Wilcoxon rank, P11-12, 1st quartile p=0.385, 3rd quartile p=0.162, LMEM, P23-25, 1st quartile p=0.470, 3rd quartile p=0.315, P38-40, 1st quartile p=0.537, 3rd quartile p=0.019). (**d**) Kolmogorov-Smirnov test score of the distance between pre and stim cumulative density function of correlation coefficients for control and ES mice. (Wilcoxon rank, P11-12, p=0.418, LMEM, P23-25, p=0.631, P38-40, p=0.033). Asterisks (* p<0.05, ** p<0.01, *** p<0.001) indicate significant differences (see Extended Data Tab. 1 for detailed statistics).

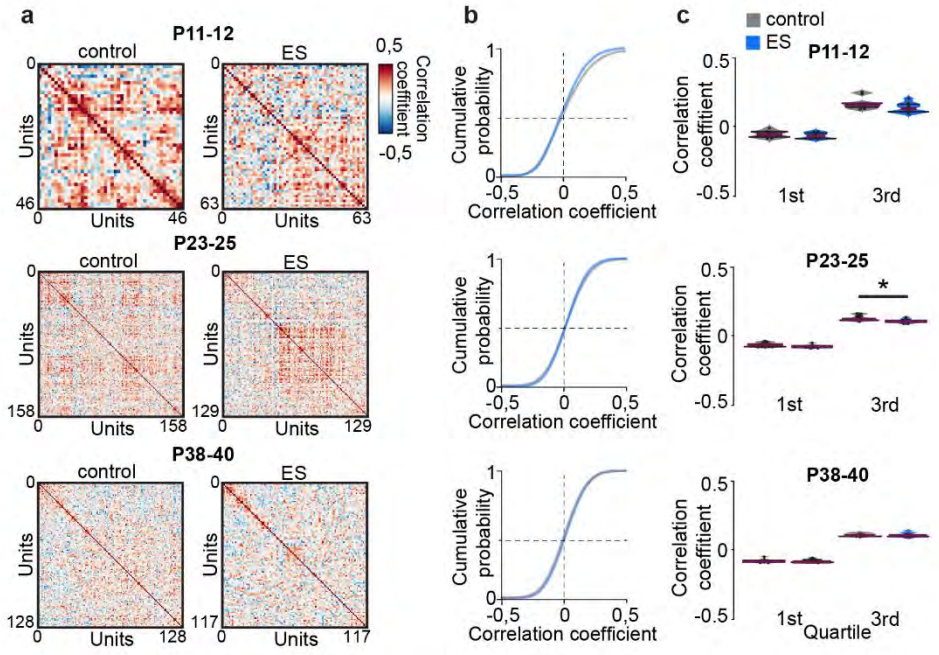

Extended Data Fig. 7. Transient early stimulation mildly affects network synchrony during spontaneous activity in the mPFC. (**a**) Representative pairwise correlations of L2/3 single units before acute ramp light stimulation for a control (left) and ES mouse (right) at different developmental stages. (**b**) Average cumulative density functions of pairwise correlations before acute ramp light stimulation for control and ES mice at P11-12 (control n=11 recordings, 11 mice, ES n=10 recordings, 10 mice), P23-25 (control n=13 recordings, 6 mice, ES n=14 recordings, 5 mice) and P38-40 (control n=12 recordings, 5 mice, ES n=12 recordings, 5 mice). (**c**) Average intercept at 1st and 3rd quartile of correlation coefficients before acute ramp light stimulation for control and ES mice at different age. (Wilcoxon rank, P11-12, 1st quartile p=0.241, 3rd quartile p=0.104, LMEM, P23-25, 1st quartile p=0.100, 3rd quartile p=0.036, P38-40, 1st quartile p=0.970, 3rd quartile p=0.911). Asterisks (* p<0.05, ** p<0.01, *** p<0.001) indicate significant differences (see Extended Data Tab. 1 for detailed statistics).

Transient increase of neonatal activity alters excitation/inhibition balance in the adult mPFC

Network synchronization in gamma frequency results from interactions between excitatory and inhibitory units[36,37]. To elucidate the mechanisms of abnormal network synchronization upon stimulation in ES mice, we analyzed the response of individual units in L2/3 of the mPFC to acute ramp light stimulations. At P11-12, 25.3% of units in control mice and 20.3% of units in ES mice significantly increased their firing rate during ramp light stimulation. Only few units (control 0.9%, ES 3.4%) decreased their firing rates. In older mice, units with significantly increased (P23-25, control 31.2%, ES 32.7%; P38-40, control 33.7%, ES 25.5%) and decreased (P23-25, control 27.0%, ES 23.6%; P38-40,

426 control 24.5%, ES 30.6%) firing rates were detected (Fig. 7a,b). The ratio of activated vs.
427 inactivated neurons per mouse was similar across groups at P11-12 and P23-25, yet
428 significantly reduced in ES mice at P38-40 compared to controls.

429 Decreased gamma synchrony and stronger inhibition in P38-40 ES mice suggest
430 that the transient increase of prefrontal activity at neonatal age causes long-term
431 alterations of the balance between excitation and inhibition in the prefrontal circuitry. To
432 test this hypothesis, we performed whole-cell patch-clamp recordings from non-
433 transfected prefrontal L2/3 PYRs in coronal slices from control and ES mice. During acute
434 light stimulation of ChR2(ET/TC)-transfected L2/3 PYRs (473 nm, square pulse, 1 s) the
435 ratio of excitatory postsynaptic currents (EPSCs) to inhibitory postsynaptic currents
436 (IPSCs) in non-transfected L2/3 PYRs was shifted towards inhibition for P38-40 ES mice
437 compared to controls (Fig. 7c). In contrast, the ratio was similar between groups at
438 younger age. Basic active and passive membrane properties as well as spontaneous
439 inputs were not affected in ES mice (Fig. 7c, Extended Data Fig. 8).

440

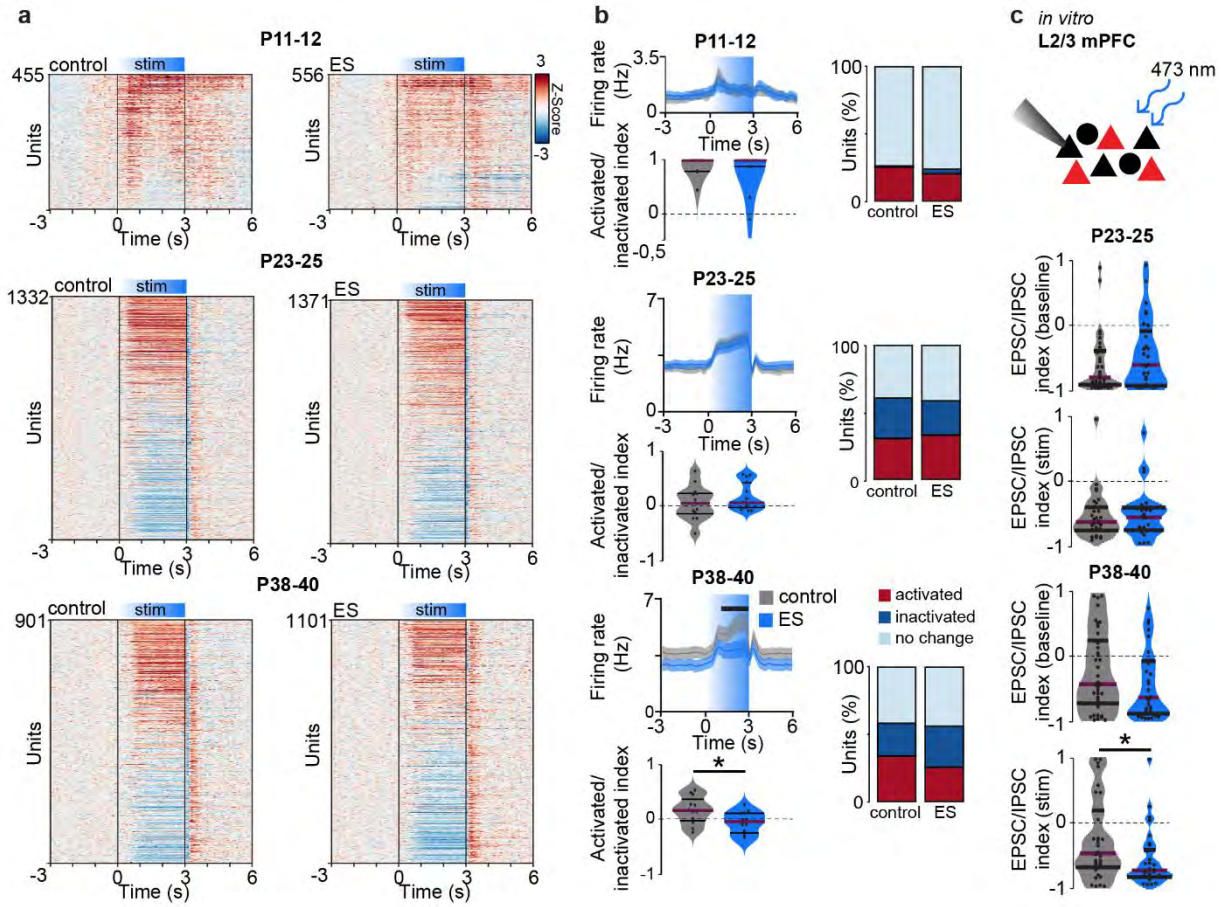

Fig. 7. Transient early stimulation alters excitation/inhibition balance in the adult mPFC during acute light stimulation. (**a**) Single unit firing rates z-scored to pre-stimulation in response to acute ramp light stimulation (473 nm, 3 s) displayed for control (left) and ES mice (right) at P11-12 (control n=455 units, 11 mice, ES n=556 units, 10 mice), P23-25 (control n=1332 units, 6 mice, ES n=1371 units, 5 mice) and P38-40 (control n=901 units, 5 mice, ES n=1101 units, 5 mice). (**b**) Line plots displaying average firing rates during acute light stimulations (top left), violin plots showing the index of significantly activated vs. inactivated units (bottom left) and bar diagrams of the percentage of significantly activated and inactivated units for control and ES mice at P11-12, P23-25 and P38-40. (P11-12, LMEM, firing rate $p<0.001$, Wilcoxon rank, activated/inactivated index $p=0.982$, LMEM, P23-25, firing rate $p=0.004$, activated/inactivated index $p=0.317$, P38-40, firing rate $p<0.001$, activated/inactivated index $p=0.033$). (**c**) Top, schematic showing the protocol for in vitro whole-cell patch-clamp recordings from non-transfected L2/3 PYRs (black) during optogenetic stimulation of neighboring transfected cells (red) in the mPFC. Bottom, violin plots displaying EPSC/IPSC index during baseline and acute light stimulation (473 nm, square pulse, 1 s) for control and ES mice at P23-25 (control n=35 neurons, 5 mice, ES n=30 neurons, 5 mice) and P38-40 (control n=41 neurons, 6 mice, ES n=33 neurons, 4 mice). (LMEM, P23-25, baseline $p=0.218$, stim $p=0.840$, P38-40, baseline $p=0.402$, stim $p=0.030$). Black lines and asterisks (* $p<0.05$, ** $p<0.01$, *** $p<0.001$) indicate significant differences (see Extended Data Tab. 1 for detailed statistics).

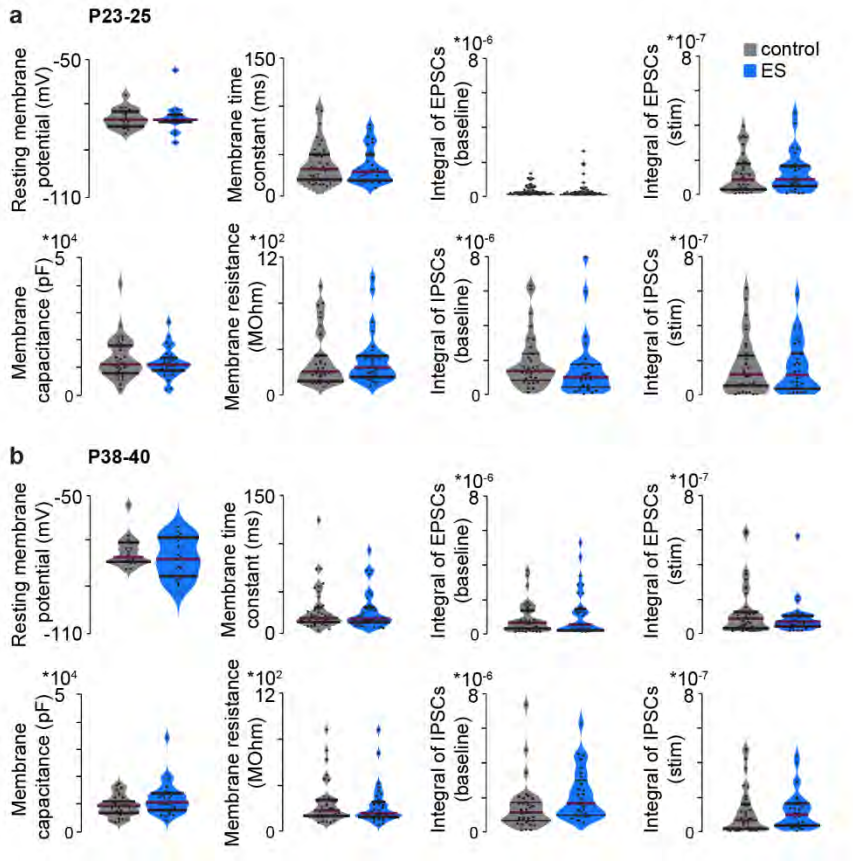

Extended Data Fig. 8. Transient early stimulation does not alter the passive and active membrane properties of non-transfected L2/3 PYRs. (**a**) Violin plots displaying passive and active membrane properties as well as properties of EPSCs and IPSCs induced by light stimulation in non-transfected L2/3 PYRs from control and ES mice at P23-25 (control n=35 neurons, 5 mice, ES n=30 neurons,5 mice). (LMEM, resting membrane potential p=0.545, membrane time constant p=0.426, EPSCs baseline p=0.743, EPSCs stim p=0.415 membrane capacitance p=0.218, membrane resistance p=0.564, IPSCs baseline p=0.234, IPSCs stim p=0.881). (**b**) Same as (a) for control and ES mice at P38-40 (control n=41 neurons, 6 mice, ES n=33 neurons, 4 mice). (LMEM, resting membrane potential p=0.526, membrane time constant p=0.907, EPSCs baseline p=0.339, EPSCs stim p=0.349 membrane capacitance p=0.304, membrane resistance p=0.436, IPSCs baseline p=0.332, IPSCs stim p=0.309). (See Extended Data Tab. 1 for detailed statistics).

Stronger inhibition might result from a higher survival rate of interneurons after transient activity increase during neonatal age[38]. To test this hypothesis, we performed immunohistochemical stainings for parvalbumin (PV) and somatostatin (SOM) and quantified the distribution of these two distinct subsets of inhibitory interneurons in the mPFC of control and ES mice during development. The density of SOM-positive neurons was significantly reduced, whereas the density of PV-positive neurons was significantly increased at P38-40 (Extended Data Fig. 9).

Fast-spiking (FS) PV-expressing interneurons that mature towards the end of the developmental period are critical for the generation of adult cortical gamma activity[36,39]. Therefore, the late emerging decrease of gamma synchrony in adult ES mice may result from disruption of these neurons. To test this hypothesis, we distinguished regular spiking (RS) and FS units in extracellular recordings from control and ES mice based on their spike waveform (Fig. 8a). This distinction revealed that the spontaneous firing rate of RS units is altered in ES mice at P23-25 and P38-40 compared to controls, whereas no changes were detected for FS units. In contrast, evoked activity during acute ramp light stimulation was reduced for RS and FS units in ES mice at P38-40, but normal earlier during development (Fig. 8c). Reduced evoked activity of FS units seems to be in opposition with the increased numbers of PV-positive neurons in adult ES mice. However, the FS firing rate is mainly reduced during the late phase of the ramp, whereas the initial peak is not altered. Taking into account that PV neurons inhibit pyramidal neurons but also other PV neurons[40], we hypothesize that FS putatively PV neurons provide more potent inhibition and thereby reduce RS and FS firing rates after initial activation in ES mice.

Gamma synchronization in the adult cortex results from temporally coordinated excitatory drive and inhibitory feedback[37,39]. To investigate the timing of RS and FS firing, we performed acute stimulations with short light pulses of 3 ms duration. RS and FS units showed a pronounced peak in their firing rate for 5-10 ms in response to short light pulses (Fig. 8d). The similar peak time of RS and FS units indicates that the RS cluster contains a substantial number of non-transfected, indirectly activated units, in agreement with the sparse transfection achieved with IUE. FS units in control mice showed a second peak in their firing rate about 20 ms after the light pulse in P23-25 and P38-40 mice. The delay of 20 ms suggest the contribution of these units to gamma oscillations that have a typical cycle duration of 20 ms at 50 Hz. This second peak was significantly reduced in ES mice at P23-25 and P38-40. Of note, similar to ramp induced activity, the first peak was not affected for FS units, indicating that FS units provide stronger inhibition after initial activation in ES mice.

Thus, transiently increased activity at neonatal age alters the development of inhibitory feedback from FS interneurons and thereby, reduces evoked gamma synchronization of adult prefrontal circuits.

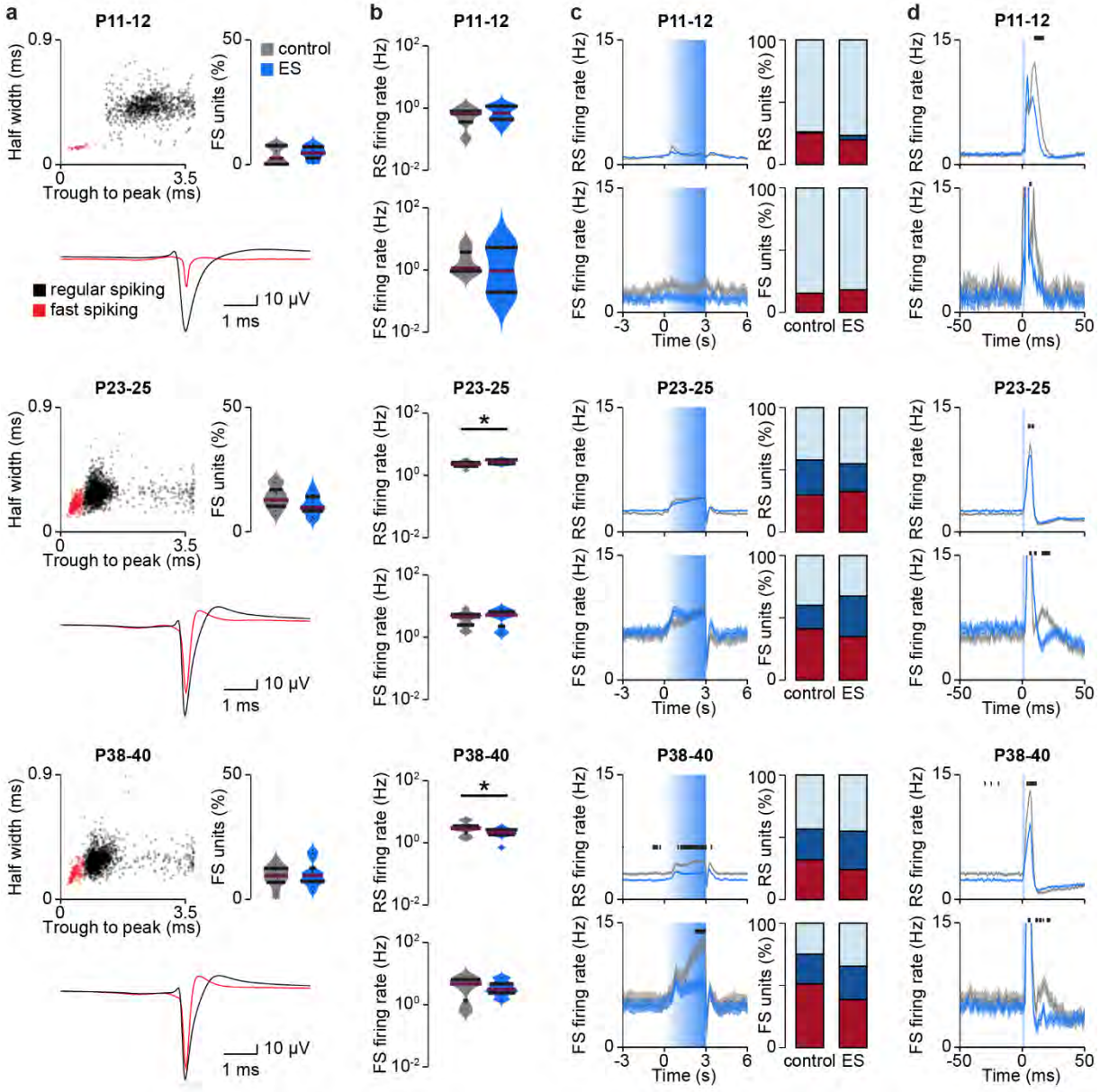

Fig. 8. Transient early stimulation alters evoked inhibitory feedback from fast spiking units in the mPFC. (**a**) Scatter plots displaying half width and trough to peak duration (top left), average waveforms for RS and FS units (bottom), as well as percent of FS units for control and ES mice at P11-12 (control 428 RS and 13 FS units, 11 mice, ES 475 RS and 22 FS units, 10 mice), P23-25 (control 1140 RS and 185 FS units, 6 mice, ES 1220 RS and 141 FS units, 5 mice) and P38-40 (control 814 RS and 84 FS units, 5 mice, ES 992 RS and 104 FS units, 5 mice). (Wilcoxon

rank, P11-12 p<0.500, LMEM, P23-25 p=0.114, P38-40 p=0.551). (**b**) Violin plots displaying spontaneous firing rate of RS and FS units for control and ES mice at P11-12, P23-25 and P38-40. (Wilcoxon rank, P11-12, RS firing rate p=0.418, FS firing rate p=0.680, LMEM, P23-25, RS firing rate p=0.020, FS firing rate p=0.357, P38-40, RS firing rate p=0.040, FS firing rate p=0.575). (**c**) Average firing rate during acute ramp light stimulation (473 nm, 3 s) and percent of significantly modulated units for control and ES mice at P11-12, P23-25 and P38-40. (LMEM, P11-12, RS firing rate p<0.001, FS firing rate p<0.001, P23-25, RS firing rate p<0.001, FS firing rate p<0.001, P38-40, RS firing rate p<0.001, FS firing rate p<0.001). (**d**) Average firing rate during acute pulse light stimulation (473 nm, 3 ms) for control and ES mice at P11-12, P23-25 and P38-40. (LMEM, P11-12, RS firing rate p<0.001, FS firing rate p<0.001, P23-25, RS firing rate p<0.001, FS firing rate p<0.001, P38-40, RS firing rate p<0.001, FS firing rate p<0.001). Black lines and asterisks (* p<0.05, ** p<0.01, *** p<0.001) indicate significant differences (see Extended Data Tab. 1 for detailed statistics).

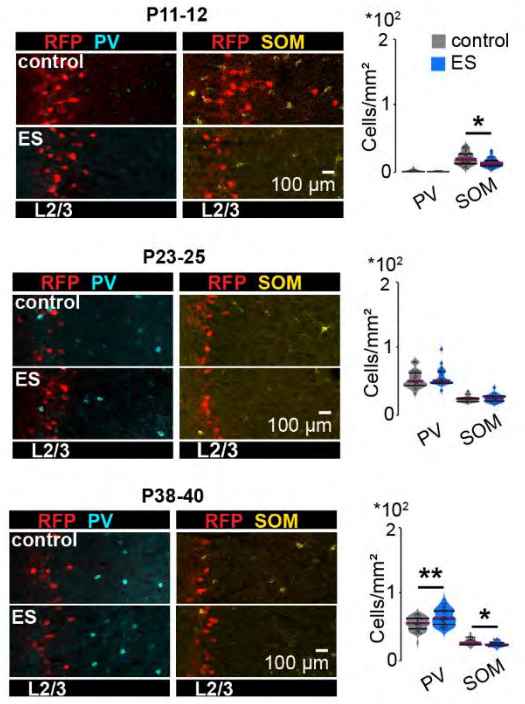

Extended Data Fig. 9. Transient early stimulation alters the density of SOM- and PV-expressing interneurons in the mPFC. Left, representative images showing PV and SOM immunostainings in the mPFC of control and ES mice at P11-12, P23-25 and P38-40. Right, violin plots displaying the density of PV-positive and SOM-positive neurons in L2/3 of the mPFC of control and ES mice at P11-12 (control: PV n=54 slices, 12 mice, SOM n=59 slices, 12 mice; ES, PV n=38 slices, 9 mice, SOM n=43 slices, 9 mice), P23-25 (control: PV n=25 slices, 5 mice, SOM n=25 slices, 5 mice; ES, PV n=27 slices, 6 mice, SOM n=25 slices, 6 mice) and P38-40 (control: PV n=36 slices, 9 mice, SOM n=36 slices, 9 mice; ES, PV n=40 slices, 10 mice, SOM n=43 slices,11 mice). (LMEM, P11-12, PV p=0.296, SOM p=0.044, P23-25, PV p=0.403, SOM p=0.390, P38-40, PV p=0.012, SOM p=0.012). Asterisks (* p<0.05, ** p<0.01, *** p<0.001) indicate significant differences (see Extended Data Tab. 1 for detailed statistics).

Discussion

Seminal research identified electrical activity as a major contributor to the development of the mammalian cerebral cortex. Early activity influences neuronal migration, differentiation, and apoptosis[19–21] as well as the establishment of synaptic connections[41,42]. Also in clinical settings, patterns of electroencephalographic activity of preterm infants provide prognostic value for neurodevelopmental outcome[43]. Several neuropsychiatric diseases have been proposed to be related to alterations in neuronal activity early in life[8,44]. However, fundamental questions still need to be addressed: how does electrical activity during early development impact adult cortical function? Does altered prefrontal activity during early development contribute to cognitive deficits later in life? Here, we address these questions and demonstrate that a transient increase of activity in the mouse mPFC during a short period of neonatal development critical for network formation causes long-lasting changes in inhibitory feedback and excitation/inhibition balance, leading to weaker evoked gamma band synchronization and ultimately, poorer cognitive abilities.

To manipulate developmental activity, we optogenetically stimulated the mPFC, inducing discontinuous activity patterns with similar dynamics as the ones spontaneously occurring. During early development the mammalian cortex shows discontinuous activity, with neuronal discharges organized in oscillatory rhythms alternating with electrically silent periods[45,46]. In the mPFC of neonatal mice, these 1-3 s-long oscillatory events with frequencies alternating between theta (4-12 Hz) and beta-low gamma (12-40 Hz) occur every 20-30 s[22,27]. The fast oscillations emerge as result of L2/3 PYRs activation[26]. Therefore, we used repeated ramp light stimulations (3 s duration, 6/min for 30 min) to activate L2/3 PYRs transfected with ChR2(ET/TC) by IUE and induced fast oscillatory discharges. At the age of transient early stimulation (P7-11), neurons have reached their final location in the cortical layers and are in the process of establishing synaptic connections[18,47]. Our stimulation protocol was designed to cause a modest increase of activity in the mPFC during this period critical for network formation. The stimulation not only augmented the level of activity but coordinated the prefrontal networks in fast oscillatory rhythms evolving from beta to gamma frequencies with age[35]. A causal link

between this rhythmic organization and the long-term effects of transient early stimulation is still missing.

How does the transient increase of neuronal activity at neonatal age influence prefrontal development and ultimately behavior? The present data demonstrate that the early manipulation triggers a cascade of structural and functional changes in the mPFC leading to the impairment of cognitive abilities. On the morphological level, increased neonatal activity induced premature growth of dendrites in stimulated L2/3 PYRs. This is consistent with the activity-dependent growth of dendrites[48] and reminiscent of the growth dynamics (i.e. initially excessive followed by arrested growth) during development in humans with autism spectrum disorders[49]. Activity of pyramidal neurons from P5 to P8 has been shown to regulate the survival of cortical interneurons[38,50]. Accordingly, we found an increased number of PV-expressing interneurons in ES mice. In contrast to previous studies[29,38,50], this effect was specific for PV-expressing neurons, whereas the number of SOM-expressing neurons was reduced. Several differences in the experimental settings might explain this disparity: (1) Stimulation a few days later during developmental (P7-11 vs. P5-8) is expected to have a stronger effect on late maturing PV-expressing interneurons[29]; (2) Increased activity of a subset of pyramidal neurons (L2/3 PYRs vs. all PYRs) might cause different activation of interneuron subtypes; (3) Optogenetic (vs. chemogenetic) stimulation triggering fast oscillatory network activity might specifically engage PV-expressing interneurons.

Premature growth of dendrites likely affects the connectivity of stimulated neurons. Together with altered interneuron numbers, these structural changes led to a shift in the excitation/inhibition balance in the mPFC of ES mice towards inhibition. In addition to the general increase in inhibition, the timing of FS, presumably PV-expressing interneurons, was altered. In juvenile and adult control mice, brief activation of L2/3 PYRs induced a sharp peak in the firing rate of FS interneurons followed by a second peak about 20 ms later. This second peak, supposedly critical for synchronization in gamma frequency, was absent in ES mice. Accordingly, the transient increase of neuronal activity at neonatal age led to impaired synchronization of the prefrontal network in gamma frequency in young adults. This is consistent with the importance of PV-expressing FS interneurons for the generation of cortical gamma activity[37,39]. The late maturation of PV-expressing

interneurons[29] and gamma activity in the mPFC[35] most likely underlie the delayed onset of these physiological effects. Of note, these effects were only evident during evoked activity, whereas spontaneous activity in the mPFC was largely normal, reflecting the moderate effects of stimulation protocol. This is consistent with alterations in evoked activity related to the early emergence of sensory symptoms in humans with autism spectrum disorders[44].

Abnormal FS interneuron development impairs prefrontal gamma activity and cognitive flexibility in adults[51]. Accordingly, transient increase of neuronal activity at neonatal age ultimately resulted in impaired cognitive abilities in juvenile and young adult mice. Gamma activity in prefrontal L2/3 is particularly important for the maintenance of information during working memory tasks[52]. This is consistent with the specific impairment of ES mice in short-term memory and working memory tasks, as well as reduced social preference.

In conclusion, these data demonstrate that altered neuronal activity during early development induces structural and functional changes in the mPFC, ultimately resulting in impaired cognitive abilities. Even though cognitive symptoms are not the core deficits, they represent a devastating burden in neuropsychiatric diseases[3–5]. Altered cortical excitation/inhibition balance and impaired gamma activity are critical for cognitive dysfunctions[53–55]. Thus, altered developmental activity of cortical circuits might actively contribute to cognitive symptoms in neuropsychiatric diseases[14–18].

Furthermore, the mechanisms described here might explain cognitive difficulties of preterm born humans experiencing excessive sensory stimulation in neonatal intensive care units (NICUs) (frequent handling associated with medical or nursing care, excessive noise and light levels) at a comparable stage of brain development (2nd-3rd gestational trimester)[56]. These stressful stimuli might trigger premature neuronal activity, perturbing the activity-dependent maturation of cortical networks[57]. Frontal regions are particularly vulnerable to conditions in NICUs [58]. Correspondingly, preterm children are highly prone to frontally confined impairment, such as memory and attention deficits[59]. Thus, our findings lend experimental proof to the concept that neuronal activity during early development accounts for adult cortical function and cognitive performance, playing a critical role in neurodevelopmental and neuropsychiatric diseases[12,14,17].

Methods

Animals

All experiments were performed in compliance with the German laws and the guidelines of the European Community for the use of animals in research and were approved by the local ethical committee (G132/12, G17/015, N18/015). Experiments were carried out on C57Bl/6J mice of both sexes. Timed-pregnant mice from the animal facility of the University Medical Center Hamburg-Eppendorf were housed individually at a 12 h light/12 h dark cycle and were given access to water and food ad libitum. The day of vaginal plug detection was considered E0.5, the day of birth was considered P0.

In utero electroporation

Pregnant mice received additional wet food daily, supplemented with 2-4 drops Metacam (0.5 mg/ml, Boehringer-Ingelheim, Germany) one day before until two days after IUE. At E15.5, pregnant mice were injected subcutaneously with buprenorphine (0.05 mg/kg body weight) 30 min before surgery. Surgery was performed under isoflurane anesthesia (induction 5%, maintenance 3.5%) on a heating blanket. Eyes were covered with eye ointment and pain reflexes and breathing were monitored to assess anesthesia depth. Uterine horns were exposed and moistened with warm sterile phosphate-buffered saline (PBS). 0.75-1.25 µl of opsin- and fluorophore-encoding plasmid (pAAV-CAG-ChR2(E123T/T159C)-2A-tDimer2, 1.25 µg/µl) purified with NucleoBond (Macherey-Nagel, Germany) in sterile PBS with 0.1% fast green dye was injected in the right lateral ventricle of each embryo using pulled borosilicate glass capillaries. Electroporation tweezer paddles of 5 mm diameter were oriented at a rough 20° leftward angle from the midline of the head and a rough 10° downward angle from the anterior to posterior axis to transfect precursor cells of medial prefrontal L2/3 PYRs with 5 electroporation pulses (35 V, 50 ms, 950 ms interval, CU21EX, BEX, Japan). Uterine horns were placed back into the abdominal cavity that was filled with warm sterile PBS. Abdominal muscles and skin were sutured with absorbable and non-absorbable suture thread, respectively. After recovery from anesthesia, mice were returned to their home cage, placed half on a heating blanket for two days after surgery. Fluorophore expression in pups was detected

669 at P2 with a portable fluorescence flashlight (Nightsea, MA, USA) through the intact skin
670 and skull and confirmed in brain slices postmortem.

671 ***Transient early stimulation***

672 A stimulation window was made at P7 for chronic transcranial optogenetic stimulation in
673 mice transfected by in utero electroporation. Mice were placed on a heating blanket and
674 anesthetized with isoflurane (5% induction, 2% maintenance). Breathing and pain
675 reflexes were monitored to assess anesthesia depth. The skin above the skull was cut
676 along the midline at the level of the mPFC and gently spread with forceps. The exposed
677 skull was covered with transparent tissue adhesive (Surgibond, SMI, Belgium). Mice were
678 returned to the dam in the home cage after recovery from anesthesia. From P7-11 mice
679 were stimulated daily under isoflurane anesthesia (5% induction, 2% maintenance) with
680 ramp stimulations of linearly increasing light power (473 nm wavelength, 3 s duration, 7
681 s interval, 180 repetitions, 30 min total duration). Light stimulation was performed using
682 an Arduino uno (Arduino, Italy) controlled laser system (Omicron, Austria) coupled to a
683 200 µm diameter light fiber (Thorlabs, NJ, USA) positioned directly above the tissue
684 adhesive window. Light power attenuation was set to reach 10 mW in the brain, adjusted
685 for measured light attenuation by the tissue adhesive (~30%) and the immature skull
686 (~25%). Control animals were treated identical but stimulated with light of 594 nm
687 wavelength that does not activate the expressed opsin ChR2(ET/TC).

688 ***Electrophysiology and optogenetics in vivo***

689 *Acute extracellular recordings*. Multi-site extracellular recordings were performed
690 unilaterally or bilaterally in the mPFC of non-anesthetized and anesthetized P7-40 mice.
691 Under isoflurane anesthesia (induction: 5%; maintenance: 2.5%), a craniotomy was
692 performed above the mPFC (0.5 mm anterior to bregma, 0.1-0.5 mm lateral to the
693 midline). Mice were head-fixed into a stereotaxic apparatus using two plastic bars
694 mounted on the nasal and occipital bones with dental cement. Multi-site electrodes
695 (NeuroNexus, MI, USA) were inserted into the mPFC (four-shank, A4x4 recording sites,
696 100 µm spacing, 125 µm shank distance, 1.8-2.0 mm deep). A silver wire was inserted
697 into the cerebellum and served as ground and reference. Pups were allowed to recover
698 for 30 min prior to recordings. For recordings in anesthetized mice, urethane (1 mg/g body

699 weight) was injected intraperitoneally prior to the surgery. Extracellular signals were band-
700 pass filtered (0.1-9,000 Hz) and digitized (32 kHz) with a multichannel extracellular
701 amplifier (Digital Lynx SX; Neuralynx, Bozeman, MO, USA). Electrode position was
702 confirmed in brain slices postmortem.

703 *Chronic extracellular recordings*. Multi-site extracellular recordings were performed in the
704 mPFC of P23-25 and P38-40 mice. Under isoflurane anesthesia (5% induction, 2.5%
705 maintenance), a metal head-post for head fixation (Luigs and Neumann, Germany) was
706 implanted at least 5 days before recordings. Above the mPFC (0.5-2.0 mm anterior to
707 bregma, 0.1-0.5 mm right to the midline) a craniotomy was performed and protected by a
708 customized synthetic window. A silver wire was implanted between skull and brain tissue
709 above the cerebellum and served as ground and reference. 0.5% bupivacaine / 1%
710 lidocaine was locally applied to cutting edges. After recovery from anesthesia, mice were
711 returned to their home cage. Mice were allowed to recover from the surgery, accustomed
712 to head-fixation and trained to run on a custom-made spinning disc. For recordings,
713 craniotomies were uncovered and a multi-site electrode (NeuroNexus, MI, USA) was
714 inserted into the mPFC (one-shank, A1x16 recording sites, 100 µm spacing, 2.0 mm
715 deep). Extracellular signals were band-pass filtered (0.1-9000 Hz) and digitized (32 kHz)
716 with a multichannel extracellular amplifier (Digital Lynx SX; Neuralynx, Bozeman, MO,
717 USA). Electrode position was confirmed in brain slices postmortem.

718 *Acute light stimulation*. Ramp (i.e. linearly increasing light power) light stimulation was
719 performed using an Arduino uno (Arduino, Italy) controlled laser system (473 nm / 594
720 nm wavelength, Omicron, Austria) coupled to a 50 µm (4 shank electrodes) or 105 µm (1
721 shank electrodes) diameter light fiber (Thorlabs, NJ, USA) glued to the multisite
722 electrodes, ending 200 µm above the top recording site. Acute stimulations were repeated
723 30 times.

724 ***Electrophysiology and optogenetics in vitro***

725 *Patch-clamp recordings*. Whole-cell patch-clamp recordings were performed from tDimer-
726 negative L2/3 PYRs in the mPFC of P23–25 and P38-40 mice. Under anesthesia, mice
727 were decapitated, brains were removed and sectioned coronally at 300 mm in ice-cold
728 oxygenated high sucrose-based artificial cerebral spinal fluid (ACSF) (in mM: 228

sucrose, 2.5 KCl, 1 NaH2PO4, 26.2 NaHCO3, 11 glucose, 7 MgSO4; 310 mOsm). Slices were incubated in oxygenated ACSF (in mM: 119 NaCl, 2.5 KCl, 1 NaH2PO4, 26.2 NaHCO3, 11 glucose, 1.3 MgSO4; 310 mOsm) at 37°C for 45 min before cooling to room temperature. Slices were superfused with oxygenated ACSF in the recording chamber. Neurons were patched under optical control using pulled borosilicate glass capillaries (tip resistance of 3-7 MΩ) filled with pipette solution (in mM: 130 D-glucononic acid 49-53%, 130 Cesium-OH 50%, 10 HEPES, 0.5 EGTA, 4 Mg-ATP, 0.3 Na2-GTP, 8 NaCl, 5 QX-314-Cl; 285 mOsm, pH 7.3). Data was acquired using PatchMaster (HEKA Elektronik, MA, USA). Capacitance artifacts and series resistance were minimized using the built-in circuitry of the patch-clamp amplifier (EPC 10; HEKA Elektronik, MA, USA). Responses of neurons were digitized at 10 kHz in voltage-clamp mode.

Light stimulation. Square light stimuli of 472 nm wavelength and 1 s duration were delivered with the pE-2 LED system (CoolLED, Andover, UK).

Histology

P5-40 mice were anesthetized with 10% ketamine (aniMedica, Germanry) / 2% xylazine (WDT, Germany) in 0.9% NaCl (10 µg/g body weight, intraperitoneal) and transcardially perfused with 4% paraformaldehyde (Histofix, Carl Roth, Germany). Brains were removed and postfixed in 4% paraformaldehyde for 24 h. Brains were sectioned coronally with a vibratom at 50 µm for immunohistochemistry or 100 µm for examination of dendritic complexity.

Immunohistochemistry. Free-floating slices were permeabilized and blocked with PBS containing 0.8% Triton X-100 (Sigma-Aldrich, MO, USA), 5% normal bovine serum (Jackson Immuno Research, PA, USA) and 0.05% sodium azide. Slices were incubated over night with primary antibody rabbit-anti-Ca2+/calmodulin-dependent protein kinase II (1:200, #PA5-38239, Thermo Fisher, MA, USA; 1:500, #ab52476, Abcam, UK), rabbit-anti-parvalbumin (1:500, #ab11427, Abcam, UK) or rabbit-anti-somatostatin (1:250, #sc13099, Santa Cruz, CA, USA), followed by 2 h incubation with secondary antibody goat-anti-rabbit Alexa Fluor 488 (1:500, #A11008, Invitrogen-Thermo Fisher, MA, USA). Sections were transferred to glass slides and covered with Fluoromount (Sigma-Aldrich, MO, USA).

Cell quantification. Images of immunostainings and IUE-induced tDimer2 expression in the right mPFC were acquired on a confocal microscope (DM IRBE, Leica, Germany) using a 10x objective (numerical aperture 0.3). tDimer2-positive and immunopositive cells were automatically quantified with custom-written algorithms in ImageJ environment. The region of interest (ROI) was manually defined over L2/3 of the mPFC. Image contrast was enhanced before applying a median filter. Local background was subtracted to reduce background noise and images were binarized and segmented using the watershed function. Counting was done after detecting the neurons with the extended maxima function of the MorphoLibJ plugin.

Dendritic complexity. Image stacks of tDimer2-positive neurons were acquired on a confocal microscope (LSN700, Zeiss, Germany) using a 40x objective. Stacks of 6 neurons per animal were acquired as 2048x2048 pixel images (voxel size 156*156*500 nm). Dendritic complexity was quantified by Sholl analysis in ImageJ environment. Images were binarized using auto threshold function and the dendrites were traced using the semi-automatic simple neurite tracer plugin. The geometric center was identified, and the traced dendritic tree was analyzed with the Sholl analysis plugin.

Behavior

Mice were handled and adapted to the investigation room two days prior to behavioral examination. Arenas and objects were cleaned with 0.1% acetic acid before each trial. Animals were tracked online using video Mot2 software (Video Mot2, TSE Systems GmbH, Germany) or offline using the python-based tracking system ezTrack[60].

Developmental milestones. Somatic and reflex development was examined every third day in P2-20 mice. Weight, body length, and tail length were measured. Grasping reflex was assessed by touching front paws with a toothpick. Vibrissa placing was measured as head movement in response to gently touching the vibrissa with a toothpick. Auditory startle was assessed in response to finger snapping. The days of pinnae detachment and eye opening were monitored. Surface righting was measured as time to turn around after being positioned on the back (max 30 s). Cliff avoidance was measured as time until withdrawing after being positioned with forepaws and snout over an elevated edge (max

30 s). Bar holding was measured as time hanging on a toothpick grasped with the forepaws (max 10 s).

Open field. At P16, Mice were positioned in the center of a circular arena (34 cm in diameter) and allowed to explore for 10 min. Behavior was quantified as discrimination index of time spent in the center and the border of the arena ((time in surround - time in center) / (time in surround + time in center)), grooming time, average velocity and number of rearing, wall rearing and jumping.

Object recognition. Novel object recognition (NOR, P17), object location recognition (OLR, P18) and recency recognition (RR, P21) were performed in the same arena as the open field examination. Mouse center, tail and snout position were tracked automatically. Object interaction was defined as the snout being within <1 cm distance from an object. For NOR, each mouse explored two identical objects for 10 min during the sample phase. After a delay period of 5 min in a break box, the mouse was placed back in the arena for the test phase, where one of the objects was replaced by a novel object. Behavior was quantified as discrimination index of time spent interacting with the novel and familiar object ((time novel object - time familiar object) / (time novel object + time familiar object)). OLR was performed similarly, but one object was relocated for the test phase instead of being exchanged. For RR, each mouse explored two identical objects during the first sample phase for 10 min, followed by a delay phase of 30 min, and a second sample phase of 10 min with two novel identical objects. After a second break of 5 min, the interaction time with an object of the first sample phase (old) and an object from the second sample phase (recent) was assessed during the test phase for 2 min. Behavior was quantified as discrimination index of time spent interacting with the novel and familiar object ((time old object – time recent object) / (time old object + time recent object)).

Maternal interaction. Maternal interaction was performed at P21 in the same arena as the open field examination. Two plastic containers were added to the arena, one empty and one containing the dam of the investigated mouse. Small holes in the containers allowed the mouse and the dam to interact. Behavior was quantified as discrimination index of time spent interacting with the empty container and the container containing the dam ((time dam container – time empty container) / (time dam container + time empty container)).

Spatial working memory. At P36-38, mice were positioned in the center of an elevated 8-arm radial maze. 4 arms contained a food pellet at the distal end (baited). On the first day, mice were allowed to examine the maze for 20 min or until all arms were visited. During the following 10 trials (2 trials on day 1 and 4 trials on day 2 and 3), mice were allowed to examine the maze until all baited arms were visited (for max 20 min) and arm entries were assessed. Visit of a non-baited arm was considered as reference memory error, repeated visit of the same arm in one trial as working memory error.

Spontaneous alteration. At P39, each mouse was positioned in the start arm of an elevated Y-maze. Visited arms during free exploration were monitored for 10 min. Percentage of alternations was calculated as (number of alternations / (entries - 2)). The test was used as habituation for delayed non-match-to-sample task.

Delayed non-match-to-sample task. At P39-40, mice were positioned in the start arm of an elevated Y-maze with access to the other arms containing a food pellet. After entering one arm, a central door was closed (sample choice). After the food pellet was consumed the mice were placed in the start arm for a second run (test choice) after a 30 s break. Each mouse performed 6 trials / day. Test choice was considered correct when visiting the arm not explored during sample phase.

Data analysis

Data from in vivo and in vitro recordings were analyzed with custom-written algorithms in Matlab environment. In vivo data were band-pass filtered (500-9000 Hz for spike analysis or 1-100 Hz for LFP) using a third-order Butterworth filter forward and backward to preserve phase information before down-sampling to analyze LFP. For in vitro data, all potentials were corrected for liquid junction potentials (-10 mV). The resting membrane potential was measured immediately after obtaining the whole-cell configuration. To assess input resistance and membrane properties, 600 ms long hyperpolarizing current pulses were applied.

Power spectral density. For power spectral density analysis, 2 s-long windows of LFP signal were concatenated and the power was calculated using Welch's method with non-overlapping windows. Spectra were multiplied with squared frequency.

Imaginary coherence. The imaginary part of complex coherence, which is insensitive to volume conduction, was calculated by taking the absolute value of the imaginary component of the normalized cross-spectrum.

Modulation index. For optogenetic stimulations, modulation index was calculated as (value stimulation - value pre stimulation) / (value stimulation + value pre stimulation).

Peak frequency and strength. Peak frequency and peak strength were calculated for the most prominent peak in the spectrum defined by the product of peak amplitude, peak half width and peak prominence.

Single unit analysis. Single unit activity (SUA) was detected and clustered using klusta[61] and manually curated using phy (https://github.com/cortex-lab/phy). Modulation index of SUA firing rate was calculated on 3 s long windows pre- and during stimulation. Significance level was set at $p<0.01$ and calculated using Wilcoxon signed rank test for zero median for single stimulation trials. Single unit autocorrelation histogram was calculated using 0.5 ms bins followed by frequency spectrum computation using discrete Fourier transform. Oscillation score was calculated by dividing peak magnitude of detected peak frequency by average spectrum magnitude for pre- and during stimulation periods. For pairwise neuronal correlation SUA spike trains were convolved using a gaussian window with a standard deviation of 20 ms. Correlation of convolved spike trains was computed using Spearman's rho. Cumulative distribution functions from before and during stimulations were compared using the two-sample Kolmogorov-Smirnov test. RS and FS units were distinguished by manually setting a threshold based on spike half width and trough-to-peak duration (FS, P11-12 halfwidth<0.31 ms, trough-to-peak<1.28 ms, P23-25 and P38-40 halfwidth<0.31 ms, trough-to-peak<0.64 ms).

EPSCs and IPSCs extraction. Voltage-clamp traces were demeaned and detrended with a median filter (mdefilt1). Traces were then deconvolved using a double exponential kernel using the OASIS toolbox (https://github.com/zhoupc/OASIS_matlab)[62]. After manual optimization of two separate kernels for EPSCs and IPSCs, the software was run with the "foopsi" model and a regularization parameter "lambda" set at the value of 10^{-11}. The parameters "smin" and "b" were automatically optimized, separately for each trace. The

deconvolved traces were then used to compute the integral of EPSCs and IPSCs for baseline and stimulation periods.

Statistics. Statistical analyses were performed in the Matlab environment or in R Statistical Software (Foundation for Statistical Computing, Austria). Data are presented as median ± median absolute deviation (MAD). Data were tested for significant differences (*P<0.05, **P<0.01 and ***P<0.001) using non-parametric Wilcoxon rank sum test for unpaired and Wilcoxon signed rank test for paired data or Kruskal-Wallis test with Bonferroni corrected post hoc analysis or Fisher's exact test for binary data analysis. Nested data were analyzed with linear mixed-effect models with animal as fixed effect and Turkey multi comparison correction for post hoc analysis. See Extended Data Tab. 1 for detailed statistics.

References

1. Frith, C. & Dolan, R. The role of the prefrontal cortex in higher cognitive functions. *Brain Res. Cogn. Brain Res.* **5**, 175–181 (1996).
2. Miller, E. K. The prefrontal cortex and cognitive control. *Nat. Rev. Neurosci.* **1**, 59–65 (2000).
3. van Os, J. & Kapur, S. Schizophrenia. *The Lancet* **374**, 635–645 (2009).
4. Baron-Cohen, S. The cognitive neuroscience of autism. *J. Neurol. Neurosurg. Psychiatry* **75**, 945–948 (2004).
5. Stuchlik, A. & Sumiyoshi, T. Cognitive Deficits in Schizophrenia and Other Neuropsychiatric Disorders: Convergence of Preclinical and Clinical Evidence. *Front. Behav. Neurosci.* **8**, (2014).
6. Clifton, N. E. *et al.* Dynamic expression of genes associated with schizophrenia and bipolar disorder across development. *Transl. Psychiatry* **9**, 1–9 (2019).
7. Sahin, M. & Sur, M. Genes, circuits, and precision therapies for autism and related neurodevelopmental disorders. *Science* **350**, (2015).
8. Marín, O. Developmental timing and critical windows for the treatment of psychiatric disorders. *Nat. Med.* **22**, 1229–1238 (2016).
9. Hall, J., Trent, S., Thomas, K. L., O'Donovan, M. C. & Owen, M. J. Genetic risk for schizophrenia: convergence on synaptic pathways involved in plasticity. *Biol. Psychiatry* **77**, 52–58 (2015).
10. Schmitt, A., Malchow, B., Hasan, A. & Falkai, P. The impact of environmental factors in severe psychiatric disorders. *Front. Neurosci.* **8**, (2014).
11. Geschwind, D. H. Genetics of autism spectrum disorders. *Trends Cogn. Sci.* **15**, 409–416 (2011).
12. Leicht, G. *et al.* EEG-Informed fMRI Reveals a Disturbed Gamma-Band–Specific Network in Subjects at High Risk for Psychosis. *Schizophr. Bull.* **42**, 239–249 (2016).
13. Mikanmaa, E. *et al.* Towards a neurodynamical understanding of the prodrome in schizophrenia. *NeuroImage* **190**, 144–153 (2019).
14. Chini, M. *et al.* Resolving and Rescuing Developmental Miswiring in a Mouse Model of Cognitive Impairment. *Neuron* **105**, 60-74.e7 (2020).
15. Hartung, H. *et al.* From Shortage to Surge: A Developmental Switch in Hippocampal-Prefrontal Coupling in a Gene-Environment Model of Neuropsychiatric Disorders. *Cereb. Cortex N. Y. N 1991* **26**, 4265–4281 (2016).
16. Peixoto, R. T., Wang, W., Croney, D. M., Kozorovitskiy, Y. & Sabatini, B. L. Early hyperactivity and precocious maturation of corticostriatal circuits in Shank3B−/− mice. *Nat. Neurosci.* **19**, 716–724 (2016).
17. Richter, M. *et al.* Altered TAOK2 activity causes autism-related neurodevelopmental and cognitive abnormalities through RhoA signaling. *Mol. Psychiatry* **24**, 1329–1350 (2019).
18. Kirischuk, S. *et al.* Modulation of Neocortical Development by Early Neuronal Activity: Physiology and Pathophysiology. *Front. Cell. Neurosci.* **11**, (2017).

19. Kirkby, L. A., Sack, G. S., Firl, A. & Feller, M. B. A Role for Correlated Spontaneous Activity in the Assembly of Neural Circuits. *Neuron* **80**, 1129–1144 (2013).
20. Katz, L. C. & Shatz, C. J. Synaptic Activity and the Construction of Cortical Circuits. *Science* **274**, 1133–1138 (1996).
21. Blanquie, O. *et al.* Electrical activity controls area-specific expression of neuronal apoptosis in the mouse developing cerebral cortex. *eLife* **6**, e27696 (2017).
22. Brockmann, M. D., Pöschel, B., Cichon, N. & Hanganu-Opatz, I. L. Coupled Oscillations Mediate Directed Interactions between Prefrontal Cortex and Hippocampus of the Neonatal Rat. *Neuron* **71**, 332–347 (2011).
23. Ahlbeck, J., Song, L., Chini, M., Bitzenhofer, S. H. & Hanganu-Opatz, I. L. Glutamatergic drive along the septo-temporal axis of hippocampus boosts prelimbic oscillations in the neonatal mouse. *eLife* **7**, (2018).
24. Janiesch, P. C., Krüger, H.-S., Pöschel, B. & Hanganu-Opatz, I. L. Cholinergic control in developing prefrontal-hippocampal networks. *J. Neurosci. Off. J. Soc. Neurosci.* **31**, 17955–17970 (2011).
25. Hartung, H., Brockmann, M. D., Pöschel, B., De Feo, V. & Hanganu-Opatz, I. L. Thalamic and Entorhinal Network Activity Differently Modulates the Functional Development of Prefrontal-Hippocampal Interactions. *J. Neurosci. Off. J. Soc. Neurosci.* **36**, 3676–3690 (2016).
26. Bitzenhofer, S. H. *et al.* Layer-specific optogenetic activation of pyramidal neurons causes beta-gamma entrainment of neonatal networks. *Nat. Commun.* **8**, 14563 (2017).
27. Bitzenhofer, S. H., Sieben, K., Siebert, K. D., Spehr, M. & Hanganu-Opatz, I. L. Oscillatory activity in developing prefrontal networks results from theta-gamma-modulated synaptic inputs. *Cell Rep.* **11**, 486–497 (2015).
28. Workman, A. D., Charvet, C. J., Clancy, B., Darlington, R. B. & Finlay, B. L. Modeling transformations of neurodevelopmental sequences across mammalian species. *J. Neurosci. Off. J. Soc. Neurosci.* **33**, 7368–7383 (2013).
29. Lim, L., Mi, D., Llorca, A. & Marín, O. Development and functional diversification of cortical interneurons. *Neuron* **100**, 294–313 (2018).
30. Anastasiades, P. G. & Butt, S. J. B. A Role for Silent Synapses in the Development of the Pathway from Layer 2/3 to 5 Pyramidal Cells in the Neocortex. *J. Neurosci.* **32**, 13085–13099 (2012).
31. Bitzenhofer, S. H., Ahlbeck, J. & Hanganu-Opatz, I. L. Methodological Approach for Optogenetic Manipulation of Neonatal Neuronal Networks. *Front. Cell. Neurosci.* **11**, 239 (2017).
32. Lindemann, C., Ahlbeck, J., Bitzenhofer, S. H. & Hanganu-Opatz, I. L. Spindle Activity Orchestrates Plasticity during Development and Sleep. *Neural Plast.* **2016**, 5787423 (2016).
33. Le Roy, I., Carlier, M. & Roubertoux, P. L. Sensory and motor development in mice: genes, environment and their interactions. *Behav. Brain Res.* **125**, 57–64 (2001).
34. Barker, G. R. I. & Warburton, E. C. When Is the Hippocampus Involved in Recognition Memory? *J. Neurosci.* **31**, 10721–10731 (2011).

35. Bitzenhofer, S. H., Poepplau, J. A. & Hanganu-Opatz, I. L. Gamma activity accelerates during prefrontal development. *bioRxiv* 2020.03.10.986281 (2020) doi:10.1101/2020.03.10.986281.
36. Chen, G. *et al.* Distinct Inhibitory Circuits Orchestrate Cortical beta and gamma Band Oscillations. *Neuron* **96**, 1403-1418.e6 (2017).
37. Atallah, B. V. & Scanziani, M. Instantaneous modulation of gamma oscillation frequency by balancing excitation with inhibition. *Neuron* **62**, 566–577 (2009).
38. Wong, F. K. *et al.* Pyramidal cell regulation of interneuron survival sculpts cortical networks. *Nature* **557**, 668–673 (2018).
39. Cardin, J. A. *et al.* Driving fast-spiking cells induces gamma rhythm and controls sensory responses. *Nature* **459**, 663–667 (2009).
40. Pfeffer, C. K., Xue, M., He, M., Huang, Z. J. & Scanziani, M. Inhibition of Inhibition in Visual Cortex: The Logic of Connections Between Molecularly Distinct Interneurons. *Nat. Neurosci.* **16**, 1068–1076 (2013).
41. Clause, A. *et al.* The precise temporal pattern of prehearing spontaneous activity is necessary for tonotopic map refinement. *Neuron* **82**, 822–835 (2014).
42. Huberman, A. D., Speer, C. M. & Chapman, B. Spontaneous retinal activity mediates development of ocular dominance columns and binocular receptive fields in v1. *Neuron* **52**, 247–254 (2006).
43. Iyer, K. K. *et al.* Cortical burst dynamics predict clinical outcome early in extremely preterm infants. *Brain J. Neurol.* **138**, 2206–2218 (2015).
44. Robertson, C. E. & Baron-Cohen, S. Sensory perception in autism. *Nat. Rev. Neurosci.* **18**, 671–684 (2017).
45. Khazipov, R. *et al.* Early motor activity drives spindle bursts in the developing somatosensory cortex. *Nature* **432**, 758–761 (2004).
46. Hanganu, I. L., Ben-Ari, Y. & Khazipov, R. Retinal Waves Trigger Spindle Bursts in the Neonatal Rat Visual Cortex. *J. Neurosci.* **26**, 6728–6736 (2006).
47. Hoerder-Suabedissen, A. & Molnár, Z. Development, evolution and pathology of neocortical subplate neurons. *Nat. Rev. Neurosci.* **16**, 133–146 (2015).
48. Wayman, G. A. *et al.* Activity-Dependent Dendritic Arborization Mediated by CaM-Kinase I Activation and Enhanced CREB-Dependent Transcription of Wnt-2. *Neuron* **50**, 897–909 (2006).
49. Courchesne, E. Brain development in autism: early overgrowth followed by premature arrest of growth. *Ment. Retard. Dev. Disabil. Res. Rev.* **10**, 106–111 (2004).
50. Denaxa, M. *et al.* Modulation of Apoptosis Controls Inhibitory Interneuron Number in the Cortex. *Cell Rep.* **22**, 1710–1721 (2018).
51. Cho, K. K. A. *et al.* Gamma Rhythms Link Prefrontal Interneuron Dysfunction with Cognitive Inflexibility in Dlx5/6+/− Mice. *Neuron* **85**, 1332–1343 (2015).

52. Bastos, A. M., Loonis, R., Kornblith, S., Lundqvist, M. & Miller, E. K. Laminar recordings in frontal cortex suggest distinct layers for maintenance and control of working memory. *Proc. Natl. Acad. Sci.* **115**, 1117–1122 (2018).
53. Sohal, V. S. & Rubenstein, J. L. R. Excitation-inhibition balance as a framework for investigating mechanisms in neuropsychiatric disorders. *Mol. Psychiatry* **24**, 1248–1257 (2019).
54. Uhlhaas, P. J. & Singer, W. Abnormal neural oscillations and synchrony in schizophrenia. *Nat. Rev. Neurosci.* **11**, 100–113 (2010).
55. Gallinat, J., Winterer, G., Herrmann, C. S. & Senkowski, D. Reduced oscillatory gamma-band responses in unmedicated schizophrenic patients indicate impaired frontal network processing. *Clin. Neurophysiol. Off. J. Int. Fed. Clin. Neurophysiol.* **115**, 1863–1874 (2004).
56. Altimier, L. & Phillips, R. The Neonatal Integrative Developmental Care Model: Advanced Clinical Applications of the Seven Core Measures for Neuroprotective Family-centered Developmental Care. *Newborn Infant Nurs. Rev.* **16**, 230–244 (2016).
57. Moiseev, A., Doesburg, S. M., Herdman, A. T., Ribary, U. & Grunau, R. E. Altered Network Oscillations and Functional Connectivity Dynamics in Children Born Very Preterm. *Brain Topogr.* **28**, 726–745 (2015).
58. Als, H. *et al.* Early experience alters brain function and structure. *Pediatrics* **113**, 846–857 (2004).
59. Taylor, H. G. & Clark, C. A. C. Executive function in children born preterm: Risk factors and implications for outcome. *Semin. Perinatol.* **40**, 520–529 (2016).
60. Pennington, Z. T. *et al.* ezTrack: An open-source video analysis pipeline for the investigation of animal behavior. *Sci. Rep.* **9**, 1–11 (2019).
61. Rossant, C. *et al.* Spike sorting for large, dense electrode arrays. *Nat. Neurosci.* **19**, 634–641 (2016).
62. Friedrich, J., Zhou, P. & Paninski, L. Fast online deconvolution of calcium imaging data. *PLOS Comput. Biol.* **13**, e1005423 (2017).

2.6 Prefrontal Cortex Development in Health and Disease: Lessons from Rodents and Humans

Mattia Chini and Ileana L. Hanganu-Opatz

Trends in Neurosciences 2020; DOI: https://doi.org/10.1016/j.tins.2020.10.017

Personal contribution

I helped conceptualizing the review. I wrote the original draft, reviewed and edited the manuscript.

Trends in Neurosciences

CellPress OPEN ACCESS

Review

Prefrontal Cortex Development in Health and Disease: Lessons from Rodents and Humans

Mattia Chini[1,*] and Ileana L. Hanganu-Opatz[1,*]

The role of the prefrontal cortex (PFC) takes center stage among unanswered questions in modern neuroscience. The PFC has a Janus-faced nature: it enables sophisticated cognitive and social abilities that reach their maximum expression in humans, yet it underlies some of the devastating symptoms of psychiatric disorders. Accordingly, appropriate prefrontal development is crucial for many high-order cognitive abilities and dysregulation of this process has been linked to various neuropsychiatric diseases. Reviewing recent advances in the field, with a primary focus on rodents and humans, we highlight why, despite differences across species, a cross-species approach is a fruitful strategy for understanding prefrontal development. We briefly review the developmental contribution of molecules and extensively discuss how electrical activity controls the early maturation and wiring of prefrontal areas, as well as the emergence and refinement of input–output circuitry involved in cognitive processing. Finally, we highlight the mechanisms of developmental dysfunction and their relevance for psychiatric disorders.

PFC: A Cognitive Hub across Mammalian Species

Our successful survival in a permanently changing environment would not be possible without the ability to store and update new evidence, (re-)evaluate our choices, and make decisions. This ability to adapt according to the situation is a product of the cognitive flexibility of our minds. It depends on low-level sensory and motor processes being internally coordinated and endowing the brain with the capacity to adapt internal goals and act accordingly. It is widely thought that such processes involve a neural circuitry that extends over much of the brain, yet it is commonly held that the PFC, the cortical region of the anterior pole of the mammalian brain, is a critical hub. The PFC not only is involved in emotional and social behavior, but provides executive 'top-down' control when behavior is guided by internal states or goals [1]. Accordingly, it is involved in a series of cognitive processes such as attention, salience detection, **working memory** (see Glossary), and inhibitory control, all having as final output the ability to adapt to various conditions and switch between tasks [1].

Despite a wealth of studies, a clear-cut, widely accepted and species-independent definition of the PFC is still lacking [2–4]. Traditionally, **structural** and **functional homology** are used as a basis for brain area classification across species. This enables knowledge to be gained from one species, usually more amenable to invasive interventions, and transferred to other, less-accessible ones, such as humans. The unique relative size, connectivity patterns, parcellation, migration pathways, and layer structure of the human PFC [1,2,5,6] hamper a direct cross-species comparison based on structural homology. Thus, functional homology might be a more fruitful approach for translating PFC studies [7]. For example, while the agranular medial PFC of rats and mice, which is the focus in this review, is not the anatomical equivalent of the primate and human dorsolateral PFC [8], it underlies the same kind of processes (e.g., working memory, decision-making, attention). It can thus be considered its functional homolog [3].

Highlights

The prefrontal cortex (PFC) comprises a conglomeration of brain areas with a largely heterogeneous cross-species anatomical definition that accounts for numerous cognitive abilities.

Abnormal structure and function of the PFC is linked to lower performance in various cognitive domains and is associated with several neuropsychiatric diseases.

Prefrontal development, while protracted compared with sensory cortices, is similarly controlled by molecular cues that set the proliferation, migration, differentiation, and eventual boundaries of prefrontal neurons.

During development, under the driving force of the hippocampus and thalamic nuclei, prefrontal circuits start to generate characteristic patterns of coordinated electrical activity that dynamically change with age in their cellular mechanisms, spectral structure, and synchrony.

Patterns of electrical activity and connectivity underlie the reorganization of prefrontal areas in line with the maturation of cognitive abilities, such as working memory and decision making.

Miswiring of prefrontal areas, resulting from genetic factors or environmental stressors acting during development, can contribute to cognitive impairment in psychiatric disorders.

[1]Institute of Developmental Neurophysiology, Center for Molecular Neurobiology, University Medical Center Hamburg-Eppendorf, 20246 Hamburg, Germany

*Correspondence:
mattia.chini@zmnh.uni-hamburg.de (M. Chini) and
hangop@zmnh.uni-hamburg.de (I.L. Hanganu-Opatz).

While some of the PFC-dependent abilities listed earlier are typically thought of as exquisitely human, many also exist in a basic form in rodents, although rodents clearly do not have the behavioral complexity or finesse that is characteristic of humans. However, to a certain extent, most mammals adapt and develop flexible strategies to thrive in their environment. The topic of cross-species comparison of the PFC has been reviewed in detail elsewhere [2]. As an additional note, it is worth mentioning that modern transcriptomic approaches might also prove to be insightful for this aim, especially in the context of neural development [9].

In contrast to sensory and motor performance, most cognitive abilities that have been assigned to prefrontal areas emerge late in life in all mammalian species. Correspondingly, it has been proposed that prefrontal areas, at least in some aspects, have a protracted development compared with sensory and motor cortices [10,11]. Abundant knowledge on the structural maturation of the PFC in rodents, monkeys, and humans has been accumulated over decades. By contrast, the picture on the functional development remains patchy and substantial gaps persist, especially for early ages. Technical and ethical difficulties related to pre- and perinatal human investigations might account for part of these gaps (Box 1). While rodents are an **altricial species**, that is relatively easily accessible already at a developmental stage that generally corresponds to human fetal development, it is difficult to relate and translate the timing of neurodevelopmental events in prefrontal areas across species. Some of these events are protracted in humans compared with rodents, and humans and rodents vary considerably in their maturational trajectory (Figure 1). Despite all these obstacles, attempts to uncover the developmental mechanisms of prefrontal function have been emerging in recent years [12,13]. Even if still far from the ultimate goal of direct application of knowledge on prefrontal maturation from animal models to questions about human development, these studies are of high value in elaborating research hypotheses, especially regarding neurodevelopmental diseases.

Here, we review recent advances on the development of prefrontal architecture and function in rodents and humans. Rodents are particularly amenable to early investigation and genetic interventions that have been proven to provide deep insights into circuit wiring. We will review findings

Box 1. Measures for Monitoring Brain Function during Development in Rodents and Humans

The functional properties of the developing brain have been studied with different methodologies leading to different readout measures. One of these measures is brain oscillations, assessed via intra- or extracranial recordings yielding LFP and EEG signal, respectively. These two signals are thought of as mostly being the product of the summation of postsynaptic currents derived from hundreds (LFP) to millions (EEG) of nearby neurons [131]. Brain oscillations are an important functional readout of brain activity, not only because they are readily available in both animal models and humans, but also because they are thought to represent the coordinated activity of neuronal ensembles and, potentially, specific microcircuit configurations [131,132]. While certain aspects of the relationship between EEG and LFP remain not well understood, the main difference between the two is that the EEG signal is spatiotemporally smoother. The EEG signal is thought to be mostly influenced by electrical currents in the apical dendrites of layer V cortical pyramidal neurons and conveys limited information on deep-brain oscillations [131]. To this end, particularly for human studies, the blood-oxygen level-dependent (BOLD) signal obtained with functional MRI (fMRI) is a complementary measure. The BOLD signal is indirectly related to neuronal activity, as it reflects local changes in blood flow [133,134]. It has a poor temporal resolution (on the order of seconds), but allows sampling of deep brain structures. While the relationship between BOLD and EEG/LFP is complex and still debated, BOLD is thought to be correlated with EEG/LFP gamma activity [133,134] and, importantly for developmental studies, with infraslow (<1 Hz) neuronal oscillations [135]. Acquisition of fMRI data during early development, however, is limited, as it usually requires the subject to stay immobile for an extended period of time. Another readout measure of early brain function in animal models is single-neuron activity that is monitored using single-unit activity (SUA) recordings or calcium indicators coupled with multiphoton microscopy. SUA is readily coupled to LFP acquisition. It has submillisecond temporal resolution and provides direct access to what is thought to be the fundamental unit of brain computation [136]. On the flipside, SUA is biased towards detecting action potentials of large neurons with a high firing rate, which leads to a low yield in the low-firing-rate regime of the developing brain. Calcium imaging, conversely, indirectly samples action potentials via their nonlinear effect on intracellular calcium concentration. It has poorer temporal resolution (hundreds of milliseconds to seconds) than SUA recordings and not always allows the detection of single action potentials under behaviorally relevant conditions [136]. However, calcium imaging has superior spatial resolution and allows the sampling of larger numbers of neurons simultaneously as well as easier characterization of specific neuronal (sub)populations [136].

Glossary

Adolescence: the period following the onset of puberty that ends with the transition into adulthood. In humans this roughly corresponds to 11–18 years of age and in mice to 20–40 days of age.
Altricial species: a species that is born in an underdeveloped state.
Functional homology: similarity of functions subserved by brain areas of different taxa.
Local field potential (LFP): electrical field potential that is recorded by intracranial electrodes and is thought to represent the temporal and spatial summation of local postsynaptic potentials.
Molecular cues: gradients of molecules that direct the early steps of the formation, migration, and differentiation of neurons.
Neonatal mouse: mouse in the first stages of post-birth development. The term is generally used for mice that are younger than 10–12 days of age.
Network oscillations: repetitive LFP or EEG patterns of activity that derive from the synchronous activity of local neuronal populations.
Parvalbumin interneurons: a class of inhibitory neurons that is particularly abundant in cortical areas towards the brain's posterior pole and that preferentially targets the soma or axon initial segment of pyramidal neurons and other parvalbumin interneurons.
Sharp-wave ripples: highly synchronous neuronal firing events that occur primarily in the CA1 area of the hippocampus mostly during consummatory behavior and that have been implicated in memory consolidation.
Somatostatin interneurons: a class of inhibitory neurons that is particularly abundant in cortical areas towards the brain's frontal pole and that preferentially targets the dendrites of pyramidal neurons and parvalbumin interneurons.
Structural homology: similarity of input/output connectivity and parcellation between brain areas of different taxa.
Subplate: a transient layer of neurons in the cortex of placental mammals that emerges early during development and resides underneath the cortical plate. It facilitates the ingrowth of afferents and efferents. In humans, it appears at GW 5–6 and disappears around GW 40 (but persists up to 2 years of age in the PFC). In rodents, it persists as layer Vib.

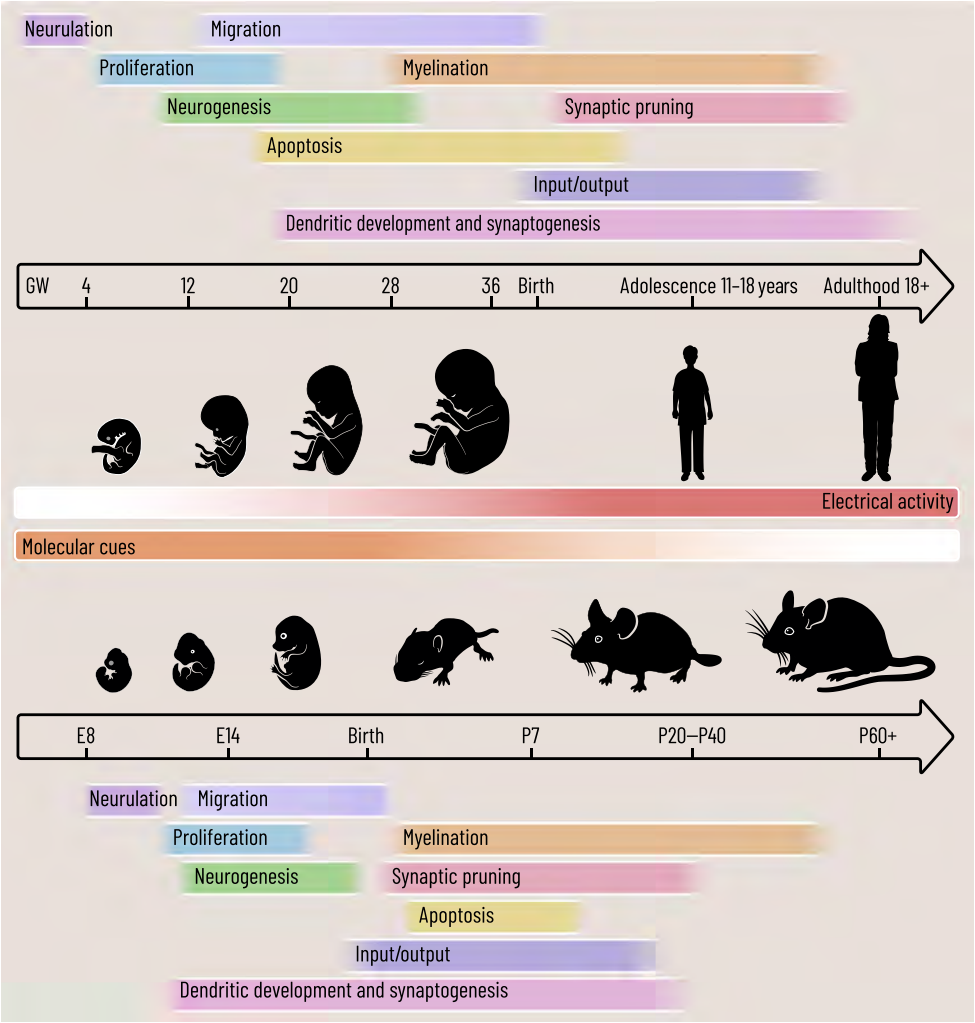

Figure 1. Schematic Representation of the Processes Guiding Human and Rodent Prefrontal Development.
The development of the PFC, its local structure, and its input/output connectivity largely follows the same maturational steps in humans and mice. It is initially guided by molecular cues, whose importance declines with age, while the relevance of electrical activity increases throughout development. While the overall development is similar in the two species, individual processes occur at different relative time points and with different time courses. Not only are mice born at a more premature state but, even when accounting for this, synaptogenesis, as an example, is less protracted than in humans, and synaptic pruning occurs at an earlier stage. Abbreviations: E, embryonic day; GW, gestational week; P, postnatal day.

Supra/infragranular layers: cortical layers that reside above (layers II/III) or below (layers V/VI) the granular layer of the cerebral cortex (layer IV).
Synaptic pruning: a process of excessive synapse removal by glial cells such as microglia and astrocytes.
Topographic organization: arrangement of neurons according to sensory receptors (e.g., retinotopic organization of the retina, tonotopic organization of the cochlea) or skeletal muscles (e.g., somatotopic organization of the primary motor cortex).
Working memory: cognitive ability that relies on short-term memory and allows the processing of information that is only temporarily stored.

uncovering the structural and functional development of the PFC in relationship to cognitive maturation. Functional assessment mainly but not exclusively relies on the investigation of **network oscillations**. Being aware of the aforementioned cross-species translation pitfalls, we will discuss the mechanisms of disrupted development and their possible implications for disease.

Molecular Control of Prefrontal Development

Mammals share a similar sequence of developmental events culminating in the formation of the neocortex. In both rodents and humans, the initial processes, including neurulation, proliferation, migration, and differentiation, are mostly under the control of genetic cues, whereas the later events, such as dendritic, synapse, and afferent–efferent development and refinement, are

considered to be largely controlled by electrical activity. However, molecules and activity not only temporally overlap in shaping cortical development but also interact with each other during this process [14,15].

Neocortical maturation starts at about day 16 of gestation in humans [16] and embryonic day (E) 7 in rodents, with neurulation followed by regional specification and expansion of the PFC. The process is controlled by intrinsic transcription factors and extrinsic growth factors that tightly interact to delimit the prefrontal boundaries [17]. Once the neural tube is formed, at around 5 weeks of gestation in humans and E10 in rodents, neurons destined to form the neocortex are born as neuroblasts. Their proliferation is a long-lasting process with an area-specific dynamic that generally peaks between 6 and 18 weeks gestation in humans [18] and E10 and E15 in rodents [19]. Excitatory neurons are generated from apical progenitors located in the ventricular zone as result of a complex interplay of cell-autonomous mechanisms and local and long-range environmental cues [20,21]. Towards the end of the neurogenic period, glial cells are generated [22]. Similar to other neocortical areas, the PFC expands and the generated neurons migrate under the influence of Fgfs radially (for glutamatergic pyramidal neurons) and of Dlx and Gad1 tangentially (for GABAergic interneurons) [23,24]. Initially [gestational week (GW) 10–12 in humans and E11–E12 in rodents], the PFC comprises the marginal zone, the cortical plate, and the **subplate**, a transiently expressed layer of heterogeneous neurons located at the border with white matter [25]. In the human PFC, the subplate is the thickest layer at GW 17–25. It persists longer (i.e., 6–12 months after birth in humans) than in the primary sensory cortices and it has been hypothesized to have a critical role in the development of prefrontal circuitry [26]. The migrating cortical neurons build the layers in an 'inside-out' spatial–temporal pattern with the earliest born neurons forming deep layers and later-born neurons embedded in upper layers [27]. The migration of prefrontal neurons is controlled by many signaling pathways that are largely common to all neocortical areas and have been reviewed elsewhere [24].

Once the neurons reach their final destination (in humans around birth to the end of the first year; in rodents at the first to second postnatal week), their axons extend and the dendrites arborize to enable the assembly of prefrontal circuits. Growth cones of developing axons are instructed by guidance molecules, such as semaphorins, to reach their targets. Subsequently, synaptic contact formation is mediated by adhesion molecules [28]. Further, genes such as Reln have been reported to control the synaptogenesis of prefrontal pyramidal neurons [29], whereas Erbb4 regulates dendritic spine formation on prefrontal interneurons [30]. During this period, overproduction of synaptic contacts and wiring occur, but synaptic density peaks relatively late in the PFC (2–4 years of age in humans and after the fourth postnatal week in rodents) compared with sensory cortices [18,31,32]. Newly established connections are highly dynamic and refined as development advances. In the PFC, this process extends until **adolescence** [~16 years in humans, postnatal day (P) 20–40 in rodents], and in humans, particularly in layer III, it leads to the most dramatic and long-lasting decrease of synaptic density [25,33,34]. While **molecular cues**, such as semaphorins, Cdk5/p35, Disc1, and Dcc, modulate to a certain extent the pruning of branches [35], the refinement of connectivity is considered to be mainly controlled by electrical activity (see next section).

The molecular orchestration of early developmental processes in prefrontal areas is prone to disruption that, despite efficient compensatory mechanisms, might lead to abnormal function and, ultimately, cognitive impairments. The molecular underpinnings and downstream pathways of prefrontal development as well as their disruption in neuropsychiatric disorders have been recently reviewed [36,37].

Early Patterns of Electrical Activity in the PFC

During the developmental time window of decreasing influence of molecular cues and increasing influence of electrical activity, the neocortex generates patterns of electrical activity with unique features (Box 2). Knowledge on the early electrical activity of the PFC is rather recent and considerably sparser than that available for sensory cortices and the hippocampus.

Topographically organized sensory cortices display spontaneous patters of activity with highly stereotypical motifs [38–40], but such network-level descriptions of early prefrontal activity remain largely elusive. However, recent studies in **neonatal mice**, conducted with and without anesthesia (Box 3), identified transient bouts of beta–low-gamma rhythmic oscillations as an early prefrontal activity signature with important functional correlates [12,41,42]. This activity is generated by pyramidal neurons residing in **supragranular layers** of the PFC ($PYRs_{II/III}$) [41,43,44], is elicited by light activation of $PYRs_{II/III}$, and occurs naturally in response to incoming stimuli from the hippocampus [12,45]. Unpublished results from our group suggest that this oscillatory motif persists and evolves smoothly from the first postnatal week throughout adulthood, gradually becoming longer, faster (the average frequency increases from ~15 Hz up to ~50 Hz), and of higher amplitude [44]. This maturation parallels and might be caused by the unfolding of inhibitory feedback [44] (Figure 2). Similar to other neocortical areas, inhibition shifts from an early environment in which **somatostatin interneurons** dominate the GABAergic landscape, to one in which **parvalbumin interneurons** progressively gain relevance ([46,47] but see also [48]). Across the first 3 postnatal weeks, the strength of somatostatin-to-pyramidal neuron synapses decreases, whereas the opposite occurs for parvalbumin interneurons [46]. Of note, early bouts of gamma activity are also present in the rodent barrel [49] and visual [50,51] cortices, but distinct mechanisms underlie their generation.

While it remains unclear what kind of information (if any) is carried by early prefrontal activity or the extent to which it serves as a functional output source for downstream areas, its relevance for the refinement of prefrontal circuits and behavior has been highlighted by a number of recent studies. In developmental mouse models of mental disorders, beta–gamma prefrontal oscillations are impaired from the first postnatal days up to adulthood, leading to cognitive deficits [42,52]. Severely

Box 2. General Features of Early Brain Activity

Brain activity in the developing brain has several unique functional properties. The most directly observable is the alternation between long periods of electrical silence (i.e., an isoelectric LFP/EGG trace and the almost complete absence of spiking) and sporadic bursts of activity. In the EEG literature, this phenomenon takes the name *tracé discontinu*. Such isoelectric electrical traces are unparalleled in the healthy adult brain, as they are indicative of *bona fide* neuronal silence and not, for instance, uncorrelated neuronal activity. This unique property of immature brain activity appears to be a brain-wide phenomenon and has been described not only in human newborns and preterm babies [137] but also in other species that are phylogenetically far apart such as rodents [138] and fishes [139].

Rodent studies have shown that, at birth, these waves of activity travel in the occipitofrontal direction [140]. Transient bursts of activity have been particularly well characterized along sensory pathways according to their frequency (i.e., the number of deflections occurring in 1 s), amplitude (i.e., the magnitude of deflections), and power (i.e., the oscillatory amplitude at a defined frequency and during a defined temporal window). The oscillatory bursts have been shown to share some characteristic features: they organize neuronal firing in the infraslow timescale [141]; they are subplate and acetylcholine dependent [38]; they are periphery driven but develop before the sensory pathway is mature [39,40,50,51]; and they become longer [142–144], less correlated [48,142,143], and more periphery independent as the brain matures [145,146]. These early patterns of spontaneous activity in brain sensory areas have been shown to be homeostatically regulated [40] and to instruct the further development of adult sensory activity [39]. While it remains a matter of debate whether they carry any sensory information (see [146,147] for one perspective and [138,148] for the other), their disruption is detrimental to the development of sensory perception [149,150] and local circuitry [151]. The exact way in which early activity influences adult sensory perception is still debated. It has been hypothesized that spontaneous activity might present the specific brain area with activity statistics that are similar to those that it will be exposed to once it is fully developed [139]. From a predictive coding perspective, this would be akin to serving the role of providing the correct priors.

Box 3. Anesthesia in the Developing Brain

Anesthesia is a behavioral state that is characterized by loss of consciousness, retrograde amnesia, immobility, and analgesia. Its neuronal correlates in the adult brain have long been characterized. With few exceptions (e.g., when ketamine is the main anesthetic), anesthesia induces a dramatic change in the dominant brain dynamics that are picked up by scalp EEG (mostly cortical activity). While during wakefulness low-amplitude and high-frequency oscillations prevail in the EEG signal, anesthesia shifts the regime towards slower oscillations of higher amplitude [152]. This phenomenon is so robust that it underlies the most common strategies used to monitor anesthesia depth during surgery [153]. Several of the pioneering studies on early brain activity, especially in rodents, were conducted under anesthesia. One might therefore ask to what extent such results are representative of what occurs in the non-anaesthetized brain. Anesthesia's effect on the immature brain is strikingly different from the adult case. In rodents, until the beginning of the second postnatal week, rather than slowing the dominant cortical rhythm, anesthesia enhances the discontinuity of the signal, leaving most of its spectral/dynamical properties relatively untouched [154]. Anesthetics increase the naturally occurring periods of electrical silence in several cortical and subcortical regions in a dose-dependent manner [154]. This is accompanied by a global decrease in firing rate and broadband suppression of LFP power that leaves the ratio of fast:slow oscillations relatively unaffected [154]. Similar findings have also been reported from scalp EEG recordings in humans of roughly equivalent age (i.e., preterm or newborn babies) [154,155]. The lack of frequency-specific effects of anesthesia on the immature brain is in stark contrast to what occurs in the adult brain and is thought to underlie the particularly poor performance of EEG-based anesthesia-depth monitoring methods in newborn babies [156]. In rodents, anesthesia begins to favor slow oscillations at the expense of faster ones around P12 [144], when activity starts to be continuous [144] and slow waves during sleep emerge [157]. In babies, such a shift occurs around 4 months of age, when anesthesia starts to induce theta and alpha oscillatory activity [158]. Of note, the age-dependent differences in how anesthesia impacts the brain somewhat resemble those of developmental changes in sleep patterns. At adulthood, deep non-rapid eye movement (REM) sleep favors slow and delta waves over faster frequencies [159]. By contrast, in preterm babies and in rats of less than 2 weeks of age, sleep increases signal discontinuity [160].

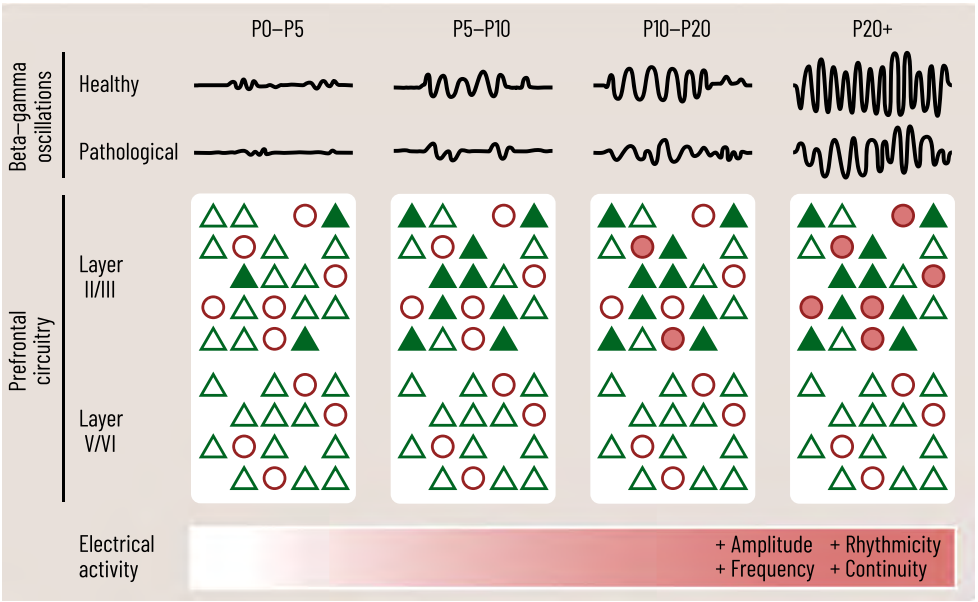

Figure 2. Schematic Representation of the Development of Beta–Gamma Prefrontal Oscillations in Health and Disease. Developmental time windows (top) refer to mice, indicated as postnatal days. Bouts of beta–gamma oscillations are one of the hallmarks of early prefrontal activity. In mice, they are mainly generated by layer II/III pyramidal neurons. In the first stages of development, when brain activity is highly discontinuous, these oscillations are slow (~15 Hz), have low amplitude, and are mostly bolstered by pyramidal neurons. As brain activity gradually becomes continuous and inhibition takes on a larger role, prefrontal oscillations increase in amplitude and frequency (~50 Hz). In mouse models of mental disorders that are often characterized by deficits in layer II/III pyramidal neurons, these rhythms are impaired throughout life, in a manner that is predictive of later-emerging cognitive deficits. In mouse models of schizophrenia, this impairment occurs in the form of beta–low-gamma oscillations of smaller amplitude and a more fragmented nature. Green triangles and red circles represent pyramidal and inhibitory neurons, respectively. Filled shapes depict neurons that are thought to actively participate in the generation of beta–gamma oscillations. Abbreviation: P, postnatal day.

simplified dendritic arborization as well as decreased spine density and firing rate of $PYRs_{II/III}$ underlies these abnormalities [31,42]. Further, selective disruption of this neuronal population recapitulates the phenotype of a pan-pyramidal neuron genetic mutation [52,53]. Intriguingly, excessive microglial pruning has been suggested as being upstream of these deficits [31,42]. It is therefore tempting to speculate that the interplay between activity and microglial phagocytosis might be one of the mechanisms through which early activity sculpts the developing prefrontal circuits. If reduced early $PYRs_{II/III}$ activity is deleterious, the opposite effect is equally detrimental. Unpublished results from our group suggest, for instance, that a protracted but subtle increase of $PYRs_{II/III}$ firing across the first two postnatal weeks results in long-term prefrontal microcircuit disruption and an excitation/inhibition (E/I) imbalance that worsens over time, equally leading to cognitive and social deficits [43]. Similar deficits have also been described in mouse models of autism spectrum disorder, which are characterized by increased prefrontal activity [54–56]. Another important piece of the puzzle is the role of inhibitory neurons in prefrontal development. Sparse experimental evidence suggests that developmental ablation of NMDA receptors on corticolimbic interneurons or disruption of MGE-derived interneurons results in altered prefrontal gamma activity [57,58].

Such a level of definition is difficult to attain in human studies. However, electroencephalography (EEG) recordings revealed patterns of coordinated activity in newborns and premature babies (Box 2). For example, early prefrontal activity and connectivity within the frontal networks of premature babies are reduced and relate to individual neurological performance [59,60]. Moreover, delayed maturation of prefrontal activity patterns has been shown to predict impaired behavioral abilities [61]. From the disease perspective, at adulthood, altered prefrontal activity in the gamma band is a robust biomarker for cognitive deficits in mental disorders [62,63]. Reduced spine density of layer III pyramidal neurons in schizophrenia patients has been proposed as an underlying disease mechanism [64]. Thus, converging evidence highlights the impact that $PYRs_{II/III}$ and early fast prefrontal activity have on the refinement of the prefrontal circuitry and the behavioral functions it subserves. Further studies are needed to uncover whether and how processes described in rodents relate to human circuit development.

Input–Output Circuitry of the Developing PFC

The functional maturation of the PFC during early stages of development is driven by other cortical and subcortical regions. Among them, the hippocampal, thalamic, ventral tegmental area (VTA), and striatal projections play critical roles.

Hippocampus

The hippocampus not only generates patterns of coordinated activity before the PFC but also critically contributes to its functional maturation [12,45]. In rodents, starting from the first postnatal days, distinct activity patterns characterize the hippocampal **local field potential (LFP)**. The most prominent are **sharp-wave ripple** events, which dominate hippocampal activity in the first postnatal week [65]. These hippocampal events are preceded by bursts of synchronous firing occurring in the entorhinal cortex, which, in turn, seem to be triggered by myoclonic movements [66]. Another hippocampal pattern is the network oscillations, whose dominant frequency ranges from theta to the beta–low-gamma range [12,45,65]. They organize single-unit firing around 8 Hz [52] and are driven by sensory [67] and motor [68] signals.

Already at neonatal age, the CA1 area of the intermediate and ventral hippocampus [45] represents a major source of glutamatergic input for the developing PFC [12,45,69]. Sharp waves induce a strong and long-lasting increase in prefrontal firing and a broadband increment of LFP power in neonatal mice [45]. Hippocampal theta bursts are relayed via monosynaptic axonal

projections to the deeper layers of PFC, where they boost intracortical coupling and the emergence of prefrontal oscillatory rhythms [12,45].

Disruption of hippocampal inputs to the PFC has life-long consequences for cognitive performance. Poorer working memory in schizophrenia patients and mouse models has been related to abnormal prefrontal–hippocampal communication [70,71]. This dysfunction emerges early in life and persists throughout the entire development, switching from insufficient to excessive hippocampal drive [52,72,73]. Correspondingly, developmental rescue of prefrontal–hippocampal communication in a mouse model of mental illness restores working memory deficits [74].

While probing the functionality of the hippocampal–prefrontal pathway in human babies is challenging, a study on newborns reported a temporal–frontal gradient in brain communication and maturation that might represent a functional equivalent of early rodent hippocampus–PFC synchrony [75]. Further, connectivity between the PFC and temporal areas is impaired in infants carrying mutations that predispose to mental disorders [76,77].

Striatum

The PFC is involved in the formation of corticostriatal circuits that are relevant for motor skill acquisition, action selection, and planning. Already in the first postnatal week, the connectivity between the mouse neocortex and striatum is established, including a direct monosynaptic afferent pathway and indirect efferents via the mediodorsal thalamus (MD) [78]. This connectivity shapes striatal development and synaptogenesis [79]. The striatum is particularly sensitive to cortical inputs early in life, and this responsiveness decreases with age [56]. Early cortical hyperactivity, as described in mouse models of autism disorders, results in imbalanced striatal circuit development and behavioral abnormalities, such as repetitive behavior and increased anxiety [55,56]. The downstream striatal response to excessive cortical activity is twofold: at the beginning of the first postnatal week, it induces striatal hyperactivity and hyperconnectivity in cortical–striatal circuits, whereas the contrary occurs towards the third postnatal week [55,73]. Further, according to preliminary results, selectively increasing the firing of pyramidal neurons from P4 to P14 leads to an imbalanced prefrontal network, decreased corticostriatal connectivity at adulthood, and behavioral abnormalities reminiscent of autism spectrum disorder [54]. On the flipside, transiently increasing the activity of D2 dopamine receptors in the mouse striatum impacts prefrontal development and PFC-dependent cognitive abilities [80]. While connectomics investigations on the homology of corticostriatal circuits between mammalian species warrant some prudence when translating mouse data to humans [81], similar deficits have also been reported in the clinical human literature. Altered prefrontal and striatal activity is present in a correlated fashion in schizophrenia patients during the prodromal phase [82,83]. Moreover, corticostriatal connectivity is similarly disrupted in humans and mice carrying a genetic mutation in the NF1 gene, which predisposes to autism spectrum disorders [84].

Thalamus and VTA

Several anatomical and lesion studies have documented the relevance of afferents from the MD and VTA to the PFC during development, but their early function is poorly understood. In rodents, a monosynaptic connection between the MD and PFC is already in place at P1, when the lamination of prefrontal deep layers is still immature and virtually absent in the more superficial ones [85,86]. This innervation pattern distinguishes the PFC from primary sensory cortices, where thalamic axons initially target the subplate and only around P3–P4 invade the newly formed cortical layers [10,85,86]. It is thus tempting to hypothesize that the early thalamic innervation of prefrontal layers contributes to the development of the supragranular layers. Despite the critical role of prefrontal–thalamic communication for executive functions in adult mice [87,88], and the fact that in

humans prefrontal–thalamic communication is disrupted in young adults carrying a 22q11.2 deletion [77], lesions of the rodent MD in the first postnatal weeks lead to only mild cognitive impairment [86]. More thorough functional investigations of this pathway throughout development are necessary. Similarly, the contribution of the ventral midline thalamus to the development of prefrontal circuits, and in particular of the nucleus reuniens, remains largely unknown, despite experimental data documenting the synchronization of the two areas in neonatal mice [89].

In rats, dense innervation from the VTA to the PFC has been described as already having a trophic function during the first postnatal week [90]. Dopaminergic axons reach the prefrontal subplate at embryonic stages of development [91]. After birth, these axons start to invade the cortical layers starting from layer VI and progressively reaching the more superficial ones [91]. At P4–P6, the VTA projections are thought to be functional but continue to grow in density, particularly in the superficial layers, where they reach maturity only weeks later. Developmental studies on the behavioral relevance of this pathway are scarce, but its neonatal lesioning has been found to alter behavioral responses to stress [92].

Adolescent PFC as Substrate of Cognitive Maturation

With ongoing development from childhood to adulthood, prefrontal areas undergo massive changes as result of gray matter decrease, white matter augmentation, and myelination processes, which have been reviewed elsewhere [93]. In the human PFC, the exuberant synapse formation is followed by a decrease in spine density [18,94]. A similar phenomenon occurs in the PFC of mice, in which spine density and turnover both peak around P30 [33,34]. **Synaptic pruning** in the PFC is protracted compared with other neocortical areas and accompanied by augmented myelination [95]. This anatomical reorganization of the PFC during adolescence has profound functional implications that have been documented both in humans and rodents. Imaging studies showed that adolescents have less-focal patterns of activation than adults [96]. At this age, the PFC becomes more strongly linked to sensory and subcortical brain areas [97,98]. EEG recordings documented a frequency change of activity at rest, with a decrease at slower rhythms (0–7 Hz) and an increase at faster ones (7–30 Hz) [99,100]. Besides synaptic pruning [33,34] and refinement of oscillatory entrainment [12,101], major changes in cellular interactions in the adolescent rodent PFC have been documented. Parvalbumin expression increases [102] and the composition of GABA and NMDA receptors changes compared with earlier ages [103,104]. These developmental processes promote gamma oscillations, the power of which increases at adolescence [100,105]. Diverse experience (e.g., environmental exploration, sexual experience, social interactions, play behavior) profoundly impacts the development of prefrontal areas and contributes to the refinement of connectivity [106,107].

Flexible adaptation to new situational tasks, salience detection, attention, recognition memory, and working memory improve considerably around adolescence and have been linked, as highlighted above, to the functional development of the PFC [108,109]. These changes in cognitive processing mirror the dramatic reorganization of prefrontal networks during adolescence [110]. While several abilities, such as working and recognition memory, gradually improve with age, risk behavior is thought to peak at adolescence [111]. The mechanisms underlying this difference between the two developmental trajectories are largely unknown, but one of the leading hypotheses is that the risk-seeking behavior of adolescents results from the imbalance between early-maturating subcortical areas, involved in reward, and later-developing prefrontal areas, guiding control behavior [110]. The development of the reward-controlling dopaminergic system has been extensively investigated and reviewed elsewhere [112]. While starting in early childhood, the interactions between the dopaminergic system and the PFC strengthen during late development. The ingrowing dopaminergic innervation as well as the density of D1 and D2 receptors in

the PFC of both rodents and humans peaks during adolescence [113,114]. Dopamine has been shown to facilitate inhibitory circuit function and to decrease the E/I balance [115,116]. It may bias behavior towards risk and sensation seeking as well as cognitive flexibility, some of the most characteristic traits of adolescent behavior.

On the flipside, the high adaptability of the adolescent PFC might make it particularly vulnerable to abnormal formation and refinement of connections [112,117]. The considerable scientific interest in the adolescent PFC results from the dynamics of numerous psychiatric disorders, such as schizophrenia, anxiety, and depression, with onset of symptoms towards the end of this developmental period [95]. In line with the increased hormonal stress response, stressful experience of various kinds (e.g., social isolation, drug abuse) has a particularly strong impact at adolescence [118]. A prominent example of disease with adolescent onset and dual genetic–environmental etiology is schizophrenia [119]. Substantial efforts in schizophrenia research have focused on the development of strategies for risk prediction and early intervention [120]. One candidate is the coordinated oscillatory activity and neuronal dynamics [121,122] that reflect the altered connectivity of prefrontal circuits [123]. E/I imbalance and abnormal long-range connectivity have been hypothesized to underlie the behavioral deficits in schizophrenia patients and animal models of disease [124,125]. Weaker gamma band activity has been detected in high-risk individuals during the prodromal phase [122]. Moreover, interneuron hypomyelination throughout development has been related to cognitive inflexibility in a schizophrenia rat model [126].

Mirroring the profound dysfunction of prefrontal circuits, cognitive impairment represents a serious, life-long burden of mental illness [127]. Even before the emergence of clinical symptoms, poorer executive abilities have been detected in adolescent offspring of schizophrenia patients [128]. Similarly, memory deficits have been reported in mouse models of disease at juvenile age [42,72]. Adolescence has been proposed as a critical period for prefrontal function similar to that characterized in sensory systems [129]. Consequently, it might offer an appropriate time window for intervention/rescue. Understanding the mechanisms underlying prefrontal dysfunction at this stage as well as the identification of reliable biomarkers represent two critical steps for the development of future therapies and diagnostics.

Concluding Remarks and Future Perspectives

Overviewing its functional complexity, the developing PFC appears as a neurobiological double-edged sword: it enables amazing complex cognition and social behavior, yet it underlies devastating symptomatology. While the maturation of PFC-dependent behaviors has been extensively investigated, the mechanisms of functional development of the PFC are less well understood. The knowledge gap is due to: (i) the lack of prefrontal homology across mammalian species; (ii) the protracted dynamics of developmental processes; and (iii) the absence of direct experimentally addressable links with the environment that differentiate the PFC from other neocortical areas (e.g., V1, S1, A1). Despite these difficulties, recent studies provided first insights into the wiring mechanisms of prefrontal areas and highlighted the role of genetic cues and electrical activity in health and psychiatric diseases.

The principles of PFC development have just begun to be uncovered. Several key questions still need to be addressed (see Outstanding Questions). The developmental features of disorders such as schizophrenia and autism remain largely unexploited partly because the principles of prefrontal development are poorly understood. To overcome this, at least two steps are necessary. First, clearer definitions of how prefrontal areas and developmental time windows compare across mammalian species would facilitate the translation of findings between species [2,4]. This will allow clearer understanding of the relevance of animal-model findings for human disease

Outstanding Questions

How do molecules and signaling pathways interact to achieve the correct parcellation and structure of prefrontal areas? Are distinct molecular programs responsible for the structural differences across mammalian species?

How does (multi)sensory maturation impact the development of prefrontal areas and behavioral performance? When does sensory information reach the PFC? How is it represented? Does this occur at the same time for all sensory modalities? Is it equally as important for PFC maturation as the hippocampal drive? When does the PFC's role as a multisensory integration area begin?

Is there a human correlate to beta/low-gamma mouse rhythms?

Which mechanisms link prefrontal development and the emergence of cognitive flexibility, working memory, and attention? Is prefrontal function at early stages of development (perinatal, childhood) a prerequisite for the maturation of cognitive performance?

How do projection-defined prefrontal populations of neurons initially assemble to encode diverse tasks? How do they enable the switch between tasks?

Which specific prefrontal features (e.g., $PYR_{II/III}$ firing, power or rhythmicity of beta/gamma rhythms) are relevant for cognitive development? What is the minimal set of these features that should be restored in a mouse model of cognitive impairment to restore impaired cognitive abilities?

Do different prefrontal neuronal subpopulations, projecting to different brain areas, follow developmental trajectories with different time courses?

Does the PFC during 'critical periods' of augmented vulnerability (i.e., perinatal age and adolescence) show characteristic signatures of neuronal and network activity across species that might serve as biomarkers for disease?

How does behavioral maturation map onto biomarkers of functional maturation (e.g., prefrontal oscillations)?

and hopefully enable the identification of meaningful biomarkers. Second, we advocate for a detailed dissection of cellular and network interactions during development using recent powerful technologies such as high-density recordings, imaging, and optogenetics. Towards translation to humans, EEG/magnetoencephalography (MEG) approaches should be complemented by the investigation of human brain organoids [130], which appear to be a powerful tool for modeling cellular interactions, neural circuit dysfunctions, and the complex genetic landscape related to neurodevelopmental pathologies.

How is the crosstalk between the PFC and basal ganglia tuned across development? Do specific patterns of activity, topographically organized firing, or firing rates code the weight of the areas? How does this change over development, especially at adolescence when risk-taking behavior is a dominant trait?

Acknowledgments

This work was funded by grants from the European Research Council (ERC-2015-CoG 681577 to I.L.H.-O.), the German Research Foundation (Ha 4466/10-1, Ha4466/11-1, Ha4466/12-1, SPP 1665, SFB 936 B5 to I.L.H-O.), and Landesforschungsförderung Hamburg (LFF-FV76 to I.L. H.-O.). I.L.H-O. is funding member of the FENS Kavli Network of Excellence. We thank Guido Hegasy (www.hegasy.de) for help with figure preparation.

References

1. Fuster, J.M. (2015) *The Prefrontal Cortex*, Academic Press
2. Carlen, M. (2017) What constitutes the prefrontal cortex? *Science* 358, 478–482
3. Laubach, M. *et al.* (2018) What, if anything, is rodent prefrontal cortex? *eNeuro* 5 ENEURO.0315-0318.2018
4. van Heukelum, S. *et al.* (2020) Where is cingulate cortex? A cross-species view. *Trends Neurosci.* 43, 285–299
5. Uylings, H.B.M. *et al.* (2003) Do rats have a prefrontal cortex? *Behav. Brain Res.* 146, 3–17
6. Sanai, N. *et al.* (2011) Corridors of migrating neurons in the human brain and their decline during infancy. *Nature* 478, 382–386
7. Ahrlund-Richter, S. *et al.* (2019) A whole-brain atlas of monosynaptic input targeting four different cell types in the medial prefrontal cortex of the mouse. *Nat. Neurosci.* 22, 657–668
8. Preuss, T.M. (1995) Do rats have prefrontal cortex – the Rose–Woolsey–Akert program reconsidered. *J. Cogn. Neurosci.* 7, 1–24
9. Gyllborg, D. *et al.* (2020) Hybridization-based *in situ* sequencing (HybISS) for spatially resolved transcriptomics in human and mouse brain tissue. *Nucleic Acids Res.* 48, e112
10. Vaneden, C.G. *et al.* (1990) The development of the rat prefrontal cortex – its size and development of connections with thalamus, spinal-cord and other cortical areas. *Prog. Brain Res.* 85, 169–183
11. Gogtay, N. *et al.* (2004) Dynamic mapping of human cortical development during childhood through early adulthood. *Proc. Natl. Acad. Sci. U. S. A.* 101, 8174–8179
12. Brockmann, M.D. *et al.* (2011) Coupled oscillations mediate directed interactions between prefrontal cortex and hippocampus of the neonatal rat. *Neuron* 71, 332–347
13. Spencer-Smith, M. and Anderson, V. (2009) Healthy and abnormal development of the prefrontal cortex. *Dev. Neurorehabil.* 12, 279–297
14. Williams, M.E. *et al.* (2010) Molecular mechanisms of synaptic specificity in developing neural circuits. *Neuron* 68, 9–18
15. Flavell, S.W. and Greenberg, M.E. (2008) Signaling mechanisms linking neuronal activity to gene expression and plasticity of the nervous system. *Annu. Rev. Neurosci.* 31, 563–590
16. Orahilly, R. and Gardner, E. (1979) Initial development of the human-brain. *Acta Anat.* 104, 123–133
17. Cholfin, J.A. and Rubenstein, J.L.R. (2007) Patterning of frontal cortex subdivisions by Fgf17. *Proc. Natl. Acad. Sci. U. S. A.* 104, 7652–7657
18. Lenroot, R.K. and Giedd, J.N. (2006) Brain development in children and adolescents: insights from anatomical magnetic resonance imaging. *Neurosci. Biobehav. Rev.* 30, 718–729
19. Rice, D. and Barone, S. (2000) Critical periods of vulnerability for the developing nervous system: evidence from humans and animal models. *Environ. Health Perspect.* 108, 511–533
20. Telley, L. *et al.* (2019) Temporal patterning of apical progenitors and their daughter neurons in the developing neocortex. *Science* 364, eaav2522
21. Oberst, P. *et al.* (2019) Temporal plasticity of apical progenitors in the developing mouse neocortex. *Nature* 573, 370–374
22. Gao, P. *et al.* (2014) Deterministic progenitor behavior and unitary production of neurons in the neocortex. *Cell* 159, 775–788
23. Lim, L. *et al.* (2018) Optimization of interneuron function by direct coupling of cell migration and axonal targeting. *Nat. Neurosci.* 21, 920–931
24. Marín, O. *et al.* (2010) Guiding neuronal cell migrations. *Cold Spring Harb. Perspect. Biol.* 2, a001834
25. Mrzljak, L. *et al.* (1990) Neuronal development in human prefrontal cortex in prenatal and postnatal stages. *Prog. Brain Res.* 85, 185–222
26. Molnar, Z. *et al.* (2019) New insights into the development of the human cerebral cortex. *J. Anat.* 235, 432–451
27. Nadarajah, B. and Parnavelas, J.G. (2002) Modes of neuronal migration in the developing cerebral cortex. *Nat. Rev. Neurosci.* 3, 423–432
28. Kiryushko, D. *et al.* (2004) Regulators of neurite outgrowth: role of cell adhesion molecules. *Ann. N. Y. Acad. Sci.* 1014, 140–154
29. Iafrati, J. *et al.* (2014) Reelin, an extracellular matrix protein linked to early onset psychiatric diseases, drives postnatal development of the prefrontal cortex via GluN2B-NMDARs and the mTOR pathway. *Mol. Psychiatry* 19, 417–426
30. Cooper, M.A. and Koleske, A.J. (2014) Ablation of ErbB4 from excitatory neurons leads to reduced dendritic spine density in mouse prefrontal cortex. *J. Comp. Neurol.* 522, 3351–3362
31. Comer, A.L. *et al.* (2020) Increased expression of schizophrenia-associated gene C4 leads to hypoconnectivity of prefrontal cortex and reduced social interaction. *PLoS Biol.* 18, e3000604
32. Kroon, T. *et al.* (2019) Early postnatal development of pyramidal neurons across layers of the mouse medial prefrontal cortex. *Sci. Rep.* 9, 5037
33. Zuo, Y. *et al.* (2005) Development of long-term dendritic spine stability in diverse regions of cerebral cortex. *Neuron* 46, 181–189
34. Pattwell, S.S. *et al.* (2016) Dynamic changes in neural circuitry during adolescence are associated with persistent attenuation of fear memories. *Nat. Commun.* 7, 11475
35. Vanderhaeghen, P. and Cheng, H.J. (2010) Guidance molecules in axon pruning and cell death. *Cold Spring Harb. Perspect. Biol.* 2, a001859
36. Schubert, D. *et al.* (2015) Molecular underpinnings of prefrontal cortex development in rodents provide insights into the etiology of neurodevelopmental disorders. *Mol. Psychiatry* 20, 795–809
37. Parenti, I. *et al.* (2020) Neurodevelopmental disorders: from genetics to functional pathways. *Trends Neurosci.* 43, 608–621
38. Dupont, E. *et al.* (2006) Rapid developmental switch in the mechanisms driving early cortical columnar networks. *Nature* 439, 79–83
39. Ackman, J.B. *et al.* (2012) Retinal waves coordinate patterned activity throughout the developing visual system. *Nature* 490, 219–225

40. Babola, T.A. *et al.* (2018) Homeostatic control of spontaneous activity in the developing auditory system. *Neuron* 99, 511–524
41. Bitzenhofer, S.H. *et al.* (2017) Layer-specific optogenetic activation of pyramidal neurons causes beta–gamma entrainment of neonatal networks. *Nat. Commun.* 8, 14563
42. Chini, M. *et al.* (2020) Resolving and rescuing developmental miswiring in a mouse model of cognitive impairment. *Neuron* 105, 60–74
43. Bitzenhofer, S.H. *et al.* (2020) Transient developmental increase of prefrontal activity alters network maturation and causes cognitive dysfunction in adult mice. *bioRxiv*. Published online April 8, 2020. https://doi.org/10.1101/558957
44. Bitzenhofer, S.H. *et al.* (2020) Gamma activity accelerates during prefrontal development. *eLife* 9, e56795
45. Ahlbeck, J. *et al.* (2018) Glutamatergic drive along the septotemporal axis of hippocampus boosts prelimbic oscillations in the neonatal mouse. *eLife* 7, e33158
46. Guan, W.Q. *et al.* (2017) Eye opening differentially modulates inhibitory synaptic transmission in the developing visual cortex. *eLife* 6, e32337
47. Marques-Smith, A. *et al.* (2016) A transient translaminar GABAergic interneuron circuit connects thalamocortical recipient layers in neonatal somatosensory cortex. *Neuron* 89, 536–549
48. Modol, L. *et al.* (2020) Assemblies of perisomatic GABAergic neurons in the developing barrel cortex. *Neuron* 105, 93–105
49. Minlebaev, M. *et al.* (2011) Early gamma oscillations synchronize developing thalamus and cortex. *Science* 334, 226–229
50. Colonnese, M.T. *et al.* (2010) A conserved switch in sensory processing prepares developing neocortex for vision. *Neuron* 67, 480–498
51. Hanganu, I.L. *et al.* (2006) Retinal waves trigger spindle bursts in the neonatal rat visual cortex. *J. Neurosci.* 26, 6728–6736
52. Xu, X.X. *et al.* (2019) Transient knock-down of prefrontal DISC1 in immune-challenged mice causes abnormal long-range coupling and cognitive dysfunction throughout development. *J. Neurosci.* 39, 1222–1235
53. Niwa, M. *et al.* (2010) Knockdown of DISC1 by *in utero* gene transfer disturbs postnatal dopaminergic maturation in the frontal cortex and leads to adult behavioral deficits. *Neuron* 65, 480–489
54. Medendorp, W.E. *et al.* (2020) Selective postnatal excitation of neocortical pyramidal neurons results in distinctive behavioral and circuit deficits in adulthood. *bioRxiv*. Published online January 18, 2020. https://doi.org/10.1101/2020.01.18.911347
55. Peixoto, R.T. *et al.* (2019) Abnormal striatal development underlies the early onset of behavioral deficits in Shank3B$^{-/-}$ mice. *Cell Rep.* 29, 2016–2027
56. Peixoto, R.T. *et al.* (2016) Early hyperactivity and precocious maturation of corticostriatal circuits in Shank3B$^{-/-}$ mice. *Nat. Neurosci.* 19, 716–724
57. Belforte, J.E. *et al.* (2010) Postnatal NMDA receptor ablation in corticolimbic interneurons confers schizophrenia-like phenotypes. *Nat. Neurosci.* 13, 76–83
58. Cho, K.K. *et al.* (2015) Gamma rhythms link prefrontal interneuron dysfunction with cognitive inflexibility in Dlx5/6$^{+/-}$ mice. *Neuron* 85, 1332–1343
59. Guo, T. *et al.* (2017) Quantitative assessment of white matter injury in preterm neonates: association with outcomes. *Neurology* 88, 614–622
60. Tokariev, A. *et al.* (2019) Preterm birth changes networks of newborn cortical activity. *Cereb. Cortex* 29, 814–826
61. McLaughlin, K.A. *et al.* (2010) Delayed maturation in brain electrical activity partially explains the association between early environmental deprivation and symptoms of attention-deficit/hyperactivity disorder. *Biol. Psychiatry* 68, 329–336
62. Senkowski, D. and Gallinat, J. (2015) Dysfunctional prefrontal gamma-band oscillations reflect working memory and other cognitive deficits in schizophrenia. *Biol. Psychiatry* 77, 1010–1019
63. Uhlhaas, P.J. and Singer, W. (2015) Oscillations and neuronal dynamics in schizophrenia: the search for basic symptoms and translational opportunities. *Biol. Psychiatry* 77, 1001–1009
64. Kolluri, N. *et al.* (2005) Lamina-specific reductions in dendritic spine density in the prefrontal cortex of subjects with schizophrenia. *Am. J. Psychiatry* 162, 1200–1202
65. Leinekugel, X. *et al.* (2002) Correlated bursts of activity in the neonatal hippocampus *in vivo*. *Science* 296, 2049–2052
66. Valeeva, G. *et al.* (2019) Emergence of coordinated activity in the developing entorhinal-hippocampal network. *Cereb. Cortex* 29, 906–920
67. Del Rio-Bermudez, C. *et al.* (2020) Active sleep promotes coherent oscillatory activity in the cortico-hippocampal system of infant rats. *Cereb. Cortex* 30, 2070–2082
68. Del Rio-Bermudez, C. *et al.* (2017) Theta oscillations during active sleep synchronize the developing rubro-hippocampal sensorimotor network. *Curr. Biol.* 27, 1413–1424
69. Bitzenhofer, S.H. *et al.* (2015) Oscillatory activity in developing prefrontal networks results from theta-gamma-modulated synaptic inputs. *Cell Rep.* 11, 486–497
70. Sigurdsson, T. *et al.* (2010) Impaired hippocampal–prefrontal synchrony in a genetic mouse model of schizophrenia. *Nature* 464, 763–767
71. Adams, R.A. *et al.* (2020) Impaired theta phase coupling underlies frontotemporal dysconnectivity in schizophrenia. *Brain* 143, 1261–1277
72. Hartung, H. *et al.* (2016) From shortage to surge: a developmental switch in hippocampal–prefrontal coupling in a gene–environment model of neuropsychiatric disorders. *Cereb. Cortex* 26, 4265–4281
73. Zerbi, V. *et al.* (2018) Dysfunctional autism risk genes cause circuit-specific connectivity deficits with distinct developmental trajectories. *Cereb. Cortex* 28, 2495–2506
74. Tamura, M. *et al.* (2016) Developmental inhibition of Gsk3 rescues behavioral and neurophysiological deficits in a mouse model of schizophrenia predisposition. *Neuron* 89, 1100–1109
75. Omidvarnia, A. *et al.* (2014) Functional bimodality in the brain networks of preterm and term human newborns. *Cereb. Cortex* 24, 2657–2668
76. Bertero, A. *et al.* (2018) Autism-associated 16p11.2 microdeletion impairs prefrontal functional connectivity in mouse and human. *Brain* 141, 2055–2065
77. Schleifer, C. *et al.* (2019) Dissociable disruptions in thalamic and hippocampal resting-state functional connectivity in youth with 22q11.2 deletions. *J. Neurosci.* 39, 1301–1319
78. Haber, S.N. and Calzavara, R. (2009) The cortico-basal ganglia integrative network: the role of the thalamus. *Brain Res. Bull.* 78, 69–74
79. Kozorovitskiy, Y. *et al.* (2012) Recurrent network activity drives striatal synaptogenesis. *Nature* 485, 646–650
80. Kellendonk, C. *et al.* (2006) Transient and selective overexpression of dopamine D2 receptors in the striatum causes persistent abnormalities in prefrontal cortex functioning. *Neuron* 49, 603–615
81. Balsters, J.H. *et al.* (2020) Primate homologs of mouse cortico-striatal circuits. *eLife* 9, e53680
82. Fusar-Poli, P. *et al.* (2011) Abnormal prefrontal activation directly related to pre-synaptic striatal dopamine dysfunction in people at clinical high risk for psychosis. *Mol. Psychiatry* 16, 67–75
83. Fusar-Poli, P. *et al.* (2010) Abnormal frontostriatal interactions in people with prodromal signs of psychosis: a multimodal imaging study. *Arch. Gen. Psychiatry* 67, 683–691
84. Shofty, B. *et al.* (2019) Autism-associated Nf1 deficiency disrupts corticocortical and corticostriatal functional connectivity in human and mouse. *Neurobiol. Dis.* 130, 104479
85. Vaneden, C.G. (1986) Development of connections between the mediodorsal nucleus of the thalamus and the prefrontal cortex in the rat. *J. Comp. Neurol.* 244, 349–359
86. Ferguson, B.R. and Gao, W.J. (2015) Development of thalamocortical connections between the mediodorsal thalamus and the prefrontal cortex and its implication in cognition. *Front. Hum. Neurosci.* 8, 1027
87. DeNicola, A.L. *et al.* (2020) Differential roles of mediodorsal nucleus of the thalamus and prefrontal cortex in decision-making and state representation in a cognitive control task measuring deficits in schizophrenia. *J. Neurosci.* 40, 1650–1667

88. Parnaudeau, S. *et al.* (2013) Inhibition of mediodorsal thalamus disrupts thalamofrontal connectivity and cognition. *Neuron* 77, 1151–1162
89. Hartung, H. *et al.* (2016) Thalamic and entorhinal network activity differently modulates the functional development of prefrontal–hippocampal interactions. *J. Neurosci.* 36, 3676–3690
90. Kalsbeek, A. *et al.* (1989) Monoamine and metabolite levels in the prefrontal cortex and the mesolimbic forebrain following neonatal lesions of the ventral tegmental area. *Brain Res.* 479, 339–343
91. Kalsbeek, A. *et al.* (1988) Development of the dopaminergic innervation in the prefrontal cortex of the rat. *J. Comp. Neurol.* 269, 58–72
92. Feenstra, M.G.P. *et al.* (1992) Neonatal lesions of the ventral tegmental area affect monoaminergic responses to stress in the medial prefrontal cortex and other dopamine projection areas in adulthood. *Brain Res.* 596, 169–182
93. Mount, C.W. and Monje, M. (2017) Wrapped to adapt: experience-dependent myelination. *Neuron* 95, 743–756
94. Petanjek, Z. *et al.* (2011) Extraordinary neoteny of synaptic spines in the human prefrontal cortex. *Proc. Natl. Acad. Sci. U. S. A.* 108, 13281–13286
95. Paus, T. *et al.* (2008) Why do many psychiatric disorders emerge during adolescence? *Nat. Rev. Neurosci.* 9, 947–957
96. Casey, B.J. and Jones, R.M. (2010) Neurobiology of the adolescent brain and behavior: implications for substance use disorders. *J. Am. Acad. Child Adolesc. Psychiatry* 49, 1189–1201
97. Nagy, Z. *et al.* (2004) Maturation of white matter is associated with the development of cognitive functions during childhood. *J. Cogn. Neurosci.* 16, 1227–1233
98. Liston, C. *et al.* (2006) Frontostriatal microstructure modulates efficient recruitment of cognitive control. *Cereb. Cortex* 16, 553–560
99. Marek, S. *et al.* (2018) Adolescent development of cortical oscillations: power, phase, and support of cognitive maturation. *PLoS Biol.* 16, e2004188
100. Uhlhaas, P.J. *et al.* (2009) The development of neural synchrony reflects late maturation and restructuring of functional networks in humans. *Proc. Natl. Acad. Sci. U. S. A.* 106, 9866–9871
101. de Almeida, J. *et al.* (2013) Refinement of neuronal synchronization with gamma oscillations in the medial prefrontal cortex after adolescence. *PLoS One* 8, e62978
102. Caballero, A. *et al.* (2014) Differential regulation of parvalbumin and calretinin interneurons in the prefrontal cortex during adolescence. *Brain Struct. Funct.* 219, 395–406
103. Konstantoudaki, X. *et al.* (2018) Prefrontal cortical-specific differences in behavior and synaptic plasticity between adolescent and adult mice. *J. Neurophysiol.* 119, 822–833
104. Datta, D. *et al.* (2015) Developmental expression patterns of $GABA_A$ receptor subunits in layer 3 and 5 pyramidal cells of monkey prefrontal cortex. *Cereb. Cortex* 25, 2295–2305
105. Gonzalez-Burgos, G. *et al.* (2015) Alterations in cortical network oscillations and parvalbumin neurons in schizophrenia. *Biol. Psychiatry* 77, 1031–1040
106. van Kerkhof, L.W.M. *et al.* (2013) Social play behavior in adolescent rats is mediated by functional activity in medial prefrontal cortex and striatum. *Neuropsychopharmacology* 38, 1899–1909
107. Glasper, E.R. *et al.* (2015) Sexual experience enhances cognitive flexibility and dendritic spine density in the medial prefrontal cortex. *Neurobiol. Learn. Mem.* 125, 73–79
108. Crone, E.A. and Dahl, R.E. (2012) Understanding adolescence as a period of social-affective engagement and goal flexibility. *Nat. Rev. Neurosci.* 13, 636–650
109. Blakemore, S.J. and Choudhury, S. (2006) Development of the adolescent brain: implications for executive function and social cognition. *J. Child Psychol. Psychiatry* 47, 296–312
110. Casey, B.J. *et al.* (2008) The adolescent brain. *Dev. Rev.* 28, 62–77
111. Steinberg, L. (2004) Risk taking in adolescence: what changes, and why? *Ann. N. Y. Acad. Sci.* 1021, 51–58
112. Larsen, B. and Luna, B. (2018) Adolescence as a neurobiological critical period for the development of higher-order cognition. *Neurosci. Biobehav. Rev.* 94, 179–195
113. Lidow, M.S. and Rakic, P. (1992) Scheduling of monoaminergic neurotransmitter receptor expression in the primate neocortex during postnatal-development. *Cereb. Cortex* 2, 401–416
114. Rosenberg, D.R. and Lewis, D.A. (1995) Postnatal maturation of the dopaminergic innervation of monkey prefrontal and motor cortices – a tyrosine-hydroxylase immunohistochemical analysis. *J. Comp. Neurol.* 358, 383–400
115. O'Donnell, P. (2010) Adolescent maturation of cortical dopamine. *Neurotox. Res.* 18, 306–312
116. Porter, L.L. *et al.* (1999) Dopamine affects parvalbumin expression during cortical development *in vitro*. *J. Neurosci.* 19, 8990–9003
117. Sakurai, T. and Gamo, N.J. (2019) Cognitive functions associated with developing prefrontal cortex during adolescence and developmental neuropsychiatric disorders. *Neurobiol. Dis.* 131, 104322
118. McEwen, B.S. and Morrison, J.H. (2013) The brain on stress: vulnerability and plasticity of the prefrontal cortex over the life course. *Neuron* 79, 16–29
119. Insel, T.R. (2010) Rethinking schizophrenia. *Nature* 468, 187–193
120. Fusar-Poli, P. *et al.* (2013) The psychosis high-risk state: a comprehensive state-of-the-art review. *JAMA Psychiatry* 70, 107–120
121. Leicht, G. *et al.* (2016) EEG-informed fMRI reveals a disturbed gamma-band-specific network in subjects at high risk for psychosis. *Schizophr. Bull.* 42, 239–249
122. Andreou, C. *et al.* (2015) Resting-state theta-band connectivity and verbal memory in schizophrenia and in the high-risk state. *Schizophr. Res.* 161, 299–307
123. Lewis, D.A. (2012) Cortical circuit dysfunction and cognitive deficits in schizophrenia – implications for preemptive interventions. *Eur. J. Neurosci.* 35, 1871–1878
124. O'Donnell, P. (2011) Adolescent onset of cortical disinhibition in schizophrenia: insights from animal models. *Schizophr. Bull.* 37, 484–492
125. Gonzalez-Burgos, G. and Lewis, D.A. (2008) GABA neurons and the mechanisms of network oscillations: implications for understanding cortical dysfunction in schizophrenia. *Schizophr. Bull.* 34, 944–961
126. Maas, D.A. *et al.* (2020) Interneuron hypomyelination is associated with cognitive inflexibility in a rat model of schizophrenia. *Nat. Commun.* 11, 2329
127. van Os, J. and Kapur, S. (2009) Schizophrenia. *Lancet* 374, 635–645
128. Diwadkar, V.A. *et al.* (2011) Working memory and attention deficits in adolescent offspring of schizophrenia or bipolar patients: comparing vulnerability markers. *Prog. Neuro-Psychopharmacol. Biol. Psychiatry* 35, 1349–1354
129. Piekarski, D.J. *et al.* (2017) Does puberty mark a transition in sensitive periods for plasticity in the associative neocortex? *Brain Res.* 1654, 123–144
130. Trujillo, C.A. *et al.* (2019) Complex oscillatory waves emerging from cortical organoids model early human brain network development. *Cell Stem Cell* 25, 558–569
131. Buzsaki, G. *et al.* (2012) The origin of extracellular fields and currents – EEG, ECoG, LFP and spikes. *Nat. Rev. Neurosci.* 13, 407–420
132. Cohen, M.X. (2017) Where does EEG come from and what does it mean? *Trends Neurosci.* 40, 208–218
133. Nir, Y. *et al.* (2007) Coupling between neuronal firing rate, gamma LFP, and BOLD fMRI is related to interneuronal correlations. *Curr. Biol.* 17, 1275–1285
134. Mateo, C. *et al.* (2017) Entrainment of arteriole vasomotor fluctuations by neural activity is a basis of blood-oxygenation-level-dependent "resting-state" connectivity. *Neuron* 96, 936–948. e933
135. Pan, W.J. *et al.* (2013) Infraslow LFP correlates to resting-state fMRI BOLD signals. *Neuroimage* 74, 288–297
136. Wei, Z. *et al.* (2020) A comparison of neuronal population dynamics measured with calcium imaging and electrophysiology. *PLoS Comput. Biol.* 16, e1008198
137. Vanhatalo, S. and Kaila, K. (2006) Development of neonatal EEG activity: from phenomenology to physiology. *Semin. Fetal Neonatal Med.* 11, 471–478

138. Khazipov, R. *et al.* (2004) Early motor activity drives spindle bursts in the developing somatosensory cortex. *Nature* 432, 758–761
139. Avitan, L. and Goodhill, G.J. (2018) Code under construction: neural coding over development. *Trends Neurosci.* 41, 599–609
140. Adelsberger, H. *et al.* (2005) Cortical calcium waves in resting newborn mice. *Nat. Neurosci.* 8, 988–990
141. Colonnese, M. and Khazipov, R. (2012) Spontaneous activity in developing sensory circuits: implications for resting state fMRI. *Neuroimage* 62, 2212–2221
142. Golshani, P. *et al.* (2009) Internally mediated developmental desynchronization of neocortical network activity. *J. Neurosci.* 29, 10890–10899
143. Rochefort, N.L. *et al.* (2009) Sparsification of neuronal activity in the visual cortex at eye-opening. *Proc. Natl. Acad. Sci. U. S. A.* 106, 15049–15054
144. Shen, J. and Colonnese, M.T. (2016) Development of activity in the mouse visual cortex. *J. Neurosci.* 36, 12259–12275
145. Gribizis, A. *et al.* (2019) Visual cortex gains independence from peripheral drive before eye opening. *Neuron* 104, 711–723
146. Mizuno, H. *et al.* (2018) Patchwork-type spontaneous activity in neonatal barrel cortex layer 4 transmitted via thalamocortical projections. *Cell Rep.* 22, 123–135
147. Anton-Bolanos, N. *et al.* (2019) Prenatal activity from thalamic neurons governs the emergence of functional cortical maps in mice. *Science* 364, 987–990
148. Dooley, J.C. *et al.* (2020) Self-generated whisker movements drive state-dependent sensory input to developing barrel cortex. *Curr. Biol.* 30, 2404–2410.e2404
149. Batista-Brito, R. *et al.* (2017) Developmental dysfunction of VIP interneurons impairs cortical circuits. *Neuron* 95, 884–895
150. Che, A. *et al.* (2018) Layer I interneurons sharpen sensory maps during neonatal development. *Neuron* 99, 98–116
151. Duan, Z.R.S. *et al.* (2020) GABAergic restriction of network dynamics regulates interneuron survival in the developing cortex. *Neuron* 105, 75–92
152. Purdon, P.L. *et al.* (2015) Clinical electroencephalography for anesthesiologists part I: background and basic signatures. *Anesthesiology* 123, 937–960
153. Kertai, M.D. *et al.* (2012) Brain monitoring with electroencephalography and the electroencephalogram-derived bispectral index during cardiac surgery. *Anesth. Analg.* 114, 533–546
154. Chini, M. *et al.* (2019) Neural correlates of anesthesia in newborn mice and humans. *Front. Neural Circuits* 13, 38
155. Agrawal, U. *et al.* (2019) Electroencephalographic features of discontinuous activity in anesthetized infants and children. *PLoS One* 14, e0223324
156. Poorun, R. *et al.* (2016) Electroencephalography during general anaesthesia differs between term-born and premature-born children. *Clin. Neurophysiol.* 127, 1216–1222
157. Blumberg, M.S. *et al.* (2020) The developing brain revealed during sleep. *Curr. Opin. Physiol.* 15, 14–22
158. Cornelissen, L. *et al.* (2018) Clinical signs and electroencephalographic patterns of emergence from sevoflurane anaesthesia in children: an observational study. *Eur. J. Anaesthesiol.* 35, 49–59
159. Niethard, N. *et al.* (2018) Cortical circuit activity underlying sleep slow oscillations and spindles. *Proc. Natl. Acad. Sci. U. S. A.* 115, E9220–E9229
160. O'Toole, J.M. *et al.* (2016) Estimating functional brain maturity in very and extremely preterm neonates using automated analysis of the electroencephalogram. *Clin. Neurophysiol.* 127, 2910–2918

2.7 Neural Correlates of Anesthesia in Newborn Mice and Humans

Mattia Chini, Sabine Gretenkord, Johanna K. Kostka, Jastyn A. Pöpplau, Laura Cornelissen, Charles B. Berde, Ileana L. Hanganu-Opatz and Sebastian H. Bitzenhofer

Frontiers in neural circuits 2019; DOI: https://doi.org/10.3389/fncir.2019.00038

Personal contribution

I designed the project. I performed *in vivo* electrophysiology experiments. I carried out formal analysis and data curation. I helped writing the original draft, reviewed and edited the manuscript.

frontiers in Neural Circuits

ORIGINAL RESEARCH
published: 22 May 2019
doi: 10.3389/fncir.2019.00038

Neural Correlates of Anesthesia in Newborn Mice and Humans

Mattia Chini[1], *Sabine Gretenkord*[1], *Johanna K. Kostka*[1], *Jastyn A. Pöpplau*[1], *Laura Cornelissen*[2,3], *Charles B. Berde*[2,3], *Ileana L. Hanganu-Opatz*[1*†] *and Sebastian H. Bitzenhofer*[1*†‡]

[1]Developmental Neurophysiology, Institute of Neuroanatomy, University Medical Center Hamburg-Eppendorf, Hamburg, Germany, [2]Department of Anesthesiology, Critical Care and Pain Medicine, Boston Children's Hospital, Boston, MA, United States, [3]Department of Anesthesia, Harvard Medical School, Boston, MA, United States

Monitoring the hypnotic component of anesthesia during surgeries is critical to prevent intraoperative awareness and reduce adverse side effects. For this purpose, electroencephalographic (EEG) methods complementing measures of autonomic functions and behavioral responses are in use in clinical practice. However, in human neonates and infants existing methods may be unreliable and the correlation between brain activity and anesthetic depth is still poorly understood. Here, we characterized the effects of different anesthetics on brain activity in neonatal mice and developed machine learning approaches to identify electrophysiological features predicting inspired or end-tidal anesthetic concentration as a proxy for anesthetic depth. We show that similar features from EEG recordings can be applied to predict anesthetic concentration in neonatal mice and humans. These results might support a novel strategy to monitor anesthetic depth in human newborns.

Keywords: development, anesthesia, LFP, EEG, mouse, human, machine learning, network dynamics

OPEN ACCESS

Edited by:
Tommaso Pizzorusso, University of Florence, Italy

Reviewed by:
Paola Binda, University of Pisa, Italy
Laura Baroncelli, Italian National Research Council (CNR), Italy

***Correspondence:**
Ileana L. Hanganu-Opatz
hangop@zmnh.uni-hamburg.de
Sebastian H. Bitzenhofer
sbitzenhofer@ucsd.edu

†These authors have contributed equally to this work

‡Present address:
Sebastian H. Bitzenhofer, Center for Neural Circuits and Behavior, Department of Neurosciences, University of California, San Diego, La Jolla, CA, United States

Received: *31 January 2019*
Accepted: *03 May 2019*
Published: *22 May 2019*

Citation:
Chini M, Gretenkord S, Kostka JK, Pöpplau JA, Cornelissen L, Berde CB, Hanganu-Opatz IL and Bitzenhofer SH (2019) Neural Correlates of Anesthesia in Newborn Mice and Humans. Front. Neural Circuits 13:38. doi: 10.3389/fncir.2019.00038

INTRODUCTION

Reliable monitoring of anesthesia depth is critical during surgery. It allows for loss of consciousness, analgesia and immobility without incurring the risk of side effects and complications due to anesthetic misdosing. Typically used measures to monitor anesthesia depth are inspired and end-tidal anesthetic concentrations as well as physiologic parameters, including respiratory rate and depth (in the absence of neuromuscular blockade or controlled ventilation), heart rate, blood pressure, and responses to noxious stimuli (Punjasawadwong et al., 2014). These measures all respond to spinal and brainstem reflexes and are not specific for arousal or cortical responses to noxious events.

Anesthesia-induced changes in brain activity can be measured with electroencephalographic (EEG) recordings. Specific algorithms have been developed to predict anesthesia depth in adults (Glass et al., 1997; Prichep et al., 2004; Kreuzer, 2017). The most commonly used of such methods, the Bispectral Index, has been shown to significantly reduce intraoperative awareness, amount of anesthetic used, recovery time and post-anesthesia care unit stay in a recent Cochrane meta-analysis (Punjasawadwong et al., 2014), but see (Kalkman et al., 2011; Hajat et al., 2017). However, evidence of similar benefits in infants and younger children is sparse, as recently shown (Cornelissen et al., 2015, 2017, 2018a). EEG in anesthetized infants changes dramatically depending on postnatal age. Slow oscillations are present from birth on, whereas theta and alpha oscillations

occur 3 months after birth, but lack the frontal dominance typically seen in adults (Davidson et al., 2005; Lo et al., 2009; Hayashi et al., 2012; Cornelissen et al., 2015; Koch et al., 2017).

EEG recordings mainly monitor neocortical activity. Converging evidence from animal and human studies has shown that most anesthetics slow EEG oscillations (Alkire et al., 2008; Chauvette et al., 2011; Purdon et al., 2015). While power at high frequency oscillations is reduced (>40 Hz), power at slower frequencies (<15 Hz) is enhanced (Purdon et al., 2015). The computations underlying proprietary indexes such as the Bispectral index or Narcotrend are thought to take advantage of these phenomena (Kertai et al., 2012). However, in preterm and term neonates for the first weeks of life, EEG during sleep-wake cycles is weakly correlated with behavioral states and shows characteristic bursts or spontaneous activity transients (Milh et al., 2007; O'Toole et al., 2016). Anesthesia-induced theta and alpha oscillations have been reported to emerge around 3–4 months of age, albeit with less frontal predominance than in older children and adults (Cornelissen et al., 2015, 2018a). Moreover, high concentrations/doses of anesthetics have been reported to depress brain activity and enhance signal discontinuity in both human and rodent neonates (Chang et al., 2016; Cornelissen et al., 2017; Stolwijk et al., 2017). However, to our knowledge, a comprehensive algorithmic approach identifying EEG parameters that robustly correlate with anesthetic depth during early postnatal development is still lacking.

Here, we developed a novel strategy to model anesthesia depth by using common electrophysiological features that correlate with inhaled anesthetic concentrations during early development of mice and humans at similar stage of brain development. We performed intracranial electrophysiological recordings to study the temporal and dose-dependent dynamics of brain activity in neonatal mice [postnatal day (P) 8–10] during bolus urethane administration, and during dose-titrated isoflurane general anesthesia, respectively. Dominant local field potential (LFP) features of anesthetic state were identified and used to develop a machine-learning algorithm that distinguishes non-anesthetized from deeply anesthetized states and predicts anesthetic concentration as a proxy for anesthetic depth. Using a similar approach, we used multielectrode EEG recordings to study the dose-dependent dynamics of brain activity in a secondary analysis of a combined new and previously reported data set (Cornelissen et al., 2018a) of human infants 0–6 months of age during induction, maintenance and emergence from general anesthesia (sevoflurane, isoflurane, or desflurane) administered for routine surgical care. Dominant EEG features of anesthetic state were identified and used to develop a machine-learning algorithm to predict end-tidal volume anesthetic concentration (an indirect measure of anesthetic concentration in the brain, and anesthetic depth).

MATERIALS AND METHODS

Animals

All experiments were performed in compliance with the German laws and the guidelines of the European Community for the use of animals in research and were approved by the local ethical committee (G132/12, G17/015, N18/015). Experiments were carried out on C57Bl/6J mice of both sexes. Timed-pregnant mice from the animal facility of the University Medical Center Hamburg-Eppendorf were housed individually at a 12 h light/12 h dark cycle, with *ad libitum* access to water and food. Day of birth was considered P0.

In vivo Electrophysiology in Neonatal Mice

Multisite extracellular recordings were performed in the prefrontal cortex (PFC) and HP, or lateral entorhinal cortex (LEC) and olfactory bulb (OB) of P8–10 mice. Pups were on a heating blanket during the entire procedure. Under isoflurane anesthesia (induction: 5%; maintenance: 2.5%), craniotomies were performed above PFC (0.5 mm anterior to Bregma, 0.1–0.5 mm right to Bregma) and HP (3.5 mm posterior to Bregma, 3.5 mm right to Bregma), or LEC (0 mm anterior to lambda, 6.5 mm right to lambda) and OB (0.5–0.8 mm anterior from the frontonasal suture, 0.5 mm right from internasal suture). Pups were head-fixed into a stereotaxic apparatus using two plastic bars mounted on the nasal and occipital bones with dental cement. Multisite electrodes (NeuroNexus, MI, USA) were inserted into PFC (four-shank, A4x4 recording sites, 100 μm spacing, 2.0 mm deep) and HP (one-shank, A1x16 recording sites, 50 μm spacing, 1.6 mm deep, 20° angle from the vertical plane), or LEC (one-shank, A1x16 recording sites, 100 μm spacing, 2 mm deep, 10° angle from the vertical plane) and OB (one-shank, A1x16 recording sites, 50 μm spacing, 1.4–1.8 mm deep). A silver wire was inserted into the cerebellum and served as ground and reference electrode. Pups were allowed to recover for 30 min prior to recordings. Extracellular signals were band-pass filtered (0.1–9,000 Hz) and digitized (32 kHz) with a multichannel extracellular amplifier (Digital Lynx SX, Neuralynx, Bozeman, MO, USA).

In vivo Electrophysiology in Juvenile Mice

Multisite extracellular recordings were performed in the PFC of P24–39 mice. Under isoflurane anesthesia (induction: 5%; maintenance: 2.5%), a metal head-post (Luigs and Neumann) was attached to the skull with dental cement and 2-mm craniotomies were performed above PFC (0.5–2.0 mm anterior to Bregma, 0.1–0.5 mm right to Bregma) and protected by a customized synthetic window. A silver wire was implanted in the cerebellum as ground and reference electrode. Surgery was performed at least 5 days before recordings. After recovery mice were trained to run on a custom-made spinning-disc. For recordings, craniotomies were uncovered and multisite electrodes (NeuroNexus, MI, USA) were inserted into PFC (one-shank, A1x16 recording sites, 50 μm spacing, 2.0 mm deep). Extracellular signals were band-pass filtered (0.1–9,000 Hz) and digitized (32 kHz) with a multichannel extracellular amplifier (Digital Lynx SX, Neuralynx, Bozeman, MO, USA).

Recordings Under Urethane

Activity was recorded for 15 min without anesthesia before intraperitoneally injecting urethane (1 mg/g body weight; Sigma-Aldrich, St. Louis, MO, USA). Activity was recorded for further 45 min. Animals were transcardially perfused after recordings,

brains were sectioned coronally, and wide field images were acquired to verify recording electrode positions.

Recordings Under Isoflurane

Mouth piece of an isoflurane evaporator (Harvard Apparatus, Holliston, MA, USA) was placed in front of the pups in the recording setup until animals accustomed to it. Activity was recorded for 15 min 0% isoflurane, but with the evaporator running (1.4 l/min). Afterward, isoflurane was added to the airflow and increased every 15 min (1%, 2%, 3%). Animals were transcardially perfused after recordings, brains were sectioned coronally, and wide field images were acquired to verify recording electrode positions.

Electroencephalographic Recordings in Human Neonates and Young Infants

Neonates and infants who were scheduled for an elective surgical procedure were recruited from the pre-operative clinic at Boston Children's Hospital from 12/2012 to 08/2018 (under Institutional Review Board P-3544, with written informed consent obtained from parents/legal guardians). Subjects required surgery below the neck, were clinically stable on the day of study and American Society of Anesthesiologists' physical status I or II. Exclusion criteria were born with congenital malformations or other genetic conditions thought to influence brain development, diagnosed with a neurological or cardiovascular disorder, or born at <32 weeks post-menstrual age. Datasets from previously published work (n = 25; Cornelissen et al., 2018a) and new subjects (n = 10) were included in the analysis. Data are presented from 35 subjects aged 0–6 months.

Anesthetic Management

Each patient received anesthesia induced with sevoflurane (32 subjects), isoflurane (two subjects) or desflurane (one subject) alone or a combination of one of the previous and nitrous oxide. Epochs used for analysis were comprised of sevoflurane, isoflurane or desflurane administration with air and oxygen, titrated to clinical signs; end-tidal anesthetic concentration was adjusted per the anesthetist's impression of clinical need, not a pre-set end-tidal anesthetic concentration.

EEG Recording

EEG data were acquired using an EEG cap (WaveGuard EEG cap, Advanced NeuroTechnology, Netherlands). Thirty-three- or 41-recording electrodes were positioned per the modified international 10/20 electrode placement system. Reference and ground electrodes were located at Fz and AFz respectively. EEG activity from 0.1 to 500 Hz was recorded with an Xltek EEG recording system (EMU40EX, Natus Medical Inc., Canada). Signals were digitized at a sampling rate of 1,024 Hz and a resolution of 16-bit. The EEG recording was started prior to anesthetic induction to capture the loss of consciousness and stopped once the participant reached the Post-Anesthesia Recovery to capture recovery of consciousness. For some infants, the EEG recording was started after anesthetic induction.

Clinical Data Collection

Demographics and clinical information were collected from the electronic medical records and from the in-house Anesthesia Information Management System (AIMS; **Supplementary Table S1**). None of the pathologies causing the need of surgery presented a risk for brain maturation. End-tidal sevoflurane, oxygen, and nitrous oxide concentrations were downloaded from the anesthetic monitoring device (Dräger Apollo, Dräger Medical Inc., Telford, PA, USA) to a recording computer in real-time using ixTrend software (ixcellence, Germany). Signals were recorded at a 1 Hz sampling rate.

Data Analysis

In vivo data were analyzed with custom-written algorithms in the Matlab environment. Data were processed as following: band-pass filtered (500–5,000 Hz) to analyze multi-unit activity (MUA) and band-pass filtered (2–100 Hz) using a third-order Butterworth filter before downsampling to analyze LFP. Filtering procedures were performed in a phase preserving manner.

Multi-Unit Activity

MUA was detected as the peak of negative deflections exceeding five times the standard deviation of the filtered signal and having a prominence larger than half the peak itself. Firing rates were computed by dividing the total number of spikes by the duration of the analyzed time window.

Detection of Oscillatory Activity

Discontinuous active periods were detected with a modified version of a previously developed algorithm for unsupervised analysis of neonatal oscillations (Cichon et al., 2014). Briefly, deflections of the root mean square of band-pass filtered signals (1–100 Hz) exceeding a variance-depending threshold were considered as network oscillations. The threshold was determined by a Gaussian fit to the values ranging from 0 to the global maximum of the root-mean-square histogram. If two oscillations occurred within 200 ms of each other they were considered as one. Only oscillations lasting >1 s were included, and their occurrence, duration and amplitude were computed.

Power Spectral Density

For power spectral density analysis, 1 s-long windows of full signal or network oscillations were concatenated, and the power was calculated using Welch's method with non-overlapping windows.

Imaginary Coherence

The imaginary part of coherence, which is insensitive to volume-conduction-based effects (Nolte et al., 2004), was calculated by taking the absolute value of the imaginary component of the normalized cross-spectrum.

Pairwise Phase Consistency

Pairwise phase consistency (PPC) was computed as previously described (Vinck et al., 2010). Briefly, the phase in the band of interest was extracted using Hilbert transform and the mean of the cosine of the absolute angular distance among all pairs of phases was calculated.

1/f Slope

1/f slope was computed as previously described (Gao et al., 2017). We used robust linear regression (MATLAB function *robustfit*)

to find the best fit over 20–40 Hz frequency range of the power spectral density, in 1-min bins.

Sample Entropy

Sample Entropy was computed using the SampEn function (MATLAB File Exchange) in 1.5 s windows and in 2 Hz frequency bins. Tolerance was set to 0.2 * std (signal), and tau to 1.

EEG Data Analysis

EEG signal was visually inspected to detect and reject channels with low signal to noise ratio and re-referenced to a common average reference. The signal was automatically scored in 5 s epochs, and channels in which signal was significantly contaminated by artifacts (patient handling, surgical electrocautery etc.) were discarded. Epochs were rejected if signal was saturated due to electrocautery, signal exceeded 150 μV, or the median signal across all EEG channels exceeds 30 μV (**Supplementary Figure S5**). Minutes containing more than 10 s of contaminated signal were removed from further analysis. On average 14 ± 9% (median ± median absolute deviation) of the signal was discarded. To compute EEG amplitude, we smoothed the absolute value of the signal, using a moving average filter with a window of 1,024 points (1 s). If more than one volatile anesthetic was used, we retained only epochs in which the main anesthetic was used in isolation. Subjects with epidural anesthesia halfway through the surgery (n = 2 subjects), or with less than 20 min of artifact-free signal (n = 5 subjects) were excluded from further analysis.

Feature Engineering

Features to predict anesthetic concentration in neonatal mice were calculated in 1-min bins. LFP power in the 1–100 Hz range in 10 Hz bins, the percentage of active periods, median length and number of oscillations, median and maximum signal amplitude were computed. All features were computed for both PFC and HP and were normalized to their median value in the non-anesthetized 15 min of recordings. Features to predict anesthetic concentration in human infants were also calculated in 1-min bins. The median amplitude of the smoothed EEG signal and the percentage of the EEG envelope that fell into each amplitude quartile was computed. Amplitude quartiles were computed on the entire EEG trace, averaged over channels. All features were calculated for unfiltered signal, and in the 1–50 Hz range in 5 Hz bins, averaged over channels. Features were normalized to their median value in the non-anesthetized portion of the recording, or lowest anesthetic concentration, if no artifact-free minute was available.

Regressors

Machine-learning analyses were performed using Python (Python Software Foundation, NH, USA) in the Spyder (Pierre Raybaut, The Spyder Development Team) development environment. Model training and performance evaluation were carried out using the scikit-learn toolbox. The set was iteratively (n = 100) divided between a training (2/3 of the set) and a cross-validation (1/3) set. Hyper-parameter of the model was tuned on the training set, which was further split using the standard three-fold cross-validation split implemented by the function "GridSearchCV," to which a "pipeline" object was passed. The "pipeline" object was built using the "Pipeline" function, and concatenating quantile transformation of the input features ("Quantile Transformer," tuning the number of quantiles), feature selection ("Select Percentile," using mutual information and tuning the percentage of features to select) and Radial Basis Function (RBF) kernel support-vector classification/regression (tuning the regularization parameters C and epsilon (regression only), and the kernel coefficient gamma). The classifier input was fed to the regressor as an additional feature. Performance assessment was then computed on the cross-validation set. Regressor decision space was reduced and plotted with t-sne. The decision space was approximated by imposing a Voronoi tessellation on the 2d plot, using k-nearest regression on the t-sne coordinates (Migut et al., 2015).

Statistics

Statistical analyses were performed using R Statistical Software (Foundation for Statistical Computing, Austria). Data were tested for significant differences ($^{*}p < 0.05$, $^{**}p < 0.01$ and $^{***}p < 0.001$) using non-parametric one- and two-way repeated-measures ANOVA (ARTool R package) with Bonferroni corrected *post hoc* analysis (emmeans R package). Correlations were computed using Spearman's rank correlation coefficient (rho). No statistical measures were used to estimate the sample size since the effect size was unknown. For the main experimental results, more information about tests used, values and parameters are provided in the supplementary material (**Supplementary Table S2**).

Data Availability

Electrophysiological data for hippocampus and prefrontal cortex mouse recordings, under both urethane and isoflurane condition, is available at the following open-access repository: https://web.gin.g-node.org/mchini/Neural_correlates_of_anesthesia_in_newborn_mice_and_humans.

RESULTS

Anesthesia Affects the Occurrence but Not the Spectral and Temporal Structure of Oscillatory Events in Neonatal Mice

We monitored the impact of anesthesia on immature brain activity in several cortical areas [PFC, hippocampus (HP), and LEC] as well as in a sensory area OB. For this, multi-site extracellular recordings of LFP and MUA were performed from P8 to 10 mice before and for 45 min after induction of anesthesia by intraperitoneal urethane injection (**Figure 1A**), an anesthetic commonly used in rodents (Khazipov et al., 2004; Colonnese and Khazipov, 2010).

The recorded network activity had a highly fragmented structure (defined as discontinuous activity) in all investigated areas (PFC, HP, LEC and OB). The full signal (i.e., entire LFP trace) consisted of transient episodes of oscillatory discharges with mixed frequencies (from here referred to as "active periods"), alternating with periods of relative electrical silence

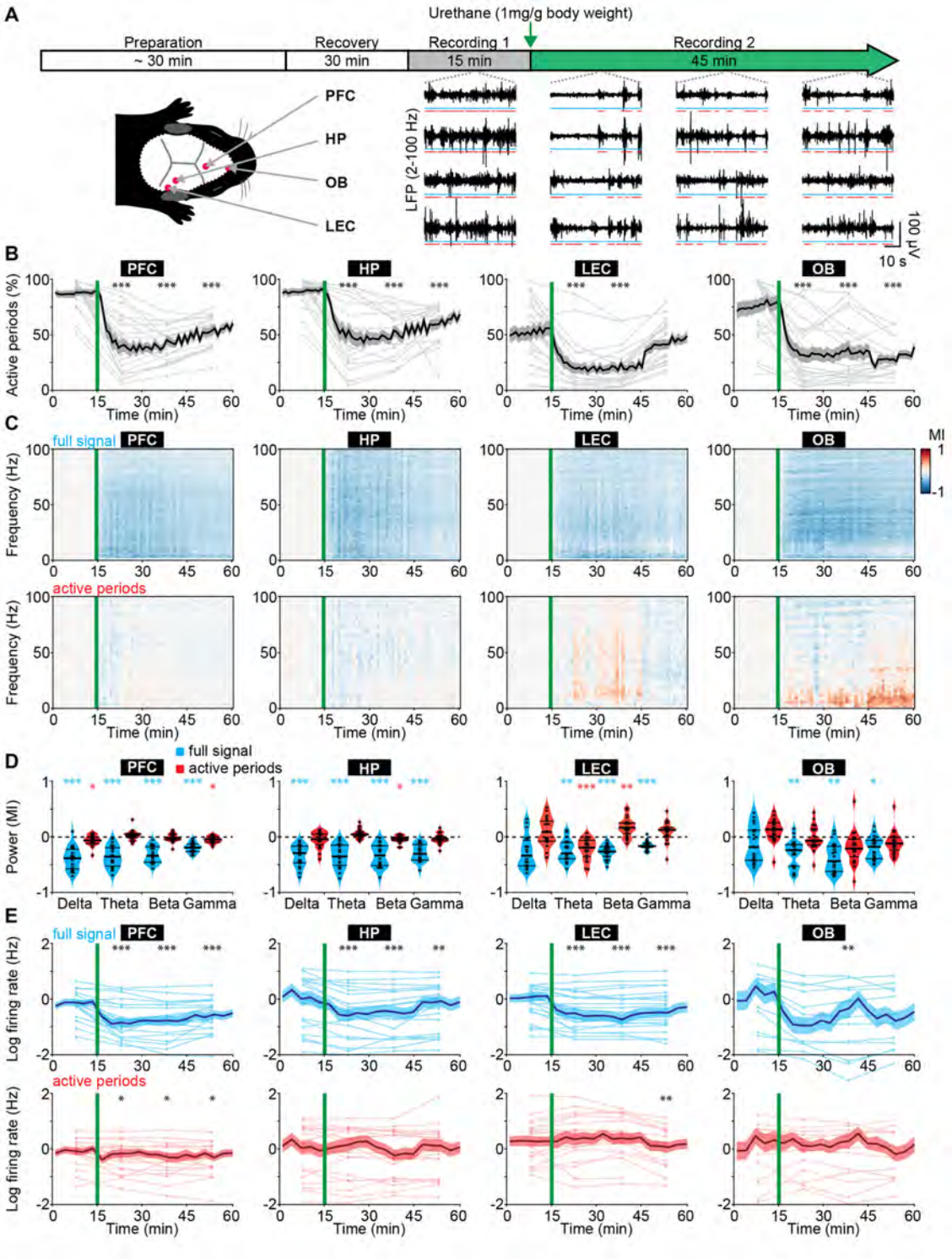

FIGURE 1 | Frequency-unspecific dampening of neuronal activity during urethane anesthesia in neonatal mice. **(A)** Schematic representation of experimental paradigm and recording sites as well as characteristic local field potential (LFP) recordings of discontinuous activity in the prefrontal cortex (PFC), HP, lateral entorhinal cortex (LEC), and olfactory bulb (OB) of neonatal mice (P8–10) during non-anesthetized and urethane-anesthetized state. Time windows of active periods are marked by red lines. **(B)** Line plots displaying the relative occurrence of active periods normalized to total recording time in PFC, HP, OB and LEC before and after urethane injection. **(C)** Color-coded MI of power spectra for full signal (top) and active periods (bottom) recorded in PFC, HP, LEC and OB of neonatal mice before and after urethane injection. **(D)** Violin plots displaying the MI of power in delta (2–4 Hz), theta-alpha (4–12 Hz), beta (12–30 Hz) and gamma (30–100 Hz) frequency bands for full signal (blue) and active periods (red) recorded in the PFC, HP, LEC and OB. **(E)** Line plots displaying multi-unit activity (MUA) rates during full signal (blue) and active periods (red). In **(B,C,E)** green lines correspond to the time point of urethane injection.

and suppressed activity (from here referred to as "silent periods"; **Figure 1A**; Khazipov et al., 2004; Hanganu et al., 2006; Brockmann et al., 2011; Bitzenhofer et al., 2017; Gretenkord et al., 2019). The prevalence of active periods decreased rapidly and robustly over time in all investigated brain areas upon urethane injection (**Figure 1B**). The most prominent reduction was observed 5–15 min after urethane injection. A partial recovery towards baseline levels during the following 30 min was detected in cortical areas, and to a lesser extent in OB (**Figure 1B**). The temporal sequence of events likely reflects the pharmacokinetics of urethane and is line with the previously reported quick onset (few minutes) and long-lasting effects of urethane anesthesia (2–4 h; Huh and Cho, 2013).

The anesthesia-induced reduced occurrence of active periods was reflected in a broadband (1–100 Hz) decrease in oscillatory power shown as modulation index (MI) defined as $(power_{post} - power_{pre})/(power_{post} + power_{pre})$. In contrast, power spectra during active periods were largely unaffected (**Figure 1C**). Of note, for OB, delta and theta power during active periods increased over time after urethane injection and might be related to an observed augmentation of respiration amplitude. Spectral properties of full signal and active periods were quantified for delta (2–4 Hz), theta-alpha (4–12 Hz), beta (12–30 Hz) and gamma (30–100 Hz) frequency bands for the first 15 min post urethane administration, the time window of strongest reduction of active periods. In contrast to the significant reduction of full signal power in all frequency bands, the power during active periods was only marginally affected by anesthesia (**Figure 1D**). Thus, urethane anesthesia affected network activity in the immature rodent brain predominantly by decreasing the amount of active periods without perturbing the frequency structure of active periods. This is in stark contrast with the well-characterized switch from a low-amplitude high-frequency regime to a high-amplitude low-frequency regime of electrical activity that has been reported for the adult rodent and human brain (Voss and Sleigh, 2007; Alkire et al., 2008).

Anesthesia was shown to induce alterations of long-range network interactions in adult rodents (Bettinardi et al., 2015) and humans (Ferrarelli et al., 2010; Lewis et al., 2012; Sarasso et al., 2015). We examined whether similar alterations are present in the immature mouse brain. Simultaneous recordings of HP and PFC, as well as OB and LEC were analyzed to assess the effects of anesthesia on long-range functional coupling. We previously showed that at the end of the first postnatal week hippocampal theta bursts drive the oscillatory entrainment of local circuits in the PFC, whereas discontinuous activity in OB controls the network activity in LEC (Brockmann et al., 2011; Ahlbeck et al., 2018; Gretenkord et al., 2019). Urethane did not modify these interactions. The synchrony within networks quantified by HP-PFC and OB-LEC coherence was similar during baseline (no urethane anesthesia) and in the presence of urethane (**Supplementary Figure S1A**). These data indicate that the core features of long-range functional coupling are retained under anesthesia in neonatal mice.

Anesthesia modified neuronal firing in all investigated areas. Firing rates in PFC, HP, LEC and OB decreased after urethane injection and only partially recovered during the following 45 min (**Figure 1E**). However, firing rates during active periods were only marginally affected. To examine whether the timing of neuronal firing to the phase of oscillatory activity was altered by anesthesia, we calculated PPC, a firing rate-independent measure of spike-LFP phase locking (Vinck et al., 2010). All four brain regions showed similar frequency-resolved phase locking profiles before and after urethane injection (**Supplementary Figures S1B,C**).

Anesthetics have been shown to alter the excitation/inhibition balance in the adult brain through their action on specific ion channels involved in synaptic transmission (Gao et al., 2017). Such alteration is usually monitored by changes in the 1/f slope of power spectral density. Further, signal complexity and information content measured by sample entropy have been correlated with behavioral states of adults, such as consciousness, sleep/wake states and anesthesia (Liang et al., 2015; Liu et al., 2018). For neonatal mice, we observed similar values of 1/f slope and sample entropy before and during urethane anesthesia (**Supplementary Figures S1D–F**), suggesting that urethane does not perturb cortical excitation/inhibition balance and signal complexity at this early age. The findings provide additional evidence to the hypothesis that anesthesia has unique effects on the immature brain.

To add additional evidence for this hypothesis, we extended the time window of investigation and performed extracellular recordings from the PFC of juvenile mice (P24–39). At this age oscillatory activity is continuous, thus a distinction between active and inactive periods is not possible. In contrast to the frequency-unspecific reduction of active periods in neonates, urethane anesthesia increased the oscillatory power in the delta frequency band and suppressed power in beta and gamma frequency bands (**Supplementary Figure S2**), confirming the anesthetic effects in the adult brain (Alkire et al., 2008; Chauvette et al., 2011; Purdon et al., 2015).

Taken together, these results indicate that urethane anesthesia dampened neonatal brain activity mainly by augmenting the discontinuity of network activity, i.e., reducing the proportion of time the brain spent in active periods. However, the active periods were largely unaffected in their temporal structure and firing dynamics. In contrast, urethane anesthesia in older mice led to frequency-specific changes. Thus, urethane anesthesia differently impacts neonatal and adult brain activity in mice.

Suppression of Active Periods Predicts Anesthetic Concentration in Neonatal Mice

To test whether the effects of urethane on neonatal brain activity generalize to other anesthetics, we performed LFP and MUA recordings from HP and PFC of P8–10 mice at increasing doses of isoflurane-induced anesthesia (0, 1, 2 and 3%; 15 min per concentration; **Figure 2A**). Urethane hyperpolarizes neurons by potentiating a resting potassium conductance (Pagliardini et al., 2013), whereas most other anesthetics, such as isoflurane and sevoflurane, mainly act by potentiating $GABA_A$ receptor-mediated transmission (Franks, 2006). Isoflurane reduced the incidence of active periods in a dose-dependent manner (**Figure 2B**). Accordingly, the broadband reduction of LFP power

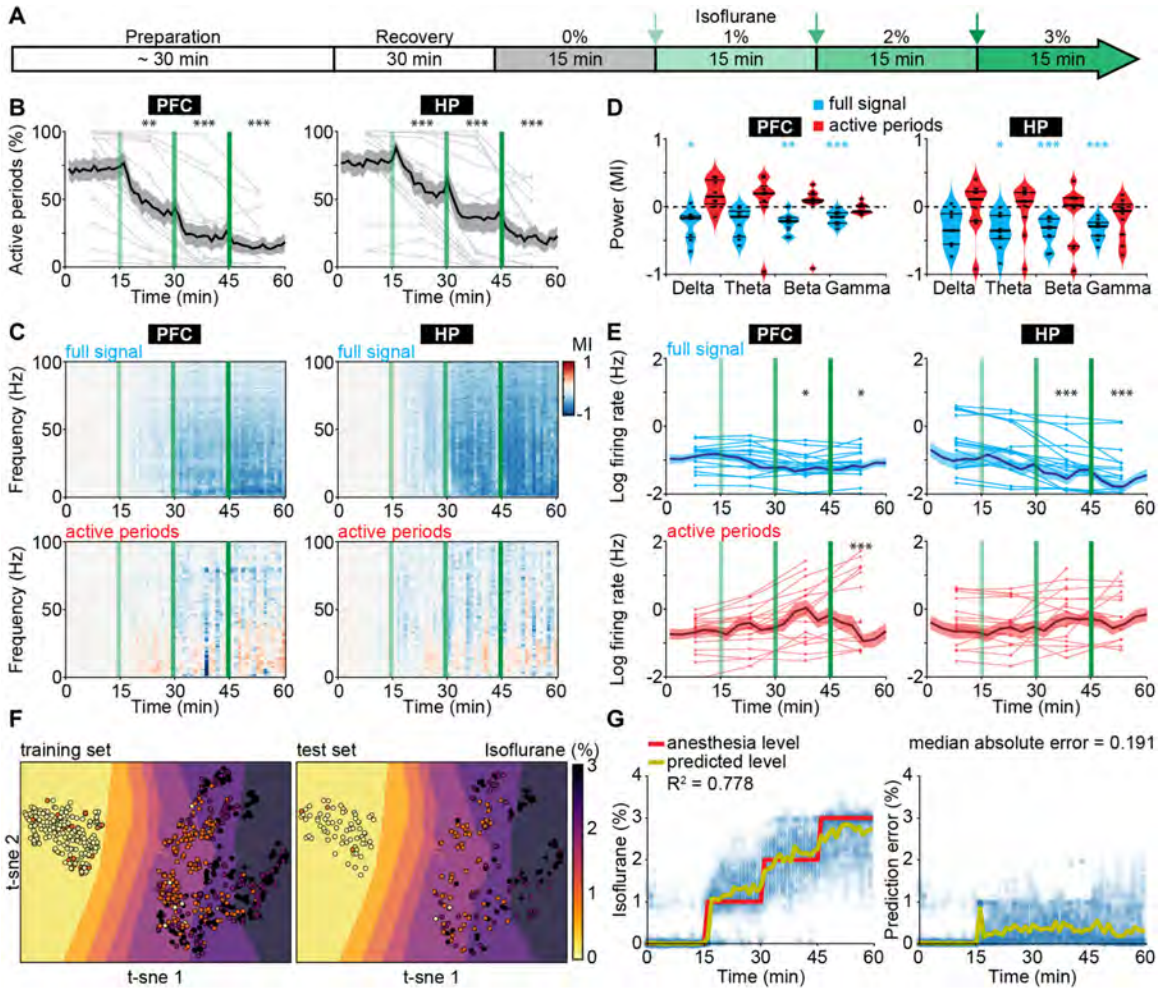

FIGURE 2 | Suppression of active periods in relationship with the depth of isoflurane anesthesia in neonatal mice. **(A)** Schematic representation of experimental protocol for LFP recordings without anesthesia and during increasing levels of isoflurane anesthesia in neonatal mice (P8–10). **(B)** Line plots displaying the relative occurrence of active periods in PFC and HP during increasing levels of isoflurane anesthesia. **(C)** Color-coded MI of power spectra for full signal (top) and active periods (bottom) during increasing levels of isoflurane anesthesia. **(D)** Violin plots displaying the MI of power in delta (2–4 Hz), theta (4–12 Hz), beta (12–30 Hz) and gamma (30–100 Hz) frequency bands for full signal (blue) and active periods (red). **(E)** Line plots displaying MUA firing rates during full signal (blue) and active periods (red). In **(B,C,E)** green lines correspond to the time points of increasing isoflurane anesthesia. **(F)** Visualization of anesthesia depth prediction by t-sne plots. Background color codes for predicted anesthesia depth, while the color of the dots represents the actual anesthesia level in the training (left) and test set (right). **(G)** Scatter plots displaying anesthesia depth predictions with support vector regression (left) and absolute errors between anesthesia depth prediction and actual anesthesia depth (right).

was also dependent on isoflurane concentration (**Figures 2C,D**). Power spectra of active periods remained largely unaffected in the presence of isoflurane, similarly to the urethane effects (**Figures 2C,D**). MUA rates during active periods in PFC and HP were hardly modified in the presence of isoflurane, yet the overall firing decreased corresponding to the reduced occurrence of active periods (**Figure 2E**). Together, these findings identify the suppression of active periods as the main effect of bolus urethane injection and isoflurane anesthesia in the neonatal mouse brain.

The development-specific response of the immature brain to anesthesia might represent the main obstacle when trying to predict anesthesia depth in infants using algorithms based on the mature brain activity of adults. Therefore, we next aimed to use electrophysiological properties specific for anesthetized neonatal mice to predict the concentration of administered isoflurane. We used support vector regression (**Supplementary Figure S3**), with the following input features: median amplitude of broadband LFP, percent of time spent in active periods, and spectral power from 1 to 100 Hz in 10 Hz bins for both hippocampal and prefrontal activity. An additional feature was the output of a support vector classifier that received the same features as for the support vector regression, and that was designed to predict whether the animal was under anesthesia or not. The algorithm accurately predicted anesthesia depth across all levels of isoflurane concentration (**Figures 2F,G**). Estimation of information content of the different features identified the median amplitude of broadband LFP as the most informative feature (**Supplementary Figure S4A**). As the power of active

periods was only marginally affected by anesthesia, this feature mainly mirrors the suppression of active periods. Interestingly, the algorithm was also able to distinguish non-anesthetized from anesthetized recordings from neonatal mice under urethane, even though it had not been exposed to this dataset during training (**Supplementary Figure S4B**).

Thus, features of electrophysiological activity that capture the particularities of immature neuronal networks can predict anesthetic concentration in neonatal mice. The generalization of the classifier to a different anesthetic indicates that it can identify general anesthesia-related features of brain activity in neonatal mice.

Frequency-Unspecific Suppression of Activity in Anesthetized Human Neonates and Young Infants

To test if human neonates and infants, similarly to mice, respond to anesthesia with a broadband decrease of periods of oscillatory activity, we examined EEG recordings from humans aged 0–6 months postnatal age, who received general anesthesia with volatile anesthetics (sevoflurane 32 subjects, isoflurane two subjects, desflurane one subject) for surgery (**Supplementary Table S1**).

In neonatal mice, the median LFP amplitude of broadband activity was identified as the most informative feature to predict anesthetic depth. We, therefore, applied the same data analysis approach to human EEG data (**Supplementary Figure S5**). We found the median amplitude of broadband EEG activity (averaged across all recording electrodes across the scalp) was negatively correlated with end-tidal anesthetic concentration (etAnesthetic) in human neonates from birth until 2 months postnatal age (**Figures 3A,B**). For older human infants, the correlation of the median EEG amplitude with the anesthetic concentration switched to a positive correlation, in agreement with adult human data (Hagihira, 2015). This relationship was even stronger using expected birth age, corrected for conceptional age (**Supplementary Figure S6A**). This switch from negative to positive correlation was also visible in the normalized median EEG amplitude when averaged for age-grouped babies (0–2, 2–4, 4–6 months; **Figure 3C**).

Quantification of median EEG amplitude across frequencies revealed a broadband suppression of EEG activity in human neonates of 0–2 months (**Figure 3D**). In contrast, the relationship between activity amplitude and etAnesthetic indicated frequency-specificity in human infants of 2–4 and 4–6 months, as previously reported (Cornelissen et al., 2017). Frontal activity has been shown to be particularly sensitive to age-varying anesthesia-related effects in human neonates (Cornelissen et al., 2015). Analysis of only frontal electrodes (Fp1, Fp2, F3, F4, F7, F8, Fpz) showed the same age-dependent anesthesia-induced changes as analysis of full scalp electrodes (**Supplementary Figures S6B–D**).

Thus, analogous to what we found in neonatal mice, general anesthesia in human infants younger than 2 months suppressed neuronal population activity, as reported previously (Cornelissen et al., 2015), while at older age anesthesia induced frequency-specific effects.

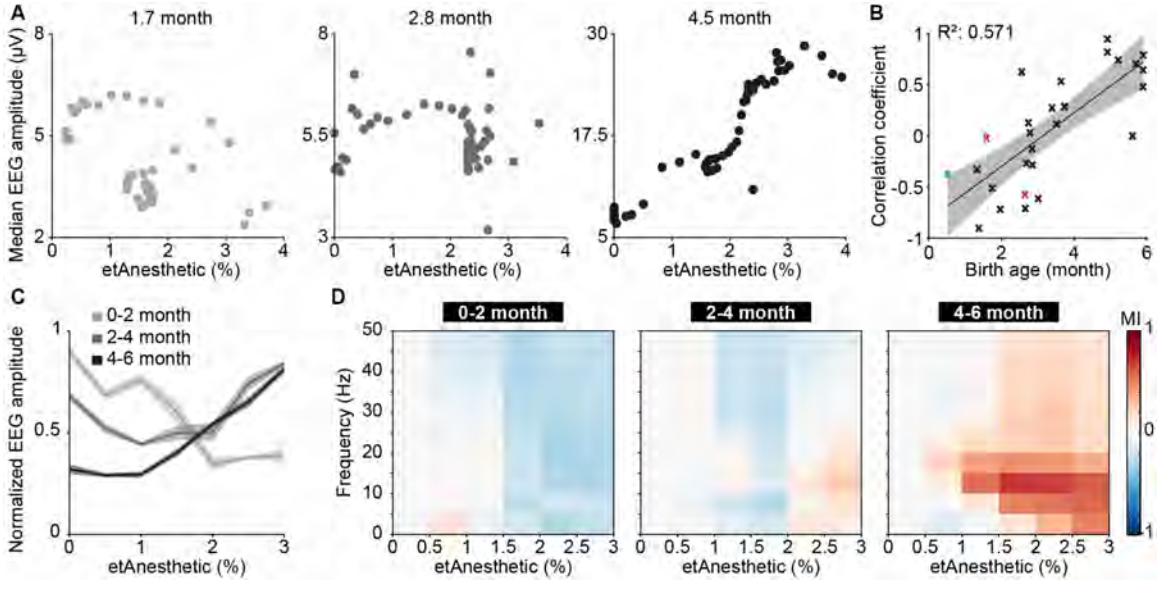

FIGURE 3 | Age-dependent switch from broadband suppression to frequency-specific effects of general anesthesia on electroencephalographic (EEG) activity in human neonates and infants. **(A)** Scatter plots displaying the median EEG amplitude as a function of anesthetic concentration for representative examples of 0–2, 2–4 and 4–6 months of age. **(B)** Scatter plot displaying the correlation coefficient of median EEG amplitude and anesthetic concentration in relation to birth age for sevoflurane (black), isoflurane (red), and desflurane (blue). **(C)** Line plots displaying normalized EEG amplitude as a function of anesthetic concentration. **(D)** Color-coded MI of median EEG amplitudes in different frequency bands as a function of anesthetic concentration for human babies of 0–2 months (left), 2–4 months (middle) and 4–6 months (right).

A Model to Predict End-Tidal Volume of Sevoflurane Anesthesia in Human Neonates and Infants

The correlation of EEG activity with etAnesthetic as well as the similar effects of anesthesia in neonatal mice and in humans from birth to 2 months old, suggests that anesthetic depth in babies might be predicted using similar features to those used in neonatal mice. To test this, we used a machine-learning algorithm with a similar architecture as the one we developed for neonatal mice (**Supplementary Figure S3**). The algorithm was modified to account for the developmental switch from broadband suppression to frequency-specific modulation by training three different regressors using 2 and 4 months as cut-offs. All regressors received the same input features (see "Materials and Methods" section and **Supplementary Figure S5**). Features derived from EEG activity were able to predict etAnesthetic with high accuracy for all age groups (0–2 months R^2 = 0.806, 2–4 months R^2 = 0.688, 4–6 months R^2 = 0.787; **Figures 4A–C**). In line with the frequency-specific alterations observed only in the older age groups, frequency-related features were rated more important for prediction of anesthesia depth in infants of 2–4 and 4–6 months than in neonates of 0–2 months (**Supplementary Figures S7A–C**). Predicting anesthesia depth for all ages with a single classifier considering age as an input feature performed with high accuracy (0–6 months R^2 = 0.689; **Figure 4D**, **Supplementary Figure S7D**). Training the predictor with only 20% of the data and testing it on the remaining 80% resulted in a reduced, but still solid prediction (R^2 = 0.512, median absolute error = 0.209) indicating the robustness of the predictor (**Supplementary Figure S8A**). This result confirms the age-varying effects of anesthesia on the brain and stresses the importance of considering age when developing algorithms aiming to assess anesthetic depth. Predicting anesthesia depth with a reduced number of four EEG channels (F4, P4, F3, P3) or two EEG channels (P4, P3) often used for long-term monitoring yielded similar results (four channels R^2 = 0.713, median absolute error = 0.134; two channels R^2 = 0.671, median absolute error = 0.161; **Supplementary Figures S8B,C**).

Thus, mouse and human neonates show similar changes in network activity in response to anesthesia. These results highlight how neurophysiological activity could be beneficial for future attempts at predicting anesthetic depth in clinical settings.

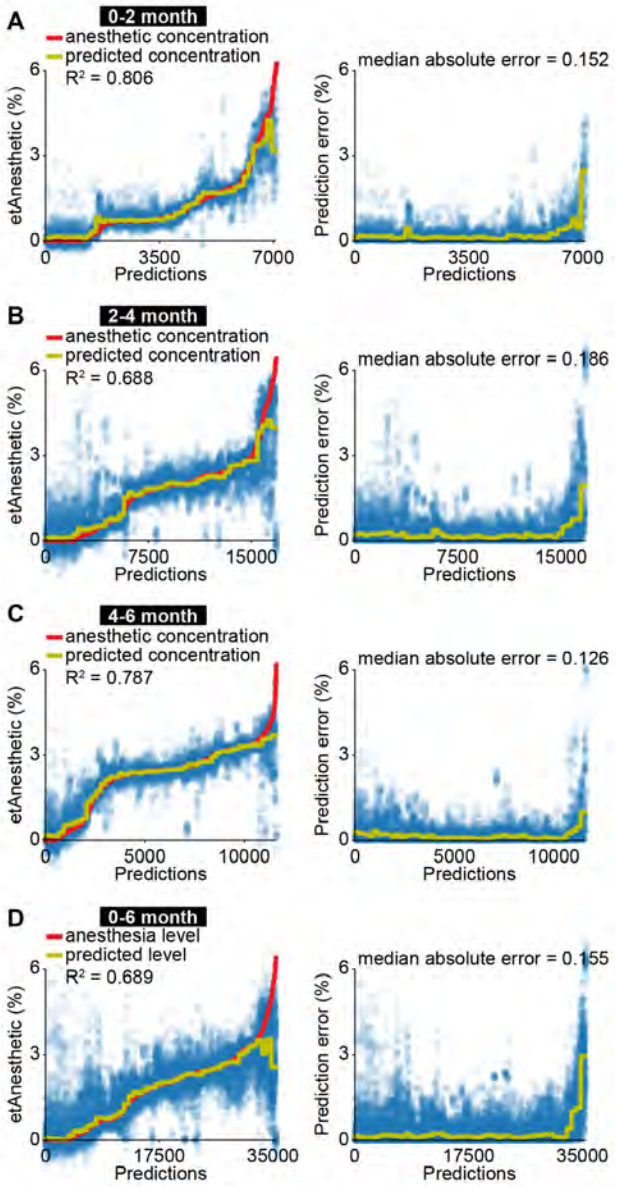

FIGURE 4 | EEG activity is predictive for anesthetic concentration in human infants. **(A)** Scatter plots displaying measured anesthetic concentration and predicted anesthetic concentration of support vector regression for all predictions (left) and absolute difference between measured and predicted anesthetic concentration (right) for human neonates of 0–2 months. **(B)** Same as **(A)** for human infants of 2–4 months. **(C)** Same as **(A)** for human infants of 4–6 months. **(D)** Same as **(A)** for human neonates and infants of 0–6 months.

DISCUSSION

Monitoring brain function during anesthesia is desirable to avoid intraoperative awareness and side effects resulting from unnecessarily high doses of anesthetics. Since consciousness is an elusive concept and cannot be directly measured, EEG features have been used to guide anesthesia delivery during human surgery. Monitoring methods developed for adults perform poorly in human neonates and infants, particularly during the first months of life (Davidson et al., 2005; Hayashi et al., 2012; Poorun et al., 2016; Koch et al., 2017). Age-specific effects of anesthetics on immature brain activity are considered the main reason for such poor performance. Implementation of neonate- and infant-specific anesthesia monitors requires elucidation of distinct anesthesia-induced EEG features during early development. We took advantage of a translational approach to address this open question. We first carried out an in-depth investigation of anesthetic effects on brain activity in neonatal mice, and then applied this knowledge to develop features that would correlate with an anesthetic concentration in human neonates.

In contrast to the continuous EEG signal observed in adults, neonatal EEG around birth is characterized by a highly discontinuous and fragmented temporal organization, with bursts of cerebral activity (active periods) alternating with interburst intervals lacking activity (silent periods; Anderson et al., 1985; Connell et al., 1987; Stockard-Pope et al., 1992; Lamblin et al., 1999; Vecchierini et al., 2003, 2007; Stevenson et al., 2017). Neonatal mice show a similar discontinuous organization of cortical activity (Khazipov et al., 2004; Hanganu et al., 2006; Brockmann et al., 2011). In accordance with the similar organization of early activity patterns in age-matched mouse pups and human infants, we found comparable effects of anesthesia on LFP and EEG signals, respectively.

It is well established that in the adult rodent and human brain most anesthetics favor slow oscillations at the expense of faster ones, thereby slowing the EEG rhythm (Alkire et al., 2008; Chauvette et al., 2011; Purdon et al., 2015). This principle is thought to underlie most algorithms that are clinically used to predict anesthesia depth (Davidson et al., 2005). Indeed, such algorithms perform poorly with anesthetics, such as ketamine, that do not share this mechanism of action (Hans et al., 2005). In line with previous studies (Ackman et al., 2014; Kirmse et al., 2015), we report that both urethane and isoflurane anesthesia affect brain activity in a different way in neonatal mice. Instead of favoring slow oscillations at the expense of faster ones, anesthesia in neonatal mice broadly suppresses activity in a frequency-unspecific manner. The dampening of cortical activity for human infants of 0–2 months suggests a development specific effect of anesthesia on immature brain activity that translates between mice and humans.

In rodents, the switch from activity suppression to frequency-specific modulation of neuronal activity by anesthesia has been reported to occur around P12 (Ackman et al., 2014). This coincides with the emergence of slow oscillations during sleep, suggested to depend on the maturation of thalamocortical networks (Steriade et al., 1993; Ackman et al., 2014). Consistent with our previous studies evaluating EEG properties of this data set, we found that theta and alpha oscillatory activity under anesthesia emerges in humans at around 4 months postnatal age (Cornelissen et al., 2015, 2017, 2018a). Developmental changes in the brain explain the changes in EEG dynamics that occur with postnatal age. In humans, gross brain development occurs in a caudal to rostral direction, with myelination of the medulla, pons, and thalamus starting within the first few postnatal weeks, and frontal cortex myelination starting around 3–4 postnatal months (Brody et al., 1987; Kinney et al., 1988). Regional differences in the rate of synaptogenesis, glucose metabolism and myelination across the cortex occur between subcortical and cortical regions, and between different regions of the cortex during the first 12 postnatal months in human infants (Huttenlocher and Dabholkar, 1997; Tau and Peterson, 2010; Dehorter et al., 2012; Catts et al., 2013; Semple et al., 2013; Murata and Colonnese, 2019). A key role in brain development is played by subplate neurons, the first neurons generated in the cerebral cortex, which guide the formation of thalamocortical connections (Kanold and Luhmann, 2010; Kostović and Judas, 2010). The subplate cells form the first functional connections and relay oscillatory activity in the developing brain (Kanold and Luhmann, 2010). Alpha oscillations in the anesthetized brain are postulated to be produced by thalamocortical circuits, and the gradual emergence of highly powered alpha oscillations at 4-months of age suggests an important developmental milestone has been reached in the processes guided by the subplate neurons. Future studies with a wider age range in mice and humans, including data of human infants studied at preterm, and children in older than 6 months of age, may deepen the understanding of anesthetic effects on brain activity throughout development.

The anesthetics evaluated across species in this study were comparable but not identical in terms of mechanism of action. Moreover, anesthetic management practices used in mice were simplified compared to commonly-used anesthetic practices in the clinic. Multimodal anesthesia requires the use of low-dose anesthetics in combination with analgesic and neuromuscular blocking agents to provide optimal anesthesia and reduce the side effect. These agents act on different drug targets in the nervous system and may have subtle but different effects on brain oscillatory activity (Brown et al., 2018).

In adult human volunteers, the correlation with anesthetic depth and EEG parameters can be performed using verbal reports to establish a threshold for unconsciousness (Purdon et al., 2015). However, in non-verbal populations such as human infants, one must rely on indirect behavioral measures which are more readily performed on emergence rather than induction and incision (Cornelissen et al., 2018b). Future investigations need to include surgical incision and other stimuli into the mouse models to understand with greater granularity the anesthetic titration around the minimal concentrations required to suppress movement, autonomic, and cortical responses to noxious stimuli.

In summary, we report that the suppression of brain activity in mouse and human neonates correlates with anesthetic concentration. The detailed understanding of anesthesia effects on network activity in mice allowed us to identify features and develop a machine-learning algorithm that is able to predict anesthetic concentration from EEG recordings in human neonates. We propose that, after appropriate training, an algorithm based on what we introduce here could learn to associate specific EEG effects with certain anesthetic doses. Eventual mismatches between administered and predicted anesthetic dose would then identify patients that are particularly sensitive/insensitive to an anesthetic, thus helping the anesthetist in administering appropriate levels of anesthetics. By these means, the risk of adverse neurodevelopmental outcome might be mitigated.

ETHICS STATEMENT

All animal experiments were performed in compliance with the German laws and the guidelines of the European Community for the use of animals in research and were approved by the local ethical committee (G132/12, G17/015, N18/015). Human neonates and infants who were scheduled for an elective surgical procedure were recruited from the pre-operative clinic at Boston Children's Hospital from 12/2012 to 08/2018 (under Institutional

Review Board P-3544, with written informed consent obtained from parents/legal guardians).

AUTHOR CONTRIBUTIONS

MC, SB and IH-O designed the experiments. MC, SB, SG, JK, JP, and LC carried out the experiments. MC, SB, SG, JK and JP analyzed the data. MC, SB, LC, CB and IH-O interpreted the data and wrote the article. All authors discussed and commented on the manuscript.

FUNDING

This work was funded by grants from the European Research Council (ERC-2015-CoG 681577 to IH-O), the German Research Foundation (Ha 4466/10-1, SPP 1665, SFB 936 B5 to IH-O) and the International Anesthesia Research Society (to LC). IH-O is a founding member of FENS Kavli Network of Excellence. This manuscript has been released as a Pre-Print at BioRxiv.

ACKNOWLEDGMENTS

We thank P. Putthoff, A. Marquardt, A. Dahlmann, and K. Titze for excellent technical assistance.

SUPPLEMENTARY MATERIAL

The Supplementary Material for this article can be found online at: https://www.frontiersin.org/articles/10.3389/fncir.2019.00038/full#supplementary-material

REFERENCES

Ackman, J. B., Zeng, H., and Crair, M. C. (2014). Structured dynamics of neural activity across developing neocortex. *BioRxiv* [Preprint]. doi: 10.1101/012237

Ahlbeck, J., Song, L., Chini, M., Bitzenhofer, S. H., and Hanganu-Opatz, I. L. (2018). Glutamatergic drive along the septo-temporal axis of hippocampus boosts prelimbic oscillations in the neonatal mouse. *Elife* 7:e33158. doi: 10.7554/eLife.33158

Alkire, M. T., Hudetz, A. G., and Tononi, G. (2008). Consciousness and anesthesia. *Science* 322, 876–880. doi: 10.1126/science.1149213

Anderson, C. M., Torres, F., and Faoro, A. (1985). The EEG of the early premature. *Electroencephalogr. Clin. Neurophysiol.* 60, 95–105. doi: 10.1016/0013-4694(85)90015-X

Bettinardi, R. G., Tort-Colet, N., Ruiz-Mejias, M., Sanchez-Vives, M. V., and Deco, G. (2015). Gradual emergence of spontaneous correlated brain activity during fading of general anesthesia in rats: evidences from fMRI and local field potentials. *Neuroimage* 114, 185–198. doi: 10.1016/j.neuroimage.2015.03.037

Bitzenhofer, S. H., Ahlbeck, J., Wolff, A., Wiegert, J. S., Gee, C. E., Oertner, T. G., et al. (2017). Layer-specific optogenetic activation of pyramidal neurons causes beta-gamma entrainment of neonatal networks. *Nat. Commun.* 8:14563. doi: 10.1038/ncomms14563

Brockmann, M. D., Pöschel, B., Cichon, N., and Hanganu-Opatz, I. L. (2011). Coupled oscillations mediate directed interactions between prefrontal cortex and hippocampus of the neonatal rat. *Neuron* 71, 332–347. doi: 10.1016/j.neuron.2011.05.041

Brody, B. A., Kinney, H. C., Kloman, A. S., and Gilles, F. H. (1987). Sequence of central-nervous-system myelination in human infancy: I. An autopsy study of myelination. *J. Neuropath. Exp. Neurol.* 46, 283–301. doi: 10.1097/00005072-198705000-00005

Brown, E. N., Pavone, K. J., and Naranjo, M. (2018). Multimodal general anesthesia: theory and practice. *Anesth. Analg.* 127, 1246–1258. doi: 10.1213/ANE.0000000000003668

Catts, V. S., Fung, S. J., Long, L. E., Joshi, D., Vercammen, A., Allen, K. M., et al. (2013). Rethinking schizophrenia in the context of normal neurodevelopment. *Front. Cell. Neurosci.* 7:60. doi: 10.3389/fncel.2013.00060

Chang, P. S., Walker, S. M., and Fitzgerald, M. (2016). Differential suppression of spontaneous and noxious-evoked somatosensory cortical activity by isoflurane in the neonatal rat. *Anesthesiology* 124, 885–898. doi: 10.1097/ALN.0000000000001017

Chauvette, S., Crochet, S., Volgushev, M., and Timofeev, I. (2011). Properties of slow oscillation during slow-wave sleep and anesthesia in cats. *J. Neurosci.* 31, 14998–15008. doi: 10.1523/JNEUROSCI.2339-11.2011

Cichon, N. B., Denker, M., Grün, S., and Hanganu-Opatz, I. L. (2014). Unsupervised classification of neocortical activity patterns in neonatal and pre-juvenile rodents. *Front. Neural Circuits* 8:50. doi: 10.3389/fncir.2014.00050

Colonnese, M. T., and Khazipov, R. (2010). "Slow activity transients" in infant rat visual cortex: a spreading synchronous oscillation patterned by retinal waves. *J. Neurosci.* 30, 4325–4337. doi: 10.1523/JNEUROSCI.4995-09.2010

Connell, J. A., Oozeer, R., and Dubowitz, V. (1987). Continuous 4-channel EEG monitoring: a guide to interpretation, with normal values, in preterm infants. *Neuropediatrics* 18, 138–145. doi: 10.1055/s-2008-1052466

Cornelissen, L., Bergin, A. M., Lobo, K., Donado, C., Soul, J. S., and Berde, C. B. (2017). Electroencephalographic discontinuity during sevoflurane anesthesia in infants and children. *Paediatr. Anaesth.* 27, 251–262. doi: 10.1111/pan.13061

Cornelissen, L., Donado, C., Lee, J. M., Liang, N. E., Mills, I., Tou, A., et al. (2018a). Clinical signs and electroencephalographic patterns of emergence from sevoflurane anaesthesia in children: an observational study. *Eur. J. Anaesthesiol.* 35, 49–59. doi: 10.1097/EJA.0000000000000739

Cornelissen, L., Kim, S. E., Lee, J. M., Brown, E. N., Purdon, P. L., and Berde, C. B. (2018b). Electroencephalographic markers of brain development during sevoflurane anaesthesia in children up to 3 years old. *Br. J. Anaesth.* 120, 1274–1286. doi: 10.1016/j.bja.2018.01.037

Cornelissen, L., Kim, S. E., Purdon, P. L., Brown, E. N., and Berde, C. B. (2015). Age-dependent electroencephalogram (EEG) patterns during sevoflurane general anesthesia in infants. *Elife* 4:e06513. doi: 10.7554/eLife.06513

Davidson, A. J., Huang, G. H., Rebmann, C. S., and Ellery, C. (2005). Performance of entropy and bispectral index as measures of anaesthesia effect in children of different ages. *Br. J. Anaesth.* 95, 674–679. doi: 10.1093/bja/aei247

Dehorter, N., Vinay, L., Hammond, C., and Ben-Ari, Y. (2012). Timing of developmental sequences in different brain structures: physiological and pathological implications. *Eur. J. Neurosci.* 35, 1846–1856. doi: 10.1111/j.1460-9568.2012.08152.x

Ferrarelli, F., Massimini, M., Sarasso, S., Casali, A., Riedner, B. A., Angelini, G., et al. (2010). Breakdown in cortical effective connectivity during midazolam-induced loss of consciousness. *Proc. Natl. Acad. Sci. U S A* 107, 2681–2686. doi: 10.1073/pnas.0913008107

Franks, N. P. (2006). Molecular targets underlying general anaesthesia. *Br. J. Pharmacol.* 147, S72–S81. doi: 10.1038/sj.bjp.0706441

Gao, R., Peterson, E. J., and Voytek, B. (2017). Inferring synaptic excitation/inhibition balance from field potentials. *Neuroimage* 158, 70–78. doi: 10.1016/j.neuroimage.2017.06.078

Glass, P. S., Bloom, M., Kearse, L., Rosow, C., Sebel, P., and Manberg, P. (1997). Bispectral analysis measures sedation and memory effects of propofol, midazolam, isoflurane and alfentanil in healthy volunteers. *Anesthesiology* 86, 836–847. doi: 10.1097/00000542-199704000-00014

Gretenkord, S., Kostka, J. K., Hartung, H., Watznauer, K., Fleck, D., Minier-Toribio, A., et al. (2019). Coordinated electrical activity in the olfactory bulb

gates the oscillatory entrainment of entorhinal networks in neonatal mice. *PLoS. Biol.* 17:e2006994. doi: 10.1371/journal.pbio.2006994

Hagihira, S. (2015). Changes in the electroencephalogram during anaesthesia and their physiological basis. *Br. J. Anaesth.* 115, i27–i31. doi: 10.1093/bja/aev212

Hajat, Z., Ahmad, N., and Andrzejowski, J. (2017). The role and limitations of EEG-based depth of anaesthesia monitoring in theatres and intensive care. *Anaesthesia* 72, 38–47. doi: 10.1111/anae.13739

Hanganu, I. L., Ben-Ari, Y., and Khazipov, R. (2006). Retinal waves trigger spindle bursts in the neonatal rat visual cortex. *J. Neurosci.* 26, 6728–6736. doi: 10.1523/JNEUROSCI.0752-06.2006

Hans, P., Dewandre, P. Y., Brichant, J. F., and Bonhomme, V. (2005). Comparative effects of ketamine on bispectral index and spectral entropy of the electroencephalogram under sevoflurane anaesthesia. *Br. J. Anaesth.* 94, 336–340. doi: 10.1093/bja/aei047

Hayashi, K., Shigemi, K., and Sawa, T. (2012). Neonatal electroencephalography shows low sensitivity to anesthesia. *Neurosci. Lett.* 517, 87–91. doi: 10.1016/j.neulet.2012.04.028

Huh, Y., and Cho, J. (2013). Urethane anesthesia depresses activities of thalamocortical neurons and alters its response to nociception in terms of dual firing modes. *Front. Behav. Neurosci.* 7:141. doi: 10.3389/fnbeh.2013.00141

Huttenlocher, P. R., and Dabholkar, A. S. (1997). Regional differences in synaptogenesis in human cerebral cortex. *J. Comp. Neurol.* 387, 167–178. doi: 10.1002/(sici)1096-9861(19971020)387:2<167::aid-cne1>3.0.co;2-z

Kalkman, C. J., Peelen, L. M., and Moons, K. G. (2011). Pick up the pieces: depth of anesthesia and long-term mortality. *Anesthesiology* 114, 485–487. doi: 10.1097/ALN.0b013e31820c2ba2

Kanold, P. O., and Luhmann, H. J. (2010). The subplate and early cortical circuits. *Annu. Rev. Neurosci.* 33, 23–48. doi: 10.1146/annurev-neuro-060909-153244

Kertai, M. D., Whitlock, E. L., and Avidan, M. S. (2012). Brain monitoring with electroencephalography and the electroencephalogram-derived bispectral index during cardiac surgery. *Anesth. Analg.* 114, 533–546. doi: 10.1213/ANE.0b013e31823ee030

Khazipov, R., Sirota, A., Leinekugel, X., Holmes, G. L., Ben-Ari, Y., and Buzsaki, G. (2004). Early motor activity drives spindle bursts in the developing somatosensory cortex. *Nature* 432, 758–761. doi: 10.1038/nature03132

Kinney, H. C., Brody, B. A., Kloman, A. S., and Gilles, F. H. (1988). Sequence of Central Nervous-System Myelination in Human Infancy .2. Patterns of Myelination in Autopsied Infants. *J. Neuropathol. Exp. Neurol.* 47, 217–234. doi: 10.1097/00005072-198805000-00003

Kirmse, K., Kummer, M., Kovalchuk, Y., Witte, O. W., Garaschuk, O., and Holthoff, K. (2015). GABA depolarizes immature neurons and inhibits network activity in the neonatal neocortex *in vivo*. *Nat. Commun.* 6:7750. doi: 10.1038/ncomms8750

Koch, S., Stegherr, A. M., Morgeli, R., Kramer, S., Toubekis, E., Lichtner, G., et al. (2017). Electroencephalogram dynamics in children during different levels of anaesthetic depth. *Clin. Neurophysiol.* 128, 2014–2021. doi: 10.1016/j.clinph.2017.07.417

Kostović, I., and Judas, M. (2010). The development of the subplate and thalamocortical connections in the human foetal brain. *Acta Paediatr.* 99, 1119–1127. doi: 10.1111/j.1651-2227.2010.01811.x

Kreuzer, M. (2017). EEG based monitoring of general anesthesia: taking the next steps. *Front. Comput. Neurosci.* 11:56. doi: 10.3389/fncom.2017.00056

Lamblin, M. D., André, M., Challamel, M. J., Curzi-Dascalova, L., d'Allest, A. M., De Giovanni, E., et al. (1999). Electroencephalography of the premature and term newborn. Maturational aspects and glossary. *Neurophysiol. Clin.* 29, 123–219. doi: 10.1016/S0987-7053(99)80051-3

Lewis, L. D., Weiner, V. S., Mukamel, E. A., Donoghue, J. A., Eskandar, E. N., Madsen, J. R., et al. (2012). Rapid fragmentation of neuronal networks at the onset of propofol-induced unconsciousness. *Proc. Natl. Acad. Sci. U S A* 109, E3377–E3386. doi: 10.1073/pnas.1210907109

Liang, Z., Wang, Y., Sun, X., Li, D., Voss, L. J., Sleigh, J. W., et al. (2015). EEG entropy measures in anesthesia. *Front. Comput. Neurosci.* 9:16. doi: 10.3389/fncom.2015.00016

Liu, Q., Ma, L., Fan, S. Z., Abbod, M. F., and Shieh, J. S. (2018). Sample entropy analysis for the estimating depth of anaesthesia through human EEG signal at different levels of unconsciousness during surgeries. *PeerJ* 6:e4817. doi: 10.7717/peerj.4817

Lo, S. S., Sobol, J. B., Mallavaram, N., Carson, M., Chang, C., Grieve, P. G., et al. (2009). Anesthetic-specific electroencephalographic patterns during emergence from sevoflurane and isoflurane in infants and children. *Paediatr. Anaesth.* 19, 1157–1165. doi: 10.1111/j.1460-9592.2009.03128.x

Migut, M. A., Worring, M., and Veenman, C. J. (2015). Visualizing multi-dimensional decision boundaries in 2D. *Data Min. Knowl. Discov.* 29, 273–295. doi: 10.1007/s10618-013-0342-x

Milh, M., Kaminska, A., Huon, C., Lapillonne, A., Ben-Ari, Y., and Khazipov, R. (2007). Rapid cortical oscillations and early motor activity in premature human neonate. *Cereb. Cortex* 17, 1582–1594. doi: 10.1093/cercor/bhl069

Murata, Y., and Colonnese, M. T. (2019). Thalamic inhibitory circuits and network activity development. *Brain Res.* 1706, 13–23. doi: 10.1016/j.brainres.2018.10.024

Nolte, G., Bai, O., Wheaton, L., Mari, Z., Vorbach, S., and Hallett, M. (2004). Identifying true brain interaction from EEG data using the imaginary part of coherency. *Clin. Neurophysiol.* 115, 2292–2307. doi: 10.1016/j.clinph.2004.04.029

O'Toole, J. M., Boylan, G. B., Vanhatalo, S., and Stevenson, N. J. (2016). Estimating functional brain maturity in very and extremely preterm neonates using automated analysis of the electroencephalogram. *Clin. Neurophysiol.* 127, 2910–2918. doi: 10.1016/j.clinph.2016.02.024

Pagliardini, S., Funk, G. D., and Dickson, C. T. (2013). Breathing and brain state: urethane anesthesia as a model for natural sleep. *Respir. Physiol. Neurobiol.* 188, 324–332. doi: 10.1016/j.resp.2013.05.035

Poorun, R., Hartley, C., Goksan, S., Worley, A., Boyd, S., Cornelissen, L., et al. (2016). Electroencephalography during general anaesthesia differs between term-born and premature-born children. *Clin. Neurophysiol.* 127, 1216–1222. doi: 10.1016/j.clinph.2015.10.041

Prichep, L. S., Gugino, L. D., John, E. R., Chabot, R. J., Howard, B., Merkin, H., et al. (2004). The patient state index as an indicator of the level of hypnosis under general anaesthesia. *Br. J. Anaesth.* 92, 393–399. doi: 10.1093/bja/aeh082

Punjasawadwong, Y., Phongchiewboon, A., and Bunchungmongkol, N. (2014). Bispectral index for improving anaesthetic delivery and postoperative recovery. *Cochrane Database Syst. Rev.* 6:CD003843. doi: 10.1002/14651858.CD003843

Purdon, P. L., Sampson, A., Pavone, K. J., and Brown, E. N. (2015). Clinical electroencephalography for anesthesiologists: Part I: background and basic signatures. *Anesthesiology* 123, 937–960. doi: 10.1097/ALN.0000000000000841

Sarasso, S., Boly, M., Napolitani, M., Gosseries, O., Charland-Verville, V., Casarotto, S., et al. (2015). Consciousness and complexity during unresponsiveness induced by propofol, Xenon and Ketamine. *Curr. Biol.* 25, 3099–3105. doi: 10.1016/j.cub.2015.10.014

Semple, B. D., Blomgren, K., Gimlin, K., Ferriero, D. M., and Noble-Haeusslein, L. J. (2013). Brain development in rodents and humans: identifying benchmarks of maturation and vulnerability to injury across species. *Prog. Neurobiol.* 106–107, 1–16. doi: 10.1016/j.pneurobio.2013.04.001

Steriade, M., Nuñez, A., and Amzica, F. (1993). Intracellular analysis of relations between the slow (<1 Hz) neocortical oscillation and other sleep rhythms of the electroencephalogram. *J. Neurosci.* 13, 3266–3283. doi: 10.1523/jneurosci.13-08-03266.1993

Stevenson, N. J., Oberdorfer, L., Koolen, N., O'Toole, J. M., Werther, T., Klebermass-Schrehof, K., et al. (2017). Functional maturation in preterm infants measured by serial recording of cortical activity. *Sci. Rep.* 7:12969. doi: 10.1038/s41598-017-13537-3

Stockard-Pope, J. E., Werner, S. S., and Bickford, R. G. (1992). *Atlas of Neonatal Electroencephalography*. New York, NY: Raven Press.

Stolwijk, L. J., Weeke, L. C., de Vries, L. S., van Herwaarden, M. Y. A., van der Zee, D. C., van der Werff, D. B. M., et al. (2017). Effect of general anesthesia on neonatal aEEG-A cohort study of patients with non-cardiac

congenital anomalies. *PLoS One* 12:e0183581. doi: 10.1371/journal.pone.0183581

Tau, G. Z., and Peterson, B. S. (2010). Normal development of brain circuits. *Neuropsychopharmacology* 35, 147–168. doi: 10.1038/npp.2009.115

Vecchierini, M. F., André, M., and d'Allest, A. M. (2007). Normal EEG of premature infants born between 24 and 30 weeks gestational age: terminology, definitions and maturation aspects. *Neurophysiol. Clin.* 37, 311–323. doi: 10.1016/j.neucli.2007.10.008

Vecchierini, M. F., d'Allest, A. M., and Verpillat, P. (2003). EEG patterns in 10 extreme premature neonates with normal neurological outcome: qualitative and quantitative data. *Brain Dev.* 25, 330–337. doi: 10.1016/s0387-7604(03)00007-x

Vinck, M., van Wingerden, M., Womelsdorf, T., Fries, P., and Pennartz, C. M. (2010). The pairwise phase consistency: a bias-free measure of rhythmic neuronal synchronization. *Neuroimage* 51, 112–122. doi: 10.1016/j.neuroimage.2010.01.073

Voss, L., and Sleigh, J. (2007). Monitoring consciousness: the current status of EEG-based depth of anaesthesia monitors. *Best Pract. Res. Clin. Anaesthesiol.* 21, 313–325. doi: 10.1016/j.bpa.2007.04.003

Conflict of Interest Statement: The authors declare that the research was conducted in the absence of any commercial or financial relationships that could be construed as a potential conflict of interest.

2.8 Anesthetics uniquely decorrelate hippocampal network activity, alter spine dynamics and affect memory consolidation

Wei Yang, Mattia Chini, Jastyn A. Pöpplau, Andrey Formozov, Alexander Dieter, Patrick Piechocinski, Cynthia Rais, Fabio Morellini, Olaf Sporns, Ileana L. Hanganu-Opatz and J. Simon Wiegert

Biorxiv, accepted in *PLOS Biology* 2021; DOI: https://doi.org/10.1101/2020.06.05.135905

Personal contribution

I helped designing the project. I carried out formal analysis and data curation. I helped writing the original draft, reviewed and edited the manuscript.

Anesthetics uniquely decorrelate hippocampal network activity, alter spine dynamics and affect memory consolidation

Wei Yang[1,6], Mattia Chini[2,6], Jastyn A. Pöpplau[2], Andrey Formozov[1], Patrick Piechocinski[1], Cynthia Rais[1], Fabio Morellini[3], Olaf Sporns[4,5], Ileana L. Hanganu-Opatz[2] and J. Simon Wiegert[1*]

[1]Research Group Synaptic Wiring and Information Processing, Center for Molecular Neurobiology Hamburg, University Medical Center Hamburg-Eppendorf, 20251 Hamburg, Germany

[2]Developmental Neurophysiology, Center for Molecular Neurobiology, University Medical Center Hamburg-Eppendorf, 20251 Hamburg, Germany

[3]Research Group Behavioral Biology, Center for Molecular Neurobiology Hamburg, University Medical Center Hamburg-Eppendorf, 20251 Hamburg, Germany

[4]Department of Psychological and Brain Sciences, Indiana University, Bloomington, Indiana, USA

[5]Indiana University Network Science Institute, Indiana University, Bloomington, Indiana, USA

[6]These authors contributed equally

*Correspondence: simon.wiegert@zmnh.uni-hamburg.de, @SimWieg

SUMMARY

General anesthesia is characterized by reversible loss of consciousness accompanied by transient amnesia. Yet, long-term memory impairment is an undesirable side-effect. How different types of general anesthetics (GAs) affect the hippocampus, a brain region central to memory formation and consolidation, is poorly understood. Using extracellular recordings, chronic 2-photon imaging and behavioral analysis, we monitor the effects of isoflurane (Iso), medetomidine/midazolam/fentanyl (MMF), and ketamine/xylazine (Keta/Xyl) on network activity and structural spine dynamics in the hippocampal CA1 area of adult mice. GAs robustly reduced spiking activity, decorrelated cellular ensembles, albeit with distinct activity signatures, and altered spine dynamics. Iso anesthesia most closely resembled wakefulness, and network alterations recovered more readily than with Keta/Xyl and MMF. Correspondingly, memory consolidation was impaired after exposure to Keta/Xyl and MMF, but not Iso. Thus, different anesthetics distinctly alter hippocampal network dynamics, synaptic connectivity, and memory consolidation, with implications for GA strategy appraisal in animal research and clinical settings.

KEYWORDS

General anesthesia, isoflurane, ketamine, fentanyl, hippocampus, population dynamics, network activity, spine turnover, episodic memory

INTRODUCTION

General anesthesia is a drug-induced, reversible behavioral condition encompassing unconsciousness, amnesia, sedation, immobility, and analgesia (Rudolph and Antkowiak, 2004; Urban and Bleckwenn, 2002). Together, these aspects represent a state where surgery can be tolerated without the requirement for further drugs (Urban and Bleckwenn, 2002). The behavioral effects of GAs are dose-dependent. At clinical (i.e. highest) dosage, they should induce unconsciousness, even though experimental evidence of this phenomenon is challenging to collect (in absence of a verifiable consciousness theory). At lower doses, some GAs cause unresponsiveness and loss of working memory, phenomena that have been both hypothesized to potentially confound the apparent loss of consciousness (Alkire et al., 2008; Sanders et al., 2012). At much lower doses still, GAs cause profound retrograde amnesia. When general anesthesia fails to induce such behavioral effects, intraoperative awareness ensues, a condition that is associated with long-term negative health consequences (Mashour et al., 2011). While loss of memory is required for the time period of anesthesia, so that no memories of the surgical procedure are formed (Antognini and Carstens, 2002; Rudolph and Antkowiak, 2004), long-term impairments of retrograde or anterograde memories are not desired. Although general anesthesia is generally considered a safe procedure, growing literature points to the possibility of long-term negative effects on the central nervous system (Vutskits and Xie, 2016). This is particularly true for specific categories of patients, such as the elderly, infants and children (Vutskits and Xie, 2016). Among the observed side effects, the most common are post-operative cognitive dysfunction syndromes, including post-operative delirium (POD) and post-operative cognitive decline (POCD). Post-operative cognitive disturbances are positively correlated with the duration of anesthesia and a single exposure to GAs can cause retrograde and anterograde memory deficits that persist for days to weeks in rodent models (Zurek et al., 2014). These aspects point to a generalized action of GAs on the memory system.

Given that amnesia is a fundamental part of general anesthesia and that the hippocampus controls memory formation and consolidation, it is important to understand how anesthetics affect hippocampal function. Together with subiculum, the CA1 area constitutes the main hippocampal output region. CA1 pyramidal cells receive excitatory input mainly from CA3 (in strata oriens & radiatum) and layer 3 of entorhinal cortex at spine synapses (Neves et al., 2008), relaying information about external and internal state, respectively (Larkum, 2012). Thus, CA1 pyramidal cells have been suggested to integrate information about the environment and internal representations (Bittner et al., 2015; Larkum, 2012), with synaptic spines being possible sites of memory storage (Frey and Morris, 1997; Kasai et al., 2010; Segal, 2005; Yang et al., 2009). Moreover, dynamic modulation of spine stability has been linked to synaptic plasticity (De Roo et al., 2008; Nagerl et al., 2004; Wiegert and Oertner, 2013; Wiegert et al., 2018). Synaptic plasticity, in turn, underlies learning and memory formation (Whitlock et al., 2006), suggesting that spine turnover in the hippocampus directly reflects these processes (Attardo et al., 2015; Schmid et al., 2016). Considering the low concentrations of anesthetics required to induce amnesia, these compounds are thought of affecting in particular the hippocampus. One possible explanation of this sensitivity is the fact that a class of γ-aminobutyric acid receptors (GABARs), which is strongly modulated by some anesthetics, is predominantly expressed in the hippocampus (Bonin and Orser, 2008; Sur et al., 1999). However, a systematic, in-depth investigation of the effects of anesthetics on the hippocampus bridging synaptic, network and behavioral levels, is still lacking.

Here, using behavioral analysis, extracellular recordings and chronic 2-photon calcium imaging, we systematically assessed how memory performance, CA1 network dynamics and synaptic structure are affected by three commonly used combinations of GAs: isoflurane (Iso), midazolam/medetomidine/fentanyl (MMF), and ketamine in combination with xylazine (Keta/Xyl). All three GAs strongly reduced overall neuronal spiking and, opposite to what has been found in the neocortex (Goltstein et al., 2015; Greenberg et al., 2008; Wenzel et al., 2019), decorrelated network activity, leading to a fragmented network state. However, the induced patterns of activity were highly distinct between the three different conditions and recovered to the pre-anesthetic status with disparate rates. Testing the effect of repeated anesthesia on spine dynamics revealed that Keta/Xyl, the condition which most strongly affected calcium activity, significantly reduced spine turnover, leading to an overall (over)stabilization of hippocampal synapses. In contrast, Iso and MMF mildly increased spine turnover. Finally, we show that the two anesthetic conditions which induce longer-lasting network alterations, Keta/Xyl and MMF, negatively influenced hippocampus-dependent memory consolidation. Thus, different anesthetics, despite reaching a similar physiological state, strongly differ in their effects on synaptic stability, hippocampal network activity, and memory consolidation.

RESULTS

Iso, Keta/Xyl and MMF induce distinct patterns of network activity

Iso, Keta/Xyl and MMF have distinct molecular targets and modes of action in the brain. We therefore hypothesized that electrical activity in the hippocampus is uniquely altered by each of the three anesthesia strategies. To test this hypothesis, we investigated local field potentials (LFPs) and firing of individual neurons (single unit activity, SUA) extracellularly recorded in the CA1 area of dorsal hippocampus (dCA1) during wakefulness followed by 45 min of anesthesia and 45 min of recovery (Fig. 1A, S1A). We found that the anesthetics differently affected network activity, inducing characteristic modulation of various frequency bands (Fig. 1B). During wakefulness, LFP power in CA1 was highest in the theta (4-12 Hz) and low-gamma (40-60 Hz) bands (Fig. S1B). Exposure to 2-2.5% Iso led to a strong reduction of LFP power > 4 Hz within the first 2 minutes that was accompanied by complete loss of mobility of the animal (Fig. 1C, S1B,C). Similarly, MMF injection promptly decreased LFP power in the same frequency bands. In contrast, Keta/Xyl increased power across all frequencies during the first 10 min after injection, the most prominent effect being observed for activity at 5-30 Hz. This is consistent with previous reports, finding enhanced theta and low-gamma power in CA1 of rats under ketamine anesthesia (Soltesz and Deschenes, 1993). The initial LFP power increase was followed by a gradual, significant decrease of 30-100 Hz activity (Fig. 1C, S1B,C).

It is widely accepted that, in the neocortex, GAs favor slow oscillations at the expense of faster ones (Purdon et al., 2015). To determine whether this is also the case in the hippocampus, we next asked how the investigated anesthetics affect slow network oscillations. Consistent with previous reports (Collins et al., 2001; Contreras and Steriade, 1995; Steriade et al., 1993), Keta/Xyl strongly enhanced LFP power at 0.5-4 Hz throughout the entire recording period (Fig. 1C,D, S1C), but suppressed frequencies lower than 0.5 Hz. In contrast, Iso strongly augmented LFP power below 0.5 Hz, peaking at 0.1-0.2 Hz (Fig. 1C,D, S1C), whereas MMF induced no significant increase in the low-frequency regime. However, similar to Keta/Xyl, a significant reduction was present below 0.5 Hz, which persisted throughout the entire recording period (Fig. 1C,D). The power-law decay exponent (1/f slope) of the LFP power spectrum has

been hypothesized to track excitation/inhibition (E/I) balance, and is reduced under anesthesia (Gao et al., 2017), indicating a shift towards inhibition. Considering the robust effects on LFP power that we reported, we reasoned that a similar phenomenon might also occur in the hippocampus. Indeed, all anesthetics significantly decreased the power-law decay exponent, albeit with a different temporal profile. While the effect of Iso occurred within a few minutes, MMF and Keta/Xyl operated on a longer timescale (Fig. 1E). Moreover, periods of activity were consistently and strongly reduced immediately under Iso and MMF, but delayed by 30 min under Keta/Xyl (Fig. 1F). These results indicate that all anesthetics shift the LFP to lower frequencies and the E/I balance towards inhibition, albeit with different temporal profiles.

In contrast to Keta/Xyl-anesthesia, Isoflurane- and MMF-anesthesia can be efficiently antagonized by removing the face mask or injecting a wake-up cocktail (Flumazenil, Atipamezol and Buprenorphine, FAB) (Albrecht et al., 2014; Fleischmann et al., 2016), respectively. 20-30 min after Iso withdrawal, animals regained motility and periods of silence in the LFP receded (Fig. 1C,F). However, in contrast to post-Iso, LFP power did not fully recover after FAB, remaining significantly reduced at frequencies below 0.5 and above 30 Hz for the entire 45 min-post anesthesia recording period (Fig. 1C,D). In contrast, elevated LFP power in the 0.5-4 Hz band and reduction in active periods remained significant throughout the entire recording in the presence of Keta/Xyl. In line with these results, the 1/f slope promptly reverted to values similar to baseline after Iso discontinuation. In contrast, the recovery was only transitory and partial after MMF antagonization, and virtually absent for Keta/Xyl (Fig. 1E), indicating that the E/I balance recovered only after Iso within 45 min.

Cross-frequency coupling between theta and gamma oscillations has been suggested to underlie information transfer in the hippocampus (Canolty and Knight, 2010). Given the strong decrease of theta power in the presence of Iso and MMF, we reasoned the phase modulation of the gamma rhythm could also be altered. To test this, we used phase-amplitude coupling (PAC) to measure whether the phase of slow LFP oscillations modulates the amplitude of the signal at a higher frequency. In line with previous results (Scheffer-Teixeira et al., 2012; Schomburg et al., 2014) a significant coupling between theta and gamma frequency bands, as well as between frequencies in the 1-2 Hz range and gamma was present in the awake state (Fig. 1G). Moreover, anesthesia strongly altered PAC. In accordance with the LFP power analysis, the coupling reached a maximum strength between the dominant slow-frequency oscillations induced by the various anesthetics (<0.5 Hz for isoflurane, ~1 Hz for MMF and 0.5-4 Hz for Keta/Xyl) and gamma (Fig. 1G). For all anesthetics, the range of phase-modulated amplitudes was wide, suggesting that the modulating phase corresponds to the identified slow-wave activity.

Taken together, these data show that all three GAs differently and persistently modulated the network oscillations in dCA1, a full recovery of activity being detected within 45 min only for Iso.

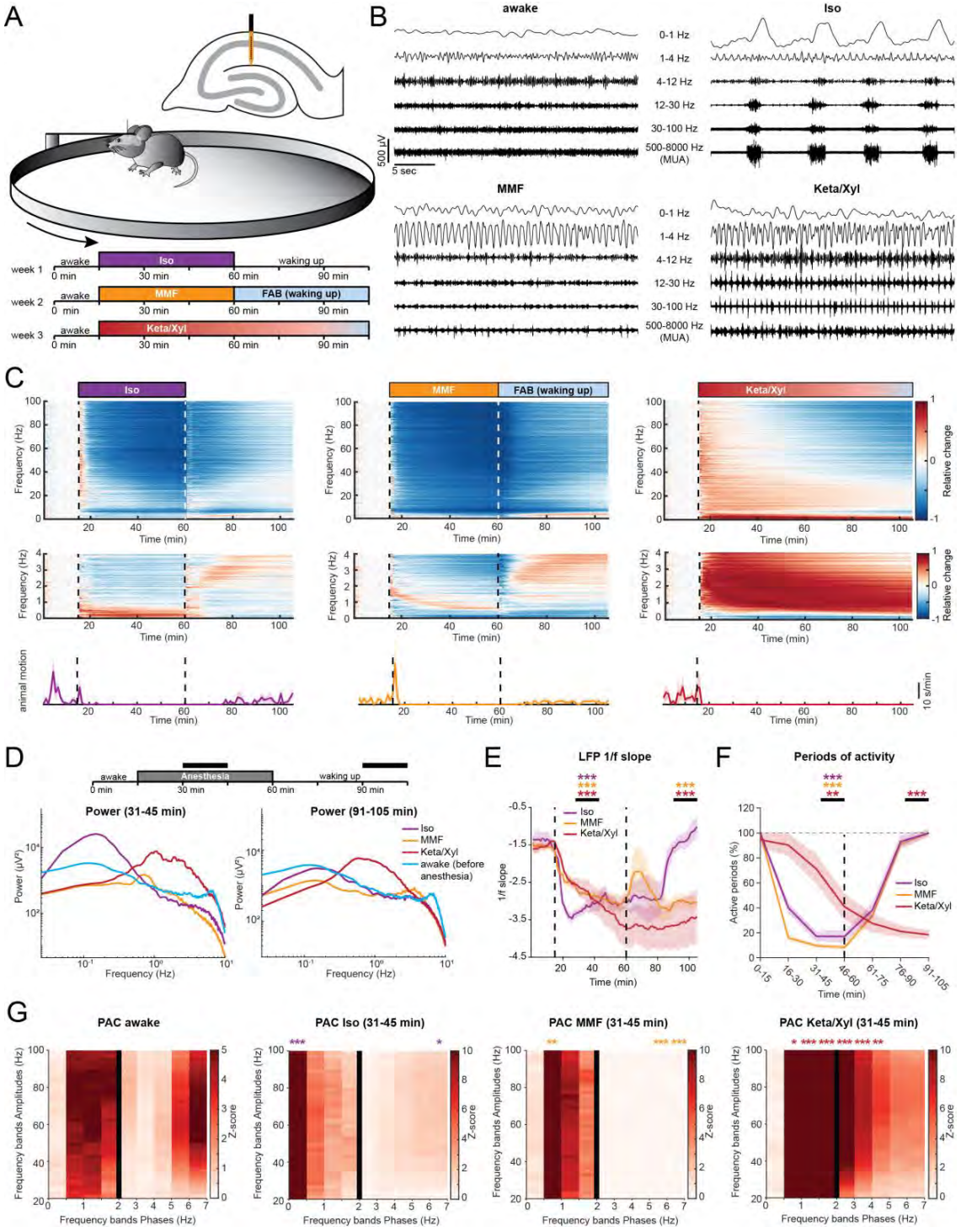

Figure 1: LFP recordings in dorsal CA1 during wakefulness and anesthesia reveal distinct and complex alterations by Iso, Keta/Xyl and MMF. (A) *Experimental setup. Extracellular electrical recordings in dorsal CA1 were performed in four head-fixed mice for 105 min, continuously. Each animal was recorded under all anesthesia as indicated in the scheme. Order of anesthetics was pseud-randomized.* ***(B)*** *Characteristic local field potential (LFP) recordings during wakefulness and under three different anesthetics.* ***(C)*** *Color-coded modulation index (MI) plots (upper and middle panels) for LFP power and motion profiles (lower panels) for the three different anesthetic conditions. Upper panels display LFP power for 0-100 Hz frequency range, lower panels for 0-4 Hz.* ***(D)*** *Line plot displaying LFP power spectra for the two time periods indicated by horizontal black bars. For comparison, the 15-min*

spectrum of the awake period before anesthesia induction is plotted in both graphs. Statistical differences are indicated in Fig. S1C ***(E)*** *Line plot displaying the power law decay exponent (1/f) of the LFP power spectrum for the 30-50 Hz range. Lines display mean ± SEM.* ***(F)*** *Line plot displaying the fraction of active periods compared to the pre-anesthetic wakeful state, in 15 min bins throughout the entire recording duration. Lines display mean ± SEM.* ***(G)*** *Heat map displaying Phase-amplitude-coupling (PAC) for pre-anesthetic wakeful state (left) and for the indicated time periods during anesthesia. Different bin sizes (0.5 Hz and 1 Hz, separated by vertical black line) are used to resolve low- and high-frequency PAC. Vertical dashed lines in (C) and (E) indicate time points of anesthesia induction (Iso, MMF, Keta/Xyl) and reversal (Iso & MMF only). Vertical dashed line in (F) indicates time point of anesthesia reversal (Iso & MMF only). Asterisks in (E) and (F) indicate significance of time periods indicated by black horizontal line compared to 15-min period before anesthesia. Anesthetic conditions are color-coded. Asterisks in (G) indicate significant differences compared to the corresponding frequency band during wakefulness. * $p < 0.05$, ** $p < 0.01$, *** $p < 0.001$, $n = 4$ mice. For full report of statistics, see statistics table.*

Delayed recovery of neuronal spiking patterns after anesthesia

While the LFP provides information about general network states in the hippocampus, it is influenced by long-range activity and highly active regions in the vicinity of CA1 (Buzsaki et al., 2012). To assess the effects of GAs on CA1 neurons, we analyzed the spiking of individual units (56-72 units per animal, n=4 mice) before, during and after each of the anesthetic conditions. All anesthetics significantly and rapidly (<1 min) decreased spiking activity in CA1 neurons (Fig. 2A,B, S2), with MMF leading to the most potent suppression, followed by Iso and Keta/Xyl. Although the bulk spike rate was strongly reduced, the number of active neurons (see Methods) was only mildly affected (Fig. 2C), reaching a significant reduction only with MMF. This observation suggests that anesthesia broadly reduces neuronal activity, and does not modulate only a discrete subpopulation of neurons. Both firing rate and the number of active neurons recovered within 45 min after reversal for MMF and Iso (Fig. 2A-C, S2).

To investigate whether the rhythmicity of single neuron firing was affected similarly to the LFP, we analyzed the spectral properties of 1 ms-binned SUA firing (i.e. power of SUA spike trains, for details see Methods). In the presence of Iso, SUA power was consistently increased in the range between 0 and 0.5 Hz (Fig. 2A,D, S2), in line with the strong modulation of LFP at 0.1-0.2 Hz. Of note, this effect did not vanish after Iso removal, suggesting that Iso has a long-lasting impact on firing rhythmicity. In contrast, and in line with its effects on the LFP, MMF generally reduced, albeit less strongly, SUA power, including the low frequencies. A significant reduction of SUA power was still present 45 min after antagonization in the 0-0.5 Hz band. Keta/Xyl, on the other hand, only showed a tendency towards reduced SUA power in the frequency band below 0.5 Hz, but increased SUA power significantly in the range between 0.5 and 4 Hz, consistent with its effect on the LFP (Fig. 2D). This modulation was present throughout the entire recording. At higher frequencies, Iso led to a peak in the theta frequency range, similar to wakefulness (Fig. 2E), yet it reduced the SUA power in the beta/gamma range. Keta/Xyl and MMF caused an overall reduction in SUA power at frequencies >5 Hz (Fig. 2E). Thus, GAs differentially impair spiking rhythmicity. These changes appeared to follow similar dynamics than those in the LFP.

To confirm the synchrony between spikes and low-frequency oscillations, we calculated their pairwise phase consistency (PPC) (Vinck et al., 2012). When compared to pre-anesthesia, PPC values for the 0-0.5 Hz frequency band were augmented by Iso. Keta/Xyl increased

coupling of spikes to the LFP between 0.5 and 1 Hz, whereas MMF showed a weak, but significant increase of coupling at frequencies below 1 Hz (Fig. 2F).

Similar to the LFP, the SUA firing rate nearly fully recovered during the 45 min post-Iso (Fig. 2A,B, S2), with even a slight, but significant increase at the end of the recording period. In contrast, after FAB-induced MMF reversal, CA1 spiking activity remained slightly reduced, reflecting the lack of LFP recovery. For Keta/Xyl, SUA remained suppressed during the entire recording period (Fig. 2B). Strikingly, SUA power did not fully recover for any of the tested anesthetics (Fig. 2E).

Taken together, we show that all investigated GAs caused a persistent and robust reduction of CA1 firing. Moreover, spiking during anesthesia was phase-locked to the GA-induced slow network oscillations.

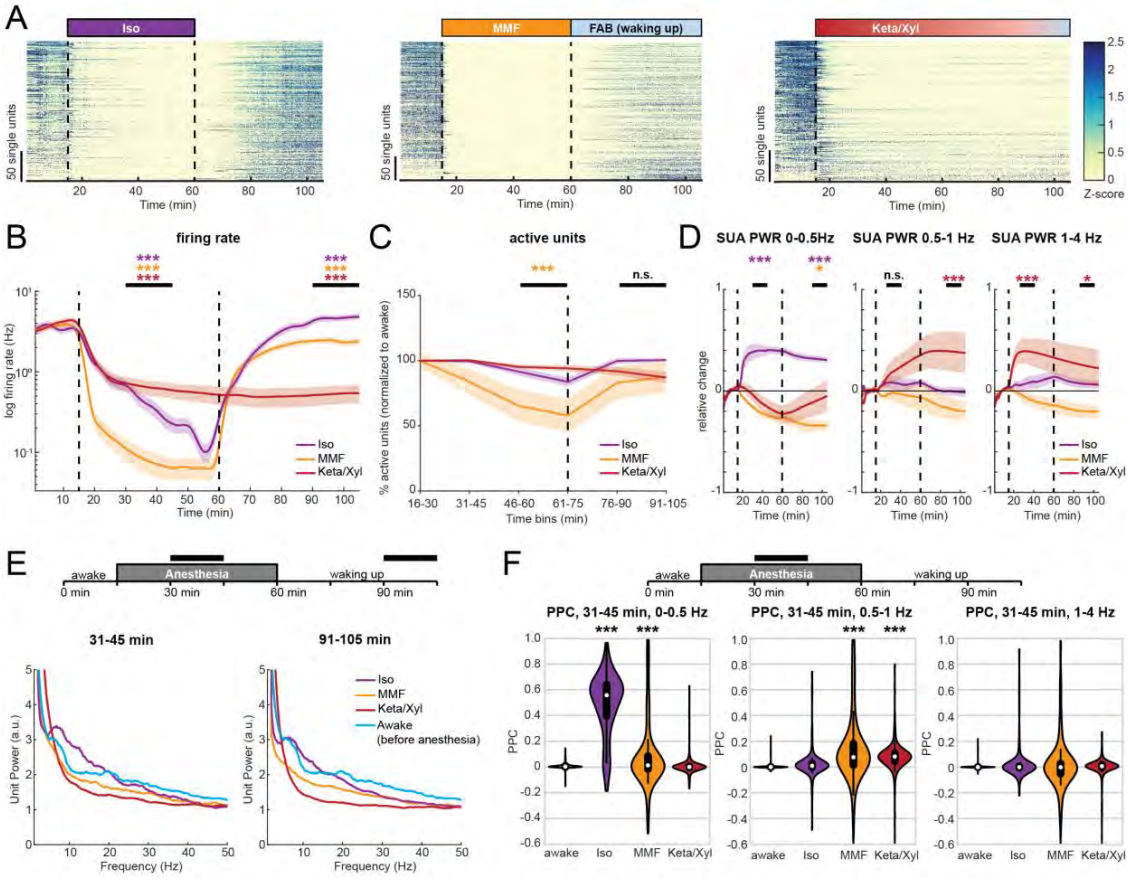

Figure 2: Single unit activity in dorsal CA1 is strongly reduced during anesthesia, and remains significantly altered long after its termination. (A) *Raster plots of z-scored single-unit activity (SUA) for the three different anesthetic strategies in four mice. Units are sorted according to initial activity during wakefulness.* ***(B)*** *Line plot of SUA firing rate before, during and after anesthesia induction.* ***(C)*** *Line plot displaying the fraction of active units compared to the pre-anesthetic wakeful state, for all three anesthetics in 15 min bins throughout the entire recording duration.* ***(D)*** *Relative change of population firing rate power in the 0-0.5, 0.5-1 and 1-4 Hz frequency band. SUA PWR = power of SUA spike trains.* ***(E)*** *Line plot displaying the normalized power spectra of population firing rate for the two time periods indicated by horizontal black bars. For comparison, the 15-min spectrum for pre-anesthetic wakeful state is plotted in both graphs.* ***(F)*** *Pairwise phase consistency (PPC) at low frequencies in the same frequency bands as (D), for the indicated time points during anesthesia. White dots indicate median, vertical thick and thin lines indicate 1st-3rd quartile and interquartile range, respectively. Colored lines in (B) - (D)*

*display mean ± SEM. Vertical dashed lines in panels (A), (B) and (D) indicate time points of anesthesia induction (Iso, MMF, Keta/Xyl) and reversal (Iso & MMF only). Vertical dashed line in (C) indicates time point of anesthesia reversal (Iso & MMF only). Asterisks in (B) - (D) indicate significance of time periods indicated by black horizontal line compared to period before anesthesia. Anesthetic conditions are color-coded. Asterisks in (F) indicate significant differences to wakefulness. * $p < 0.05$, ** $p < 0.01$, *** $p < 0.001$, $n = 4$ mice. For full report of statistics, see statistics table.*

Iso, Keta/Xyl and MMF reduce number, amplitude, and duration of calcium transients

To monitor the population dynamics of CA1 neurons in the presence of different anesthetics, we imaged the same field of view (FOV) using the genetically encoded indicator GCaMP6f (Chen et al., 2013) and systematically compared the activity of identified neurons during quiet wakefulness and in the presence of different anesthetics (Fig. 3A).

First, we considered all active neurons in each condition and analyzed the average rate (i.e., the number of transients), amplitude, and duration (i.e., the decay constant) of calcium transients across all imaging sessions in 7 mice. In line with the results of SUA analysis (see Fig. 2C), a large number of CA1 pyramidal neurons were active in the presence of all three GAs. Using extraction parameters that restricted the number of ROIs but maximized signal quality (see Methods), we obtained a median of 311 (min-max of 16-817) active neurons per FOV, for a total of 189 five-minutes recordings. All GAs significantly altered calcium dynamics in CA1 neurons, reducing the activity (Fig. 3C,D), as previously shown for neuronal spiking (Fig. 2B). However, each condition could be characterized by a specific signature in their calcium dynamics. Iso yielded only a mild decrease of rate and amplitude, but a strong reduction of duration of calcium transients (Fig. 3D). Consistent with effects on LFP and SUA, calcium transients showed a spectral peak between 0.1 and 0.2 Hz (Fig. S4). In contrast to Iso, MMF did not significantly affect the duration of transients but reduced their rate and amplitude when compared to wakefulness. Keta/Xyl-anesthesia had the strongest effect on calcium transients, leading to a reduction of all three parameters compared to wakefulness (Fig. 3D). Unlike for electrophysiological recordings, no spectral peak was present in calcium transients, most likely due to the strong suppression of calcium activity by Keta/Xyl. Considering all parameters, the four groups tended to segregate into clusters, one consisting mostly of recordings under Keta/Xyl, and another one consisting of awake and Iso recordings. Most recordings under MMF clustered between these two groups (Fig. 3E). Importantly, these findings were robust to changes in the signal extraction pipeline. Varying the threshold for calcium transient detection across a wide range of values did not affect the reported effects on rate and height of transients (Fig. S3B). Further, conducting the same analysis on neuronal activity metrics that are independent of calcium transients detection (integral and standard deviation) or on dF/F calcium signals also yielded analogous results (Fig. S3C-E).

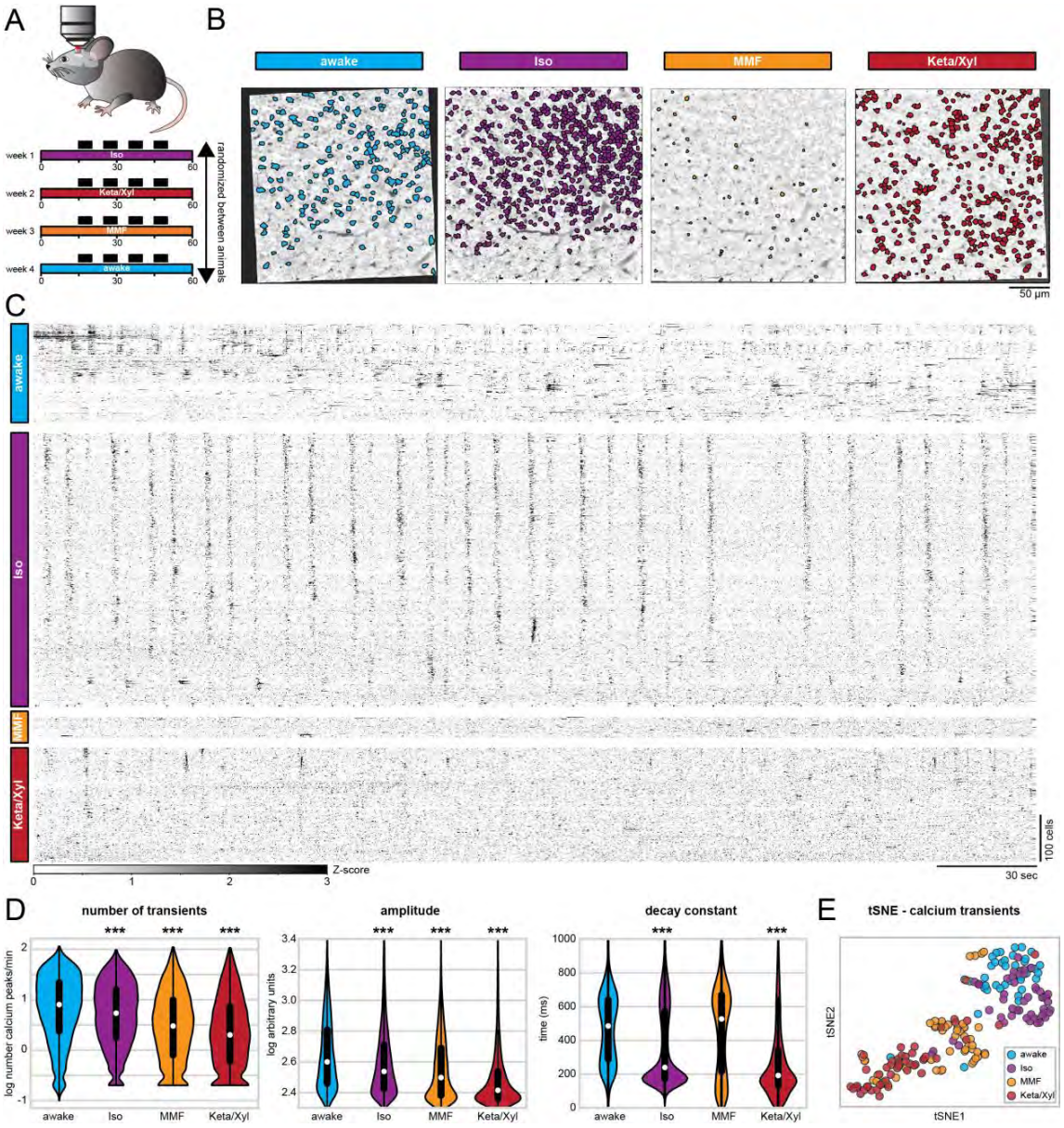

Figure 3: Repeated calcium imaging in dorsal CA1 reveals distinct activity profiles for Iso, MMF and Keta/Xyl. (A) *Experimental strategy for chronic calcium imaging of cellular activity in dorsal CA1. For each condition, mice were imaged four times for five minutes in seven mice, as indicated by black fields in the scheme. The order of imaging conditions was pseudo-randomized.* ***(B)*** *Time-averaged, two-photon images of the same FOV in CA1 aligned to the Iso condition. ROIs of automatically extracted, active neurons are overlaid for each condition.* ***(C)*** *Raster plots of z-scored calcium transients in the same animal under different conditions. Traces are sorted by similarity.* ***(D)*** *Violin plots quantifying the number (left), amplitude (middle), and decay (right) of detected calcium transients. White dots indicate median, vertical thick and thin lines indicate 1st-3rd quartile and interquartile range, respectively.* ***(E)*** *tSNE plot summarizing the average calcium transients properties. Each data point represents one recording session. Asterisks in (D) indicate significant differences to wakefulness. *** p < 0.001. Note, to facilitate readability, only differences to wakefulness are indicated. For full report of statistics, see statistics table.*

Iso, Keta/Xyl and MMF distinctly modulate cellular calcium dynamics in a given neuron

One possible explanation for these distinct modes of calcium activity could be that each anesthetic condition recruits a unique set of neurons characterized by particular spiking properties. We tested this possibility by analyzing calcium transients in neurons that were active during all conditions (Fig. 4A, S5, S6). To obtain a sufficient number of active neurons, we extracted calcium transients using a lower quality threshold, accepting more neurons per recording (see Methods). In this manner, we obtained a median of 783 neurons per recording (min-max of 156-1641). While this shifted the overall distribution of calcium parameters to lower values, the relative ratios between the four conditions remained the same and the differences between anesthesia groups were preserved (Fig. S3F-G). Also, when considering only neurons that were active in all four conditions, rate as well as amplitude of calcium peaks were generally reduced under anesthesia being lowest in the Keta/Xyl condition (Fig. 4B,C). Compared to the whole dataset, differences in decay constant were less pronounced. The median decay constant strongly decreased for awake and MMF conditions, while it increased for Iso and Keta/Xyl. These results indicate that both the between- as well as the within-condition variance strongly decreased when considering only neurons active under all conditions.

The relatively low number of neurons active in all four conditions (335 neurons) limited the statistical analysis. Therefore, we additionally compared neurons that were active in any two combinations of conditions (Fig. S7). This analysis further corroborated the similarity of neurons active during wakefulness and Iso anesthesia (Fig. 4C, S7). Rate, amplitude, and duration of calcium transients were most similar between wakefulness and Iso compared to the other GAs. In contrast, neurons active during wakefulness and either Keta/Xyl or MMF showed decreased rate, amplitude and duration under anesthesia, with Keta/Xyl causing the strongest phenotype (Fig S7). Overall, this indicates that anesthetics influence the firing properties of hippocampal neurons. However, the magnitude and the direction of these effects vary considerably. Iso anesthesia has the mildest effect, and it most likely arises from distinct neuronal populations being active in the two conditions (wakefulness vs. Iso anesthesia), as the firing properties of cells that are active in both are barely affected (Fig. 4B,C). On the other hand, the strong effects of MMF and Keta/Xyl on all calcium parameters in the same cells indicate that different anesthetics directly alter the firing properties of individual neurons. Thus, alterations in firing properties of neuronal populations (e.g. SUA, Fig. 2B-D) are not solely explainable by different subpopulations of neurons being active between awake and anesthesia.

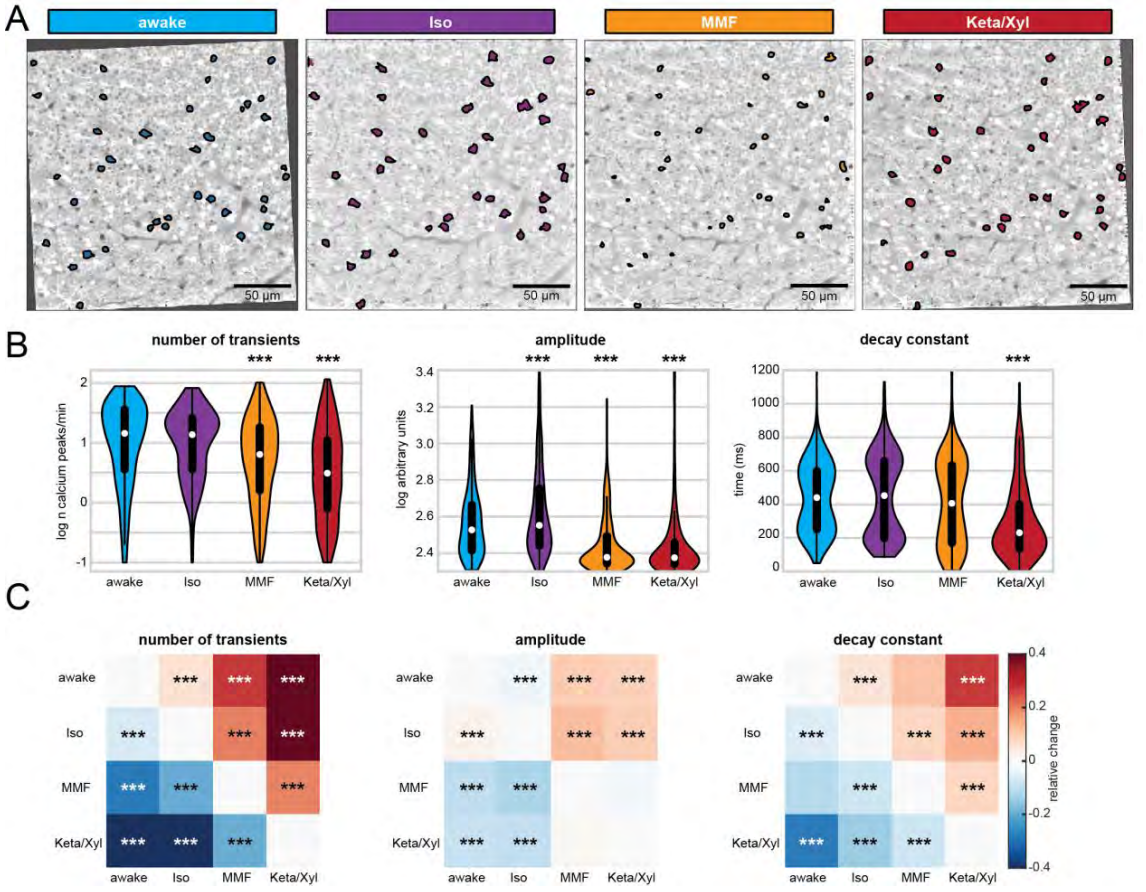

Figure 4: Calcium activity profiles in neurons active during all conditions are similar between wakefulness and Iso. (A) *Two-photon time-averaged images of the same FOV in CA1, aligned to the Iso condition (same images as in figs. 3). ROIs show neurons that were active in each condition, allowing direct comparison of calcium transients in the same cells under different conditions.* ***(B)*** *Violin plots quantifying the number (left), amplitude (middle), and decay (right) of detected calcium transients. White dots indicate median, vertical thick and thin lines indicate 1st-3rd quartile and interquartile range, respectively.* ***(C)*** *Heat maps displaying the relative change in the number (left), amplitude (middle), and decay (right) of calcium transients between neurons active in pairs of conditions (see also Fig. S7). Asterisks in (B) and (C) indicate significant differences to wakefulness. *** p < 0.001. Note, to facilitate readability, only differences to wakefulness are indicated. For full report of statistics, see statistics table.*

Anesthesia decorrelates hippocampal activity

Calcium imaging studies in the visual cortex of ketamine anesthetized rats (Greenberg et al., 2008) and isoflurane anesthetized mice (Goltstein et al., 2015) showed that anesthesia increases the overall pairwise correlations between firing neurons, and consequently, induces more structured patterns of activity in the neocortex. While neocortical L2/3 cells typically show a high degree of local interconnectivity (Harris and Mrsic-Flogel, 2013), this is not the case for CA1, where pyramidal cells receive their main excitatory input from CA3 and entorhinal cortex and send their efferents to subiculum and extrahippocampal areas (Neves et al., 2008). Another difference between neocortex and hippocampal CA1 area is that the neocortex receives strong direct input from primary thalamus, which is a major source for slow oscillations during anesthesia-induced unconsciousness and sleep (Franks, 2008; Klinzing et al., 2019; Rudolph and Antkowiak, 2004). In comparison to neocortex, hippocampus shows different

patterns of activity, including sharp waves, which are generated intrinsically in the hippocampus, likely originating in CA3 (Buzsaki, 1986). To investigate whether these differences cause a different impact of anesthesia on the population activity in CA1 when compared to the neocortex, we analyzed the dynamical structure of population activity using both calcium imaging and SUA of extracellular recordings in vivo. First, we analyzed Fisher-corrected Pearson pairwise correlation between neuropil-corrected, raw fluorescence traces. We found that both correlation and anticorrelation were highest in animals during quiet wakefulness (Fig 5A-B). In particular, the awake condition had a higher proportion of correlation coefficients both in the 1st as well as in the 4th quartile of the entire distribution and, accordingly, higher absolute correlation values (Fig. 5B, S8A). Similar to the firing properties, Iso induced the milder changes, whereas Keta/Xyl caused the strongest phenotype. This relationship was preserved in neurons active during all conditions (Fig. S8B), indicating that anesthesia generally reduces correlated activity between neurons and that this effect is not attributable to the activity of particular neuronal subpopulations. Moreover, these effects were not influenced by the distance between the pair of neurons whose correlation was quantified (Fig. 5C). These findings highlight the major differences between the anesthesia-induced effects on neuronal coupling in hippocampal CA1 and neocortex. In accordance with the anatomy of CA1, the correlation between pairs of neurons was only mildly affected by the distance between them, with or without anesthesia. Not only were neurons less highly correlated to each other under anesthesia, but their coupling to the whole population activity (Okun et al., 2015) was reduced as well. The proportion of neurons with population coupling in the 4th quartile of the entire distribution was highest for awake, and most strongly reduced under Keta/Xyl and MMF, while Iso showed only mild effects (Fig. 5D).

To further relate the calcium imaging data to extracellular recordings of neuronal firing, we carried out an analogous analysis on SUA. To avoid the confounding effect of firing rate, we quantified the correlation between pairs of neurons using the Spike-Time Tiling Coefficient (Cutts and Eglen, 2014), a measure that is largely insensitive to variations of the firing rate (see Methods). To be consistent with the calcium data, we quantified correlations within 1 second, a timescale of the same magnitude as the decay constant used to extract calcium signals (700 ms). This analysis confirmed that all anesthetics decorrelated neuronal activity (Fig. 5E). This effect was still present, albeit less strongly pronounced, using an integration window of 10 ms, which is closer to the duration of electrically measured spikes (Fig. S9). Overall, the decorrelation was milder under Iso anesthesia and stronger under Keta/Xyl and MMF. Thus, all three GAs decorrelated calcium transients and spiking activity in the CA1 area, with MMF and Keta/Xyl inducing the most prominent effects.

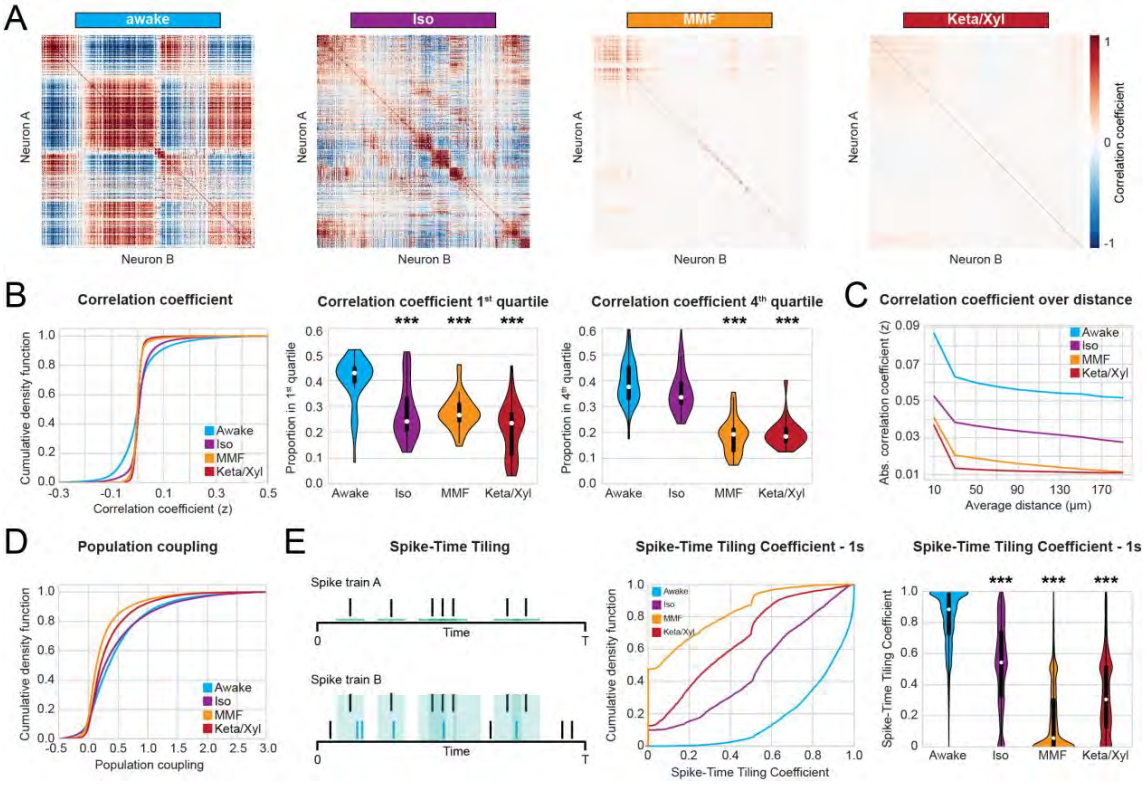

Fig. 5. Correlation analysis of CA1 calcium and spiking shows decorrelation under anesthesia. ***(A)*** *Heat maps displaying representative correlation matrices between pairs of neurons during wakefulness and the three different anesthetic conditions, in the same animal. Matrices are sorted by similarity.* ***(B)*** *Left: Line plot displaying cumulative distribution of Fisher-corrected Pearson correlation coefficients between pairs of neurons. Center: violin plot displaying the proportion of pairs found in the 1st (most negative) and 4th (most positive) quartile of the distribution.* ***(C)*** *Line plot displaying the absolute pairwise correlation coefficients over distance (25 micrometer bins).* ***(D)*** *Line plot displaying cumulative distribution of population coupling.* ***(E)*** *Quantification of correlation between pairs of extracellularly recorded single units using the Spike-Time Tiling Coefficient (STTC). Left: Schematic illustration of the STTC quantification. Center: cumulative distribution of the STTC with a 1000 ms integration window. Right: violin plot quantifying the STTC. In violin plots, white dots indicate median, vertical thick and thin lines indicate 1st-3rd quartile and interquartile range, respectively. Asterisks in (B) and (E) indicate significant differences to wakefulness. *** $p < 0.001$. Note, only differences to wakefulness are indicated. For comparison between conditions, see statistics table.*

Anesthesia fragments temporal and spatial structure of hippocampal activity

The decorrelation of neuronal activity during anesthesia suggests that GAs might impact the spatial and temporal organization of CA1 neuronal ensembles (see Fig. 5A). To test this hypothesis, we analyzed the same number of active neurons for each condition, since a different number of neurons in each condition potentially influences the number and size of detected clusters (Wenzel et al., 2019). First, we monitored the impact of GAs on the temporal structure of CA1 activity. We defined the number of clusters identified by principal component analysis (PCA) as the number of components that were needed to explain 90% of the variance. Moreover, we assessed the power-law slope of variance explained over the first 150 components (Fig. 6A). Both methods led to a larger number of clusters and a flatter power-law slope for anesthesia when compared to wakefulness (Fig. 6A). Further corroborating these

findings, both tSNE dimensionality reduction and affinity propagation (AP) clustering (see Methods) also revealed a larger number of clusters for anesthesia compared to wakefulness (Fig. 6B,C). These observations indicate that activity is less structured under anesthesia. In line with previous results, Iso had the weakest effect, whereas Keta/Xyl consistently induced the most pronounced phenotype. Analysis on the deconvolved calcium traces led to comparable results (Fig S10A,B). These findings support the idea that GAs cause a fragmentation of the network consisting of a more diverse repertoire of microstates.

Second, we tested whether anesthesia disrupted the spatial structure of hippocampal activity, employing a modularity maximization approach (Newman and Girvan, 2004; Sporns and Betzel, 2016) designed to detect internally densely connected communities (modules). To allow detection of modules at varying sizes, we carried out our analysis while varying a resolution parameter (gamma) and thus focusing on different spatial scales. Using this approach, we showed that GAs increase the number of detected communities over a wide range of resolution parameter values (Fig 6D). Moreover, the modularity of these communities was lower than in wakefulness (Fig 6E). These results indicate that anesthesia results in a more fractured network with, on average, smaller and less coherent communities. A multi-resolution approach (Jeub et al., 2018) followed by the selection of partitions based on hierarchical consensus clustering yielded similar results (Fig. S10C). Among GAs, Iso induced the mildest phenotype, whereas Keta/Xyl had the most prominent effects. Thus, GAs not only decorrelate hippocampal activity, but also consistently fragment both its temporal and spatial structure.

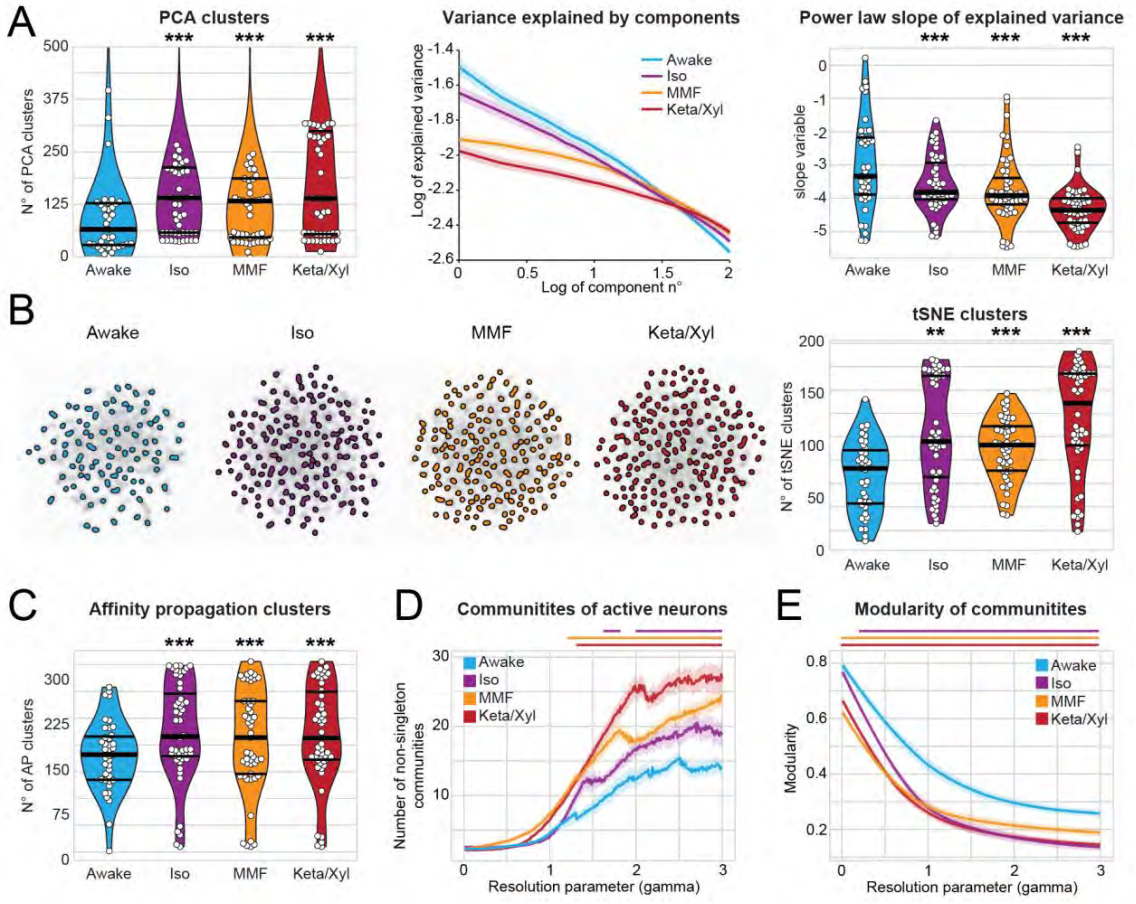

Fig. 6. Calcium activity in CA1 is temporally and spatially fragmented during anesthesia. (A) *Left: violin plot quantifying the number of principal component analysis (PCA) clusters during wakefulness or anesthesia, as indicated. Middle: loglog line plot displaying the variance explained by the first 100 components for each condition. Right: violin plot quantifying the power-law slope of the variance explained by the first 100 components for each condition.* ***(B)*** *Left: tSNE plots of network events recorded in the same animal under the four indicated conditions. Right: Violin plot quantifying the number of tSNE clusters obtained from calcium recordings during the four different treatments.* ***(C)*** *Violin plot quantifying the number of clusters obtained by affinity propagation from calcium recordings during the four different treatments.* ***(D)*** *and* ***(E)*** *Line plots quantifying the number of detected communities and the modularity of the detected communities with the resolution parameter gamma ranging from 0 to 3. Horizontal lines in violin plots indicate median and 1st-3rd quartile. Asterisks in (A) - (C) indicate significant differences to wakefulness. ** p < 0.01, *** p < 0.001. Horizontal lines above plots in (D) - (E) indicate significant difference to wakefulness. Anesthetic conditions are color-coded. Note, only differences to wakefulness are indicated. For comparison between conditions, see statistics table.*

Repeated anesthesia alters spine dynamics in CA1

The impact of Iso, MMF, and Keta/Xyl on CA1 activity might alter spine dynamics at CA1 pyramidal neurons. This issue is of critical relevance, since GAs disrupt activity patterns during development (Chini et al., 2019) also involving alteration of synaptic connectivity (Briner et al., 2010; Briner et al., 2011; De Roo et al., 2009), but less is known about the impact of GAs on hippocampal synaptic structure during adulthood. So far, spine dynamics in hippocampus were only investigated under anesthesia, lacking comparison to the wake state. Moreover, the reported turnover rates varied strongly between studies (Attardo et al., 2015; Gu et al., 2014; Pfeiffer et al., 2018). Thus, it is unknown how repeated anesthesia in itself affects spine stability.

We repeatedly imaged the same basal, oblique, and tuft dendritic segments of CA1 pyramidal neurons under all four conditions (five times per condition, every four days), interrupted by a 30-day recovery period between conditions (Fig. 7A, S11A). To rule out time-effects, we pseudo-randomized the order of anesthetics (Fig. S11A). During wakefulness, without any anesthesia in between, the turnover ratio of spines on all dendrites was on average 18.6 - 20.5 % per four days. This turnover ratio was stable and did not change systematically over successive imaging sessions (Fig. 7B). Notably, all anesthetics affected spine turnover. Both MMF and Iso anesthesia mildly increased the turnover ratio compared to wakefulness (21.1 – 23.8 % for MMF, 24.0 – 24.7 % for Iso). Iso did not alter the surviving fraction of spines. Together with the significant increase in spine density over time (Fig. 7B) these results indicate that the elevated turnover ratio was due to a rise in the gained fraction of spines (Fig. S11B). In contrast, MMF led to a slight increase in the fraction of lost spines (Fig. S11B) and correspondingly, slightly decreased the surviving fraction compared to wakefulness. Spine density did not change over time. Keta/Xyl anesthesia showed the strongest effect on spine turnover (13.4 - 15.7 %), which was opposite to MMF and Iso, and therefore significantly lower rather than higher compared to the awake condition (Fig. 7B). This lower turnover ratio was accompanied by a higher surviving fraction and an increase in density with time (Fig. 7B). Consistently, the fraction of lost spines was most strongly reduced (Fig. S11B). Thus, Keta/Xyl anesthesia resulted in marked stabilization of existing spines and a reduction in the formation of new spines, indicative of a significant effect on structural plasticity.

To rule out that the age of the animal influenced spine dynamics in the awake condition, we measured spine turnover in a group of age-matched animals to the first anesthesia group (Fig.

S11A,C). Moreover, to rule out that the chronic imaging procedure per se and anesthesia in general had a long-lasting effect on the awake imaging condition, we added another awake-imaging control group with naïve, age-matched animals to the awake imaging time point in the experimental group (Fig. S11A,C). In all three groups, spine turnover was indistinguishable, indicating that neither age nor previous imaging under anesthesia impacted spine dynamics in the awake-imaging group (Fig. S11C).

Next, we asked whether the modulation of spine turnover by GAs was due to acute remodeling of spines during the time of anesthesia. Alternatively, spine turnover might be driven by long-lasting changes in network activity imposed by the slow reversal of all GAs. To capture fast events such as filopodia formation, we acquired image stacks every 10 min (Fig. 7C). Spine turnover, survival, or density were not significantly altered during the one hour of imaging (Fig. 7D). Thus, spines were stable during the one hour irrespective of the treatment. While mature spines typically show low elimination/formation rates over one hour, filopodia are more dynamic (Dailey and Smith, 1996; Lendvai et al., 2000; Portera-Cailliau et al., 2003). Unlike other reports, that observed an acute selective formation of filopodia under Keta/Xyl, but not Iso (Yang et al., 2011), we did not detect any acute effects of GAs on filopodia turnover of CA1 pyramidal cell dendrites. Thus, chronic exposure to all GAs consistently impacted spine dynamics, whereas acute effects were lacking. Keta/Xyl caused a strong decrease in spine turnover, accompanied by a higher surviving fraction and an increased density over time.

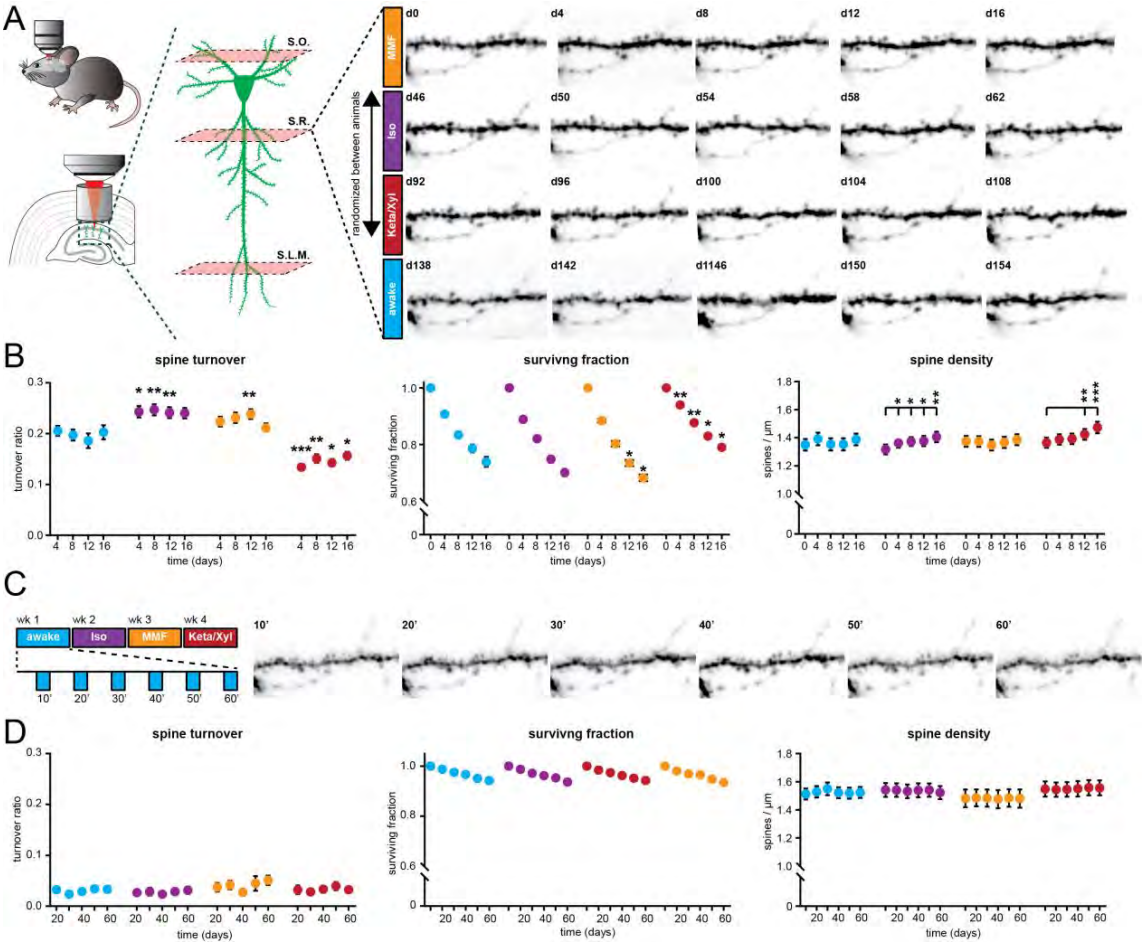

Fig. 7. Spine turnover at CA1 pyramidal neurons is distinctly altered by repeated application of Iso, MMF and Keta/Xyl. (A) *Left: Schematic illustration of in vivo spine imaging strategy. In each animal,*

spines were imaged on basal dendrites located in stratum oriens (S.O.), oblique dendrites in stratum radiatum (S.R.) and tuft dendrites in stratum lacunosum moleculare (S.L.M.). Right: Example showing an oblique dendrite in S.R. imaged chronically during all conditions. The order of anesthetic treatments was pseudo-randomized between mice (see Fig. S11). ***(B)*** *Dot plots showing quantification of spine turnover (left), spine survival (middle) and spine density (right) under the four indicated treatments. Note that spines were imaged on the same dendrites across all conditions. Dots indicate mean ± SEM. Asterisks indicate significant differences to wakefulness in the left and middle panel. In the right panel, asterisks denote significant changes within each treatment compared to day 0. * $p < 0.05$, ** $p < 0.01$, *** $p < 0.001$.* ***(C)*** *Imaging of acute spine dynamics during four different conditions. Left: schematic of the experimental timeline. Right: example of dendrite imaged during wakefulness in 10 min intervals (same dendrite as in A).* ***(D)*** *Dot plots showing quantification of acute spine turnover (left), spine survival (center) and spine density (right) under the four indicated treatments. Dots indicate mean ± SEM.*

Episodic memory consolidation is impaired by MMF and Keta/Xyl, but not by Iso

Episodic memory formation and consolidation require hippocampal activity. Newly learned experiences are thought of being consolidated via replay events that co-occur with low-frequency oscillations (Klinzing et al., 2019; Moscovitch et al., 2016; Nadel and Moscovitch, 1997; O'Neill et al., 2010). In the hippocampus, these low-frequency events typically occur as sharp waves (Buzsaki, 1986) during sleep, but also during awake resting behavior (O'Neill et al., 2010). The above results from electrophysiological recordings and imaging showed that GAs strongly altered network oscillations in the CA1 area, in the case of MMF and Keta/Xyl, also long after anesthesia discontinuation. Spine turnover of CA1 pyramidal neurons was also affected, especially after Keta/Xyl administration. Therefore, we tested whether inducing anesthesia for 1 hour shortly after the acquisition of a new episodic memory affected its consolidation (Fig. 8A). In line with previous experiments, we restricted Iso and MMF anesthesia to one hour, while Keta/Xyl anesthesia was left to recede spontaneously. We assessed episodic-like memory with a water maze protocol for reversal learning, when the hidden platform was moved to the quadrant opposite the initial target location (Fig. 8A). Specifically, we tested the effects of the different anesthetics on the consolidation of the memory of the new platform location. We compared the performance of the mice during the probe trial done on day 3 immediately after the reversal learning protocol (and 30 min before anesthesia), with the performance during the probe trial on day 4, twenty-four-hours after anesthesia. During the probe trial on day 3, animals of all four groups spent significantly more time in the new target quadrant compared to chance (25 %), indicating that they learned the new platform position successfully (Fig. 8B,C).

On day 4, control animals that did not undergo anesthesia showed the same performance as on day 3, suggesting that they had retained the memory of the new platform location (Fig. 8B,C). However, animals that were anesthetized with Keta/Xyl or MMF spent significantly less time in the new target quadrant and showed a significantly larger mean distance to the target platform position compared to the probe trial on day 3. In the Iso group, no significant difference compared to day 3 was detectable (Fig. 8B,C, S12). Notably, the effects were relatively mild, and the decrease in performance on day 4 was not significantly different between treatment groups. In summary, consistent with long-lasting effects on CA1 network activity, Keta/Xyl, and MMF impaired episodic-like memory consolidation. In contrast, Iso, which overall caused a weaker disturbance of neuronal population activity and a faster recovery profile, did not significantly affect memory consolidation.

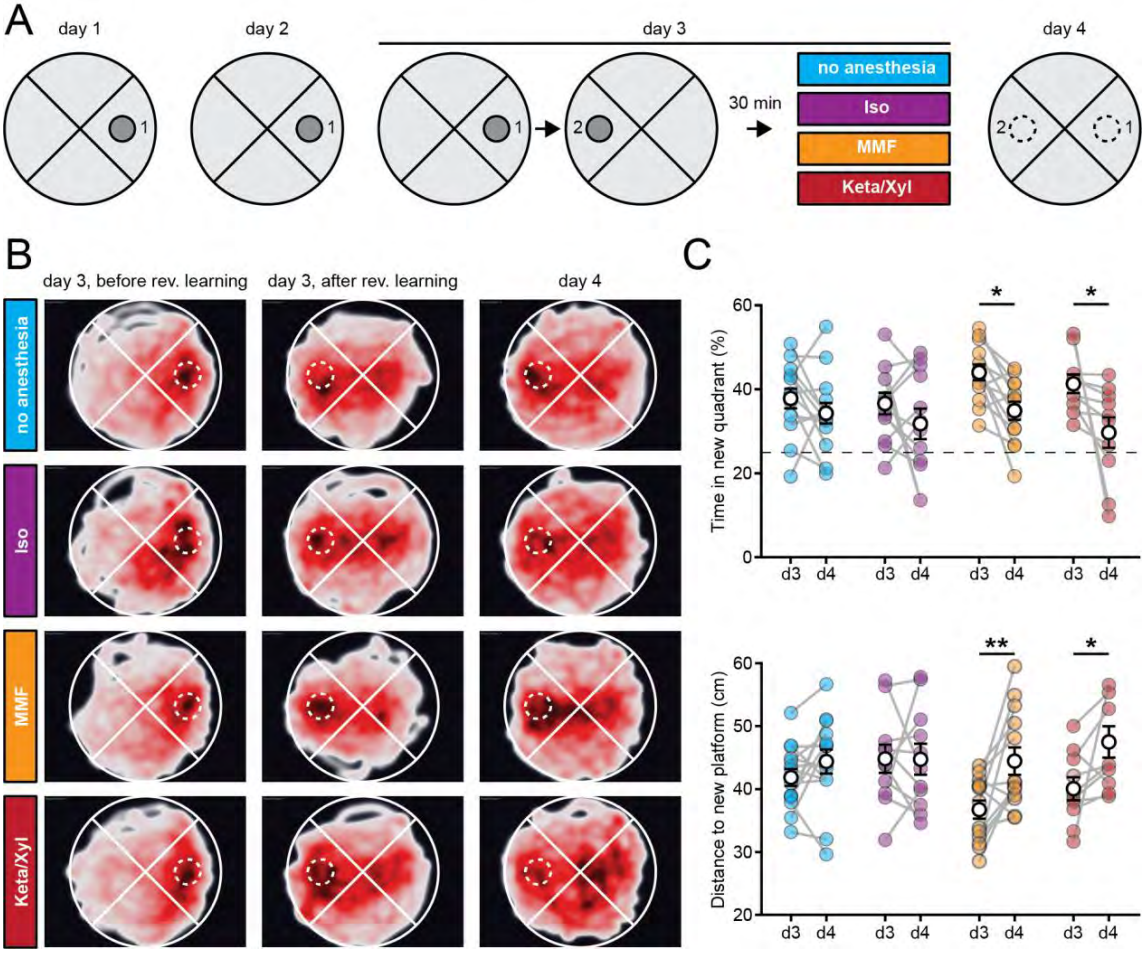

Fig. 8. Episodic memory consolidation is impaired by MMF and Keta/Xyl, but not by Iso. (A) *Experimental design to test episodic-like memory in a Morris water maze. On days 1 and 2 animals were trained to find the platform in position 1. Reversal learning was performed on day 3 where animals had to learn that the platform was moved to position 2. Training was followed 30 min later by a 1-h period of one of the four indicated treatments per group. On day 4, consolidation of the memory for the platform in position 2 was tested.* ***(B)*** *Heat maps showing trajectories of all mice during the first probe trial before reversal learning on day 3 (left column), after reversal learning on day 3 (middle column) and after treatment on day 4 (right column). Position of the target zone is indicated by dashed circles.* ***(C)*** *Scatter plots showing quantification of time spent in the new target quadrant (top) and distance to the new platform (bottom) after reversal learning on day 3 and on day 4. Filled, colored circles indicate individual animals, White circles indicate mean ± SEM. Asterisks in (C) indicate significant differences between days. * $p < 0.05$, ** $p < 0.01$.*

DISCUSSION

We investigated and systematically compared the intra- and post-anesthetic effects of different commonly used anesthetic strategies on the mouse hippocampus across multiple levels of analysis. Despite sharing some common traits, brain and cellular network states differ substantially under the influence of various types of anesthetics (Clark and Rosner, 1973; Sarasso et al., 2015; Steriade et al., 1993). Indeed, at the neuronal level, compared with awake state, all three anesthetics showed robustly reduced spiking activity in single neurons, reduced power in high oscillation frequency band, and decorrelated cellular population activity.

However, the induced network states in CA1 were highly distinct between the three different conditions, with Iso leading to prominent network oscillations at around 0.1 Hz, which timed the spiking activity of single units and neuronal calcium transients. Keta/Xyl caused pronounced oscillations between 0.5 and 4 Hz and the strongest reduction in calcium dynamics. MMF, in contrast, most strongly reduced LFP and SUA and impaired population dynamics as assessed with calcium imaging. Differences were also present in the long-term effects on spine dynamics, with Keta/Xyl stabilizing spines, leading to reduced turnover and increased density. MMF, on the other hand, mildly increased spine dynamics. Keta/Xyl cannot be antagonized and therefore changes of the CA1 network mediated by this anesthetic strategy had the longest duration, in agreement with long-lasting overall changes of global animal physiology (Albrecht et al., 2014). More unexpectedly, and in contrast to overall effects on physiology (Albrecht et al., 2014), CA1 network dynamics were still disturbed long after antagonization of MMF anesthesia. These long-lasting alterations were associated with impairment of episodic memory consolidation after exposure to Keta/Xyl- or MMF, but not Iso. Thus, despite fulfilling all the hallmarks of general anesthesia, different GAs distinctly alter hippocampal network dynamics, synaptic connectivity, and memory consolidation.

Iso, MMF and Keta/Xyl have different molecular targets and distinctly modulate functional and structural features of CA1

The GAs used here represent three different strategies based on the large repertoire of currently available anesthetics. Isoflurane represents the class of halogenated diethyl ether analogues, which are volatile and therefore administered via inhalation. Fentanyl, in combination with the analgesic medetomidine and the sedative midazolam (MMF), represents an anesthetic approach based on injection of a combination of drugs with sedative, analgesic and anxiolytic properties. In the clinic, propofol can be used instead of midazolam. Finally, ketamine is used both as an anesthetic and, at lower dosage, as a treatment against depression. For anesthesia it is combined with xylazine, which acts sedative, analgesic and as a muscle relaxant. All three strategies differ markedly in their molecular targets. Consequently, they uniquely modulate general animal physiology (Albrecht et al., 2014) and brain activity (Sarasso et al., 2015). Isoflurane is a potent GABA- and glycine receptor agonist. Moreover, it activates two-pore potassium channels and acts as α-amino-3-hydroxy-5-methyl-4-isoxazolepropionic acid receptor (AMPAR) inhibitor (Alkire et al., 2008). Similar to Iso, midazolam, the hypnotic component of the MMF mix, mainly acts as a GABAR agonist with little effect on NMDARs. In contrast, ketamine is a potent, use-dependent NMDAR blocker with less pronounced effects on potassium channels, GABA, glycine and other glutamate receptors such AMPA or kainite receptors (Alkire et al., 2008). Moreover, while most anesthetics reduce activity of thalamic nuclei, ketamine increases thalamic drive (Langsjo et al., 2005), leading to enhanced rather than reduced oscillations in mid-to-high frequency bands such as theta and gamma (Lee et al., 2013; Soltesz and Deschenes, 1993). In accordance with this, our study reveals major differences in the action of the different anesthetics on functional and structural features of CA1. With both electrical recordings and calcium imaging we report a robust reduction of neuronal spiking and pairwise neuronal correlation. Notably, effects on electrical activity and calcium activity were well in line for both Iso and MMF, despite the different recording methods. However, we observed some divergence for Keta/Xyl.

Comparison of electrophysiological recordings and calcium imaging

Generally, differences in electrophysiological recordings and calcium imaging data may stem from the location where the signal is detected. In the calcium imaging experiments, the signal

was sampled in a horizontal plane located inside and parallel to stratum pyramidale of CA1. In this configuration, somatic, action-potential driven calcium transients mainly from pyramidal neurons dominate the signal. Due to the kinetics and calcium-binding properties of GCaMP6f, action potentials can only be resolved below approx. 5 Hz and are reported non-linearly (Chen et al., 2013). In contrast, the electrodes on linear probes are arranged orthogonally to the strata of CA1 and parallel to the dendrites of CA1 cells. Thus, synaptic potentials mainly constitute the LFP across all layers and spikes are picked up from both pyramidal cells (in stratum pyramidale) and GABAergic neurons in all layers. Moreover, the first method samples neurons that spatially distribute over a large area. In contrast, the second one is biased towards large, active neurons that are in close proximity of the electrode.

More specifically, under Keta/Xyl, the overall firing rate of single units showed the smallest reduction of all three anesthetics. At the same time, imaging revealed the most substantial reduction in rate, amplitude and duration of calcium transients (compare Fig. 2B and 3D). One reason for this discrepancy may be the inhibitory action of ketamine on NMDARs. CA1 pyramidal cells display large, NMDAR-driven dendritic plateau potentials and calcium spikes (Katz et al., 2009). Moreover, ketamine likely inhibits L-type voltage-gated calcium channels (Yamakage et al., 1995) and reduces burst firing (Yang et al., 2018), leading to calcium transients with reduced amplitude and a faster decay constant. In contrast, ketamine has little influence on sodium spikes and AMPAR-mediated synaptic potentials, which are detected in electrical recordings as SUA and LFP, respectively. In accordance with electrical recordings, calcium transients showed increased power at 0.1-0.2 Hz under Iso. However, we did not detect a clear peak at 1-4 Hz in the presence of Keta/Xyl, as seen in LFP and SUA, probably due to its strongly dampening effect on calcium transients. The (low-pass) filtering of neuronal activity imposed by calcium indicators might also play a role.

Notably, the differences between electrical recordings and calcium imaging under Keta/Xyl are relevant. Calcium is a second messenger central to neuronal plasticity and metabolism (West et al., 2002; Wiegert and Bading, 2011). NMDARs are a major source for activity-dependent calcium entry into the cell, involved in regulating synaptic plasticity, metabolism, and pathology (Hardingham and Bading, 2010). The present findings suggest that Keta/Xyl has a particularly strong effect on neuronal calcium activity, uncoupling action potential firing from associated cytosolic calcium transients, leading to reduced intracellular calcium signaling. In contrast, calcium transients under MMF and Iso anesthesia closely matched the electrical activity profile of neurons. Therefore, aside from overall effects on network activity, Keta/Xyl may selectively alter neuronal plasticity by suppressing NMDAR-dependent postsynaptic calcium signals.

In contrast to neocortex, GAs decorrelate neuronal activity in CA1

All anesthetics decorrelated neuronal activity in CA1, leading to an overall more fragmented network state. This is in stark contrast with what has been reported from studies on GAs and cortical activity both at adulthood (Goltstein et al., 2015; Greenberg et al., 2008; Wenzel et al., 2019) and during development (Chini et al., 2019). This discrepancy may arise from the distinct architecture of CA1 compared to L2/3 of the neocortex, the latter showing a high degree of local interconnectivity (Harris and Mrsic-Flogel, 2013). In CA1 this is not the case. Pyramidal cells receive their main excitatory input from CA3 and entorhinal cortex and send their efferents to subiculum and extrahippocampal areas without making local connections among each other (Neves et al., 2008). Afferent activity originating in various sources and converging in CA1, may arrive out-of-phase under anesthesia, leading to desynchronized firing of CA1 pyramidal cells. Such a phenomenon has been proposed as a candidate mechanism underlying

desynchronization of neuronal firing in basal ganglia under conditions of slow oscillations (slow-wave sleep) and high synchrony in the neocortex (Mizrahi-Kliger et al., 2018). Notably, pairwise correlation was not entirely independent of the distance between neurons. Synchronization of pyramidal neurons via local, GABAergic interneurons may be another factor that increases spatial correlations. Both in neocortex and hippocampus, various types of GABAergic interneurons locally connect to and synchronize pyramidal neurons such as basket or bistratified cells (Klausberger and Somogyi, 2008).

Coordinated neuronal network dynamics, including pairwise correlation of calcium transients and single units, population coupling, clustering in the temporal and spatial domain were consistently impaired most strongly with Keta/Xyl and MMF. Iso, both in electrophysiological as well as calcium recordings, showed the mildest effects and permitted hippocampal activity patterns that closely resembled the awake state. Iso and MMF, in contrast to Keta/Xyl, are thought to be immediately reversible (Albrecht et al., 2014). However, they showed significant disruption of network dynamics for at least 45 min after reversal. Thus, all anesthetics had a much longer effect on network activity than expected. We therefore further asked whether this is reflected in long-term effects of these different types of anesthetics on spine dynamics of CA1 pyramidal neurons. Recent studies investigating spine dynamics at CA1 pyramidal neurons came to incongruent conclusions reporting spine turnover ranging from 3% (Gu et al., 2014) over 12% (Attardo et al., 2015) to approx. 80% (Pfeiffer et al., 2018) over 4 days. However, all studies used either isoflurane (Attardo et al., 2015) or ketamine/xylazine-based (Gu et al., 2014; Pfeiffer et al., 2018) anesthesia during the repeated imaging sessions. Thus, to what extent anesthesia itself influences spine dynamics is not clear.

Iso, MMF and Keta/Xyl distinctly alter spine dynamics in CA1

More generally, various effects of general anesthesia on spine dynamics were reported, depending on the brain region, preparation, age of the animal and anesthetic strategy. For example, enhanced synaptogenesis has been reported with different types of anesthetics on cortical and hippocampal neurons during development (Briner et al., 2010; De Roo et al., 2009). In contrast, one study indicated that spine dynamics were not altered on cortical neurons of adult mice with Keta/Xyl or Iso (Yang et al., 2011), while another study demonstrated an increase in spine density in somatosensory cortex with ketamine (Pryazhnikov et al., 2018). Also, fentanyl-mediated, concentration-dependent bidirectional modulations of spine dynamics were reported in hippocampal cultures (Lin et al., 2009).

To systematically compare spine dynamics in CA1 in vivo under different anesthetic treatments, we imaged spines at basal, oblique and tuft dendrites in a large set of dendrites. We found small, but robust chronic effects of repeated anesthesia. Keta/Xyl decreased spine turnover leading to a mild increase in spine density over time by stabilizing existing spines. This observation agrees with recent studies that showed a stabilizing effect of ketamine in the somatosensory cortex, resulting in increased spine density (Pryazhnikov et al., 2018). Thus, repeated anesthetic doses of Keta/Xyl may limit overall synaptic plasticity and thus, spine turnover. It was further shown that sub-anesthetic, antidepressant doses of ketamine enhance spine density in the prefrontal cortex (Li et al., 2010; Phoumthipphavong et al., 2016), similar to our study for CA1 neurons. Iso and MMF had contrasting effects on spine dynamics compared to Keta/Xyl, mildly enhancing spine turnover, which might be explained by, the their different pharmacology compared to ketamine, as pointed out above. A second aspect that distinguishes Keta/Xyl from Iso and MMF is its irreversibility, which might lead to longer-lasting alterations of synaptic transmission and E/I ratios leading to differential spine dynamics. This

idea is supported by the observation that during the anesthesia period itself, spine turnover was not altered, suggesting that long-lasting and repeated disturbances are required to leave a mark in synaptic connectivity.

MMF and Keta/Xyl, but not Iso, retrogradely affect episodic-like memory formation

Notably, a single dose of anesthesia with Keta/Xyl and MMF, but not Iso disrupted memory consolidation using a water maze assay in adult mice. Our results appear at odds with a reports (Zurek et al., 2012), where a single, 1-h treatment with Iso caused deficits in the formation of contextual fear memory, object recognition memory and in the Morris water maze in the following 48 h. However, this study investigated memory acquisition after anesthesia (i.e. anterograde amnesia), while our study asked whether anesthesia affects the consolidation of a memory formed shortly before the treatment (i.e. retrograde amnesia). The induction of retrograde amnesia correlated with the magnitude and duration of CA1 network disturbance imposed by the various anesthetics. KetaXyl and MMF most strongly decorrelated CA1 network activity and these disruptions recovered only slowly, compared to Iso.

Changes in synaptic connections are considered essential for memory formation and storage (Frey and Morris, 1997; Kasai et al., 2010; Segal, 2005; Yang et al., 2009). Despite, a small effect on spine dynamics, the strong and lasting disturbance of hippocampal network activity in CA1 (and most likely other brain areas) by Keta/Xyl and MMF was sufficient to interfere with memory consolidation. The chronic alterations of spine turnover, especially by Keta/Xyl, may therefore indicate that repeated anesthesia can impact long-lasting hippocampus-dependent memories. To establish a direct link between spine dynamics, network disruptions and memory, future studies are required that investigate both spine turnover and changes in population coupling at hippocampal neurons causally involved in memory formation and maintenance.

Taken together, we report a novel effect of anesthesia on brain dynamics, namely fragmentation of network activity in hippocampus. We consistently observe this phenomenon across multiple levels of analysis. This unique response compared to the cortex may underlie its high sensitivity to anesthesia including its central role in amnesia. The extent, duration, and reversibility of network fragmentation depends on the GA used. Therefore, this study may help guide the choice of an appropriate anesthetic strategy, dependent on experimental requirements and constraints, especially in the neurosciences. More generally, our findings might also have relevance for the clinic. Postoperative delirium, a condition that involves memory loss, is still an unresolved mystery. Minimizing the disturbance of hippocampal function may be one building block to overcome this undesired condition.

AUTHOR CONTRIBUTIONS

Conceptualization, W.Y., M.C., J.S.W.; Methodology, W.Y., M.C., J.A.P., A.F., F.M., O.S., I.L.H.-O., J.S.W.; Analysis, W.Y., M.C., A.F., J.A.P., P.P., C.R., F.M., J.S.W.; Investigation , W.Y., J.A.P.; Data Curation, W.Y., M.C., J.A.P., A.F.; Writing, W.Y., M.C., O.S., I.L.H.-O., J.S.W.; Visualization, W.Y., M.C., A.F., J.S.W.; Supervision, F.M., I.L.H.-O., J.S.W.; Project Administration, J.S.W.; Funding Acquisition, W.Y., A.F., I.L.H.-O., J.S.W.

ACKNOWLEDGEMENTS

We thank Stefan Schillemeit and Kathrin Sauter for technical assistance and Thomas G. Oertner and Amit Marmelstein for critical feedback on the manuscript. This work was funded by the Deutsche Forschungsgemeinschaft (DFG, SPP1926/FOR2419/P6, SFB963/B8 to J.S.W., SPP 1665/Ha 4466/10-1/Ha4466/12-1, SFB 936/B5 to I.L.H.-O.), the European Research Council (ERC2016-StG-714762 to J.S.W., ERC-2015-CoG 681577 to I.L.H.-O.), the German Academic Exchange Service (DAAD, STG/19/5744091 to A.F.), and the Chinese Scholarship Council (CSC 201606210129 to W.Y.).

DECLARATION OF INTERESTS

The authors declare no competing interests.

STAR METHODS

Key Resources Table

Resource Availability

Lead Contact

Further information and requests for resources and reagents should be directed to and will be fulfilled by the Lead Contact, J. Simon Wiegert (simon.wiegert@zmnh.uni-hamburg.de).

Materials Availability

This study did not generate new unique reagents.

Data and Code Availability

The code generated during this study is available at https://github.com/OpatzLab/HanganuOpatzToolbox and https://github.com/mchini/Calcium-Imaging---Anesthesia

The calcium imaging and electrophysiology data sets generated during this study are available at https://gin.g-node.org/SW_lab/Anesthesia_CA1

Experimental Model and Subject Details

Mice

Adult C57BL/6J mice and transgenic Thy1-GFP-M mice of both sexes were housed and bred in pathogen-free conditions at the University Medical Center Hamburg-Eppendorf. The light/dark cycle was 12/12 h and the humidity and temperature were kept constant (40% relative humidity; 22°C). Food and water were available ad libitum. All procedures were performed in compliance with German law according and the guidelines of Directive 2010/63/EU. Protocols were approved by the Behörde für Gesundheit und Verbraucherschutz of the City of Hamburg.

Method Details

Hippocampal recording-window surgery and in-vivo electrophysiology

Chronic multisite extracellular recordings were performed in dorsal CA1. The adapter for head fixation was implanted at least 4 days before recordings. Mice were anesthetized via intraperitoneal injection of midazolam/medetomidine/fentanyl (MMF) and placed on a heating blanket to maintain the body temperature. Eyes were covered with eye ointment (Vidisic, Bausch + Lomb) to prevent drying. Prior to surgery, the depth of anesthesia and analgesia was evaluated with a toe-pinch to test the paw-withdrawal reflex. Subsequently, mice were fixed in a stereotactic frame, the fur was removed with a fine trimmer and the skin of the head was disinfected with Betaisodona. After removing the skin, 0.5% bupivacaine / 1% lidocaine was locally applied to cutting edges. A metal head-post (Neurotar) was attached to the skull with dental cement (Super Bond C&B, Sun Medical) and a craniotomy was performed above the to the dorsal CA1 area (− 2.0 mm AP, ± 1.3 mm ML relative to Bregma) which was subsequently protected by a customized synthetic window filled with Kwik-Cast sealant (World Precision Instruments). After recovery from anesthesia, mice were returned to their home cage and were provided with Meloxicam mixed into soft food for 3 days. After recovery from the surgery, mice were accustomed to head-fixation and trained to move in the Mobile HomeCage system (Neurotar). For recordings, craniotomies were reopened by removal of the Kwik-Cast sealant and multi-site electrodes (NeuroNexus, MI, USA) were inserted into the dorsal CA1 (one-shank, A1x16 recording sites, 50 µm spacing, 1.6 mm deep). A silver wire served as ground and reference in the craniotomy between skull and brain tissue. Extracellular signals were band-pass filtered (0.1-8000 Hz) and digitized (32 kHz) with a multichannel extracellular amplifier (Digital Lynx SX; Neuralynx). The same animals were recorded weekly under different anesthesia. After 15 min of non-anesthetized recording, mice received a subcutaneous injection of Keta/Xyl, MMF or inhalation of Iso in a pseudo-randomized order. The following drug combinations were administered: 2.0 % isoflurane in 100% O_2; 130 mg/kg ketamine, 10 mg/kg xylazine s.c.; 5.0 mg/kg midazolam, 0.2 mg/kg medetomidine and 0.05 mg/kg fentanyl s.c.; and for complete reversal of anesthesia, 0.5 mg/kg flumazenil, 2.5 mg/kg atipamezole and 0.1 mg/kg buprenorphine s.c. Recordings were continued for 1.5 h. After recordings craniotomy was closed and mice were returned to their home cage. Electrode position was confirmed in brain slices postmortem.

Virus injection and hippocampal window surgery for in vivo calcium imaging

C57BL/6J wild-type mice were anesthetized via intraperitoneal injection of midazolam/medetomidine/fentanyl (MMF) and placed on a heating blanket to maintain the body temperature. Eyes were covered with eye ointment (Vidisic, Bausch + Lomb) to prevent drying. Prior to surgery, the depth of anesthesia and analgesia was evaluated with a toe-pinch to test the paw-withdrawal reflex. Subsequently, mice were fixed in a stereotactic frame, the fur was removed with a fine trimmer and the skin of the head was disinfected with Betaisodona. The skin was removed by a midline scalp incision (1-3 cm), the skull was cleaned using a bone scraper (Fine Science Tools) and a small hole was drilled with a dental drill (Foredom) above the injection site. AAV2/7-syn-GCaMP6f was targeted unilaterally to the dorsal CA1 area (− 2.0 mm AP, ± 1.3 mm ML, − 1.5 mm DV relative to Bregma). 0.6 µl of virus suspension was injected. All injections were done at 100 nl*min^{-1} using a glass micropipette. After the injection, the pipette stayed in place for at least 5 min before it was withdrawn and the scalp was closed with sutures. For complete reversal of anesthesia, mice received a subcutaneous dose of Flumazenil, Atipamezol and Buprenorphine (FAB). During the two days following surgery animals were provided with Meloxicam mixed into soft food. Two weeks after virus injection,

mice were anesthetized as described above to implant the hippocampal window. After fur removal, skin above the frontal and parietal bones of the skull was removed by one horizontal cut along basis of skull and two rostral cuts. The skull was cleaned after removal of the periosteum, roughened with a bone scraper and covered with a thin layer of cyanoacrylate glue (Pattex). After polymerization a 3-mm circle was marked on the right parietal bone (anteroposterior, −2.2 mm; mediolateral, +1.8 mm relative to bregma) with a biopsy punch and the bone was removed with a dental drill (Foredom). The dura and somatosensory cortex above the hippocampus were carefully aspirated until the white matter tracts of the corpus callosum became visible. The craniotomy was washed with sterile PBS and a custom-built imaging window was inserted over the dorsal hippocampus. The window consisted of a hollow glass cylinder (diameter: 3 mm, wall thickness: 0.1 mm, height: 1.8 mm) glued to a No. 1 coverslip (diameter: 3mm, thickness: 0.17 mm) on the bottom and to a stainless-steel rim on the top with UV-curable glass glue (Norland NOA61). The steel rim and a head holder plate (Luigs & Neumann) were fixed to the skull with cyanoacrylate gel (Pattex). After polymerization, cranial window and head holder plate were covered with dental cement (Super Bond C&B, Sun Medical) to provide strong bonding to the skull bone. Following the surgery, animals were provided with Meloxicam mixed into soft food for 3 days. The position of the hippocampal window was confirmed in brain slices postmortem.

Two-photon calcium imaging in anesthetized and awake mice

The same animals were sequentially imaged under Keta/Xyl, MMF or Iso in a pseudo-randomized order (for details see above). After losing the righting reflex, generally 5–10 min after application of the anesthetics, the animals were positioned on a heating-pad to maintain body temperature at approximately 37°C during anesthesia. The intensity of anesthesia and evaluation of the different stages of anesthesia were assessed by recording the presence or absence of distinct reflex responses: righting reflex, palpebral reflex, toe-pinch reflex. Between each imaging session, mice were allowed to recover for one week.

Anesthetized mice were head fixed under the microscope on a heated blanket to maintain body temperature. Eyes were covered with eye ointment (Vidisic, Bausch + Lomb) to prevent drying. The window was centered under the two-photon microscope (MOM-scope, Sutter Instruments, modified by Rapp Optoelectronics) and GCaMP6f expression was verified in the hippocampus using epi fluorescence. Images were acquired with a 16x water immersion objective (Nikon CFI75 LWD 16X W, 0.80 NA, 3.0 mm WD). For awake imaging we used a linear treadmill, which allowed imaging during quiet and running states. 5-min-timelapse images were acquired every 10 minutes for a period of 50 minutes. Image acquisition was carried out with a Ti:Sa laser (Chameleon Vision-S, Coherent) tuned to 980 nm to excite GCaMP6f. Single planes (512x512 pixels) were acquired at 30 Hz with a resonant-galvanometric scanner at 29-60 mW (980 nm) using ScanImage 2017b (Vidrio). Emitted photons were detected by a pair of photomultiplier tubes (H7422P-40, Hamamatsu). A 560 DXCR dichroic mirror and 525/50 and 607/70 emission filters (Chroma Technology) were used to separate green and red fluorescence. Excitation light was blocked by short-pass filters (ET700SP-2P, Chroma). For the repetitive imaging, the position of the field of view (FOV) was registered in the first imaging session with the help of vascular landmarks and cell bodies of CA1 pyramidal neurons. This allowed for subsequent retrieval of the FOV for each mouse.

Two-photon spine imaging in anesthetized and awake mice

3 - 4 weeks after window implantation, chronic spine imaging started in Tg(Thy1-EGFP)MJrs/J mice with the first of a total of four imaging series (see Fig. S11A). Each imaging series was

done under one of the three anesthetic conditions (Iso, Keta/Xyl, MMF, see above for details) or during wakefulness. Within one series, mice were imaged 5 times every 4 days. Afterwards, mice were allowed to recover for three to four weeks until the next imaging series under a different anesthetic condition was started. Thus, each experiment lasted approx. 5 months. To avoid time-dependent effects, anesthetic conditions were pseudo-randomized (see Fig. S11A). For imaging sessions under anesthesia mice were head fixed under the microscope on a heated blanket to maintain body temperature. Eyes were covered with eye ointment (Vidisic, Bausch + Lomb) to prevent drying. The window was centered under the two-photon microscope (MOM-scope, Sutter Instruments, modified by Rapp Optoelectronics) and GFP expression was verified in the hippocampus using epi-fluorescence. Image acquisition was carried out with a Ti:Sa laser (Chameleon Vision-S, Coherent) tuned to 980 nm to excite GFP. Images were acquired with a 40x water immersion objective (Nikon CFI APO NIR 40X W, 0.80 NA, 3.5 mm WD). Single planes (512x512 pixels) were acquired at 30 Hz with a resonant scanner at 10-60 mW (980 nm) using ScanImage 2017b. Before the first imaging session, we registered the field of views with the help of vascular landmarks and cell bodies of CA1 pyramidal neurons and selected several regions for longitudinal monitoring across the duration of the time-lapse experiment. Each of these regions contained between 1 and 2 dendritic segments visibly expressing GFP. The imaging sessions lasted for max 60 min and mice were placed back to their home cages where they woke up.

Morris Water Maze

We designed a protocol for reversal learning in the spatial version of the water maze to assess the possible effects of the different anesthetics on episodic-like memory in mice (Chen et al., 2000; Morellini, 2013). The water maze consisted of a circular tank (145 cm in diameter) circled by dark curtains and walls. The water was made opaque by the addition of non-toxic white paint such that the white platform (14 cm diameter, 9 cm high, 1 cm below the water surface) was not visible. Four landmarks (35 X 35 cm) differing in shape and grey gradient were positioned on the wall of the maze. Four white spotlights on the floor around the swimming pool provided homogeneous indirect illumination of 60 lux on the water surface. Mice were first familiarized for one day to swim and climb onto a platform (diameter of 10 cm) placed in a small rectangular maze (42.5 x 26.5 cm and 15.5 cm high). During familiarization, the position of the platform was unpredictable since its location was randomized, and training was performed in darkness. After familiarization, mice underwent three learning days, during which they had to learn the location of a hidden platform. The starting position and the side of the maze from which mice were taken out of the maze were randomized. At day 1 mice underwent four learning trials (maximum duration of 90 seconds, inter-trial interval of 10 minutes). After staying on the platform for 15 s, mice were returned to their home cage and warmed up under red light. On day 2, mice underwent two training trials before they performed a 60 seconds-long probe trial to assess their searching strategy. Afterwards, one additional training trial was used to re-consolidate the memory of the platform position. On day 3 the long-term memory of the platform position was tested with a 45-seconds long probe trial, followed by another training trial with the platform in place to avoid extinction. Then mice underwent four reversal learning trials with the platform located in the quadrant opposite to the one in which the platform was during the previous training trials. To assess whether the mice learned the new platform position, mice underwent a 60-seconds long probe trial to followed by one more training trial to consolidate the memory of the new location. One hour after the last reversal learning trial, mice were anesthetized to analyze the effects of the anesthesia on the consolidation of the memory of the new platform position. Mice were assigned to four groups with an equal average performance during the probe trial on day 2. Each group was subjected to different conditions:

one-hour Iso anesthesia, one-hour MMF anesthesia, Keta/Xyl anesthesia (which was not antagonized), and one group was left untreated. On day 4, mice underwent a 60-seconds long probe trial to evaluate their searching strategies, namely, the "episodic-like memory" of the reversal learning trials performed one hour before having been anesthetized on day 3 (see Fig. 8A).

Quantification and Statistical Analysis

Electrophysiology

In vivo electrophysiology data were analyzed with custom-written scripts in the Matlab environment available at https://github.com/mchini/HanganuOpatzToolbox. Data were band-pass filtered (1-100 Hz or 0-100 Hz for low frequency LFP analysis) using a third-order Butterworth forward and backward filter to preserve phase information before down-sampling to analyze LFP.

Detection of active periods. Active periods were detected with an adapted version of an algorithm for ripple detection (https://github.com/buzsakilab/buzcode/blob/master/detectors/detectEvents/bz_FindRipples.m). Briefly, active periods were detected on the band-pass filtered (4-20 Hz) normalized squared signal using both absolute and relative thresholds. We first passed the signal through a boxcar filter and then performed hysteresis thresholding: we first detected events whose absolute or relative power exceeded the higher threshold, and considered as belonging to the same event all data points that were below the lower (absolute or relative) threshold. Absolute thresholds were set to 7 and 15 μV, relative thresholds to 1 and 2. Periods were merged if having an inter-period interval shorter than 900 ms, and discarded if lasted less than 500 ms. Percentage of active periods was calculated for 15 min bins. Timestamps were preserved for further analysis.

Power spectral density. Power spectral density was calculated on 30 s-long windows of 0-100 Hz filtered signal using Welch's method with a signal overlap of 15 s.

Modulation index (MI). Modulation index was calculated as (value anesthesia - value pre-anesthetized) / (value anesthesia + value pre-anesthetized).

Power law decay exponent of the LFP power spectrum. The 1/f slope was computed as in (Gao et al., 2017). We used robust linear regression (Matlab function *robustfit.m*) on the log10 of the LFP power spectrum in the 30-50 Hz frequency range.

Phase-amplitude coupling (PAC). PAC was calculated on 0-100 Hz filtered full signal using the PAC toolbox based on modulation index measure (Onslow et al., 2011). Range of phase vector was set to 0-8 Hz and range of amplitude vector was set to 20-100 Hz. Significant coupling was calculated in comparison to a shuffled dataset. Non-significant values were rejected.

Single unit analysis. Single unit activity (SUA) was detected and clustered using klusta (Rossant et al., 2016) and manually curated using phy (https://github.com/cortex-lab).

Active units: the recording was divided into 15-minute bins. Single units were considered to be active in the time interval if they fired at least five times.

Pairwise phase consistency. Pairwise phase consistency (PPC) was computed as previously described (Vinck et al., 2010). Briefly, the phase in the band of interest was extracted as mentioned above, and the mean of the cosine of the absolute angular distance (dot product) among all single unit pairs of phases was calculated.

Unit Power. SUA spike trains of each recording were summed in a population vector, and power spectral density was calculated on 30 s-long windows using Welch's method with a signal overlap of 15 s. The resulting power spectra were normalized by the firing rate in that window.

Spike-Time tiling coefficient (STTC) was computed as previously described (Cutts and Eglen, 2014). Briefly, we quantified the proportion (P_A) of spikes of spike train A that fall within ±Δt of a spike from spike train B. To this value we subtract the proportion of time that occurs within ±Δt of spikes from spike train B (T_B). This is then divided by 1 minus the product of these two values. The same is then applied after inverting spike train A and B, and the mean between the two values is kept.

$$STTC = \frac{1}{2}\left(\frac{P_A - T_B}{1 - P_A T_B} + \frac{P_B - T_A}{1 - P_B T_A}\right)$$

Importantly, this coefficient has several desirable properties. It is bounded between -1 and 1. It is symmetric with respect to the two spike trains. Computing it over different timescales is readily done by controlling the value of the parameter "Δt". Lastly, and most importantly, traditionally used methods of assessing correlations between pairs of spike trains show an inverse correlation between their value and firing rate, due to the fact that spiking is sparse with respect to the sampling frequency, and therefore quiescent period in both spike trains artificially increase the correlation. This is not the case for the spike-time tiling coefficient (Cutts and Eglen, 2014). Given that there are large differences in the average firing rate of our conditions, we chose STTC analysis over pure correlation analysis to circumvent this major bias. On the flipside, STTC cannot be straightforwardly applied to negative correlations, that were therefore not investigated in SUA data.

Calcium imaging data

In vivo calcium imaging data were analyzed with custom-written scripts in the Python and Matlab environment available at https://github.com/mchini/Calcium-Imaging---Anesthesia.

Alignment of multiple recordings. To track the activity of the same set of neurons in different anesthetic conditions and during wakefulness, we acquired two-photon time series of a defined field of view for each animal and each condition across multiple weeks. Over such long time periods, the field of view was susceptible to geometrical transformations from one recording to another and thus, any two time series were never perfectly aligned. This problem scaled with time that passed between recordings. However, optimal image alignment is critical for the successful identification and calcium analysis of the same neurons across time (Rose et al., 2016; Sheintuch et al., 2017).

To address this problem, we developed an approach based on the pystackreg package, a Python implementation of the ImageJ extension TurboReg/StackReg (Thevenaz et al., 1998). The source code that reproduces the procedure described in this section is available on github (https://pypi.org/project/pystackreg/). The *pystackreg* package is capable of using different combinations of geometrical transformations for the alignment. We considered rigid body (translation + rotation + scaling) and affine (translation + rotation + scaling + shearing) transformation methods, which we applied to mean and enhanced-mean intensity images generated by Suite2p during the registration of each single recording. We performed the alignment using all four combinations (2 transformations x 2 types of images) choosing the one with the best performance according to the following procedure. Squared difference between the central part of a reference and aligned image served as a distance function d to quantify

the alignment (since the signal is not always present on the borders of the image they were truncated):

$$d = \sum_{i,j}^{\substack{Tranc.\\images}} (x_{i,j}^{ref} - x_{i,j}^{aligned})^2,$$

where $x_{i,j}^{ref}$ and $x_{i,j}^{aligned}$ are intensities of the pixel with coordinates i, j of the reference and aligned images. The combination with the smallest score was chosen for the final transformation. In some rare cases, the algorithm of the alignment did not converge for a given transformation method and image type (mean or enhanced-mean), crumbling the aligned image in a way that most of the field of view remained empty. This combination may have the smallest distance function *d* and may be falsely identified as the best one. To overcome this issue, an additional criterion was applied, which requires the central part of the aligned picture to contain more than 90 % of the non-empty pixels. The overall performance of the algorithm was verified by visual inspection. An example of the alignment of two recordings is shown in Fig. S5. The alignment for all recordings of an example mouse is demonstrated in a supplementary video (Supplementary_video_37529_aligned_recordings.avi).

In case of relatively small distortions across recordings, for example, when consecutive acquisitions were done within one imaging session, registration can alternatively be performed simultaneously with ROI detection in Suite2p by concatenating those TIFF-stacks. In this approach, every ROI is automatically labeled with the same identification number across all recordings.

Identification of the same neurons across different recordings & unique neuron ID assignment. After the alignment procedure, we set out to identify neurons which were active across multiple recordings (and thus, multiple conditions). To achieve this, we developed an algorithm similar to the one described in Sheintuch. et al. 2017 (Sheintuch et al., 2017)

The algorithm processes in series all recordings for a given animal and assigns unique identification (ID) numbers to each ROIs of every recording. Since the recordings under Iso-anesthesia had the largest number of active neurons, we chose the first recording of this condition as reference. We assigned IDs that ranged from 1 to the total amount of neurons to all the ROIs of this recording. For every other recording of each mouse, Neuron ID assignment consisted of: 1. comparison of the properties (details below) of each ROI with each ROI that had already been processed. 2a. If the properties of the ROI matched the properties of an ROI from a previously analyzed recording, the ROI received the same Neuron ID. 2b. If no match was found, a new (in sequential order) Neuron ID was assigned to the ROI. In order to be identified as representing the same neuron in two different recordings, two ROIs had to respect the following criteria: the distance between their centroids had to be below 3 μm, and the overlap between their pixels had to be above 70%. An example of the identification of unique neuron pairs in two recordings is presented in Fig. S6A. The thresholds were chosen based on the distribution of the distances between centroids and percentage of the overlaps. An example for a single mouse is graphically illustrated in Fig. S6B. Both properties have a clearly bimodal distribution (similar to (Sheintuch et al., 2017)) with cutoffs close to the chosen thresholds.

Signal extraction and analysis. Signal extraction, correlation and spectral analysis for calcium signal was performed using Python (Python Software Foundation, NH, USA) in the Spyder (Pierre Raybaut, The Spyder Development Team) development environment. Calcium imaging

1066 data were analyzed with the Suite2p toolbox (Pachitariu et al., 2017) using the parameters
1067 given in table 1.

1068

Parameter	**Variable**	**Value**
Sampling rate, frames per second	fs	30
Registration		
Subsampled frames for finding reference image	nimg_init	2000
Number of frames per batch	batch_size	200
Maximum allowed registration shift, as a fraction of frame max(width and height)	maxregshift	0.1
Precision of subpixel registration (1/subpixel steps)	subpixel	10
Smoothing	smooth_sigma	1.15
Bad frames to be excluded	th_badframes	100.0
Non-rigid registration		
Use nonrigid registration	nonrigid	True
Block size to register (** keep this a multiple of 2 **)	block_size	[128,128]
if any nonrigid block is below this threshold, it gets smoothed until above this threshold. 1.0 results in no smoothing	snr_thresh	2.0
maximum pixel shift allowed for nonrigid, relative to rigid	maxregshiftNR	10
Cell detection		
Run ROI extraction	roidetect	True
Run sparse_mode	sparse_mode	False
Diameter for filtering and extracting	diameter	12.0
Keep ROIs fully connected (set to 0 for dendrites)	connected	True
Maximum number of binned frames for cell detection	nbinned	5000
Maximum number of iterations to do cell detection	max_iterations	20
Adjust the automatically determined threshold by this scalar multiplier	threshold_scaling	1.0 or 0.1

Cells with more overlap than this get removed during triage, before refinement	max_overlap	0.75
Running mean subtraction with window of size 'high_pass'	high_pass	100
ROI extraction		
Number of pixels to keep between ROI and neuropil donut	inner_neuropil_radius	2
Minimum number of pixels in the neuropil	min_neuropil_pixels	100
Pixels that are overlapping are thrown out (False) or added to both ROIs (True)	allow_overlap	True
Deconvolution		
Deconvolution time constant, seconds	tau	0.7

The same analytical pipeline was applied to both the raw fluorescence traces as well as the deconvolved ("spikes") signal, as extracted by the Suite2p toolbox. Generally, the raw fluorescence signal was preferred over the deconvolved one given that its extraction is more straightforward and relies on less assumptions. However, while the reported effects varied in magnitude depending on which of the two signals was considered, the same results were obtained on both datasets. The effects were entirely consistent. For raw signal analysis of each neuron, previous to any further step, we subtracted 0.7 of the corresponding neuropil fluorescence trace.

The number and height of calcium transients properties were calculated with the scipy function *find_peaks* on the raw calcium traces with the following parameters: height = 200, distance = 10 and prominence = 200. The decay was computed on the 10 best-isolated transients of each neuron, using the *OASIS* toolbox (https://github.com/j-friedrich/OASIS). We used the *deconvolve* function with the following parameters: penalty = 0, optimize_g = 10. Traces with an estimated decay over 2 seconds were considered cases of failed extraction and removed from further analysis.

The choice of the parameter values for transient detection is somewhat arbitrary. Similarly, it is debatable whether and how the calcium traces should best be normalized. Therefore, we tested the robustness of our findings by systematically varying signal extraction choices. We first varied the height and prominence threshold across a wide range of values (50 to 700 arbitrary units). We further computed transients features on normalized ΔF/F calcium traces. To normalize calcium signals, we used the baseline value as extracted by the *deconvolve* function. Also, in this case, we varied the height and prominence threshold across a wide range of values (0.5 to 3 arbitrary units). Finally, we computed two measures of neuronal activity that are independent of calcium transients detection: the average of the trace integral and its standard deviation, with and without normalization. Across all of these scenarios, the reported effects were robustly consistent.

Correlations were computed both as Pearson (numpy function *corrcoeff*) and Spearman (custom written function) coefficient on the z-scored signal. To both sets of coefficients, the

Fisher correction (the inverse of the hyperbolic tangent function, numpy function *arctanh*) was applied. For power analysis, we first created a population activity vector by summing all the single neuron z-scored signals, and then estimated the power spectral density by applying the Welch method (sampling frequency = 30 Hz, number of points for fast Fourier transformation = 1024, no overlap, window length = 1 s).

Complexity analysis was performed in the Matlab (MathWorks) environment. For complexity analysis, we limited the amount of neurons to the minimum (N_{min}) present in any recording of any condition for each single mouse (median = 265, min = 156, max = 1068). The resulting matrix therefore had the $T_{rec}xN_{min}$ dimensions, where T_{rec} represents the time vector for the recording, with a length of 5 min and a sampling rate of 30 Hz. For recordings that had a number of neurons larger than N_{min} for that mouse, we randomly sampled n = N_{min} neurons and repeated the analysis 5 times. For every extracted parameter, we then considered the median value over the 5 repetitions. For further analysis, the signal was downsampled from the original sampling frequency of 30 Hz to 10 Hz (100 ms bins). The same analytical pipeline was then applied to both the raw fluorescence traces, as well as the deconvolved signal.

tSNE clustering. tSNE clustering was performed similar to (Wenzel et al., 2019). Briefly, in a range between 5 and 45, the perplexity value that minimized the reconstruction error was selected. The number of PCA components used for this step was limited to 30. For the raw fluorescence signal, Euclidian distance was used, whereas for the deconvolved signal we opted for cosine distance, as it is better suited to a sparse signal. We computed the probability distribution of the resulting embedded matrix ($2xT_{rec}$), that was then convolved with a 2D Gaussian window (standard deviation was set to be equal to 1/40 of the total maximum value). To evaluate the number of clusters in the distribution, we then applied a series of standard steps in image analysis: background subtraction with the rolling ball method, smoothing with a median filter, thresholding, watershedding to avoid undersegmentation, and extended minima transformation. Finally, the exterior boundaries of the objects were traced and counted. This gave the number of clusters.

Affinity Propagation Clustering (APC). Affinity Propagation clustering was performed using a Matlab toolbox [https://www.psi.toronto.edu/index.php?q=affinity%20propagation] and similarly to (Wenzel et al., 2019). We first obtained a distance map, which was computed as 1 minus the pairwise cosine distance between observations of the $T_{rec}xN_{min}$ matrix. This distance matrix was then fed to the affinity propagation algorithm with the input preference set equal to the median of the distance matrix.

Principal Component Analysis (PCA) clustering and variance explained. Standard PCA was applied to the $T_{rec}xN_{min}$ matrix. The number of clusters was computed as the number of components that was needed to cumulatively explain 90% of the variance of the input matrix. Further, we computed the loglog decay coefficient of number of components versus variance explained.

Community detection. To detect communities, we used the Louvain algorithm from the Brain Connectivity Toolbox (https://sites.google.com/site/bctnet/), a modularity maximization procedure widely used in studies examining brain networks (Rubinov and Sporns, 2010). This approach aims at subdividing the network into partitions that are more internally dense than would be expected by chance (Sporns and Betzel, 2016). As input to the algorithm, we used Fisher-transformed correlation matrices obtained from calcium imaging time-series. Matrices were not thresholded, and both positive and negative correlations were taken into account to determine optimal modular partitions. The algorithm was evaluated while varying the resolution

parameter gamma between 0 and 3, in steps of 0.1. For the multiresolution approach and hierarchical consensus clustering, data was analyzed using code available at https://github.com/LJeub/HierarchicalConsensus and according to the procedure described in (Jeub et al., 2018). The number of communities detected by the finest level partition of the consensus hierarchy was used for further analysis. While neurons in the awake condition tended to be spatially closer to each other than for the other conditions (Fig. S10E), this is unlikely to have influenced the results of the analysis, as the difference was minimal and there was no correlation between median distance in a recording and the number of detected communities (Fig. S10F).

Two-Photon Spine Image Processing

In each animal, at least one GFP-expressing CA1 pyramidal neuron was selected and 1-3 dendrites of 20–50 µm length of each of the following types were analyzed: basal dendrites, oblique dendrites emerging from the apical trunk and tuft dendrites. Motion artefacts were corrected with a custom-modified Lucas-Kanade-based alignment algorithm written in Matlab. Spines that laterally emanated from the dendrite were counted by manually scrolling through the z-stacks of subsequent imaging time points of the same dendritic element, by an expert examiner blinded to the experimental condition. Protrusions from the dendrite that reached a threshold of 0.2 µm were scored as dendritic spines regardless of shape. If spine neck positions differed 0.5 µm on the subsequent images, the spine was scored as a new spine. Spines were scored as lost if they fell below the threshold of 0.2 µm. Spine density was calculated as the number of spines per µm. The turnover ratio was calculated for every time point by dividing the sum of gained and lost spines by the number of present spines. The survival fraction of spines was calculated as the percentage of remaining spines compared with the first imaging time point.

Statistical analysis

Statistical analyses were performed using R Statistical Software (Foundation for Statistical Computing, Vienna, Austria) or GraphPad Prism. All R scripts and datasets are available on github https://github.com/mchini/Calcium-Imaging---Anesthesia. Nested data were analyzed with linear mixed-effect models to account for the commonly ignored increased false positive rate inherent in nested design (Aarts et al., 2014). We used “mouse”, “recording”, “neuron” (calcium imaging), and “single unit” (electrophysiology) as random effects, according to the specific experimental design. Parameter estimation was done using the lmer function implemented in the *lme4* R package (Bates et al., 2015). Model selection was performed according to experimental design. Significance and summary tables for lmer model fits were evaluated with the *lmerTest* R package (Kuznetsova et al., 2017), using the Satterthwaite's degrees of freedom method. Post hoc analysis with Tukey multiple comparison correction was carried out using the *emmeans* R package.

REFERENCES

Aarts, E., Verhage, M., Veenvliet, J.V., Dolan, C.V., and van der Sluis, S. (2014). A solution to dependency: using multilevel analysis to accommodate nested data. Nat Neurosci 17, 491-496.

Albrecht, M., Henke, J., Tacke, S., Markert, M., and Guth, B. (2014). Effects of isoflurane, ketamine-xylazine and a combination of medetomidine, midazolam and fentanyl on

physiological variables continuously measured by telemetry in Wistar rats. BMC Vet Res 10, 198.

Alkire, M.T., Hudetz, A.G., and Tononi, G. (2008). Consciousness and anesthesia. Science 322, 876-880.

Antognini, J.F., and Carstens, E. (2002). In vivo characterization of clinical anaesthesia and its components. Br J Anaesth 89, 156-166.

Attardo, A., Fitzgerald, J.E., and Schnitzer, M.J. (2015). Impermanence of dendritic spines in live adult CA1 hippocampus. Nature 523, 592-596.

Bates, D., Machler, M., Bolker, B.M., and Walker, S.C. (2015). Fitting Linear Mixed-Effects Models Using lme4. J Stat Softw 67, 1-48.

Bittner, K.C., Grienberger, C., Vaidya, S.P., Milstein, A.D., Macklin, J.J., Suh, J., Tonegawa, S., and Magee, J.C. (2015). Conjunctive input processing drives feature selectivity in hippocampal CA1 neurons. Nat Neurosci.

Bonin, R.P., and Orser, B.A. (2008). GABA(A) receptor subtypes underlying general anesthesia. Pharmacol Biochem Behav 90, 105-112.

Briner, A., De Roo, M., Dayer, A., Muller, D., Habre, W., and Vutskits, L. (2010). Volatile anesthetics rapidly increase dendritic spine density in the rat medial prefrontal cortex during synaptogenesis. Anesthesiology 112, 546-556.

Briner, A., Nikonenko, I., De Roo, M., Dayer, A., Muller, D., and Vutskits, L. (2011). Developmental Stage-dependent persistent impact of propofol anesthesia on dendritic spines in the rat medial prefrontal cortex. Anesthesiology 115, 282-293.

Buzsaki, G. (1986). Hippocampal sharp waves: their origin and significance. Brain Res 398, 242-252.

Buzsaki, G., Anastassiou, C.A., and Koch, C. (2012). The origin of extracellular fields and currents--EEG, ECoG, LFP and spikes. Nat Rev Neurosci 13, 407-420.

Canolty, R.T., and Knight, R.T. (2010). The functional role of cross-frequency coupling. Trends in cognitive sciences 14, 506-515.

Chen, G., Chen, K.S., Knox, J., Inglis, J., Bernard, A., Martin, S.J., Justice, A., McConlogue, L., Games, D., Freedman, S.B., and Morris, R.G. (2000). A learning deficit related to age and beta-amyloid plaques in a mouse model of Alzheimer's disease. Nature 408, 975-979.

Chen, T.W., Wardill, T.J., Sun, Y., Pulver, S.R., Renninger, S.L., Baohan, A., Schreiter, E.R., Kerr, R.A., Orger, M.B., Jayaraman, V., *et al.* (2013). Ultrasensitive fluorescent proteins for imaging neuronal activity. Nature 499, 295-300.

Chini, M., Gretenkord, S., Kostka, J.K., Popplau, J.A., Cornelissen, L., Berde, C.B., Hanganu-Opatz, I.L., and Bitzenhofer, S.H. (2019). Neural Correlates of Anesthesia in Newborn Mice and Humans. Frontiers in neural circuits 13, 38.

Clark, D.L., and Rosner, B.S. (1973). Neurophysiologic effects of general anesthetics. I. The electroencephalogram and sensory evoked responses in man. Anesthesiology 38, 564-582.

Collins, D.R., Pelletier, J.G., and Pare, D. (2001). Slow and fast (gamma) neuronal oscillations in the perirhinal cortex and lateral amygdala. J Neurophysiol 85, 1661-1672.

1228 Contreras, D., and Steriade, M. (1995). Cellular basis of EEG slow rhythms: a study of dynamic
1229 corticothalamic relationships. J Neurosci 15, 604-622.

1230 Cutts, C.S., and Eglen, S.J. (2014). Detecting pairwise correlations in spike trains: an objective
1231 comparison of methods and application to the study of retinal waves. J Neurosci 34, 14288-
1232 14303.

1233 Dailey, M.E., and Smith, S.J. (1996). The dynamics of dendritic structure in developing
1234 hippocampal slices. J Neurosci 16, 2983-2994.

1235 De Roo, M., Klauser, P., Briner, A., Nikonenko, I., Mendez, P., Dayer, A., Kiss, J.Z., Muller, D.,
1236 and Vutskits, L. (2009). Anesthetics rapidly promote synaptogenesis during a critical period of
1237 brain development. PloS one 4, e7043.

1238 De Roo, M., Klauser, P., and Muller, D. (2008). LTP promotes a selective long-term
1239 stabilization and clustering of dendritic spines. PLoS Biol 6, e219.

1240 Fleischmann, T., Jirkof, P., Henke, J., Arras, M., and Cesarovic, N. (2016). Injection
1241 anaesthesia with fentanyl-midazolam-medetomidine in adult female mice: importance of
1242 antagonization and perioperative care. Lab Anim 50, 264-274.

1243 Franks, N.P. (2008). General anaesthesia: from molecular targets to neuronal pathways of
1244 sleep and arousal. Nat Rev Neurosci 9, 370-386.

1245 Frey, U., and Morris, R.G. (1997). Synaptic tagging and long-term potentiation. Nature 385,
1246 533-536.

1247 Gao, R., Peterson, E.J., and Voytek, B. (2017). Inferring synaptic excitation/inhibition balance
1248 from field potentials. NeuroImage 158, 70-78.

1249 Goltstein, P.M., Montijn, J.S., and Pennartz, C.M. (2015). Effects of isoflurane anesthesia on
1250 ensemble patterns of Ca2+ activity in mouse v1: reduced direction selectivity independent of
1251 increased correlations in cellular activity. PloS one 10, e0118277.

1252 Greenberg, D.S., Houweling, A.R., and Kerr, J.N. (2008). Population imaging of ongoing
1253 neuronal activity in the visual cortex of awake rats. Nat Neurosci 11, 749-751.

1254 Gu, L., Kleiber, S., Schmid, L., Nebeling, F., Chamoun, M., Steffen, J., Wagner, J., and
1255 Fuhrmann, M. (2014). Long-term in vivo imaging of dendritic spines in the hippocampus
1256 reveals structural plasticity. J Neurosci 34, 13948-13953.

1257 Hardingham, G.E., and Bading, H. (2010). Synaptic versus extrasynaptic NMDA receptor
1258 signalling: implications for neurodegenerative disorders. Nat Rev Neurosci.

1259 Harris, K.D., and Mrsic-Flogel, T.D. (2013). Cortical connectivity and sensory coding. Nature
1260 503, 51-58.

1261 Jeub, L.G.S., Sporns, O., and Fortunato, S. (2018). Multiresolution Consensus Clustering in
1262 Networks. Scientific reports 8.

1263 Kasai, H., Fukuda, M., Watanabe, S., Hayashi-Takagi, A., and Noguchi, J. (2010). Structural
1264 dynamics of dendritic spines in memory and cognition. Trends Neurosci 33, 121-129.

1265 Katz, Y., Menon, V., Nicholson, D.A., Geinisman, Y., Kath, W.L., and Spruston, N. (2009).
1266 Synapse distribution suggests a two-stage model of dendritic integration in CA1 pyramidal
1267 neurons. Neuron 63, 171-177.

1268 Klausberger, T., and Somogyi, P. (2008). Neuronal diversity and temporal dynamics: the unity
1269 of hippocampal circuit operations. Science 321, 53-57.

1270 Klinzing, J.G., Niethard, N., and Born, J. (2019). Mechanisms of systems memory
1271 consolidation during sleep. Nat Neurosci 22, 1598-1610.

1272 Kuznetsova, A., Brockhoff, P.B., and Christensen, R.H.B. (2017). lmerTest Package: Tests in
1273 Linear Mixed Effects Models. J Stat Softw 82, 1-26.

1274 Langsjo, J.W., Maksimow, A., Salmi, E., Kaisti, K., Aalto, S., Oikonen, V., Hinkka, S., Aantaa,
1275 R., Sipila, H., Viljanen, T., *et al.* (2005). S-ketamine anesthesia increases cerebral blood flow
1276 in excess of the metabolic needs in humans. Anesthesiology 103, 258-268.

1277 Larkum, M. (2012). A cellular mechanism for cortical associations: an organizing principle for
1278 the cerebral cortex. Trends Neurosci.

1279 Lee, U., Ku, S., Noh, G., Baek, S., Choi, B., and Mashour, G.A. (2013). Disruption of frontal-
1280 parietal communication by ketamine, propofol, and sevoflurane. Anesthesiology 118, 1264-
1281 1275.

1282 Lendvai, B., Stern, E.A., Chen, B., and Svoboda, K. (2000). Experience-dependent plasticity
1283 of dendritic spines in the developing rat barrel cortex in vivo. Nature 404, 876-881.

1284 Li, N., Lee, B., Liu, R.J., Banasr, M., Dwyer, J.M., Iwata, M., Li, X.Y., Aghajanian, G., and
1285 Duman, R.S. (2010). mTOR-dependent synapse formation underlies the rapid antidepressant
1286 effects of NMDA antagonists. Science 329, 959-964.

1287 Lin, H., Higgins, P., Loh, H.H., Law, P.Y., and Liao, D. (2009). Bidirectional effects of fentanyl
1288 on dendritic spines and AMPA receptors depend upon the internalization of mu opioid
1289 receptors. Neuropsychopharmacology 34, 2097-2111.

1290 Mashour, G.A., Orser, B.A., and Avidan, M.S. (2011). Intraoperative awareness: from
1291 neurobiology to clinical practice. Anesthesiology 114, 1218-1233.

1292 Mizrahi-Kliger, A.D., Kaplan, A., Israel, Z., and Bergman, H. (2018). Desynchronization of slow
1293 oscillations in the basal ganglia during natural sleep. Proc Natl Acad Sci U S A 115, E4274-
1294 E4283.

1295 Morellini, F. (2013). Spatial memory tasks in rodents: what do they model? Cell Tissue Res
1296 354, 273-286.

1297 Moscovitch, M., Cabeza, R., Winocur, G., and Nadel, L. (2016). Episodic Memory and Beyond:
1298 The Hippocampus and Neocortex in Transformation. Annual review of psychology 67, 105-
1299 134.

1300 Nadel, L., and Moscovitch, M. (1997). Memory consolidation, retrograde amnesia and the
1301 hippocampal complex. Curr Opin Neurobiol 7, 217-227.

1302 Nagerl, U.V., Eberhorn, N., Cambridge, S.B., and Bonhoeffer, T. (2004). Bidirectional activity-
1303 dependent morphological plasticity in hippocampal neurons. Neuron 44, 759-767.

1304 Neves, G., Cooke, S.F., and Bliss, T.V. (2008). Synaptic plasticity, memory and the
1305 hippocampus: a neural network approach to causality. Nat Rev Neurosci 9, 65-75.

1306 Newman, M.E., and Girvan, M. (2004). Finding and evaluating community structure in
1307 networks. Phys Rev E Stat Nonlin Soft Matter Phys 69, 026113.

O'Neill, J., Pleydell-Bouverie, B., Dupret, D., and Csicsvari, J. (2010). Play it again: reactivation of waking experience and memory. Trends Neurosci 33, 220-229.

Okun, M., Steinmetz, N., Cossell, L., Iacaruso, M.F., Ko, H., Bartho, P., Moore, T., Hofer, S.B., Mrsic-Flogel, T.D., Carandini, M., and Harris, K.D. (2015). Diverse coupling of neurons to populations in sensory cortex. Nature 521, 511-515.

Onslow, A.C., Bogacz, R., and Jones, M.W. (2011). Quantifying phase-amplitude coupling in neuronal network oscillations. Prog Biophys Mol Biol 105, 49-57.

Pachitariu, M., Stringer, C., Dipoppa, M., Schröder, S., Rossi, L.F., Dalgleish, H., Carandini, M., and Harris, K.D. (2017). Suite2p: beyond 10,000 neurons with standard two-photon microscopy. bioRxiv, 061507.

Pfeiffer, T., Poll, S., Bancelin, S., Angibaud, J., Inavalli, V.K., Keppler, K., Mittag, M., Fuhrmann, M., and Nagerl, U.V. (2018). Chronic 2P-STED imaging reveals high turnover of dendritic spines in the hippocampus in vivo. eLife 7.

Phoumthipphavong, V., Barthas, F., Hassett, S., and Kwan, A.C. (2016). Longitudinal Effects of Ketamine on Dendritic Architecture In Vivo in the Mouse Medial Frontal Cortex. eNeuro 3.

Portera-Cailliau, C., Pan, D.T., and Yuste, R. (2003). Activity-regulated dynamic behavior of early dendritic protrusions: evidence for different types of dendritic filopodia. J Neurosci 23, 7129-7142.

Pryazhnikov, E., Mugantseva, E., Casarotto, P., Kolikova, J., Fred, S.M., Toptunov, D., Afzalov, R., Hotulainen, P., Voikar, V., Terry-Lorenzo, R.*, et al.* (2018). Longitudinal two-photon imaging in somatosensory cortex of behaving mice reveals dendritic spine formation enhancement by subchronic administration of low-dose ketamine. Scientific reports 8, 6464.

Purdon, P.L., Sampson, A., Pavone, K.J., and Brown, E.N. (2015). Clinical Electroencephalography for Anesthesiologists: Part I: Background and Basic Signatures. Anesthesiology 123, 937-960.

Rose, T., Jaepel, J., Hubener, M., and Bonhoeffer, T. (2016). Cell-specific restoration of stimulus preference after monocular deprivation in the visual cortex. Science 352, 1319-1322.

Rossant, C., Kadir, S.N., Goodman, D.F.M., Schulman, J., Hunter, M.L.D., Saleem, A.B., Grosmark, A., Belluscio, M., Denfield, G.H., Ecker, A.S.*, et al.* (2016). Spike sorting for large, dense electrode arrays. Nat Neurosci 19, 634-641.

Rubinov, M., and Sporns, O. (2010). Complex network measures of brain connectivity: Uses and interpretations. NeuroImage 52, 1059-1069.

Rudolph, U., and Antkowiak, B. (2004). Molecular and neuronal substrates for general anaesthetics. Nat Rev Neurosci 5, 709-720.

Sanders, R.D., Tononi, G., Laureys, S., and Sleigh, J.W. (2012). Unresponsiveness not equal unconsciousness. Anesthesiology 116, 946-959.

Sarasso, S., Boly, M., Napolitani, M., Gosseries, O., Charland-Verville, V., Casarotto, S., Rosanova, M., Casali, A.G., Brichant, J.F., Boveroux, P.*, et al.* (2015). Consciousness and Complexity during Unresponsiveness Induced by Propofol, Xenon, and Ketamine. Curr Biol 25, 3099-3105.

1348 Scheffer-Teixeira, R., Belchior, H., Caixeta, F.V., Souza, B.C., Ribeiro, S., and Tort, A.B.
1349 (2012). Theta phase modulates multiple layer-specific oscillations in the CA1 region. Cereb
1350 Cortex 22, 2404-2414.

1351 Schmid, L.C., Mittag, M., Poll, S., Steffen, J., Wagner, J., Geis, H.R., Schwarz, I., Schmidt, B.,
1352 Schwarz, M.K., Remy, S., and Fuhrmann, M. (2016). Dysfunction of Somatostatin-Positive
1353 Interneurons Associated with Memory Deficits in an Alzheimer's Disease Model. Neuron 92,
1354 114-125.

1355 Schomburg, E.W., Fernandez-Ruiz, A., Mizuseki, K., Berenyi, A., Anastassiou, C.A., Koch, C.,
1356 and Buzsaki, G. (2014). Theta phase segregation of input-specific gamma patterns in
1357 entorhinal-hippocampal networks. Neuron 84, 470-485.

1358 Segal, M. (2005). Dendritic spines and long-term plasticity. Nat Rev Neurosci 6, 277-284.

1359 Sheintuch, L., Rubin, A., Brande-Eilat, N., Geva, N., Sadeh, N., Pinchasof, O., and Ziv, Y.
1360 (2017). Tracking the Same Neurons across Multiple Days in Ca(2+) Imaging Data. Cell reports
1361 21, 1102-1115.

1362 Soltesz, I., and Deschenes, M. (1993). Low- and high-frequency membrane potential
1363 oscillations during theta activity in CA1 and CA3 pyramidal neurons of the rat hippocampus
1364 under ketamine-xylazine anesthesia. J Neurophysiol 70, 97-116.

1365 Sporns, O., and Betzel, R.F. (2016). Modular Brain Networks. Annual review of psychology 67,
1366 613-640.

1367 Steriade, M., Nunez, A., and Amzica, F. (1993). A novel slow (< 1 Hz) oscillation of neocortical
1368 neurons in vivo: depolarizing and hyperpolarizing components. J Neurosci 13, 3252-3265.

1369 Sur, C., Fresu, L., Howell, O., McKernan, R.M., and Atack, J.R. (1999). Autoradiographic
1370 localization of alpha5 subunit-containing GABAA receptors in rat brain. Brain Res 822, 265-
1371 270.

1372 Thevenaz, P., Ruttimann, U.E., and Unser, M. (1998). A pyramid approach to subpixel
1373 registration based on intensity. IEEE Trans Image Process 7, 27-41.

1374 Urban, B.W., and Bleckwenn, M. (2002). Concepts and correlations relevant to general
1375 anaesthesia. Br J Anaesth 89, 3-16.

1376 Vinck, M., Battaglia, F.P., Womelsdorf, T., and Pennartz, C. (2012). Improved measures of
1377 phase-coupling between spikes and the Local Field Potential. J Comput Neurosci 33, 53-75.

1378 Vinck, M., van Wingerden, M., Womelsdorf, T., Fries, P., and Pennartz, C.M. (2010). The
1379 pairwise phase consistency: a bias-free measure of rhythmic neuronal synchronization.
1380 NeuroImage 51, 112-122.

1381 Vutskits, L., and Xie, Z. (2016). Lasting impact of general anaesthesia on the brain:
1382 mechanisms and relevance. Nat Rev Neurosci 17, 705-717.

1383 Wenzel, M., Han, S., Smith, E.H., Hoel, E., Greger, B., House, P.A., and Yuste, R. (2019).
1384 Reduced Repertoire of Cortical Microstates and Neuronal Ensembles in Medically Induced
1385 Loss of Consciousness. Cell Syst 8, 467-474 e464.

1386 West, A.E., Griffith, E.C., and Greenberg, M.E. (2002). Regulation of transcription factors by
1387 neuronal activity. Nat Rev Neurosci 3, 921-931.

1388 Whitlock, J.R., Heynen, A.J., Shuler, M.G., and Bear, M.F. (2006). Learning induces long-term
1389 potentiation in the hippocampus. Science 313, 1093-1097.

1390 Wiegert, J.S., and Bading, H. (2011). Activity-dependent calcium signaling and ERK-MAP
1391 kinases in neurons: a link to structural plasticity of the nucleus and gene transcription
1392 regulation. Cell calcium 49, 296-305.

1393 Wiegert, J.S., and Oertner, T.G. (2013). Long-term depression triggers the selective
1394 elimination of weakly integrated synapses. Proc Natl Acad Sci U S A 110, E4510-4519.

1395 Wiegert, J.S., Pulin, M., Gee, C.E., and Oertner, T.G. (2018). The fate of hippocampal
1396 synapses depends on the sequence of plasticity-inducing events. eLife 7.

1397 Yamakage, M., Hirshman, C.A., and Croxton, T.L. (1995). Inhibitory effects of thiopental,
1398 ketamine, and propofol on voltage-dependent Ca2+ channels in porcine tracheal smooth
1399 muscle cells. Anesthesiology 83, 1274-1282.

1400 Yang, G., Chang, P.C., Bekker, A., Blanck, T.J., and Gan, W.B. (2011). Transient effects of
1401 anesthetics on dendritic spines and filopodia in the living mouse cortex. Anesthesiology 115,
1402 718-726.

1403 Yang, G., Pan, F., and Gan, W.B. (2009). Stably maintained dendritic spines are associated
1404 with lifelong memories. Nature 462, 920-924.

1405 Yang, Y., Cui, Y., Sang, K., Dong, Y., Ni, Z., Ma, S., and Hu, H. (2018). Ketamine blocks
1406 bursting in the lateral habenula to rapidly relieve depression. Nature 554, 317-322.

1407 Zurek, A.A., Bridgwater, E.M., and Orser, B.A. (2012). Inhibition of alpha5 gamma-
1408 Aminobutyric acid type A receptors restores recognition memory after general anesthesia.
1409 Anesth Analg 114, 845-855.

1410 Zurek, A.A., Yu, J., Wang, D.S., Haffey, S.C., Bridgwater, E.M., Penna, A., Lecker, I., Lei, G.,
1411 Chang, T., Salter, E.W., and Orser, B.A. (2014). Sustained increase in alpha5GABAA receptor
1412 function impairs memory after anesthesia. J Clin Invest 124, 5437-5441.

1413

3 | Discussion

Current treatments of neurodevelopmental disorders are mostly symptomatic and generally administered only after the disease has reached a relatively advanced state (Millan et al. 2016; Millan et al. 2012; Pratt et al. 2012). Moreover, the drug treatment landscape of disorders such as schizophrenia has seen no significant progress in the last 50 years (Pratt et al. 2012). Nonetheless, current research points in the direction that another course of action might be possible. Given the developmental nature of several neuropsychiatric disorders, it has been postulated that an early therapy might help in course-correcting the disease, with long lasting pathophysiology effects (Millan et al. 2016). To achieve this goal, advancements in early detection of these pathologies and novel pharmacological treatments are needed. However, studies that investigate this hypothesis in clinical populations, for instance in young individuals at high-risk of developing one of these disorders, are promising but complicated by a number of obvious ethical concerns (Kaur and Cadenhead 2010). To this aim, animal studies are instrumental in gaining knowledge from one species that is more amenable to genetic and mechanistic manipulations, with the goal of transferring it to humans. Accordingly, to fill this knowledge gap, this thesis employed several mouse models of cognitive impairment, with the intent of investigating the existence of early disease biomarkers, and novel strategies that might alter the course of the disease.

3.1 Preclinical models of mental disorders

The use of rodent models in the study of cognitive dysfunction and, more generally, of mental disorders has been at the center of extensive recent debate (Pratt et al. 2012; Neill et al. 2010; Wong and Josselyn 2016; Fuccillo et al. 2016; Manning 2016). Rodents are particularly suited to this sort of investigations, not only for the vast array of genetic techniques that easily allow the researcher to manipulate a specific neuronal population or pathway, but also because rodents are an altricial species, and are born at a developmental stage that roughly corresponds to mid human gestation. Mice are thus experimentally accessible at a developmental time-point that is relevant for the risk of incurring in neurodevelopmental disorders (Meyer et al. 2007; Krakowiak et al. 2012). However, several challenges exist for the development of animal models for neurodevelopmental disorders, including the lack of specific disease biomarkers, our poor understanding of their etiology, and the relative unspecificity of their symptoms (Wong and Josselyn 2016). One common criticism that has been targeted to the use of mouse models of mental disorders is that they cannot capture certain exquisitely human categories of psychiatric symptoms and behaviors (Wong and Josselyn 2016). Further, genetic animal models often generally focus on rare but highly penetrant genetic mutations, that poorly represent the polygenic and multifactorial nature of neurodevelopmental disorders (De Rubeis et al. 2014; International Schizophrenia et al. 2009).

To mitigate these limitations, we generally resorted to investigating dual-hit mouse models of mental disorders. These models combine two mild hits, generally one genetic and one environmental, which in isolation do not give rise to a strong symptomatology, but that have a synergistic pathological effect (Chini et al. 2020; Hartung et al. 2016a; Oberlander et al. 2019). Such models induce a larger spectrum of deficits than single-hit ones, and have been proposed of better mimicking the multifactorial etiology of mental disorders (Feigenson et al. 2014). By the same token, a second approach that we applied was to seek for traits that generalize over different mouse models, which has also been proposed as being particularly informative (Arguello and Gogos 2012).

An alternative approach to mouse models that, while still in its infancy, appears to be highly promising, is the use of human induced pluripotent stem cells- (hiPSCs) derived brain organoids (Del Dosso et al. 2020; Paşca 2018). Brain organoids are 3D aggregates of hiPSCs that are grown under particular protocols aimed at reproducing *in vitro* replicas of different brain regions (Del Dosso et al. 2020). Currently, the technology is still of limited use due to high inter- and intra-protocol organoid variability, and the lack of certain cell types such as microglia (Del Dosso et al. 2020;

Paşca 2018; Quadrato et al. 2017). However, the protocols are rapidly improving and, despite these shortcomings, brain organoids have already yielded important discoveries in neuropsychiatric diseases, including neurodevelopmental disorders such as ASD (Lancaster et al. 2013; Birey et al. 2017; Klaus et al. 2019; Jin et al. 2020; Khan et al. 2020). Compared to animal models, brain organoids have the advantage of better modelling the genetic landscape associated with various diseases, as hiPSCs can be directly obtained from the clinical population affected by the disorder. Given that methods that allow network activity detection in brain organoids, via calcium imaging or microelectrode arrays, are starting to be available (Kim et al. 2019; Samarasinghe et al. 2019; Giandomenico et al. 2019; Trujillo et al. 2019; Sharf et al. 2021), it will be interesting to compare how the detected electrophysiological patterns compare to animal studies. Of note, a recent paper found organoid-generated oscillations to share several features with the network activity described in the rodent and human literature, including an increase in broadband LFP power, firing rate and increase in complexity throughout development (Trujillo et al. 2019).

3.2 Early biomarkers of neurodevelopmental disorders: the HP-PFC pathway

As previously discussed, the HP-PFC pathway plays a fundamental role in sustaining cognition across species. This communication route is already established in the very first postnatal days, and it is indispensable in instructing the early prefrontal development. Disruption of the HP-PFC circuitry has been implicated in the pathophysiology of cognitive disorders in both clinical patients and mouse models of these diseases (Sigurdsson et al. 2010; Adams et al. 2020; Tamura et al. 2016). A question that we sought out to answer is whether, in models of mental disorders, these deficits can be used as an early biomarker of the disease. To address this knowledge gap, we probed the mouse HP-PFC pathway at the beginning of the second postnatal week, long before any overt symptomatology might occur, in a number of different mouse models (Oberlander et al. 2019; Xu et al. 2019). The animal models that we investigated included:

1. Two purely genetic mouse models, characterized by a mutation in the pleiotropic gene DISC1, that has a number of important developmental functions (Niwa et al. 2016), or by a chromosomal deficiency that mimics the human 22q11.2 microdeletion

(Ellegood et al. 2014). Both genetic mutations have been linked to a broad increase in the risk of developing neurodevelopmental disorders in humans (Niwa et al. 2016; Ellegood et al. 2014).
2. Two purely environmental mouse models, characterized by a synthetic viral infection during pregnancy, which induces maternal and fetal inflammation (Estes and McAllister 2016), or by chronic administration of ketamine, whose acute administration induces psychotic-like symptoms (Lahti et al. 1995).
3. Two models (dual-hit models) consisting of a combination of a genetic mutation – analogous to the two employed for the two genetic models – plus a synthetic viral infection during pregnancy.
The investigation of several mouse models with the same experimental paradigm was a strategic approach aimed at maximizing face and construct validity of our approach (Millan et al. 2016; Pratt et al. 2012). Stressing the developmental relevance of the HP-PFC pathway (Brockmann et al. 2011), and in line with previous results (Hartung et al. 2016a; Tamura et al. 2016; Zerbi et al. 2018; Xu et al. 2021), communication deficits between the two structures were the trait that most robustly generalized across the various mouse models (Oberlander et al. 2019; Xu et al. 2019).
As previously discussed, studying this network in humans is not without challenges, but connectivity between PFC and HP is reduced also in infants that carry a genetic mutation that increases the risk of developing mental disorders (Bertero et al. 2018; Schleifer et al. 2019). Of particular relevance is the translational approach of Bertero et al., that, investigating an homologous genetic mutation in humans and mice, reported comparable deficits across species. This line of evidence thus points in the direction of deficits in the HP-PFC pathway being an early biomarker of neurodevelopmental disorders.

3.3 Early biomarkers of neurodevelopmental disorders: the PFC

A question that follows from the conclusion that altered HP-PFC communication is an early biomarker of disease is whether these alterations are due to deficits in the source brain area (the HP), in the receiver (the PFC) or in how the two brain areas are wired. We addressed this topic in the subsequent chapters of the thesis.
In light of converging evidence pointing to the PFC as being crucial in the pathophysi-

ology of cognitive deficits (Chini and Hanganu-Opatz 2020), we focused our studies on this brain area. In the first postnatal week, the prefrontal electrophysiological activity is characterized by the emergence of PNOs (Brockmann et al. 2011; Bitzenhofer et al. 2020a), that are mostly sustained by the firing of $PYRs_{II/III}$ (Bitzenhofer et al. 2017; Chini et al. 2020), and that gradually transition into oscillation of higher amplitude and duration, and with a faster average frequency (Bitzenhofer et al. 2020a). Whether PNOs have any functional relevance for the subsequent correct development of the brain area microcircuitry and functionality, similarly to their sensory-motor counterparts, is an open question.

To probe this hypothesis, we manipulated $PYRs_{II/III}$ physiology with an array of different methods, and systematically assessed the consequences on prefrontal network activity and PFC-dependent cognitive abilities. In Chini et al. 2020, we used a dual-hit, genetic-environmental mouse model (GE mice) of mental disorders. The model combines two mild hits that, *per se*, do not give rise to an apparent symptomatology, but that have a synergistic pathological effect (Hartung et al. 2016a; Chini et al. 2020). $PYRs_{II/III}$ of GE mice were characterized by a striking simplified dendritic arborization, and a reduced spine density. On the contrary, their deep layers counterpart were relatively unaffected. These morphological deficits underpinned broadband deficits in PNOs. Furthermore, $PYRs_{II/III}$ of GE mice lost the ability of generating PNOs in the beta-low gamma frequency upon specific optogenetic stimulation. To show whether these prefrontal electrophysiological alterations are robust, we trained a machine-learning algorithm on one set of control and GE mice, and obtained a classification accuracy 90% in an independent set of mice. This supports the notion that these deficits are specific and of considerable magnitude. In Xu et al. 2019 we corroborated these findings by showing that restricting the DISC1 mutation to $PYRs_{II/III}$ recapitulated the structural and physiological deficits observed in the full, pan-neuronal, GE model. This is in line with previous literature on the topic (Niwa et al. 2010) Both studies reported consistent cognitive deficits in GE mice.

In Bitzenhofer et al. 2020b we brought the investigation of this causal chain one step further. Applying a novel paradigm for chronic stimulation of $PYRs_{II/III}$ in mice of P7-P11, we transiently increased the activity of this neuronal population, inducing a premature growth of dendrites and spines. In turn, this resulted in long-term E/I imbalance and deficient PNOs. In particular, upon optogenetic stimulation of $PYRs_{II/III}$, adult early-stimulated (ES) mice displayed a different and desynchronized firing rate dynamic. We hypothesized that this might be due to increased feedback inhibition provided by PV interneurons. Indeed, we showed that PV interneurons of ES mice display an increased dendritic arborization, and a tendency towards

inducing IPSCs of higher amplitude on $PYRs_{II/III}$. This finding lends support to the aforementioned hypothesis that PV interneurons might play a fundamental role in assisting the rhythmicity that underlies mature PNOs. Further, the impaired dynamic of $PYRs_{II/III}$ activation resulted in gamma oscillations of lower amplitude and / or slower frequency. This occurred both when the PFC of ES mice was engaged in a social task, or when we directly and indirectly (via the intermediate hippocampus) optogenetically stimulated it. Taken together, this shows that not only reduced activity of $PYRs_{II/III}$, as characterized in GE mice (Chini et al. 2020; Xu et al. 2019), but also a transient increase of $PYRs_{II/III}$ firing rate is detrimental to the development of the PFC functionality. Of note, similar increased prefrontal activity and altered E/I balance are also present in diverse mouse models of autism spectrum disorder (ASD), that are equally characterized by impaired cognitive and social behavior (Richter et al. 2019; Medendorp et al. 2020; Peixoto et al. 2016; Antoine et al. 2019). Overall, these studies highlight the relevance that early PNOs have in instructing the further development of the PFC and of PFC-dependent cognitive abilities, and how even small deviations from an optimal amount and structure of activity have negative long-term consequences.
Equivalent studies in human babies are challenging, but these results are in line with connectivity within frontal network of premature babies being predictive of neurological performance (Guo et al. 2017; Tokariev et al. 2019). Further, prefrontal EEG oscillations are altered in patients affected by several psychiatric disorders (Senkowski and Gallinat 2015; Uhlhaas and Singer 2015), and post-mortem studies revealed that layer III prefrontal pyramidal neurons of patients affected by schizophrenia have reduced spine density (Kolluri et al. 2005). Thus, there is converging evidence sustaining the hypothesis that impaired early prefrontal PNOs are an early biomarker of deficient cognitive abilities.

3.4 Microglia as a mediator for altering the course of the disease

Having identified an early biomarker that predicts the impaired development of cognitive abilities, we sought out to test whether a pharmacological treatment that corrects these early deficits, equally rescues the impaired cognition accompanying it. To this aim, given the inflammatory component that characterizes GE mice, and

following the stream of evidence highlighting the relationship between inflammation and neurodevelopmental disorders (Estes and McAllister 2016; Smith et al. 2007), we investigated whether microglia cells, the immune resident cells of the brain (Li and Barres 2018), are involved in the pathophysiology of these disorders. Corroborating this hypothesis, we reported that microglia cells in GE mice were increased in number, had an altered morphology and engulfed a larger amount of synaptic terminals (Chini et al. 2020). Administration of minocycline, a non-invasive pharmacological treatment aimed at inhibiting the inflammatory response orchestrated by microglia cells (Kobayashi et al. 2013), partially rescued the microglial phenotype, and fully restored the altered $PYRs_{II/III}$ morphology and impaired PNOs (Chini et al. 2020). Ultimately, the pharmacological intervention resulted also in rescued PFC-dependent cognitive abilities. This shows not only that microglia cells are key players in the pathophysiology of this mouse model, but also extends the causal chain linking PNOs and cognition. It suggests that correcting the deficits of the early prefrontal oscillations is predictive of restored cognitive abilities, and that PNOs are a biomarker that is sensitive to changes in the disease course.

The role of microglia phagocytosis in the pathophysiology of neurodevelopmental disorders and cognitive deficits is supported by several recent studies. Overexpressing the C4 protein in the prefrontal cortex, a protein that is key to microglia pruning (Yilmaz et al. 2021), has been linked to reduced synaptic density, prefrontal circuit dysfunction and impaired cognition (Comer et al. 2020; Druart et al. 2020; Pinto et al. 2020; Kanmogne and Klein 2021; Yilmaz et al. 2021). In particular, the studies by Comer et al. 2020, and Druart et al. 2020, also focused on $PYRs_{II/III}$ and reported results that are entirely analogous to the ones in Chini et al. 2020. It is tempting to speculate that this might be the mechanisms behind the fact that the C4 genetic locus has been linked to the risk of developing schizophrenia in a genetic association study (Sekar et al. 2016). C4 is selectively upregulated in the prefrontal cortex of patients affected by schizophrenia (Rey et al. 2020). Moreover, induced pluripotent stem cell-derived microglia cells from patients affected from schizophrenia engulf synaptic terminals at a higher rate than controls, and this is partially explained by variants occurring on the C4 locus (Sellgren et al. 2019). Stressing the potential translation relevance of our approach, administration of minocycline, the same pharmacological treatment used to inhibit the microglia inflammatory response in Chini et al. 2020, reduces synapse engulfment of patient-derived microglia cells and the risk of psychotic disorders in adolescence (Sellgren et al. 2019). Of note, the effects of minocycline administration on the risk of developing psychotic disorders were not studied in a prospective manner, but rather in a retrospective fashion, taking advantage of the fact that minocycline is used in adolescents for the treatment of a common skin disease,

acne vulgaris (Sellgren et al. 2019). These results must therefore be interpreted with caution.
Taken together, these data suggest that microglia-mediated inflammation plays an important role in the pathophysiology of neuropsychiatric disorders. Converging evidence from mice and humans points in the direction of complement-mediated excessive microglia pruning of synaptic material as being upstream of the prefrontal network deficits that characterize these disorders and the corresponding mouse models. While further studies are needed, and prudence in translating rodent findings to human patients is warranted, treatments that aim at altering this process are yielding promising results in a preclinical context, and might potentially open new avenues for the prevention and course-correction of these disorders.

3.5 Concluding remarks

In this thesis, I present several new insights into the physiological and pathological network development of the murine prefrontal cortex. We confirm and expand previous literature pointing to the HP as an important input source that sustains prefrontal development, and report that altered HP-PFC communication is a trait that is shared across several mouse model of cognitive impairment. Importantly, pyramidal neurons of the superficial layers of the PFC emerge as fundamental players in the development of early network oscillations, as subtle disturbances to their development has profound consequences on the overall PFC physiology and, ultimately, PFC-depend cognitive abilities. This brings us closer to one of the aims of advocated by the RDoC: the identification of a biomarker that can be used to predict the course of a disease, and assess the potential efficacy of treatments (Wong and Josselyn 2016; Boksa 2013).

4 | General Summary

4.1 English

It has long been hypothesized that the pathophysiology of neurodevelopmental disorders begins long before the emergence of an appreciable symptomatology. In this regard, the prefrontal cortex is thought of being a major player, and disturbances to its development have been implicated in several of such disorders. However, evidence sustaining this proposition is still scarce, and there is a lack of mechanistic insights. A crucial repercussion of this shortcoming is the lack of progress in identifying early disease biomarkers and, consequently, in the development of early therapies that might help altering the course of these conditions. In this thesis, I addressed this knowledge gap by studying the physiological and pathological early development of the rodent prefrontal cortex, and the therefrom depending cognitive abilities.
While rodents clearly lack the finesse of human cognition, and the translation of rodent research on neurodevelopmental disorders to human patients is certainly not without perils, they also offer remarkable opportunities. Rodents are altricial species compared to humans, and are thus already accessible to investigations at a developmental stage that roughly corresponds to mid human gestation, a period of high vulnerability for neuropsychiatric disorders. Moreover, recent advances in genome manipulation and

viral vector targeting allow not only to causally and specifically investigate specific brain structures and networks, but also better modeling of the genetic landscape of these diseases.
Employing an array of different mouse models of mental disorders, we report that, as hypothesized, the prefrontal cortex exhibits functional disturbances already in the first days after birth, and that these deficits are predictive of impaired cognitive abilities. A reduced hippocampal drive to the prefrontal cortex is upstream of these manifestations. Particularly severely affected are layer II/III pyramidal neurons, that are characterized by a simplified dendritic arborization and reduced synaptic density. In turn, this results in impaired prefrontal network oscillations. By chronically optogenetic stimulation of this same neuronal population and of prefrontal oscillations, we show that prefrontal oscillations are homeostatically regulated, and that an overabundant level of activity is equally detrimental to the development of cognitive abilities. Taken together, this data supports the notion that early prefrontal oscillations might be an early biomarker tracking the pathophysiology of neurodevelopmental disorders. Conclusively, in a mouse model that is characterized by systemic inflammation during pregnancy, we show that microglia cells, the resident brain immune cells, are involved in the processes that ultimately result in cognitive deficits. They display an altered morphology and engulf an excessive amount of synaptic terminals. Inhibition of their inflammatory response fully rescues the deficits affecting prefrontal network oscillations and the cognitive symptomatology. While still preliminary, this body of work might help establishing new principles in the development of pharmaceutical tools that could alter the course of neurodevelopmental disorders.

4.2 German

Seit langem wird angenommen, dass die Pathophysiologie von neurologischen Entwicklungsstörungen lange vor dem Auftreten einer nennenswerten Symptomatik beginnt.

In diesem Kontext wird dem präfrontalen Kortex eine wichtige Rolle zugeschrieben und Störungen seiner Entwicklung wurden mit mehreren solcher Störungen in Verbindung gebracht. Allerdings ist die empirische Datenlage zur Unterstützung dieser Hypothese noch spärlich und es gibt einen Mangel an Erkenntnissen über die zugrundeliegenden Mechanismen. Als entscheidende Auswirkung dieses Mangels gibt es nur langsame Fortschritte in der Identifikation von frühen Krankheits-Biomarkern und damit auch in der Entwicklung von frühen Therapieansätzen, die den Krankheitsverlauf beeinflussen könnten. In dieser Thesis gehe ich diese Wissenslücke an, indem ich die physiologische und pathologische frühe Entwicklung des präfrontalen Kortex bei Nagern und davon abhängige kognitive Fähigkeiten untersuche.
Obwohl Nager offensichtlich nicht die Finesse menschlicher Kognition besitzen und die Übertragung von Forschung an Nagern zu neurologischen Entwicklungsstörungen auf menschliche Patienten nicht unproblematisch ist, bieten sie auch bemerkenswerte Möglichkeiten. Nagetiere werden im Vergleich zu Menschen in einem früheren Entwicklungsstadium geboren und sind damit bereits in einem Stadiums, das in etwa der Hälfte der menschlichen Gestation entspricht für Untersuchungen verfügbar. Darüber hinaus erlauben neue Fortschritte in der Genommanipulation und virales Vektor-Targeting es nicht nur, kausal und spezifisch bestimmte Hirnstrukturen und -netzwerke zu untersuchen, sondern auch die genetische Landschaft dieser Störungen besser zu modellieren.
Anhand einer Reihe verschiedener Mausmodelle für mentale Störungen berichten wir, dass, wie angenommen, der präfrontale Kortex bereits in den ersten Tagen nach der Geburt funktionale Störungen aufweist und dass diese Defizite eingeschränkte kognitive Fähigkeiten vorhersagen. Verminderter Input des Hippocampus in den präfrontalen Kortex liegt diesen Manifestationen zugrunde. Besonders stark betroffen sind Pyramidalneuronen aus der 2./3. kortikalen Schicht, die durch eine vereinfachte dendritische Arborisierung und verminderte synaptische Dichte charakteristisch sind. Dies wiederum führt zu beeinträchtigten Oszillationen im präfrontalen Netzwerk. Durch chronische optogenetische Stimulierungen ebendieser neuronalen Populationen und präfrontale Oszillationen zeigen wir, dass präfrontale Oszillationen homöostatisch reguliert sind und dass ein übermäßiges Level an Aktivität ebenso problematisch für die Entwicklung von kognitiven Fähigkeiten ist. Zusammengenommen unterstützen diese Daten die Annahme, dass frühe präfrontale Oszillationen ein früher Biomarker sein könnten, der die Pathophysiologie von neurologischen Entwicklungsstörungen nachzeichnet.
Abschließend zeigen wir in einem Mausmodell, das durch systemische Entzündung während der Schwangerschaft gekennzeichnet ist, dass Mikro-Gliazellen, die Immunzellen des Gehirns, in den Vorgängen, die schlussendlich zu kognitiven Defiziten führen,

involviert sind. Diese zeigen eine veränderte Morphologie und verschlingen eine exzessive Menge synaptischer Endigungen. Durch Hemmung ihrer Entzündungsantwort können die Defizite der Oszillationen des präfrontalen Netzwerks und die kognitive Symptomatik vollständig verhindert werden. Die hier berichtete Forschung ist noch vorläufig, aber sie könnte dazu beitragen neue Prinzipien in der der Entwicklung von pharmazeutischen Werkzeugen zu etablieren, die den Verlauf von neurologischen Entwicklungsstörungen beeinflussen.

5 | Bibliography

[1] E. Aarts et al. "A solution to dependency: using multilevel analysis to accommodate nested data". In: *Nature Neuroscience* 17.4 (Apr. 2014), pp. 491–496. ISSN: 1546-1726. DOI: 10.1038/nn.3648.

[2] J. B. Ackman, T. J. Burbridge, and M. C. Crair. "Retinal waves coordinate patterned activity throughout the developing visual system". In: *Nature* 490.7419 (Oct. 11, 2012). Edition: 2012/10/13, pp. 219–25. ISSN: 1476-4687 (Electronic) 0028-0836 (Linking). DOI: 10.1038/nature11529.

[3] J. B. Ackman, H. Zeng, and M. C. Crair. "Structured dynamics of neural activity across developing neocortex". In: *bioRxiv* (2014), p. 012237. DOI: 10.1101/012237.

[4] R. A. Adams et al. "Impaired theta phase coupling underlies frontotemporal dysconnectivity in schizophrenia". In: *Brain* 143.4 (Apr. 1, 2020), pp. 1261–1277. ISSN: 0006-8950. DOI: 10.1093/brain/awaa035.

[5] H. Adelsberger, O. Garaschuk, and A. Konnerth. "Cortical calcium waves in resting newborn mice". In: *Nature Neuroscience* 8.8 (Aug. 2005), pp. 988–990. ISSN: 1097-6256. DOI: 10.1038/nn1502.

[6] U. Agrawal, C. B. Berde, and L. Cornelissen. "Electroencephalographic features of discontinuous activity in anesthetized infants and children". In: *PLoS One* 14.10 (2019). Edition: 2019/10/04, e0223324. ISSN: 1932-6203 (Electronic) 1932-6203 (Linking). DOI: 10.1371/journal.pone.0223324.

[7] J. Ahlbeck et al. "Glutamatergic drive along the septotemporal axis of hippocampus boosts prelimbic oscillations in the neonatal mouse". In: *Elife* 7 (Apr. 10, 2018), e33158. ISSN: 2050-084x. DOI: 10.7554/eLife.33158.

[8] O. Akin et al. "Cell-type-Specific Patterned Stimulus-Independent Neuronal Activity in the Drosophila Visual System during Synapse Formation". In: *Neuron* 101.5 (Mar. 6, 2019), 894–904.e5. ISSN: 1097-4199. DOI: 10.1016/j.neuron.2019.01.008.

[9] M. T. Alkire, A. G. Hudetz, and G. Tononi. "Consciousness and anesthesia". In: *Science (New York, N.Y.)* 322.5903 (Nov. 7, 2008), pp. 876–880. ISSN: 1095-9203. DOI: 10.1126/science.1149213.

[10] C. Allene et al. "Sequential Generation of Two Distinct Synapse-Driven Network Patterns in Developing Neocortex". In: *Journal of Neuroscience* 28.48 (Nov. 26, 2008), pp. 12851–12863. ISSN: 0270-6474. DOI: 10.1523/Jneurosci.3733-08.2008.

[11] D. G. Amaral and M. P. Witter. "The three-dimensional organization of the hippocampal formation: a review of anatomical data". In: *Neuroscience* 31.3 (1989), pp. 571–591. ISSN: 0306-4522. DOI: 10.1016/0306-4522(89)90424-7.

[12] D. Amaral and P. Lavenex. *Hippocampal Neuroanatomy*. Pages: 37-114 Publication Title: The Hippocampus Book Section: The Hippocampus Book. Oxford University Press, 2006. ISBN: 978-0-19-986413-3.

[13] P. G. Anastasiades et al. "GABAergic interneurons form transient layer-specific circuits in early postnatal neocortex". In: *Nature Communications* 7 (Feb. 2016). ISSN: 2041-1723. DOI: 10.1038/ncomms10584.

[14] K. L. Anderson et al. "Theta oscillations mediate interaction between prefrontal cortex and medial temporal lobe in human memory". In: *Cerebral Cortex (New York, N.Y.: 1991)* 20.7 (July 2010), pp. 1604–1612. ISSN: 1460-2199. DOI: 10.1093/cercor/bhp223.

[15] M. André et al. "Electroencephalography in premature and full-term infants. Developmental features and glossary". In: *Neurophysiologie Clinique = Clinical Neurophysiology* 40.2 (May 2010), pp. 59–124. ISSN: 1769-7131. DOI: 10.1016/j.neucli.2010.02.002.

[16] M. W. Antoine et al. "Increased Excitation-Inhibition Ratio Stabilizes Synapse and Circuit Excitability in Four Autism Mouse Models". In: *Neuron* 101.4 (Feb. 20, 2019), 648–661.e4. ISSN: 1097-4199. DOI: 10.1016/j.neuron.2018.12.026.

[17] N. Anton-Bolanos et al. "Prenatal activity from thalamic neurons governs the emergence of functional cortical maps in mice". In: *Science* 364.6444 (June 7, 2019), pp. 987–990. ISSN: 0036-8075. DOI: 10.1126/science.aav7617.

[18] P. A. Arguello and J. A. Gogos. "Genetic and cognitive windows into circuit mechanisms of psychiatric disease". In: *Trends in Neurosciences* 35.1 (Jan. 2012), pp. 3–13. ISSN: 1878-108X. DOI: 10.1016/j.tins.2011.11.007.

[19] L. Avitan et al. "Spontaneous Activity in the Zebrafish Tectum Reorganizes over Development and Is Influenced by Visual Experience". In: *Current biology: CB* 27.16 (Aug. 21, 2017), 2407–2419.e4. ISSN: 1879-0445. DOI: 10.1016/j.cub.2017.06.056.

[20] N. Axmacher et al. "Interactions between Medial Temporal Lobe, Prefrontal Cortex, and Inferior Temporal Regions during Visual Working Memory: A Combined Intracranial EEG and Functional Magnetic Resonance Imaging Study". In: *Journal of Neuroscience* 28.29 (July 16, 2008). Publisher: Society for Neuroscience Section: Articles, pp. 7304–7312. ISSN: 0270-6474, 1529-2401. DOI: 10.1523/JNEUROSCI.1778-08.2008.

[21] T. A. Babola et al. "Homeostatic Control of Spontaneous Activity in the Developing Auditory System". In: *Neuron* 99.3 (Aug. 8, 2018). Edition: 2018/08/06, pp. 511–524. ISSN: 1097-4199 (Electronic) 0896-6273 (Linking). DOI: 10.1016/j.neuron.2018.07.004.

[22] A. R. Backus et al. "Hippocampal-Prefrontal Theta Oscillations Support Memory Integration". In: *Current biology: CB* 26.4 (Feb. 22, 2016), pp. 450–457. ISSN: 1879-0445. DOI: 10.1016/j.cub.2015.12.048.

[23] F. Bähner et al. "Hippocampal–Dorsolateral Prefrontal Coupling as a Species-Conserved Cognitive Mechanism: A Human Translational Imaging Study". In: *Neuropsychopharmacology* 40.7 (June 2015). Number: 7 Publisher: Nature Publishing Group, pp. 1674–1681. ISSN: 1740-634X. DOI: 10.1038/npp.2015.13.

[24] H. Barbas and G. J. Blatt. "Topographically specific hippocampal projections target functionally distinct prefrontal areas in the rhesus monkey". In: *Hippocampus* 5.6 (1995), pp. 511–533. ISSN: 1050-9631. DOI: 10.1002/hipo.450050604.

[25] D. Bates et al. "Fitting Linear Mixed-Effects Models using lme4". In: *arXiv:1406.5823 [stat]* (June 23, 2014). arXiv: 1406.5823.

[26] R. Batista-Brito et al. "Developmental Dysfunction of VIP Interneurons Impairs Cortical Circuits". In: *Neuron* 95.4 (Aug. 16, 2017), pp. 884–895. ISSN: 0896-6273. DOI: 10.1016/j.neuron.2017.07.034.

[27] Y. Ben-Ari. "Excitatory actions of gaba during development: the nature of the nurture". In: *Nature Reviews. Neuroscience* 3.9 (Sept. 2002), pp. 728–739. ISSN: 1471-003X. DOI: 10.1038/nrn920.

[28] K. Benchenane et al. "Coherent theta oscillations and reorganization of spike timing in the hippocampal- prefrontal network upon learning". In: *Neuron* 66.6 (June 24, 2010), pp. 921–936. ISSN: 1097-4199. DOI: 10.1016/j.neuron.2010.05.013.

[29] A. Bertero et al. "Autism-associated 16p11.2 microdeletion impairs prefrontal functional connectivity in mouse and human". In: *Brain: A Journal of Neurology* 141.7 (July 1, 2018), pp. 2055–2065. ISSN: 1460-2156. DOI: 10.1093/brain/awy111.

[30] F. Birey et al. "Assembly of functionally integrated human forebrain spheroids". In: *Nature* 545.7652 (May 4, 2017), pp. 54–59. ISSN: 1476-4687. DOI: 10.1038/nature22330.

[31] S. H. Bitzenhofer et al. "Layer-specific optogenetic activation of pyramidal neurons causes beta-gamma entrainment of neonatal networks". In: *Nature Communications* 8 (Feb. 20, 2017). ISSN: 2041-1723. DOI: 10.1038/ncomms14563.

[32] S. H. Bitzenhofer et al. "Oscillatory Activity in Developing Prefrontal Networks Results from Theta-Gamma-Modulated Synaptic Inputs". In: *Cell Reports* 11.3 (Apr. 21, 2015), pp. 486–497. ISSN: 2211-1247. DOI: 10.1016/j.celrep.2015.03.031.

[33] S. H. Bitzenhofer, J. A. Pöpplau, and I. Hanganu-Opatz. "Gamma activity accelerates during prefrontal development". In: *eLife* 9 (Nov. 18, 2020). Ed. by M. Vinck et al. Publisher: eLife Sciences Publications, Ltd, e56795. ISSN: 2050-084X. DOI: 10.7554/eLife.56795.

[34] S. H. Bitzenhofer et al. "Transient developmental increase of prefrontal activity alters network maturation and causes cognitive dysfunction in adult mice". In: *bioRxiv* (2020), p. 558957. DOI: 10.1101/558957.

[35] A. G. Blankenship and M. B. Feller. "Mechanisms underlying spontaneous patterned activity in developing neural circuits". In: *Nature Reviews. Neuroscience* 11.1 (Jan. 2010), pp. 18–29. ISSN: 1471-0048. DOI: 10.1038/nrn2759.

[36] P. Boksa. "A way forward for research on biomarkers for psychiatric disorders". In: *Journal of psychiatry & neuroscience: JPN* 38.2 (Mar. 2013), pp. 75–77. ISSN: 1488-2434. DOI: 10.1503/jpn.130018.

[37] P. Bregestovski and C. Bernard. "Excitatory GABA: How a Correct Observation May Turn Out to be an Experimental Artifact". In: *Frontiers in Pharmacology* 3 (2012), p. 65. ISSN: 1663-9812. DOI: 10.3389/fphar.2012.00065.

[38] M. D. Brockmann et al. "Coupled Oscillations Mediate Directed Interactions between Prefrontal Cortex and Hippocampus of the Neonatal Rat". In: *Neuron* 71.2 (July 28, 2011), pp. 332–347. ISSN: 0896-6273. DOI: 10.1016/j.neuron.2011.05.041.

[39] D. L. Buhl and G. Buzsaki. "Developmental emergence of hippocampal fast-field "ripple" oscillations in the behaving rat pups". In: *Neuroscience* 134.4 (2005), pp. 1423–1430. ISSN: 0306-4522. DOI: 10.1016/j.neuroscience.2005.05.030.

[40] S. J. B. Butt et al. "The temporal and spatial origins of cortical interneurons predict their physiological subtype". In: *Neuron* 48.4 (Nov. 23, 2005), pp. 591–604. ISSN: 0896-6273. DOI: 10.1016/j.neuron.2005.09.034.

[41] G. Buzsáki and E. I. Moser. "Memory, navigation and theta rhythm in the hippocampal-entorhinal system". In: *Nature Neuroscience* 16.2 (Feb. 2013), pp. 130–138. ISSN: 1546-1726. DOI: 10.1038/nn.3304.

[42] J. A. Cardin et al. "Driving fast-spiking cells induces gamma rhythm and controls sensory responses". In: *Nature* 459.7247 (June 4, 2009), pp. 663–667. ISSN: 1476-4687. DOI: 10.1038/nature08002.

[43] M. Carlen. "What constitutes the prefrontal cortex?" In: *Science* 358.6362 (Oct. 27, 2017). Edition: 2017/10/28, pp. 478–482. ISSN: 1095-9203 (Electronic) 0036-8075 (Linking). DOI: 10.1126/science.aan8868.

[44] P.-s. Chang, S. M. Walker, and M. Fitzgerald. "Differential Suppression of Spontaneous and Noxious-evoked Somatosensory Cortical Activity by Isoflurane in the Neonatal Rat". In: *Anesthesiology* 124.4 (Apr. 2016), pp. 885–898. ISSN: 1528-1175. DOI: 10.1097/ALN.0000000000001017.

[45] A. Che et al. "Layer I Interneurons Sharpen Sensory Maps during Neonatal Development". In: *Neuron* 99.1 (July 11, 2018), pp. 98–116. ISSN: 0896-6273. DOI: 10.1016/j.neuron.2018.06.002.

[46] G. Chen et al. "Distinct Inhibitory Circuits Orchestrate Cortical beta and gamma Band Oscillations". In: *Neuron* 96.6 (Dec. 20, 2017), 1403–1418.e6. ISSN: 1097-4199. DOI: 10.1016/j.neuron.2017.11.033.

[47] M. Chini et al. "Neural Correlates of Anesthesia in Newborn Mice and Humans". In: *Front Neural Circuits* 13 (2019). Edition: 2019/06/14, p. 38. ISSN: 1662-5110 (Electronic) 1662-5110 (Linking). DOI: 10.3389/fncir.2019.00038.

[48] M. Chini et al. "Resolving and Rescuing Developmental Miswiring in a Mouse Model of Cognitive Impairment". In: *Neuron* 105.1 (Jan. 8, 2020). Edition: 2019/11/18, pp. 60–74. ISSN: 1097-4199 (Electronic) 0896-6273 (Linking). DOI: 10.1016/j.neuron.2019.09.042.

[49] M. Chini and I. L. Hanganu-Opatz. "Prefrontal Cortex Development in Health and Disease: Lessons from Rodents and Humans". In: *Trends in Neurosciences* (Nov. 24, 2020). ISSN: 1878-108X. DOI: 10.1016/j.tins.2020.10.017.

[50] C. Cirelli and G. Tononi. "Cortical development, electroencephalogram rhythms, and the sleep/wake cycle". In: *Biological Psychiatry* 77.12 (June 15, 2015), pp. 1071–1078. ISSN: 1873-2402. DOI: 10.1016/j.biopsych.2014.12.017.

[51] M. Colonnese and R. Khazipov. "Spontaneous activity in developing sensory circuits: Implications for resting state fMRI". In: *Neuroimage* 62.4 (Oct. 1, 2012). Edition: 2012/03/06, pp. 2212–21. ISSN: 1095-9572 (Electronic) 1053-8119 (Linking). DOI: 10.1016/j.neuroimage.2012.02.046.

[52] M. T. Colonnese et al. "A Conserved Switch in Sensory Processing Prepares Developing Neocortex for Vision". In: *Neuron* 67.3 (Aug. 12, 2010), pp. 480–498. ISSN: 0896-6273. DOI: 10.1016/j.neuron.2010.07.015.

[53] A. L. Comer et al. "Increased expression of schizophrenia-associated gene C4 leads to hypoconnectivity of prefrontal cortex and reduced social interaction". In: *PLoS Biology* 18.1 (Jan. 14, 2020). ISSN: 1544-9173. DOI: 10.1371/journal.pbio.3000604.

[54] L. Cornelissen et al. "Age-dependent electroencephalogram (EEG) patterns during sevoflurane general anesthesia in infants". In: *Elife* 4 (June 23, 2015). ISSN: 2050-084x. DOI: 10.7554/eLife.06513.

[55] L. Cornelissen et al. "Clinical signs and electroencephalographic patterns of emergence from sevoflurane anaesthesia in children: An observational study". In: *European Journal of Anaesthesiology* 35.1 (Jan. 2018), pp. 49–59. ISSN: 0265-0215. DOI: 10.1097/Eja.0000000000000739.

[56] V. Crépel et al. "A parturition-associated nonsynaptic coherent activity pattern in the developing hippocampus". In: *Neuron* 54.1 (Apr. 5, 2007), pp. 105–120. ISSN: 0896-6273. DOI: 10.1016/j.neuron.2007.03.007.

[57] C. S. Cutts and S. J. Eglen. "Detecting pairwise correlations in spike trains: an objective comparison of methods and application to the study of retinal waves". In: *The Journal of Neuroscience: The Official Journal of the Society for Neuroscience* 34.43 (Oct. 22, 2014), pp. 14288–14303. ISSN: 1529-2401. DOI: 10.1523/JNEUROSCI.2767-14.2014.

[58] S. De Rubeis et al. "Synaptic, transcriptional and chromatin genes disrupted in autism". In: *Nature* 515.7526 (Nov. 13, 2014), 209–U119. ISSN: 0028-0836. DOI: 10.1038/nature13772.

[59] A. Del Dosso et al. "Upgrading the Physiological Relevance of Human Brain Organoids". In: *Neuron* 107.6 (Sept. 23, 2020), pp. 1014–1028. ISSN: 1097-4199. DOI: 10.1016/j.neuron.2020.08.029.

[60] C. Del Rio-Bermudez et al. "Active Sleep Promotes Coherent Oscillatory Activity in the Cortico-Hippocampal System of Infant Rats". In: *Cereb Cortex* 30.4 (Apr. 14, 2020). Edition: 2020/01/11, pp. 2070–2082. ISSN: 1460-2199 (Electronic) 1047-3211 (Linking). DOI: 10.1093/cercor/bhz223.

[61] C. Del Rio-Bermudez et al. "Theta Oscillations during Active Sleep Synchronize the Developing Rubro-Hippocampal Sensorimotor Network". In: *Current Biology* 27.10 (May 22, 2017), pp. 1413–1424. ISSN: 0960-9822. DOI: 10.1016/j.cub.2017.03.077.

[62] J. C. Dooley et al. "Self-Generated Whisker Movements Drive State-Dependent Sensory Input to Developing Barrel Cortex". In: *Current Biology* 30.12 (2020), 2404–2410.e4. ISSN: 0960-9822. DOI: 10.1016/j.cub.2020.04.045.

[63] M. Druart et al. "Elevated expression of complement C4 in the mouse prefrontal cortex causes schizophrenia-associated phenotypes". In: *bioRxiv* (Nov. 27, 2020). Publisher: Cold Spring Harbor Laboratory Section: New Results, p. 2020.11.27.400960. DOI: 10.1101/2020.11.27.400960.

[64] Z. R. S. Duan et al. "GABAergic Restriction of Network Dynamics Regulates Interneuron Survival in the Developing Cortex". In: *Neuron* 105.1 (Jan. 8, 2020), pp. 75–92. ISSN: 0896-6273. DOI: 10.1016/j.neuron.2019.10.008.

[65] E. Dupont et al. “Rapid developmental switch in the mechanisms driving early cortical columnar networks”. In: *Nature* 439.7072 (Jan. 5, 2006), pp. 79–83. ISSN: 0028-0836. DOI: 10.1038/nature04264.

[66] A. V. Egorov and A. Draguhn. “Development of coherent neuronal activity patterns in mammalian cortical networks: common principles and local hetereogeneity”. In: *Mechanisms of Development* 130.6 (Aug. 2013), pp. 412–423. ISSN: 1872-6356. DOI: 10.1016/j.mod.2012.09.006.

[67] H. Eichenbaum. “Prefrontal-hippocampal interactions in episodic memory”. In: *Nature Reviews. Neuroscience* 18.9 (Sept. 2017), pp. 547–558. ISSN: 1471-0048. DOI: 10.1038/nrn.2017.74.

[68] J. Ellegood et al. “Neuroanatomical phenotypes in a mouse model of the 22q11.2 microdeletion”. In: *Molecular Psychiatry* 19.1 (Jan. 2014), pp. 99–107. ISSN: 1476-5578. DOI: 10.1038/mp.2013.112.

[69] C. T. Ellis et al. “Re-imagining fMRI for awake behaving infants”. In: *Nature Communications* 11.1 (Sept. 9, 2020), p. 4523. ISSN: 2041-1723. DOI: 10.1038/s41467-020-18286-y.

[70] M. L. Estes and A. K. McAllister. “Maternal immune activation: Implications for neuropsychiatric disorders”. In: *Science (New York, N.Y.)* 353.6301 (Aug. 19, 2016), pp. 772–777. ISSN: 1095-9203. DOI: 10.1126/science.aag3194.

[71] K. A. Feigenson, A. W. Kusnecov, and S. M. Silverstein. “Inflammation and the Two-Hit Hypothesis of Schizophrenia”. In: *Neuroscience and biobehavioral reviews* 38 (Jan. 2014), pp. 72–93. ISSN: 0149-7634. DOI: 10.1016/j.neubiorev.2013.11.006.

[72] F. Ferino, A. M. Thierry, and J. Glowinski. “Anatomical and electrophysiological evidence for a direct projection from ammon’s horn to the medial prefrontal cortex in the rat”. In: *Experimental Brain Research* 65.2 (Jan. 1, 1987), pp. 421–426. ISSN: 1432-1106. DOI: 10.1007/BF00236315.

[73] T. A. Ferreira et al. “Neuronal morphometry directly from bitmap images”. In: *Nature Methods* 11.10 (Oct. 2014), pp. 982–984. ISSN: 1548-7105. DOI: 10.1038/nmeth.3125.

[74] M. V. Fuccillo, P. E. Rothwell, and R. C. Malenka. “From Synapses to Behavior: What Rodent Models Can Tell Us About Neuropsychiatric Disease”. In: *Biological Psychiatry* 79.1 (Jan. 1, 2016), pp. 4–6. ISSN: 1873-2402. DOI: 10.1016/j.biopsych.2015.02.009.

[75] J. M. Fuster. *The prefrontal cortex*. Fifth edition. Amsterdam ; Boston: Elsevier/AP, Academic Press is an imprint of Elsevier, 2015. 444 pp. ISBN: 978-0-12-407815-4.

[76] O. Garaschuk et al. "Large-scale oscillatory calcium waves in the immature cortex". In: *Nature Neuroscience* 3.5 (May 2000), pp. 452–459. ISSN: 1097-6256.

[77] N. V. D. Garcia, T. Karayannis, and G. Fishell. "Neuronal activity is required for the development of specific cortical interneuron subtypes". In: *Nature* 472.7343 (Apr. 21, 2011), 351–U116. ISSN: 0028-0836. DOI: 10.1038/nature09865.

[78] F. Ghezzi et al. "Non-canonical role for Lpar1-EGFP subplate neurons in early postnatal somatosensory cortex". In: *bioRxiv* (May 13, 2020). Publisher: Cold Spring Harbor Laboratory Section: New Results, p. 2020.05.12.088450. DOI: 10.1101/2020.05.12.088450.

[79] S. L. Giandomenico et al. "Cerebral organoids at the air-liquid interface generate diverse nerve tracts with functional output". In: *Nature Neuroscience* 22.4 (Apr. 2019), pp. 669–679. ISSN: 1546-1726. DOI: 10.1038/s41593-019-0350-2.

[80] B. P. Godsil et al. "The hippocampal-prefrontal pathway: the weak link in psychiatric disorders?" In: *European Neuropsychopharmacology: The Journal of the European College of Neuropsychopharmacology* 23.10 (Oct. 2013), pp. 1165–1181. ISSN: 1873-7862. DOI: 10.1016/j.euroneuro.2012.10.018.

[81] P. Golshani et al. "Internally Mediated Developmental Desynchronization of Neocortical Network Activity". In: *Journal of Neuroscience* 29.35 (Sept. 2, 2009), pp. 10890–10899. ISSN: 0270-6474. DOI: 10.1523/Jneurosci.2012-09.2009.

[82] S. Gretenkord et al. "Coordinated electrical activity in the olfactory bulb gates the oscillatory entrainment of entorhinal networks in neonatal mice". In: *PLoS biology* 17.1 (Jan. 2019), e2006994. ISSN: 1545-7885. DOI: 10.1371/journal.pbio.2006994.

[83] W. Q. Guan et al. "Eye opening differentially modulates inhibitory synaptic transmission in the developing visual cortex". In: *Elife* 6 (Dec. 11, 2017), e32337. ISSN: 2050-084x. DOI: 10.7445/eLife.32337.

[84] T. Guo et al. "Quantitative assessment of white matter injury in preterm neonates: Association with outcomes". In: *Neurology* 88.7 (Feb. 14, 2017). Edition: 2017/01/20, pp. 614–622. ISSN: 1526-632X (Electronic) 0028-3878 (Linking). DOI: 10.1212/WNL.0000000000003606.

[85] I. L. Hanganu, Y. Ben-Ari, and R. Khazipov. "Retinal waves trigger spindle bursts in the neonatal rat visual cortex". In: *Journal of Neuroscience* 26.25 (June 21, 2006), pp. 6728–6736. ISSN: 0270-6474. DOI: 10.1523/Jneurosci.0752-06.2006.

[86] I. L. Hanganu, W. Kilb, and H. J. Luhmann. "Functional synaptic projections onto subplate neurons in neonatal rat somatosensory cortex". In: *Journal of Neuroscience* 22.16 (Aug. 15, 2002), pp. 7165–7176. ISSN: 0270-6474.

[87] I. L. Hanganu and H. J. Luhmann. "Functional nicotinic acetylcholine receptors on subplate neurons in neonatal rat somatosensory cortex". In: *Journal of Neurophysiology* 92.1 (July 2004), pp. 189–198. ISSN: 0022-3077. DOI: 10.1152/jn.00010.2004.

[88] I. L. Hanganu-Opatz et al. "The Logic of Developing Neocortical Circuits in Health and Disease". In: *The Journal of Neuroscience: The Official Journal of the Society for Neuroscience* (Jan. 8, 2021). ISSN: 1529-2401. DOI: 10.1523/JNEUROSCI.1655-20.2020.

[89] H. Hartung et al. "From Shortage to Surge: A Developmental Switch in Hippocampal-Prefrontal Coupling in a Gene-Environment Model of Neuropsychiatric Disorders". In: *Cerebral Cortex* 26.11 (Nov. 2016), pp. 4265–4281. ISSN: 1047-3211. DOI: 10.1093/cercor/bhw274.

[90] H. Hartung et al. "Thalamic and Entorhinal Network Activity Differently Modulates the Functional Development of Prefrontal-Hippocampal Interactions". In: *J Neurosci* 36.13 (Mar. 30, 2016). Edition: 2016/04/01, pp. 3676–90. ISSN: 1529-2401 (Electronic) 0270-6474 (Linking). DOI: 10.1523/JNEUROSCI.3232-15.2016.

[91] N. A. Herweg et al. "Theta-Alpha Oscillations Bind the Hippocampus, Prefrontal Cortex, and Striatum during Recollection: Evidence from Simultaneous EEG–fMRI". In: *Journal of Neuroscience* 36.12 (Mar. 23, 2016). Publisher: Society for Neuroscience Section: Articles, pp. 3579–3587. ISSN: 0270-6474, 1529-2401. DOI: 10.1523/JNEUROSCI.3629-15.2016.

[92] S. van Heukelum et al. "Where is Cingulate Cortex? A Cross-Species View". In: *Trends in Neurosciences* 43.5 (May 2020), pp. 285–299. ISSN: 0166-2236. DOI: 10.1016/j.tins.2020.03.007.

[93] S. K. Hill et al. "Effect of second-generation antipsychotics on cognition: current issues and future challenges". In: *Expert Review of Neurotherapeutics* 10.1 (Jan. 2010), pp. 43–57. ISSN: 1744-8360. DOI: 10.1586/ern.09.143.

[94] S. E. Hyman. "Can neuroscience be integrated into the DSM-V?" In: *Nature Reviews. Neuroscience* 8.9 (Sept. 2007), pp. 725–732. ISSN: 1471-003X. DOI: 10.1038/nrn2218.

[95] T. Insel et al. "Research domain criteria (RDoC): toward a new classification framework for research on mental disorders". In: *The American Journal of Psychiatry* 167.7 (July 2010), pp. 748–751. ISSN: 1535-7228. DOI: 10.1176/appi.ajp.2010.09091379.

[96] C. International Schizophrenia et al. "Common polygenic variation contributes to risk of schizophrenia and bipolar disorder". In: *Nature* 460.7256 (Aug. 6, 2009). Edition: 2009/07/03, pp. 748–52. ISSN: 1476-4687 (Electronic) 0028-0836 (Linking). DOI: 10.1038/nature08185.

[97] L. Izhikevich et al. "Measuring the average power of neural oscillations". In: *bioRxiv* (Oct. 22, 2018). Publisher: Cold Spring Harbor Laboratory Section: New Results, p. 441626. DOI: 10.1101/441626.

[98] P. C. Janiesch et al. "Cholinergic control in developing prefrontal-hippocampal networks". In: *The Journal of Neuroscience: The Official Journal of the Society for Neuroscience* 31.49 (Dec. 7, 2011), pp. 17955–17970. ISSN: 1529-2401. DOI: 10.1523/JNEUROSCI.2644-11.2011.

[99] T. M. Jay and M. P. Witter. "Distribution of hippocampal CA1 and subicular efferents in the prefrontal cortex of the rat studied by means of anterograde transport of Phaseolus vulgaris-leucoagglutinin". In: *The Journal of Comparative Neurology* 313.4 (Nov. 22, 1991), pp. 574–586. ISSN: 0021-9967. DOI: 10.1002/cne.903130404.

[100] X. Jin et al. "In vivo Perturb-Seq reveals neuronal and glial abnormalities associated with autism risk genes". In: *Science (New York, N.Y.)* 370.6520 (Nov. 27, 2020). ISSN: 1095-9203. DOI: 10.1126/science.aaz6063.

[101] M. Kanmogne and R. S. Klein. "Neuroprotective versus Neuroinflammatory Roles of Complement: From Development to Disease". In: *Trends in Neurosciences* 44.2 (Feb. 2021), pp. 97–109. ISSN: 1878-108X. DOI: 10.1016/j.tins.2020.10.003.

[102] K. A. E. Karlsson et al. "On the co-occurrence of startles and hippocampal sharp waves in newborn rats". In: *Hippocampus* 16.11 (2006), pp. 959–965. ISSN: 1050-9631. DOI: 10.1002/hipo.20224.

[103] T. Kaur and K. S. Cadenhead. "Treatment Implications of the Schizophrenia Prodrome". In: *Current topics in behavioral neurosciences* 4 (2010), pp. 97–121. ISSN: 1866-3370.

[104] J. F. Keeler and T. W. Robbins. "Translating cognition from animals to humans". In: *Biochemical Pharmacology* 81.12 (June 15, 2011), pp. 1356–1366. ISSN: 1873-2968. DOI: 10.1016/j.bcp.2010.12.028.

[105] T. A. Khan et al. "Neuronal defects in a human cellular model of 22q11.2 deletion syndrome". In: *Nature Medicine* 26.12 (Dec. 2020), pp. 1888–1898. ISSN: 1546-170X. DOI: 10.1038/s41591-020-1043-9.

[106] R. Khazipov et al. "Early motor activity drives spindle bursts in the developing somatosensory cortex". In: *Nature* 432.7018 (Dec. 9, 2004), pp. 758–761. ISSN: 0028-0836. DOI: 10.1038/nature03132.

[107] H. Kim et al. "Pluripotent Stem Cell-Derived Cerebral Organoids Reveal Human Oligodendrogenesis with Dorsal and Ventral Origins". In: *Stem Cell Reports* 12.5 (May 14, 2019), pp. 890–905. ISSN: 2213-6711. DOI: 10.1016/j.stemcr.2019.04.011.

[108] K. Kirmse et al. "GABA depolarizes immature neurons and inhibits network activity in the neonatal neocortex in vivo". In: *Nature Communications* 6 (July 16, 2015), p. 7750. ISSN: 2041-1723. DOI: 10.1038/ncomms8750.

[109] J. Klaus et al. "Altered neuronal migratory trajectories in human cerebral organoids derived from individuals with neuronal heterotopia". In: *Nature Medicine* 25.4 (Apr. 2019), pp. 561–568. ISSN: 1546-170X. DOI: 10.1038/s41591-019-0371-0.

[110] J. G. Klinzing, N. Niethard, and J. Born. "Mechanisms of systems memory consolidation during sleep". In: *Nature Neuroscience* 22.10 (Oct. 2019), pp. 1598–1610. ISSN: 1546-1726. DOI: 10.1038/s41593-019-0467-3.

[111] K. Kobayashi et al. "Minocycline selectively inhibits M1 polarization of microglia". In: *Cell Death & Disease* 4 (Mar. 7, 2013), e525. ISSN: 2041-4889. DOI: 10.1038/cddis.2013.54.

[112] N. Kolluri et al. "Lamina-specific reductions in dendritic spine density in the prefrontal cortex of subjects with schizophrenia". In: *American Journal of Psychiatry* 162.6 (June 2005), pp. 1200–1202. ISSN: 0002-953x. DOI: 10.1176/appi.ajp.162.6.1200.

[113] I. Kostovic and P. Rakic. "Developmental History of the Transient Subplate Zone in the Visual and Somatosensory Cortex of the Macaque Monkey and Human Brain". In: *Journal of Comparative Neurology* 297.3 (July 15, 1990), pp. 441–470. ISSN: 0021-9967. DOI: 10.1002/cne.902970309.

[114] P. Krakowiak et al. "Maternal metabolic conditions and risk for autism and other neurodevelopmental disorders". In: *Pediatrics* 129.5 (May 2012), e1121–1128. ISSN: 1098-4275. DOI: 10.1542/peds.2011-2583.

[115] D. J. Kupfer and D. A. Regier. "Neuroscience, clinical evidence, and the future of psychiatric classification in DSM-5". In: *The American Journal of Psychiatry* 168.7 (July 2011), pp. 672–674. ISSN: 1535-7228. DOI: 10.1176/appi.ajp.2011.11020219.

[116] A. Kuznetsova, P. B. Brockhoff, and R. H. B. Christensen. "lmerTest Package: Tests in Linear Mixed Effects Models". In: *Journal of Statistical Software* 82.1 (Dec. 6, 2017). Number: 1, pp. 1–26. ISSN: 1548-7660. DOI: 10.18637/jss.v082.i13.

[117] A. C. Lahti et al. "Subanesthetic doses of ketamine stimulate psychosis in schizophrenia". In: *Neuropsychopharmacology: Official Publication of the American College of Neuropsychopharmacology* 13.1 (Aug. 1995), pp. 9–19. ISSN: 0893-133X. DOI: 10.1016/0893-133X(94)00131-I.

[118] M. A. Lancaster et al. "Cerebral organoids model human brain development and microcephaly". In: *Nature* 501.7467 (Sept. 19, 2013), pp. 373–379. ISSN: 1476-4687. DOI: 10.1038/nature12517.

[119] M. Laubach et al. "What, If Anything, Is Rodent Prefrontal Cortex?" In: *eNeuro* 5.5 (Sept. 1, 2018). Publisher: Society for Neuroscience Section: Review. ISSN: 2373-2822. DOI: 10.1523/ENEURO.0315-18.2018.

[120] X. Leinekugel et al. "Correlated bursts of activity in the neonatal hippocampus in vivo". In: *Science* 296.5575 (June 14, 2002), pp. 2049–2052. ISSN: 0036-8075. DOI: 10.1126/science.1071111.

[121] R. V. Lenth et al. *emmeans: Estimated Marginal Means, aka Least-Squares Means*. Version 1.5.3. Dec. 9, 2020.

[122] Q. Li and B. A. Barres. "Microglia and macrophages in brain homeostasis and disease". In: *Nature Reviews. Immunology* 18.4 (Apr. 2018), pp. 225–242. ISSN: 1474-1741. DOI: 10.1038/nri.2017.125.

[123] R. S. Mackin et al. "The Effect of Cognitive Impairment on Mental Healthcare Costs for Individuals With Severe Psychiatric Illness". In: *The American Journal of Geriatric Psychiatry* 19.2 (Feb. 1, 2011), pp. 176–184. ISSN: 1064-7481. DOI: 10.1097/JGP.0b013e3181e56cfa.

[124] E. E. Manning. "There Is Much to Be Learned From Animal Models of Obsessive-Compulsive Disorder". In: *Biological Psychiatry* 79.1 (Jan. 1, 2016), e1–3. ISSN: 1873-2402. DOI: 10.1016/j.biopsych.2015.10.010.

[125] A. Marques-Smith et al. "A Transient Translaminar GABAergic Interneuron Circuit Connects Thalamocortical Recipient Layers in Neonatal Somatosensory Cortex". In: *Neuron* 89.3 (Feb. 3, 2016), pp. 536–549. ISSN: 0896-6273. DOI: 10.1016/j.neuron.2016.01.015.

[126] W. E. Medendorp et al. "Selective Postnatal Excitation of Neocortical Pyramidal Neurons Results in Distinctive Behavioral and Circuit Deficits in Adulthood". In: *bioRxiv* (2020), p. 2020.01.18.911347. DOI: 10.1101/2020.01.18.911347.

[127] U. Meyer, B. K. Yee, and J. Feldon. "The neurodevelopmental impact of prenatal infections at different times of pregnancy: the earlier the worse?" In: *The Neuroscientist: A Review Journal Bringing Neurobiology, Neurology and Psychiatry* 13.3 (June 2007), pp. 241–256. ISSN: 1073-8584. DOI: 10.1177/1073858406296401.

[128] M. R. Milad et al. "Recall of Fear Extinction in Humans Activates the Ventromedial Prefrontal Cortex and Hippocampus in Concert". In: *Biological Psychiatry*. Neurocircuitry and Neuroplasticity Abnormalities in Mood and Anxiety Disorders 62.5 (Sept. 1, 2007), pp. 446–454. ISSN: 0006-3223. DOI: 10.1016/j.biopsych.2006.10.011.

[129] M. J. Millan et al. "Altering the course of schizophrenia: progress and perspectives". In: *Nature Reviews. Drug Discovery* 15.7 (July 2016), pp. 485–515. ISSN: 1474-1784. DOI: 10.1038/nrd.2016.28.

[130] M. J. Millan et al. "Cognitive dysfunction in psychiatric disorders: characteristics, causes and the quest for improved therapy". In: *Nature Reviews Drug Discovery* 11.2 (Feb. 2012). Number: 2 Publisher: Nature Publishing Group, pp. 141–168. ISSN: 1474-1784. DOI: 10.1038/nrd3628.

[131] M. Minlebaev et al. "Early Gamma Oscillations Synchronize Developing Thalamus and Cortex". In: *Science* 334.6053 (Oct. 14, 2011), pp. 226–229. ISSN: 0036-8075. DOI: 10.1126/science.1210574.

[132] H. Mizuno et al. "Patchwork-Type Spontaneous Activity in Neonatal Barrel Cortex Layer 4 Transmitted via Thalamocortical Projections". In: *Cell Reports* 22.1 (Jan. 2, 2018), pp. 123–135. ISSN: 2211-1247. DOI: 10.1016/j.celrep.2017.12.012.

[133] L. Modol et al. "Assemblies of Perisomatic GABAergic Neurons in the Developing Barrel Cortex". In: *Neuron* 105.1 (Jan. 8, 2020), pp. 93–105. ISSN: 0896-6273. DOI: 10.1016/j.neuron.2019.10.007.

[134] E. J. Mohns and M. S. Blumberg. "Synchronous bursts of neuronal activity in the developing hippocampus: modulation by active sleep and association with emerging gamma and theta rhythms". In: *The Journal of Neuroscience: The Official Journal of the Society for Neuroscience* 28.40 (Oct. 1, 2008), pp. 10134–10144. ISSN: 1529-2401. DOI: 10.1523/JNEUROSCI.1967-08.2008.

[135] Z. Molnár, H. J. Luhmann, and P. O. Kanold. "Transient cortical circuits match spontaneous and sensory-driven activity during development". In: *Science (New York, N.Y.)* 370.6514 (Oct. 16, 2020). ISSN: 1095-9203. DOI: 10.1126/science.abb2153.

[136] Y. Murata and M. T. Colonnese. "GABAergic interneurons excite neonatal hippocampus in vivo". In: *Science Advances* 6.24 (June 12, 2020). ISSN: 2375-2548. DOI: 10.1126/sciadv.aba1430.

[137] J. C. Neill et al. "Animal models of cognitive dysfunction and negative symptoms of schizophrenia: focus on NMDA receptor antagonism". In: *Pharmacology & Therapeutics* 128.3 (Dec. 2010), pp. 419–432. ISSN: 1879-016X. DOI: 10.1016/j.pharmthera.2010.07.004.

[138] N. Niethard et al. "Cortical circuit activity underlying sleep slow oscillations and spindles". In: *Proceedings of the National Academy of Sciences of the United States of America* 115.39 (Sept. 25, 2018), E9220–E9229. ISSN: 0027-8424. DOI: 10.1073/pnas.1805517115.

[139] M. Niwa et al. "DISC1 a key molecular lead in psychiatry and neurodevelopment: No-More Disrupted-in-Schizophrenia 1". In: *Mol Psychiatry* 21.11 (Nov. 2016). Edition: 2016/10/21, pp. 1488–1489. ISSN: 1476-5578 (Electronic) 1359-4184 (Linking). DOI: 10.1038/mp.2016.154.

[140] M. Niwa et al. "Knockdown of DISC1 by in utero gene transfer disturbs postnatal dopaminergic maturation in the frontal cortex and leads to adult behavioral deficits". In: *Neuron* 65.4 (Feb. 25, 2010). Edition: 2010/03/02, pp. 480–9. ISSN: 1097-4199 (Electronic) 0896-6273 (Linking). DOI: 10.1016/j.neuron.2010.01.019.

[141] S. O'Mara. "The subiculum: what it does, what it might do, and what neuroanatomy has yet to tell us". In: *Journal of Anatomy* 207.3 (Sept. 2005), pp. 271–282. ISSN: 0021-8782. DOI: 10.1111/j.1469-7580.2005.00446.x.

[142] P.-K. O'Neill, J. A. Gordon, and T. Sigurdsson. "Theta Oscillations in the Medial Prefrontal Cortex Are Modulated by Spatial Working Memory and Synchronize with the Hippocampus through Its Ventral Subregion". In: *The Journal of Neuroscience* 33.35 (Aug. 28, 2013), pp. 14211–14224. ISSN: 0270-6474. DOI: 10.1523/JNEUROSCI.2378-13.2013.

[143] J. M. O'Toole et al. "Estimating functional brain maturity in very and extremely preterm neonates using automated analysis of the electroencephalogram". In: *Clinical Neurophysiology* 127.8 (Aug. 2016), pp. 2910–2918. ISSN: 1388-2457. DOI: 10.1016/j.clinph.2016.02.024.

[144] V. C. Oberlander et al. "Developmental dysfunction of prefrontal-hippocampal networks in mouse models of mental illness". In: *The European Journal of Neuroscience* 50.6 (Sept. 2019), pp. 3072–3084. ISSN: 1460-9568. DOI: 10.1111/ejn.14436.

[145] W. C. Oh et al. "De novo synaptogenesis induced by GABA in the developing mouse cortex". In: *Science (New York, N.Y.)* 353.6303 (Sept. 2, 2016), pp. 1037–1040. ISSN: 1095-9203. DOI: 10.1126/science.aaf5206.

[146] A. Omidvarnia et al. "Functional bimodality in the brain networks of preterm and term human newborns". In: *Cereb Cortex* 24.10 (Oct. 2014). Edition: 2013/05/08, pp. 2657–68. ISSN: 1460-2199 (Electronic) 1047-3211 (Linking). DOI: 10.1093/cercor/bht120.

[147] N. Padilla-Coreano et al. "Hippocampal-Prefrontal Theta Transmission Regulates Avoidance Behavior". In: *Neuron* 104.3 (Nov. 6, 2019), pp. 601–+. ISSN: 0896-6273. DOI: 10.1016/j.neuron.2019.08.006.

[148] N. Padilla-Coreano et al. "Direct Ventral Hippocampal-Prefrontal Input Is Required for Anxiety-Related Neural Activity and Behavior". In: *Neuron* 89.4 (Feb. 17, 2016), pp. 857–866. ISSN: 1097-4199. DOI: 10.1016/j.neuron.2016.01.011.

[149] A. Pan-Vazquez et al. "Activity-Dependent Plasticity of Axo-axonic Synapses at the Axon Initial Segment". In: *Neuron* 106.2 (Apr. 22, 2020), pp. 265–+. ISSN: 0896-6273. DOI: 10.1016/j.neuron.2020.01.037.

[150] S. P. Paşca. "Building three-dimensional human brain organoids". In: *Nature Neuroscience* (Mar. 28, 2018). ISSN: 1546-1726. DOI: 10.1038/s41593-018-0107-3.

[151] R. T. Peixoto et al. "Early hyperactivity and precocious maturation of corticostriatal circuits in Shank3B(-/-) mice". In: *Nature Neuroscience* 19.5 (May 2016), pp. 716–724. ISSN: 1097-6256. DOI: 10.1038/nn.4260.

[152] B. Pinto et al. "Rescuing Over-activated Microglia Restores Cognitive Performance in Juvenile Animals of the Dp(16) Mouse Model of Down Syndrome". In: *Neuron* 108.5 (Dec. 9, 2020), 887–904.e12. ISSN: 1097-4199. DOI: 10.1016/j.neuron.2020.09.010.

[153] F. Pizzo et al. "Deep brain activities can be detected with magnetoencephalography". In: *Nature Communications* 10.1 (Feb. 27, 2019), p. 971. ISSN: 2041-1723. DOI: 10.1038/s41467-019-08665-5.

[154] R. Place et al. "Bidirectional prefrontal-hippocampal interactions support context-guided memory". In: *Nature Neuroscience* 19.8 (Aug. 2016), pp. 992–994. ISSN: 1546-1726. DOI: 10.1038/nn.4327.

[155] J. Pratt et al. "Advancing schizophrenia drug discovery: optimizing rodent models to bridge the translational gap". In: *Nature Reviews. Drug Discovery* 11.7 (June 22, 2012), pp. 560–579. ISSN: 1474-1784. DOI: 10.1038/nrd3649.

[156] Y. Pu et al. "Non-invasive Investigation of Human Hippocampal Rhythms Using Magnetoencephalography: A Review". In: *Frontiers in Neuroscience* 12 (Apr. 26, 2018). ISSN: 1662-4548. DOI: 10.3389/fnins.2018.00273.

[157] P. L. Purdon et al. "Clinical Electroencephalography for Anesthesiologists Part I: Background and Basic Signatures". In: *Anesthesiology* 123.4 (Oct. 2015), pp. 937–960. ISSN: 0003-3022. DOI: 10.1097/Aln.0000000000000841.

[158] G. Quadrato et al. "Cell diversity and network dynamics in photosensitive human brain organoids". In: *Nature* 545.7652 (May 4, 2017), pp. 48–53. ISSN: 1476-4687. DOI: 10.1038/nature22047.

[159] A. Reiner. "Is prefrontal cortex found only in mammals?" In: *Trends in Neurosciences* 9 (Jan. 1, 1986). Publisher: Elsevier, pp. 298–300. ISSN: 0166-2236, 1878-108X. DOI: 10.1016/0166-2236(86)90086-X.

[160] R. Rey et al. "Overexpression of complement component C4 in the dorsolateral prefrontal cortex, parietal cortex, superior temporal gyrus and associative striatum of patients with schizophrenia". In: *Brain, Behavior, and Immunity* 90 (Nov. 2020), pp. 216–225. ISSN: 1090-2139. DOI: 10.1016/j.bbi.2020.08.019.

[161] M. Richter et al. "Altered TAOK2 activity causes autism-related neurodevelopmental and cognitive abnormalities through RhoA signaling". In: *Molecular Psychiatry* 24.9 (Sept. 2019), pp. 1329–1350. ISSN: 1359-4184. DOI: 10.1038/s41380-018-0025-5.

[162] G. Rinetti-Vargas et al. “Periadolescent Maturation of GABAergic Hyperpolarization at the Axon Initial Segment”. In: *Cell Reports* 20.1 (July 5, 2017), pp. 21–29. ISSN: 2211-1247. DOI: 10.1016/j.celrep.2017.06.030.

[163] A. C. Roberts and H. F. Clarke. “Why we need nonhuman primates to study the role of ventromedial prefrontal cortex in the regulation of threat- and reward-elicited responses”. In: *Proceedings of the National Academy of Sciences* 116.52 (Dec. 26, 2019). Publisher: National Academy of Sciences Section: Colloquium Paper, pp. 26297–26304. ISSN: 0027-8424, 1091-6490. DOI: 10.1073/pnas.1902288116.

[164] N. L. Rochefort et al. “Sparsification of neuronal activity in the visual cortex at eye-opening”. In: *Proceedings of the National Academy of Sciences of the United States of America* 106.35 (Sept. 1, 2009), pp. 15049–15054. ISSN: 0027-8424. DOI: 10.1073/pnas.0907660106.

[165] J. M. Rosin and D. M. Kurrasch. “In utero electroporation induces cell death and alters embryonic microglia morphology and expression signatures in the developing hypothalamus”. In: *Journal of Neuroinflammation* 15.1 (June 12, 2018), p. 181. ISSN: 1742-2094. DOI: 10.1186/s12974-018-1213-6.

[166] C. Rossant et al. “Spike sorting for large, dense electrode arrays”. In: *Nature Neuroscience* 19.4 (Apr. 2016), pp. 634–641. ISSN: 1546-1726. DOI: 10.1038/nn.4268.

[167] R. A. Samarasinghe et al. “Identification of neural oscillations and epileptiform changes in human brain organoids”. In: *bioRxiv* (Oct. 28, 2019). Publisher: Cold Spring Harbor Laboratory Section: New Results, p. 820183. DOI: 10.1101/820183.

[168] C. Schleifer et al. “Dissociable Disruptions in Thalamic and Hippocampal Resting-State Functional Connectivity in Youth with 22q11.2 Deletions”. In: *J Neurosci* 39.7 (Feb. 13, 2019). Edition: 2018/11/28, pp. 1301–1319. ISSN: 1529-2401 (Electronic) 0270-6474 (Linking). DOI: 10.1523/JNEUROSCI.3470-17.2018.

[169] A. Sekar et al. “Schizophrenia risk from complex variation of complement component 4”. In: *Nature* 530.7589 (Feb. 11, 2016), pp. 177–183. ISSN: 1476-4687. DOI: 10.1038/nature16549.

[170] C. M. Sellgren et al. “Increased synapse elimination by microglia in schizophrenia patient-derived models of synaptic pruning”. In: *Nature Neuroscience* 22.3 (Mar. 2019), pp. 374–385. ISSN: 1546-1726. DOI: 10.1038/s41593-018-0334-7.

[171] D. Senkowski and J. Gallinat. "Dysfunctional Prefrontal Gamma-Band Oscillations Reflect Working Memory and Other Cognitive Deficits in Schizophrenia". In: *Biological Psychiatry* 77.12 (June 15, 2015), pp. 1010–1019. ISSN: 0006-3223. DOI: 10.1016/j.biopsych.2015.02.034.

[172] T. Sharf et al. "Intrinsic network activity in human brain organoids". In: *bioRxiv* (Jan. 28, 2021). Publisher: Cold Spring Harbor Laboratory Section: New Results, p. 2021.01.28.428643. DOI: 10.1101/2021.01.28.428643.

[173] J. Shen and M. T. Colonnese. "Development of Activity in the Mouse Visual Cortex". In: *Journal of Neuroscience* 36.48 (Nov. 30, 2016), pp. 12259–12275. ISSN: 0270-6474. DOI: 10.1523/Jneurosci.1903-16.2016.

[174] A. G. Siapas, E. V. Lubenov, and M. A. Wilson. "Prefrontal phase locking to hippocampal theta oscillations". In: *Neuron* 46.1 (Apr. 7, 2005), pp. 141–151. ISSN: 0896-6273. DOI: 10.1016/j.neuron.2005.02.028.

[175] T. Sigurdsson et al. "Impaired hippocampal-prefrontal synchrony in a genetic mouse model of schizophrenia". In: *Nature* 464.7289 (Apr. 1, 2010), 763–U139. ISSN: 0028-0836. DOI: 10.1038/nature08855.

[176] S. E. P. Smith et al. "Maternal immune activation alters fetal brain development through interleukin-6". In: *The Journal of Neuroscience: The Official Journal of the Society for Neuroscience* 27.40 (Oct. 3, 2007), pp. 10695–10702. ISSN: 1529-2401. DOI: 10.1523/JNEUROSCI.2178-07.2007.

[177] T. Spellman et al. "Hippocampal-prefrontal input supports spatial encoding in working memory". In: *Nature* 522.7556 (June 18, 2015), pp. 309–+. ISSN: 0028-0836. DOI: 10.1038/nature14445.

[178] L. J. Stolwijk et al. "Effect of general anesthesia on neonatal aEEG - A cohort study of patients with non-cardiac congenital anomalies". In: *Plos One* 12.8 (Aug. 31, 2017). ISSN: 1932-6203. DOI: 10.1371/journal.pone.0183581.

[179] C. Summerfield and J. A. Mangels. "Coherent theta-band EEG activity predicts item-context binding during encoding". In: *NeuroImage* 24.3 (Feb. 1, 2005), pp. 692–703. ISSN: 1053-8119. DOI: 10.1016/j.neuroimage.2004.09.012.

[180] H. Supèr and E. Soriano. "The organization of the embryonic and early postnatal murine hippocampus. II. Development of entorhinal, commissural, and septal connections studied with the lipophilic tracer DiI". In: *The Journal of Comparative Neurology* 344.1 (June 1, 1994), pp. 101–120. ISSN: 0021-9967. DOI: 10.1002/cne.903440108.

[181] M. Tamura et al. "Developmental Inhibition of Gsk3 Rescues Behavioral and Neurophysiological Deficits in a Mouse Model of Schizophrenia Predisposition". In: *Neuron* 89.5 (Mar. 2, 2016), pp. 1100–1109. ISSN: 0896-6273. DOI: 10.1016/j.neuron.2016.01.025.

[182] A. Tokariev et al. "Preterm Birth Changes Networks of Newborn Cortical Activity". In: *Cereb Cortex* 29.2 (Feb. 1, 2019). Edition: 2018/10/16, pp. 814–826. ISSN: 1460-2199 (Electronic) 1047-3211 (Linking). DOI: 10.1093/cercor/bhy012.

[183] M. Tolonen et al. "Development of the spontaneous activity transients and ongoing cortical activity in human preterm babies". In: *Neuroscience* 145.3 (Mar. 30, 2007), pp. 997–1006. ISSN: 0306-4522. DOI: 10.1016/j.neuroscience.2006.12.070.

[184] R. Tremblay, S. Lee, and B. Rudy. "GABAergic Interneurons in the Neocortex: From Cellular Properties to Circuits". In: *Neuron* 91.2 (July 20, 2016), pp. 260–292. ISSN: 1097-4199. DOI: 10.1016/j.neuron.2016.06.033.

[185] C. A. Trujillo et al. "Complex Oscillatory Waves Emerging from Cortical Organoids Model Early Human Brain Network Development". In: *Cell Stem Cell* 25.4 (Oct. 3, 2019), pp. 558–569. ISSN: 1934-5909. DOI: 10.1016/j.stem.2019.08.002.

[186] S. N. Tuncdemir et al. "Early Somatostatin Interneuron Connectivity Mediates the Maturation of Deep Layer Cortical Circuits". In: *Neuron* 89.3 (Feb. 3, 2016), pp. 521–535. ISSN: 0896-6273. DOI: 10.1016/j.neuron.2015.11.020.

[187] P. J. Uhlhaas and W. Singer. "Oscillations and Neuronal Dynamics in Schizophrenia: The Search for Basic Symptoms and Translational Opportunities". In: *Biological Psychiatry* 77.12 (June 15, 2015), pp. 1001–1009. ISSN: 0006-3223. DOI: 10.1016/j.biopsych.2014.11.019.

[188] C. Vagnoni et al. "Ontogeny of the VIP+ interneuron sensory-motor circuit prior to active whisking". In: *bioRxiv* (July 2, 2020). Publisher: Cold Spring Harbor Laboratory Section: New Results, p. 2020.07.01.182238. DOI: 10.1101/2020.07.01.182238.

[189] G. Valeeva et al. "Bilateral Synchronization of Hippocampal Early Sharp Waves in Neonatal Rats". In: *Frontiers in Cellular Neuroscience* 13 (Feb. 7, 2019). ISSN: 1662-5102. DOI: 10.3389/fncel.2019.00029.

[190] G. Valeeva et al. "Early Sharp Wave Synchronization along the Septo-Temporal Axis of the Neonatal Rat Hippocampus". In: *Neuroscience and Behavioral Physiology* 50.9 (Nov. 2020), pp. 1195–1202. ISSN: 0097-0549, 1573-899X. DOI: 10.1007/s11055-020-01021-x.

[191] G. Valeeva et al. "Emergence of Coordinated Activity in the Developing Entorhinal-Hippocampal Network". In: *Cereb Cortex* 29.2 (Feb. 1, 2019). Edition: 2018/12/12, pp. 906–920. ISSN: 1460-2199 (Electronic) 1047-3211 (Linking). DOI: 10.1093/cercor/bhy309.

[192] G. Valeeva et al. "An Optogenetic Approach for Investigation of Excitatory and Inhibitory Network GABA Actions in Mice Expressing Channelrhodopsin-2 in GABAergic Neurons". In: *The Journal of Neuroscience: The Official Journal of the Society for Neuroscience* 36.22 (June 1, 2016), pp. 5961–5973. ISSN: 1529-2401. DOI: 10.1523/JNEUROSCI.3482-15.2016.

[193] S. Vanhatalo and K. Kaila. "Development of neonatal EEG activity: From phenomenology to physiology". In: *Seminars in Fetal & Neonatal Medicine* 11.6 (Dec. 2006), pp. 471–478. ISSN: 1744-165x. DOI: 10.1016/j.siny.2006.07.008.

[194] S. Vanhatalo et al. "Slow endogenous activity transients and developmental expression of K+-Cl- cotransporter 2 in the immature human cortex". In: *European Journal of Neuroscience* 22.11 (Dec. 2005), pp. 2799–2804. ISSN: 0953-816x. DOI: 10.1111/j.1460-9568.2005.04459.x.

[195] J. Veit et al. "Cortical gamma band synchronization through somatostatin interneurons". In: *Nature Neuroscience* 20.7 (July 2017), pp. 951–959. ISSN: 1546-1726. DOI: 10.1038/nn.4562.

[196] M. Vinck et al. "The pairwise phase consistency: a bias-free measure of rhythmic neuronal synchronization". In: *NeuroImage* 51.1 (May 15, 2010), pp. 112–122. ISSN: 1095-9572. DOI: 10.1016/j.neuroimage.2010.01.073.

[197] A. H. C. Wong and S. A. Josselyn. "Caution When Diagnosing Your Mouse With Schizophrenia: The Use and Misuse of Model Animals for Understanding Psychiatric Disorders". In: *Biological Psychiatry* 79.1 (Jan. 1, 2016), pp. 32–38. ISSN: 1873-2402. DOI: 10.1016/j.biopsych.2015.04.023.

[198] X. X. Xu et al. "Transient Knock-Down of Prefrontal DISC1 in Immune-Challenged Mice Causes Abnormal Long-Range Coupling and Cognitive Dysfunction throughout Development". In: *Journal of Neuroscience* 39.7 (Feb. 13, 2019), pp. 1222–1235. ISSN: 0270-6474. DOI: 10.1523/Jneurosci.2170-18.2018.

[199] X. Xu, L. Song, and I. L. Hanganu-Opatz. "Knock-Down of Hippocampal DISC1 in Immune-Challenged Mice Impairs the Prefrontal-Hippocampal Coupling and the Cognitive Performance Throughout Development". In: *Cerebral Cortex (New York, N.Y.: 1991)* 31.2 (Jan. 5, 2021), pp. 1240–1258. ISSN: 1460-2199. DOI: 10.1093/cercor/bhaa291.

[200] J. W. Yang et al. "Thalamic Network Oscillations Synchronize Ontogenetic Columns in the Newborn Rat Barrel Cortex". In: *Cerebral Cortex* 23.6 (June 2013), pp. 1299–1316. ISSN: 1047-3211. DOI: 10.1093/cercor/bhs103.

[201] W. Yang et al. "Anesthetics fragment hippocampal network activity, alter spine dynamics and affect memory consolidation". In: *bioRxiv* (Jan. 15, 2021). Publisher: Cold Spring Harbor Laboratory Section: New Results, p. 2020.06.05.135905. DOI: 10.1101/2020.06.05.135905.

[202] M. Yilmaz et al. "Overexpression of schizophrenia susceptibility factor human complement C4A promotes excessive synaptic loss and behavioral changes in mice". In: *Nature Neuroscience* 24.2 (Feb. 2021), pp. 214–224. ISSN: 1546-1726. DOI: 10.1038/s41593-020-00763-8.

[203] V. Zerbi et al. "Dysfunctional Autism Risk Genes Cause Circuit-Specific Connectivity Deficits With Distinct Developmental Trajectories". In: *Cerebral Cortex* 28.7 (July 2018), pp. 2495–2506. ISSN: 1047-3211. DOI: 10.1093/cercor/bhy046.

6 | Acknowledgments

This work would have never been possible without the support of many people.
I would like to express my deepest gratitude to my supervisor Ileana Hanganu-Opatz for her continuous supervision and encouragement, for fostering an environment that has profoundly shaped my scientific thinking, for her availability, and for allowing me the freedom to pursue my own interests.
I am particularly thankful to Sebastian Bitzenhofer, Joachim Ahlbeck and Christoph Lindemann, for tutoring me in my early days as PhD student. I would have been lost without their help.
I would like to thank all the members of the Hanganu-Opatz lab, for the animated scientific discussions and the precious critical feedback. In particular, I would like to thank Johanna Kostka, Marilena Hnida, Jastyn Pöpplau, Steven Schepanski, Lingzhen Song and Xiaxia Xu with whom I have shared many memorable moments inside and outside of the lab.
I would like to thank Peggy Putthoff, Annette Marquard and Achim Dahlmann for their patient and expert technical assistance.
Science is a cooperative effort. As such, I was lucky to have collaborated with several great scientists throughout my time as a PhD student. I thank them for providing a different point of view, sharing their knowledge, ideas and criticisms with me.
One of my favorite aspects of my life as a PhD students has been the convivial atmosphere of ZMNH. Through social events, courses, talks and seminars, I have met

countless friends that have brought me great joy. I am thankful to the organizers of these events, and everyone that took part.
I want to thank my family and my friends, for their unconditional support, for making me the person I am, for reminding me what really matters, and for brightening every day of my life. Special thanks to Lukas Neugebauer for translating the "General Summary" into German.
Finally, I want to thank Noemi. None of this would mean anything without her.

7 | Curriculum Vitae

Lebenslauf aus datenschutzrechtlichen Gründen nicht enthalten

Publications

Yang W*, **Chini M***, Pöpplau JA, Formozov A, Dieter A, Piechocinski P, Rais C, Morellini F, Sporns O, Hanganu-Opatz IL and Wiegert SJ (2021) Anesthetics uniquely decorrelate hippocampal network activity, alter spine dynamics and affect memory consolidation. *In press, PLOS Biology.*

Bitzenhofer SH*, Pöpplau JA*, **Chini M**, Marquardt A and Hanganu-Opatz IL. (2021) Transient developmental increase of prefrontal activity alters network maturation and causes cognitive dysfunction in adult mice. *In press, Neuron.*

Chini M and Hanganu-Opatz IL. (2020) Prefrontal Cortex Development in Health and Disease: Lessons from Rodents and Humans. *Trends in Neurosciences.*

Chini M, Pöpplau JA, Lindemann C, Carol-Perdiguer L, Hnida M, Oberländer V, Xu X, Ahlbeck J, Bitzenhofer SH, Mulert C and Hanganu-Opatz IL. (2020) Resolving and Rescuing Developmental Miswiring in a Mouse Model of Cognitive Impairment. *Neuron.*

Chini M, Gretenkord S, Kostka JK, Pöpplau JA, Cornelissen L, Berde CB, Hanganu-Opatz IL* and Bitzenhofer SH* (2019) Neural Correlates of Anesthesia in Newborn Mice and Humans. *Frontiers in neural circuits.*

Xu X, **Chini M**, Bitzenhofer SH and Hanganu-Opatz IL. (2019) Transient Knock-Down of Prefrontal DISC1 in Immune-Challenged Mice Causes Abnormal Long-Range Coupling and Cognitive Dysfunction throughout Development. *Journal of Neuroscience.*

Oberländer V, Xu X, **Chini M** and Hanganu-Opatz IL. (2019) Developmental dysfunction of prefrontal–hippocampal networks in mouse models of mental illness. *European Journal of Neuroscience.*

Ahlbeck J, Song L, **Chini M**, Bitzenhofer SH, Hanganu-Opatz IL. (2018) Glutamatergic drive along the septo-temporal axis of hippocampus boosts prelimbic oscillations in the neonatal mouse. *eLife.*

Bellesi M, De vivo L, **Chini M**, Gilli F, Tononi G and Cirelli C. (2017) Sleep Loss Promotes Astrocytic Phagocytosis and Microglial Activation in Mouse Cerebral Cortex. *Journal of Neuroscience.*

Bellesi M, Bushey D, **Chini M**, Tononi G and Cirelli C. (2016) Contribution of sleep to the repair of neuronal DNA double-strand breaks: evidence from flies and mice. *Scientific Reports*.

8 | Eidesstattliche Versicherung

Ich versichere ausdrücklich, dass ich die Arbeit selbständig und ohne fremde Hilfe verfasst, andere als die von mir angegebenen Quellen und Hilfsmittel nicht benutzt und die aus den benutzten Werken wörtlich oder inhaltlich entnommenen Stellen einzeln nach Ausgabe (Auflage und Jahr des Erscheinens), Band und Seite des benutzten Werkes kenntlich gemacht habe. Ferner versichere ich, dass ich die Dissertation bisher nicht einem Fachvertreter an einer anderen Hochschule zur Überprüfung vorgelegt oder mich anderweitig um Zulassung zur Promotion beworben habe. Ich erkläre mich einverstanden, dass meine Dissertation vom Dekanat der Medizinischen Fakultät mit einer gängigen Software zur Erkennung von Plagiaten überprüft werden kann.